Fluid Mechanics and Thermodynamics of Turbomachinery

Seventh Edition

Fluid Mechanics and Thermodynamics of Turbomachinery

Seventh Edition

S. L. Dixon, B. Eng., Ph.D.
Honorary Senior Fellow,
Department of Engineering,
University of Liverpool, UK

C. A. Hall, Ph.D.
University Senior Lecturer in Turbomachinery,
University of Cambridge, UK

AMSTERDAM • BOSTON • HEIDELBERG • LONDON • NEW YORK • OXFORD • PARIS
SAN DIEGO • SAN FRANCISCO • SINGAPORE • SYDNEY • TOKYO

Butterworth-Heinemann is an imprint of Elsevier

Butterworth-Heinemann is an imprint of Elsevier
The Boulevard, Langford Lane, Kidlington, Oxford, OX5 1GB, UK
225 Wyman Street, Waltham, MA 02451, USA

First published by Pergamon Press Ltd. 1966
Second edition 1975
Third edition 1978
Reprinted 1979, 1982 (twice), 1984, 1986, 1989, 1992, 1995
Fourth edition 1998
Fifth edition 2005 (twice)
Sixth edition 2010
Seventh edition 2014

Notices

Knowledge and best practice in this field are constantly changing. As new research and experience broaden our understanding, changes in research methods, professional practices, or medical treatment may become necessary.

Practitioners and researchers must always rely on their own experience and knowledge in evaluating and using any information, methods, compounds, or experiments described herein. In using such information or methods they should be mindful of their own safety and the safety of others, including parties for whom they have a professional responsibility.

To the fullest extent of the law, neither the Publisher nor the authors, contributors, or editors, assume any liability for any injury and/or damage to persons or property as a matter of products liability, negligence or otherwise, or from any use or operation of any methods, products, instructions, or ideas contained in the material herein.

Library of Congress Cataloging-in-Publication Data
A catalog record for this book is available from the Library of congress

British Library Cataloguing-in-Publication Data
A catalogue record for this book is available from the British Library

ISBN: 978-0-12-415954-9

Typeset by MPS Limited, Chennai, India
www.adi-mps.com

Printed in the US

14 15 16 17 18 10 9 8 7 6 5 4 3 2 1

Dedication

In memory of Avril (22 years) and baby Paul.

Preface to the Seventh Edition

This book was originally conceived as a text for students in their final year reading for an honors degree in engineering that included turbomachinery as a main subject. It was also found to be a useful support for students embarking on postgraduate courses at masters level. The book was written for engineers rather than for mathematicians, although some knowledge of mathematics will prove most useful. Also, it is assumed from the start that readers will have completed preliminary courses in fluid mechanics. The stress is placed on the actual physics of the flows and the use of specialized mathematical methods is kept to a minimum.

Compared to the sixth edition, this new edition has had a large number of changes made in terms of presentation of ideas, new material, and additional examples. In Chapter 1, following the definition of a turbomachine, the fundamental laws of flow continuity, the energy and entropy equations are introduced as well as the all-important Euler work equation. In addition, the properties of working fluids other than perfect gases are covered and a steam chart is included in the appendices. In Chapter 2, the main emphasis is given to the application of the "similarity laws," to dimensional analysis of all types of turbomachine and their performance characteristics. Additional types of turbomachine are considered and examples of high-speed characteristics are presented. The important ideas of specific speed and specific diameter emerge from these concepts and their application is illustrated in the Cordier Diagram, which shows how to select the machine that will give the highest efficiency for a given duty. Also, in this chapter the basics of cavitation are examined for pumps and hydraulic turbines.

The measurement and understanding of cascade aerodynamics is the basis of modern axial turbomachine design and analysis. In Chapter 3, the subject of cascade aerodynamics is presented in preparation for the following chapters on axial turbines and compressors. This chapter was completely reorganized in the previous edition. In this edition, further emphasis is given to compressible flow and on understanding the physics that constrain the design of turbomachine blades and determine cascade performance. In addition, a completely new section on computational methods for cascade design and analysis has been added, which presents the details of different numerical approaches and their capabilities.

Chapters 4 and 5 cover axial turbines and axial compressors, respectively. In Chapter 4, new material has been added to give better coverage of steam turbines. Sections explaining the numerous sources of loss within a turbine have been added and the relationships between loss and efficiency are further detailed. The examples and end-of-chapter problems have also been updated. Within this chapter, the merits of different styles of turbine design are considered including the implications for mechanical design such as centrifugal stress levels and cooling in high-speed and high temperature turbines. Through the use of some relatively simple correlations, the trends in turbine efficiency with the main turbine parameters are presented.

In Chapter 5, the analysis and preliminary design of all types of axial compressors are covered. Several new figures, examples, and end-of-chapter problems have been added. There is new coverage of compressor loss sources and, in particular, shock wave losses within high-speed rotors are explored in detail. New material on off-design operation and stage matching in multistage compressors has been added, which enables the performance of large compressors to be quantified.

Several new examples and end-of-chapter problems have also been added that reflect the new material on design, off-design operation, and compressible flow analysis of high-speed compressors.

Chapter 6 covers three-dimensional effects in axial turbomachinery and it possibly has the most new features relative to the sixth edition. There are extensive new sections on three-dimensional flows, three-dimensional design features, and three-dimensional computational methods. The section on through-flow methods has also been reworked and updated. Numerous explanatory figures have been added and there are new worked examples on vortex design and additional end-of-chapter problems.

Radial turbomachinery remains hugely important for a vast number of applications, such as turbocharging for internal combustion engines, oil and gas transportation, and air liquefaction. As jet engine cores become more compact there is also the possibility of radial machines finding new uses within aerospace applications. The analysis and design principles for centrifugal compressors and radial inflow turbines are covered in Chapters 7 and 8. Improvements have been made relative to the fifth edition, including new examples, corrections to the material, and reorganization of some sections.

Renewable energy topics were first added to the fourth edition of this book by way of the Wells turbine and a new chapter on hydraulic turbines. In the fifth edition, a new chapter on wind turbines was added. Both of these chapters have been retained in this edition as the world remains increasingly concerned with the very major issues surrounding the use of various forms of energy. There is continuous pressure to obtain more power from renewable energy sources and hydroelectricity and wind power have a significant role to play. In this edition, hydraulic turbines are covered in Chapter 9, which includes coverage of the Wells turbine, a new section on tidal power generators, and several new example problems. Chapter 10 covers the essential fluid mechanics of wind turbines, together with numerous worked examples at various levels of difficulty. In this edition, the range of coverage of the wind itself has been increased in terms of probability theory. This allows for a better understanding of how much energy a given size of wind turbine can capture from a normally gusting wind. Instantaneous measurements of wind speeds made with anemometers are used to determine average velocities and the average wind power. Important aspects concerning the criteria of blade selection and blade manufacture, control methods for regulating power output and rotor speed, and performance testing are touched upon. Also included are some very brief notes concerning public and environmental issues, which are becoming increasingly important as they, ultimately, can affect the development of wind turbines.

To develop the understanding of students as they progress through the book, the expounded theories are illustrated by a selection of worked examples. As well as these examples, each chapter contains problems for solution, some easy, some hard. See what you make of them—answers are provided in Appendix F!

Acknowledgments

The authors are indebted to a large number of people in publishing, teaching, research, and manufacturing organizations for their help and support in the preparation of this volume. In particular, thanks are given for the kind permission to use photographs and line diagrams appearing in this edition, as listed below:

ABB (Brown Boveri, Ltd.)
American Wind Energy Association
Bergey Windpower Company
Dyson Ltd.
Elsevier Science
Hodder Education
Institution of Mechanical Engineers
Kvaener Energy, Norway
Marine Current Turbines Ltd., UK
National Aeronautics and Space Administration (NASA)
NREL
Rolls-Royce plc
The Royal Aeronautical Society and its Aeronautical Journal
Siemens (Steam Division)
Sirona Dental
Sulzer Hydro of Zurich
Sussex Steam Co., UK
US Department of Energy
Voith Hydro Inc., Pennsylvania
The Whittle Laboratory, Cambridge, UK

I would like to give my belated thanks to the late Professor W.J. Kearton of the University of Liverpool and his influential book *Steam Turbine Theory and Practice*, who spent a great deal of time and effort teaching us about engineering and instilled in me an increasing and life-long interest in turbomachinery. This would not have been possible without the University of Liverpool's award of the W.R. Pickup Foundation Scholarship supporting me as a university student, opening doors of opportunity that changed my life.

Also, I give my most grateful thanks to Professor (now Sir) John H. Horlock for nurturing my interest in the wealth of mysteries concerning the flows through compressors and turbine blades during his tenure of the Harrison Chair of Mechanical Engineering at the University of Liverpool. At an early stage of the sixth edition some deep and helpful discussions of possible additions to the new edition took place with Emeritus Professor John P. Gostelow (a former undergraduate student of mine). There are also many members of staff in the Department of Mechanical Engineering during my career who helped and instructed me for which I am grateful.

Also, I am most grateful for the help given to me by the staff of the Harold Cohen Library, University of Liverpool, in my frequent searches for new material needed for the seventh edition.

Last, but by no means least, to my wife Rosaleen, whose patient support and occasional suggestions enabled me to find the energy to complete this new edition.

S. Larry Dixon

I would like to thank the University of Cambridge, Department of Engineering, where I have been a student, researcher, and now lecturer. Many people there have contributed to my development as an academic and engineer. Of particular importance is Professor John Young who initiated my enthusiasm for thermofluids through his excellent teaching of the subject. I am also very grateful to Rolls-Royce plc, where I worked for several years. I learned a huge amount about compressor and turbine aerodynamics from my colleagues there and they continue to support me in my research activities.

Almost all the contributions I made to this new edition were written in my office at King's College, Cambridge, during a sabbatical. As well as providing accommodation and food, King's is full of exceptional and friendly people who I would like to thank for their companionship and help during the preparation of this book.

As a lecturer in turbomachinery, there is no better place to be based than the Whittle Laboratory. I would like to thank the members of the laboratory, past and present, for their support and all they have taught me. I would like to make a special mention of Dr. Tom Hynes, my Ph.D. supervisor, for encouraging my return to academia from industry and for handing over the teaching of a turbomachinery course to me when I started as a lecturer. During my time in the laboratory, Dr. Rob Miller has been a great friend and colleague and I would like to thank him for the sound advice he has given on many technical, professional, and personal matters. Several laboratory members have also helped in the preparation of suitable figures for this book. These include Dr. Graham Pullan, Dr. Liping Xu, Dr Martin Goodhand, Vicente Jerez-Fidalgo, Ewan Gunn, and Peter O'Brien.

Finally, special personal thanks go to my parents, Hazel and Alan, for all they have done for me. I would like to dedicate my work on this book to my wife Gisella and my son Sebastian.

Cesare A. Hall

List of Symbols

A	area
a	sonic velocity
$\overline{a}, a'$	axial-flow induction factor, tangential flow induction factor
b	axial chord length, passage width, maximum camber
C_c, C_f	chordwise and tangential force coefficients
C_L, C_D	lift and drag coefficients
CF	capacity factor ($= \overline{P}_W/P_R$)
C_p	specific heat at constant pressure, pressure coefficient, pressure rise coefficient
C_v	specific heat at constant volume
C_X, C_Y	axial and tangential force coefficients
c	absolute velocity
c_o	spouting velocity
d	internal diameter of pipe
D	drag force, diameter
D_h	hydraulic mean diameter
D_s	specific diameter
DF	diffusion factor
E, e	energy, specific energy
F	force, Prandtl correction factor
F_c	centrifugal force in blade
f	friction factor, frequency, acceleration
g	gravitational acceleration
H	blade height, head
H_E	effective head
H_f	head loss due to friction
H_G	gross head
H_S	net positive suction head (NPSH)
h	specific enthalpy
I	rothalpy
i	incidence angle
J	wind turbine tip−speed ratio
j	wind turbine local blade-speed ratio
K, k	constants
L	lift force, length of diffuser wall
l	blade chord length, pipe length
M	Mach number
m	mass, molecular mass
N	rotational speed, axial length of diffuser
n	number of stages, polytropic index
o	throat width
P	power

P_R	rated power of wind turbine
$\overline{P}_W$	average wind turbine power
p	pressure
p_a	atmospheric pressure
p_v	vapor pressure
q	quality of steam
Q	heat transfer, volume flow rate
R	reaction, specific gas constant, diffuser radius, stream tube radius
Re	Reynolds number
R_H	reheat factor
R_o	universal gas constant
r	radius
S	entropy, power ratio
s	blade pitch, specific entropy
T	temperature
t	time, thickness
U	blade speed, internal energy
u	specific internal energy
V, v	volume, specific volume
W	work transfer, diffuser width
ΔW	specific work transfer
W_x	shaft work
w	relative velocity
X	axial force
x, y	dryness fraction, wetness fraction
x, y, z	Cartesian coordinate directions
Y	tangential force
Y_p	stagnation pressure loss coefficient
Z	number of blades, Zweifel blade loading coefficient
α	absolute flow angle
β	relative flow angle, pitch angle of blade
Γ	circulation
γ	ratio of specific heats
δ	deviation angle
ε	fluid deflection angle, cooling effectiveness, drag−lift ratio in wind turbines
ζ	enthalpy loss coefficient, incompressible stagnation pressure loss coefficient
η	efficiency
θ	blade camber angle, wake momentum thickness, diffuser half angle
κ	angle subtended by log spiral vane
λ	profile loss coefficient, blade loading coefficient, incidence factor
μ	dynamic viscosity
ν	kinematic viscosity, hub−tip ratio, velocity ratio
ξ	blade stagger angle
ρ	density

σ	slip factor, solidity, Thoma coefficient
σ_b	blade cavitation coefficient
σ_c	centrifugal stress
τ	torque
ϕ	flow coefficient, velocity ratio, wind turbine impingement angle
ψ	stage loading coefficient
Ω	speed of rotation
Ω_S	specific speed
Ω_{SP}	power specific speed
Ω_{SS}	suction specific speed
ω	vorticity

Subscripts

0	stagnation property
b	blade
c	compressor, centrifugal, critical
cr	critical value
d	design
D	diffuser
e	exit
h	hydraulic, hub
i	inlet, impeller
id	ideal
m	mean, meridional, mechanical, material
max	maximum
min	minimum
N	nozzle
n	normal component
o	overall
opt	optimum
p	polytropic, pump, constant pressure
R	reversible process, rotor
r	radial
ref	reference value
rel	relative
s	isentropic, shroud, stall condition
ss	stage isentropic
t	turbine, tip, transverse
ts	total-to-static
tt	total-to-total

$\mathbf{v}$	velocity
x, y, z	Cartesian coordinate components
θ	tangential

Superscripts

$\dot{}$	time rate of change
$\bar{}$	average
$'$	blade angle (as distinct from flow angle)
*	nominal condition, throat condition
$\hat{}$	nondimensionalized quantity

CHAPTER

Introduction: Basic Principles

1

Take your choice of those that can best aid your action.
Shakespeare, *Coriolanus*

1.1 Definition of a turbomachine

We classify as turbomachines all those devices in which energy is transferred either to, or from, a continuously flowing fluid by the *dynamic action* of one or more moving blade rows. The word *turbo* or *turbinis* is of Latin origin and implies that which spins or whirls around. Essentially, a rotating blade row, a *rotor* or an *impeller* changes the stagnation enthalpy of the fluid moving through it by doing either positive or negative work, depending upon the effect required of the machine. These enthalpy changes are intimately linked with the pressure changes occurring simultaneously in the fluid.

Two main categories of turbomachine are identified: first, those that *absorb* power to increase the fluid pressure or head (ducted and unducted fans, compressors, and pumps); second, those that *produce* power by expanding fluid to a lower pressure or head (wind, hydraulic, steam, and gas turbines). Figure 1.1 shows, in a simple diagrammatic form, a selection of the many varieties of turbomachines encountered in practice. The reason that so many different types of either pump (compressor) or turbine are in use is because of the almost infinite range of service requirements. Generally speaking, for a given set of operating requirements one type of pump or turbine is best suited to provide optimum conditions of operation.

Turbomachines are further categorized according to the nature of the flow path through the passages of the rotor. When the path of the *through-flow* is wholly or mainly parallel to the axis of rotation, the device is termed an *axial flow turbomachine* (e.g., Figures 1.1(a) and (e)). When the path of the *through-flow* is wholly or mainly in a plane perpendicular to the rotation axis, the device is termed a *radial flow turbomachine* (e.g., Figure 1.1(c)). More detailed sketches of radial flow machines are given in Figures 7.3, 7.4, 8.2, and 8.3. *Mixed flow turbomachines* are widely used. The term *mixed flow* in this context refers to the direction of the through-flow at the rotor outlet when both radial and axial velocity components are present in significant amounts. Figure 1.1(b) shows a mixed flow pump and Figure 1.1(d) a mixed flow hydraulic turbine.

One further category should be mentioned. All turbomachines can be classified as either *impulse* or *reaction* machines according to whether pressure changes are absent or present, respectively, in the flow through the rotor. In an impulse machine all the pressure change takes place in one or more nozzles, the fluid being directed onto the rotor. The Pelton wheel, Figure 1.1(f), is an example of an impulse turbine.

Fluid Mechanics and Thermodynamics of Turbomachinery. DOI: http://dx.doi.org/10.1016/B978-0-12-415954-9.00001-2

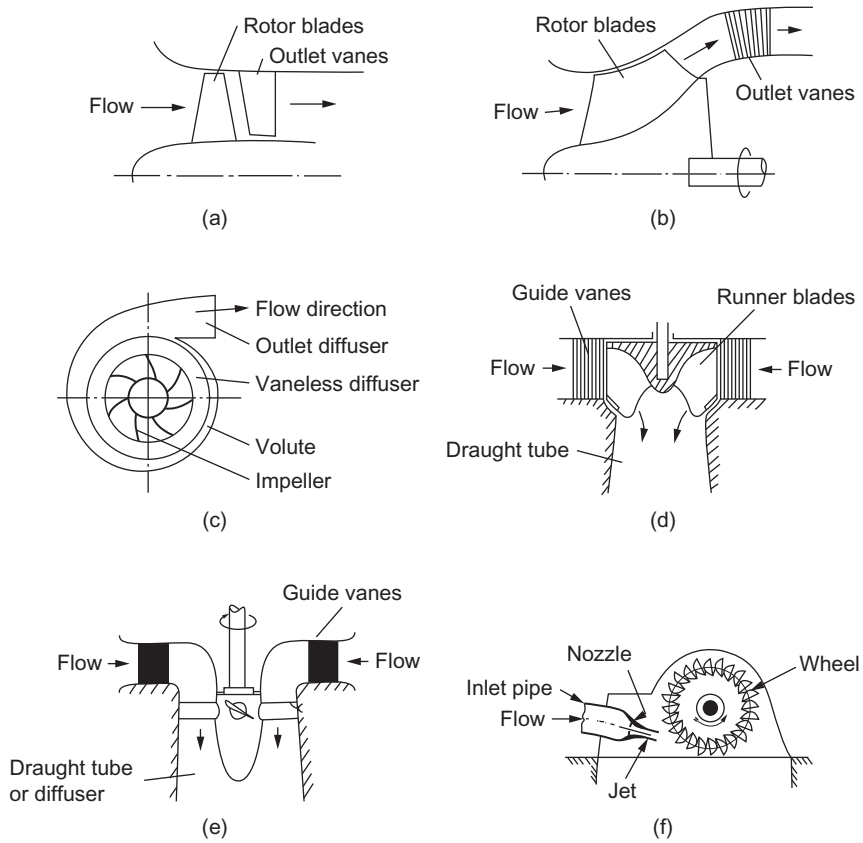

FIGURE 1.1

Examples of turbomachines. (a) Single stage axial flow compressor or pump, (b) mixed flow pump, (c) centrifugal compressor or pump, (d) Francis turbine (mixed flow type), (e) Kaplan turbine, and (f) Pelton wheel.

The main purpose of this book is to examine, through the laws of fluid mechanics and thermodynamics, the means by which the energy transfer is achieved in the chief types of turbomachines, together with the differing behavior of individual types in operation. Methods of analyzing the flow processes differ depending upon the geometrical configuration of the machine, whether the fluid can be regarded as incompressible or not, and whether the machine absorbs or produces work. As far as possible, a unified treatment is adopted so that machines having similar configurations and function are considered together.

1.2 Coordinate system

Turbomachines consist of rotating and stationary blades arranged around a common axis, which means that they tend to have some form of cylindrical shape. It is therefore natural to use a

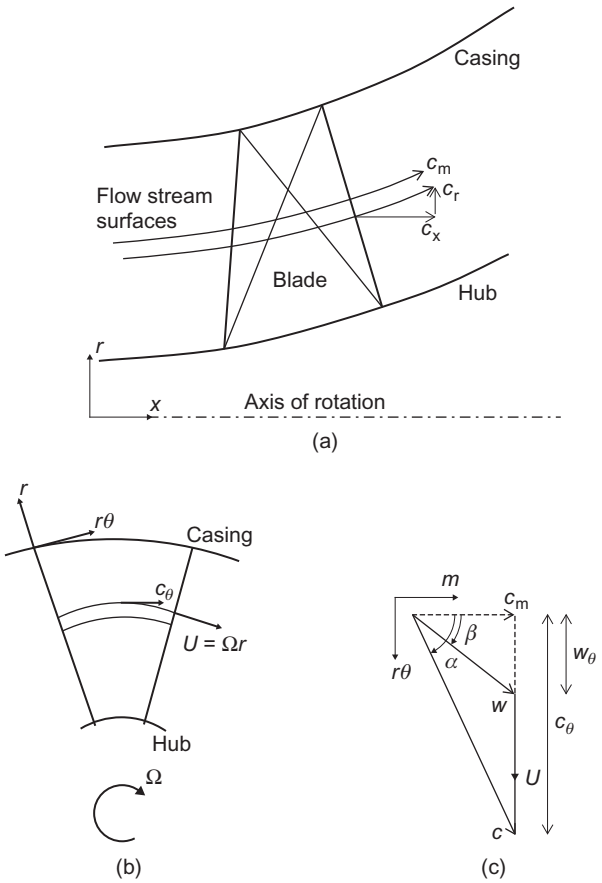

FIGURE 1.2

The coordinate system and flow velocities within a turbomachine. (a) Meridional or side view, (b) view along the axis, and (c) view looking down onto a stream surface.

cylindrical polar coordinate system aligned with the axis of rotation for their description and analysis. This coordinate system is pictured in Figure 1.2. The three axes are referred to as axial x, radial r, and tangential (or circumferential) $r\theta$.

In general, the flow in a turbomachine has components of velocity along all three axes, which vary in all directions. However, to simplify the analysis it is usually assumed that the flow does not vary in the tangential direction. In this case, the flow moves through the machine on *axi-symmetric stream surfaces*, as drawn on Figure 1.2(a). The component of velocity along an axi-symmetric stream surface is called the *meridional* velocity,

$$c_m = \sqrt{c_x^2 + c_r^2} \tag{1.1}$$

In purely axial flow machines the radius of the flow path is constant and, therefore, referring to Figure 1.2(c) the radial flow velocity will be zero and $c_m = c_x$. Similarly, in purely radial flow machines the axial flow velocity will be zero and $c_m = c_r$. Examples of both of these types of machines can be found in Figure 1.1.

The total flow velocity is made up of the meridional and tangential components and can be written

$$c = \sqrt{c_x^2 + c_r^2 + c_\theta^2} = \sqrt{c_m^2 + c_\theta^2} \tag{1.2}$$

The swirl, or tangential, angle is the angle between the flow direction and the meridional direction:

$$\alpha = \tan^{-1}(c_\theta / c_m) \tag{1.3}$$

Relative velocities

The analysis of the flow-field within the rotating blades of a turbomachine is performed in a frame of reference that is stationary relative to the blades. In this frame of reference the flow appears as *steady*, whereas in the absolute frame of reference it would be *unsteady*. This makes any calculations significantly easier, and therefore the use of relative velocities and relative flow quantities is fundamental to the study of turbomachinery.

The relative velocity w is the vector subtraction of the local velocity of the blade U from the absolute velocity of the flow c, as shown in Figure 1.2(c). The blade has velocity only in the tangential direction, and therefore the components of the relative velocity can be written as

$$w_\theta = c_\theta - U, w_x = c_x, w_r = c_r \tag{1.4}$$

The relative flow angle is the angle between the relative flow direction and the meridional direction:

$$\beta = \tan^{-1}(w_\theta / c_m) \tag{1.5}$$

By combining Eqs. (1.3), (1.4), and (1.5) a relationship between the relative and absolute flow angles can be found:

$$\tan\beta = \tan\alpha - U/c_m \tag{1.6}$$

Sign convention

Equations (1.4) and (1.6) suggest that negative values of flow angles and velocities are possible. In many turbomachinery courses and texts, the convention is to use positive values for tangential velocities that are in the direction of rotation (as they are in Figure 1.2(b) and (c)), and negative values for tangential velocities that are opposite to the direction of rotation. The convention adopted in this book is to ensure that the correct vector relationship between the relative and absolute velocities is applied using only positive values for flow velocities and flow angles.

Velocity diagrams for an axial flow compressor stage

A typical stage of an axial flow compressor is shown schematically in Figure 1.3 (looking radially inwards) to show the arrangement of the blading and the flow onto the blades.

The flow enters the stage at an angle α_1 with a velocity c_1. This inlet velocity is set by whatever is directly upstream of the compressor stage: an inlet duct, another compressor stage or an inlet guide vane (IGV). By vector subtraction the relative velocity entering the rotor will have a magnitude w_1 at a relative flow angle β_1. The rotor blades are designed to smoothly accept this relative flow and change its direction so that at outlet the flow leaves the rotor with a relative velocity w_2 at a relative flow angle β_2. As shown later in this chapter, work will be done by the rotor blades on the gas during this process and, as a consequence, the gas stagnation pressure and stagnation temperature will be increased.

By vector addition the absolute velocity at rotor exit c_2 is found at flow angle α_2. This flow should smoothly enter the stator row which it then leaves at a reduced velocity c_3 at an absolute angle α_3. The diffusion in velocity from c_2 to c_3 causes the pressure and temperature to rise further. Following this the gas is directed to the following rotor and the process goes on repeating through the remaining stages of the compressor.

The purpose of this brief explanation is to introduce the reader to the basic fluid mechanical processes of turbomachinery via an axial flow compressor. It is hoped that the reader will follow the description given in relation to the velocity changes shown in Figure 1.3 as this is fundamental to understanding the subject of turbomachinery. Velocity triangles will be considered in further detail for each category of turbomachine in later chapters.

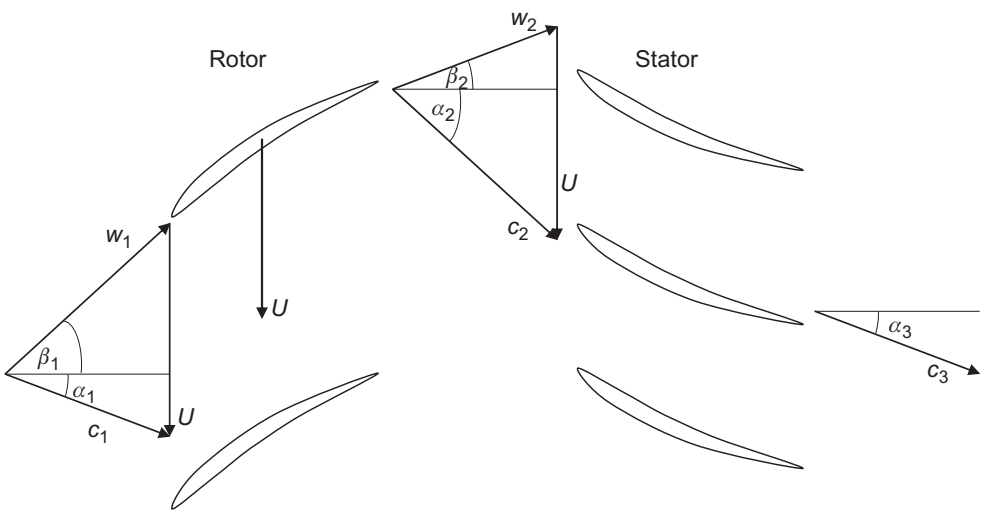

FIGURE 1.3

Velocity triangles for an axial compressor stage.

EXAMPLE 1.1

The axial velocity through an axial flow fan is constant and equal to 30 m/s. With the notation given in Figure 1.3, the flow angles for the stage are α_1 and β_2 are 23° and β_1 and α_2 are 60°.

From this information determine the blade speed U and, if the mean radius of the fan is 0.15 m, find the rotational speed of the rotor.

Solution

The velocity components are easily calculated as follows:

$$w_{\theta 1} = c_x \tan \beta_1 \quad \text{and} \quad c_{\theta 1} = c_x \tan \alpha_1$$

$$\therefore U_m = c_{\theta 1} + w_{\theta 1} = c_x(\tan \alpha_1 + \tan \beta_1) = 64.7 \text{ m/s}$$

The speed of rotation is

$$\Omega = \frac{U_m}{r_m} = 431.3 \text{ rad/}s \text{ or } 431.3 \times 30/\pi = 4119 \text{ rpm}$$

1.3 The fundamental laws

The remainder of this chapter summarizes the basic physical laws of fluid mechanics and thermodynamics, developing them into a form suitable for the study of turbomachines. Following this, the properties of fluids, compressible flow relations and the efficiency of compression and expansion flow processes are covered.

The laws discussed are

i. the *continuity of flow equation*;
ii. the *first law of thermodynamics* and the *steady flow energy equation*;
iii. the *momentum equation*;
iv. the *second law of thermodynamics*.

All of these laws are usually covered in first-year university engineering and technology courses, so only the briefest discussion and analysis is given here. Some textbooks dealing comprehensively with these laws are those written by Çengel and Boles (1994), Douglas, Gasiorek and Swaffield (1995), Rogers and Mayhew (1992), and Reynolds and Perkins (1977). It is worth remembering that these laws are completely general; they are independent of the nature of the fluid or whether the fluid is compressible or incompressible.

1.4 The equation of continuity

Consider the flow of a fluid with density ρ, through the element of area dA, during the time interval dt. Referring to Figure 1.4, if c is the stream velocity the elementary mass is $dm = \rho c dt dA \cos\theta$, where θ is the angle subtended by the normal of the area element to the stream direction.

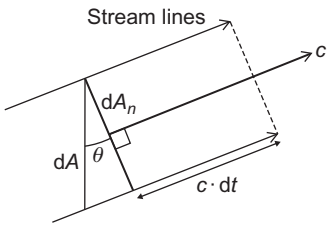

FIGURE 1.4

Flow across an element of area.

The element of area perpendicular to the flow direction is $dA_n = dA\cos\theta$ and so $dm = \rho c dA_n dt$. The elementary rate of mass flow is therefore

$$d\dot{m} = \frac{dm}{dt} = \rho c dA_n \tag{1.7}$$

Most analyses in this book are limited to one-dimensional steady flows where the velocity and density are regarded as constant across each section of a duct or passage. If A_{n1} and A_{n2} are the areas normal to the flow direction at stations 1 and 2 along a passage respectively, then

$$\dot{m} = \rho_1 c_1 A_{n1} = \rho_2 c_2 A_{n2} = \rho c A_n \tag{1.8}$$

since there is no accumulation of fluid within the control volume.

1.5 The first law of thermodynamics

The *first law of thermodynamics* states that, if a system is taken through a complete cycle during which heat is supplied and work is done, then

$$\oint (dQ - dW) = 0 \tag{1.9}$$

where $\oint dQ$ represents the heat supplied to the system during the cycle and $\oint dW$ the work done by the system during the cycle. The units of heat and work in Eq. (1.9) are taken to be the same.

During a change from state 1 to state 2, there is a change in the energy within the system:

$$E_2 - E_1 = \int_1^2 (dQ - dW) \tag{1.10a}$$

where $E = U + (1/2)mc^2 + mgz$.

For an infinitesimal change of state,

$$dE = dQ - dW \tag{1.10b}$$

The steady flow energy equation

Many textbooks, e.g., Çengel and Boles (1994), demonstrate how the first law of thermodynamics is applied to the steady flow of fluid through a control volume so that the steady flow energy equation is obtained. It is unprofitable to reproduce this proof here and only the final result is quoted. Figure 1.5 shows a control volume representing a turbomachine, through which fluid passes at a steady rate of mass flow $\dot{m}$, entering at position 1 and leaving at position 2. Energy is transferred from the fluid to the blades of the turbomachine, positive work being done (via the shaft) at the rate $\dot{W}_x$. In the general case positive heat transfer takes place at the rate $\dot{Q}$, *from* the surroundings *to* the control volume. Thus, with this sign convention the steady flow energy equation is

$$\dot{Q} - \dot{W}_x = \dot{m}\left[(h_2 - h_1) + \frac{1}{2}(c_2^2 - c_1^2) + g(z_2 - z_1)\right] \tag{1.11}$$

where h is the specific enthalpy, $1/2c^2$, the kinetic energy per unit mass and gz, the potential energy per unit mass.

For convenience, the specific enthalpy, h, and the kinetic energy, $1/2c^2$, are combined and the result is called the *stagnation enthalpy*:

$$h_0 = h + \frac{1}{2}c^2 \tag{1.12}$$

Apart from hydraulic machines, the contribution of the $g(z_2 - z_1)$ term in Eq. (1.11) is small and can usually be ignored. In this case, Eq. (1.11) can be written as

$$\dot{Q} - \dot{W}_x = \dot{m}(h_{02} - h_{01}) \tag{1.13}$$

The stagnation enthalpy is therefore constant in any flow process that does not involve a work transfer or a heat transfer. Most turbomachinery flow processes are adiabatic (or very nearly so) and it is permissible to write $\dot{Q} = 0$. For work producing machines (turbines) $\dot{W}_x > 0$, so that

$$\dot{W}_x = \dot{W}_t = \dot{m}(h_{01} - h_{02}) \tag{1.14}$$

For work absorbing machines (compressors) $\dot{W}_x < 0$, so that it is more convenient to write

$$\dot{W}_c = -\dot{W}_x = \dot{m}(h_{02} - h_{01}) \tag{1.15}$$

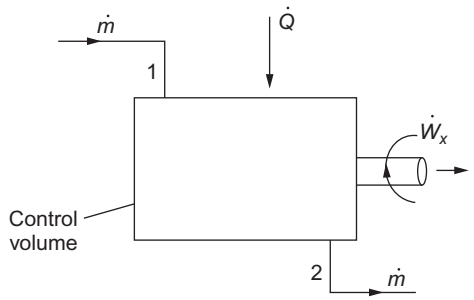

FIGURE 1.5

Control volume showing sign convention for heat and work transfers.

1.6 The momentum equation

One of the most fundamental and valuable principles in mechanics is *Newton's second law of motion*. The momentum equation relates the sum of the external forces acting on a fluid element to its acceleration, or to the rate of change of momentum in the direction of the resultant external force. In the study of turbomachines many applications of the momentum equation can be found, e.g., the force exerted upon a blade in a compressor or turbine cascade caused by the deflection or acceleration of fluid passing the blades.

Considering a system of mass m, the sum of all the body and surface forces acting on m along some arbitrary direction x is equal to *the time rate of change of the total x-momentum of the system*, i.e.,

$$\sum F_x = \frac{\mathrm{d}}{\mathrm{d}t}(mc_x) \tag{1.16a}$$

For a control volume where fluid enters steadily at a uniform velocity c_{x1} and leaves steadily with a uniform velocity c_{x2}, then

$$\sum F_x = \dot{m}(c_{x2} - c_{x1}) \tag{1.16b}$$

Equation (1.16b) is the one-dimensional form of the steady flow momentum equation.

Moment of momentum

In dynamics useful information can be obtained by employing Newton's second law in the form where it applies to the moments of forces. This form is of central importance in the analysis of the energy transfer process in turbomachines.

For a system of mass m, the vector sum of the moments of all external forces acting on the system about some arbitrary axis $A-A$ fixed in space is equal to the time rate of change of angular momentum of the system about that axis, i.e.,

$$\tau_A = m\frac{\mathrm{d}}{\mathrm{d}t}(rc_\theta) \tag{1.17a}$$

where r is distance of the mass center from the axis of rotation measured along the normal to the axis and c_θ the velocity component mutually perpendicular to both the axis and radius vector r.

For a control volume the *law of moment of momentum* can be obtained. Figure 1.6 shows the control volume enclosing the rotor of a generalized turbomachine. Swirling fluid enters the control volume at radius r_1 with tangential velocity $c_{\theta 1}$ and leaves at radius r_2 with tangential velocity $c_{\theta 2}$. For one-dimensional steady flow,

$$\tau_\mathrm{A} = \dot{m}(r_2 c_{\theta 2} - r_1 c_{\theta 1}) \tag{1.17b}$$

which states that the sum of the moments of the external forces acting on fluid temporarily occupying the control volume is equal to the net time rate of efflux of angular momentum from the control volume.

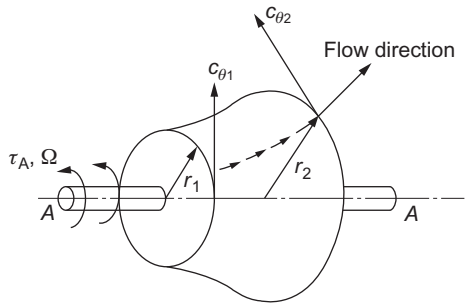

FIGURE 1.6

Control volume for a generalized turbomachine.

The Euler work equation

For a pump or compressor rotor running at angular velocity Ω, the rate at which the rotor does work on the fluid is

$$\dot{W}_c = \tau_A \Omega = \dot{m}(U_2 c_{\theta 2} - U_1 c_{\theta 1}) \tag{1.18a}$$

where the blade speed $U = \Omega r$.

Thus, the work done on the fluid per unit mass or specific work is

$$\Delta W_c = \frac{\dot{W}_c}{\dot{m}} = \frac{\tau_A \Omega}{\dot{m}} = U_2 c_{\theta 2} - U_1 c_{\theta 1} > 0 \tag{1.18b}$$

This equation is referred to as *Euler's pump or compressor equation*.

For a turbine the fluid does work *on* the rotor and the sign for work is then reversed. Thus, the specific work is

$$\Delta W_t = \frac{\dot{W}_t}{\dot{m}} = U_1 c_{\theta 1} - U_2 c_{\theta 2} > 0 \tag{1.18c}$$

Equation (1.18c) is referred to as *Euler's turbine equation*.

Note that, for any adiabatic turbomachine (turbine or compressor), applying the steady flow energy equation, Eq. (1.13), gives

$$\Delta W_x = (h_{01} - h_{02}) = U_1 c_{\theta 1} - U_2 c_{\theta 2} \tag{1.19a}$$

Alternatively, this can be written as

$$\Delta h_0 = \Delta(U c_\theta) \tag{1.19b}$$

Equations (1.19a) and (1.19b) are the general forms of the *Euler work equation*. By considering the assumptions used in its derivation, this equation can be seen to be valid for adiabatic flow for any streamline through the blade rows of a turbomachine. It is applicable to both viscous and inviscid flow, since the torque provided by the fluid on the blades can be exerted by pressure forces or frictional forces. It is strictly valid only for steady flow but it can also be applied to time-averaged unsteady flow provided the averaging is done over a long enough time period. In all cases, all of the torque from the fluid must be transferred to the blades. Friction on the hub and casing of a

turbomachine can cause local changes in angular momentum that are not accounted for in the Euler work equation.

Note that for any stationary blade row, $U = 0$ and therefore $h_0 =$ constant. This is to be expected since a stationary blade cannot transfer any work to or from the fluid.

Rothalpy and relative velocities

The Euler work equation, Eq. (1.19), can be rewritten as

$$I = h_0 - Uc_\theta \tag{1.20a}$$

where I is a constant along the streamlines through a turbomachine. The function I was first introduced by Wu (1952) and has acquired the widely used name *rothalpy*, a contraction of rotational stagnation enthalpy, and is a fluid mechanical property of some importance in the study of flow within rotating systems. The rothalpy can also be written in terms of the static enthalpy as

$$I = h + \frac{1}{2}c^2 - Uc_\theta \tag{1.20b}$$

The Euler work equation can also be written in terms of relative quantities for a rotating frame of reference. The relative tangential velocity, as given in Eq. (1.4), can be substituted in Eq. (1.20b) to produce

$$I = h + \frac{1}{2}(w^2 + U^2 + 2Uw_\theta) - U(w_\theta + U) = h + \frac{1}{2}w^2 - \frac{1}{2}U^2 \tag{1.21a}$$

Defining a relative stagnation enthalpy as $h_{0,\text{rel}} = h + (1/2)w^2$, Eq. (1.21a) can be simplified to

$$I = h_{0,\text{rel}} - \frac{1}{2}U^2 \tag{1.21b}$$

This final form of the Euler work equation shows that, for rotating blade rows, the relative stagnation enthalpy is constant through the blades provided the blade speed is constant. In other words, $h_{0,\text{rel}} =$ constant, if the radius of a streamline passing through the blades stays the same. This result is important for analyzing turbomachinery flows in the relative frame of reference.

1.7 The second law of thermodynamics—entropy

The *second law of thermodynamics*, developed rigorously in many modern thermodynamic textbooks, e.g., Çengel and Boles (1994), Reynolds and Perkins (1977), and Rogers and Mayhew (1992), enables the concept of entropy to be introduced and ideal thermodynamic processes to be defined.

An important and useful corollary of the second law of thermodynamics, known as the *Inequality of Clausius*, states that, for a system passing through a cycle involving heat exchanges,

$$\oint \frac{\mathrm{d}Q}{T} \leq 0 \tag{1.22a}$$

where dQ is an element of heat transferred to the system at an absolute temperature T. If all the processes in the cycle are reversible, then $dQ = dQ_R$, and the equality in Eq. (1.22a) holds true, i.e.,

$$\oint \frac{dQ_R}{T} = 0 \tag{1.22b}$$

The property called *entropy*, for a finite change of state, is then defined as

$$S_2 - S_1 = \int_1^2 \frac{dQ_R}{T} \tag{1.23a}$$

For an incremental change of state

$$dS = m ds = \frac{dQ_R}{T} \tag{1.23b}$$

where m is the mass of the system.

With steady one-dimensional flow through a control volume in which the fluid experiences a change of state from condition 1 at entry to 2 at exit,

$$\int_1^2 \frac{d\dot{Q}}{T} \leq \dot{m}(s_2 - s_1) \tag{1.24a}$$

Alternatively, this can be written in terms of an entropy production due to irreversibility, ΔS_{irrev}:

$$\dot{m}(s_2 - s_1) = \int_1^2 \frac{d\dot{Q}}{T} + \Delta S_{irrev} \tag{1.24b}$$

If the process is adiabatic, $d\dot{Q} = 0$, then

$$s_2 \geq s_1 \tag{1.25a}$$

If the process is *reversible* as well, then

$$s_2 = s_1 \tag{1.25b}$$

Thus, for a flow undergoing a process that is both adiabatic and reversible, the entropy will remain unchanged (this type of process is referred to as *isentropic*). Since turbomachinery is usually adiabatic, or close to adiabatic, an isentropic compression or expansion represents the best possible process that can be achieved. To maximize the efficiency of a turbomachine, the irreversible entropy production ΔS_{irrev} must be minimized, and this is a primary objective of any design.

Several important expressions can be obtained using the preceding definition of *entropy*. For a system of mass m undergoing a reversible process $dQ = dQ_R = mTds$ and $dW = dW_R = mpdv$. In the absence of motion, gravity, and other effects the first law of thermodynamics, Eq. (1.10b) becomes

$$Tds = du + pdv \tag{1.26a}$$

With $h = u + pv$, then $dh = du + pdv + vdp$, and Eq. (1.26a) then gives

$$Tds = dh + vdp \tag{1.26b}$$

Equations (1.26a) and (1.26b) are extremely useful forms of the second law of thermodynamics because the equations are written only in terms of properties of the system (there are no terms involving Q or W). These equations can therefore be applied to a system undergoing any process.

Entropy is a particularly useful property for the analysis of turbomachinery problems. Any increase of entropy in the flow path of a machine can be equated to a certain amount of "lost work" and thus a loss in efficiency. The value of entropy is the same in both the absolute and relative frames of reference (see Figure 1.9) and this means it can be used to track the sources of inefficiency through all the rotating and stationary parts of a machine. The application of entropy to account for lost performance is very powerful and will be demonstrated in later chapters.

1.8 Bernoulli's equation

Consider the steady flow energy equation, Eq. (1.11). For adiabatic flow, with no work transfer,

$$(h_2 - h_1) + \frac{1}{2}(c_2^2 - c_1^2) + g(z_2 - z_1) = 0 \tag{1.27}$$

If this is applied to a control volume whose thickness is infinitesimal in the stream direction (Figure 1.7), the following differential form is derived:

$$\mathrm{d}h + c\mathrm{d}c + g\mathrm{d}z = 0 \tag{1.28}$$

If there are no shear forces acting on the flow (no mixing or friction), then the flow will be isentropic and, from Eq. (1.26b), $\mathrm{d}h = v\mathrm{d}p = \mathrm{d}p/\rho$, giving

$$\frac{1}{\rho}\mathrm{d}p + c\mathrm{d}c + g\mathrm{d}z = 0 \tag{1.29a}$$

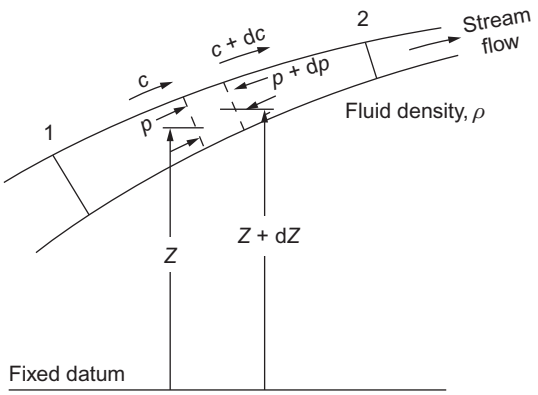

FIGURE 1.7

Control volume in a streaming fluid.

Equation (1.29a) is often referred to as the *one-dimensional form* of Euler's equation of motion. Integrating this equation in the stream direction we obtain

$$\int_1^2 \frac{1}{\rho}\mathrm{d}p + \frac{1}{2}(c_2^2 - c_1^2) + g(z_2 - z_1) = 0 \tag{1.29b}$$

which is Bernoulli's equation. For an incompressible fluid, ρ is constant and Eq. (1.29b) becomes

$$\frac{1}{p}(p_{02} - p_{01}) + g(z_2 - z_1) = 0 \tag{1.29c}$$

where the stagnation pressure for an incompressible fluid is $p_0 = p + (1/2)\rho c^2$.

When dealing with hydraulic turbomachines, the term *head*, H, occurs frequently and describes the quantity $z + p_0/(\rho g)$. Thus, Eq. (1.29c) becomes

$$H_2 - H_1 = 0 \tag{1.29d}$$

If the fluid is a gas or vapor, the change in gravitational potential is generally negligible and Eq. (1.29b) is then

$$\int_1^2 \frac{1}{\rho}\mathrm{d}p + \frac{1}{2}(c_2^2 - c_1^2) = 0 \tag{1.29e}$$

Now, if the gas or vapor is subject to only small pressure changes the fluid density is sensibly constant and integration of Eq. (1.29e) gives

$$p_{02} = p_{01} = p_0 \tag{1.29f}$$

i.e., the stagnation pressure is constant (it is shown later that this is also true for a *compressible isentropic process*).

1.9 The thermodynamic properties of fluids

The three most familiar fluid properties are the pressure p, the temperature T and the density ρ. We also need to consider how other associated thermodynamic properties such as the internal energy u, the enthalpy h, the entropy s, and the specific heats C_p and C_v change during a flow process.

It is known from studies of statistical thermodynamics that in all fluid processes involving a change in pressure, an enormous number of molecular collisions take place in an extremely short interval which means that the fluid pressure rapidly adjusts to an equilibrium state. We can thus safely assume that all the properties listed above will follow the laws and state relations of classical equilibrium thermodynamics. We will also restrict ourselves to the following pure and homogenous substances: ideal gases, perfect gases, and steam.

Ideal gases

Air is a mixture of gases but, in the temperature range 160−2100 K, it can be regarded as a pure substance. Within this temperature range air obeys the ideal gas relationship:

$$p = \rho RT \quad \text{or} \quad pv = RT \tag{1.30}$$

where $R = C_p - C_v$ is the gas constant.

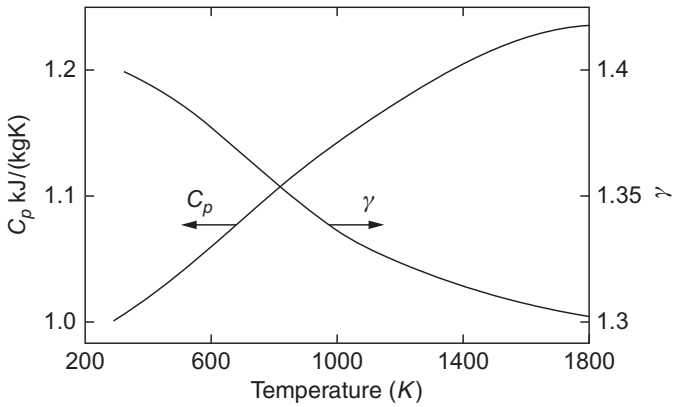

FIGURE 1.8

Variation of gas properties with temperature for dry air .

(Data from Rogers and Mayhew, 1995)

The value of the gas constant R for any ideal gas is equal to a Universal Gas Constant $R_0 = 8314$ J/kmol divided by the molecular weight of the gas. In this book many of the problems concern air so it is useful to evaluate a value for this gas mixture which has a molecular weight $M = 28.97$ kg/kmol.

$$R_{\text{air}} = \frac{8314}{28.97} = 287\ J/\text{kg K}$$

For air under standard sea-level conditions, the pressure $p_a = 1.01$ bar and the temperature $T_a = 288$ K. Thus, the density of air under standardized sea-level conditions is

$$\rho_a = \frac{p_a}{RT_a} = \frac{1.01 \times 10^5}{287 \times 288} = 1.222\ \text{kg}/m^3$$

All gases at high temperatures and at relatively low pressures conform to the ideal gas law.
An ideal gas can be either a *semi-perfect gas* or a *perfect gas*.
In a semi-perfect gas, the specific heat capacities are functions of temperature only:

$$C_p = \left(\frac{\partial h}{\partial T}\right)_p = \frac{\mathrm{d}h}{\mathrm{d}T} = \mathrm{C}_p(T) \text{ and } \mathrm{C}_v = \left(\frac{\partial u}{\partial T}\right)_p = \frac{\mathrm{d}u}{\mathrm{d}T} = C_v(T)$$

Over large temperature differences, air and many other common gases should be treated as semi-perfect gases. The variation in the values of C_p and γ for air are shown in Figure 1.8. Note that $\gamma = C_p/C_v$ is the ratio of the specific heats, which is a particularly important parameter in compressible flow analysis (see Section 1.10).

Perfect gases

A perfect gas is an ideal gas for which C_p, C_v, and γ, are constants. Many real gases can be treated as perfect gases over a limited range of temperature and pressure. In the calculation of expansion or compression processes in turbomachines the normal practice is to use weighted mean values for C_p and γ according to the mean temperature of the process. Accordingly, in the problems in this book values have been selected for C_p and γ appropriate to the gas and the temperature range. For example, in air flow at temperatures close to ambient the value of γ is taken to be 1.4.

Note that the entropy change for a perfect gas undergoing any process can be calculated from the properties at the start and end of the process. Substituting $\mathrm{d}h = C_p \mathrm{d}T$ and $pv = RT$ into Eq. (1.26b) gives:

$$T\mathrm{d}s = C_P \mathrm{d}T - RT\,\mathrm{d}p/p$$

This equation can be integrated between the start state (1) and end state (2) of a process:

$$\int_1^2 \mathrm{d}s = C_p \int_1^2 \frac{\mathrm{d}T}{T} - R\int_1^2 \frac{\mathrm{d}p}{p}$$

$$\therefore s_2 - s_1 = C_p \ln\frac{T_2}{T_1} - R\ln\frac{p_2}{p_1} \tag{1.31}$$

EXAMPLE 1.2

a. A quantity of carbon dioxide undergoes an *isentropic* process. Initially the pressure $p_1 = 120$ kPa and the temperature $T_1 = 120°\mathrm{C}$. Finally, at the end of the process, the pressure $p_2 = 100$ kPa. Determine the final temperature T_2.

b. Heat is now supplied to the gas at constant volume and the temperature rises to 200°C. Determine how much heat is supplied per unit mass of the gas, the final pressure, and the specific entropy increase of the gas due to the heat transfer.

Consider CO_2 to be a perfect gas with $R = 189\ J/\mathrm{kg\ K}$ and $\gamma = 1.30$.

Solution

a. From Eq. (1.31), with $s_2 = s_1$

$C_p \ln(T_2/T_1) = R\ln(p_2/p_1)$ from which you can find:

$$T_2 = T_1\left(\frac{p_2}{p_1}\right)^{(\gamma-1)/\gamma} = 393 \times 0.9588 = 376.8\ \mathrm{K}$$

b. Applying the first law of thermodynamics to a system, Eq. (1.10b):

$$Q = \Delta U = C_v \Delta T,\ T_3 = 473\ \mathrm{K}\ \therefore Q = C_v(T_3 - T_2) = \frac{R}{\gamma - 1}(T_3 - T_2)$$

$$\therefore Q = \frac{189}{0.3}(96.2) = 60.6 \text{ kJ/kg}$$

At constant volume, from

$$pv = RT, \quad \frac{p_3}{p_2} = \frac{T_3}{T_2} \quad \therefore p_3 = 100 \times \frac{473}{376.8} = 125.5 \text{ kPa}$$

The increase in entropy, from Eq. (1.31) is given by:

$$\Delta s = C_P \ln\left(\frac{T_3}{T_2}\right) - R \ln\left(\frac{p_3}{p_2}\right) = \frac{\gamma R}{\gamma - 1} \ln\left(\frac{T_3}{T_2}\right) - R \ln\left(\frac{p_3}{p_2}\right)$$

$$\therefore \Delta s = \frac{1.3 \times 189}{0.3} \ln\left(\frac{473}{376.8}\right) - 189 \ln\left(\frac{125.5}{100}\right) = 142.9 \, J/\text{kg K}$$

Steam

Steam is the gaseous phase of water formed when pure water is boiled. When steam is in the two-phase region, where liquid and gaseous water coexist, it is known as *wet steam*. Steam turbines use the expansion of high-pressure steam to generate power. They typically operate close to or within the two-phase region, where the ideal gas law is highly inaccurate. No simple formulae apply and it is necessary to use tabulations of property values obtained by experiment and compiled as steam tables or steam charts to determine the effects of a change of state.

The thermodynamic properties of steam were the subject of many *difficult investigations* by groups of scientists and engineers over many years. An interesting summary of the methods used and the difficulties encountered are given in a paper by Harvey and Levelt Sengers (2001). The latest state-of-the-art account of the thermodynamic properties of water was adopted by the *International Association for the Properties of Water and Steam* (IAPWS) (Wagner and Pruss (2002)). The properties calculated from the current IAPWS standards for general and scientific use are distributed in a computer program by the National Institute of Standards and Technology (NIST) Standard Reference Data Program (Harvey, Peskin and Klein (2000)). These properties are also available via a free online calculator and in tabulated form (National Institute of Standards and Technology (2012)).

As well as steam tables the most immediate aid for performing calculations (although less accurate) is the Mollier diagram. This shows the enthalpy h (kJ/kg) plotted against entropy s (kJ/kg K) for various values of pressure p (MPa). A small, single-page Mollier chart is shown in Appendix E, but poster size charts can be obtained which, of course, enable greater accuracy.

Commonly used thermodynamic terms relevant to steam tables

i. Saturation curve

This is the boundary between the different phases on a property diagram. *Saturated liquid* refers to a state where all the water is in the liquid phase and *saturated vapor* refers to a state where all the water is in the gaseous phase. The two-phase region lies between the liquid and vapor saturation curves. Note that within the two-phase region temperature and pressure are no

longer independent properties. For example, at 1 bar pressure, when water is boiling, all the liquid and gas is at 100°C.

ii. Quality or dryness fraction

This applies within the two-phase region and is the ratio of the vapor mass to the total mass of liquid and vapor. The value of any intensive property within the two-phase region is the mass weighted average of the values on the liquid and vapor saturation curves at the same pressure and temperature. Hence, the quality or dryness fraction can be used to specify the thermodynamic state of the steam.

For example, consider a quantity of wet steam at a state with dryness fraction x. The specific enthalpy of the steam at this state will be given by:

$$h = (1 - x)h_f + xh_g \tag{1.32}$$

where h_f is the enthalpy on the liquid saturation curve, and h_g is the enthalpy on the vapor saturation curve, both at the same temperature and pressure of the wet steam. The above approach can be used for other intensive properties, such as u, v, s.

iii. Degree of superheat of steam.

When steam is heated at constant pressure in the gaseous phase it will be at a higher temperature than the corresponding saturation temperature. The temperature difference between the steam temperature and the saturation temperature at the same pressure is the degree of superheat.

iv. The Triple Point and the Critical Point.

The triple point for water is the unique temperature and pressure where all three phases coexist: ice, liquid water, and steam. The critical point is the state where the liquid and vapor saturation curves meet at the highest temperature and pressure possible in the two-phase region.

1.10 Compressible flow relations for perfect gases

The Mach number of a flow is defined as the velocity divided by the local speed of sound. For a perfect gas, such as air over a limited temperature range, the Mach number can be written as

$$M = \frac{c}{a} = \frac{c}{\sqrt{\gamma RT}} \tag{1.33}$$

Whenever the Mach number in a flow exceeds about 0.3, the flow becomes compressible, and the fluid density can no longer be considered as constant. High power turbomachines require high flow rates and high blade speeds and this inevitably leads to compressible flow. The static and stagnation quantities in the flow can be related using functions of the local Mach number and these are derived later.

Starting with the definition of stagnation enthalpy, $h_0 = h + (1/2)c^2$, this can be rewritten for a perfect gas as

$$C_pT_0 = C_pT + \frac{c^2}{2} = C_pT + \frac{\mathrm{M}^2\gamma RT}{2} \tag{1.34a}$$

Given that $\gamma R = (\gamma - 1)C_P$, Eq. (1.34a) can be simplified to

$$\frac{T_0}{T} = 1 + \frac{\gamma - 1}{2}\mathrm{M}^2 \tag{1.34b}$$

The stagnation pressure in a flow is the static pressure that is measured if the flow is brought *isentropically* to rest. From Eq. (1.26b), for an isentropic process $\mathrm{d}h = \mathrm{d}p/\rho$. If this is combined with the equation of state for a perfect gas, $p = \rho RT$, the following equation is obtained:

$$\frac{\mathrm{d}p}{p} = \frac{Cp}{R}\frac{\mathrm{d}T}{T} = \frac{\mathrm{d}T}{T}\frac{\gamma}{\gamma - 1} \tag{1.35}$$

This can be integrated between the static and stagnation conditions to give the following compressible flow relation between the stagnation and static pressure:

$$\frac{p_0}{p} = \left(\frac{T_0}{T}\right)^{\gamma/(\gamma-1)} = \left(1 + \frac{\gamma - 1}{2}\mathrm{M}^2\right)^{\gamma/(\gamma-1)} \tag{1.36}$$

Equation (1.35) can also be integrated along a streamline between any two arbitrary points 1 and 2 within an isentropic flow. In this case, the stagnation temperatures and pressures are related:

$$\frac{p_{02}}{p_{01}} = \left(\frac{T_{02}}{T_{01}}\right)^{\gamma/(\gamma-1)} \tag{1.37}$$

If there is no heat or work transfer to the flow, $T_0 =$ constant. Hence, Eq. (1.37) shows that, in isentropic flow with no work transfer, $p_{02} = p_{01} =$ constant, which was shown to be the case for incompressible flow in Eq. (1.29f).

Combining the equation of state, $p = \rho RT$ with Eqs. (1.34b) and (1.36) the corresponding relationship for the stagnation density is obtained:

$$\frac{\rho_0}{\rho} = \left(1 + \frac{\gamma - 1}{2}\mathrm{M}^2\right)^{1/(\gamma-1)} \tag{1.38}$$

Arguably the most important compressible flow relationship for turbomachinery is the one for nondimensional mass flow rate, sometimes referred to as *capacity*. It is obtained by combining Eqs. (1.34b), (1.36), and (1.38) with continuity, Eq. (1.8):

$$\frac{\dot{m}\sqrt{C_P T_0}}{A_n p_0} = \frac{\gamma}{\sqrt{\gamma - 1}}\mathrm{M}\left(1 + \frac{\gamma - 1}{2}\mathrm{M}^2\right)^{-\frac{1}{2}\left(\frac{\gamma+1}{\gamma-1}\right)} \tag{1.39}$$

This result is important since it can be used to relate the flow properties at different points within a compressible flow turbomachine. The application of Eq. (1.39) is demonstrated in Chapter 3.

Note that the compressible flow relations given previously can be applied in the relative frame of reference for flow within rotating blade rows. In this case relative stagnation properties and relative Mach numbers are used:

$$\frac{p_{0,\mathrm{rel}}}{p}, \frac{T_{0,\mathrm{rel}}}{T}, \frac{\rho_{0,\mathrm{rel}}}{\rho}, \frac{\dot{m}\sqrt{C_p T_{0,\mathrm{rel}}}}{A p_{0,\mathrm{rel}}} = f(\mathrm{M}_{\mathrm{rel}})$$

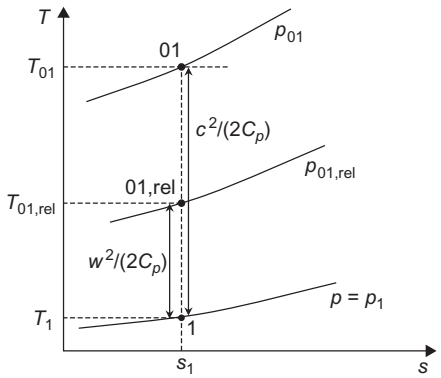

FIGURE 1.9

Relationship between stagnation and static quantities on a temperature–entropy diagram.

Figure 1.9 shows the relationship between stagnation and static conditions on a temperature–entropy diagram, in which the temperature differences have been exaggerated for clarity. This shows the relative stagnation properties as well as the absolute properties for a single point in a flow. Note that all of the conditions have the same entropy because the stagnation states are defined using an isentropic process. The pressures and temperatures are related using Eq. (1.36).

EXAMPLE 1.3

Air flows adiabatically and at high subsonic speed through a duct. At a station which we will call A, flow measurements indicate that the velocity c_A is 250 m/s, the static temperature T_A is 315 K and the static pressure p_A is 180 kPa. Determine the values of the stagnation temperature T_{0A}, the Mach number M_A the stagnation pressure p_{0A} and the stagnation density ρ_A. If the duct cross-sectional area is 0.1 m^2, calculate the air mass flow rate. For air take $R = 287$ J/kg K and $\gamma = 1.4$.

Solution

From Eq. (1.34a)

$$T_{0A} = T_A + \frac{c_A^2}{2C_p} = 346 \text{ K}$$

From Eq. (1.33)

$$M_A = \frac{c_A}{\sqrt{\gamma R T_A}} = 0.703$$

From Eq. (1.36)

$$p_{0A} = p_A \left(1 + \frac{\gamma - 1}{2} M_A^2\right)^{\frac{\gamma}{\gamma - 1}} = 250 \text{ kPa}$$

From Eq. (1.38)

$$\rho_{0A} = \rho_A \left(1 + \frac{\gamma - 1}{2} M_A^2\right)^{\frac{1}{\gamma - 1}} \text{ where } \rho_A = \frac{p_A}{RT_A} = 1.991 \text{ kg/m}^3$$

$$\therefore \rho_{0A} = 2.52 \text{ kg/m}^3$$

Here, it will be obvious that the stagnation density can be evaluated more directly using the gas law:

$$\rho_{0A} = \frac{p_{0A}}{RT_{0A}} = 2.52 \text{ kg/m}^3$$

There are also two ways to evaluate the air mass flow rate. Using Eq. (1.8)

$$\dot{m} = \rho_A A_A c_A = 1.99 \times 0.1 \times 250 = 49.8 \text{ kg/s}$$

Alternatively, from Eq. (1.39) or Table C.1,

$$\frac{\dot{m}\sqrt{C_P T_{0A}}}{p_{0A} A_A} = f(0.703) = 1.1728$$

$$\therefore \dot{m} = 1.1728 \times \frac{p_{0A} A_A}{\sqrt{C_P T_{0A}}} = 49.7 \text{ kg/s}$$

Note that Appendix C includes tabulated results for Eqs. (1.34), (1.36), (1.38), and (1.39).

Choked flow

For subsonic flow, as flow speed and Mach number increase, the mass flow per unit area increases. This is because, from Eq. (1.8), the mass flow per unit area is $\dot{m}/A = \rho c$ and as Mach number rises, the flow speed c increases more rapidly than the density ρ reduces. However, this is not true for supersonic flow and, above $M = 1$, as flow speed and Mach number increase, the mass flow per unit area decreases. There is, therefore, a maximum mass flow per unit area which occurs at sonic conditions ($M = 1$). This maximum can be readily observed by plotting out the nondimensional mass flow function given in Eq. (1.39) for a Mach number range from 0 to 2 using a fixed value of γ.

An important consequence of this is that the mass flow through any turbomachinery component reaches a maximum once $M = 1$ across the section of minimum flow area. The flow is said to be *choked* and it is not possible to increase the mass flow further (without changing the inlet stagnation conditions). The section of minimum flow area is known as the *throat* and the size of the throat is a critical design parameter since it determines the maximum mass flow that can pass through a transonic turbomachine. Under choked conditions, because pressure waves in the flow travel at $M = 1$, changes to the flow downstream of the throat cannot have any effect on the flow upstream of the throat.

Choking is considered in further detail for compressor and turbine blade rows within Sections 3.5 and 3.6, respectively.

1.11 Definitions of efficiency

A large number of efficiency definitions are included in the literature of turbomachines and most workers in this field would agree there are too many. In this book only those considered to be important and useful are included.

Efficiency of turbines

Turbines are designed to convert the available energy in a flowing fluid into useful mechanical work delivered at the coupling of the output shaft. The efficiency of this process, the *overall efficiency* η_0, is a performance factor of considerable interest to both designer and user of the turbine. Thus,

$$\eta_0 = \frac{\text{mechanical energy available at coupling of output shaft in unit time}}{\text{maximum energy difference possible for the fluid in unit time}}$$

Mechanical energy losses occur between the turbine rotor and the output shaft coupling as a result of the work done against friction at the bearings, glands, etc. The magnitude of this loss as a fraction of the total energy transferred to the rotor is difficult to estimate as it varies with the size and individual design of turbomachine. For small machines (several kilowatts) it may amount to 5% or more, but for medium and large machines this loss ratio may become as little as 1%. A detailed consideration of the mechanical losses in turbomachines is beyond the scope of this book and is not pursued further.

The *isentropic efficiency* η_t or *hydraulic efficiency* η_h for a turbine is, in broad terms,

$$\eta_t (\text{or } \eta_h) = \frac{\text{mechanical energy supplied to the rotor in unit time}}{\text{maximum energy difference possible for the fluid in unit time}}$$

Comparing these definitions it is easily deduced that the *mechanical efficiency* η_m, which is simply the ratio of shaft power to rotor power, is

$$\eta_m = \eta_0/\eta_t (\text{or } \eta_0/\eta_h) \tag{1.40}$$

The preceding isentropic efficiency definition can be concisely expressed in terms of the work done by the fluid passing through the turbine:

$$\eta_t (\text{or } \eta_h) = \frac{\text{actual work}}{\text{ideal (maximum) work}} = \frac{\Delta W_x}{\Delta W_{\max}} \tag{1.41}$$

The *actual work* is unambiguous and straightforward to determine from the steady flow energy equation, Eq. (1.11). For an adiabatic turbine, using the definition of stagnation enthalpy,

$$\Delta W_x = \dot{W}_x/\dot{m} = (h_{01} - h_{02}) + g(z_1 - z_2)$$

The *ideal work* is slightly more complicated as it depends on how the ideal process is defined. The process that gives maximum work will always be an isentropic expansion, but the question is one of how to define the exit state of the ideal process relative to the actual process. In the following paragraphs the different definitions are discussed in terms of to what type of turbine they are applied.

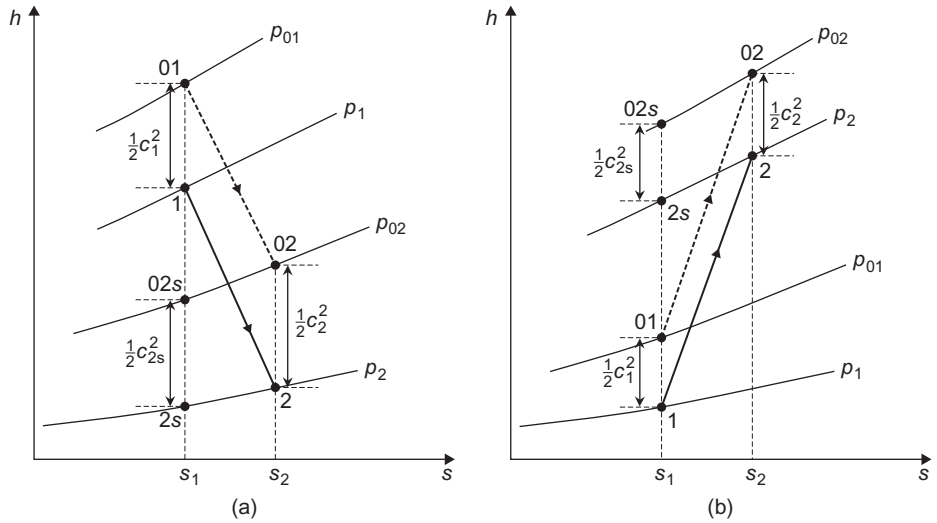

FIGURE 1.10

Enthalpy–entropy diagrams for the flow through an adiabatic turbine and an adiabatic compressor. (a) Turbine expansion process and (b) compression process.

Steam and gas turbines

Figure 1.10(a) shows a simplified Mollier diagram representing the expansion process through an adiabatic turbine. Line 1−2 represents the actual expansion and line 1−2*s* the ideal or reversible expansion. The fluid velocities at entry to and exit from a turbine may be quite high and the corresponding kinetic energies significant. On the other hand, for a compressible fluid the potential energy terms are usually negligible. Hence, the *actual* turbine rotor *specific work* is

$$\Delta W_x = \dot{W}_x/\dot{m} = h_{01} - h_{02} = (h_1 - h_2) + \frac{1}{2}(c_1^2 - c_2^2)$$

There are two main ways of expressing the isentropic efficiency, the choice of definition depending largely upon whether the *exit kinetic energy* is usefully employed or is wasted. If the exhaust kinetic energy is useful, then the ideal expansion is to the same stagnation (or total) pressure as the actual process. The ideal work output is, therefore, that obtained between state points 01 and 02*s*,

$$\Delta W_{\max} = \dot{W}_{\max}/\dot{m} = h_{01} - h_{02s} = (h_1 - h_{2s}) + \frac{1}{2}(c_1^2 - c_{2s}^2)$$

The relevant adiabatic efficiency, η, is called the *total-to-total efficiency* and it is given by

$$\eta_{\text{tt}} = \Delta W_x/\Delta W_{\max} = (h_{01} - h_{02})/(h_{01} - h_{02s}) \tag{1.42a}$$

If the difference between the inlet and outlet kinetic energies is small, i.e., $(1/2)c_1^2 \cong (1/2)c_2^2$, then

$$\eta_{\text{tt}} = (h_1 - h_2)/(h_1 - h_{2s}) \tag{1.42b}$$

An example where the exhaust kinetic energy is not wasted is from the last stage of an aircraft gas turbine where it contributes to the jet propulsive thrust. Likewise, the exit kinetic energy from one stage of a multistage turbine where it can be used in the following stage provides another example.

If, instead, the exhaust kinetic energy cannot be usefully employed and is entirely wasted, the ideal expansion is to the same static pressure as the actual process with zero exit kinetic energy. The ideal work output in this case is that obtained between state points 01 and 2*s*:

$$\Delta W_{\max} = \dot{W}_{\max}/\dot{m} = h_{01} - h_{2s} = (h_1 - h_{2s}) + \frac{1}{2}c_1^2$$

The relevant adiabatic efficiency is called the *total-to-static efficiency* η_{ts} and is given by

$$\eta_{\text{ts}} = \Delta W_x/\Delta W_{\max} = (h_{01} - h_{02})/(h_{01} - h_{2s}) \tag{1.43a}$$

If the difference between inlet and outlet kinetic energies is small, Eq. (1.43a) becomes

$$\eta_{\text{ts}} = (h_1 - h_2)/\left(h_1 - h_{2s} + \frac{1}{2}c_1^2\right) \tag{1.43b}$$

A situation where the outlet kinetic energy is wasted is a turbine exhausting directly to the surroundings rather than through a diffuser. For example, auxiliary turbines used in rockets often have no exhaust diffusers because the disadvantages of increased mass and space utilization are greater than the extra propellant required as a result of reduced turbine efficiency.

By comparing Eqs. (1.42) and (1.43) it is clear that the total-to-static efficiency will always be lower than the total-to-total efficiency. The total-to-total efficiency relates to the internal losses (entropy creation) within the turbine, whereas the total-to-static efficiency relates to the internal losses plus the wasted kinetic energy.

EXAMPLE 1.4

A steam turbine receives 10 kg/s of superheated steam at 20 bar and 350°C which then expands through the turbine to a pressure of 0.3 bar and a dryness fraction of 0.95. Neglecting any changes in kinetic energy, determine

a. the change in enthalpy of the steam in its passage through the turbine
b. the increase in entropy of the steam
c. the total-to-total efficiency of the turbine.
d. the power output of the turbine

Solution

A small Mollier diagram for steam is shown in Appendix E. This can be used to verify the enthalpy and entropy values for the expansion given below.

	T°C	*h* kJ/kg	*s* kJ/kg K
Inlet Steam at 20 bar	350	3140	6.96
Saturated Liquid at 0.3 bar	69.1	289.3	0.944
Saturated Vapor at 0.3 bar	69.1	2624.5	7.767

a. First determine the specific enthalpy and entropy at exit from the steam turbine (state 2). Using Eq. (1.32) for a dryness fraction of 0.95:

$$h_2 = 0.95h_g + 0.05h_f = 0.95 \times 2624.5 + 0.05 \times 289.3 = 2510 \text{ kJ/kg}$$

$$s_2 = 0.95s_g + 0.05s_f = 0.95 \times 7.767 + 0.05 \times 0.944 = 7.43 \text{ kJ/kg K}$$

$$\Delta h_0 = 630 \text{ kJ/kg}$$

b. $$\Delta s = 0.47 \text{ kJ/kg K}$$

c. The efficiency of the turbine expansion process is

$$\eta_{tt} = \frac{h_{01} - h_{02}}{h_{01} - h_{02s}} = \frac{630}{790} = 0.797$$

Note that $h_{02s} = 2350$ kJ/kg is the enthalpy where $p = 0.3$ bar and $s = 6.96$ kJ/kg K.

d. The power output is $\dot{W} = \dot{m}(h_{01} - h_{02}) = 10 \times 630 = 6.3$ MW

Hydraulic turbines

The turbine hydraulic efficiency is a form of the total-to-total efficiency expressed previously. The steady flow energy equation (Eq. 1.11) can be written in differential form for an adiabatic turbine as

$$\mathrm{d}\dot{W}_x = \dot{m}\left[\mathrm{d}h + \frac{1}{2}\mathrm{d}(c^2) + g\mathrm{d}z\right]$$

For an isentropic process, $T\mathrm{d}s = 0 = \mathrm{d}h - \mathrm{d}p/\rho$. The maximum work output for an expansion to the same exit static pressure, kinetic energy, and height as the actual process is, therefore,

$$\dot{W}_{\max} = \dot{m}\left[\int_1^2 \frac{1}{\rho}\mathrm{d}p + \frac{1}{2}(c_1^2 - c_2^2) + g(z_1 - z_2)\right]$$

For an incompressible fluid, the maximum work output from a hydraulic turbine (ignoring frictional losses) can be written

$$\dot{W}_{\max} = \dot{m}\left[\frac{1}{\rho}(p_1 - p_2) + \frac{1}{2}(c_1^2 - c_2^2) + g(z_1 - z_2)\right] = \dot{m}g(H_1 - H_2)$$

where $gH = p/\rho + (1/2)c^2 + gz$ and $\dot{m} = \rho Q$.

The turbine hydraulic efficiency, η_h, is the work supplied by the rotor divided by the hydrodynamic energy difference of the fluid, i.e.,

$$\eta_h = \frac{\dot{W}_x}{\dot{W}_{\max}} = \frac{\Delta W_x}{g[H_1 - H_2]} \tag{1.44}$$

Efficiency of compressors and pumps

The isentropic *efficiency*, η_c, of a compressor or the *hydraulic efficiency* of a pump, η_h, is broadly defined as

$$\eta_c (\text{or } \eta_h) = \frac{\text{useful (hydrodynamic) energy input to fluid in unit time}}{\text{power input to rotor}}$$

The power input to the rotor (or impeller) is always less than the power supplied at the coupling because of external energy losses in the bearings, glands, etc. Thus, the overall efficiency of the compressor or pump is

$$\eta_o = \frac{\text{useful (hydrodynamic) energy input to fluid in unit time}}{\text{power input to coupling of shaft}}$$

Hence, the mechanical efficiency is

$$\eta_m = \eta_o / \eta_c (\text{or } \eta_o / \eta_h) \tag{1.45}$$

For a complete adiabatic compression process going from state 1 to state 2, the specific work input is

$$\Delta W_c = (h_{02} - h_{01}) + g(z_2 - z_1)$$

Figure 1.10(b) shows a Mollier diagram on which the actual compression process is represented by the state change 1−2 and the corresponding ideal process by 1−2s. For an adiabatic compressor in which potential energy changes are negligible, the most meaningful efficiency is the total-to-total efficiency, which can be written as

$$\eta_c = \frac{\text{ideal (minimum) work input}}{\text{actual work input}} = \frac{h_{02s} - h_{01}}{h_{02} - h_{01}} \tag{1.46a}$$

If the difference between inlet and outlet kinetic energies is small, $(1/2)c_1^2 \cong (1/2)c_2^2$ then

$$\eta_c = \frac{h_{2s} - h_1}{h_2 - h_1} \tag{1.46b}$$

For *incompressible* flow, the minimum work input is given by

$$\Delta W_{\min} = \dot{W}_{\min} / \dot{m} = \left[(p_2 - p_1)/p + \frac{1}{2}(c_2^2 - c_1^2) + g(z_2 - z_1) \right] = g[H_2 - H_1]$$

For a pump the hydraulic efficiency is therefore defined as

$$\eta_h = \frac{\dot{W}_{\min}}{\dot{W}_c} = \frac{g[H_2 - H_1]}{\Delta W_c} \tag{1.47}$$

EXAMPLE 1.5

A hydraulic pump delivers 0.4 m^3/s of water against a head of 6.0 m. If the efficiency of the pump is known to be 85%, how much power is needed to drive the pump?

Solution

From Eq. (1.47)

$$\eta_h = \frac{g\Delta H}{\Delta W_c} \quad \therefore \Delta W_c = g\Delta H/\eta_h = \frac{9.81 \times 6}{0.85} = 69.25 \text{ J/kg}$$

$$\therefore P = \rho Q \Delta W_c = 10^3 \times 0.4 \times 69.25 = 27.7 \text{ kW}$$

1.12 Small stage or polytropic efficiency

The isentropic *efficiency* described in the preceding section, although fundamentally valid, can be misleading if used for comparing the efficiencies of turbomachines of differing pressure ratios. Now, any turbomachine may be regarded as being composed of a large number of very small stages, irrespective of the actual number of stages in the machine. If each small stage has the same efficiency, then the isentropic efficiency of the whole machine will be different from the small stage efficiency, the difference depending upon the pressure ratio of the machine. This perhaps rather surprising result is a manifestation of a simple thermodynamic effect concealed in the expression for isentropic efficiency and is made apparent in the following argument.

Compression process

Figure 1.11 shows an enthalpy–entropy diagram on which adiabatic compression between pressures p_1 and p_2 is represented by the change of state between points 1 and 2. The corresponding reversible process is represented by the isentropic line 1 to 2s. It is assumed that the compression process may be divided into a large number of small stages of equal efficiency η_p. For each small stage the actual work input is δW and the corresponding ideal work in the isentropic process is $\delta W_{\min}$. With the notation of Figure 1.11,

$$\eta_P = \frac{\delta W_{\min}}{\delta W} = \frac{h_{xs} - h_1}{h_x - h_1} = \frac{h_{ys} - h_x}{h_y - h_x} = \cdots$$

Since each small stage has the same efficiency, then $\eta_p = (\Sigma \delta W_{\min}/\Sigma \delta W)$ is also true.

From the relation $T\mathrm{d}s = \mathrm{d}h - v\mathrm{d}p$, for a constant pressure process, $(\partial h/\partial s)_{p1} = T$. This means that the higher the fluid temperature, the *greater* is the slope of the constant pressure lines on the Mollier diagram. For a gas where h is a function of T, constant pressure lines diverge and the slope of the line p_2 is greater than the slope of line p_1 at the same value of entropy. At equal values of T, constant pressure lines are of equal slope as indicated in Figure 1.11. For the special case of a

perfect gas (where C_p is constant), $C_p(\mathrm{d}T/\mathrm{d}s) = T$ for a constant pressure process. Integrating this expression results in the equation for a constant pressure line, $s = C_p \log T + \text{constant}$.

Returning now to the more general case, since

$$\Sigma \mathrm{d}W = \{(h_x - h_1) + (h_y - h_x) + \cdots\} = (h_2 - h_1)$$

then

$$\eta_P = [(h_{xs} - h_1) + (h_{ys} - h_s) + \cdots]/(h_2 - h_1)$$

The adiabatic efficiency of the *whole* compression process is

$$\eta_c = (h_{2s} - h_1)/(h_2 - h_1)$$

Due to the divergence of the constant pressure lines

$$\{(h_{xs} - h_1) + (h_{ys} - h_x) + \cdots\} > (h_{2s} - h_1)$$

i.e.,

$$\Sigma \delta W_{\min} > W_{\min}$$

Therefore,

$$\eta_P > \eta_c$$

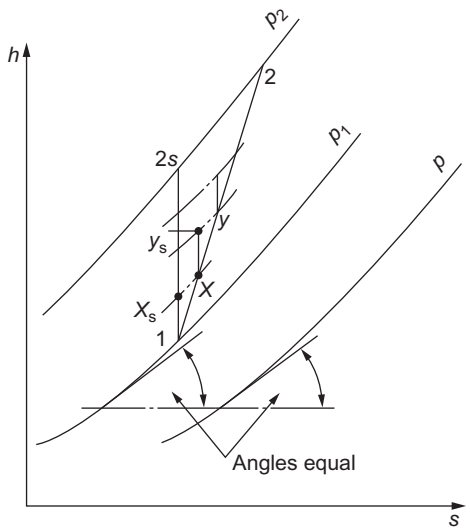

FIGURE 1.11

Compression process by small stages.

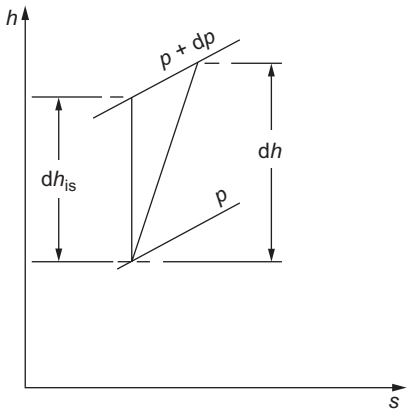

FIGURE 1.12

Incremental change of state in a compression process.

Thus, for a compression process the isentropic efficiency of the machine is *less* than the small stage efficiency, the difference being dependent upon the divergence of the constant pressure lines. Although the foregoing discussion has been in terms of static states it also applies to stagnation states since these are related to the static states via isentropic processes.

Small stage efficiency for a perfect gas

An explicit relation can be readily derived for a perfect gas between small stage efficiency, the overall isentropic efficiency and the pressure ratio. The analysis is for the limiting case of an infinitesimal compressor stage in which the incremental change in pressure is dp as indicated in Figure 1.12. For the actual process the incremental enthalpy rise is dh and the corresponding ideal enthalpy rise is dh_{is}.

The polytropic efficiency for the small stage is

$$\eta_P = \frac{\mathrm{d}h_{is}}{\mathrm{d}h} = \frac{v\mathrm{d}p}{C_p\mathrm{d}T} \tag{1.48}$$

since for an isentropic process $T\mathrm{d}s = 0 = \mathrm{d}h_{is} - v\mathrm{d}p$. Substituting $v = RT/p$ into Eq. (1.48) and using $C_p = \gamma R/(\gamma - 1)$ gives

$$\frac{\mathrm{d}T}{T} = \frac{(\gamma - 1)}{\gamma\eta_P}\frac{\mathrm{d}p}{p} \tag{1.49}$$

Integrating Eq. (1.49) across the whole compressor and taking equal efficiency for each infinitesimal stage gives

$$\frac{T_2}{T_1} = \left(\frac{p_2}{p_1}\right)^{(\gamma-1)/\eta_P\gamma} \tag{1.50}$$

Now the isentropic efficiency for the whole compression process is

$$\eta_c = (T_{2s} - T_1)/(T_2 - T_1) \tag{1.51}$$

if it is assumed that the velocities at inlet and outlet are equal.

For the *ideal* compression process put $\eta_p = 1$ in Eq. (1.50) and so obtain

$$\frac{T_{2s}}{T_1} = \left(\frac{p_2}{p_1}\right)^{(\gamma-1)/\gamma} \tag{1.52}$$

which is equivalent to Eq. (1.37). Substituting Eqs. (1.50) and (1.52) into Eq. (1.51) results in the expression

$$\eta_c = \left[\left(\frac{p_2}{p_1}\right)^{(\gamma-1)/\gamma} - 1\right] \Bigg/ \left[\left(\frac{p_2}{p_1}\right)^{(\gamma-1)/\eta_P\gamma} - 1\right] \tag{1.53}$$

Values of "overall" isentropic efficiency have been calculated using Eq. (1.53) for a range of pressure ratio and different values of η_p; these are plotted in Figure 1.13. This figure amplifies the observation made earlier that the isentropic efficiency of a finite compression process is *less* than the efficiency of the small stages. Comparison of the isentropic efficiency of two machines of different pressure ratios is not a valid procedure since, for equal polytropic efficiency, the compressor with the higher pressure ratio is penalized by the *hidden* thermodynamic effect.

EXAMPLE 1.6

An axial flow air compressor is designed to provide an overall total-to-total pressure ratio of 8 to 1. At inlet and outlet the stagnation temperatures are 300 and 586.4 K, respectively.

Determine the overall total-to-total efficiency and the polytropic efficiency for the compressor. Assume that γ for air is 1.4.

Solution

From Eq. (1.46), substituting $h = C_pT$, the efficiency can be written as

$$\eta_C = \frac{T_{02s} - T_{01}}{T_{02} - T_{01}} = \frac{(p_{02}/p_{01})^{(\gamma-1)/\gamma} - 1}{T_{02}/T_{01} - 1} = \frac{8^{1/3.5} - 1}{586.4/300 - 1} = 0.85$$

From Eq. (1.50), taking logs of both sides and rearranging, we get

$$\eta_p = \frac{\gamma - 1}{\gamma}\frac{\ln(p_{02}/p_{01})}{\ln(T_{02}/T_{01})} = \frac{1}{3.5} \times \frac{\ln 8}{\ln 1.9547} = 0.8865$$

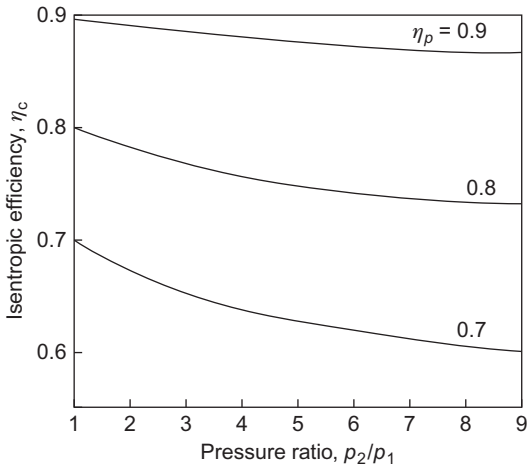

FIGURE 1.13

Relationship between isentropic (overall) efficiency, pressure ratio, and small stage (polytropic) efficiency for a compressor ($\gamma = 1.4$).

Turbine polytropic efficiency

A similar analysis to the compression process can be applied to a perfect gas expanding through an adiabatic turbine. For the turbine the appropriate expressions for an expansion, from a state 1 to a state 2, are

$$\frac{T_2}{T_1} = \left(\frac{p_2}{p_1}\right)^{\eta_p(\gamma-1)/\gamma} \tag{1.54}$$

$$\eta_t = \left[1 - \left(\frac{p_2}{p_1}\right)^{\eta_p(\gamma-1)/\gamma}\right] \Bigg/ \left[1 - \left(\frac{p_2}{p_1}\right)^{(\gamma-1)/\gamma}\right] \tag{1.55}$$

The derivation of these expressions is left as an exercise for the student. "Overall" isentropic efficiencies have been calculated for a range of pressure ratios and polytropic efficiencies, and these are shown in Figure 1.14. The most notable feature of these results is that, in contrast with a compression process, for an expansion, isentropic efficiency *exceeds* small stage efficiency.

Reheat factor

The foregoing relations cannot be applied to steam turbines as vapors do not obey the perfect gas laws. It is customary in steam turbine practice to use a *reheat factor* R_H as a measure of the inefficiency of the complete expansion. Referring to Figure 1.15, the expansion process through an

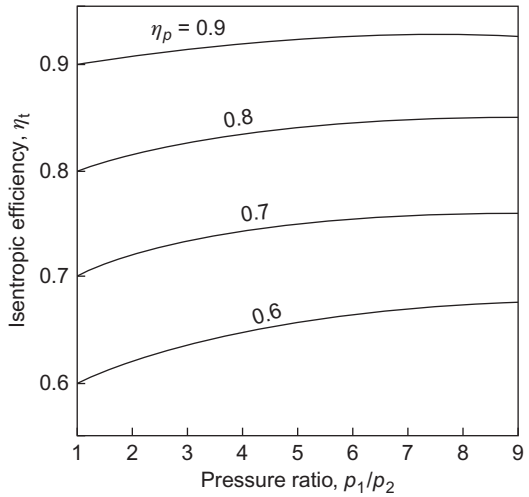

FIGURE 1.14

Turbine isentropic efficiency against pressure ratio for various polytropic efficiencies ($\gamma = 1.4$).

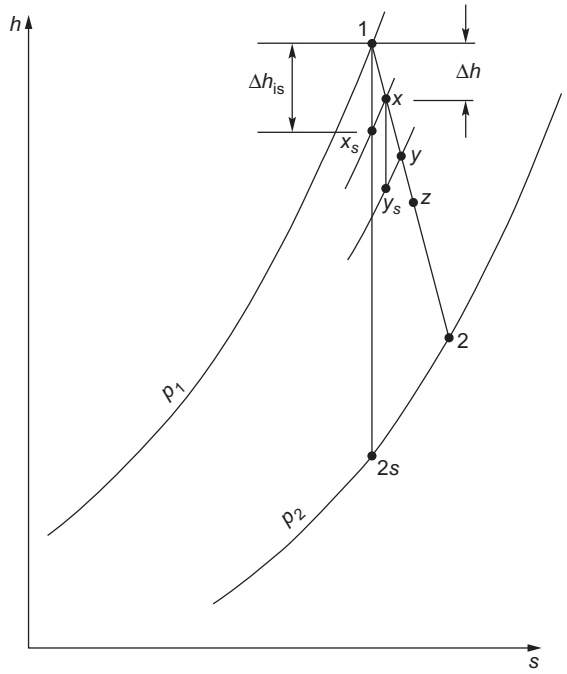

FIGURE 1.15

Mollier diagram showing expansion process through a turbine split up into a number of small stages.

adiabatic turbine from state 1 to state 2 is shown on a Mollier diagram, split into a number of small stages. The reheat factor is defined as

$$R_H = [(h_1 - h_{xs}) + (h_x - h_{ys}) + \cdots]/(h_1 - h_{2s}) = (\Sigma \Delta h_{is})/(h_1 - h_{2s})$$

Due to the gradual divergence of the constant pressure lines on a Mollier chart, R_H is always greater than unity. The actual value of R_H for a large number of stages will depend upon the position of the expansion line on the Mollier chart and the overall pressure ratio of the expansion. In normal steam turbine practice the value of R_H is usually between 1.03 and 1.08.

Now, since the isentropic efficiency of the turbine is

$$\eta_t = \frac{h_1 - h_2}{h_1 - h_{2s}} = \frac{h_1 - h_2}{\Sigma \Delta h_{is}} \times \frac{\Sigma \Delta h_{is}}{h_1 - h_{2s}}$$

then

$$\eta_t = \eta_P R_H \tag{1.56}$$

which establishes the connection between polytropic efficiency, reheat factor and turbine isentropic efficiency.

1.13 The inherent unsteadiness of the flow within turbomachines

It is a less well-known fact often ignored by designers of turbomachinery that turbomachines can only work the way they do because of *flow unsteadiness*. This subject was discussed by Dean (1959), Horlock and Daneshyar (1970), and Greitzer (1986). Here, only a brief introduction to an extensive subject is given.

In the absence of viscosity, the equation for the stagnation enthalpy change of a fluid particle moving through a turbomachine is

$$\frac{Dh_0}{Dt} = \frac{1}{\rho}\frac{\partial p}{\partial t} \tag{1.57}$$

where D/Dt is the rate of change following the fluid particle. Eq. (1.57) shows us that any change in stagnation enthalpy of the fluid is a result of unsteady variations in static pressure. In fact, without unsteadiness, no change in stagnation enthalpy is possible and thus no work can be done by the fluid. This is the so-called "*Unsteadiness Paradox*." Steady approaches can be used to determine the work transfer in a turbomachine, yet the underlying mechanism is fundamentally unsteady.

A physical situation considered by Greitzer (1986) is the axial compressor rotor as depicted in Figure 1.16a. The pressure field associated with the blades is such that the pressure increases from the suction surface (S) to the pressure surface (P). This pressure field moves with the blades and is therefore steady in the relative frame of reference. However, for an observer situated at the point* (in the absolute frame of reference), a pressure that varies with time would be recorded, as shown

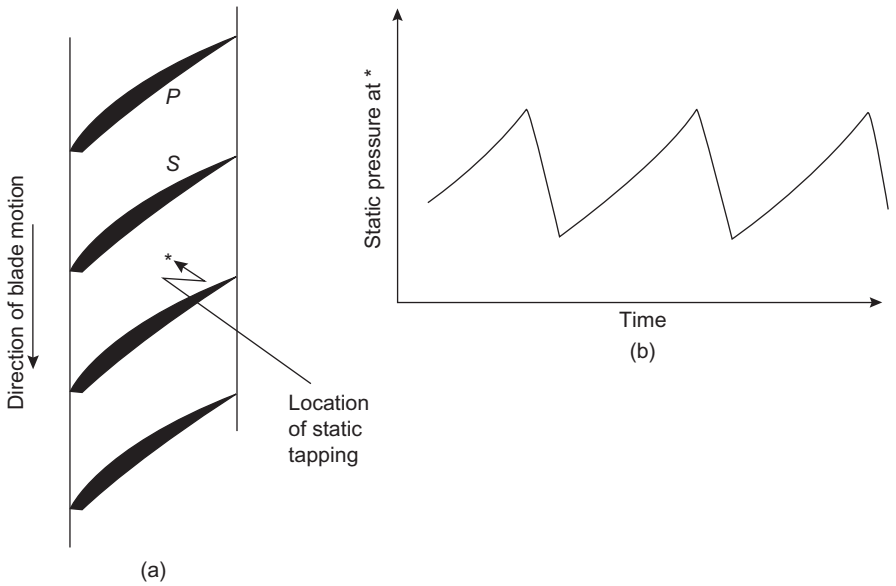

FIGURE 1.16

Measuring the unsteady pressure field of an axial compressor rotor: (a) pressure measured at point* on the casing, (b) fluctuating pressure measured at point*.

in Figure 1.16b. This unsteady pressure variation is directly related to the blade pressure field via the rotational speed of the blades,

$$\frac{\partial p}{\partial t} = \Omega \frac{\partial p}{\partial \theta} = U \frac{\partial p}{r \partial \theta} \tag{1.58}$$

Thus, the fluid particles passing through the rotor experience a positive pressure increase with time (i.e., $\partial p/\partial t > 0$) enthalpies are increased.

PROBLEMS

1. **a.** Air flows adiabatically through a long straight horizontal duct, 0.25 m diameter, at a measured mass flow rate of 40 kg/s. At a particular section along the duct the measured values of static temperature $T = 150°C$ and static pressure $p = 550$ kPa. Determine the average velocity of the airflow and its stagnation temperature.

b. At another station further along the duct, measurements reveal that the static temperature has dropped to 147°C as a consequence of wall friction. Determine the average velocity and the static pressure of the airflow at this station.

Also determine the change in entropy per unit of mass flow between the two stations.

For air assume that $R = 287$ J/(kg K) and $\gamma = 1.4$.

2. Nitrogen gas at a stagnation temperature of 300 K and a static pressure of 2 bar flows adiabatically through a pipe duct of 0.3 m diameter. At a particular station along the duct length the Mach number is 0.6. Assuming the flow is frictionless, determine
a. the static temperature and stagnation pressure of the flow;
b. the mass flow of gas if the duct diameter is 0.3 m.
For nitrogen gas take $R = 297$ J/(kg K) and $\gamma = 1.4$.

3. Air flows adiabatically through a horizontal duct and at a section numbered (1) the static pressure $p_1 = 150$ kPa, the static temperature $T_1 = 200°C$ and the velocity $c_1 = 100$ m/s. At a station further downstream the static pressure $p_2 = 50$ kPa and the static temperature $T_2 = 150°C$. Determine the velocity c_2 and the change in entropy per unit mass of air. For air take $R = 287$ J/(kg K) and $\gamma = 1.4$.

4. For the adiabatic expansion of a perfect gas through a turbine, show that the overall efficiency η_t and small stage efficiency η_p are related by

$$\eta_t = (1 - \varepsilon^{\eta_p})/(1 - \varepsilon)$$

where $\varepsilon = r^{(1-\gamma)/\gamma}$, and r is the expansion pressure ratio, γ is the ratio of specific heats. An axial flow turbine has a small stage efficiency of 86%, an overall pressure ratio of 4.5 to 1 and a mean value of γ equal to 1.333. Calculate the overall turbine efficiency.

5. Air is expanded in a multistage axial flow turbine, the pressure drop across each stage being very small. Assuming that air behaves as a perfect gas with ratio of specific heats γ, derive pressure–temperature relationships for the following processes:
a. reversible adiabatic expansion;
b. irreversible adiabatic expansion, with small stage efficiency η_p;
c. reversible expansion in which the heat loss in each stage is a constant fraction k of the enthalpy drop in that stage;
d. reversible expansion in which the heat loss is proportional to the absolute temperature T.
Sketch the first three processes on a T, s diagram. If the entry temperature is 1100 K and the pressure ratio across the turbine is 6 to 1, calculate the exhaust temperatures in each of the first three cases. Assume that γ is 1.333, that $\eta_p = 0.85$, and that $k = 0.1$.

6. Steam at a pressure of 80 bar and a temperature of 500°C is admitted to a turbine where it expands to a pressure of 0.15 bar. The expansion through the turbine takes place adiabatically with an isentropic efficiency of 0.9 and the power output from the turbine is 40 MW. Using a Mollier chart and/or steam tables determine the enthalpy of the steam at exit from the turbine and the flow rate of the steam.

7. A multistage high-pressure steam turbine is supplied with steam at a stagnation pressure of 7 MPa and a stagnation temperature of 500°C. The corresponding specific enthalpy is 3410 kJ/kg. The steam exhausts from the turbine at a stagnation pressure of 0.7 MPa, the steam having been in a superheated condition throughout the expansion. It can be assumed that the steam behaves like a perfect gas over the range of the expansion and that $\gamma = 1.3$. Given that the turbine flow process has a small-stage efficiency of 0.82, determine

a. the temperature and specific volume at the end of the expansion;
b. the reheat factor.
The specific volume of superheated steam is represented by $pv = 0.231(h - 1943)$, where p is in kPa, v is in m^3/kg, and h is in kJ/kg.

8. A 20 MW back-pressure turbine receives steam at 4 MPa and 300°C, exhausting from the last stage at 0.35 MPa. The stage efficiency is 0.85, reheat factor 1.04, and external losses 2% of the actual isentropic enthalpy drop. Determine the rate of steam flow. At the exit from the first stage nozzles, the steam velocity is 244 m/s, specific volume 68.6 dm^3/kg, mean diameter 762 mm, and steam exit angle 76° measured from the axial direction. Determine the nozzle exit height of this stage.

9. Steam is supplied to the first stage of a five-stage pressure-compounded steam turbine at a stagnation pressure of 1.5 MPa and a stagnation temperature of 350°C. The steam leaves the last stage at a stagnation pressure of 7.0 kPa with a corresponding dryness fraction of 0.95. By using a Mollier chart for steam and assuming that the stagnation state point locus is a straight line joining the initial and final states, determine
a. the stagnation conditions between each stage assuming that each stage does the same amount of work;
b. the total-to-total efficiency of each stage;
c. the overall total-to-total efficiency and total-to-static efficiency assuming the steam enters the condenser with a velocity of 200 m/s;
d. the reheat factor based upon stagnation conditions.

10. Carbon dioxide gas (CO_2) flows *adiabatically* along a duct. At station 1 the static pressure $p_1 = 120$ kPa and the static temperature $T_1 = 120$°C. At station 2 further along the duct the static pressure $p_2 = 75$ kPa and the velocity $c_2 = 150$ m/s.
Determine
a. the Mach number M_2;
b. the stagnation pressure p_{02};
c. stagnation temperature T_{02};
d. the Mach number M_1.
For CO_2 take $R = 188$ J/(kg K) and $\gamma = 1.30$.

11. Air enters the first stage of an axial flow compressor at a stagnation temperature of 20°C and at a stagnation pressure of 1.05 bar and leaves the compressor at a stagnation pressure of 11 bar. The total-to-total efficiency of the compressor is 83%. Determine, the exit stagnation temperature of the air and the polytropic efficiency of the compressor. Assume for air that $\gamma = 1.4$.

References

Çengel, Y. A., & Boles, M. A. (1994). *Thermodynamics: An engineering approach* (2nd ed.). New York, NY: McGraw-Hill.

Dean, R. C. (1959). On the necessity of unsteady flow in fluid mechanics. *Journal of Basic Engineering, Transactions of the American Society of Mechanical Engineers*, *81*, 24–28.

Douglas, J. F., Gasioreck, J. M., & Swaffield, J. A. (1995). *Fluid mechanics* New York, NY: Longman.

Greitzer, E. M. (1986). An introduction to unsteady flow in turbomachines. In D. Japikse (Ed.), *Advanced topics in turbomachinery, principal lecture series no. 2*. Wilder, VT: Concepts ETI.

Harvey, A. H., & Levelt Sengers, J. M. H. (2001). *Thermodynamic properties of water and steam for power generation* (pp. 49–52). Special Publication 958, National Institute of Standards and Technology.

Harvey, A. H., Peskin, A. P. & Klein, S. A. (2000). *NIST/ASME Steam Properties*, NIST Standard Reference Database 10, Version 2.2, National Institute of Standards and Technology.

Horlock, J. H., & Daneshyar, H. (1970). Stagnation pressure changes in unsteady flow. *Aeronautical Quarterly*, *22*, 207–224.

National Institute of Standards and Technology. (2012). Websites for access to thermodynamic properties of water and steam. Online property calculator:<http://webbook.nist.gov/chemistry/fluid/> Tabulated data: <http://www.nist.gov/srd/upload/NISTIR5078.htm>.

Reynolds, C., & Perkins, C. (1977). *Engineering Thermodynamics* (2nd ed.). New York, NY: McGraw-Hill.

Rogers, G. F. C., & Mayhew, Y. R. (1992). *Engineering Thermodynamics, Work and Heat Transfer* (4th ed.). New York, NY: Longman.

Rogers, G. F. C., & Mayhew, Y. R. (1995). *Thermodynamic and Transport Properties of Fluids (SI Units)* (5th ed.). Malden, MA: Blackwell.

Wagner, W., & Pruss, A. (2002). The IAPWS formulation 1995 for the thermodynamic properties of ordinary water substance for general and scientific use. *The Journal of Physical Chemistry Reference Data*, *31*, 387–535.

Wu, C. H. (1952). A general theory of three-dimensional flow in subsonic and supersonic turbomachines in radial and mixed flow types. NACA TN 2604. National Aeronautics and Space Administration, Washington DC.

CHAPTER

Dimensional Analysis: Similitude

2

If you have known one you have known all.
Terence, *Phormio*

2.1 Dimensional analysis and performance laws

The widest comprehension of the general behavior of all turbomachines is, without doubt, obtained from *dimensional analysis*. This is the formal procedure whereby the group of variables representing some physical situation is reduced to a smaller number of dimensionless groups. When the number of independent variables is not too great, dimensional analysis enables experimental relations between variables to be found with the greatest economy of effort. Dimensional analysis applied to turbomachines has two further important uses: (a) prediction of a prototype's performance from tests conducted on a scale model (similitude), and (b) determination of the most suitable type of machine, on the basis of maximum efficiency, for a specified range of head, speed, and flow rate. Several methods of constructing nondimensional groups have been described by Douglas, Gasiorek, and Swaffield (1995) and Shames (1992), among other authors. The subject of dimensional analysis was made simple and much more interesting by Taylor (1974) in his comprehensive account of the subject and this approach is the one adopted in this book.

Adopting the simple approach of elementary thermodynamics, a control surface of fixed shape, position, and orientation is drawn around the turbomachine (Figure 2.1). Across this boundary, fluid flows steadily, entering at station 1 and leaving at station 2. As well as the flow of fluid, there is a flow of work across the control surface, transmitted by the shaft either to or from the machine. All details of the flow within the machine can be ignored and only externally observed features such as shaft speed, flow rate, torque, and change in fluid properties across the machine need be considered. To be specific, let the turbomachine be a *pump* (although the analysis could apply to other classes of turbomachine) driven by an electric motor. The speed of rotation Ω can be adjusted by altering the current to the motor; the volume flow rate Q can be *independently* adjusted by means of a throttle valve. For fixed values of the set Q and Ω, all other variables, such as torque, τ, and head, H, are thereby established. The choice of Q and Ω as *control variables* is clearly arbitrary and any other pair of independent variables such as τ and H could equally well have been chosen. The important point to recognize is that there are, for this pump, *two* control variables.

If the fluid flowing is changed for another of different density, ρ and viscosity, μ, the performance of the machine will be affected. Note also that, for a turbomachine handling compressible fluids, other *fluid properties* are important and these are discussed later.

Fluid Mechanics and Thermodynamics of Turbomachinery. DOI: http://dx.doi.org/10.1016/B978-0-12-415954-9.00002-4

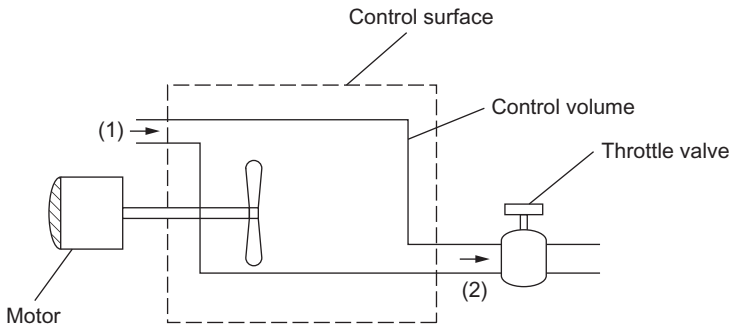

FIGURE 2.1

Turbomachine considered as a control volume.

So far we have considered only one particular turbomachine, namely a pump of a given size. To extend the range of this discussion, the effect of the *geometric variables* on the performance must now be included. The size of machine is characterized by the impeller diameter, D, the shape can be expressed by a number of length ratios, l_1/D, l_2/D, etc., and the surface finish can be characterized by a representative roughness length, e.

2.2 Incompressible fluid analysis

The performance of a turbomachine can be expressed in terms of the control variables, geometric variables, and fluid properties. Take as an example a hydraulic pump. It is convenient to regard the net energy transfer, gH, the efficiency, η, and the power supplied, P, as dependent variables and to write the three functional relationships as

$$gH = f_1\left(Q, \Omega, D, \rho, \mu, e, \frac{l_1}{D}, \frac{l_2}{D}, \ldots\right) \tag{2.1a}$$

$$\eta = f_2\left(Q, \Omega, D, \rho, \mu, e, \frac{l_1}{D}, \frac{l_2}{D}, \ldots\right) \tag{2.1b}$$

$$P = f_3\left(Q, \Omega, D, \rho, \mu, e, \frac{l_1}{D}, \frac{l_2}{D}, \ldots\right) \tag{2.1c}$$

For a family of *geometrically similar* machines, the shape parameters, l_1/D and l_2/D are constant and may be omitted. Dimensional analysis[1] can then be applied to determine the dimensionless

[1]This is the approach used to reduce the experimental variables in a fluid mechanical problem (and in other areas, as well) to the minimum number of nondimensional parameters. It is explained at some length in elementary textbooks such as Franzini and Finnemore (1997) and White (2011).

groups that are needed to describe *dynamic similarity*. The number of dimensionless groups required can be found using Buckingham's π-theorem (Buckingham, 1914). This theorem states that for M independent variables and N dimensions, there must be at least $M - N$ nondimensional groups. In this case, for 6 variables $(Q, \Omega, D, \rho, \mu, e)$ and 3 dimensions (mass, length, time), there must be $6 - 3 = 3$ independent nondimensional groups. However, the form of the nondimensional groups required is not obvious and consideration of the physics is necessary. For a pump, the selection of ρ, Ω, and D as common factors avoids the appearance of special fluid terms (e.g., μ, Q) in more than one group and allows gH, η, and P to be made explicit. Hence, the three relationships in Eqs. (2.1a–c) can be reduced to the following easily verified forms:

Energy transfer coefficient, sometimes called head coefficient:

$$\psi = \frac{gH}{(\Omega D)^2} = f_4\left(\frac{Q}{\Omega D^3}, \frac{\rho \Omega D^2}{\mu}, \frac{e}{D}\right) \tag{2.2a}$$

Efficiency, which is already nondimensional:

$$\eta = f_5\left(\frac{Q}{\Omega D^3}, \frac{\rho \Omega D^2}{\mu}, \frac{e}{D}\right) \tag{2.2b}$$

Power coefficient:

$$\hat{P} = \frac{P}{\rho \Omega^3 D^5} = f_4\left(\frac{Q}{\Omega D^3}, \frac{\rho \Omega D^2}{\mu}, \frac{e}{D}\right) \tag{2.2c}$$

The nondimensional group $Q/(\Omega D^3)$ is a volumetric flow coefficient. In nonhydraulic flow turbomachines, an alternative to $Q/(\Omega D^3)$ that is frequently used is the velocity (or flow) coefficient $\Phi = c_m/U$, where U is the mean blade speed and c_m the average meridional velocity. Since

$$Q = c_m \times \text{flow area} \propto c_m D^2 \quad \text{and} \quad U \propto \Omega D$$

then

$$\frac{Q}{\Omega D^3} \propto \frac{c_m}{U} = \Phi$$

Both of these nondimensional groups are usually referred to as a flow coefficient, Φ.

The nondimensional group $\rho \Omega D^2/\mu$ is a form of Reynolds number, denoted Re. Physically, Reynolds number represents the ratio between the inertial forces and the viscous forces within a fluid flow. For low viscosity fluid moving at high velocity, the Reynolds number is high; conversely for slow moving fluid with high viscosity, the Reynolds number is low. It is found experimentally that provided $Re > 2 \times 10^5$, the effects of Re on the performance of turbomachines is small. This is true because at high Re, the viscous boundary layers on the blades of a turbomachine are generally turbulent and very thin. They, therefore, have little impact on the global flow field. Efficiency is the variable that can be most affected by Reynolds number and typically η will rise up to a few per cent as Re increases an order of magnitude. Note that for turbomachines handling water, the kinematic viscosity, $\nu = \mu/\rho$, is very small and, therefore, the corresponding Reynolds number is always high and its effects may be ignored to a first approximation.

The effects of surface finish are captured by the nondimensional group, e/D, called the roughness ratio or relative roughness. At high Reynolds numbers, greater surface roughness tends to increase skin friction losses and thus reduce the efficiency. The effects at lower Reynolds numbers are more complex as the boundary layers may be laminar or undergoing transition to turbulence. If it is assumed that both the surface finish effects are small and that the Reynolds numbers are high, the functional relationships for geometrically similar hydraulic turbomachines are:

$$\psi = f_4(Q/\Omega D^3) \tag{2.3a}$$

$$\eta = f_5(Q/\Omega D^3) \tag{2.3b}$$

$$\hat{P} = f_6(Q/\Omega D^3) \tag{2.3c}$$

This is as far as the reasoning with dimensional analysis alone can be taken; the actual *form* of the functions f_4, f_5, and f_6 must be ascertained by experiment.

One relation between ψ, Φ, η, and $\hat{P}$ may be immediately stated. For a pump, the *net hydraulic power*, P_N, equals ρQgH, which is the minimum shaft power required in the absence of all losses. As shown in Chapter 1, we define pump efficiency as $\eta = P_N/P = \rho QgH/P$, where P is the actual power to drive the pump. Therefore,

$$P = \frac{1}{\eta}\left(\frac{Q}{\Omega D^3}\right)\frac{gH}{\Omega^2 D^2}\rho\Omega^3 D^5 \tag{2.4}$$

Thus, f_6 may be derived from f_4 and f_5 since $\hat{P} = \Phi\psi/\eta$. For a turbine, the net hydraulic power supplied to it, P_N, is clearly greater than the actual power output from the machine and the efficiency $\eta = P/P_N$. By reasoning similar to that provided for the pump, we can see that for a turbine $\hat{P} = \Phi\psi\eta$.

2.3 Performance characteristics for low-speed machines

The operating condition of a turbomachine will be *dynamically similar* at two different rotational speeds if all fluid velocities at *corresponding points* within the machine are in the same direction and proportional to the blade speed. In other words, the flow is dynamically similar if the streamline patterns relative to the blades are geometrically similar. When two flow fields are dynamically similar, then *all* the dimensionless groups are the same. As shown by Eqs. (2.3a–c), for an incompressible flow machine (one in which $M < 0.3$ everywhere) operating at high Reynolds number, dynamic similarity is achieved once the flow coefficient is the same. Thus, the nondimensional presentation of performance data has the important practical advantage of collapsing results into a single curve that would otherwise require a multiplicity of curves if plotted dimensionally.

Evidence in support of the foregoing assertion is provided in Figure 2.2, which shows experimental results obtained by one author (at the University of Liverpool) on a simple centrifugal laboratory pump. Within the normal operating range of this pump, $0.03 < Q/(\Omega D^3) < 0.06$, very little systematic scatter is apparent, which might be associated with a Reynolds number effect, for the range of speeds $2500 \le \Omega \le 5000$ rpm. For smaller flows, $Q/(\Omega D^3) < 0.025$, the flow became unsteady and the manometer readings of uncertain accuracy, but nevertheless, dynamically similar

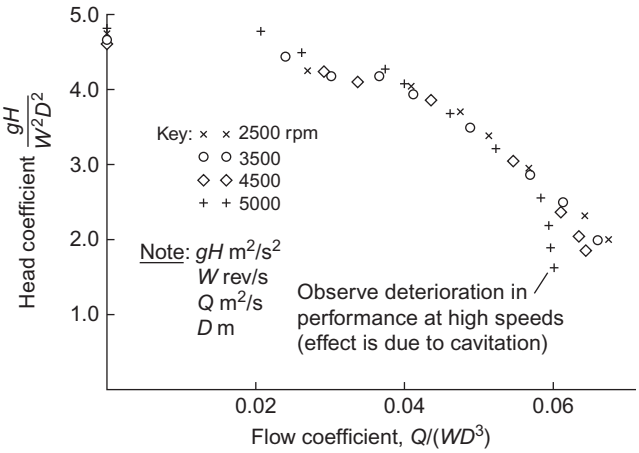

FIGURE 2.2

Dimensionless head–volume characteristic of a centrifugal pump.

conditions still appear to hold true. At high flow rates there is a systematic deviation away from the "single-curve" law at higher rotational speeds. This effect is due to *cavitation*, a high-speed phenomenon of hydraulic machines caused by the release of vapor bubbles at low pressures, which is discussed later in this chapter. It will be clear at this stage that under cavitating flow conditions, dynamical similarity is not possible.

The nondimensional results shown in Figure 2.2 have, of course, been obtained for a particular pump. They would also be approximately valid for a range of *different* pump sizes so long as all these pumps are geometrically similar and cavitation is absent. Thus, neglecting any change in performance due to change in Reynolds number, the dynamically similar results in Figure 2.2 can be applied to predicting the dimensional performance of a given pump for a series of required speeds. Figure 2.3 shows such a dimensional presentation. It will be clear from the preceding discussion that the locus of dynamically similar points in the $H-Q$ field lies on a parabola since H varies as Ω^2 and Q varies as Ω.

EXAMPLE 2.1

A model centrifugal pump with an efficiency of 88% is tested at a rotational speed of 3000 rpm and delivers 0.12 m^3/s of water against a head of 30 m. Using the similarity rules given above, determine the rotational speed, volume flow rate, and power requirement of a geometrically similar prototype at eight times the scale of the model and working against a head of 50 m.

Solution

From the similarity laws, for the same head coefficient,

$$H_p/(\Omega_p^2 D_p^2) = H_m/(\Omega_m^2 D_m^2)$$

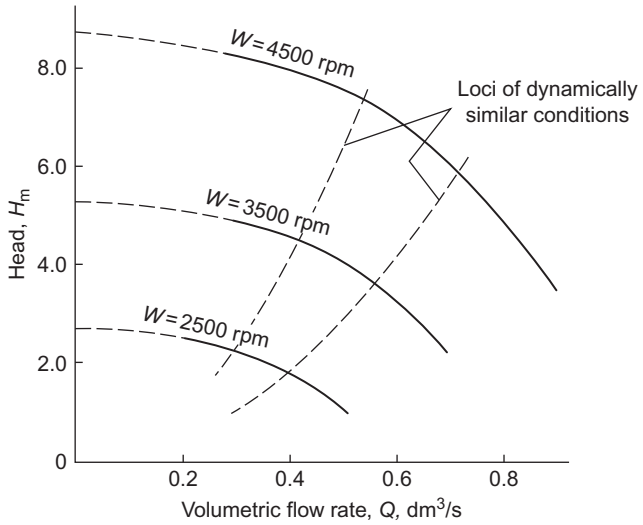

FIGURE 2.3

Extrapolation of characteristic curves for dynamically similar conditions at $\Omega = 3500$ rpm.

where subscript m is for the model and p for the prototype. Hence,

$$\Omega_p = \Omega_m \left(\frac{D_m}{D_p}\right)\left(\frac{H_p}{H_m}\right)^{\frac{1}{2}} = 3000 \times \frac{1}{8} \times \left(\frac{50}{30}\right)^{\frac{1}{2}} = 484.1 \text{ rpm}$$

Operating at the same volumetric flow coefficient,

$$\frac{Q_p}{\Omega_p D_p^3} = \frac{Q_m}{\Omega_m D_m^3}$$

$$Q_p = Q_m \frac{\Omega_p}{\Omega_m}\left(\frac{D_p}{D_m}\right)^3 = 0.12 \times \frac{484.1}{3000} \times 8^3 = 9.914 \text{ m}^3/\text{s}$$

Finally, the power for the prototype can be determined assuming the efficiency is the same as the model:

$$P_p = \frac{\rho g Q_p H_p}{\eta_p} = (10^3 \times 9.81 \times 9.914 \times 50)/0.88 = 5.526 \times 10^6 = 5.536 \text{ MW}$$

2.4 Compressible flow analysis

The application of dimensional analysis to compressible flow increases, not unexpectedly, the complexity of the functional relationships obtained in comparison with those already found for

incompressible fluids. Even if the fluid is regarded as a perfect gas, in addition to the previously used fluid properties, two further characteristics are required; these are a_{01}, the stagnation speed of sound at entry to the machine, and γ, the ratio of specific heats C_p/C_ν. In the following analysis, the compressible fluids under discussion are either perfect gases or dry vapors approximating in behavior to a perfect gas.

Another choice of variables is preferred when appreciable density changes occur across the machine. Instead of volume flow rate Q, the mass flow rate $\dot{m}$ is used; likewise for the head change H, the isentropic *stagnation enthalpy* change Δh_{0s} is employed. The choice of this last variable is a significant one for, in an ideal and adiabatic process, Δh_{0s} is equal to the work done per unit mass of fluid. Since heat transfer from the casings of turbomachines is, in general, of negligible magnitude compared with the flux of energy through the machine, temperature on its own may be safely excluded as a fluid variable. However, temperature is an easily observable characteristic and, for a perfect gas, can be easily introduced by means of the equation of state, $p/\rho = RT$.

The performance parameters Δh_{0s}, η, and P, for a turbomachine handling a compressible flow, can be expressed functionally as

$$\Delta h_{0s}, \eta, P = f(\mu, \Omega, D, \dot{m}, \rho_{01}, a_{01}, \gamma) \tag{2.5}$$

Because ρ_0 and a_0 change through a turbomachine, the values of these fluid variables are selected at inlet, denoted by subscript 1. Equation (2.5) expresses *three* separate functional relationships, each of which consists of eight variables. Again, selecting ρ_{01}, Ω, and D as common factors, each of these three relationships may be reduced to five dimensionless groups:

$$\frac{\Delta h_{0s}}{\Omega^2 D^2}, \eta, \frac{P}{\rho_{01}\Omega^3 D^5} = f\left(\frac{\dot{m}}{\rho_{01}\Omega D^3}, \frac{\rho_{01}\Omega D^2}{\mu}, \frac{\Omega D}{a_{01}}, \gamma\right) \tag{2.6a}$$

The group $\Omega D/a_{01}$ can be regarded as a *blade Mach number* because ΩD is proportional to blade speed. Since this appears as an independent variable on the right-hand side of the equation, it can be used to rewrite the preceding relationships in terms of the inlet stagnation speed of sound a_{01}:

$$\frac{\Delta h_{0s}}{a_{01}^2}, \eta, \frac{P}{\rho_{01} a_{01}^3 D^2} = f\left(\frac{\dot{m}}{\rho_{01} a_{01} D^2}, \frac{\rho_{01} a_{01} D}{\mu}, \frac{\Omega D}{a_{01}}, \gamma\right) \tag{2.6b}$$

For a machine handling a perfect gas, a different set of functional relationships is often more useful. These may be found either by selecting the appropriate variables for a perfect gas and working through again from first principles or, by means of some rather straightforward transformations, rewriting Eq. (2.6b) to give more suitable groups. The latter procedure is preferred here as it provides a useful exercise. As an example, consider an adiabatic compressor handling a perfect gas. The isentropic stagnation enthalpy rise can be written as $C_p(T_{02s} - T_{01})$ for a perfect gas. As shown in Chapter 1, the isentropic relationship between temperature and pressure is given by

$$\frac{T_{02s}}{T_{01}} = \left(\frac{p_{02}}{p_{01}}\right)^{(\gamma-1)/\gamma}$$

The isentropic stagnation enthalpy rise can therefore be written as

$$\Delta h_{0s} = C_p T_{01}[(p_{02}/p_{01})^{(\gamma-1)/\gamma} - 1] \tag{2.7}$$

Since $C_p = \gamma R/(\gamma - 1)$ and $a_{01}^2 = \gamma R T_{01}$, then $a_{01}^2 = (\gamma - 1) C_p T_{01}$ and thus,

$$\frac{\Delta h_{0s}}{a_{01}^2} = \frac{\Delta h_{0s}}{(\gamma - 1) C_p T_{01}} = \frac{1}{(\gamma - 1)} \left[\left(\frac{p_{02}}{p_{01}} \right)^{(\gamma-1)/\gamma} - 1 \right] = f(p_{02}/p_{01}, \gamma)$$

Using the equation of state, $p/\rho = RT$, the nondimensional mass flow can be more conveniently expressed as

$$\hat{m} = \frac{\dot{m}}{\rho_{01} a_{01} D^2} = \frac{\dot{m} R T_{01}}{p_{01} \sqrt{\gamma R T_{01}} D^2} = \frac{\dot{m} \sqrt{\gamma R T_{01}}}{D^2 p_{01} \gamma}$$

The power coefficient can also be rewritten as

$$\hat{P} = \frac{P}{\rho_{01} a_{01}^3 D^2} = \frac{\dot{m} C_p \Delta T_0}{(\rho_{01} a_{01} D^2) a_{01}^2} = \hat{m} \frac{C_p \Delta T_0}{a_{01}^2} = \frac{\hat{m}}{(\gamma - 1)} \frac{\Delta T_0}{T_{01}}$$

Collecting together these newly formed nondimensional groups and inserting them in Eq. (2.6b) leads to a simpler and more useful functional relationship:

$$\frac{p_{02}}{p_{01}}, \eta, \frac{\Delta T_0}{T_{01}} = f\left(\frac{\dot{m} \sqrt{\gamma R T_{01}}}{D^2 p_{01}}, \frac{\Omega D}{\sqrt{\gamma R T_{01}}}, Re, \gamma \right) \tag{2.8}$$

A key advantage of Eq. (2.8) over Eq. (2.6b) is that the nondimensional groups are in terms of inlet and exit stagnation temperatures and pressures, which are parameters that are readily measured for a turbomachine. For a machine handling a single gas, γ can be dropped as an independent variable. If, in addition, the machine operates only at high Reynolds numbers (or over a small speed range), Re can also be dropped. Equation (2.8) can then be written with just two nondimensional groups on the right-hand side:

$$\frac{p_{02}}{p_{01}}, \eta, \frac{\Delta T_0}{T_{01}} = f\left(\frac{\dot{m} \sqrt{C_p T_{01}}}{D^2 p_{01}}, \frac{\Omega D}{\sqrt{\gamma R T_{01}}} \right) \tag{2.9a}$$

In this equation, the nondimensional group, $\dot{m} \sqrt{C_p T_{01}}/D^2 p_{01}$ is often referred to as the *flow capacity*, introduced in Section 1.10 of Chapter 1. This is the most widely used form of nondimensional mass flow, although the forms in Eqs (2.6b) and (2.8) are also valid. For machines of a known size and fixed working fluid, it has become customary, in industry at least, to delete γ, R, C_p, and D from Eq. (2.9a) and similar expressions. Under these conditions, Eq. (2.9a) becomes

$$\frac{p_{02}}{p_{01}}, \eta, \frac{\Delta T_0}{T_{01}} = f\left(\frac{\dot{m} \sqrt{T_{01}}}{p_{01}}, \frac{\Omega}{\sqrt{T_{01}}} \right) \tag{2.9b}$$

Note that by omitting the diameter D and gas constant R, the independent variables on the right-hand side of Eq. (2.9b) are no longer dimensionless.

For a given turbomachine, Eq. (2.9b) is sometimes expressed in terms of *corrected flow* and *corrected speed*. These are the mass flow and speed that would be measured if the machine was operating at standard sea-level atmospheric pressure and temperature, p_a and T_a.

The corrected mass flow and corrected speed are defined as

$$\frac{\dot{m}\sqrt{\theta}}{\delta} \quad \text{and} \quad \frac{\Omega}{\sqrt{\theta}}$$

where

$$\theta = \frac{T_{01}}{T_a} \quad \text{and} \quad \delta = \frac{p_{01}}{p_a}$$

The functional relationships in Eq. (2.9b) can then be rewritten as

$$\frac{p_{02}}{p_{01}}, \eta, \frac{\Delta T_0}{T_{01}} = f\left(\frac{\dot{m}\sqrt{\theta}}{\delta}, \frac{\Omega}{\sqrt{\theta}}\right) \tag{2.9c}$$

Note that the parameters on the right-hand side are no longer nondimensional. The units of the first parameter are kg/s and that of the second are rad/s. To nondimensionalize these parameters, they can be normalized by their values at the design point.

Equations (2.9a–c) show that two variables are required to fix the operating point of a compressible flow machine. This compares to the one variable needed to fix the operating point of an incompressible flow machine, Eqs. (2.3a–c). In all cases, for dynamic similarity, the streamline pattern relative to the blades must be geometrically similar. In an incompressible flow machine, it is enough just to fix the relative inlet angle to the blades (via the flow coefficient). In a compressible flow machine, the streamline pattern within the blade rows also depends on the variation of density through the blade passages. Therefore, a second parameter is needed to fix the flow Mach numbers and thus fix the variation of density.

Similarly to the incompressible case, the performance parameters, p_{02}/p_{01}, η, and $\Delta T_0/T_{01}$ are not entirely independent and it is straightforward to write an equation relating the three. For a compressor, the isentropic efficiency is defined in Chapter 1 and can be written as

$$\eta_c = \frac{\Delta h_{0s}}{\Delta h_0} = \frac{((p_{02}/p_{01})^{\gamma/(\gamma-1)} - 1)}{\Delta T_0/T_{01}} \tag{2.10a}$$

The corresponding isentropic efficiency for a turbine is

$$\eta_t = \frac{\Delta h_0}{\Delta h_{0s}} = \frac{\Delta T_0/T_{01}}{[(p_{01}/p_{02})^{(\gamma-1/\gamma)} - 1]} \tag{2.10b}$$

where p_{01}/p_{02} is the overall total pressure ratio of the turbine.

Flow coefficient and stage loading

In compressible flow machines, the flow coefficient, Φ, is an important parameter for design and analysis. It is defined in the same way as given earlier for incompressible machines, i.e., $\Phi = c_m/U$, where U is the mean blade speed and c_m the average meridional velocity. However, in the compressible case, the flow coefficient alone cannot be used to fix the operating condition of a

machine. This is because the flow coefficient is also a function of the nondimensional parameters given in Eq. (2.9a). It is straightforward to show this via the following algebraic manipulation:

$$\varphi = \frac{c_m}{U} = \frac{\dot{m}}{\rho_{01} A_1 U} = \frac{\dot{m} R T_{01}}{p_{01} A_1 U} \propto \frac{\dot{m}\sqrt{(C_p T_{01})}}{D^2 p_{01}} \times \frac{\sqrt{(C_p T_{01})}}{U} = f\left(\frac{\dot{m}\sqrt{C_p T_{01}}}{D^2 p_{01}}, \frac{\Omega D}{\sqrt{\gamma R T_{01}}}\right)$$

Note that the nondimensional mass flow, $\dot{m}\sqrt{C_p T_{01}}/D^2 p_{01}$ is distinct from a flow coefficient because it does not involve the blade speed.

The stage loading, ψ, is another key design parameter for all nonhydraulic turbomachines. It is defined as

$$\psi = \frac{\Delta h_0}{U^2} \tag{2.11}$$

This parameter is similar in form to the head coefficient ψ used in hydraulic machines (Eq. (2.2a)), but there are subtle differences. Most importantly, stage loading is a nondimensional form of the actual specific stagnation enthalpy change, whereas the head coefficient is a nondimensional measure of the maximum, or isentropic, work that a hydraulic machine can achieve. Note that the stage loading can be related to the nondimensional parameters in Eq. (2.9a) as follows:

$$\psi = \frac{\Delta h_0}{U^2} = \frac{C_p \Delta T_0}{C_p T_{01} U^2} \times \frac{C_p T_{01}}{U^2} = \frac{\Delta T_0}{T_{01}} \Big/ \left(\frac{U}{\sqrt{(C_p T_{01})}}\right)^2 = f\left\{\frac{\dot{m}\sqrt{(C_p T_{01})}}{D^2 p_{01}}, \frac{\Omega D}{\sqrt{(\gamma R T_{01})}}\right\}$$

Thus, the stage loading is also fixed once both the nondimensional mass flow and the nondimensional blade speed (or blade Mach number) are fixed. In many cases, the stage loading is used in place of the power coefficient $\Delta T_0/T_0$ given in Eq. (2.9a).

2.5 Performance characteristics for high-speed machines

Compressors

The performance (or characteristic) map of a high-speed compressor is essentially a graphical representation of the functional relationships given in Eq. (2.9b). Figure 2.4 shows a performance map for a transonic fan and Figure 2.5 shows a performance map for a high-speed multistage axial compressor. In both cases, the pressure ratio across the machine is plotted as a function of $\dot{m}\sqrt{T_{01}}/p_{01}$ for several fixed values of $\Omega/\sqrt{T_{01}}$, which is the usual method of presentation. Figures 2.4 and 2.5 also show contours of compressor isentropic efficiency on the same axes.

Each of the constant speed curves on the compressor characteristic terminate at the instability line (often referred to as the surge or stall line). Beyond this point, the operation is unstable. A discussion of the phenomena of surge and stall is included in Chapter 5. At high speeds and low pressure ratios, the constant speed curves become vertical. In these regions of the characteristic, no further increase in $\dot{m}\sqrt{T_{01}}/p_{01}$ is possible since the Mach number across a section of the machine has reached unity and the flow is *choked*.

A compressor is able to operate anywhere below and to the right of the surge line. However, it is usually constrained to a single *operating line*, which is set by the flow area downstream of the compressor. A single operating line is shown in Figure 2.4. The design operating line is usually

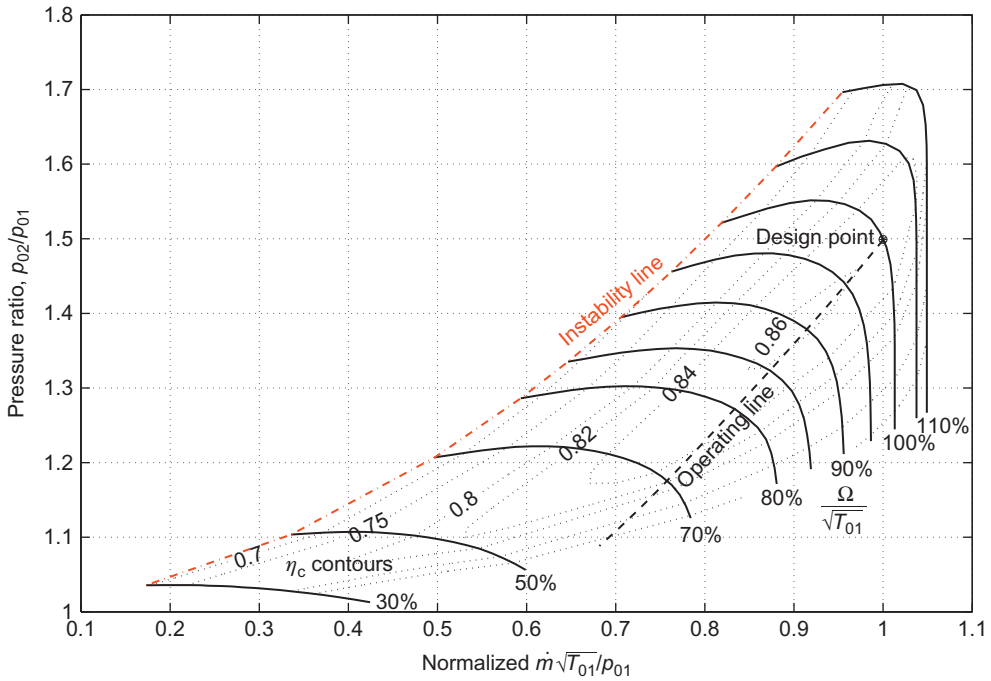

FIGURE 2.4

Characteristic map of a transonic fan for a civil aircraft jet engine.

(*Based on data from Cornell, 1975*)

specified so that it passes as close as possible to the point of peak compressor efficiency. However, its exact position is a matter of judgment for the compressor designer. The term *stall margin* is often used to describe the relative position of the operating line and the surge line. There are several ways of defining the surge margin (*SM*) and a fairly simple one often used is

$$SM = \frac{(pr)_s - (pr)_o}{(pr)_o} \tag{2.12}$$

where $(pr)_o$ is a pressure ratio at a point on the operating line at a certain corrected speed $\Omega/\sqrt{T_{01}}$ and $(pr)_s$ is the corresponding pressure ratio on the surge line at the same corrected speed. With this definition a surge margin of 20% would be typical for a compressor used within a turbojet engine. Several other definitions of *stall margin* and their merits are discussed by Cumpsty (1989).

Turbines

Figure 2.6 shows a typical high-speed axial turbine characteristic. The behavior of turbines is very different to that of compressors and this is reflected in the way the characteristic has been presented. Turbines are able to operate with a high-pressure ratio across each stage because the

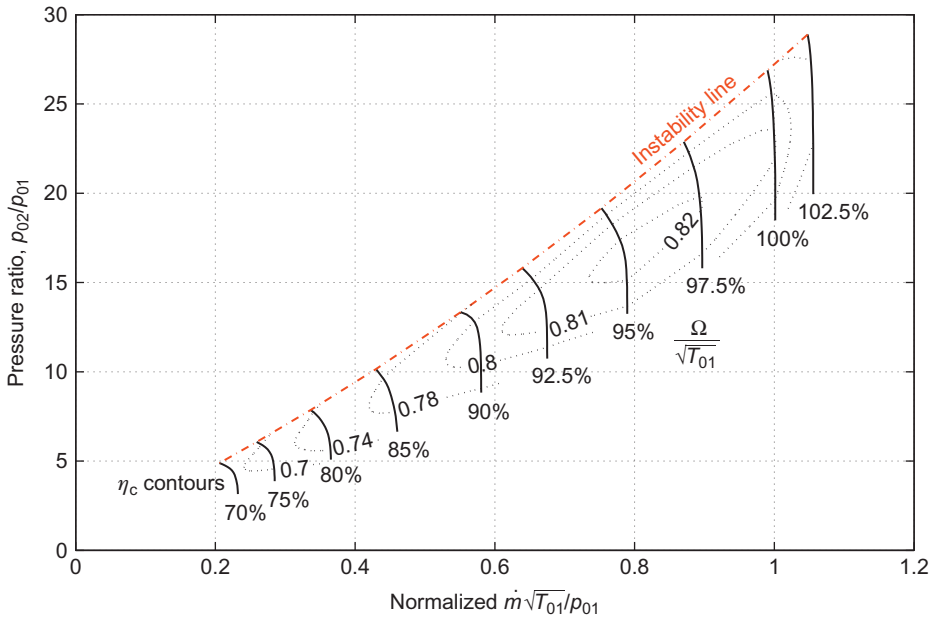

FIGURE 2.5

Performance map of a 10-stage high-speed axial compressor.

(*Adapted from Cline et al., 1983*)

boundary layers on the surfaces of the turbine blades are accelerating and therefore stable. The high-pressure ratios soon lead to choking in the turbine stator blades and therefore a fixed nondimensional mass flow through the machine. Once the turbine stators are fully choked, the operating point is independent of $\Omega/\sqrt{T_{01}}$ because the rotation of the blades has virtually no influence on either the turbine pressure ratio or the nondimensional mass flow rate.

As shown by Figure 2.6, it is more revealing to plot the flow capacity and turbine efficiency as a function of the turbine pressure ratio rather than the other way around, since it is usually the pressure ratio across a turbine that is specified and, for a high-speed case, there is limited variation in $\dot{m}\sqrt{T_{01}}/p_{01}$ for different values of $\Omega/\sqrt{T_{01}}$.

EXAMPLE 2.2

The compressor with the performance map shown in Figure 2.5 is tested at sea level on a stationary test bed on a day when the atmospheric temperature and pressure is 298 K and 101 kPa, respectively. When running at its design operating point, the mass flow rate through the compressor is measured as 15 kg/s and the rotational speed is 6200 rpm. Determine the mass flow rate and rotational speed when the compressor is operating at the design operating point during high altitude cruise with an inlet stagnation temperature of 236 K and an inlet stagnation pressure of 10.2 kPa.

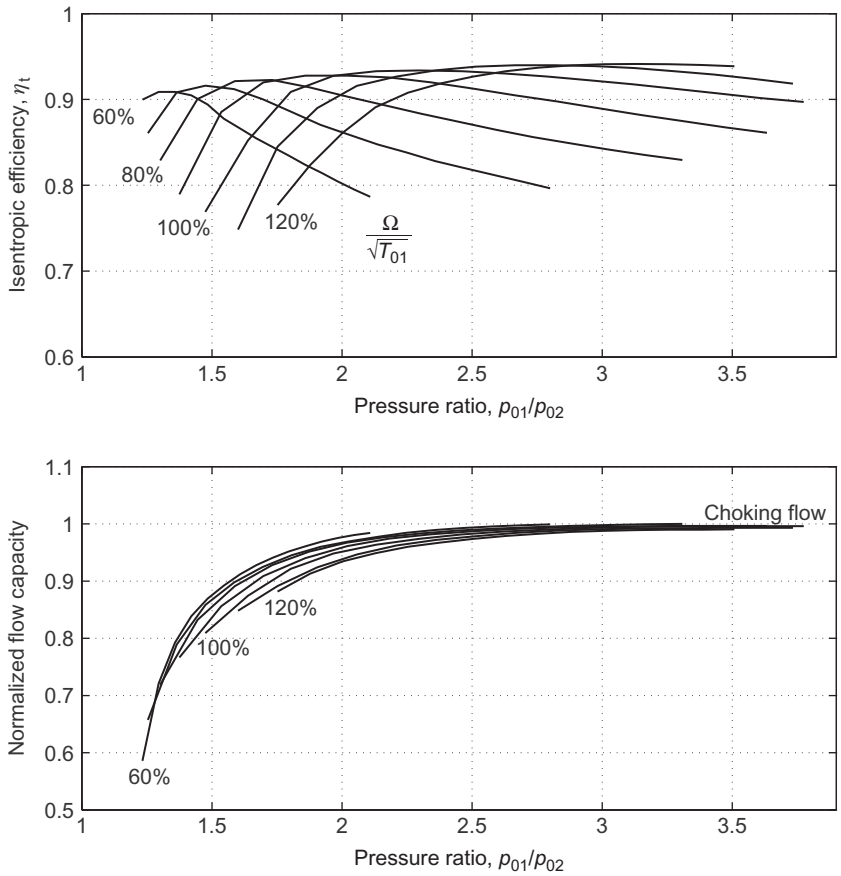

FIGURE 2.6

Overall characteristic of a two-stage high-speed axial turbine.

The design pressure ratio of the compressor is 22. Using the compressor characteristic in Figure 2.5, determine the compressor isentropic and polytropic efficiency at the design point. Hence calculate the required power input at the cruise condition. Assume throughout for air that $\gamma = 1.4$ and $C_p = 1005$ J/kg/K.

Solution

At cruise and during the test the compressor is operating at its design nondimensional operating point. Therefore, all the nondimensional performance parameters of the compressor will be the same at both conditions.

The nondimensional mass flow is

$$\left[\frac{\dot{m}\sqrt{\gamma RT_{01}}}{D^2 p_{01}}\right]_{\text{cruise}} = \left[\frac{\dot{m}\sqrt{\gamma RT_{01}}}{D^2 p_{01}}\right]_{\text{test}}$$

Since there is no change in the dimensions of the compressor or in the gas properties of the working fluid, this reduces to

$$\left[\frac{\dot{m}\sqrt{T_{01}}}{p_{01}}\right]_{\text{cruise}} = \left[\frac{\dot{m}\sqrt{T_{01}}}{p_{01}}\right]_{\text{test}}$$

During the test, the compressor is stationary and therefore the inlet air stagnation temperature and pressure are equal to the atmospheric static temperature and pressure. The mass flow at cruise is thus

$$\dot{m}_{\text{cruise}} = \left[\frac{p_{01}}{\sqrt{T_{01}}}\right]_{\text{cruise}} \times \left[\frac{\dot{m}\sqrt{T_{01}}}{p_{01}}\right]_{\text{test}} = \frac{10.2}{\sqrt{236}} \times \frac{15 \times \sqrt{298}}{101} = \underline{1.70 \text{ kg/s}}$$

Similarly for the nondimensional speed,

$$\left[\frac{\Omega}{\sqrt{T_{01}}}\right]_{\text{cruise}} = \left[\frac{\Omega}{\sqrt{T_{01}}}\right]_{\text{test}}$$

and thus,

$$\Omega_{\text{cruise}} = \sqrt{T_{01,\text{cruise}}} \times \left[\frac{\Omega}{\sqrt{T_{01}}}\right]_{\text{test}} = \sqrt{236} \times \left[\frac{6200}{\sqrt{298}}\right] = \underline{5520 \text{ rpm}}$$

From, Figure 2.5, at 100% speed and a pressure ratio of 22, $\underline{\eta_c = 0.81}$.

$$\frac{T_{02}}{T_{01}} = \frac{(p_{02}/p_{01})^{(\gamma-1)/\gamma} - 1}{\eta_c} + 1 = \frac{22^{1/3.5} - 1}{0.81} + 1 = 2.751$$

From Eq. (1.50), the polytropic efficiency is given by

$$\eta_p = \frac{\gamma - 1}{\gamma}\frac{\ln(p_{02}/p_{01})}{\ln(T_{02}/T_{01})} = \frac{1}{3.5}\frac{\ln(22)}{\ln(2.751)} = \underline{0.873}$$

As expected, the polytropic efficiency is significantly higher than the isentropic efficiency at this pressure ratio. The input power to the compressor at the cruise condition can be found using the fact that the nondimensional power coefficient $\Delta T_0/T_0$ is unchanged between the two conditions:

$$\frac{\Delta T_0}{T_{01}} = \frac{T_{02}}{T_{01}} - 1 = 1.751$$

$$P_{\text{cruise}} = [\dot{m}C_p\Delta T_0]_{\text{cruise}} = [\dot{m}C_p T_{01}]_{\text{cruise}} \frac{\Delta T_0}{T_{01}} = 1.70 \times 1005 \times 236 \times 1.751 = \underline{706 \text{ kW}}$$

2.6 Specific speed and specific diameter

The turbomachine designer is often faced with the basic problem of deciding what type of machine will be the best choice for a given duty. At the outset of the design process, some overall requirements of the machine will usually be known. For a hydraulic pump, these would include the head required, H, the volume flow rate, Q, and the rotational speed, Ω. In contrast, if a high-speed gas turbine was being considered, the initial specification would probably cover the mass flow rate, $\dot{m}$, the specific work, Δh_0, and the preferred rotational speed, Ω.

Two nondimensional parameters called the *specific speed*, Ω_s, and *specific diameter*, D_s, are often used to decide upon the choice of the most appropriate machine (see Balje (1981)). The specific speed is derived from the nondimensional groups defined in Eqs. (2.3a–c) in such a way that the characteristic diameter D of the turbomachine is eliminated. The value of Ω_s gives the designer a guide to the type of machine that will provide the normal requirement of high efficiency at the design condition. Similarly, the specific diameter is derived from these groups by eliminating the speed, Ω.

Consider a hydraulic turbomachine with fixed geometry. As shown by Eq. (2.3b), there will be a unique relationship between efficiency and flow coefficient if Reynolds number effects are negligible and cavitation absent. If the maximum efficiency $\eta = \eta_{max}$ occurs at a unique value of flow coefficient $\Phi = \Phi_1$ and corresponding unique values of $\psi = \psi_1$ and $\hat{P} = \hat{P}_1$, it is possible to write

$$\frac{Q}{\Omega D^3} = \Phi_1 = \text{constant} \tag{2.13a}$$

$$\frac{gH}{\Omega^2 D^2} = \psi_1 = \text{constant} \tag{2.13b}$$

$$\frac{P}{\rho \Omega^3 D^5} = \hat{P}_1 = \text{constant} \tag{2.13c}$$

It is a simple matter to combine any pair of these expressions in such a way as to eliminate the diameter. For a pump, the customary way of eliminating D is to divide $\Phi_1^{1/2}$ by $\psi_1^{3/4}$. Thus, at the operating point giving maximum efficiency,

$$\Omega_s = \frac{\Phi_1^{1/2}}{\psi_1^{3/4}} = \frac{\Omega Q^{1/2}}{(gH)^{3/4}} \tag{2.14}$$

where Ω_s is called the *specific speed*. The term *specific speed* is justified only to the extent that Ω_s is directly proportional to Ω. It is sometimes referred to as a *shape factor* since its value characterizes the shape of the machine required.

In the case of a hydraulic turbine, the *power specific speed* Ω_{sp} is often used and it is defined by

$$\Omega_{sp} = \frac{\hat{P}_1^{1/2}}{\psi_1^{5/4}} = \frac{\Omega (P/\rho)^{1/2}}{(gH)^{5/4}} \tag{2.15}$$

There is a simple connection between Ω_s and Ω_{sp}. By dividing Eq. (2.15) by Eq. (2.14), we obtain, for a hydraulic turbine,

$$\frac{\Omega_{sp}}{\Omega_s} = \frac{\Omega (P/\rho)^{1/2}}{(gH)^{5/4}} \frac{(gH)^{3/4}}{\Omega Q^{1/2}} = \left(\frac{P}{\rho g Q H} \right)^{1/2} = \sqrt{\eta} \tag{2.16}$$

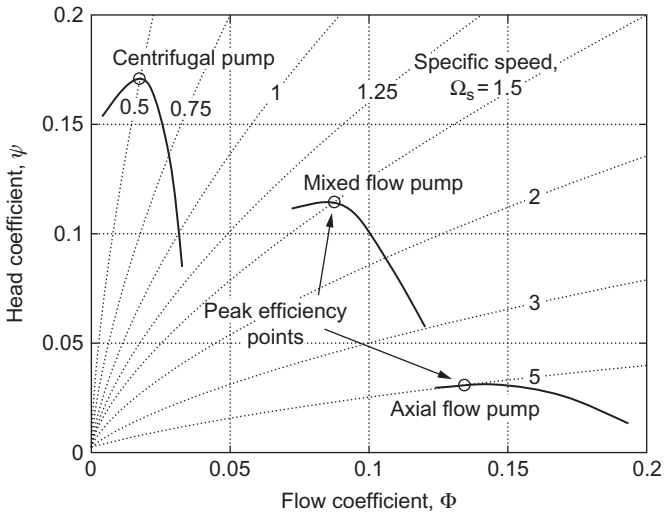

FIGURE 2.7

Contours of specific speed showing characteristics of various pump types.

Similarly to specific speed, to form the *specific diameter*, any pair of expressions in Eqs. (2.13a–c) can be used to eliminate the speed, Ω. In the case of a pump, we divide $\psi^{1/4}$ by $\Phi^{1/2}$. Thus,

$$D_s = \frac{\psi_1^{1/4}}{\Phi_1^{1/2}} = \frac{D(gH)^{1/4}}{Q^{1/2}} \tag{2.17}$$

Equations (2.14), (2.15), and (2.17) are *dimensionless*. It is *always* safer and less confusing to calculate specific speed and specific diameter in one or another of these forms rather than dropping the factors g and ρ, which would make the equations *dimensional* and any values of specific speed or specific diameter obtained using them would then depend upon the choice of the units employed. The dimensionless forms of Ω_s (and Ω_{sp}) and D_s are the only ones used in this book. Another point arises from the fact that the rotational speed, Ω, can be expressed in rad/s, rev/s or rpm, and therefore, although Ω_s is dimensionless, numerical values of specific speed are sometimes specified in rev/s rather than rad/s. In this book, unless otherwise stated, the speed of rotation is taken to be in rad/s.

The concept of specific speed just described is illustrated in Figure 2.7. This shows contours of Ω_s plotted as a function of flow coefficient, Φ, and head coefficient, ψ, using Eq. (2.14). Also plotted on the same axes are typical characteristics of three types of hydraulic pumps. This plot demonstrates how for a given type of machine, one value of Ω_s passes through the operating point of peak efficiency. In other words, once the specific speed is known, the machine type giving peak efficiency can be determined. Figure 2.7 also shows how a low specific speed suits radial machines, since these tend to give a high pressure change to a low mass flow rate. In contrast, axial flow stages with widely spaced blades are suited to high specific speed applications because they impart a small pressure change to a large mass flow rate.

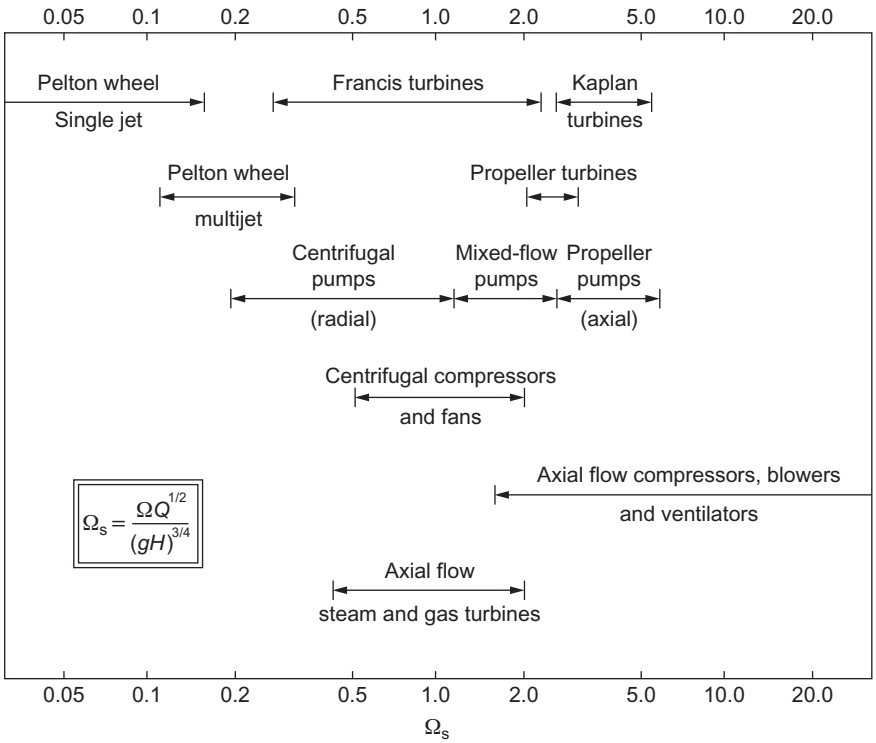

FIGURE 2.8

Range of specific speeds for various types of turbomachine.

(*From Csanady, 1964*)

Given that specific speed is defined at the point of maximum efficiency of a turbomachine, it becomes a parameter of great importance in selecting the type of machine required for a given duty. The maximum efficiency condition *replaces* the condition of geometric similarity, so that any alteration in specific speed implies that the machine design changes. Broadly speaking, each different class of machine has its optimum efficiency within its own fairly narrow range of specific speed. Figure 2.8 shows the ranges of specific speed appropriate to different types of turbomachine. Once the specific speed at the design condition is found, a well-designed machine selected using Figure 2.8 should give the maximum possible design efficiency.

EXAMPLE 2.3

a. A hydraulic turbine with a runner outside diameter of 4.31 m operates with an effective head, H, of 543 m at a volume flow rate of 71.5 m^3/s and produces 350 MW of shaft power at a rotational speed of 333 rpm. Determine the specific speed, the specific diameter, and efficiency of this turbine.

b. Another geometrically and dynamically similar turbine with a runner 6.0 m diameter is to be built to operate with an effective head of 500 m. Determine the required flow rate, the expected power output, and the rotational speed of the turbine.

Solution

a. *Note*: All speeds are first converted to rad/s; therefore, $\Omega = 333 \times \pi/30 = 34.87$ rad/s.

Using Eq. (2.14), the specific speed is

$$\Omega_s = \Omega Q^{1/2}/(gH)^{3/4} = \frac{34.87 \times 71.5^{0.5}}{(9.81 \times 543)^{0.75}} = 0.473 \text{ rad}$$

Using Eq. (2.17), the specific diameter is

$$D_s = \frac{D(gH)^{1/4}}{Q^{1/2}} = \frac{4.31 \times (9.81 \times 543)^{1/4}}{71.4^{1/2}} = 4.354$$

For the turbine, the net hydraulic power is

$$P_n = \rho g Q H = 9810 \times 71.5 \times 543 = 380.9 \times 10^6 = 380.9 \text{ MW}$$

The turbine efficiency is

$$\eta = 350/380.9 = 0.919$$

b. Transposing Eq. (2.17), we can find the volume flow rate:

$$Q = (D/D_s)^2 (gH)^{1/2} = (6/4.354)^2 (9.81 \times 500)^{1/2} = 133 \text{ m}^3/\text{s}$$

and the power output is

$$P = \eta \rho g Q H = 0.919 \times 9810 \times 133 \times 500 = 599.5 \text{ MW}$$

We can determine the rotational speed in rpm from Eq. (2.14) as

$$\Omega = \Omega_s (gH)^{3/4}/Q^{1/2} = 0.473 \times \frac{30}{\pi} \times (9.81 \times 500)^{3/4}/133^{1/2} = 229.6 \text{ rpm}$$

The Cordier diagram

A rough but useful guide to the selection of the most appropriate type and size of compressor, pump, or fan for a given duty and optimum efficiency is obtained by means of the Cordier diagram, Figure 2.9. Although the method was originally devised by Cordier (1953), further details are more readily accessed from the work of Csanady (1964) and, with some added elaboration, by Lewis (1996). Figure 2.9 shows, on the right-hand side, the recommended ranges for various types of turbomachines for which the method applies. It must be mentioned that the line presented is, in fact, a mean curve based upon results obtained from a large number of machines, so it represents a fairly broad spread of results on either side of the line. For many designs, it would be possible to diverge from the line and still obtain high-performance pumps, fans, or compressors.

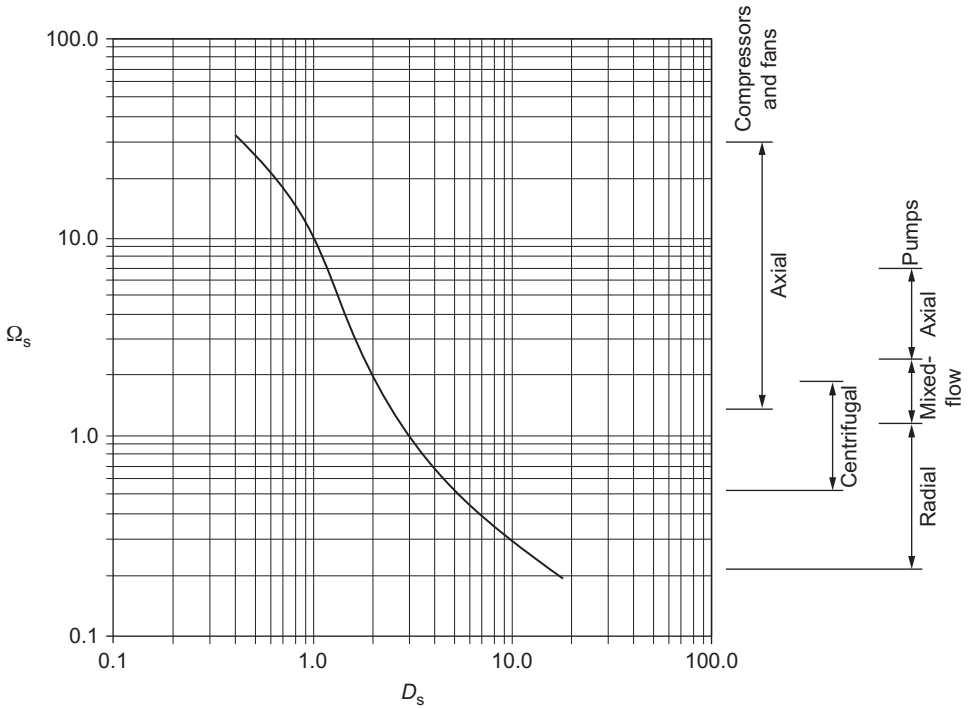

FIGURE 2.9

Cordier diagram for machine selection.

Following Lewis, an interesting and useful alternative presentation of the Cordier diagram can be made with ordinates Φ and ψ from the relationships already given. From Eqs (2.14) and (2.17), we can derive the flow coefficient, Φ, and stage loading coefficient, ψ, as

$$\Phi = 1/(\Omega_s D_s^3) \tag{2.18}$$

$$\psi = 1/(\Omega_s^2 D_s^2) \tag{2.19}$$

By introducing the Cordier line data into these last two equations and replotting this information, a new and more definite shape of the optimum machine curves results, shown in Figure 2.10. The new curve is clearly divided into two main parts with centrifugal pumps operating at a fairly constant head coefficient at roughly $\psi = 0.1$ over a flow coefficient range of $0.001 \leq \Phi \leq 0.04$ and axial machines operating with a wide range of stage loading coefficients, $0.005 \leq \psi \leq 0.05$ and also a wide range of Φ. Casey, Zwyssig, and Robinson (2010) show that the shape of the Cordier line and the two distinct parts of the curve in Figure 2.10 are caused by the variation in centrifugal effects in the different compressor types: In radial machines, almost all the pressure change is due to the centrifugal effects generated by a change in flow radius, whereas these effects are absent in axial machines (see Chapter 7).

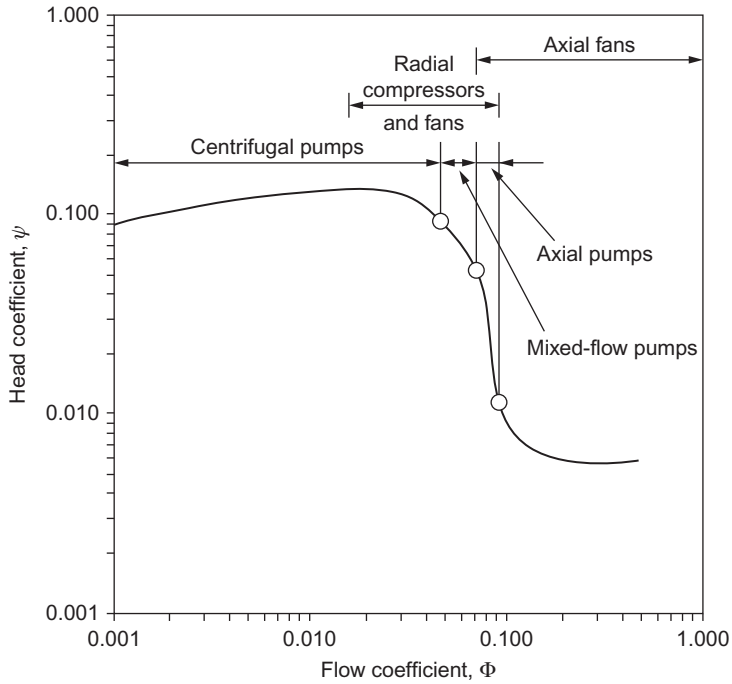

FIGURE 2.10

Chart of ψ versus Φ for various pumps and fans.

Mixed-flow machines are stuck in between axials and radials with quite a narrow range of both ψ and Φ. However, in some cases, mixed-flow machines are the crucial choice. Lewis (1996) points out that applications that require a high mass flow at a high pressure ratio, such as gas cooled nuclear reactors and hovercraft lift fans, are ideally suited for mixed-flow fans rather than a single-stage axial compressor. Recently, mixed-flow turbomachinery has found application in specialist domestic appliances. Figure 2.11 shows a mixed-flow fan used for air movement.

EXAMPLE 2.4

The mixed-flow fan shown in Figure 2.11 is designed to provide a pressure rise of 450 Pa to air at a volume flow rate of 27 L/s. The impeller design rotational speed is 8300 rpm and its tip diameter is 90 mm.

Calculate the specific speed and specific diameter of the fan and mark the location of the design on the Cordier line in Figure 2.9. Also determine the design flow coefficient and head coefficient. Assuming that the required flow rate and pressure rise cannot be changed, estimate the rotational speed that would be needed for an axial flow fan to be suitable for the design.

Take air density to be 1.21 kg/m^3.

FIGURE 2.11

Mixed flow impeller used for efficient air movement.

(*With kind permission of Dyson Ltd.*)

Solution

The specific speed can be calculated from the design specification, as follows:

$$\Omega_s = \frac{\Omega Q^{1/2}}{(gH)^{3/4}} = \frac{\Omega Q^{1/2}}{(\Delta p/\rho)^{3/4}} = \frac{8300 \times \pi/30 \times \sqrt{27 \times 10^{-3}}}{(450/1.21)^{0.75}} \cong \underline{1.69 \text{ rad}}$$

Similarly, the specific diameter can be calculated:

$$D_s = \frac{D(gH)^{1/4}}{Q^{1/2}} = \frac{D(\Delta p/\rho)^{1/4}}{Q^{1/2}} = \frac{0.09 \times (450/1.21)^{.25}}{\sqrt{27 \times 10^{-3}}} \cong \underline{2.41}$$

Marking these values on Figure 2.9, it is clear that the design lies close to the Cordier line and that a mixed-flow device is most suitable. The design flow coefficient and head coefficient, using Eqs (2.18) and (2.19), are

$$\Phi = \frac{Q}{\Omega D^3} = \frac{1}{(\Omega_s D_s^3)} = \frac{1}{1.69 \times 2.41^3} = \underline{0.042}$$

$$\psi = \frac{\Delta p/\rho}{\Omega^2 D^2} = \frac{1}{(\Omega_s^2 D_s^2)} = \frac{1}{1.69^2 \times 2.41^2} = \underline{0.060}$$

For an axial machine to be suitable, Figures 2.8 and 2.9 suggest that the specific speed must be increased to a value of around 3 or higher. With a fixed flow and pressure rise, the specific speed is proportional to the rotational speed. Therefore, a specific speed greater than 3 requires a rotational speed:

$$\Omega_2 \geq \Omega_1 \frac{\Omega_{s2}}{\Omega_{s1}} = 8300 \times \frac{3}{1.69} = \underline{14700 \text{ rpm}}$$

Compressible specific speed

Specific speed as defined in Eq. (2.14) has mostly been applied to the design and selection of low-speed and hydraulic turbomachines. However, the notion of specific speed can equally be applied to a compressible flow machine, and it is particularly useful for determining whether an axial or a radial flow machine is best for a particular requirement. As described in Baskharone (2006), the application of the important concept of specific speed to compressible turbomachines has to be modified because of the large variation in the values of volume flow rate, Q, as well as the particular meaning of the head, H. The specific speed when applied to high-speed turbomachines is therefore expressed in terms of parameters appropriate to compressible flow:

$$\Omega_s = \Omega\left(\frac{\dot{m}}{\rho_e}\right)^{1/2}(\Delta h_{0s})^{-3/4} \tag{2.20}$$

Note that in Eq. (2.20), the isentropic specific work, Δh_{0s}, is used rather than the actual specific work, Δh_0. In the case of a compressor, this makes sense since the isentropic specific work can be determined from the required pressure ratio p_{02}/p_{01} using Eq. (2.7). The required pressure ratio is likely to be known at the outset of the design process, whereas the actual specific work input depends on the compressor efficiency, which in general will not be known. In the case of a turbine, the actual specific work is more likely to be a known requirement. The efficiency can be estimated or the isentropic work approximated to be equal to the actual work required.

Equation (2.20) also requires the density of the working fluid at exit ρ_e. This can be estimated from $\rho_e = p_e/RT_e$, with p_e and T_e taken as the isentropic static pressure and temperature at exit from the machine. Other definitions are sometimes used, but this is the simplest and any extra uncertainty introduced is likely to be small and will have no effect on the preferred type of machine selected.

EXAMPLE 2.5

An air turbine is required for a dentist's drill. For the drill bit to effectively abrade tooth enamel, the turbine must rotate at high speed, around 300,000 rpm. The turbine must also be very small so that it can be used to access all parts of a patient's mouth and an exit air flow rate in the region of 10 L/min is required for this. The turbine is to be driven by supply air at a pressure of 3 bar and a temperature of 300 K.

Calculate the specific speed of the turbine and use this to determine the type of machine required. Also estimate the power consumption of the turbine and account for how this power is used.

Solution

Putting the quantities into standard SI units,

$$\text{the rotational speed, } \Omega = 300,000 \times \pi/30 = 10,000\pi \text{ rad}/s$$

$$\text{the exit volume flow rate, } \dot{m}/\rho_e = Q_e = 10/(1000 \times 60) = 0.000167 \text{ m}^3/\text{s}$$

The isentropic specific work can be estimated assuming an isentropic expansion through the turbine. Treating air as a perfect gas with $\gamma = 1.4$ and $C_p = 1005$ J/kg/K,

$$\Delta h_{0s} = C_p T_{01}\left[1 - (p_{02}/p_{01})^{(\gamma-1)/\gamma}\right] = 1005 \times 300 \times \left[1 - \left(\frac{1}{3}\right)^{0.4/1.4}\right] = 81.29 \text{ kJ/kg}$$

The specific speed can now be calculated from the information provided using Eq. (2.20):

$$\Omega_s = \frac{\Omega Q^{1/2}}{(gH)^{3/4}} = \Omega\left(\frac{\dot{m}}{\rho_e}\right)^{1/2}(\Delta h_{0s})^{-3/4} = \frac{10,000 \times \pi \times 0.000167^{1/2}}{(81,290)^{3/4}} \cong \underline{0.084 \text{ rad}}$$

Using the plot of machine type versus specific speed presented in Figure 2.8, it is immediately apparent that the only kind of turbine suitable for this very low specific speed is a Pelton wheel. In fact, all modern high-speed dentist drills use Pelton wheels and a photograph of a typical impeller from one is shown in Figure 2.12.

The power used by the turbine can be approximated from the mass flow rate and the specific isentropic work output. Using a typical value for the exit air density, this gives

$$P = \dot{m}\Delta h_{0s} = \rho_e Q_e \Delta h_{0s} \cong 1.16 \times 0.000167 \times 81,290 = \underline{15.7W}$$

The majority of this power will be dissipated as heat through friction in the bearings, losses in the Pelton wheel, and friction with the tooth. This heat dissipation is the reason why an appreciable amount of cooling water is required for modern high-speed dentist drills!

FIGURE 2.12

Pelton Wheel Turbine Impeller from a High Speed Dental Drill, Tip Diameter 10 mm.

(*With kind permission of Sirona Dental*)

2.7 Cavitation

Cavitation is the boiling of a liquid at normal temperature when the static pressure is made sufficiently low. It may occur at the entry to pumps or at the exit from hydraulic turbines in the vicinity of the moving blades. The dynamic action of the rotor blades causes the static pressure to reduce

locally in a region that is already normally below atmospheric pressure and cavitation can commence. The phenomenon is accentuated by the presence of dissolved gases that are released with a reduction in pressure.

For the purpose of illustration, consider a centrifugal pump operating at constant speed and capacity. By steadily reducing the inlet pressure head, a point is reached when streams of small vapor bubbles appear within the liquid and close to solid surfaces. This is called *cavitation inception* and commences in the regions of lowest pressure. These bubbles are swept into regions of higher pressure where they collapse. This condensation occurs suddenly, the liquid surrounding the bubbles either hitting the walls or adjacent liquid. The pressure wave produced by bubble collapse (with a magnitude on the order of 400 MPa) momentarily raises the pressure level in the vicinity and the action ceases. The cycle then repeats itself and the frequency may be as high as 25 kHz (Shepherd, 1956). The repeated action of bubbles collapsing near solid surfaces leads to the well-known cavitation erosion.

The collapse of vapor cavities generates noise over a wide range of frequencies—up to 1 MHz has been measured (Pearsall, 1972), i.e., so-called white noise. Apparently the collapsing smaller bubbles cause the higher frequency noise, and the larger cavities the lower frequency noise. Noise measurement can be used as a means of detecting cavitation (Pearsall, 1967). Pearsall and McNulty (1968) have shown experimentally that there is a relationship between cavitation noise levels and erosion damage on cylinders and conclude that a technique could be developed for predicting the occurrence of erosion.

Up to this point, no detectable deterioration in performance occurs. However, with further reduction in inlet pressure, the bubbles increase both in size and number, coalescing into pockets of vapor that affects the whole field of flow. This growth of vapor cavities is usually accompanied by a sharp drop in pump performance as shown conclusively in Figure 2.2 (for the 5000 rpm test data). It may seem surprising to learn that, with this large change in bubble size, the solid surfaces are much less likely to be damaged than at inception of cavitation. The avoidance of cavitation inception in conventionally designed machines can be regarded as one of the essential tasks of both pump and turbine designers. However, in certain recent specialized applications, pumps have been designed to operate under *supercavitating* conditions. Under these conditions, large size vapor bubbles are formed, but bubble collapse takes place *downstream* of the impeller blades. An example of the specialized application of a supercavitating pump is the fuel pumps of rocket engines for space vehicles, where size and mass must be kept low at all costs. Pearsall (1973) has shown that the supercavitating principle is most suitable for axial flow pumps of high specific speed and has suggested a design technique using methods similar to those employed for conventional pumps.

Pearsall (1973) was one of the first to show that operating in the supercavitating regime was practicable for axial flow pumps, and he proposed a design technique to enable this mode of operation to be used. A detailed description was published in Pearsall (1972), and the cavitation performance was claimed to be much better than that of conventional pumps. Some further details are given in Chapter 7.

Cavitation limits

In theory, cavitation commences in a liquid when the static pressure is reduced to the vapor pressure corresponding to the liquid's temperature. However, in practice, the physical state of the liquid will determine the pressure at which cavitation starts (Pearsall, 1972). Dissolved gases come out of

solution as the pressure is reduced, forming gas cavities at pressures in excess of the vapor pressure. Vapor cavitation requires the presence of nuclei—submicroscopic gas bubbles or solid non-wetted particles—in sufficient numbers. It is an interesting fact that in the absence of such nuclei, a liquid can withstand negative pressures (i.e., *tensile stresses*)! Perhaps the earliest demonstration of this phenomenon was that performed by Reynolds (1882) before a learned society. He showed how a column of mercury more than twice the height of the barometer could be (and was) supported by the internal cohesion (stress) of the liquid. More recently Ryley (1980) devised a simple centrifugal apparatus for students to test the tensile strength of both plain, untreated tap water in comparison with water that had been filtered and then deaerated by boiling. Young (1989) gives an extensive literature list covering many aspects of cavitation including the tensile strength of liquids. At room temperature, the theoretical tensile strength of water is quoted as being as high as 1000 atm (100 MPa)! Special pretreatment (i.e., rigorous filtration and pre-pressurization) of the liquid is required to obtain this state. In general, the liquids flowing through turbomachines will contain some dust and dissolved gases and under these conditions negative pressure does not arise.

A useful parameter is the available suction head at entry to a pump or at exit from a turbine. This is usually referred to as the *net positive suction head*, NPSH, defined as

$$H_s = (p_o - p_v)/(\rho g) \tag{2.21}$$

where p_o and p_v are the absolute stagnation and vapor pressures, respectively, at pump inlet or at turbine outlet.

To take into account the effects of cavitation, the performance laws of a hydraulic turbomachine should include the additional independent variable H_s. Ignoring the effects of Reynolds number, the performance laws of a constant geometry hydraulic turbomachine are then dependent on two groups of variable. Thus, the efficiency,

$$\eta = f(\varphi, \Omega_{ss}) \tag{2.22}$$

where the *suction specific speed* $\Omega_{ss} = \Omega Q^{1/2}/(gH_s)^{3/4}$, determines the effect of cavitation, and $\Phi = Q/(\Omega D^3)$, as before.

It is known from experiments made by Wislicenus (1965) that cavitation inception occurs for an almost constant value of Ω_{ss} for all pumps (and, separately, for all turbines) designed to resist cavitation. This is because the blade sections at the inlet to these pumps are broadly similar (likewise, the exit blade sections of turbines are similar) and the *shape* of the low-pressure passages influences the onset of cavitation.

Using the alternative definition of suction specific speed $\Omega_{ss} = \Omega Q^{1/2}/(gH_s)^{3/4}$, where Ω is the rotational speed in rad/s, Q is the volume flow in m^3/s, and gH_s is in m^2/s^2. Wislicenus showed that

$$\Omega_{ss} = 3.0 \text{ (rad)} \tag{2.23a}$$

for pumps, and

$$\Omega_{ss} = 4.0 \text{ (rad)} \tag{2.23b}$$

for turbines.

Pearsall (1967) describes a supercavitating pump with a cavitation performance much better than that of conventional pumps. For this pump, suction specific speeds Ω_{ss} up to 9.0 were readily obtained and, it was claimed, even better values might be possible but at the cost of reduced head

and efficiency. It is likely that supercavitating pumps will be increasingly used in the search for higher speeds, smaller sizes, and lower costs.

PROBLEMS

1. A fan operating at 1750 rpm at a volume flow rate of 4.25 m^3/s develops a head of 153 mm measured on a water-filled U-tube manometer. It is required to build a larger, geometrically similar fan that will deliver the same head at the same efficiency as the existing fan but at a speed of 1440 rpm. Calculate the volume flow rate of the larger fan.

2. An axial flow fan 1.83 m diameter is designed to run at a speed of 1400 rpm with an average axial air velocity of 12.2 m/s. A quarter scale model has been built to obtain a check on the design and the rotational speed of the model fan is 4200 rpm. Determine the axial air velocity of the model so that dynamical similarity with the full-scale fan is preserved. The effects of Reynolds number change may be neglected. A sufficiently large pressure vessel becomes available in which the complete model can be placed and tested under conditions of complete similarity. The viscosity of the air is independent of pressure and the temperature is maintained constant. At what pressure must the model be tested?

3. The water pump used to generate the plot shown in Figure 2.2 has an impeller diameter of 56 mm. When tested at a speed of 4500 rpm, the head−volume flow rate characteristic produced can be approximated by the equation

$$H = 8.6 - 5.6Q^2$$

where H is in meters and Q in dm^3/s. Show that, provided viscous and cavitation effects are negligible, the characteristic of all geometrically similar pumps may be written in dimensionless form as

$$\psi = 0.121(1 - 4460\Phi^2)$$

where ψ is the dimensionless head coefficient, gH/Ω^2D^2, Φ is the flow coefficient, $Q/\Omega D^3$, and Ω is expressed in rad/s. Show that this result is consistent with Figure 2.2, where Ω is expressed in rev/s.

4. A water turbine is to be designed to produce 27 MW when running at 93.7 rpm under a head of 16.5 m. A model turbine with an output of 37.5 kW is to be tested under dynamically similar conditions with a head of 4.9 m. Calculate the model speed and scale ratio. Assuming a model efficiency of 88%, estimate the volume flow rate through the model. It is estimated that the force on the thrust bearing of the full-size machine will be 7.0 GN. For what thrust must the model bearing be designed?

5. Derive the nondimensional groups that are normally used in the testing of gas turbines and compressors. A compressor has been designed for normal atmospheric conditions (101.3 kPa and 15°C). To economize on the power required, it is being tested with a throttle in the entry duct to reduce the entry pressure. The characteristic curve for its normal design speed of

4000 rpm is being obtained on a day when the ambient temperature is 20°C. At what speed should the compressor be run? At the point on the characteristic curve at which the mass flow would normally be 58 kg/s, the entry pressure is 55 kPa. Calculate the mass flow rate during the test.

6. Describe, with the aid of sketches, the relationship between geometry and specific speed for pumps.

a. A model centrifugal pump with an impeller diameter of 20 cm is designed to rotate at 1450 rpm and to deliver 20 dm^3/s of freshwater against a pressure of 150 kPa. Determine the specific speed and diameter of the pump. How much power is needed to drive the pump if its efficiency is 82%?

b. A prototype pump with an impeller diameter of 0.8 m is to be tested at 725 rpm under dynamically similar conditions as the model. Determine the head of water the pump must overcome, the volume flow rate, and the power needed to drive the pump.

7. A hydraulic turbine is to be installed where the net head is 120 m and the normal available flow rate is 1.5 m^3/s. A 48 pole synchronous generator is available (to operate with a 60 Hz electrical system) and has an adequate power capacity matching the turbine. Determine

a. the rotational speed and the electrical power that can be delivered if the system efficiency (turbine and generator) is 85%;

b. the power specific speed of the turbine;

What type of turbine is being used in this application?

8. A hydraulic turbine running at 160 rpm, discharges 11 m^3/s and develops 2400 kW at a net head of 25 m. Determine

a. the efficiency of the turbine;

b. the speed, flow rate, and power output of this turbine when running under a net head of 40 m assuming homologous conditions and the same efficiency.

9. A hydraulics engineer is planning to utilize the water flowing in a stream, normally able to provide water at a flow rate of 2.7 m^3/s, and a head of 13 m for power generation. The engineer is planning to use a 2.0 m diameter turbine operating at a rotational speed of 360 rpm and at a hoped for efficiency of 88%.

a. Determine the likely power developed by the turbine, the specific speed and specific diameter, and the most suitable type of turbine for this duty.

b. The engineer then decides, first of all, to test a geometrically similar model turbine with a diameter of 0.5 m (operating at the same specific speed and specific diameter as the prototype) and with a head of 4.0 m. Determine, for the model, the volume flow rate, the rotational speed, and the power.

10. A single-stage axial flow gas turbine is to be tested in a "cold rig" so as to simulate the design-point operation. The two sets of operating conditions are:

1. *Design—point operation of turbine*

Stage—inlet total pressure, $p_{01} = 11$ bar

Stage—inlet total temperature, $T_{01} = 1400$ K

Stage—exit total pressure, $p_{02} = 5.0$ bar

Speed of rotation, $N = 55{,}000$ rpm
Stage efficiency, $\eta_t = 87\%$
Mass flow rate $\dot{m} = 3.5\ \mathrm{kg}/s$

2. *Cold—rig operation*
Stage—inlet total pressure, $p_{01(cr)} = 2.5$ bar
Stage—inlet total temperature, $T_{01(cr)} = 365$ K

For both sets of conditions, assume that the axial velocity across the stage remains constant. Determine

a. the stage—exit total temperature $T_{02(cr)}$;
b. the power output in the cold rig.

Assume that the average specific heat ratio for both operating conditions is given by $\gamma = 1.36$.

References

Balje, O. E. (1981). *Turbomachines: A guide to design selection and theory.* New York, NY: John Wiley & Sons.

Baskharone, E. A. (2006). *Principles of turbomachinery in air breathing engines.* Cambridge, UK: Cambridge University Press.

Buckingham, E. (1914). On physically similar systems: illustrations of the use of dimensional equations. *Physical Review*, *4*(4), 345–376.

Casey, M., Zwyssig, C., & Robinson, C. (2010). The Cordier line for mixed flow compressors. *ASME IGTI conference*. Glasgow, UK. Paper GT2010-22549.

Cline, S. J., Fesler, W., Liu H. S., Lovewell, R. C., & Shaffer, S. J. (1983). Energy efficient engine—high pressure compressor component performance report. NASA CR-168245, Washington, D.C.: National Aeronautics and Space Administration.

Cornell, W. G. (1975). Experimental quiet engine program. NASA-CR-2519, Washington, D.C.: National Aeronautics and Space Administration.

Cordier, O. (1953). Ähnlichkeitsbedingungen für Strömungsmaschinen. In *Brennstoff-Wärme-Kraft*, 5, 337.

Csanady, G. T. (1964). *Theory of turbomachines.* New York, NY: McGraw-Hill.

Cumpsty, N. A. (1989). *Compressor aerodynamics.* New York, NY: Longman.

Douglas, J. F., Gasiorek, J. M., & Swaffield, J. A. (1995). *Fluid mechanics.* New York, NY: Longman.

Franzini, J. B., & Finnemore, E. J. (1997). *Fluid mechanics with engineering applications.* McGraw-Hill.

Lewis, R. I. (1996). *Turbomachinery performance analysis.* London: Arnold.

Pearsall, I. S (1973). The supercavitating pump. *Proceedings of the Institution of Mechanical Engineers*, *187*(1), 649–665.

Pearsall, I. S. (1966). Acoustic Detection of Cavitation. *Proceedings of the Institution of Mechanical Engineers*, 1966–67, 181, Part 3A, Paper 14.

Pearsall, I. S. (1972). Cavitation. M & B Monograph ME/10. London: Mills & Boon.

Pearsall, I. S. & McNulty, P. J. (1968). *Comparison of cavitation noise with erosion* (6–7). *Cavitation forum* American Society of Mechanical Engineers. New York, NY.

Reynolds O. (1882). On the internal cohesion of liquids and the suspension of a column of mercury to a height of more than double that of a barometer. *Memoirs of the Literary and Philosophical Society of Manchester*, 3rd series, vol. 7, pp 1–19.

Ryley, D. J. (1980). Hydrostatic stress in water. *International Journal of Mechanical Engineering Education*, *8*, 2.

Shames, I. H. (1992). *Mechanics of fluids.* New York, NY: McGraw-Hill.
Shepherd, D. G. (1956). *Principles of turbomachinery.* New York, NY: Macmillan.
Taylor, E. S. (1974). *Dimensional analysis for engineers.* Oxford: Clarendon.
Wislicenus, G. F. (1965). *Fluid mechanics of turbomachinery.* New York, NY: McGraw-Hill.
White, F. M. (2011). *Fluid mechanics.* New York, NY: McGraw-Hill.
Young, F. R. (1989). *Cavitation.* New York, NY: McGraw-Hill.

CHAPTER

Two-Dimensional Cascades

3

Let us first understand the facts and then we may seek the causes.
Aristotle

3.1 Introduction

The design and performance prediction of axial flow compressors and turbines has been based, in the main, upon measurements of the flow-through two-dimensional cascades of blades. However, to an increasing extent, computational fluid dynamic (CFD) methods are now being used to simulate cascade testing. The flow within a turbomachine is, in general, unsteady and three dimensional. For cascade analysis, the flow across individual blade rows is treated as two dimensional and steady. This approach is appropriate for many compressor and turbine designs and the derived flow characteristics obtained from cascade tests have usually been found to be satisfactory, although laborious to collect.

Reviews of the many types of cascade tunnels, which includes low-speed, high-speed, intermittent blowdown, suction tunnels, are available in the literature, e.g., Sieverding (1985), Baines, Oldfield, Jones, Schulz, King, and Daniels (1982), and Hirsch (1993). The range of Mach numbers in axial flow turbomachines can be considered to extend from $M = 0.1$ to 2.5:

i. low speed, operating in the range 20−60 m/s;
ii. high speed, for the compressible flow range of testing.

A typical low-speed, continuous running cascade tunnel is shown in Figure 3.1(a). This linear cascade of blades comprises a number of identical blades, equally spaced and parallel to one another. Figure 3.1(b) shows the test section of a cascade facility for transonic and moderate supersonic inlet velocities. The upper wall is slotted and equipped for suction, allowing operation in the transonic regime. The flexible section of the upper wall allows for a change of geometry so that a convergent−divergent nozzle can be formed, allowing the flow to expand to supersonic speeds upstream of the cascade.

It is most important that the flow across the central region of the cascade blades (where the flow measurements are made) is a good approximation to two-dimensional flow and that the flow repeats (i.e., is periodic) across several blade pitches. This effect could be achieved by employing a large number of long blades, but then an excessive amount of power would be required to operate the tunnel. With a tunnel of more compact size, aerodynamic difficulties become apparent and arise from the tunnel wall boundary layers interacting with the blades. In particular, and as illustrated in Figure 3.2(a), the tunnel wall boundary layer merges with the end blade boundary

Fluid Mechanics and Thermodynamics of Turbomachinery. DOI: http://dx.doi.org/10.1016/B978-0-12-415954-9.00003-6

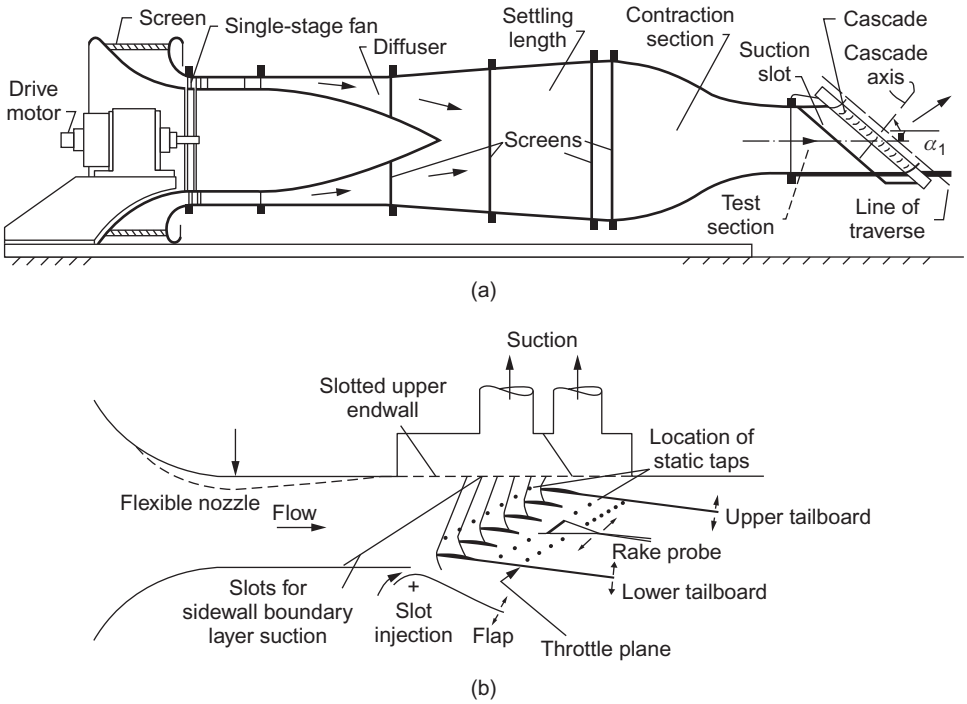

FIGURE 3.1

Compressor cascade wind tunnels: (a) conventional low speed, continuous running cascade tunnel and (b) transonic/supersonic cascade tunnel.

((a) Adapted from Carter, Andrews, and Shaw, 1950 and (b) adapted from Sieverding, 1985)

layer, and as a consequence, this blade usually stalls, resulting in a nonuniform flow across the cascade.

In a compressor cascade, the rapid increase in pressure across the blades causes a marked thickening of the wall boundary layers and produces an effective contraction of the flow, as depicted in Figure 3.3. A *contraction coefficient*, used as a measure of the boundary layer growth through the cascade, is defined by $\rho_1 c_1 \cos \alpha_1 / (\rho_2 c_2 \cos \alpha_2)$. Carter et al. (1950) quoted values of 0.9 for a good tunnel dropping to 0.8 in normal high-speed tunnels and even less in bad cases. These are values for compressor cascades; with turbine cascades higher values can be expected, since the flow is accelerating and therefore the boundary layers will not be thickened.

Because of the contraction of the main through-flow, the theoretical pressure rise across a compressor cascade, even allowing for losses, is never achieved. This will be evident since a contraction (in a subsonic flow) accelerates the fluid, which is in conflict with the diffuser action of the cascade.

To counteract these effects, it has been customary (in Great Britain) to use *at least* seven blades in a compressor cascade, each blade having a minimum aspect ratio (blade span/chord length) of 3.

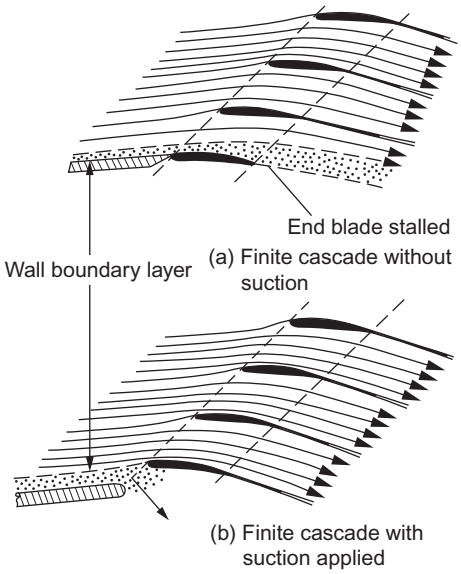

FIGURE 3.2

(a) Flow entering cascade without boundary layer control causes end blade stalling: (b) Application of suction to bottom wall boundary layer results in a more uniform flow without blade stall.

(Adapted from Carter et al., 1950)

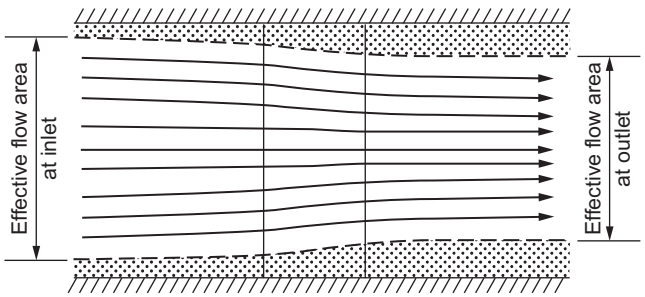

FIGURE 3.3

Contraction of streamlines due to boundary layer thickening.

(Adapted from Carter et al., 1950)

With seven blades, suction is desirable in a compressor cascade, but it is not usual in a turbine cascade. In the United States, much lower aspect ratios have been commonly employed in compressor cascade testing, the technique being the almost complete removal of tunnel wall boundary layers from all four walls using a combination of suction slots and perforated end walls to which

suction is applied. Figure 3.2(b) illustrates the effective application of suction to produce a more uniform flow-field.

For axial flow machines of high hub−tip radius ratios, radial velocities are negligible and the flow may be described as two dimensional. The flow in the cascade is then likely to be a good model of the flow in the machine. With lower hub−tip radius ratios, the blades of a turbomachine will normally have an appreciable amount of twist along their length and a varying *space−chord ratio*. In such cases, a number of cascade test measurements can be applied to cover the design of the blade sections at a number of radial locations. However, it should be emphasized that, in all cases, the two-dimensional cascade is a simplified model of the flow within a turbomachine, which in reality can include various three-dimensional flow features. For sections of a turbomachine where there are separated flow regions, leakage flows or significant spanwise flows, the cascade model will not be accurate and careful consideration of the three-dimensional effects is required. Further details of three-dimensional flows in axial turbomachines are given in Chapter 6.

3.2 Cascade geometry

A cascade blade profile can be conceived as a curved *camber line* upon which a *profile thickness distribution* is symmetrically superimposed. In Figure 3.4, two blades of a compressor cascade are shown together with the notation needed to describe the geometry. Several geometric parameters that characterize the cascade are:

- **i.** the *stagger angle*, ξ, the angle between the chord line and the reference direction;[1]
- **ii.** the *space−chord ratio*, s/l (in American practice the *solidity*, $\sigma = l/s$, is more frequently used);
- **iii.** the *camber angle*, θ;
- **iv.** the *blade inlet angle*, α'_1;
- **v.** the *blade outlet angle*, α'_2.

Further parameters that are needed to describe the cascade blade shape include its camber line shape, thickness distribution, the radii at the leading and trailing edges, and the maximum thickness to chord ratio, t_{max}/l.

The camber angle, θ, is the change in angle of the camber line between the leading and trailing edges that equals $\alpha'_1 - \alpha'_2$ in the notation of Figure 3.4. For circular arc camber lines, the stagger angle is $\xi = (1/2)(\alpha'_1 + \alpha'_2)$. The change in angle of the flow is called the *deflection*, $\varepsilon = \alpha_1 - \alpha_2$, and in general this will be different to the camber angle due to flow incidence at the leading edge and deviation at the trailing edge. The incidence is the difference between the inlet flow angle and the blade inlet angle:

$$i = \alpha_1 - \alpha'_1 \tag{3.1}$$

[1]Throughout this book, all fluid and blade angles are measured from this reference direction, which is a line perpendicular to the cascade front (this is the axial direction, when the blades are in an annular arrangement).

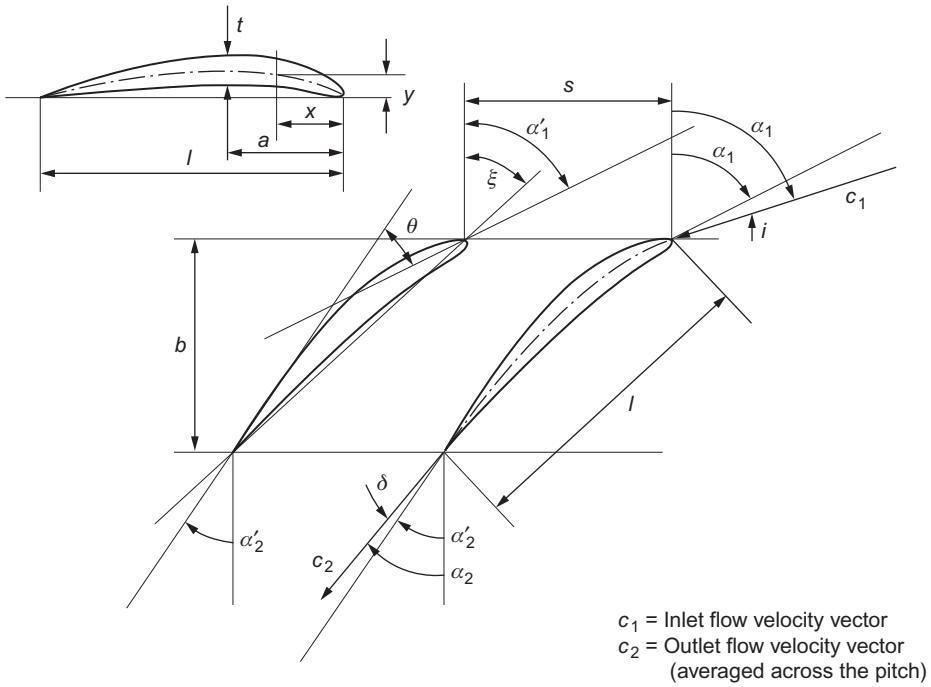

FIGURE 3.4

Compressor cascade and blade notation.

The deviation is the difference between the exit flow angle and the blade exit angle:

$$\delta = \alpha_2 - \alpha'_2 \tag{3.2}$$

Compressor blade profiles

The modern approach in compressor design is to use blade profiles designed by the so-called prescribed velocity distribution (PVD) method. In this approach, the designer will select a blade surface velocity distribution and a computational method determines the aerofoil thickness and curvature variation required to achieve the desired aerodynamics. Despite this, many blade designs are still in use based upon geometrically prescribed profiles. The most commonly used geometric families are the American National Advisory Committee for Aeronautics (NACA) 65 Series, the British C Series, and the double circular arc (DCA) or biconvex blade.

The NACA 65 Series blades originated from the NACA aircraft wing aerofoil and were designed for approximately uniform loading. Figure 3.5 compares the profiles of the most widely used blade sections drawn at a maximum thickness to chord ratio of 20%, for the purpose of clarity. In fact, the maximum t/l ratios of compressor blade sections are nowadays normally less than 10%

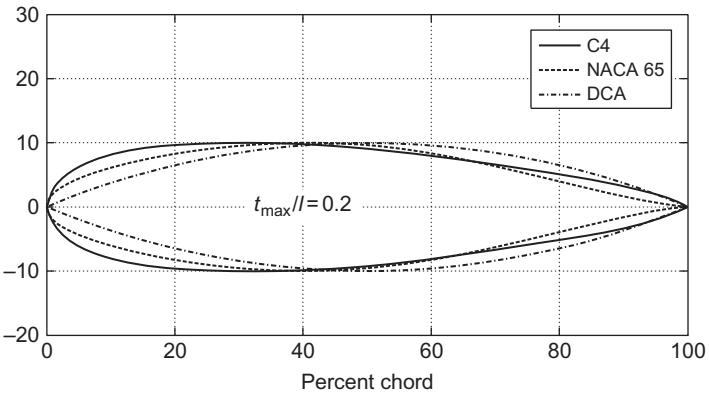

FIGURE 3.5

Thickness distributions for various compressor blade profiles.

and often a value of 5% is used because of the superior high Mach number performance that can be achieved with thinner blades. The NACA 65 Series has its maximum thickness at 40%, whereas the C Series is at 30% and the DCA Series is at 50%. These differences have a marked effect on the velocity distributions measured around the blades surfaces. Aerofoils with the maximum thickness near the leading edge and, consequently, with a well rounded leading edge have a wide operating range but a poorer high speed performance than blades with a sharp leading edge and the maximum thickness point further back.

The exact details of the different profiles are very well documented, e.g., Mellor (1956), Cumpsty (1989), Johnson and Bullock (1965), Aungier (2003), and it is not thought useful or necessary to reproduce these in this book.

The actual blade shape is defined by one of these profile shapes superimposed on a camber line. This can be a simple circular arc although, as shown by Aungier (2003), a parabolic arc allows a more flexible style of blade loading. The blade profile is laid out with the selected scaled thickness distribution plotted normal to the chosen camber line. Correlations for the performance of the different styles of compressor aerofoil are discussed within Section 3.5 later in this chapter.

Turbine blade profiles

The shape of turbine blades is less critical than it is in a compressor cascade. However, the designer still needs to exercise some care in the selection of blades to attain good efficiency with highly loaded blade rows. Nowadays, the process of specifying blade row geometry (blade shape, flow angles, and space–chord ratio) is accomplished by computational methods but, ultimately, the designs still need to be backed up by cascade tests. Figure 3.6 shows a photograph of a typical high-speed turbine cascade that is used to represent the aerofoils of a conventional low-pressure turbine within an aero engine. The blade profiles illustrate the high turning and the contraction of the passage flow area within a turbine blade row.

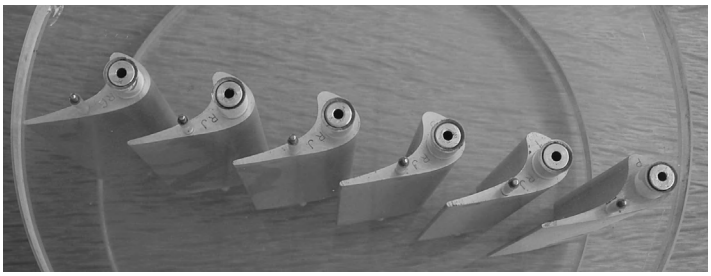

FIGURE 3.6

A cascade of high-speed turbine aerofoils.

(Courtesy of the Whittle Laboratory)

During the early design phase of a turbine, or when cascade results are unavailable, one-dimensional calculations and correlation methods can be used to estimate the blade row performance of turbine blade rows. These are discussed within Section 3.6.

3.3 Cascade flow characteristics

The fluid approaches the cascade from far upstream[2] with velocity c_1 at an angle α_1 and leaves far downstream of the cascade with velocity c_2 at an angle α_2 as shown in Figure 3.7. The aims of a cascade test are to measure the deviation angle, δ, and to characterize the losses generated within the flow as it is passes through the blade passages.

Deviation arises through inviscid and viscous effects. The flow mechanisms are different for compressors and turbines and they will be described in detail later. Essentially though, the flow is unable to follow the blade angle precisely, such that it is *underturned* and thus leaves the trailing edge at a slightly different angle to the blade exit angle. Cascade losses arise from the growth of the boundary layers on the suction and pressure surfaces of the blades. These boundary layers combine at the blade trailing edge where they form the blade wake. As a result, a local defect in stagnation pressure is created. As the flow moves downstream the wake widens, as shown in Figure 3.7, and becomes less intense. In addition, cascades operating at high Mach numbers have losses due to shock waves and shock–boundary layer interaction at the blade surfaces.

The deviation and loss for a cascade are measured (or computed) at a range of conditions, because as well as determining the design performance, it is important to check the tolerance to changes in the inlet flow conditions, i.e., to show good off-design behavior. Note that cascade tests can be made on both rotor and stator blades. For rotors, the absolute velocities in the cascade are equivalent to the relative velocities that would be present in the actual machine.

[2]*Far upstream*, usually implies an indefinite distance of ½ to 1 chord upstream of the leading edge at a location where the influence of the cascade static pressure field on the flow is negligible, similarly for *far downstream*.

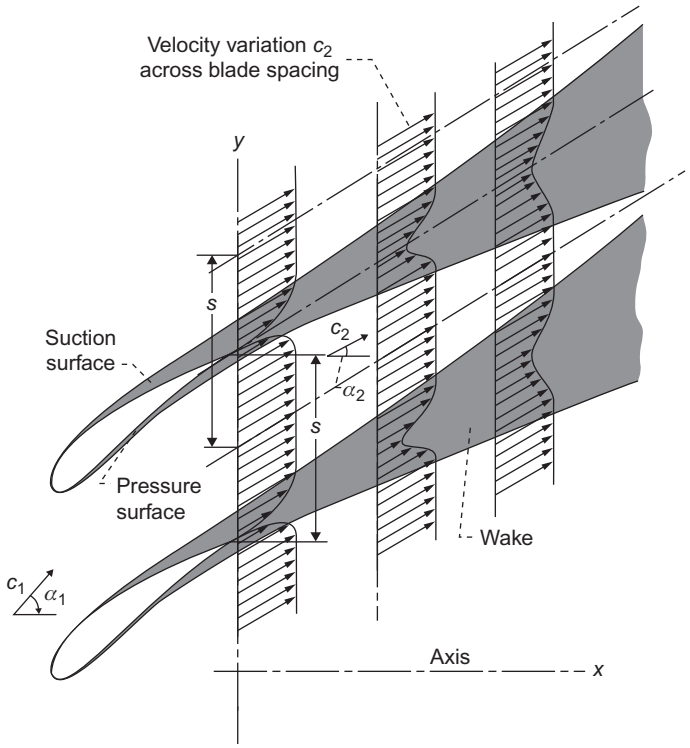

FIGURE 3.7

The flow through a blade cascade and the formation of the wakes.

(From Johnson and Bullock, 1965)

Streamtube thickness variation

When considering the flow through the blade passage of a compressor cascade, it is often assumed that the mean streamtube thickness remains constant. However, this may not be true because the rapid increase in pressure of the flow through the blades can cause a marked thickening of the end wall boundary layers resulting in an effective contraction of the flow as already indicated in Figure 3.3. This effect can be countered by the use of suction to remove the end wall boundary layers.

In general, for all flows, the conservation of mass flow rate per blade passage is

$$\dot{m} = \rho_1 c_1 H_1 s \cos \alpha_1 = \rho_2 c_2 H_2 s \cos \alpha_2 \tag{3.3}$$

where Hs is the projected frontal area of the control volume, A_a. The parameter $H_1 s \cos \alpha_1$ is the flow area measured *perpendicular to the inlet flow direction*. This is the area perceived by the flow and is therefore referred to as the *true flow area*. This is an important factor when compressible flow is considered.

It is useful to define an axial velocity density ratio (AVDR), i.e.,

$$\text{AVDR} = (\rho_2 c_{x2})/(\rho_1 c_{x1}) = H_1/H_2 \tag{3.4}$$

Equation (3.4) can be used in relating flow properties at the different positions along the mean streamtube. Note that AVDR is the inverse of the contraction coefficient described in the introduction. In compressors AVDR > 1 due to the thickening boundary layers, but in turbine cascades AVDR may be less than 1 due to the possible thinning of the boundary layers in accelerating flow.

Cascade performance parameters

For a known AVDR, as just defined, the primary aerodynamic input data for a cascade test are:

i. the inlet flow angle, α_1;
ii. the inlet Mach number, M_1;
iii. the blade Reynolds number, $Re = \rho_1 c_1 l/\mu$, where l is the blade chord.

The data from cascade traverses are used to provide the following parameters for use in the design and performance prediction of axial flow compressors and turbines:

i. exit flow angle, α_2;
ii. stagnation pressure loss, Y_p, or an energy loss coefficient, ζ.

The performance characteristics of a cascade can therefore be expressed by the following functional relationships:

$$\alpha_2 = \text{fn}(M_1, \alpha_1, Re); Y_p = \text{fn}(M_1, \alpha_1, Re); \quad \text{or} \quad \zeta = \text{fn}(M_1, \alpha_1, Re)$$

The exit flow angle, α_2, is a critical performance parameter because it determines the work transfer within a turbomachinery stage. If we revisit the Euler work equation from Chapter 1, $\Delta h_0 = \Delta(Uc_\theta)$, it is clear that the work input or output from a turbomachine will depend on the exit flow angles since $c_\theta = c \sin \alpha$.

The *stagnation pressure loss coefficient* is an overall measure of the aerodynamic losses through the blade row. Generally, it is defined as

$$Y_p = \text{loss of stagnation pressure} \div \text{reference (dynamic) pressure}$$

The aerodynamic losses in a cascade blade row translate into efficiency losses within a real turbomachine with the same blade shapes. The sources of losses can include:

i. boundary layers on the blades;
ii. flow separation;
iii. shock waves in the flow.

If no shock waves are present, most of the "loss" due to irreversibility is confined to a narrow wake downstream of the trailing edge as shown in Figure 3.7.

For *compressors*, the total pressure loss coefficient is based on *reference inlet conditions*, i.e.,

$$Y_p = (p_{01} - p_{02})/(p_{01} - p_1) \tag{3.5}$$

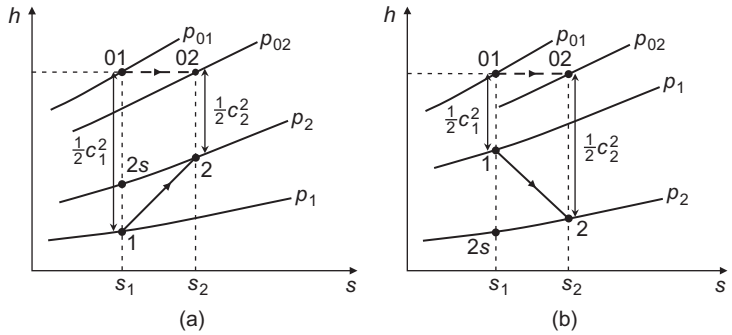

FIGURE 3.8

Mollier diagrams for the flow through: (a) a compressor blade cascade and (b) a turbine blade cascade.

A Mollier diagram with the pressures and salient points for a compressor blade cascade is shown in Figure 3.8(a).

For *turbines*, the total pressure loss coefficient is based on *reference exit conditions*, i.e.,

$$Y_p = (p_{01} - p_{02})/(p_{01} - p_2) \tag{3.6}$$

In this case the reference dynamic pressure is the dynamic pressure at exit if the flow were isentropic. Other variations of the turbine loss coefficient are used in the literature and Horlock (1966) gives a comprehensive list of the definitions possible.

An alternative loss parameter is sometimes used for turbines, called the *energy loss coefficient*, ζ, which measures the lost kinetic energy relative to the *isentropic* exit kinetic energy:

$$\zeta = (c_{2\text{is}}^2 - c_2^2)/c_{2\text{is}}^2, \quad \text{where} \quad 0.5c_{2\text{is}}^2 = h_{01} - h_{2\text{s}} \tag{3.7}$$

Figure 3.8(b) is a Mollier diagram[3] indicating the pressures and enthalpies for the flow through a turbine cascade blade row.

The two definitions of loss coefficient yield numerical values that are almost identical at low Mach numbers, but their values rapidly diverge as M_2 increases with $Y_p > \zeta$.

A primary objective of a compressor blade is to produce a rise in static pressure as well as a deflection of the flow angle. A relevant performance parameter is, therefore, the static pressure rise coefficient. For compressible flow this is usually defined as

$$C_p = (p_2 - p_1)/(p_{01} - p_1) \tag{3.8a}$$

and for incompressible flow

$$C_p = (p_2 - p_1)/\left(\frac{1}{2}\rho c_1^2\right) \tag{3.8b}$$

Flow measurements are made usually across either one or two blade pitches of the varying values of stagnation and static pressures, p_{02} and p_2, and the values of α_2. Mass-averaged values of

[3]The enthalpy changes for the turbine and compressor cascades are drawn roughly equal only for expediency. In fact, the turbine enthalpy drop will be three or four times larger than the enthalpy rise in the compressor blade row.

the performance parameters are then derived from these flow measurements. For example, the mass flow rate is given by

$$\dot{m} = \int_0^s \rho c H \cos\alpha \, \mathrm{d}y = \int_0^s \rho c_x H \, \mathrm{d}y \tag{3.9}$$

A mean value of the air angle α_2 can be found from integrals of tangential and axial momentum across the pitch:

$$\tan\alpha_2 = \int_0^s \rho c_x c_y \, \mathrm{d}y \Big/ \int_0^s \rho c_x^2 \, \mathrm{d}y \tag{3.10}$$

Finally, the mass-averaged stagnation pressure loss coefficient is

$$Y_p = \int_0^s \{(p_{01} - p_{02})/(p_{01} - p_1)\} \rho c_x \, \mathrm{d}y \Big/ \int_0^s \rho c_x \, \mathrm{d}y \tag{3.11}$$

Figure 3.9 shows representative traverse results of Y_p and α_2 for a compressor cascade together with the mass-averaged values of these parameters. The odd-looking "kinks" in the plot of α_2 are caused by the variation in the gradient of p_{02} across the wake and the response of a yaw meter used in measuring flow direction. Further details are given in a paper by Dixon (1978).

Note: From this point onward, all parameters, e.g., α_2, Y_p, are taken as having been mass-averaged according to the formulae just outlined.

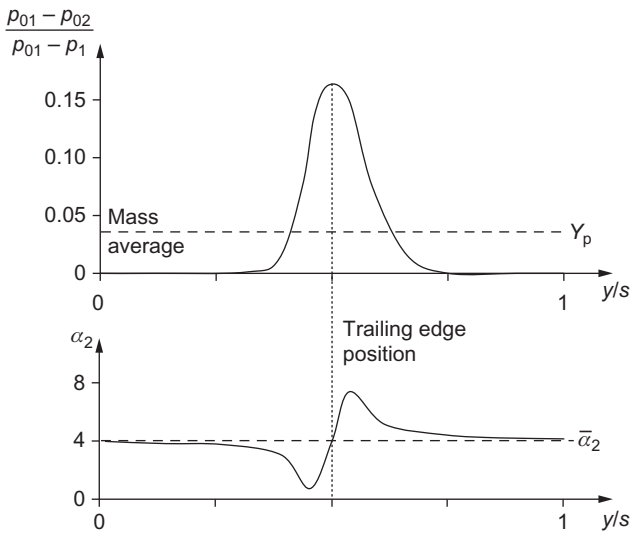

FIGURE 3.9

Typical traverse results for a compressor cascade.

Blade surface velocity distributions

The details of the flow and velocity variations within the blade passages are not required to derive the cascade performance metrics. However, blade surface velocity (and pressure) distributions are used to show whether a blade achieves the velocity distributions intended in the design, and they are helpful for understanding the way a cascade blade performs. In particular, the velocity variation on the blade suction surface can give an indication of imminent flow separation, which would lead to reduced turning and high loss. The relationship between surface velocity distribution and blade performance is discussed further in Section 3.5.

3.4 Analysis of cascade forces

Lift and drag coefficients are frequently referred to in the general literature and in many later parts of this book, especially with regard to low-speed fans and wind turbines. However, with the advent of much higher blade speeds in compressors and turbines, the effects of compressibility have become complicated matters and their usage has almost vanished. Instead, it is now common practice just to use flow deflection and nondimensional total pressure loss in calculating performance, as described previously. This section is included for completeness, but it should be remembered that the material is, strictly speaking, only applicable to low-speed turbomachines.

Consider a portion of a compressor blade cascade, as shown in Figure 3.10. The forces X and Y exerted by a unit depth of blade upon the fluid are exactly equal and opposite to the forces exerted by the fluid upon the blade. A control surface is drawn with end boundaries far upstream and downstream of the cascade and with side boundaries coinciding with the median streamlines.

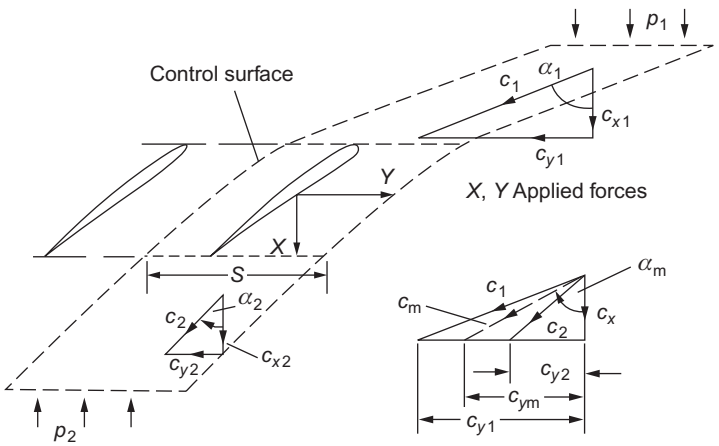

FIGURE 3.10

Forces and velocities in a compressor blade cascade.

The momentum equation is applied in the x and y directions assuming constant axial velocity, c_x, gives the force components:

$$X = (p_2 - p_1)s \tag{3.12}$$

$$Y = \rho s c_x (cy_1 - cy_2) \tag{3.13a}$$

and

$$Y = \rho s c_x^2 (\tan \alpha_1 - \tan \alpha_2) \tag{3.13b}$$

Equations (3.12) and (3.13b) are valid only for incompressible flow with total pressure losses in the cascade but with no change in axial velocity.

Lift and drag forces

A mean velocity c_m is defined by

$$c_m = c_x / \cos \alpha_m \tag{3.14}$$

where α_m is itself defined by

$$\tan \alpha_m = \frac{1}{2}(\tan \alpha_1 + \tan \alpha_2) \tag{3.15}$$

Considering unit depth of a cascade blade, a lift force L acts in a direction perpendicular to c_m and a drag force D in a direction parallel to c_m. Figure 3.11 shows L and D as the reaction forces exerted *by* the blade *upon* the fluid.

Experimental data are often presented in terms of lift and drag when, in fact, the data could be of more use in the form of tangential force and total pressure loss. The lift and drag forces will now be resolved in terms of the axial and tangential forces. Referring to Figure 3.12,

$$L = X \sin \alpha_m + Y \cos \alpha_m \tag{3.16}$$

$$D = Y \sin \alpha_m - X \cos \alpha_m \tag{3.17}$$

There is an immediate connection between the drag force D and the mass-averaged stagnation pressure loss coefficient, Y_p. If we consider a unit blade length, the *force deficit* acting over the

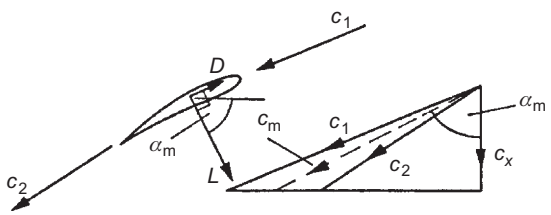

FIGURE 3.11

Lift and drag forces exerted by a unit span of a cascade blade upon the fluid.

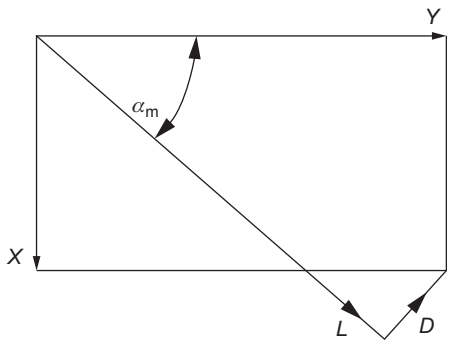

FIGURE 3.12

Axial and tangential forces exerted by unit span of a blade upon the fluid.

span as a result of the total pressure losses is $s\Delta p_0$, where $\Delta p_0 = p_{01} - p_{02}$ for the cascade. The drag is the force component shown in Figure 3.12, which is

$$D = s\Delta p_0 \cos \alpha_m \tag{3.18}$$

This is a result of fundamental importance, but it is only applicable to incompressible flows. Clearly, the drag force $D = 0$ when $\Delta p_0 = 0$. From Eqs (3.17) and (3.18), the drag force is

$$D = \cos \alpha_m (Y \tan \alpha_m - X) = s\Delta p_0 \cos \alpha_m \tag{3.19}$$

Rearranging the above equation, we obtain X

$$X = Y \tan \alpha_m - s\Delta p_0 \tag{3.20}$$

Substituting Eq. (3.20) into Eq. (3.16), we find

$$L = \sin \alpha_m (Y \tan \alpha_m - s\Delta p_0) + Y \cos \alpha_m = Y \sec \alpha_m - s\Delta p_0 \sin \alpha_m \tag{3.21}$$

Substituting for Y using Eq. (3.13b), the lift becomes

$$L = \rho s c_x^2 (\tan \alpha_1 - \tan \alpha_2) \sec \alpha_m - s\Delta p_0 \sin \alpha_m \tag{3.22}$$

Lift and drag coefficients

These coefficients are normally defined in terms of *incompressible flow* parameters. The lift coefficient is conventionally defined as

$$C_L = L / \left(\frac{1}{2} \rho c_m^2 l \right) \tag{3.23}$$

where $c_m = c_x / \cos \alpha_m$ and l = blade chord. The drag coefficient, similarly, is defined as

$$C_D = D / \left(\frac{1}{2} \rho c_m^2 l \right) \tag{3.24a}$$

Using the following incompressible definition of stagnation pressure loss coefficient,

$$\zeta = \Delta p_0 / \left(\frac{1}{2} \rho c_{\mathrm{m}}^2 \right) \tag{3.24b}$$

and substituting for D with Eq. (3.18) then using Eq. (3.24b), we find

$$C_D = \frac{s \Delta p_0 \cos \alpha_{\mathrm{m}}}{1/2 \rho c_{\mathrm{m}}^2 l} = \frac{s \zeta 1/2 \rho c_{\mathrm{m}}^2 \cos \alpha_{\mathrm{m}}}{1/2 \rho c_{\mathrm{m}}^2 l} = \frac{s}{l} \zeta \cos \alpha_{\mathrm{m}} \tag{3.25}$$

Again, we can write C_L in a more convenient form. From Eq. (3.22),

$$C_L = [\rho s c_x^2 (\tan \alpha_1 - \tan \alpha_2) \sec \alpha_{\mathrm{m}} - s \Delta p_0 \sin \alpha_{\mathrm{m}}] / \left(\frac{1}{2} \rho c_{\mathrm{m}}^2 l \right)$$

Therefore,

$$C_L = 2 \frac{s}{l} \cos \alpha_{\mathrm{m}} (\tan \alpha_1 - \tan \alpha_2) - C_D \tan \alpha_{\mathrm{m}} \tag{3.26a}$$

Within the normal range of operation of the flow through a cascade, values of C_D are very much less than those of C_L. Thus, the approximation is occasionally found to be useful, i.e.,

$$\frac{L}{D} = \frac{C_L}{C_D} = \frac{2}{\zeta} (\tan \alpha_1 - \tan \alpha_2) \tag{3.26b}$$

Circulation and lift

Note: The classical analysis of the lift developed by a single isolated aerofoil is based upon the ideal case, when $D = 0$, and the flow is incompressible, i.e., ρ is constant.

The *Kutta–Joukowski theorem* states that the lift force L is

$$L = \Gamma \rho c \tag{3.27}$$

where c is the relative velocity between the aerofoil and the fluid at infinity and Γ is the circulation about the aerofoil. This theorem is of fundamental importance in the development of the theory of aerofoils (Glauert, 1959).

With the assumption that stagnation pressure losses are absent, the lift force per unit span of a blade *in cascade*, using Eq. (3.22), becomes

$$L = \rho s c_x^2 (\tan \alpha_1 - \tan \alpha_2) \sec \alpha_{\mathrm{m}} = \rho s c_{\mathrm{m}} (c_{y1} - c_{y2}) \tag{3.28}$$

Now the *circulation* is the contour integral of velocity around a closed curve. For the cascade blade, the circulation is

$$\Gamma = s (c_{y1} - c_{y2}) \tag{3.29}$$

Combining Eqs (3.28) and (3.29),

$$L = \Gamma \rho c_{\mathrm{m}} \tag{3.30}$$

As the spacing between the cascade blades is increased without limit (i.e., $s \to \infty$), the inlet and outlet velocities to the cascade, c_1 and c_2, become equal in magnitude and direction. Thus, $c_1 = c_2 = c_{\mathrm{m}}$ and Eq. (3.30) becomes the same as the theorem of Kutta–Joukowski stated previously for an isolated aerofoil.

3.5 Compressor cascade performance

Within compressor blades, the flow is moving from a low static pressure at inlet toward a higher static pressure at exit. The fundamental difficulty in compressors is getting the flow to negotiate this pressure rise without generating high loss or separating. The axial compressor designer must choose an appropriate level of blade loading, such that the flow can achieve the required pressure rise, while not overdesigning the compressor, such that there are too many blades. In addition, compressors are required to perform satisfactorily over a range of operating conditions and the designer must produce a blade geometry that can tolerate variations in the operating point.

This section describes the key phenomena present in compressor cascades that determine their design and performance. It also presents some research into the aerodynamics of compressor blades and the correlations that these past studies have established.

Compressor loss and blade loading

Many experimental investigations have confirmed that the efficient performance of compressor cascade blades is limited by the growth and separation of the blade surface boundary layers. One of the aims of cascade research is to establish the generalized loss characteristics and stall limits of conventional blades. This task is made difficult because of the large number of factors that can influence the growth of the blade surface boundary layers, including surface velocity distribution, blade Reynolds number, inlet Mach number, free-stream turbulence and unsteadiness, and surface roughness. However, the analysis of experimental data have led to several correlation methods that enable the first-order behavior of the blade losses and fluid deflection to be predicted with sufficient accuracy for many engineering purposes.

The correlations of Lieblein (1959) and Johnson and Bullock (1965) are based on observations that high levels of velocity diffusion on the surfaces of compressor blades tend to produce thick boundary layers and eventual flow separation. Lieblein showed that in the region of minimum loss, the wake thickness and consequently the loss in total pressure are primarily related to the diffusion in velocity on the suction surface of the blade. He reasoned that the boundary layer on the *suction surface* of conventional compressor blades contributes the largest share of the blade wake, and, therefore, the suction-surface velocity distribution becomes the main factor in determining the total pressure loss.

A typical velocity distribution is shown in Figure 3.13 derived from surface pressure measurements on a compressor cascade blade operating in the region of minimum loss. From this it is clear that the fall in velocity on the suction surface is high and much greater than the overall

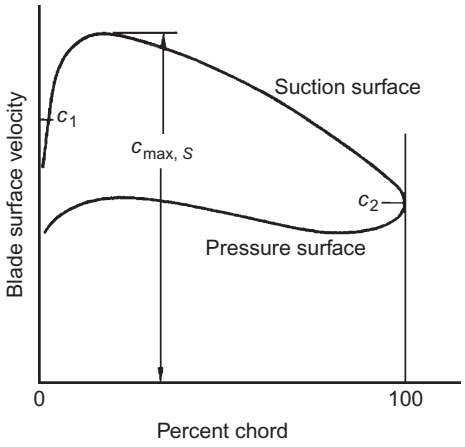

FIGURE 3.13

Typical velocity distribution on a compressor cascade blade (at or near minimum loss condition).

change, i.e., $c_{\max,s} - c_2 \gg c_1 - c_2$. Lieblein defined a term to quantify this diffusion on the suction surface, which he called the *local diffusion factor*,

$$\mathrm{DF}_{\mathrm{loc}} = (c_{\max,s} - c_2)/c_{\max,s} \tag{3.31}$$

Since the local diffusion factor was relatively hard to determine, Lieblein, Schwenk, and Broderick (1953) developed the much used *diffusion factor* (DF) based on a theoretical surface velocity distribution similar to those actually measured on the NACA 65 Series and the British C4 Series cascades. This parameter requires knowledge of only the inlet and exit velocities from the blade and the pitch–chord ratio and is therefore very useful for preliminary design purposes:

$$\mathrm{DF} = (1 - c_2/c_1) + \left(\frac{c_{\theta 1} - c_{\theta 2}}{2c_1}\right)\frac{s}{l} \tag{3.32}$$

The first term on the right-hand side, $1 - c_2/c_1$, represents the mean deceleration of the flow. The second term, $(c_{\theta 1} - c_{\theta 2})/2c_1$, represents the flow turning. The pitch–chord ratio, s/l, is important as this determines how well the flow is guided by the blades. A low value implies lower pressure gradients across the blade passages required to turn the flow and, hence, less diffusion. Lieblein showed that the loss in a blade row increases rapidly as the flow starts to separate, which occurs when the diffusion factor exceeds about 0.6. Typically, a well-designed blade with moderate loading will operate with a diffusion factor around 0.45. Although it was developed using just a small range of compressor blade designs operating at a minimum loss condition, the diffusion factor is widely applied to a range of compressor designs, both compressible and incompressible, for preliminary design purposes.

Another, even simpler, measure of the overall amount of diffusion through a compressor blade row is known as the *De Haller number*, c_2/c_1. This parameter, first proposed in De Haller (1953),

is still often used to limit the maximum pressure rise across a compressor blade row. De Haller's rule recommends that:

$$c_2/c_1 \geq 0.72 \tag{3.33}$$

Fluid deviation

The flow leaving a compressor blade does not follow the blade camber line at the trailing edge. This deviation arises partly because the flow is diffusing within the blade passages. This means that the streamlines are diverging and therefore the flow is not moving in a single direction. This effect is exacerbated by the spacing of the blades because the flow is guided less by the blades when they are further apart. The deviation is further increased by viscous effects since any boundary layer growth on the blade surfaces will generate a blockage that modifies the effective blade shape.

Howell (1945a, b) and Carter (1950) developed an empirical relationship between the nominal deviation, δ^*, occurring at the nominal (design) incidence angle i^*, and the blade geometry:

$$\delta * = m\theta(s/l)^n \tag{3.34}$$

where $n \approx 0.5$ for compressor cascades and $n \approx 1$ for compressor *inlet guide vanes* (these can be considered as turbine blades because they accelerate the flow). Equation (3.34) is now widely referred to as Carter's rule. It demonstrates that the deviation increases with pitch−chord ratio and blade camber. The value of m depends upon the precise shape of the camber line and the blade stagger. A typical correlation for m in a compressor cascade is

$$m = 0.23(2a/l)^2 + \alpha_2^*/500 \tag{3.35}$$

where the maximum camber of the blade is at distance a from the leading edge.

Deviation increases further as the incidence changes from the nominal condition and any flow separation will cause a rapid increase in deviation. An example of the detailed variation of exit angle with incidence and inlet Mach number is shown later, in Figure 3.20.

EXAMPLE 3.1

At its design operating point, a cascade has an inlet flow velocity of 150 m/s at an angle of 50° and an exit flow velocity of 114 m/s at an angle of 30°. Calculate the diffusion factor, *DF*, and the De Haller number if the pitch/chord ratio is 0.85. If the blade has a circular arc camber line and operates with 3° of incidence, find the deviation and the blade camber using Carter's rule.

Solution

$$\mathrm{DF} = (1 - c_2/c_1) + \left(\frac{c_{\theta 1} - c_{\theta 2}}{2c_1}\right)\frac{s}{l} = \left(1 - \frac{114}{150}\right) + \left(\frac{150\sin 50^\circ - 114\sin 30^\circ}{2 \times 150}\right)0.85$$

$$\Rightarrow \text{DF} = 0.24 + 0.193 \times 0.85 = \underline{0.404}$$

The De Haller number,

$$c_2/c_1 = 114/150 = \underline{0.76}$$

The above values are reasonable for a compressor blade at design.

Carter's deviation rule for a compressor blade is $\delta^* = m\theta(s/l)^{0.5}$

This can be written as $\alpha_2^* - \alpha_2' = m(\alpha_1' - \alpha_2')(s/l)^{0.5}$

The parameter m can be estimated directly from Eq. (3.35). For a circular arc blade, $a/l = 0.5$ and the exit flow angle is known,

$$m = 0.23(2a/l)^2 + \alpha_2^*/500 = 0.23 \times 1 + 30/500 = 0.29$$

The inlet metal angle is $\alpha_1' = \alpha_1 - \text{i} = 50 - 3 = 47^\circ$

The deviation equation can now be rearranged to find the exit metal angle:

$$\alpha_2' = \frac{\alpha_2^* - \alpha_1' m\sqrt{s/l}}{1 - m\sqrt{s/l}} = \frac{30 - 47 \times 0.29 \times \sqrt{0.85}}{1 - 0.29 \times \sqrt{0.85}} = 23.8^\circ$$

Hence, the deviation and camber are $\delta^* = \alpha_2^* - \alpha_2' = 30 - 23.8 = \underline{6.2^\circ}$

$$\theta = \alpha_1' - \alpha_2' = 47 - 23.8 = \underline{23.2^\circ}$$

Incidence effects

Figure 3.14 shows a schematic of the flow around a compressor blade for different incidence conditions as well as the corresponding surface velocity distributions for a compressor cascade. At the design point of a compressor blade, the inlet flow angle is almost parallel to the camber line at the leading edge (i.e., the inlet blade angle). Hence, there is close to zero incidence and the surface pressure distribution for the blade should be smooth and continuous. In this case, almost all the deflection, or turning, of the flow is achieved via the camber of the blades. As the incidence is increased, the flow impinges on the blade pressure surface, and the flow on the suction surface must rapidly accelerate around the leading edge then decelerate to a speed comparable with the mainstream flow. This leads to very high local diffusion close to the front of the blade and sometimes what is referred to as a *leading edge spike* on the blade suction surface. The diffusion can cause boundary layer transition and, thus, higher blade losses, and at very high incidences the flow will separate, leading to stall. With positive incidence, the blade loading is higher and the flow deflection increased. Some of the turning can be thought of as being due to the blade camber, and some due to the incidence. At negative incidence, the flow accelerates around the leading edge onto the pressure surface. The pressure distributions on the front of the suction and pressure surfaces swap and the diffusion on the pressure surface is increased. The flow deflection is reduced and the loading is low. At very high values of negative incidence, the diffusion becomes so high that the flow can separate on the pressure surface.

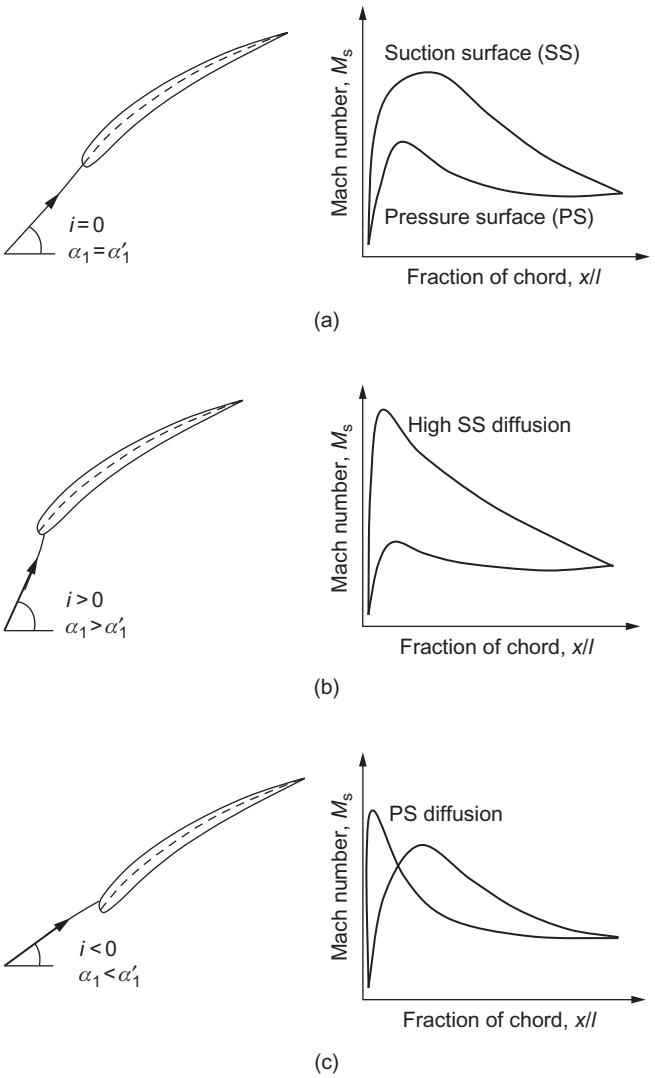

FIGURE 3.14

Effect of incidence on the surface velocity distributions around a compressor blade: (a) design incidence, (b) positive incidence, and (c) negative incidence.

The tolerance of the compressor blades to incidence variations is critical to enable stable and efficient off-design operation of a compressor. When a compressor operates at mass flow rates or rotational speeds that are away from the design point, the blades will be subject to incidence variations, as detailed in Chapter 5. Typically, a compressor blade needs to tolerate at least $\pm 5^{\circ}$ variation of incidence without stalling, although the exact requirements will depend on the

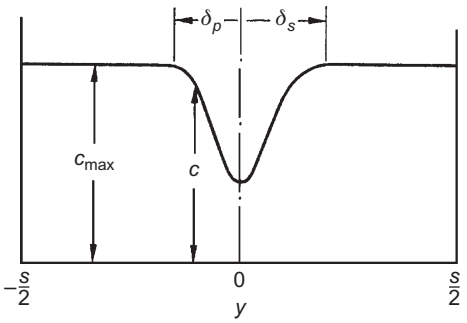

FIGURE 3.15

Blade wake downstream of the exit of a compressor blade cascade.

application. As shown later, the variations in incidence that can be tolerated by a compressor aerofoil reduce as the inlet Mach number increases.

Incompressible cascade analysis

Many studies of compressor cascades are carried out at low speed, where compressibility effects can be neglected. This enables several simplifications to be made. In incompressible flow with constant axial velocity, the Lieblein diffusion factor in Eq. (3.32) can be rewritten as

$$\mathrm{DF} = \left(1 - \frac{\cos\alpha_1}{\cos\alpha_2}\right) + \frac{s}{l}\frac{\cos\alpha_1}{2}(\tan\alpha_1 - \tan\alpha_2) \tag{3.36}$$

Thus, once the inlet and exit flow angles are fixed, a required level of diffusion factor can be used to set the pitch−chord ratio.

Lieblein (1965) developed a correlation between local diffusion factor and the wake momentum thickness to chord ratio, θ_2/l, at the reference incidence (midpoint of working range) for a range of compressor blades. The wake momentum thickness, with the parameters of the flow model in Figure 3.16, is defined as

$$\theta_2 = \int_{-s/2}^{s/2} (c/c_{\max})(1 - c/c_{\max})\mathrm{d}y \tag{3.37}$$

Figure 3.16 shows the full blade wake in the exit plane of the cascade. Using Newton's second law of motion, we now equate the total loss in momentum due to friction with the drag force. This, of course, includes the boundary layers on both blade surfaces. Using Eq. (3.18), we get

$$D = s\,\Delta p_0 \cos\alpha_\mathrm{m} = \theta_2 \rho c_2^2 \tag{3.38}$$

where $\theta_2 = \theta_s + \theta_p$, i.e., the sum of the momentum thicknesses on the pressure and suction surfaces at the trailing edge plane.

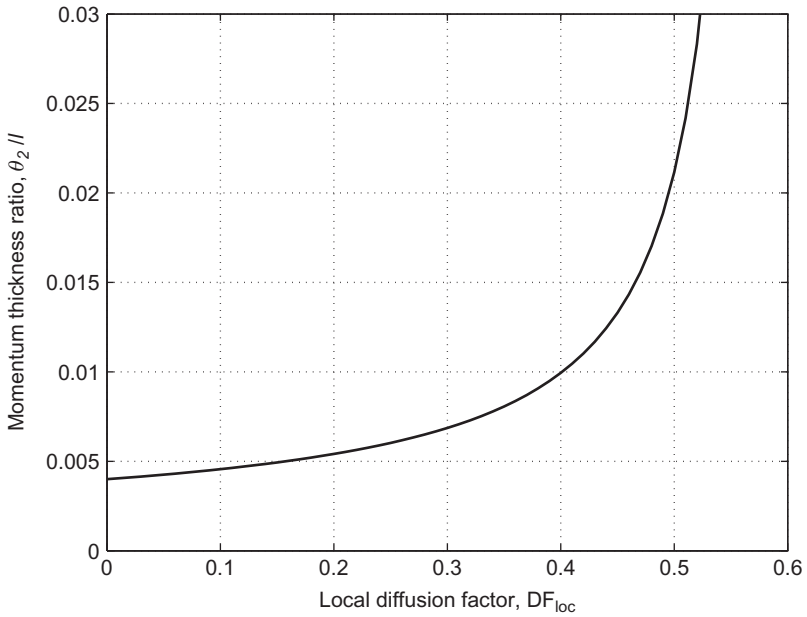

FIGURE 3.16

Blade wake downstream of the exit of a compressor blade cascade.

From the definition of drag coefficient, Eq. (3.24a) combined with Eq. (3.38), it can be shown that

$$C_D = \zeta(s/1)\cos\alpha_m = 2(\theta_2/l)\cos^2\alpha_m/\cos^2\alpha_2 \tag{3.39}$$

This equation provides a useful link between the drag coefficient and the wake momentum thickness.

Lieblein's correlation of momentum thickness to chord ratio with the local diffusion factor is plotted in Figure 3.17. This curve represents the equation

$$\frac{\theta_2}{l} = 0.004/[1 + 1.17\ln(1 - DF_{loc})] \tag{3.40}$$

where DF_{loc} is as defined in Eq. (3.31). Equations (3.39) and (3.40) provide a simple relationship between the blade stagnation pressure loss coefficient and the suction-surface velocity distribution. Note that the *practical limit of efficient operation* corresponds to a local diffusion factor of around 0.5.

EXAMPLE 3.2

A low-speed compressor cascade is to be tested with a flow inlet angle, $\alpha_1 = 55°$, and a flow exit angle, $\alpha_2 = 30°$. The expected design value of the local diffusion ratio, DF_{loc}, is 0.4. Find a safe value for the pitch–chord ratio if the maximum value of the diffusion factor, DF, is assumed to be 0.6. Using Eqs (3.26), (3.39), and (3.40), determine values for ζ, C_D, and C_L.

Solution

Using Eq. (3.33) with DF = 0.6, the maximum allowable pitch–chord ratio is

$$\frac{s}{l} \leq \frac{2\cos\alpha_1/\cos\alpha_2 - 0.8}{\cos\alpha_1(\tan\alpha_1 - \tan\alpha_2)} = \frac{2 \times 0.5736/0.866 - 0.8}{0.5736 \times (1.4281 - 0.5774)} = \underline{1.075}$$

From Eq. (3.40), $\theta_2/l = 0.004/[1 + 1.17\ln(1 - 0.4)] = 0.01$.
From Eq. (3.39), $C_D = 2(\theta_2/l)\cos^2\alpha_m/\cos^2\alpha_2$, where $\tan\alpha_m = (1/2)(\tan\alpha_1 + \tan\alpha_2) = 1.00275$.
Therefore, $\alpha_m = 45.08°$, and

$$C_D = 2 \times 0.01 \times \cos^2 45.08/\cos^2 30 = \underline{0.013}$$

From Eq. (3.25), the loss coefficient,

$$\zeta = C_D \Big/ \frac{s}{l}\cos\alpha_m = 0.013/(1.075 \times \cos 45) = \underline{0.017}$$

From Eq. (3.26a), $C_L = 2s/l\cos\alpha_m(\tan\alpha_1 - \tan\alpha_2) - C_D\tan\alpha_m$; therefore,

$$C_L = 2 \times 1.075 \times \cos 45.08 \times (\tan 55 - \tan 30) - 0.013 \times \tan 45.08 = \underline{1.28}$$

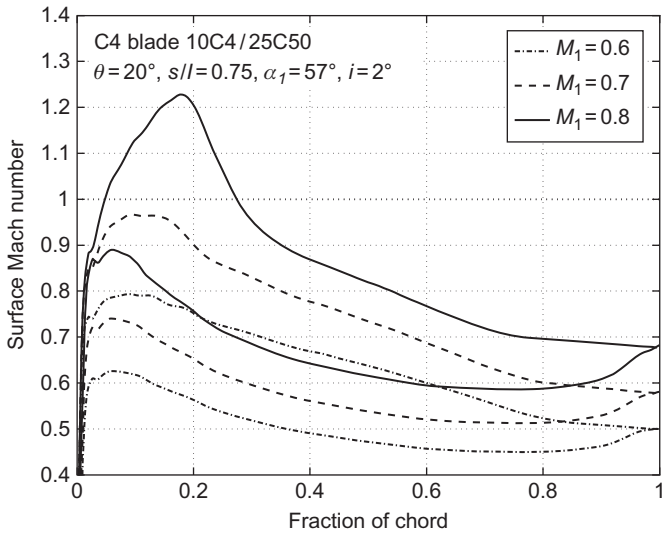

FIGURE 3.17

Mean variation of wake momentum thickness–chord ratio with suction-surface local diffusion factor at reference incidence condition.

(Adapted from Lieblein, 1959.)

Effects of Mach number

When flow velocities through a cascade are such that Mach numbers are above 0.3, the flow can no longer be treated as incompressible. The peak Mach number on the surface of a conventional compressor blade is significantly higher than the inlet Mach number. If the inlet Mach number exceeds about 0.7, the flow over the blade will become transonic, leading to performance deterioration. Figure 3.18 shows the surface Mach number distribution around a compressor aerofoil in a cascade at low incidence for different levels of inlet Mach number. Once the local Mach number on the suction surface exceeds 1, additional losses arise due to the presence of shock waves. In addition, the rapid pressure rise across the shock waves leads to thicker boundary layers and therefore greater viscous losses. The higher diffusion on the suction surface at high inlet Mach number means that the blade boundary layers are likely to separate at modest levels of positive incidence.

In practice, the effects of high inlet Mach numbers are alleviated by using very thin blades and low camber. These features help to make the peak suction-surface Mach number not much higher than the inlet Mach number. As shown in Chapter 5, such blades can be used for highly efficient transonic compressor rotors with relative inlet Mach numbers up to 1.5.

Figure 3.19 is a diagram showing the mean-line flow through a high-speed compressor cascade. For any cascade, given the inlet angle, α_1, the inlet Mach number, M_1, and the exit Mach number, M_2, it is possible to calculate the exit angle, and thus the deviation, if the cascade loss coefficient,

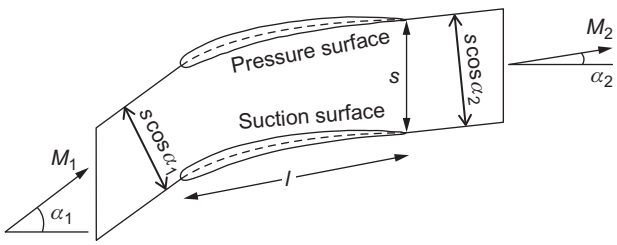

FIGURE 3.18

Variation of surface Mach number with inlet Mach number for a C4 compressor blade at low incidence

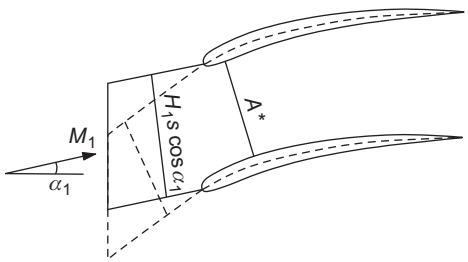

FIGURE 3.19

Mean-line analysis of compressible flow through a compressor cascade.

Y_p, is known. This is done using the one-dimensional compressible flow relations for the flow through the cascade. The ratio of stagnation to static pressure and the nondimensional mass flow are both functions of inlet Mach number:

$$\frac{p_{01}}{p_1} = \left(1 + \frac{\gamma - 1}{2} M_1^2\right)^{\gamma/(\gamma-1)} \qquad \text{(from Eq.(1.36))}$$

$$\dot{m}\frac{\sqrt{CpT_{01}}}{sH_1 \cos\alpha_1 p_{01}} = Q(M_1) \qquad \text{(from Eq.(1.39))}$$

From the definition of loss coefficient, Y_p (Eq. (3.5)), the cascade stagnation pressure ratio can be found:

$$\frac{p_{02}}{p_{01}} = 1 - Y_p\left(1 - \frac{p_1}{p_{01}}\right) \tag{3.41}$$

For a stationary blade row, $T_{01} = T_{02}$. Thus, the nondimensional mass flow at exit from the cascade can be written:

$$\frac{\dot{m}\sqrt{CpT_{02}}}{H_2 s \cos\alpha_2 p_{02}} = Q(M_2) = Q(M_1) \times \frac{H_1}{H_2} \times \frac{p_{01}}{p_{02}} \times \frac{\cos\alpha_1}{\cos\alpha_2}$$

Assuming the AVDR of the cascade is equal to 1, then $H_1/H_2 = 1$, and the preceding can be written in the following form to give the flow exit angle:

$$\cos\alpha_2 = \frac{Q(M_1)}{Q(M_2)} \times \frac{p_{01}}{p_{02}} \times \cos\alpha_1 \tag{3.42}$$

Combining Eqs (3.41) and (3.42) gives the exit angle in terms of the inlet conditions, the loss coefficient, and the exit Mach number. Equally, the preceding expression can be used to find the exit Mach number or the loss coefficient in terms of the other quantities.

The effect of negative incidence at a high inlet Mach number can be demonstrated using an analysis similar to that presented previously to find when a compressor cascade will choke. Consider a compressor cascade with a minimum flow area, A^*, as pictured in Figure 3.20. This minimum flow area is usually referred to as the *throat* of the blade passage. Applying conservation of mass between the inlet and the throat,

$$\frac{\dot{m}\sqrt{CpT_{01}}}{H_1 s \cos\alpha_1 p_{01}} = Q(M_1) = \frac{\dot{m}\sqrt{CpT_{01}}}{A * P_0^*}\frac{p_0^*}{p_{01}} \times \frac{A*}{H_1 s \cos\alpha_1} \tag{3.43}$$

When the flow chokes in the blade passage, the Mach number at the throat is unity and, therefore,

$$\frac{\dot{m}\sqrt{CpT_{01}}}{A * P_0^*} = Q(1) = \text{constant}$$

In the best case, there will be little loss in stagnation pressure between inlet and the throat and $p_0^* = p_{01}$. In this case, Eq. (3.43) can be simplified to give the inlet flow angle at which choking occurs:

$$\cos\alpha_1 = \frac{Q(1)}{Q(M_1)}\frac{A^*}{H_1 s} \tag{3.44}$$

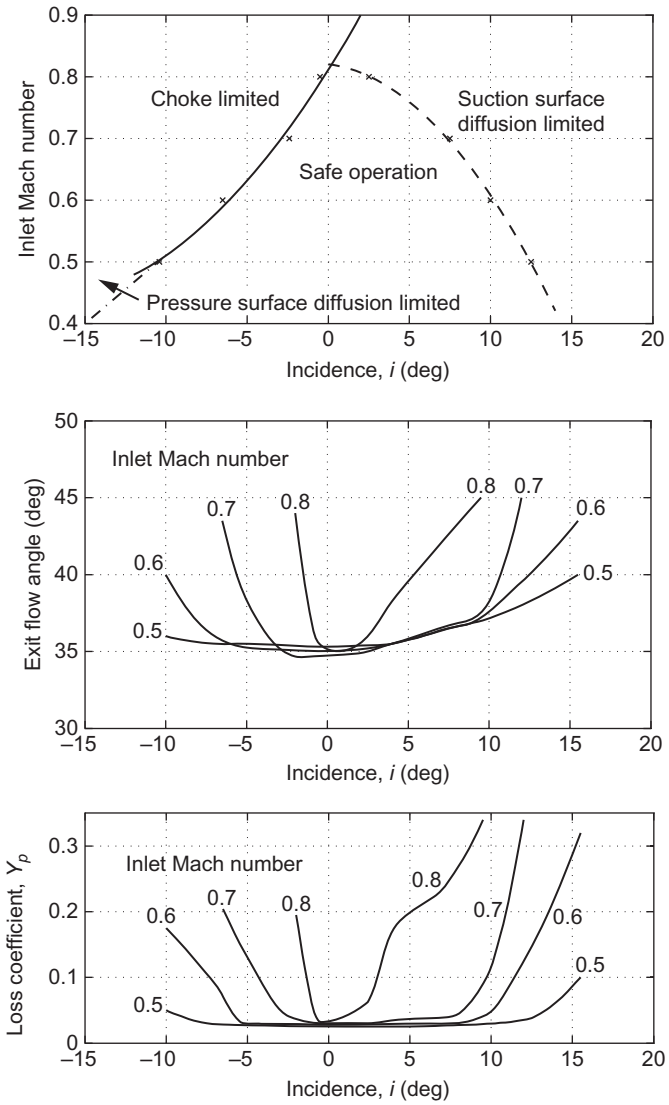

FIGURE 3.20

Choking of a compressor cascade at negative incidence.

All the terms on the right-hand side of Eq. (3.44) are constant except $Q(M_1)$. This equation shows that, as the inlet Mach number increases, the cosine of the inlet angle when choking occurs decreases (and thus the actual angle increases). Therefore, the amount of negative incidence possible before choking occurs is reduced as the inlet Mach number increases. To avoid choking either the inlet angle must be increased or the inlet Mach number reduced.

To conclude this section, Figure 3.14 shows typical variations in loss coefficient and exit angle for a compressor cascade as a function of the inlet incidence angle and inlet Mach number. The exact form of these plots will depend on the detailed cascade geometry, and they can only be determined by a series of cascade tests or detailed numerical analysis. However, the trends shown are seen in all compressor blades. For a given inlet Mach number, there is a range of incidence for which the cascade is low loss and low deviation. Outside this range, both the loss and deviation rise rapidly. The variation of a compressor blade row loss coefficient with incidence is often referred to as a *loss bucket* or a *loss loop*. The results plotted in Figure 3.14 clearly show that as Mach number increases the tolerance of the cascade to incidence is reduced. The reduced tolerance to positive incidence occurs due to the greater suction-surface diffusion present at higher inlet Mach numbers. The reduced tolerance to negative incidence occurs due to choking of the cascade blade passage. It is only at low inlet Mach numbers that diffusion on the pressure surface can limit the performance at negative incidence.

3.6 Turbine cascades

There is a fundamental difference between the flow in turbine cascades and that in compressor cascades that needs emphasizing. In turbine blade rows, the pressure is falling and the flow is accelerating. This means that

i. the boundary layers are much more stable and remain attached to the blades;
ii. the blades can accept a much higher loading without the danger of boundary layer separation;
iii. the flow deflection in a turbine blade row can be greater than 120°;
iv. the ratio of exit to inlet velocity, c_2/c_1, can be between 2 and 4;
v. the diffusion factor on the suction surface, DF, is typically only about 0.15, so there is no danger of boundary layer separation except at very low values of Reynolds number.

Figure 3.21 shows a sketch of the flow through an axial flow turbine cascade with the corresponding surface velocity distribution. This illustrates many of the features described previously and it is worth noting the rapid reduction in flow area through the cascade, which is what generates the high acceleration along the streamtube. The high acceleration and low levels of diffusion throughout the flow-field lead to turbine cascades having a wide range of low loss performance. This is in contrast to compressor cascades, which have a rather narrow range. This is also the basic reason why the pressure drop across turbine blades can be much higher than the pressure rise across compressor blades and why there are far fewer turbine stages than compressor stages in a turbojet engine.

Turbine loss correlations

A number of approaches have been made to predict the total pressure loss coefficients and flow deviation angles to the geometry of the turbine cascade and the incoming flow. A detailed account of the different methods and comparison of results found have been given by Horlock (1966), Dunham and Came (1970), Kacker and Okapuu (1981), Craig and Cox (1971), and others. In the

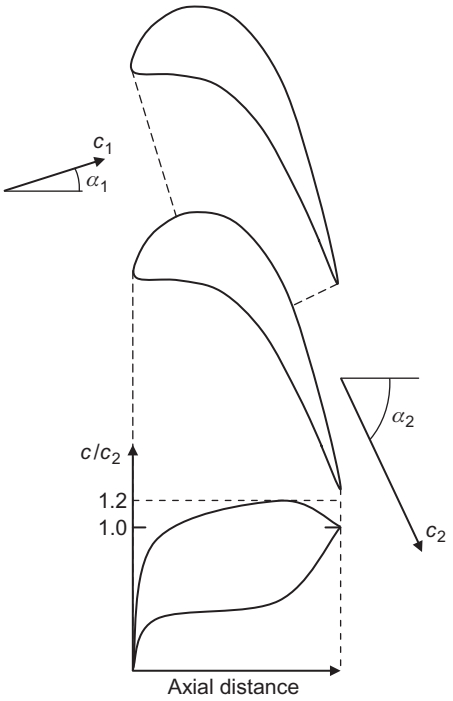

FIGURE 3.21

Flow through an axial flow turbine cascade.

following account, it seems reasonable to limit the discussion to just two of the more prominent methods, namely,

i. the correlation of Ainley and Mathieson (1951);
ii. the correlation of Soderberg (1949).

Before embarking on the details of these correlations, it seems only fair to mention that so far as their accuracy goes that Soderberg's method is adequate for making rapid estimates of turbine efficiency (which is dealt with in Chapter 4) and, according to Horlock (1966), can give efficiencies within $\pm 3\%$. However, these correlations are now quite dated and are not expected to be accurate for modern, highly loaded transonic turbine blade rows. Nowadays, correlations may be used during the preliminary design of turbines, but detailed cascade testing or computational analysis would always be applied to accurately determine the blade losses.

Correlation of Ainley and Mathieson

Ainley and Mathieson (1951) (A&M) reported a way of estimating the performance of an axial flow turbine, which has been widely used. The method determines the total pressure loss and gas efflux angle for each row of a turbine stage at a single *reference* diameter (the mean of the blade row inner

and outer diameters) and under a wide range of inlet conditions. Dunham and Came (1970) gathered together details of several improvements to the method, which gave better performance prediction than the original method, particularly for *small* turbines. When the blading is *competently designed*, the revised method has been found to give reliable predictions of efficiency to within $\pm 2\%$.

According to A&M's method, the total pressure loss in a turbine is composed of three parts:

i. a profile loss;
ii. a secondary loss;
iii. a tip clearance loss

and all of these are needed to determine the overall performance of a turbine stage.

In the following analysis, we are concerned only with the profile loss, since this is the component relevant to turbine cascades. The other two components of turbine loss, which require fairly extensive descriptions, are considered in Chapter 4.

The profile loss coefficient, defined by Eq. (3.6), is determined initially at zero incidence ($i = 0$). At any other incidence, the profile loss ratio $Y_p/Y_{p(i=0)}$ is assumed to be defined by a unique function of the incidence ratio i/i_s as shown in Figure 3.22, where i_s is the *stalling incidence*, which is defined as the incidence where the profile loss ratio $Y_p/Y_{p(i=0)} = 2.0$.

Next, A&M correlated the profile losses of turbine blade rows against space–chord ratio s/l, fluid outlet angle α_2, blade maximum thickness–chord ratio t_{max}/l, and blade inlet angle. The variation of $Y_{p(i=0)}$ against the space–chord ratio s/l is shown in Figure 3.23(a) for *nozzle blade rows* and in Figure 3.23(b)*for impulse blading*, both at various flow outlet angles.

For the sort of blading normally employed (intermediate between nozzle blades and impulse blades), the zero incidence total pressure loss coefficient devised by A&M is

$$Y_{p(i=0)} = \left\{ Y_{p(\alpha_1=0)} + \left(\frac{\alpha_1}{\alpha_2}\right)^2 \left[Y_{p(\alpha_1=\alpha_2)} - Y_{p(\alpha_1=0)} \right] \right\} \left(\frac{t_{max}/l}{0.2} \right)^{\alpha_1/\alpha_2} \tag{3.45}$$

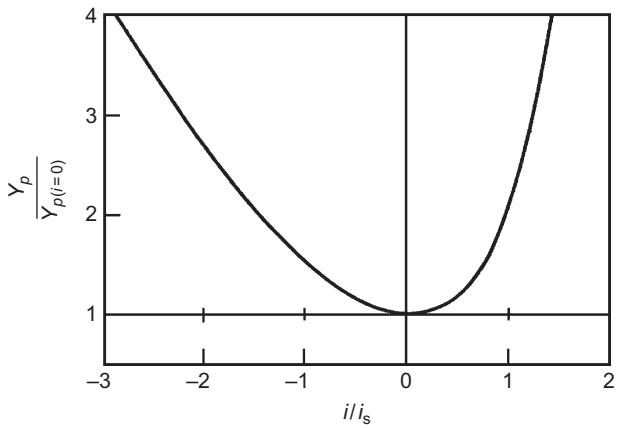

FIGURE 3.22

Variation of profile loss with incidence for typical turbine blading.

(Adapted from Ainley and Mathieson, 1951.)

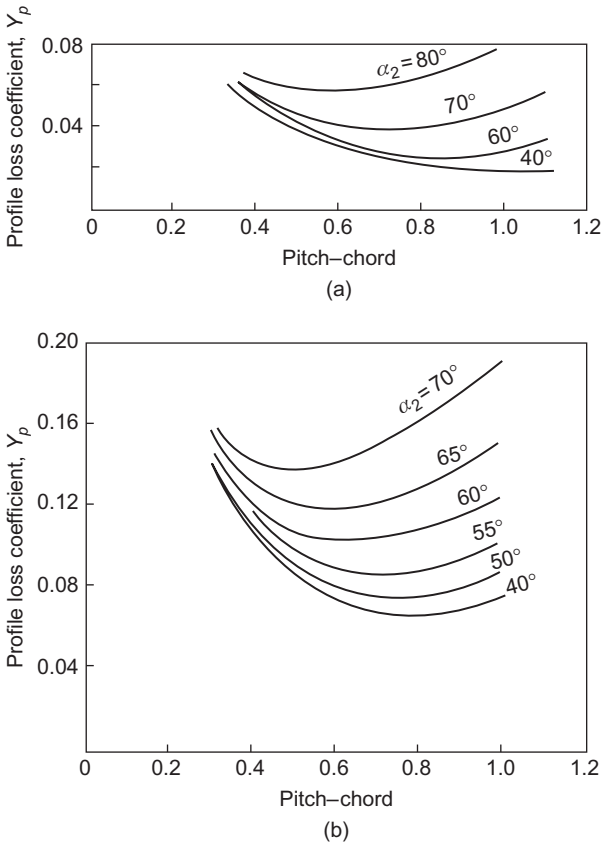

FIGURE 3.23

Profile loss coefficients of turbine nozzle and impulse blading at zero incidence: (a) nozzle blades, $\alpha_1 = 0$ and (b) impulse blades, $\alpha_1 = \alpha_2$ ($(t_{max}/l = 0.2$; $Re = 2 \times 10^5$; $M < 0.6$).

(Adapted from Ainley and Mathieson, 1951.)

All the values of Y_p are taken at the same space−chord ratio and outlet flow angle. Equation (3.45) includes a correction for the effect of the thickness−chord ratio and is valid in the range $0.15 \leq t_{max}/l \leq 0.25$. If the actual blade has a t_{max}/l greater or less than the limits quoted, A&M recommended that the loss should be taken as equal to a blade having t_{max}/l either 0.25 or 0.15.

A feature of the losses given in Figure 3.23 is that, compared with the impulse blades, the nozzle blades have a much lower total pressure loss coefficient. This observation confirms the results shown in Figure 3.24, that flows in which the mean pressure is falling always have a lower loss coefficient than flows in which the mean pressure is constant or increasing.

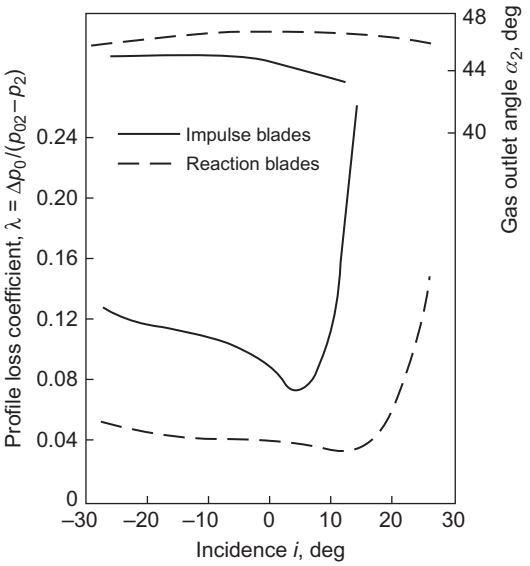

FIGURE 3.24

Variation in profile loss with incidence for typical turbine cascade blades.

(Adapted from Ainley, 1948.)

Reynolds number correction

A&M obtained their data for a mean Reynolds number of 2×10^5 based on the mean chord and exit flow conditions from the turbine state. They recommended that, for lower Reynolds numbers, down to 5×10^4, a correction be made to stage efficiency according to the rough rule

$$(1 - \eta_{tt}) \propto Re^{-1/5}$$

Soderberg's correlation

A relatively simple method of estimating turbine blade row losses is to assemble the performance data on the overall efficiencies from a wide variety of turbines and from this determine the individual blade row stagnation pressure losses. Such a system was developed by Soderberg (1949) from a large number of tests performed on steam turbines and on cascades and extended to fit data obtained from small turbines with very low aspect ratio blading (small height−chord). Soderberg's method was intended only for turbines conforming to the standards of "good design," discussed later.

Horlock (1960) critically reviewed several widely used methods of obtaining design data for turbines. His paper confirms the claim made for Soderberg's correlation that, although based on relatively few parameters, its accuracy is comparable with the best of the other methods available at the time. Soderberg found that with the *optimum* space−chord ratio (using Zweifel's criterion),

turbine blade losses could be correlated with space−chord ratio, blade aspect ratio, blade thickness−chord ratio, and Reynolds number.

For turbine blade rows operating at the optimum load coefficient, with a Reynolds number of 10^5 and aspect ratio, H/b = blade height/axial chord, of 3, the "nominal" loss coefficient, ζ^* (defined by Eq. (3.7)) is a simple function of the fluid deflection angle, $\varepsilon = \alpha_1 + \alpha_2$, for a given thickness−chord ratio (t_{max}/l):

$$\zeta^* = 0.04 + 0.06\left(\frac{\varepsilon}{100}\right)^2 \tag{3.46}$$

where ε is in degrees. Values of ζ^* are drawn in Figure 3.25 as a function of deflection angle ε for several ratios of t_{max}/l.

This expression fits the Soderberg curve (for $t_{max}/l = 0.2$) quite well with $\varepsilon \leq 120°$ but is less accurate at higher deflections. For turbine rows operating at zero incidence, which is the basis of Soderberg's correlation, the fluid deflection is little different from the blading deflection since, for *turbine cascades*, deviations are usually small. If the aspect ratio H/b is larger or less than 3, a correction to the nominal loss coefficient ζ^* is made as follows: for nozzle rows,

$$1 + \zeta_1 = (1 + \zeta^*)(0.993 + 0.021b/H) \tag{3.47a}$$

and for rotors,

$$1 + \zeta_1 = (1 + \zeta^*)(0.975 + 0.75b/H) \tag{3.47b}$$

where ζ_1 is the energy loss coefficient at a Reynolds number of 10^5.

A further correction can be made if the Reynolds number is different from 10^5. As used in this section, the Reynolds number is based upon exit velocity c_2 and the hydraulic diameter D_h at the throat section, defined by

$$Re = \rho_2 c_2 D_h/\mu$$

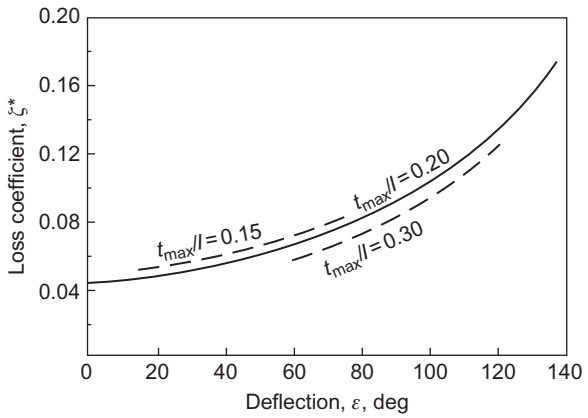

FIGURE 3.25

Soderberg's correlation of the turbine blade loss coefficient with fluid deflection.

(Adapted from Horlock, 1960.)

where for a cascade geometry, $D_h = 2sH\cos\alpha_2/(s\cos\alpha_2 + H)$. (*Note*: Hydraulic diameter = 4 × flow area ÷ perimeter.)

The Reynolds number correction is

$$\zeta_2 = \left(\frac{10^5}{Re}\right)^{1/4} \zeta_1 \tag{3.48}$$

Soderberg's method of loss prediction can be used to estimate turbine efficiencies over a wide range of Reynolds numbers and aspect ratios when additional corrections are included to allow for tip leakage and disk friction. The method has been shown to be useful by Lewis (1996) and by Sayers (1990).

Mach number effects on loss

Figure 3.26 shows plots of how the various components of loss coefficient, ζ, vary with exit Mach number, M_2, for a typical high-speed turbine cascade, taken fromMee et al. (1992). This plot demonstrates how the loss coefficient of a turbine blade rises rapidly as M_2 approaches and exceeds unity. This rise in loss is not accounted for in the previous correlations, which do not include functions of Mach number. It is partly caused by the shock waves, but it is also due to mixing and the

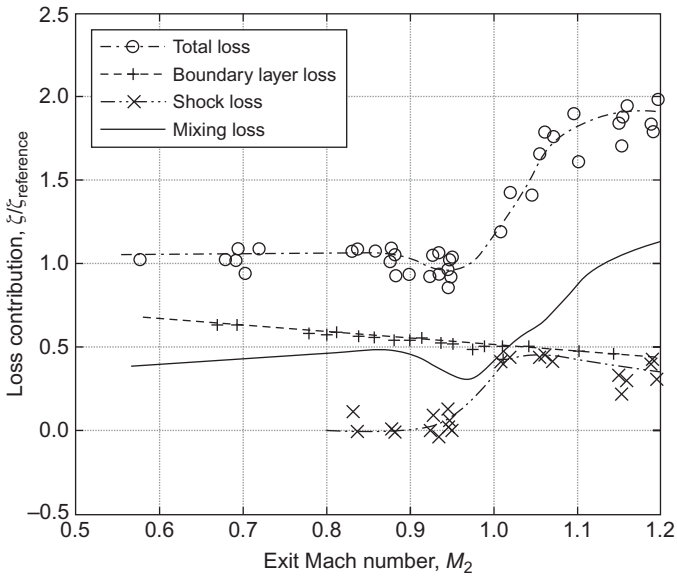

FIGURE 3.26

Variation of loss coefficient with Mach number for a turbine cascade at a Reynolds number of 1×10^6.

(From Mee et al., 1992.)

complex trailing edge flow pattern. This pattern generates a low-pressure region at the trailing edge, causing a drag force to act on the blade. This region is investigated in detail within Sieverding, Richard, and Desse (2003).

The Zweifel criterion

For turbine cascade blades, there is an optimum space−chord ratio that gives a minimum overall loss. Figure 3.27 illustrates the way the velocity distribution varies around the surface of a turbine blade in a cascade at three values of space−chord ratio. If the spacing between the blades is made small, the fluid receives the maximum amount of guidance from the blades, but the friction losses will be large. On the other hand, with the same blades spaced well apart, friction losses are small but, because of poor fluid guidance, the losses resulting from flow separation are high. These considerations led Zweifel (1945) to formulate his criterion for the optimum space−chord ratio of turbine blades having large deflection angles. Essentially, *Zweifel's criterion* is simply that the ratio of an "actual" to an "ideal" tangential blade loading has an approximately constant value for minimum losses. The tangential blade loads are obtained from the real and ideal pressure distributions on both blade surfaces, as described here.

Figure 3.28 indicates a typical pressure distribution around one blade in an incompressible turbine cascade, curves P and S corresponding to the pressure (or concave) side and suction (convex) side, respectively. The pressures are projected parallel to the cascade front so that the area enclosed between the curves S and P represents the *actual tangential blade load*:

$$Y = \dot{m}(c_{y1} + c_{y2}) \tag{3.49}$$

To give some idea of blade load capacity, the real pressure distribution is compared with an ideal pressure distribution giving a maximum load Y_{id} without risk of fluid separation on the S surface. The conditions for this ideal load are fulfilled by p_{01} acting over the *whole* P surface and p_2 acting over the *whole* S surface. With this pressure distribution, the *ideal tangential load* is

$$Y_{id} = (p_{01} - p_2)bH \tag{3.50}$$

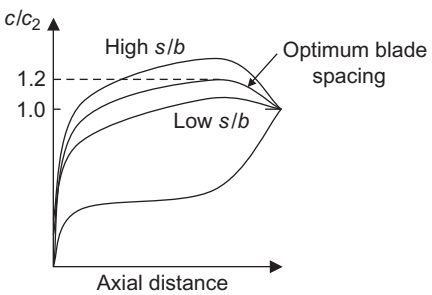

FIGURE 3.27

Optimum space−chord ratio for a turbine cascade.

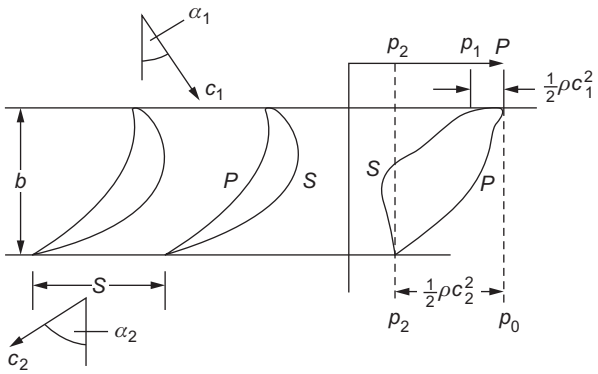

FIGURE 3.28

Typical pressure distribution around a low-speed turbine cascade blade.

where b is the axial chord of the blade. For incompressible, loss-free flow, $(p_{01} - p_2) = (1/2)\rho c_2^2$. If the axial velocity is also constant (i.e., AVDR = 1), then the mass flow, $\dot{m} = \rho H s c_x$, and the ratio of actual to ideal blade force is given by

$$Z = Y/Y_{\text{id}} = \frac{\dot{m}(c_{y1} + c_{y2})}{(p_{01} - p_2)bH} = \frac{\rho H s c_x^2(\tan\alpha_1 + \tan\alpha_2)}{1/2\rho c_x^2 \sec^2\alpha_2 bH}$$

This can be simplified to give

$$Z = Y/Y_{\text{id}} = 2(s/b)\cos^2\alpha_2(\tan\alpha_1 + \tan\alpha_2) \tag{3.51}$$

Zweifel found from a number of experiments on turbine cascades that at low Mach numbers, for minimum losses, the value of Z was approximately 0.8. Thus, for specified inlet and outlet angles, the optimum space–axial chord ratio is

$$s/b = 0.4/[\cos^2\alpha_2(\tan\alpha_1 + \tan\alpha_2)] \tag{3.52}$$

This shows that highly turning turbine blades, i.e., large $(\tan\alpha_1 + \tan\alpha_2)$, need to have a low pitch–axial chord ratio, whereas highly accelerating blades that have a high exit angle, i.e., small $\cos^2\alpha_2$, can be spaced further apart.

According to Horlock (1966), Zweifel's criterion accurately predicts optimum space–chord ratio for the data of A&M *only* for outlet angles of 60–70°. At other outlet angles, the criterion gives a less accurate estimate of optimum space–axial chord ratio, a conclusion supported by Aungier (2003). For modern blade designs, higher values of Z are common, particularly in the low-pressure turbines of jet engines, where there is a need to minimize the overall turbine weight and thus reduce the number of aerofoils required. Japikse and Baines (1994) suggest that the value of Zweifel's coefficient used may be in excess of 1 in such cases.

For compressible flow turbine cascades, the assumptions used in deriving Eq. (3.51) are no longer valid and the compressible value of Z must be derived from Eqs (3.49) and (3.50), i.e.,

$$Z = Y/Y_{\text{id}} = \frac{\dot{m}(c_{y1} + c_{y2})}{(p_{01} - p_2)bH} \tag{3.53}$$

The optimum value of Z, as just defined, is found to decrease as the exit Mach number rises. This reduction occurs because the ideal dynamic pressure $(p_{01} - p_2)$ increases rapidly with Mach number leading to a larger ideal blade force. For high Mach numbers, the coefficient can be evaluated using compressible flow relations as demonstrated in Example 3.4.

EXAMPLE 3.3

A two-dimensional linear turbine cascade operates in air with an inlet flow angle of 22° and an inlet Mach number of 0.3. The exit Mach number is measured as 0.93 with an exit flow angle of 61.4°. Calculate the ratio of inlet stagnation pressure to exit static pressure and determine the cascade stagnation pressure loss coefficient. If, for this operating condition, the Zweifel loading coefficient required for the cascade is 0.6, determine the pitch to axial chord ratio for the blades.

Solution

Applying continuity from inlet to exit of the cascade,

$$\frac{\dot{m}\sqrt{c_pT_{01}}}{Hs\cos\alpha_1 p_{01}} = Q(M_1) = \frac{\dot{m}\sqrt{c_pT_{02}}}{Hs\cos\alpha_2 p_{02}} \times \frac{\cos\alpha_2}{\cos\alpha_1} \times \frac{p_{02}}{p_{01}}$$

For a cascade, the stagnation temperature is constant, and thus, $T_{02} = T_{01}$. Rearranging the preceding equation allows the stagnation pressure ratio to be found by using compressible flow tables:

$$\frac{p_{02}}{p_{01}} = \frac{Q(M_1)}{Q(M_2)} \times \frac{\cos\alpha_1}{\cos\alpha_2} = \frac{0.6295}{1.2756} \times \frac{\cos(22^\circ)}{\cos(61.4^\circ)} = 0.9559$$

The ratio of inlet stagnation to exit pressure is found from

$$\frac{p_{01}}{p_2} = \frac{p_{02}}{p_2} \times \frac{p_{01}}{p_{02}} = \frac{1}{0.5721 \times 0.9559} = \underline{1.829}$$

The cascade loss coefficient can then be determined:

$$Y_p = \frac{p_{01} - p_{02}}{p_{01} - p_2} = \frac{1 - p_{02}/p_{01}}{1 - p_2/p_{01}} = \frac{1 - 0.9559}{1 - 1.829^{-1}} = \underline{0.0973}$$

The Zweifel coefficient can be expressed in terms of nondimensional groups that are each a function of Mach number. By expressing the Zweifel coefficient in this way, the compressible flow tables can then be used to evaluate each of the parameters required:

$$Z = \frac{\dot{m}(c_{y1} + c_{y2})}{(p_{01} - p_2)bH} = \frac{\dot{m}\sqrt{c_pT_{01}}}{Hs\cos\alpha_1 p_{01}} \times \frac{\left(c_1\sin\alpha_1/\sqrt{c_pT_{01}} + c_2\sin\alpha_2/\sqrt{c_pT_{01}}\right) \times Hs\cos\alpha_1}{(1 - p_2/p_{01})bH}$$

The Zweifel coefficient is then simplified to the following function of the blade pitch to axial chord ratio, the inlet and exit Mach numbers and the flow angles:

$$Z = Q(M_1) \times \frac{\left(c_1/\sqrt{c_pT_{01}} \times \sin\alpha_1 + c_2/\sqrt{c_pT_{01}} \times \sin\alpha_2\right) \times \cos\alpha_1}{(1 - p_2/p_{01})} \times \frac{s}{b}$$

Rearranging this equation to find the pitch to axial chord ratio gives

$$\frac{s}{b} = \frac{(1 - p_2/p_{01})Z}{Q(M_1) \times \left(c_1/\sqrt{c_p T_{01}} \times \sin\alpha_1 + c_2/\sqrt{c_p T_{01}} \times \sin\alpha_2\right) \times \cos\alpha_1}$$

Putting in the values and using the compressible flow tables where needed,

$$\frac{s}{b} = \frac{(1 - 1.829^{-1}) \times 0.6}{0.6295 \times [0.1881 \times \sin(22^\circ) + 0.5431 \times \sin(61.4^\circ)] \times \cos(22^\circ)} = \underline{0.851}$$

Flow exit angle

For turbine blades, the low amount of diffusion on the suction surface together with the thin boundary layers imply that the flow exit angle is much closer to the metal angle at the trailing edge than for a compressor cascade blade. (i.e., a small deviation angle). However, accurate prediction of the exit angle is extremely important because the downstream flow area, $Hs\cos\alpha_2$, varies rather rapidly with the exit angle α_2.

At high Mach numbers, the flow exit angle can be determined from compressible flow relationships. Figure 3.29 shows the flow through a choked turbine cascade. When the blade throat is choked the mass average, Mach number across the throat is unity, in which case (referring to Eq. (1.39)):

$$\frac{\dot{m}\sqrt{c_p T_0}}{Hop_o^*} = Q(1) \tag{3.54}$$

where o is the minimum distance at the blade throat, as shown in Figure 3.29, and p_o^* is the stagnation pressure at that location. Once the flow is choked, conditions upstream of the throat are fixed and independent of the downstream pressure.

Downstream of the cascade, the flow area is $s\cos\alpha_2$ and the Mach number is M_2,

$$\frac{\dot{m}\sqrt{c_p T_0}}{Hs\cos\alpha_2 po_2} = Q(M_2) \tag{3.55}$$

hence, by combining the preceding two equations,

$$\cos\alpha_2 = \frac{Q(1)}{Q(M_2)} \times \frac{p_0^*}{p_{02}} \times \frac{o}{s} \tag{3.56}$$

If the losses downstream of the throat are small, then $p_{02} \approx p_0^*$, so

$$\cos\alpha_2 = \frac{Q(1)}{Q(M_2)} \times \frac{o}{s} \tag{3.57}$$

In particular, when $M_2 = 1$, then $\alpha_2 = \cos^{-1}(o/s)$.

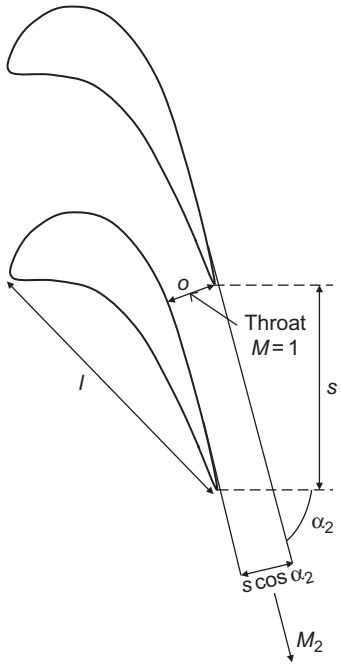

FIGURE 3.29

Flow through a choked turbine cascade.

Figure 3.30 indicates how the angle α_2 varies from subsonic to supersonic flow. For subsonic flows, the exit angle varies very little with Mach number. For supersonic exit flows, $Q(M_2) < Q(1)$ and it follows from Eq. (3.60) that α_2 decreases. This is known as *supersonic deviation*. As shown by Figure 3.30, further deviation is observed in experimental measurements. This additional deviation relative to the theory is caused by stagnation pressure losses downstream of the throat, $p_{02} < p_0^*$ and the blockage caused by the growth of boundary layers on the blade surfaces.

Turbine limit load

Turbines frequently operate with supersonic exit flows and at such conditions shock waves emanate from the trailing edge. One branch of the shock wave propagates downstream, but the other branch reflects off the suction surface of the adjacent blade. The configuration of these shock waves is shown in Figure 3.31 using a Schlieren photograph of the flow in a transonic turbine cascade at a downstream Mach number, $M_2 = 1.15$.

The back pressure of a turbine cascade can be lowered until the axial velocity component of the exit flow is equal to the sonic speed. This condition is called the *limit load* and it is the point where

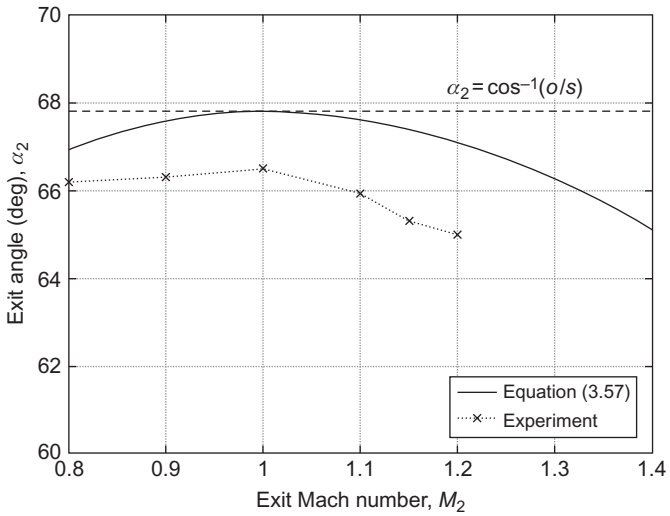

FIGURE 3.30

The variation of exit flow angle with exit Mach number for a transonic turbine cascade.

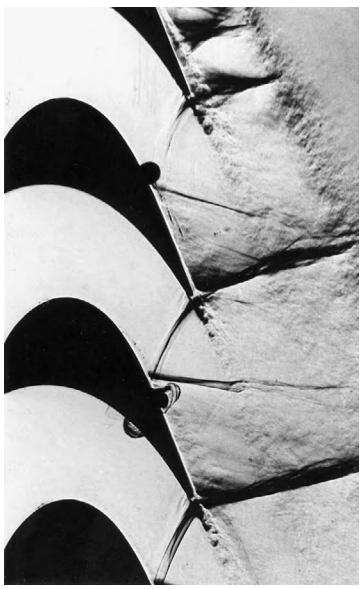

FIGURE 3.31

Schlieren photograph of flow in a highly loaded transonic turbine cascade with an exit Mach number of 1.15.

(From Xu, 1985.)

information (i.e., pressure waves) cannot travel upstream and no further increase in exit Mach number is possible. At *limit load*, $M_{x,\text{lim}} = M_{2,\text{lim}} \cos \alpha_{2,\text{lim}} = 1.0$, which implies that

$$M_{2,\text{lim}} = \frac{1}{\cos \alpha_{2,\text{lim}}} \tag{3.58}$$

Conservation of mass means that

$$\frac{\dot{m}\sqrt{c_p T_0}}{Hs \cos \alpha_{2,\text{lim}}\, p_{02}} = Q(M_{2,\text{lim}}) = \frac{\dot{m}\sqrt{c_p T_0}}{Hop_o^*} \times \frac{p_o^*}{p_{02}} \times \frac{0}{s \cos \alpha_{2,\text{lim}}}$$

Given that the throat is choked, as in Eq. (3.54),

$$\dot{m}\sqrt{\frac{c_p T}{Hop_o^*}} = Q(1)$$

so that

$$Q(M_{2,\text{lim}}) = Q(1) \times \frac{p_o^*}{p_{02}} \times \frac{o}{s \cos \alpha_{2,\text{lim}}} \tag{3.59}$$

Equations (3.58) and (3.59) can be solved simultaneously to enable both $M_{2,\text{lim}}$ and $\alpha_{2,\text{lim}}$ to be determined. Typically, the range of maximum exit Mach number is $1.4 < M_{2,\text{lim}} < 2.0$.

3.7 Cascade computational analysis

Rather than use cascade tests or correlations, computational methods are regularly applied to determine blade loading, surface velocity distributions, losses, and deviation. This section briefly outlines the key aspects of computational methods used for blade section analysis and some of the results they can produce. Further consideration of computational methods is presented in Chapter 6, including some presentation of three-dimensional CFD. However, it should be emphasized that the intention in this book is only to provide a general understanding of the capability of such methods and how they are used in turbomachinery design and analysis. Good references for further details are Stow (1989) and Denton and Dawes (1999).

Calculation geometry

Computational methods that perform the role of a cascade test are known as "blade-to-blade methods" since they compute the flow-field between adjacent blade sections on an unwrapped meridional−tangential (m-$r\theta$) streamsurface.[4] As discussed in Section 3.3, for cascade testing, the streamtube thickness does not necessarily remain constant through the blade passages and most modern blade-to-blade methods can accommodate an AVDR that is not equal to unity. Such methods are often referred to as quasi-three-dimensional (Q3D) since they are accounting for the 3D effects of streamtube divergence or convergence.

[4]In purely axial-flow cases, the flow domain will be an unwrapped axial−tangential (x−$r\theta$) plane. See Figure 1.2 for diagrams defining the turbomachinery coordinate system.

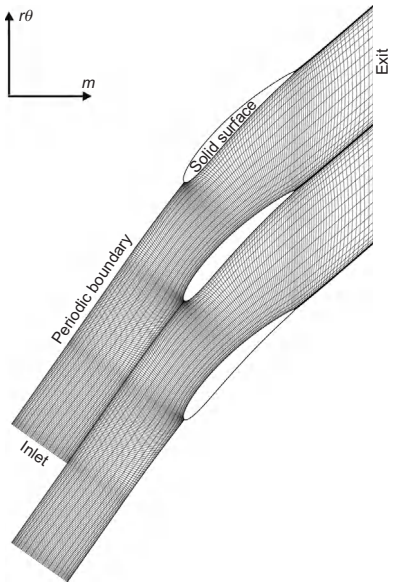

FIGURE 3.32

Calculation mesh for a blade-to-blade computation of a compressor cascade.

A typical computational mesh for a blade-to-blade method is shown in Figure 3.32. Note that in this case the mesh is for an inviscid calculation that does not resolve the boundary layers on the blade surfaces. The exact form of the mesh depends on the type of method used and the resolution required. Some meshes have regular, rectangular topology with fairly constant cell size, as in the case shown, whereas there are also methods that use triangular meshes with huge variations in cell size. In all cases, the mesh is only one cell thick and it represents a streamtube, so there can be no flow perpendicular to the plane of the mesh (into or out of the page).

Method types

The main task of a computational method is to determine, for each cell within a mesh, the flow properties that are compatible with the boundary conditions. Different numerical solvers take different approaches and include varying assumptions and simplifications. However, they are, in general, simply applying the fundamental laws of continuity, the steady flow energy equation, conservation of momentum, and the second law of thermodynamics, as presented in Chapter 1.

A technique known as a panel (or vortex) method assumes two-dimensional incompressible, inviscid flow. The method places vortices at a series of points on the blade pressure and suction surfaces. The strengths of the vortices are set such that there is no flow into or out of the blade surfaces. The flow at any point in the blade passages is then the linear sum of the influence of all of the vortices. This type of method is fairly limited for turbomachinery use since it is only applicable to incompressible, inviscid flow with uniform inflow.

A potential flow method is applicable to isentropic flow through a cascade. It essentially solves a form of the compressible continuity equation on a mesh, subject to constant stagnation enthalpy, isentropic relations, and the requirement for flow to leave a blade section trailing edge smoothly. They can be used for compressible flow cases provided there are no strong shock waves, but they cannot give any indication of blade losses. Potential flow methods such as Whitehead and Newton (1985) are still in use today to design turbine blade sections because they are very fast and the neglected viscous effects are usually small.

An Euler method treats each cell in a computational mesh as a control volume. It iteratively solves the equations for conservation of mass, momentum, and energy for each of these control volumes. A large number of iterations can be required to reach a converged, steady solution, which increases the run time, but typically Euler methods only take a minute or so on a modern computer. An Euler method can be used for compressible flow, but it does not include viscous effects. To account for boundary layers, a Navier–Stokes method can be used, which includes viscous terms in the momentum equation. Alternatively a coupled inviscid method and boundary layer solver can be used. In this, an Euler, or similar method, is used for the inviscid mainstream flow and a boundary layer solver is used to compute the development of the viscous boundary layers on the blade surface. Information is shared between these computations to account for the blockage of the boundary layer and the effects of the mainstream flow pressure distribution on the boundary layer parameters. A coupled method that is widely used today for blade section analysis and design is described in Giles and Drela (1987).

Note that many of the above methods can work in an "inverse" (or "design") mode as well as the standard "analysis" mode. In analysis mode, the geometry is fixed, analogous to a cascade test. In the inverse mode, the user prescribes a surface velocity distribution, which the code then aims to achieve by manipulating the blade section geometry.

Boundary conditions

Figure 3.32 indicates the different types of domain boundary in a blade-to-blade computation. A fundamental assumption for a cascade is that the flow is the same in all blade passages. Therefore, all flow properties should repeat along the periodic boundaries and this can be prescribed as a boundary condition. On solid blade surfaces, there can be no flow into or out of the surface and thus the velocity normal to any surface is zero and this is specified as another boundary condition.

The inlet and exit boundary conditions are specified to match the required cascade operating point. As discussed in Section 3.3, the performance of a cascade can be expressed by functional relationships of the form

$$\alpha_2 = \text{fn}(M_1, \alpha_1, Re); \quad Y_p = \text{fn}(M_1, \alpha_1, Re)$$

The boundary conditions must therefore be sufficient to fix the Mach number, inlet flow angle, and Reynolds number. For incompressible methods, the Mach number is irrelevant, and for inviscid (or isentropic) methods, the Reynolds number can also be omitted. Hence, there are fewer boundary conditions required for potential flow and panel methods.

In Euler and Navier–Stokes methods, the inlet stagnation pressure p_{01}, the inlet stagnation temperature T_{01}, and the inlet angle α_1 are usually specified, along with the exit static pressure p_2.

This is equivalent to how a cascade experiment is set up (see Figure 3.1): the inlet conditions p_{01} and T_{01} are set by the wind tunnel fan, the inlet angle α_1 is set by the angle between the cascade axis and the test section, and the exit static pressure is fixed by the ambient pressure downstream of the cascade. If viscous effects are modeled, the Reynolds number is also set, either directly, or by specifying the fluid viscosity and the geometry scale.

Transonic effects

Euler methods and Navier–Stokes methods can handle transonic flow and strong shock waves, although the accuracy of their predictions is limited by the resolution of the computational mesh. A shock wave will tend to be "smeared out" over a number of cells and the associated aerodynamic effects will not be accurately resolved. Figure 3.33 shows Mach number contours for a coupled inviscid method and boundary layer solver applied to a C4 compressor cascade operating with an inlet Mach number of 0.8 (This is the same condition and geometry as used in the surface Mach number plot in Figure 3.18). The figure shows a shock wave clearly captured on the blade suction surface. It also indicates the streamlines at the edge of the blade boundary layers that form the blade wake. This shows how in compressor blades the viscous effects can create significant blockage, which leads to an effect on the inviscid flow-field.

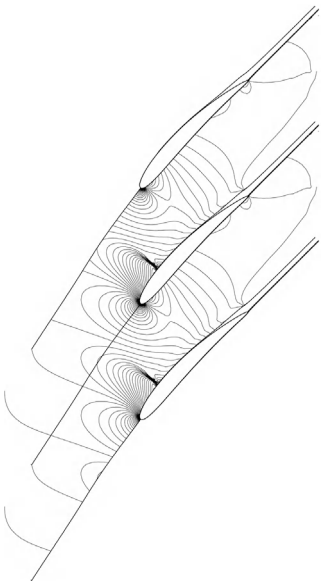

FIGURE 3.33

Contours of Mach number from a coupled inviscid and boundary layer computation of a C4 compressor cascade operating at low incidence with an inlet Mach number of 0.8.

Viscous effects

Inviscid methods cannot give an estimation of losses, but they can still be useful as they will calculate the blade surface velocity distribution, the blade loading and the diffusion levels on the surfaces. As discussed in Section 3.5, the state of the boundary layers and blade losses correlate with local diffusion levels. Inviscid methods can therefore be used to determine whether acceptable diffusion levels are maintained and what operating points lead to high diffusion. Figure 3.34 shows an example comparison between measured and computed surface velocity distributions around a turbine stator for a quasi-three-dimensional Euler method.

Methods that model viscous effects do not necessarily determine them accurately. There are several complex physical phenomena that may need to be modeled in the blade boundary layers such as laminar flow, transition to turbulence, turbulent flow, separation, and reattachment. A Navier–Stokes method requires models for turbulence and transition as well as a large number of mesh points close to any surfaces to resolve the flow gradients in the boundary layers. Denton and Dawes (1999) state that at high Reynolds number a Navier–Stokes solution should predict viscous losses accurate to within 10%, but at lower, transitional, Reynolds numbers the losses may be in error by 50%. In this case, a coupled inviscid and boundary layer method is more accurate and can provide a more detailed prediction of the boundary layer parameters. In applications where there are significant Reynolds number and transitional effects, such as low-pressure turbines for jet engines, coupled inviscid and boundary layer solvers have been shown to be accurate in reproducing cascade test results, see Stow (1989).

In all cases, a computational method user should be careful to ensure that all the relevant physics are sufficiently reproduced in their solver, that the method has been adequately calibrated, and that it has been applied correctly using a suitable mesh and appropriate boundary conditions.

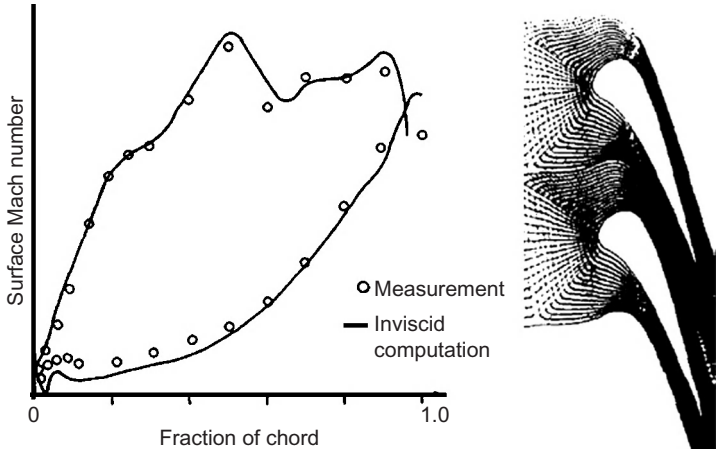

FIGURE 3.34

Comparison of surface Mach number distribution between an inviscid Euler solver and experiment for a high-pressure turbine stator.

(Adapted from Bry, 1989.)

It should then be possible to quickly generate useful cascade results (e.g., in the form shown in Figure 3.14 or 3.25) with a known level of accuracy.

PROBLEMS

1. Experimental compressor cascade results suggest that the stalling lift coefficient of a low-speed cascade blade may be expressed as

$$C_L\left(\frac{c_1}{c_2}\right)^3 = 2.2$$

where c_1 and c_2 are the entry and exit velocities, respectively. Find the stalling inlet angle for a compressor cascade of space–chord ratio unity if the outlet air angle is 30°.

2. Show, for a low-speed turbine cascade, using the angle notation of Figure 3.28, that the lift coefficient is

$$C_L = 2(s/l)(\tan\alpha_1 + \tan\alpha_2)\cos\alpha_\mathrm{m} + C_D\tan\alpha_\mathrm{m}$$

where $\tan\alpha_\mathrm{m} = (1/2)(\tan\alpha_\mathrm{m} - \tan\alpha_1)$ and $C_D = \mathrm{drag}/((1/2)\rho c_\mathrm{m}^2 l)$. A cascade of turbine nozzle vanes has a blade inlet angle α_1' of 0°, a blade outlet angle α_2' of 65.5°, a chord length l of 45 mm and an axial chord b of 32 mm. The flow entering the blades is to have zero incidence and an estimate of the deviation angle based upon similar cascades is that δ will be about 1.5° at low outlet Mach number. If the blade load ratio Z defined by Eq. (3.55) is to be 0.85, estimate a suitable space–chord ratio for the cascade. Determine the drag and lift coefficients for the cascade given that the profile loss coefficient is

$$\lambda = \Delta p_0/\left(\frac{1}{2}\rho c_2^2\right) = 0.035$$

3. **a.** Show that the pressure rise coefficient $C_p = \Delta p/((1/2)\rho c_1^2)$ of an incompressible compressor cascade is related to the total pressure loss coefficient ζ by the following expression:

$$C_p = 1 - (\sec^2\alpha_2 + \zeta)/\sec^2\alpha_1$$

$$\zeta = \Delta p_0/\left(\frac{1}{2}\rho c_x^2\right)$$

where α_1, α_2 = flow angles at cascade inlet and outlet.

b. Determine a suitable *maximum* inlet flow angle of a low-speed compressor cascade having a space–chord ratio 0.8 and $\alpha_2 = 30°$ when the diffusion factor DF is limited to 0.6. The definition of diffusion factor that should be used is the Lieblein formula (1959):

$$\mathrm{DF} = \left(1 - \frac{\cos\alpha_1}{\cos\alpha_2}\right) + \left(\frac{s}{l}\right)\frac{\cos\alpha_1}{2}(\tan\alpha_1 - \tan\alpha_2)$$

c. The stagnation pressure loss derived from flow measurements on this cascade is 149 Pa when the inlet velocity c_1 is 100 m/s at an air density ρ of 1.2 kg/m^3. Determine the values of
  i. pressure rise and
  ii. drag and lift coefficients.

4. A low-speed compressor has stator vanes that are to have an inlet flow angle of 45° and an exit flow angle of 25°.
a. Calculate the pitch−chord ratio of the stators assuming a Lieblein diffusion factor of 0.45. Using Lieblein's diffusion factor reaching 0.6 as a criterion, and assuming that the exit flow angle remains constant, determine the incidence that corresponds to the blade stalling.
b. Use Carter's deviation correlation to estimate the required metal exit angle given that a parabolic arc camber line is employed with maximum camber at 40% chord. (Note that some iteration is needed.)

5. Use $\gamma = 1.4$, $R = 287$ J/kg/K^1 and $c_p = 1005$ J/kg/K in this question.
a. A two-dimensional compressor cascade operates in air. The inlet metal angle of the blades is 55° and the exit metal angle is 37°. When the flow is at zero incidence with an inlet Mach number of 0.65, the exit Mach number is 0.44, and the stagnation pressure loss coefficient is given by

$$Y_p = \frac{p_{01} - p_{02}}{p_{01} - p_1} = 0.038$$

Determine the exit flow angle and give two reasons why this is greater than the exit metal angle.
b. Find the blade pitch-to-chord ratio needed such that DF = 0.45 when the cascade is at the operating point described in part (a).
c. Assuming that the exit flow angle and loss remain constant, estimate the new value of DF when the incidence of the flow is increased to 5° while maintaining an inlet Mach number of 0.65. Use the pitch-to-chord ratio found in part (b).
d. If the cascade throat width to pitch ratio o/s is 0.6, determine the incidence of the flow onto the blades at which the cascade will choke with an inlet Mach number of 0.65. Assume that there is no loss upstream of the cascade throat.

6. A high-speed air turbine cascade is estimated to have an AVDR of 0.97. At inlet the Mach number is 0.22 and the flow angle is 30°. The blades turn the flow through 100° and at exit the flow is just sonic. Take γ to be 1.4.
a. Determine the stagnation pressure loss coefficient based on exit conditions and the energy loss coefficient, ζ.
b. Estimate ζ using the Soderberg correlation for this cascade, Eq. (3.46), assuming an aspect ratio of 3. Compare with the value found in (a) and explain why the correlation might be expected to underestimate the loss in this case.
c. Neglecting streamtube contraction and the stagnation pressure loss downstream of the throat, estimate the opening-to-pitch ratio of the cascade.

7. A two-dimensional compressor cascade is tested in air with an inlet stagnation pressure of 1 bar and an inlet stagnation temperature of 300 K. For an inlet Mach number of 0.75 and an

inlet flow angle of 50°, the exit flow angle is measured as 15.8°. Determine the mass flow rate per unit frontal area. Assuming the flow is isentropic, calculate the exit Mach number and the static pressure ratio across the cascade.

8. A compressor blade design tested in a cascade is found to choke with an inlet Mach number of 0.9 when the inlet flow angle is 52°. If the ratio of the throat area to the frontal area, $A^*/H_1 s$, for the cascade is 0.625, calculate the loss of stagnation pressure between the far upstream and the throat and express this as a loss coefficient. Comment on what could cause this loss.

9. A turbine cascade operates in air with an inlet angle of 45° from the axial direction. The ratio of inlet stagnation pressure to exit static pressure is 2.6 and the inlet Mach number is 0.3.

a. If the stagnation pressure loss coefficient, Y_p, is measured to be 0.098, calculate the exit Mach number and show that the exit angle is 67.7°. It can be assumed that the blade height is constant through the cascade and that the growth of sidewall boundary layers is negligible.

b. The opening-to-pitch ratio of the cascade is 0.354. For the operating point described in part (a), show that approximately two-thirds of the total loss in stagnation pressure occurs downstream of the throat.

c. The exit static pressure from the cascade is lowered until limit load is achieved. The exit Mach number at this condition is measured to be 1.77. Given that the stagnation pressure loss upstream of the throat is unchanged, determine the new overall stagnation pressure loss coefficient for the cascade.

References

Ainley, D. G. (1948). Performance of axial flow turbines. *Proceedings of the Institution of Mechanical Engineers, 159.*

Ainley, D. G., & Mathieson, G. C. R. (1951). A method of performance estimation for axial flow turbines. *ARC. R. and M.*, 2974.

Aungier, R. H. (2003). *Axial-flow compressors: a strategy for aerodynamic design and analysis.* New York, NY: ASME Press.

Baines, N. C., Oldfield, M. L. G., Jones, T. V., Schulz, D. L., King, P. I., & Daniels, L. C. (1982). A short duration blowdown tunnel for aerodynamic studies on gas turbine blading. ASME Paper 82-GT-312.

Bry, P. F. (1989). Blading design for cooled high-pressure turbines. Within AGARD Lecture Series No. 167 presented June 1989.

Carter, A. D. S. (1950). Low-speed performance of related aerofoils in cascade. ARC. Current Paper, No. 29.

Carter, A. D. S., Andrews, S. J., & Shaw, H. (1950). Some fluid dynamic research techniques. *Proceedings of the Institution of Mechanical Engineers, 163.*

Craig, H. R. M., & Cox, H. J. A. (1971). Performance estimation of axial flow turbines. *Proceedings of the Institution of Mechanical Engineers*, *185*, 407–424.

Csanady, G. T. (1964). *Theory of turbomachines.* New York, NY: McGraw-Hill.

Cumpsty, N. A. (1989). *Compressor aerodynamics.* New York, NY: Longman.

De Haller, P. (1953). Das Verhalten von Tragflügelgittern in Axialverdichtern und im Windkanal. *BWK Zeitschrift*, *5*(10), 333–337.

Denton, J. D. (1993). Loss mechanisms in turbomachines. IGTI scholar lecture. *ASME Journal of Turbomachinery*, *115*, 621–656.

Denton, J. D., & Dawes, W. N. (1999). Computational fluid dynamics for turbomachinery design. *Proceedings of the Institution of Mechanical Engineers Part C*, *213*.

Dixon, S. L. (1978). Measurement of flow direction in a shear flow. *Journal of Physics E: Scientific Instruments*, *2*, 31–34.

Dunham, J. (1970). A review of cascade data on secondary losses in turbines. *Journal of Mechanical Engineering Science*, *12*.

Dunham, J., & Came, P. (1970). Improvements to the Ainley–Mathieson method of turbine performance prediction. *Transactions of the American Society of Mechanical Engineers, Series A*, 92.

Felix, A. R. (1957). Summary of 65-Series compressor blade low-speed cascade data by use of the carpet-plotting technique. NACAT.N. 3913.

Giles, M. B., & Drela, M. (1987). Two dimensional transonic aerodynamic design method. *AIAA Journal*, *25*, 9.

Glauert, H. (1959). *Aerofoil and airscrew theory* (2nd ed.). Cambridge, UK: Cambridge University Press.

Hay, N., Metcalfe, R., & Reizes, J. A. (1978). A simple method for the selection of axial fan blade profiles. *Proceedings of the Institution of Mechanical Engineers*, *192*(25), 269–275.

Hearsey, R. M. (1986). Practical compressor design. In David Japikse (Ed.), *Advanced topics in turbomachinery technology*. Norwich, VT: Concepts ETI, Inc.

Herrig, L. J., Emery, J. C., & Erwin, J. R. (1957). Systematic two-dimensional cascade tests of NACA 65-Series compressor blades at low speeds. NACA T.N. 3916.

Hirsch, C. (Ed.), (1993). Advanced methods for cascade testing. Advisory Group for Aerospace Research & Development, NATO, AGARDograph 328.

Horlock, J. H. (1958). *Axial flow compressors.* London: Butterworth (1973 reprint with supplemental material, Huntington, NY: Krieger).

Horlock, J. H. (1960). Losses and efficiency in axial-flow turbines. *International Journal of Mechanical Science*, *2*, 48.

Horlock, J. H. (1966). *Axial-Flow Turbines.* London: Butterworth (1973 reprint with corrections, Huntington, NY: Krieger).

Howell, A. R. (1945a). Design of axial compressors. *Proceedings of the Institution of Mechanical Engineers, 153*.

Howell, A. R. (1945b). Fluid dynamics of axial compressors. *Proceedings of the Institution of Mechanical Engineers, 153*.

Japikse, D., & Baines, N. C. (1994). *Introduction to turbomachinery.* Oxford, UK: Concepts ETI, Inc., Wilder, VT and Oxford University Press.

Johnsen, I. A., & Bullock, R. O. (Eds.), (1965). *Aerodynamic design of axial-flow compressors*. NASA SP 36.

Kacker, S. C., & Okapuu, U. (1981). A mean line prediction method for axial flow turbine efficiency, Paper No. 81-GT-58, ASME.

Koch, C. C., & Smith, L. H., Jr. (1976). Loss sources and magnitudes in axial-flow compressors. *ASME Journal of Engineering for Power*, 411–423.

Lewis, R. I. (1996). *Turbomachinery performance analysis.* New York, NY: Arnold and John Wiley.

Lieblein, S. (1959). Loss and stall analysis of compressor cascades. *Transactions of the American Society of Mechanical Engineers, Series D, 81*.

Lieblein, S. (1960). Incidence and deviation-angle correlations for compressor cascades. *Transactions of the American Society of Mechanical Engineers, Journal of Basic Engineering*, *82*, 575–587.

Lieblein, S. (1965). Experimental flow in two-dimensional cascades. In I. A. Johnsen R. O. Bullock (Eds.), *Aerodynamic design of axial-flow compressors*. NASA SP 36.

Lieblein, S., & Roudebush, W. H. (1956). Theoretical loss relations for low-speed 2D cascade flow. NACA T.N. 3662.

Lieblein, S., Schwenk, F. C., & Broderick, R. L. (1953). Diffusion factor for estimating losses and limiting blade loadings in axial flow compressor blade elements. NACA R.M. E53 D01.

Mee, D. J. (1991). Large chord turbine cascade testing at engine Mach and Reynolds numbers. *Experiments in fluids*, *12*, 119–124.

Mee, D. J., et al. (1992). An examination of the contributions to loss on a transonic turbine blade in cascade. *ASME Journal of Turbomachinery*, *114*, 155–124.

Mellor, G. (1956). The NACA 65-series cascade data. *MIT Gas Turbine Laboratory Report*.

Sayers, A. T. (1990). *Hydraulic and compressible flow turbomachines.* New York, NY: McGraw-Hill.

Sieverding, C. H. (1985). Aerodynamic development of axial turbomachinery blading. In A. S. Ücer, P. Stow, & C. Hirsch (Eds.), *Thermodynamics and fluid mechanics of turbomachinery* (Vol. 1, pp. 513–665). Dordrecht, The Netherlands: Martinus Nijhoff, NATO ASI Series.

Sieverding, C. H., Richard, H., & Desse, J. -M. (2003). Turbine blade trailing edge flow characteristics at high subsonic outlet Mach number. *ASME Journal of Turbomachinery*, *125*, 298–309.

Soderberg, C. R. (1949). Unpublished notes, Gas Turbine Laboratory, MIT.

Starken, H., et al. (1993). *Advanced methods for cascade testing*, Chapter 2, Linear cascades. Advisory Group for Aerospace Research and Development, AGARDograph 328.

Stow, P. (1989). Blading design for multi-stage HP compressors. Within AGARD Lecture Series No. 167 presented June 1989.

Whitehead, D. S., & Newton, S. G. (1985). Finite element method for the solution of 2D transonic flow in cascades. *International Journal of Numerical Methods in Fluid*, *5*, 115–132.

Xu, L. (1985). The base pressure and trailing edge loss of transonic turbine blades. PhD Thesis, University of Cambridge, Cambridge, UK.

Zweifel, O. (1945). The spacing of turbomachine blading, especially with large angular deflection. *Brown Boveri Review*, *32*, 12.

CHAPTER

Axial-Flow Turbines: Mean-Line Analysis and Design

4

Power is more certainly retained by wary measures than by daring counsels.
Tacitus, *Annals*

4.1 Introduction

The modern axial-flow turbine developed from a long line of inventions stretching back in time to the aeolipile of Heron (aka Hero) of Alexandria around 120 BC. Although we would regard it as a toy it did demonstrate the important principle that rotary motion could be obtained by the expansion of steam through nozzles. Over the centuries, many developments of rotary devices took place with wind and water driven mills, water driven turbines, and the early steam turbine of the Swedish engineer Carl de Laval in 1883. The main problems of the de Laval turbines arose from their enormous rotational speeds, the smallest rotors attained speeds of 26,000 rpm and the largest had peripheral speeds in excess of 400 m/s. Learning from these mistakes, Sir Charles Parsons in 1891 developed a multistage (15 stages) axial-flow steam turbine, which had a power output of 100 kW at 4800 rpm. Later, and rather famously, a Parsons steam turbine rated at 1570 kW was used to power a 30 m long ship, Turbinia, at what was regarded as an excessive speed at a grand review of naval ships at Spithead, England, in 1897. It outpaced the ships ordered to pursue it and to bring order to the review. This spectacular dash at once proved to all the capability and power of the steam turbine and was a turning point in the career of Parsons and for the steam turbine. Not long after this most capital ships of the major powers employed steam turbines rather than old-fashioned piston engines.

From this point, the design of steam turbines evolved rapidly. By 1920, General Electric was supplying turbines rated at 40 MW for generating electricity. Significant progress has since been made in the size and efficiency of steam turbines with 1000 MW now being achieved for a single shaft plant. Figure 4.1 shows the rotor of a modern double-flow low-pressure turbine with this power output.

The development of the axial-flow turbine is tied to the history of the aircraft gas turbine but clearly depended upon the design advances made previously in the field of steam turbines. In this chapter, the basic thermodynamic and aerodynamic characteristics of axial-flow turbines are presented. The simplest approach to their analysis is to assume that the flow conditions at a mean radius, called the *pitchline*, represent the flow at all radii. This two-dimensional (2D) analysis can provide a reasonable approximation to the actual flow, provided that the ratio of blade height to mean radius is

Fluid Mechanics and Thermodynamics of Turbomachinery. DOI: http://dx.doi.org/10.1016/B978-0-12-415954-9.00004-8

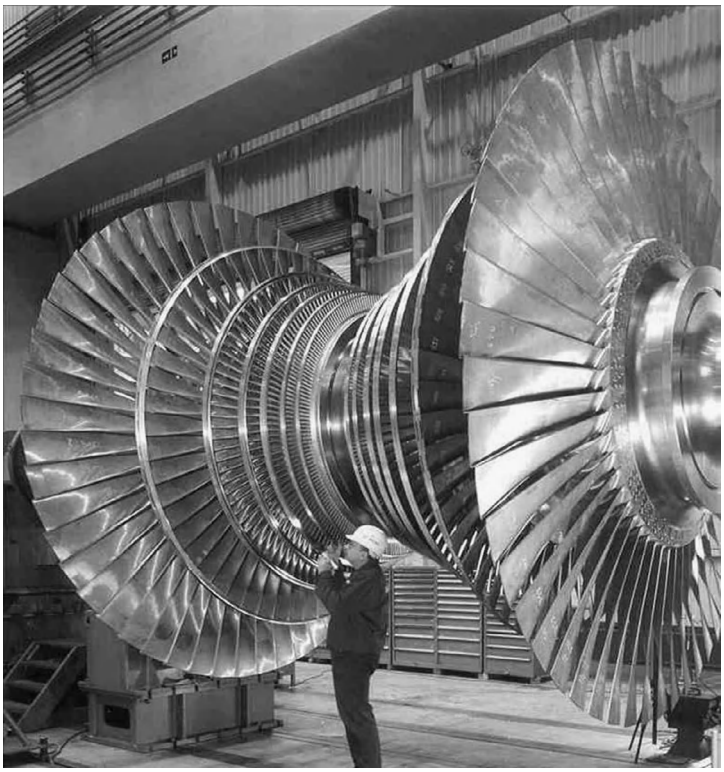

FIGURE 4.1

Large low-pressure steam turbine.

(With kind permission of Siemens Turbines)

small. However, when this ratio is large, as in the final stages of an aircraft or a steam turbine, a more elaborate *three-dimensional (3D) analysis* is necessary. Some elementary 3D analyses of the flow in axial turbomachines of low hub-to-tip ratio, e.g., $r_h/r_t \approx 0.4$, are discussed in Chapter 6. One further assumption required for the purposes of mean-line analysis is that the flow is invariant along the circumferential direction (i.e., there are no significant "blade-to-blade" flow variations).

For turbines, the analysis is presented with compressible flow effects in mind. This approach is then applicable to both steam and gas turbines provided that, in the former case, the steam condition remains wholly within the *vapor* phase (i.e., superheat region).

The modern axial-flow turbine used in aircraft engines now lies at the extreme edge of technological development; the gases leaving the combustor can be at temperatures of around 1600°C or more whilst the material used to make turbine blades melt at about 1250°C. Even more remarkable is the fact that these blades are subjected to enormous centrifugal forces and bending loads from deflecting the hot gases. The only way these temperature and stress levels can be sustained is by an adequate cooling system of high pressure (HP) air supplied from the final stage compressor. In this chapter, a brief outline of the basic ideas on centrifugal stresses

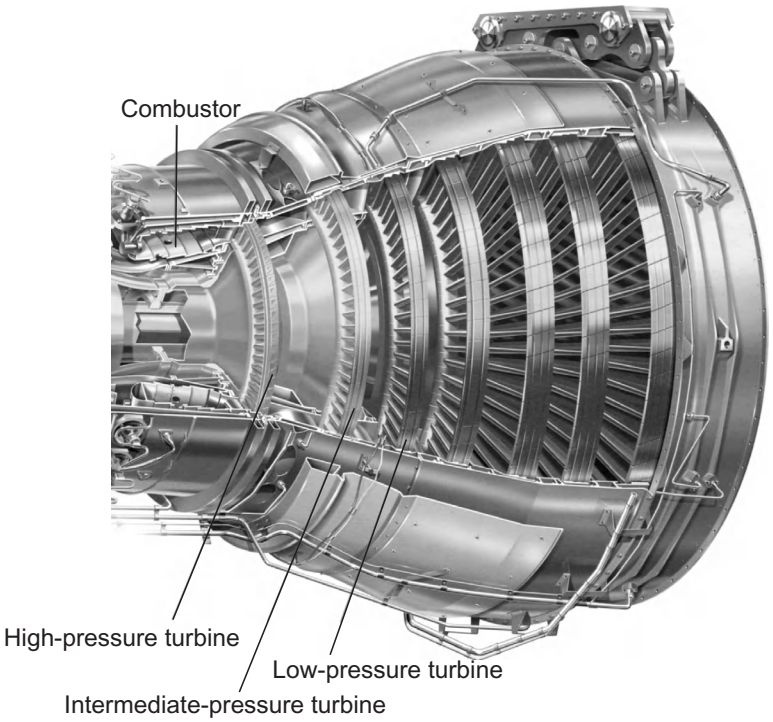

FIGURE 4.2

Turbine module of a modern turbofan jet engine.

(With kind permission from Rolls-Royce plc)

and some of the methods used for blade cooling is given. Figure 4.2 shows the three shaft axial-flow turbine system of a Rolls Royce Trent turbofan engine.

4.2 Velocity diagrams of the axial turbine stage

The axial turbine stage comprises a row of fixed guide vanes or nozzles (often called a *stator* row) and a row of moving blades or buckets (a *rotor* row). Fluid enters the stator with absolute velocity c_1 at angle α_1 and accelerates to an absolute velocity c_2 at angle α_2 (Figure 4.3). All angles are measured from the axial (x) direction. The *sign convention* is such that angles and velocities as drawn in Figure 4.3 will be taken as positive throughout this chapter. From the velocity diagram, the rotor inlet *relative* velocity w_2, at an angle β_2, is found by subtracting, vectorially, the blade speed U from the absolute velocity c_2. The relative flow within the rotor accelerates to velocity w_3 at an angle β_3 at rotor outlet; the corresponding absolute flow (c_3, α_3) is obtained by adding, vectorially, the blade speed U to the relative velocity w_3.

When drawing the velocity triangles, it is always worth sketching the nozzle and rotor rows beside them, as shown in Figure 4.3. This helps to prevent errors, since the absolute velocities are

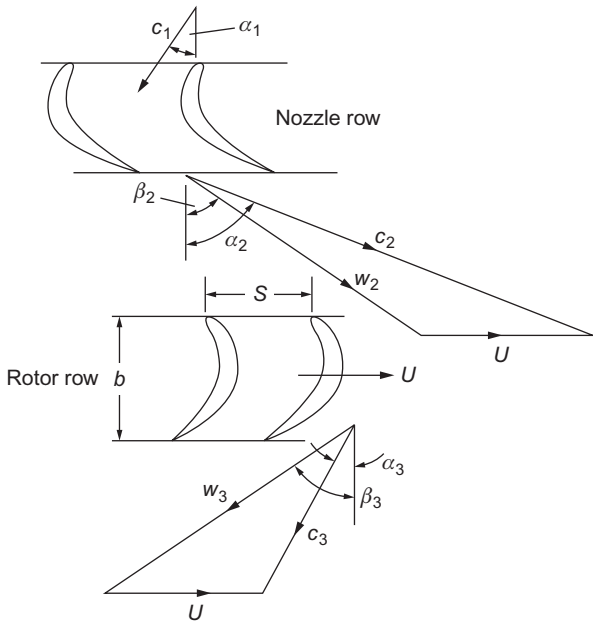

FIGURE 4.3

Turbine stage velocity diagrams.

roughly aligned with the inlet and exit angles from the nozzle row and the relative velocities are aligned with the rotor row. Note that, within an axial turbine, the levels of turning are very high and the flow is turned through the axial direction in both the rotors and nozzles.

4.3 Turbine stage design parameters

Three key nondimensional parameters are related to the shape of the turbine velocity triangles and are used in fixing the preliminary design of a turbine stage.

Design flow coefficient

This was introduced in Chapter 2. It is strictly defined as the ratio of the meridional flow velocity to the blade speed, $\phi = c_m/U$, but in a purely axial-flow machine, $\phi = c_x/U$. The value of ϕ for a stage determines the relative flow angles. A stage with a low value of ϕ implies highly staggered blades and relative flow angles close to tangential. High values imply low stagger and flow angles closer to axial. For a fixed geometry and fixed rotational speed, the mass flow through the turbine increases with increasing ϕ. This follows from the continuity equation for steady flow, which can be written for the turbine stage as

$$\dot{m} = \rho_1 A_{x1} c_{x1} = \rho_2 A_{x2} c_{x2} = \rho_3 A_{x3} c_{x3} = \rho A_x \phi U \tag{4.1}$$

Stage loading coefficient

The stage loading is defined as the ratio of the stagnation enthalpy change through a stage to the square of the blade speed, $\psi = \Delta h_0/U^2$. In an adiabatic turbine, the stagnation enthalpy change is equal to the specific work, ΔW, and for a purely axial turbine with constant radius, we can use the Euler work equation (Eq. (1.19b)) to write $\Delta h_0 = U\Delta c_\theta$. The stage loading can, therefore, be written as

$$\psi = \frac{\Delta c_\theta}{U} \tag{4.2}$$

where Δc_θ represents the change in the tangential component of absolute velocity through the rotor. Thus, high stage loading implies large flow turning and leads to highly "skewed" velocity triangles to achieve this turning. Since the stage loading is a nondimensional measure of the work extraction per stage, a high stage loading is desirable because it means fewer stages are needed to produce a required work output. However, as shown in later sections of this chapter, the stage loading is limited by the effects that high stage loadings have on efficiency.

Stage reaction

The stage reaction is defined as the ratio of the static *enthalpy* drop in the rotor to the static *enthalpy* drop across the stage. Thus,

$$R = \frac{h_2 - h_3}{h_1 - h_3} \tag{4.3a}$$

Taking the flow through a turbine as *nearly* isentropic the equation of the second law of thermodynamics, $T\mathrm{d}s = \mathrm{d}h - \mathrm{d}p/\rho$, can be approximated by $\mathrm{d}h = \mathrm{d}p/\rho$, and ignoring compressibility effects, the reaction can thus be approximated as

$$R \approx \frac{p_2 - p_3}{p_1 - p_3} \tag{4.3b}$$

The reaction, therefore, indicates the drop in pressure across the rotor compared to that for the stage. However, as a design parameter, the reaction is more significant since it describes the asymmetry of the velocity triangles and is, therefore, a statement of the blade geometries. As will be shown later, a 50% reaction turbine implies velocity triangles that are symmetrical, which leads to similar stator and rotor blade shapes. In contrast, a zero reaction turbine stage implies little pressure change through the rotor. This requires rotor blades that are highly cambered, that do not accelerate the relative flow greatly, and low cambered stator blades that produce highly accelerating flow.

4.4 Thermodynamics of the axial turbine stage

The work done on the rotor by unit mass of fluid, the specific work, equals the stagnation enthalpy drop incurred by the fluid passing through the stage (assuming adiabatic flow). From the Euler work (Eq. (1.19a)), we can write

$$\Delta W = \dot{W}/\dot{m} = h_{01} - h_{03} = U(c_{\theta 2} + c_{\theta 3}). \tag{4.4}$$

In Eq. (4.4), the absolute tangential velocity components (c_θ) are *added*, so as to adhere to the agreed sign convention of Figure 4.3. As no work is done in the nozzle row, the stagnation enthalpy across it remains constant and

$$h_{01} = h_{02} \tag{4.5}$$

In an axial turbine, the radial component of velocity is small. Writing $h_0 = h + (1/2)(c_x^2 + c_\theta^2)$ and using Eq. (4.5) in Eq. (4.4), we obtain

$$h_{02} - h_{03} = (h_2 - h_3) + \frac{1}{2}(c_{\theta 2}^2 - c_{\theta 3}^2) + \frac{1}{2}(c_{x2}^2 - c_{x3}^2) = U(c_{\theta 2} + c_{\theta 3})$$

hence

$$(h_2 - h_3) + \frac{1}{2}(c_{\theta 2} + c_{\theta 3})[(c_{\theta 2} - U) - (c_{\theta 3} + U)] + \frac{1}{2}\left(c_{x2}^2 - c_{x3}^2\right) = 0$$

It is observed from the velocity triangles of Figure 4.3 that $c_{\theta 2} - U = w_{\theta 2}$, $c_{\theta 3} + U = w_{\theta 3}$, and $c_{\theta 2} + c_{\theta 3} = w_{\theta 2} + w_{\theta 3}$. Thus,

$$(h_2 - h_3) + \frac{1}{2}\left(w_{\theta 2}^2 - w_{\theta 3}^2\right) + \frac{1}{2}\left(c_{x2}^2 - c_{x3}^2\right) = 0$$

This equation can be reduced to

$$h_2 + \frac{1}{2}w_2^2 = h_3 + \frac{1}{2}w_3^2 \quad \text{or} \quad h_{02,\text{rel}} = h_{03,\text{rel}} \tag{4.6}$$

Thus, the *relative* stagnation enthalpy, $h_{0,\text{rel}} = h + (1/2)w^2$, remains unchanged through the rotor of a purely axial turbomachine. It is assumed that no radial shift of the streamlines occurs in this flow. In some modern axial turbines, the mean flow may have a component of radial velocity, and in this case the more general form of the Euler work equation must be used to account for changes in the blade speed perceived by the flow, see Eq. (1.21a). It is then the *rothalpy* that is conserved through the rotor,

$$h_2 + \frac{1}{2}w_2^2 - \frac{1}{2}U_2^2 = h_3 + \frac{1}{2}w_3^2 - \frac{1}{2}U_3^2 \quad \text{or} \quad I_2 = I_3 \tag{4.7}$$

where U_2 and U_3 are the local blade speeds at inlet and outlet from the rotor, $U_2 = r_2\Omega$ and $U_3 = r_3\Omega$. Within the rest of this chapter, the analysis presented is directed at purely axial turbines that have a constant mean flow radius and therefore a single blade speed.

A Mollier diagram showing the change of state through a complete turbine stage, including the effects of irreversibility, is given in Figure 4.4.

Through the nozzles, the state point moves from 1 to 2 and the static pressure decreases from p_1 to p_2. In the rotor row, the absolute static pressure reduces (in general) from p_2 to p_3. It is important to note that all the conditions contained in Eqs (4.4)–(4.6) are satisfied in the figure.

4.5 Repeating stage turbines

Aeroengine and power generation applications require turbines with high-power output and high efficiency. To achieve this, an axial turbine with multiple stages is required. In these multistage axial-flow turbines, the design is often chosen to have identical, or at least very similar, mean

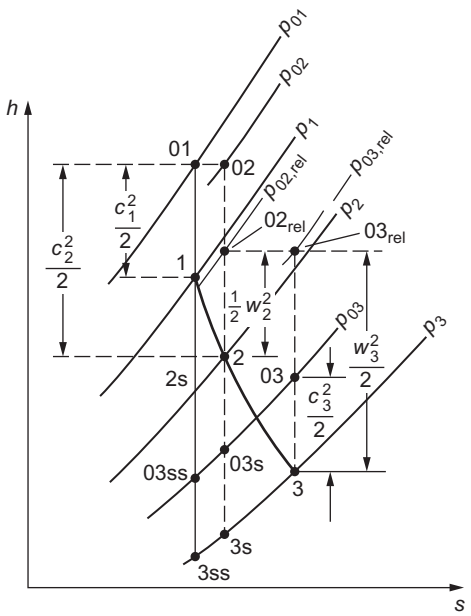

FIGURE 4.4

Mollier diagram for a turbine stage.

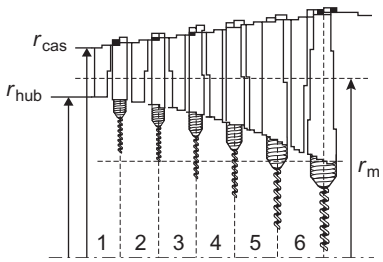

FIGURE 4.5

General arrangement of a repeating six-stage turbine.

velocity triangles for all stages. To achieve this, the axial velocity and the mean blade radius must remain constant throughout the turbine. To allow for the reduction in fluid density that arises as the flow expands through the turbine, the blade height must be continuously increasing between blade rows. Figure 4.5 shows the arrangement of a multistage turbine within an aeroengine showing the increasing blade height and the constant mean radius.

For the velocity diagrams to be the same, the flow angles at exit from each stage must be equal to those at the inlet. The requirements for a *repeating stage* can therefore be summarized as

$$c_x = \text{constant}, \quad r = \text{constant}, \quad \alpha_1 = \alpha_3.$$

Note that a single-stage turbine can also satisfy these conditions for a repeating stage. Stages satisfying these requirements are often referred to as *normal* stages.

For this type of turbine, several useful relationships can be derived relating the shapes of the velocity triangles to the flow coefficient, stage loading, and reaction parameters. These relationships are important for the preliminary design of the turbine.

Starting with the definition of reaction,

$$R = \frac{h_2 - h_3}{h_1 - h_3} = 1 - \frac{h_1 - h_2}{h_{01} - h_{03}} \tag{4.8}$$

Note that $h_{01} - h_{03} = h_1 - h_3$ since the inlet and exit velocities for the stage are equal. Through the stator no work is done, so the stagnation enthalpy stays constant across it. Given that the axial velocity is also constant, this gives

$$h_1 - h_2 = (h_{01} - h_{02}) + \frac{1}{2}\left(c_2^2 - c_1^2\right) = \frac{1}{2}c_x^2\left(\tan^2 \alpha_2 - \tan^2 \alpha_1\right) \tag{4.9}$$

From the definition of stage loading,

$$h_{01} - h_{03} = U^2\psi \tag{4.10}$$

Substituting these in the equations for the reaction (4.3) and by applying the definition of flow coefficient for a purely axial turbine, $\phi = c_x/U$, the following is obtained:

$$R = 1 - \frac{\phi^2}{2\psi}\left(\tan^2\alpha_2 - \tan^2\alpha_1\right) \tag{4.11}$$

This is true whether or not the exit angle from the stage equals the inlet angle. It shows how the three nondimensional design parameters are related to the flow angles at inlet and exit from the turbine nozzle. In a repeating stage turbine, this relationship can be further simplified, since the stage loading can be written as follows:

$$\psi = \frac{\Delta c_\theta}{U} = \frac{c_x(\tan \alpha_2 + \tan \alpha_3)}{U} = \phi(\tan \alpha_2 + \tan \alpha_1) \tag{4.12}$$

Substituting this into Eq. (4.11), we obtain

$$R = 1 - \frac{\phi}{2}(\tan \alpha_2 - \tan \alpha_1) \tag{4.13a}$$

This can be combined with Eq. (4.12) to eliminate α_2. Adding $2 \times$ Eq. (4.13a) to Eq. (4.12) gives the following relationship among stage loading, flow coefficient, and reaction:

$$\psi = 2(1 - R + \phi \tan \alpha_1) \tag{4.14}$$

This is a very useful result. It also applies to repeating stages of compressors. It shows that, for high stage loading, ψ, the reaction, R, should be low and the interstage swirl angle, $\alpha_1 = \alpha_3$, should be as large as possible. Equations (4.13a) and (4.14) also show that, once the stage loading, flow coefficient, and reaction are fixed, all the flow angles, and thus the velocity triangles, are fully specified. This is true since Eq. (4.14) gives α_1, and α_2 then follows from Eq. (4.13a). The other

angles of the velocity triangles are then fixed from the repeating stage condition, $\alpha_1 = \alpha_3$, and the relationship between relative and absolute flow angles is

$$\tan\beta_2 = \tan\alpha_2 - \frac{1}{\phi}, \quad \tan\beta_3 = \tan\alpha_3 + \frac{1}{\phi} \tag{4.15}$$

Note that by combining Eq. (4.15) with Eq. (4.13a), another useful equation for the reaction can be formed in terms of the relative flow angles,

$$R = \frac{\phi}{2}(\tan\beta_3 - \tan\beta_2) \tag{4.13b}$$

In summary, to fix the velocity triangles for a *repeating stage* a turbine designer can fix ϕ, ψ, and R or ϕ, ψ, and α_1 (or indeed any independent combination of three angles and parameters). Once the velocity triangles are fixed, key features of the turbine design can be determined, such as the turbine blade sizes and the number of stages needed. The expected performance of the turbine can also be estimated. These aspects of the preliminary design are considered further in Section 4.7.

The choice of the velocity triangles for the turbine (i.e., the choice of ϕ, ψ, and R) is largely determined by best practice and previous experience. For a company that has already designed and tested many turbines of a similar style, it will be very challenging to produce a turbine with very different values of ϕ, ψ, and R that has as good a performance as its previous designs.

4.6 Stage losses and efficiency

In Chapter 1, various definitions of efficiency for complete turbomachines were given. For a *turbine stage*, the total-to-total efficiency is

$$\eta_{\mathrm{u}} = \frac{\text{actual work output}}{\text{ideal work output when operating to same back pressure}} = \frac{h_{01} - h_{03}}{h_{01} - h_{03\mathrm{ss}}}$$

The slope of a constant pressure line on a Mollier diagram is $(\partial h/\partial s)_p = T$, obtained from Eq. (1.28). Thus, for a finite change of enthalpy in a constant pressure process, $\Delta h \cong T\Delta s$ (and $\Delta h_0 \cong T_0\Delta s$). The total-to-total efficiency can therefore be rewritten as

$$\eta_{\mathrm{tt}} = \frac{h_{01} - h_{03}}{h_{01} - h_{03\mathrm{ss}}} = \frac{h_{01} - h_{03}}{(h_{01} - h_{03}) + (h_{03} - h_{03\mathrm{ss}})} = \left[1 + \frac{h_{03} - h_{03\mathrm{ss}}}{h_{01} - h_{03}}\right]^{-1} \cong \left[1 + \frac{T_{03}(s_3 - s_{3\mathrm{ss}})}{h_{01} - h_{03}}\right]^{-1} \tag{4.16}$$

As shown by Figure 4.4, the entropy change across the whole stage, $s_3 - s_{3\mathrm{ss}}$, is the sum of the entropy increase across the nozzle row, $s_2 - s_{2\mathrm{s}} = s_{3\mathrm{s}} - s_{3\mathrm{ss}}$, and the entropy increase across the rotor row, $s_3 - s_{3\mathrm{s}}$. These increases in entropy represent the cumulative effects of irreversibility through the stator and rotor. Nondimensional enthalpy "loss" coefficients can be defined in terms of the exit kinetic energy from each blade row (Eq. (3.7)). For the nozzle row,

$$h_2 - h_{2\mathrm{s}} = \frac{1}{2}c_2^2\zeta_{\mathrm{N}}$$

Hence, the entropy change through the stator in terms of the enthalpy loss coefficient is

$$s_2 - s_{2s} \cong \frac{h_2 - h_{2s}}{T_2} = \frac{(1/2)c_2^2 \zeta_N}{T_2} \tag{4.17a}$$

For the rotor row,

$$h_3 - h_{3s} = \frac{1}{2} w_3^2 \zeta_R$$

The entropy change through the rotor in terms of the enthalpy loss coefficient is then

$$s_3 - s_{3s} \cong \frac{h_3 - h_{3s}}{T_3} = \frac{(1/2)w_3^2 \zeta_R}{T_3} \tag{4.17b}$$

Substituting Eqs (4.17a) and (4.17b) into Eq. (4.16) gives

$$\eta_{tt} \cong \left[1 + \frac{T_{03}}{T_3} \frac{\left(\zeta_N c_2^2 T_3/T_2 + w_3^2 \zeta_R\right)}{2(h_{01} - h_{03})}\right]^{-1} \tag{4.18a}$$

When the exit velocity is not recovered (in Chapter 1, examples of such cases are quoted), a total-to-static efficiency for the stage is used,

$$\begin{aligned} \eta_{ts} &= \frac{h_{01} - h_{03}}{h_{01} - h_{3ss}} = \frac{h_{01} - h_{03}}{h_{01} - h_{03} + (h_{03} - h_3) + h_3 - h_{3ss}} \cong \left[1 + \frac{0.5c_3^2 + T_3(s_3 - s_{3ss})}{h_{01} - h_{03}}\right]^{-1} \\ \Rightarrow \eta_{ts} &\cong \left[1 + \frac{\zeta_N c_2^2 T_3/T_2 + w_3^2 \zeta_R + c_3^2}{2(h_{01} - h_{03})}\right]^{-1} \end{aligned} \tag{4.19a}$$

Equations (4.18a) and (4.19a) are applicable to all turbine stages. For a repeating (or *normal*) stage, the inlet and exit flow conditions (absolute velocity and flow angle) are identical, i.e., $c_1 = c_3$ and $\alpha_1 = \alpha_3$. In this case, $h_{01} - h_{03} = h_1 - h_3$. If, in addition, the interstage absolute Mach number is fairly low, $T_{03}/T_3 \cong 1$, the total-to-total efficiency and the total-to-static efficiency can be written as

$$\eta_{tt} \cong \left[1 + \frac{\zeta_R w_3^2 + \zeta_N c_2^2 T_3/T_2}{2(h_1 - h_3)}\right]^{-1} \tag{4.18b}$$

$$\eta_{ts} \cong \left[1 + \frac{\zeta_R w_3^2 + \zeta_N c_2^2 T_3/T_2 + c_1^2}{2(h_1 - h_3)}\right]^{-1} \tag{4.19b}$$

For incompressible flow turbines, and other cases where the static temperature drop through the rotor is not large, the temperature ratio T_3/T_2 can be set equal to unity resulting in the more convenient approximations:

$$\eta_{tt} \cong \left[1 + \frac{\zeta_R w_3^2 + \zeta_N c_2^2}{2(h_1 - h_3)}\right]^{-1} \tag{4.18c}$$

$$\eta_{ts} \cong \left[1 + \frac{\zeta_R w_3^2 + \zeta_N c_2^2 + c_1^2}{2(h_1 - h_3)}\right]^{-1} \tag{4.19c}$$

So that estimates can be made of the efficiency of a proposed turbine stage, as part of the preliminary design process, some means of determining the loss coefficients, ζ_N and ζ_R, are required. Several methods for doing this are available with varying degrees of complexity. The blade row method proposed by Soderberg (1949) and reported by Horlock (1966), although old, is still useful despite its simplicity, see Eq. (3.46). Ainley and Mathieson (1951) developed a semiempirical method based on profile loss coefficient data for nozzle blades (with 100% expansion) and impulse blades (with 0% expansion), see Eq. (3.45). Full details of both these methods are given in Section 3.6.

It should be remembered that loss coefficients based on cascade testing or 2D computational fluid dynamics (CFD) represent only the 2D loss of the aerofoils and in a real turbine, various 3D effects also contribute to the loss. These 3D effects, described in further detail below, include the tip leakage jet, the mixing of any coolant flows, and the secondary flows on the turbine end walls. These effects are significant and can contribute more than 50% of the total losses.

Further preliminary methods of predicting the efficiency of axial-flow turbines have been devised, such as those of Craig and Cox (1971), Kacker and Okapuu (1982), and Wilson (1987). Also various proprietary methods are used within industry that are generally semiempirical methods based on previous test results for turbine stages of a similar design. In addition, CFD can be used to estimate efficiency. However, although CFD can often accurately predict trends in efficiency, absolute performance levels are elusive even with the latest 3D methods. In addition, CFD can only be applied once detailed turbine rotor and stator geometries have been created. It is therefore more applicable later in the design process, see Chapter 6. Advanced computational methods have not yet replaced preliminary design methods and these are still essential to converge as closely as possible to an optimum configuration before carrying out detailed design refinements using CFD.

Turbine loss sources

As stated in Chapter 1, wherever there is irreversible entropy creation within the flow path of a turbomachine, there is a loss in the available work. A loss source is therefore any flow feature that leads to entropy creation. Entropy is created by irreversible processes that involve viscous friction, mixing between flows of different properties, heat transfer across a finite temperature difference, or nonequilibrium changes like shock waves. In a turbine stage, there are numerous loss sources and they can each be quantified by the entropy they generate. The total loss is then the cumulative sum of the entropy increases, which can be used to determine a single blade row loss coefficient, as used in mean-line analysis, and applied in Eqs (4.16)–(4.19) above. However, in many cases it is very difficult to determine the entropy generation associated with a particular loss source, and loss coefficients are generally based on values derived from testing a similar machine combined with correlations.

A detailed description of all of the different loss mechanisms in turbomachinery is given by Denton (1993), and this reference is strongly recommended. Here the aim is to give a brief overview of the principal loss sources in turbines and their relative importance.

The losses in a turbine can be categorized as 2D or 3D. The 2D loss sources are those that would be present in a cascade test of a turbine blade row with infinite span (i.e., no endwall effects). The 3D losses are the additional losses that arise when the turbine stage is operating in a realistic rotating arrangement.

2D loss sources are made up of (a) the *blade boundary layers*, (b) *trailing edge mixing*, (c) *flow separation*, and (d) *shock waves*.

The loss in the *blade boundary layers* can be thought of as lost work expended against viscous shear within the boundary layers. Its magnitude depends on the development of the boundary layer and, in particular, on the blade surface pressure distribution and where transition from laminar to turbulent flow occurs. Boundary layer loss typically accounts for over 50% of the 2D loss in subsonic turbines. For incompressible flow, Denton (1993) shows that the total loss in a boundary layer can be determined using

$$\zeta_{te} = \frac{\delta_e}{s \cos \alpha_2}, \tag{4.20}$$

where $\delta_e = \int_{-s/2}^{s/2} c/c_{max}[1 - (c/c_{max})^2]dy$ is the boundary layer energy thickness at the trailing edge and c_{max} is the local velocity at the edge of the boundary layer.

The *trailing edge mixing* loss is the loss that arises from the mixing of the suction surface and pressure surface boundary layers with the region of flow just behind the trailing edge. This loss is significant, typically about 35% of the total 2D loss in subsonic turbines, and rising to around 50% in supersonic cases, see Figure 3.26. Note that for incompressible cases, the combined boundary layer loss and trailing edge loss can be accounted for by the wake momentum thickness, θ_2, as shown in Eq. (3.38),

$$\zeta = \frac{2\theta_2}{s \cos \alpha_2}$$

Combining this with Eq. (4.20) shows that the ratio of loss in a boundary layer to the total loss within the wake after mixing is given by $\delta_e/2\theta_2$.

Flow separation loss exists when the boundary layer detaches from the blade surface and a large region of reduced kinetic energy flow forms downstream. This loss is difficult to quantify, but a well-designed turbine should never exhibit large-scale 2D flow separation, so it can generally be neglected. Separation close to the trailing edge is included in the trailing edge mixing loss.

Shock loss occurs when the turbine blade passage is choked and the exit Mach number is above about 0.9. The loss caused by shock waves in a turbine passage is not as great as might be expected. For a normal shock wave, with a preshock Mach number, M_1, it can be shown, see National Advisory Committee for Aeronautics Report 1135 (1953), that the entropy generation is given by

$$\frac{\Delta s}{c_v} = \ln\left[\frac{2\gamma M_1^2 - \gamma + 1}{\gamma + 1}\right] - \gamma \ln\left[\frac{(\gamma + 1)M_1^2}{(\gamma - 1)M_1^2 + 2}\right] \tag{4.21}$$

If the above is expanded as a power series, it is found that the entropy creation varies approximately as the cube of $(M_1^2 - 1)$, which is relatively small up to Mach numbers of about 1.4. In turbine passages the shock waves are usually oblique, reducing the losses further. As shown in Figure 3.26, shock loss accounts for about 30% or less of the total 2D loss above an exit Mach number of 1.

3D loss sources can be separated into (a) *tip leakage flows*, (b) *endwall (or secondary) flows*, and (c) *coolant flows*.

In all turbomachines, a clearance gap exists between the rotating blades and the stationary casing. *Tip leakage* is the passage of flow from the pressure surface to the suction surface of the blade through this clearance gap. The leakage flow leads to a reduction in the work done by a turbine rotor because the mass flow rate through the blade passage is reduced. It also leads to a loss in efficiency. First, the leakage flow increases its entropy through viscous effects and mixing as it passes through the leakage path above the blade tip. Second, when the leakage flow emerges at the suction side it mixes with the main flow, creating a further entropy rise. These losses are demonstrated in Bindon (1989) and various models exist to determine the leakage mass flow rate and the loss generated. Tip leakage loss rises rapidly with the size of clearance gap and typically a 1% increase of clearance gap to blade height will incur a loss of 2−3% of efficiency. It is, therefore, more detrimental in small turbine stages that have relatively large clearance gaps. Note that stator rows also suffer from leakage losses if they have clearance flow paths.

Endwall loss is a large, complex subject and an area of active research. It encompasses all of the loss arising on the hub and casing surfaces, both inside and outside of the blade rows. Endwall loss is very difficult to isolate and predict, but typically it accounts for about 30% of the total loss in a turbine stage, see Denton (1993). The flow close to the annulus walls is determined by secondary flows in the blade passage, which are driven by the incoming endwall boundary layers and the turning in the blade passage, see Chapter 6.

Loss from *coolant flows* is only applicable to high-temperature cooled gas turbine stages, see Section 4.14. The overall effect must be considered in terms of the thermodynamics of the complete gas turbine system. Cooling is applied to increase the turbine entry temperature, which raises the cycle efficiency and work output. However, the cooling process itself is highly irreversible. Entropy is created by heat transfer from the mainstream flow, by the passage of the coolant through convoluted passages and by the mixing of the coolant with the mainstream flow. The last of these processes has a significant impact on the turbine stage efficiency. The coolant flow is injected into the blade passages at an angle through holes or slots and has quite different stagnation temperature and pressure to the mainstream flow. Various models have been developed that enable this mixing loss to be quantified, see Denton (1993), but accurately predicting the efficiency impact is still challenging.

Steam turbines

The above efficiency analysis and discussion of loss sources also applies to steam turbines. The main difference to keep in mind for steam turbines is that the working fluid cannot be approximated as an ideal gas and steam tables or a Mollier chart for steam (Appendix E) have to be used. As a result, the changes in properties through a steam turbine stage can be much greater than through a gas turbine stage. Equations (4.18a) and (4.19a) are still valid for a steam turbine stage, and for modern designs, typically $88\% < \eta_{tt} < 93\%$, but in a multistage turbine the loss coefficients can vary significantly between the front and rear stages, see McCloskey (2003, chap. 8). In cases where only the inlet and exit conditions to a multistage steam turbine are known it is more appropriate to use the overall isentropic efficiency. This can be related to an equivalent small-stage (or polytropic) efficiency, using the reheat factor, as shown in Eq. (1.56),

$$\eta_{tt} = \frac{h_{01} - h_{02}}{h_{01} - h_{02s}} = \eta_p R_H$$

where h_{01} is the stagnation enthalpy of the steam at the turbine inlet temperature and pressure, h_{02} is the stagnation enthalpy of the steam at the exit temperature and pressure, and h_{02s} is the stagnation enthalpy of the steam at the exit pressure and the inlet entropy.

In addition to the loss sources described previously, steam turbines suffer additional losses due to moisture in the working fluid. Water droplets form when steam crosses the saturation line into the two-phase region on the steam chart, see Appendix E. For a steam turbine in a power station, the overall efficiency typically drops by about 1% for every 1% of wetness in the final stages. This has led to turbine designs in which moisture levels in the exhaust are limited to around 10% (Hesketh & Walker, 2005). Steam turbines also suffer particularly from leakage losses and surface roughness effects. There are multiple leakage paths in steam turbines, such as over the rotor tips, the stator shrouds, and through various seals. Some surface roughness arises in manufacture, but it is rapidly worsened by the particle erosion and blade surface deposits that can occur when operating with steam. However, since the operating temperatures are lower than gas turbines, steam turbines do not have cooled blades and, therefore, avoid the additional losses and complexity required by blade cooling.

EXAMPLE 4.1

A low-pressure steam turbine within a power station has an entry temperature of 450°C and an entry pressure of 30 bar. At exit from the turbine, the condenser pressure is 0.06 bar and due to the effects of moisture, the turbine isentropic efficiency is given by $\eta_t = 0.9 - y$, where y is the wetness fraction of the steam at turbine exit (and $y = 1 - x$, where x is the dryness fraction).

1. Find the net work output from the turbine per kg of steam and determine the turbine polytropic efficiency assuming a reheat factor of 1.02.
2. The turbine consists of repeating stages designed with zero reaction, a flow coefficient of 0.8 and axial flow at inlet to each stage. If it rotates at 3000 rpm and has a mean radius of 0.9 m, determine the number of stages, the absolute flow angle at nozzle exit, and the relative angle at rotor inlet.

Use the following table of properties for water and steam:

	Specific Enthalpy (kJ/kg)	Specific Entropy (kJ/kg K)	Temperature (°C)
Saturated liquid at 0.06 bar	151.5	0.521	36.16 (state *f*)
Saturated vapor at 0.06 bar	2566.6	8.329	36.16 (state *g*)
30 bar, 450°C	3344.8	7.086	(state 1)

Solution

1. For the turbine, using Eq. (1.32), with wetness fraction y_2,

$$\eta_{LPT} = \frac{h_1 - h_2}{h_1 - h_{2s}} = \frac{h_1 - [y_2 h_f + (1 - y_2)h_g]}{h_1 - h_{2s}} = 0.9 - y_2$$

Hence we need the value of h_{2s}. We know that $s_{2s} = s_1$ and therefore can find y_{2s}, i.e.,

$$y_{2s} = \frac{S_g - S_{2s}}{S_g - S_f} = \frac{S_g - S_1}{S_g - S_f} = \frac{8.329 - 7.086}{8.329 - 0.521} = 0.1592.$$

$$\therefore \quad h_{2s} = y_{2s} h_f + (1 - y_{2s})h_g = 0.1592 \times 151.5 + (1 - 0.1592) \times 2566.6 = 2182.1 \text{ kJ/kg}$$

Rearranging the above equation for η_{LPT} gives the exit wetness fraction

$$y_2 = \frac{0.9(h_1 - h_{2s}) - (h_1 - h_g)}{(h_g - h_f) + (h_1 - h_{2s})} = \frac{0.9(3344.8 - 2182.1) - (3344.8 - 2566.6)}{(3344.8 - 2182.1) + (2566.6 - 151.5)} = 0.07497$$

Hence we can find the actual enthalpy at exit,

$$h_2 = y_2 h_f + (1 - y_2) h_g = 0.07497 \times 151.5 + (1 - 0.07497) \times 2566.6 = 2385.5 \text{ kJ/kg}$$

The net work output per kg of steam is then simply

$$\Delta W_{LPT} = h_1 - h_2 = 3344.8 - 2385.5 = 959.3 \text{ kJ/kg}$$

Note that a less accurate answer could be obtained using a steam chart.
The polytropic efficiency,

$$\eta_p = \frac{\eta_t}{R_H} = \frac{h_1 - h_2}{h_1 - h_{2s}} \frac{1}{R_H} = \frac{959.3}{3344.8 - 2182.1} \times \frac{1}{1.02} = 0.809$$

2. From Eq. (4.14), using the fact that $R = 0$ and $\alpha_1 = 0$,

$$\psi = 2(1 - R + \phi \tan \alpha_1) = 2$$

The number of stages required,

$$n_{stage} \geq \frac{\Delta W_{LPT}}{\psi U^2} = \frac{959.3 \times 10^3}{2 \times (0.9 \times 100\pi^2)} = 5.999 \Rightarrow n_{stage} = 6$$

The flow angles are found using Eqs (4.12) and (4.15),

$$\phi(\tan \alpha_2 + \tan \alpha_1) = \psi \Rightarrow \tan \alpha_2 = \psi/\phi = 2/0.8 = 2.5. \quad \therefore \alpha_2 = 68.2^\circ$$

$$\tan \beta_2 = \tan \alpha_2 - 1/\phi \Rightarrow \tan \alpha_2 = 2.5 - 1/0.8 = 1.25. \quad \therefore \beta_2 = 51.3^\circ$$

4.7 Preliminary axial turbine design

The process of choosing the best turbine design for a given application involves juggling several parameters that may be of equal importance, for instance, rotor stress, weight, outside diameter, efficiency, noise, durability, and cost, so that the final design lies within acceptable limits for each parameter. In consequence, a simple presentation can hardly do justice to the real problem of an integrated turbine design. However, a consideration of how the preliminary design choices affect the turbine basic layout and the efficiency can provide useful guidance to the designer.

As demonstrated earlier in the chapter, the main goal in the preliminary stage design of a turbine is to fix the shapes of the velocity triangles, either by setting the flow angles or by choosing values for the three dimensionless design parameters, ϕ, ψ, and R. If we now consider matching the overall (dimensioned) requirements of the turbine to the velocity triangle parameters, the general layout of the turbomachine can also be determined.

Number of stages

First, from the specification of the turbine, the design will usually have a known mass flow rate of the working fluid and a required power output. This enables the specific work output of the turbine to be calculated according to $\Delta W = \dot{W}/\dot{m}$. The specific work per stage can be determined from the stage loading and the blade speed and, thus, the required number of stages can be found as

$$n_{\text{stage}} \geq \frac{\dot{W}}{\dot{m}\psi U^2} \tag{4.22}$$

An inequality is used in Eq. (4.22) since the number of stages must be an integer value. The result shows how a large stage loading can reduce the number of stages required in a multistage turbine. It also shows that a high blade speed, U, is desirable. However, this is usually constrained by a stress limit, because centripetal loadings and vibration rise rapidly with rotor speed, see later in this chapter. In some cases, aerodynamic or acoustic considerations may limit the maximum blade speed. For example, if a turbine is required to operate with transonic flow, the blade speed may be constrained by the need to limit the maximum flow Mach number.

Blade height and mean radius

Given that the axial velocity remains constant throughout each stage, i.e., $c_{x1} = c_{x2} = c_{x3} = c_x$, then the continuity equation for the turbine, Eq. (4.1), reduces to

$$\rho_1 A_{x1} = \rho_2 A_{x2} = \rho_3 A_{x3} = \text{constant} \tag{4.23}$$

If the mass flow rate through the machine is specified the annulus area, A_x, can be determined from the continuity equation combined with the flow coefficient:

$$A_x = \frac{\dot{m}}{\rho\phi U} \approx 2\pi \times r_{\text{m}} H \tag{4.24}$$

This equation is only approximate since it assumes the mean radius is exactly midway between the hub and tip, i.e., $r_{\text{m}} = (r_{\text{t}} + r_{\text{h}})/2$. To be precise, the mean radius should be the radius that divides the annulus into two equal areas, i.e., $r_{\text{m}}^2 = (r_{\text{t}}^2 + r_{\text{h}}^2)/2$. However, for high hub-to-tip radius ratios these definitions of mean radius are equivalent. In all cases, an accurate expression for the annulus area is given by

$$A_x = \pi \times r_{\text{t}}^2 \left[1 - \left(\frac{r_{\text{h}}}{r_{\text{t}}}\right)^2\right] \tag{4.25}$$

This equation is useful for determining the annulus area if the hub-to-tip radius ratio required for the turbine is known or if the casing diameter is set by the need to fit the machine in with other components.

Often, the mean radius will be fixed by the need to rotate at a particular rotational speed (e.g., for mains electricity, $\Omega = 50$ Hz $= 3000$ rpm) and using a known blade speed, $r_{\text{m}} = U/\Omega$. The spanwise height required for the blades can then be determined from

$$r_{\text{t}} - r_{\text{h}} = H \approx \frac{\dot{m}}{\rho\phi U 2\pi \times r_{\text{m}}} \tag{4.26}$$

In compressible gas turbines, the inlet stagnation conditions and the inlet Mach number may be known. This then fixes the inlet annulus area via the mass flow function:

$$\frac{\dot{m}\sqrt{C_pT_{01}}}{A_x \cos \alpha_1 p_{01}} = Q(M_1) \tag{4.27}$$

The area found from this can then be used with Eq. (4.24) or (4.25) to find the blade span. For the subsequent, downstream stage, the stagnation temperature and pressure can be found from the following relationship for the stage loading and pressure ratio:

$$\frac{T_{03}}{T_{01}} = 1 - \frac{\psi U^2}{C_pT_{01}}, \quad \frac{p_{03}}{p_{01}} = \left(\frac{T_{03}}{T_{01}}\right)^{\eta_p \gamma/(\gamma-1)} \tag{4.28}$$

Note that the polytropic efficiency is used here since this is more appropriate for calculating changes in properties across a single stage. The Mach number at inlet to the downstream stage can then be found from the velocity using the following compressible flow relationship (included in the compressible flow tables):

$$\frac{c_3}{\sqrt{C_pT_{03}}} = M_3\sqrt{\gamma-1}\left(1+\frac{\gamma-1}{2}M_3^2\right)^{-1/2} \tag{4.29}$$

The new annulus area is then determined from Eq. (4.27) and, given the fact that the mean radius is constant, the blade span can be found. This process can be repeated for subsequent stages, enabling the general arrangement of the entire turbine to be determined in terms of the size and number of stages.

Number of aerofoils and axial chord

The number of aerofoils in each turbine row and the chord lengths of the vanes and blades can also be estimated during the preliminary design. The aspect ratio of a blade row is the height, or blade span, divided by the axial chord, H/b. A suitable value of this is set by mechanical and manufacturing considerations and will vary between applications. For jet engine, core turbines aspect ratios between 1 and 2 are usual, but low-pressure turbines and steam turbines can have much higher values, as demonstrated in Figures 4.1 and 4.2. To find the ratio of blade pitch to axial chord, s/b, the Zweifel criterion for blade loading can be applied, as detailed in Chapter 3. Equations (3.51) and (3.52) show how, given the turbine velocity triangles, the pitch to axial chord ratio can be found from an optimum value of Zweifel coefficient. For a known axial chord, knowing s/b fixes the number of aerofoils.

4.8 Styles of turbine

Often, if the stage loading and flow coefficient are fixed by the overall requirements of the turbine and the principal design constraints, only one parameter remains that the designer has the freedom to change in the preliminary design. The classification of different styles of turbine design is most conveniently described by the reaction, because this relates to the turbine blade geometries. There are two extremes: zero reaction, where the rotor and stator shapes are very different, and 50% reaction, where the rotor and stator shapes are symmetric. The advantages and disadvantages of both these styles are discussed below.

Zero reaction stage

Walker and Hesketh (1999) summarize the advantages of low reaction as enabling a high stage loading with low interstage swirl, low thrust on the rotor, robust rotor blades, and lower tip leakage flows (due to a low-pressure drop across the rotor). However, they also point out that low reaction can lead to boundary layer separation from the highly cambered rotor blades and they show how the increased stage loading almost invariably leads to lower efficiency. Low reaction designs are regularly applied in steam turbines, where their advantages are most beneficial and they enable a reduction in the total number of stages required, but they are not currently used in gas turbines.

From the definition of reaction, when $R = 0$, Eq. (4.3) indicates that $h_2 = h_3$ and, thus, all the enthalpy drop occurs across the stator. From Eq. (4.13b), we can show that

$$R = \frac{\phi}{2}(\tan \beta_3 - \tan \beta_2) \Rightarrow \beta_2 = \beta_3$$

Since the axial velocity is constant, this means that the relative speed of the flow across the rotor does not change. The Mollier diagram and velocity triangles corresponding to these conditions are sketched in Figure 4.6. From this it is also clear that, since $h_{02\text{rel}} = h_{03\text{rel}}$ and $h_2 = h_3$ for $R = 0$, it follows that $w_2 = w_3$. It will be observed in Figure 4.6 that, because of irreversibility, there is a *pressure drop* through the rotor row. The zero reaction stage is *not* the same thing as an *impulse* stage; in the latter case there is, by definition, no pressure drop through the rotor. The Mollier diagram for an impulse stage is shown in Figure 4.7, where it is seen that the enthalpy *increases* through the rotor. As shown by Eq. (4.3a) this means that the reaction is negative for the impulse turbine stage when account is taken of the irreversibility.

50% Reaction stage

Havakechian and Greim (1999) summarize the advantages of 50% reaction designs as symmetrical velocity triangles leading to similar blade shapes and reduced cost, low turning and highly

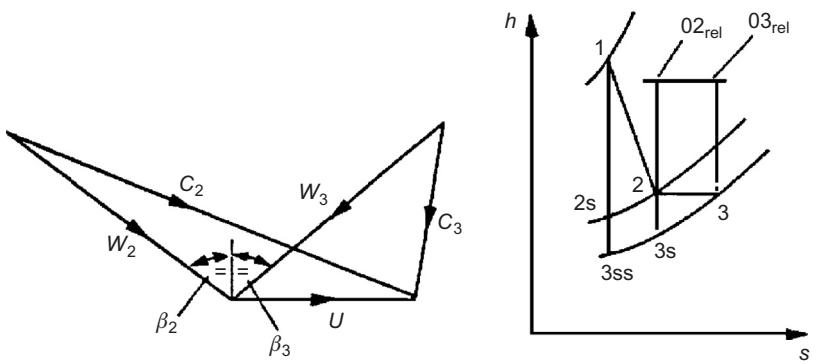

FIGURE 4.6

Velocity diagram and Mollier diagram for a zero reaction turbine stage.

accelerating passages leading to lower losses, an expansion split into two steps leading to subsonic Mach numbers, and improved performance over a range of operating conditions. However, they concede that 50% reaction designs lead to increased turbine part count relative to low reaction designs since, for low interstage swirl, roughly twice as many stages are needed. Also, the greater expansion through the rotors increases the thrust on the rotor bearings and increases leakage losses. 50% reaction designs are very common in gas turbines, where the requirement for maximum efficiency is paramount. In gas turbines higher stage loadings are achieved by increasing the interstage swirl angle, α_1. In steam turbines, both 50% reaction and low reaction designs are regularly applied and the two approaches remain competitive.

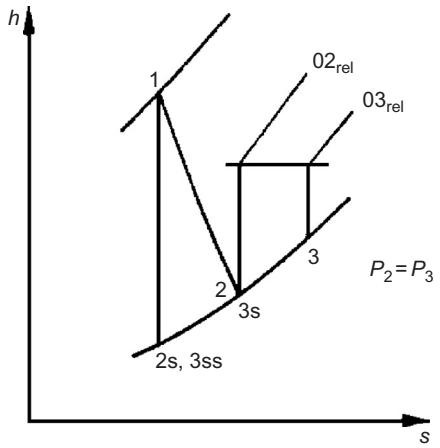

FIGURE 4.7

Mollier diagram for an impulse turbine stage.

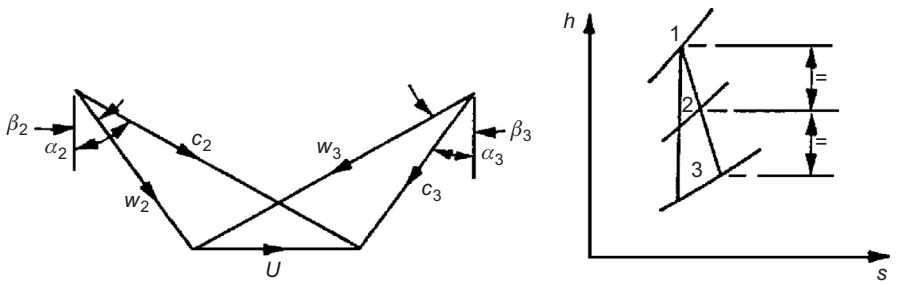

FIGURE 4.8

Velocity diagram and Mollier diagram for a 50% reaction turbine stage.

The symmetrical velocity diagram for the 50% reaction case is shown in Figure 4.8. With $R = 0.5$, from Eq. (4.13a) combined with Eq. (4.15), it is found that

$$R = 1 - \frac{\phi}{2}(\tan\alpha_2 - \tan\alpha_1) \Rightarrow 1 = \phi\left(\tan\beta_2 + \frac{1}{\phi} - \tan\alpha_1\right) \Rightarrow \beta_2 = \alpha_1 = \alpha_3$$

Similarly, it can be shown that $\beta_3 = \alpha_2$ as well, proving that the velocity triangles are indeed symmetric. Figure 4.8 has been drawn with the same values of c_x, U, and ΔW as in Figure 4.6 (the zero reaction case) to emphasize the difference in flow geometry between the 50% reaction and zero reaction stages.

EXAMPLE 4.2

A low-pressure turbine within a turbofan jet engine consists of five repeating stages. The turbine inlet stagnation temperature is 1200 K and the inlet stagnation pressure is 213 kPa. It operates with a mass flow of 15 kg/s and generates 6.64 MW of mechanical power. The stator in each turbine stage turns the flow from 15° at stator inlet to 70° at stator outlet. The turbine mean radius is 0.46 m and the rotational shaft speed is 5600 rpm.

1. Calculate the turbine stage loading coefficient and flow coefficient. Hence, show that the reaction is 0.5 and sketch the velocity triangles for one complete stage.
2. Calculate the annulus area at inlet to the turbine. Use this to estimate the blade height and the hub-to-tip radius ratio for the stator in the first turbine stage.

Take $\gamma = 1.333$, $R = 287.2$ J/kg K, and $C_p = 1150$ J/kg K.

Solution

1. The mean blade speed can be calculated from the mean radius and angular speed:

$$U = r_m\Omega = 0.46 \times \frac{5600}{60} \times 2\pi = 269.8 \text{ m/s}$$

The stage loading can then be determined from the power and mass flow:

$$\psi = \frac{\Delta h_0}{U^2} = \frac{\text{Power}/(\dot{m}/n_{\text{stage}})}{U^2} = \frac{6.64 \times 10^6}{15 \times 5 \times 269.8^2} = 1.217$$

The flow coefficient follows from Eq. (4.12):

$$\phi = \frac{\psi}{(\tan\alpha_2 + \tan\alpha_1)} = \frac{1.217}{(\tan 70^\circ + \tan 15^\circ)} = 0.403$$

The reaction can then be determined by rearranging Eq. (4.14):

$$R = 1 - \frac{\psi}{2} + \phi \tan\alpha_1 = 1 - \frac{1.217}{2} + 0.4 \tan 15^\circ = 0.5$$

Velocity triangles (symmetrical, since $R = 0.5$) are as follows:

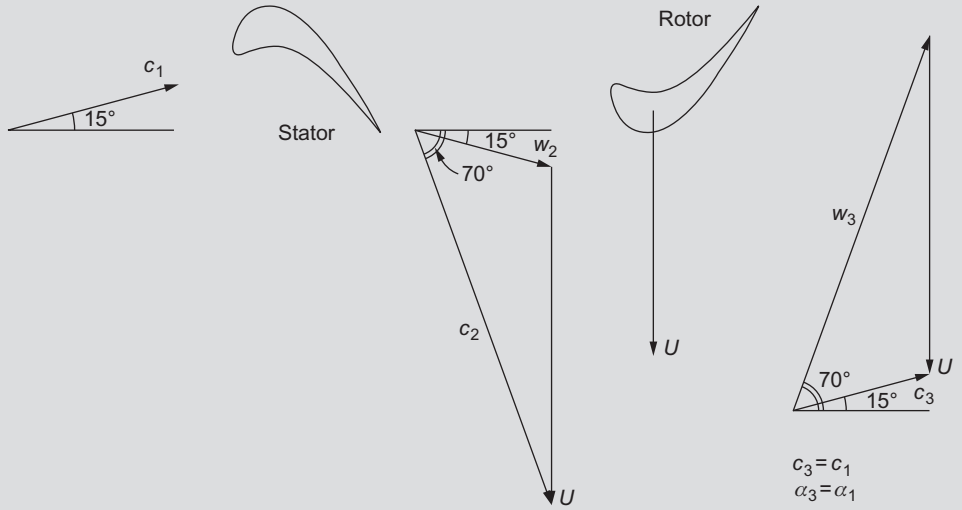

2. To calculate the inlet area, we first determine the Mach number from the inlet velocity then use the compressible mass flow function:

$$\frac{c_1}{\sqrt{C_p T_{01}}} = \frac{\phi U/\cos\alpha_1}{\sqrt{C_p T_{01}}} = \frac{0.403 \times 269.8}{\cos 15^\circ \sqrt{1150 \times 1200}} = 0.0958$$

From compressible flow tables ($\gamma = 1.333$),

$$M_1 = 0.166, \quad (\dot{m}\sqrt{C_p T_{01}})/A p_{01} = Q(0.166) = 0.3781$$

$$A_x = \frac{A}{\cos\alpha_1} = \frac{\dot{m}\sqrt{C_p T_{01}}}{Q(0.166) p_{01}} \frac{1}{\cos 15^\circ} = \frac{15\sqrt{1150 \times 1200}}{0.3781 \times 213 \times 10^3 \times 0.9659} = 0.227 \text{ m}^2$$

In this case, given the low inlet Mach number, it would also be valid to calculate the density using the inlet stagnation pressure and temperature then apply the continuity equation (4.24). Once the area is found, the blade height and hub-to-tip radius ratio can be determined. For the blade height,

$$H = \frac{A_x}{2\pi r_\text{m}} = \frac{0.227}{2\pi \times 0.46} = 0.0785$$

which implies that $H = 78.2$ mm. For the hub-to-tip ratio,

$$\text{HTR} = \frac{r_\text{m} - H/2}{r_\text{m} + H/2} = \frac{0.46 - 0.0785/2}{0.46 + 0.0785/2} = 0.843$$

4.9 Effect of reaction on efficiency

Consider the problem of selecting an axial turbine design for which the mean blade speed, U, the stage loading, ψ (or $\Delta W/U^2$), and the flow coefficient, ϕ (or c_x/U), have already been selected. The only remaining parameter required to completely define the velocity triangles is R or the interstage swirl angle, α_1, since from Eq. (4.14),

$$\psi = 2(1 - R + \phi \tan \alpha_1)$$

For different values of R the velocity triangles can be constructed, the loss coefficients determined, and η_{tt}, η_{ts} calculated. In Shapiro, Soderberg, Stenning, Taylor, and Horlock (1957), Stenning considered a family of turbines each having a flow coefficient $c_x/U = 0.4$, blade aspect ratio $H/b = 3$, and Reynolds number $Re = 10^5$, and calculated η_{tt}, η_{ts} for stage loading factors $\Delta W/U^2$ of 1, 2, and 3 using Soderberg's correlation. The results of this calculation are shown in Figure 4.9 as presented by Shapiro et al. (1957).

In the case of total-to-static efficiency, it is at once apparent that this is optimized, at a given blade loading, by a suitable choice of reaction. When $\Delta W/U^2 = 2$, the maximum value of η_{ts} occurs with approximately zero reaction. With lighter blade loading, the optimum η_{ts} is obtained with higher reaction ratios. When $\Delta W/U^2 > 2$, the highest value of η_{ts} attainable without rotor *relative* flow diffusion occurring is obtained with $R = 0$. Note that these results relate only to the 2D blading efficiency and make no allowance for losses due to tip clearance and endwall flow.

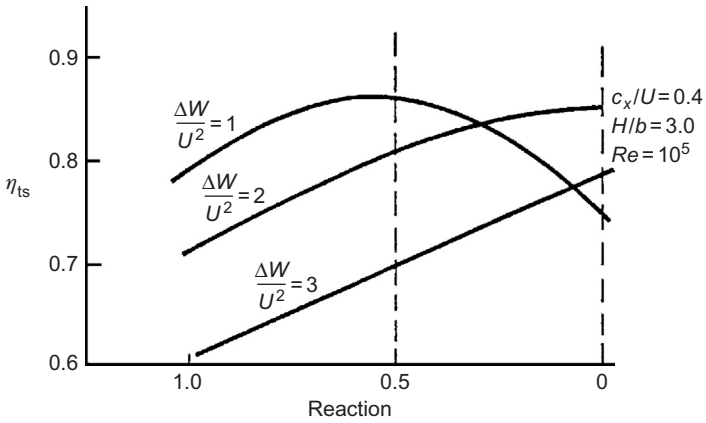

FIGURE 4.9

Influence of reaction on total-to-static efficiency with fixed values of stage loading factor.

EXAMPLE 4.3

Verify that the peak value of the total-to-static efficiency η_{ts} shown in Figure 4.9 occurs at a reaction of 50% for the curve marked $\Delta W/U^2 = 1$ and estimate its value using Soderberg's correlation.

Solution

From Eq. (4.19c),

$$\frac{1}{\eta_{ts}} = 1 + \frac{\zeta_R w_3^2 + \zeta_N c_2^2 + c_1^2}{2\Delta W}$$

As $\Delta W/U^2 = 1$ and $R = 0.5$, from $\psi = 2(1 - R + \phi \tan \alpha_1)$, $\alpha_1 = 0$ and from Eq. (4.15),

$$\tan \beta_3 = \frac{1}{\phi} = 2.5, \quad \text{and therefore,} \quad \beta_3 = 68.2^\circ$$

The velocity triangles are symmetrical, so that $\alpha_2 = \beta_3$. Also, $\theta_R = \theta_N = \alpha_2 = 68.2^\circ$; therefore

$$\zeta = 0.04 \times (1 + 1.5 \times 0.682^2) = 0.0679$$

$$\begin{aligned}\frac{1}{\eta_{ts}} &= 1 + \frac{2\zeta w_3^2 + c_x^2}{2U^2} = 1 + \zeta\phi^2 \sec^2 \beta_3 + \frac{1}{2}\phi^2 \\ &= 1 + \phi^2(\zeta \sec^2 \beta_3 + 0.5) \\ &= 1 + 0.4^2 \times (0.0679 \times 2.6928^2 + 0.5) \\ &= 1 + 0.16 \times (0.49235 + 0.5)\end{aligned}$$

Therefore,

$$\eta_{ts} = 0.863$$

This value appears to be close to the peak value of the efficiency curve $\Delta W/U^2 = 1.0$ in Figure 4.9. Note that it is almost expected that the peak total-to-static efficiency would be at a reaction of 50% for a stage loading of 1, because this is where there is no interstage swirl, and thus for a fixed axial velocity, the exit kinetic energy will be minimized. If the total-to-total efficiency was considered, this would not be greatly affected by the choice of reaction. However, the maximum value of η_{tt} is found, in general, to decrease slightly as the stage loading factor increases, see Section 4.12.

4.10 Diffusion within blade rows

Any diffusion of the flow through turbine blade rows is particularly undesirable and must, at the design stage, be avoided at all costs. This is because the adverse pressure gradient (arising from the flow diffusion), coupled with large amounts of fluid deflection (usual in turbine blade rows), makes boundary layer separation more than merely possible, with the result that large-scale losses arise. A compressor blade row, on the other hand, is designed to cause the fluid pressure to rise in

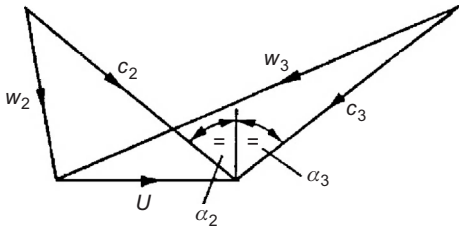

FIGURE 4.10

Velocity diagram for 100% reaction turbine stage.

the direction of flow, i.e., an *adverse* pressure gradient. The magnitude of this gradient is strictly controlled in a compressor, mainly by having a fairly limited amount of fluid deflection in each blade row.

It was shown previously that negative values of reaction indicated diffusion of the rotor relative velocity (i.e., for $R < 0$, $w_3 < w_2$). A similar condition that holds for diffusion of the nozzle absolute velocity is that, if $R > 1$, $c_2 < c_1$.

If we consider Eq. (4.13), this can be written as

$$R = 1 + \frac{\phi}{2}(\tan \alpha_3 - \tan \alpha_2)$$

Thus, when $\alpha_3 = \alpha_2$ the reaction is unity (also $c_2 = c_3$). The velocity diagram for $R = 1$ is shown in Figure 4.10 with the same values of c_x, U, and ΔW used for $R = 0$ and $R = 1/2$. It will be apparent that if R exceeds unity, then $c_2 < c_1$ (i.e., nozzle flow *diffusion*).

EXAMPLE 4.4

A single-stage gas turbine operates at its design condition with an axial absolute flow at entry and exit from the stage. The absolute flow angle at nozzle exit is 70°. At stage entry, the total pressure and temperature are 311 kPa and 850°C, respectively. The exhaust static pressure is 100 kPa, the total-to-static efficiency is 0.87, and the mean blade speed is 500 m/s.

Assuming constant axial velocity through the stage, determine

1. the specific work done;
2. the Mach number leaving the nozzle;
3. the axial velocity;
4. the total-to-total efficiency;
5. the stage reaction.

Take $C_p = 1.148$ kJ/(kg °C) and $\gamma = 1.33$ for the gas.

Solution

1. From Eq. (4.19a), total-to-static efficiency is

$$\eta_{ts} = \frac{h_{01} - h_{03}}{h_{01} - h_{3ss}} = \frac{\Delta W}{h_{01}[1 - (p_3/p_{01})^{(\gamma-1)/\gamma}]}$$

Thus, the specific work is

$$\begin{aligned}\Delta W &= \eta_{ts} C_p T_{01}[1-(p_3/p_{01})^{(\gamma-1)/\gamma}] \\ &= 0.87 \times 1148 \times 1123 \times [1-(1/3.11)^{0.248}] = 276 \text{ kJ/kg}\end{aligned}$$

2. At nozzle exit, the Mach number is

$$M_2 = c_2/(\gamma R T_2)^{1/2}$$

and it is necessary to solve the velocity diagram to find c_2 and, hence, to determine T_2. As

$$c_{\theta 3} = 0, \quad \Delta W = U c_{\theta 2}$$

$$c_{\theta 2} = \frac{\Delta W}{U} = \frac{276 \times 10^3}{500} = 552 \text{ m/s}$$

$$c_2 = \frac{c_{\theta 2}}{\sin \alpha_2} = 588 \text{ m/s}$$

Referring to Figure 4.1, across the nozzle $h_{01} = h_{02} = h_2 + (1/2)c_2^2$, thus,

$$T_2 = T_{01} - \frac{1}{2} c_2^2 / C_p = 973 \text{ K}$$

Hence, $M_2 = 0.97$ with $\gamma R = (\gamma - 1) C_p$

3. The axial velocity, $c_x = c_2 \cos \alpha_2 = 200$ m/s

4. $\eta_u = \dfrac{\Delta W}{(h_{01} + h_{3ss} - (1/2)c_3^2)}$

After some rearrangement,

$$\frac{1}{\eta_u} = \frac{1}{\eta_{ts}} - \frac{c_3^2}{2\Delta W} = \frac{1}{0.87} - \frac{200^2}{2 \times 276 \times 10^3} = 1.0775$$

Therefore, $\eta_{tt} = 0.93$

5. Using Eq. (4.13a), the reaction is

$$R = 1 - \frac{\phi}{2}(\tan \alpha_2 - \tan \alpha_1)$$

$$\therefore R = 1 - \frac{(200/500)}{2} \tan 70^\circ = 0.451$$

4.11 The efficiency correlation of Smith (1965)

All manufacturers of steam and gas turbines keep large databases of measured efficiency of axial-flow turbine stages as functions of the duty parameters (flow coefficient, ϕ, and stage loading coefficient, ψ). Smith (1965) devised a widely used efficiency correlation based upon data obtained from 70 Rolls-Royce aircraft gas turbines, such as the Avon, Dart, Spey, Conway, and others, including the special four-stage turbine test facility at Rolls-Royce, Derby, England. The data points and

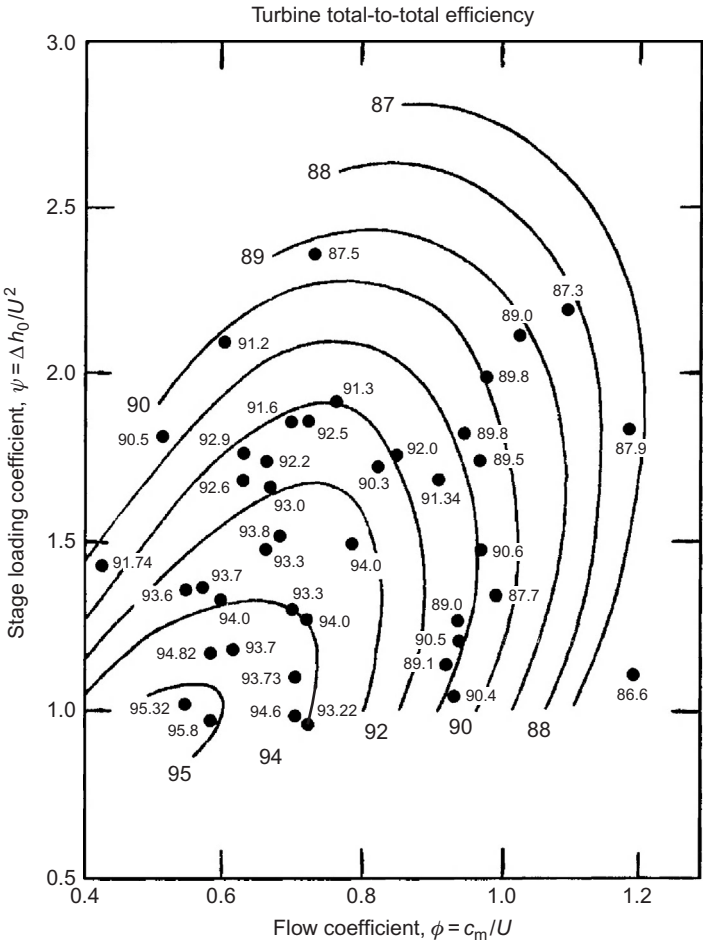

FIGURE 4.11

Smith chart for turbine stage efficiency.

(Smith, 1965, with Permission from the Royal Aeronautical Society and its Aeronautical Journal)

efficiency curves found by him are shown in Figure 4.11. It is worth knowing that all stages tested were constant axial velocity, the reactions were between 0.2 and 0.6 and the blade aspect ratio (blade height to chord ratio) was relatively large, between 3 and 4. Another important factor to remember was that all efficiencies were corrected to eliminate tip leakage loss so that, in actual operation, the efficiencies would be higher than those expected for the equivalent real turbines. The tip leakage losses (which can be very large) were found by repeating tests with different amounts of tip clearance and extrapolating the results back to zero clearance to get the desired result.

Every turbine was tested over a range of pressure ratios to find its point of maximum efficiency and to determine the corresponding values of ψ and ϕ. Each point plotted in Figure 4.11 represents

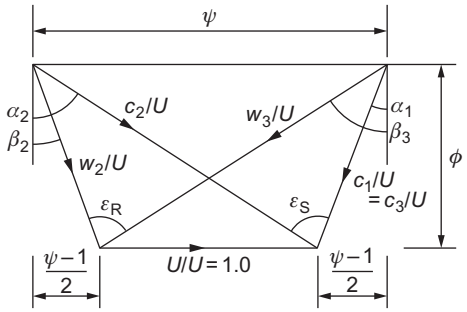

FIGURE 4.12

Dimensionless velocity triangles for a 50% reaction turbine stage.

just one test turbine at its best efficiency point and the value of its efficiency is shown adjacent to that point. Confirmatory tests made by Kacker and Okapuu (1982) and others have shown the usefulness of the chart in preliminary turbine design.

Smith developed a simple theoretical analysis to explain the shape of the efficiency curves. He argued that the losses in any blade row were proportional to the average absolute kinetic energy, $(1/2)(c_1^2 + c_2^2)$, for that row. For $R = 0.5$, Smith defined a factor, f_s, as the ratio of the shaft work output to the sum of the mean kinetic energies within the rotor and stator. Thus,

$$f_s = \frac{\Delta h_0}{c_1^2 + c_2^2} = \frac{\Delta h_0 / U^2}{(c_1^2/U^2) + (c_2^2/U^2)} \tag{4.30}$$

Following the reasoning of Smith it is helpful to nondimensionalize the velocity triangles for the complete stage, assuming $R = 0.5$, as shown in Figure 4.12. It will be observed that $\tan \alpha_1 = \tan \beta_2 = (\psi - 1)/2\phi$ and $\tan \alpha_2 = \tan \beta_3 = (\psi + 1)/2\phi$. Solving for the nondimensionalized velocities in terms of ψ and ϕ, we find

$$\frac{c_2}{U} = \frac{w_3}{U} = \sqrt{\phi^2 + \left(\frac{\psi+1}{2}\right)^2}$$

and

$$\frac{c_1}{U} = \frac{w_2}{U} = \sqrt{\phi^2 + \left(\frac{\psi+1}{2}\right)^2}$$

Substituting into Eq. (4.30), we obtain

$$f_s = \frac{\psi}{\phi^2 + ((\psi+1)/2)^2 + \phi^2 + ((\psi-1)/2)^2} = \frac{2\psi}{4\phi^2 + \psi^2 + 1} \tag{4.31}$$

From this expression the optimum stage work coefficient, ψ, for a given flow coefficient, ϕ, can be found by differentiating with respect to ψ:

$$\frac{\partial f_s}{\partial \psi} = \frac{2(4\phi^2 + \psi^2 + 1)}{(4\phi^2 + \psi^2 + 1)} = 0$$

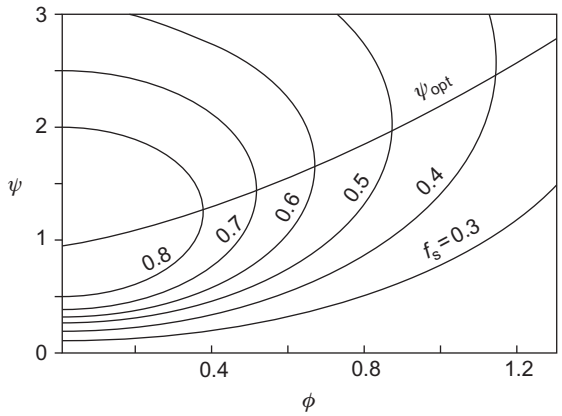

FIGURE 4.13

Smith's kinetic energy coefficient f_s and the optimum stage loading, ψ_{opt}, plotted against the stage loading coefficient and flow coefficient for a turbine stage.

From this expression, the optimum curve is easily derived as

$$\psi_{opt} = \sqrt{4\phi^2 + 1} \tag{4.32}$$

Figure 4.13 is a carpet plot of ψ versus ϕ for various values of f_s. Superimposed on this plot is the locus of the optimum curve defined by Eq. (4.32). It has been noted that this curve tends to follow the trend of the optimum efficiency of the Rolls-Royce efficiency correlation given in Figure 4.13. It has been reported by Lewis (1996) that a more accurate representation of the optimum can be picked out from the Rolls-Royce data as

$$\psi_{opt\ exp} = 0.65\sqrt{4\phi^2 + 1} \tag{4.33}$$

It is worth knowing that Lewis (1996) developed Smith's method of analysis to include the blade aerodynamics and blade loss coefficients adding further insight into the method.

4.12 Design point efficiency of a turbine stage

In this section, the performance of a turbine stage in terms of its efficiency is calculated for several types of design, i.e., 50% reaction, zero reaction, and zero exit flow angle, using the loss correlation method of Soderberg described in Chapter 3. The results are most usefully presented in the form of carpet plots of the stage loading coefficient, ψ, and flow coefficient, ϕ.

Total-to-total efficiency of 50% reaction stage

In a multistage turbine the total-to-total efficiency is the relevant performance criterion, the kinetic energy at stage exit being recovered in the next stage. After the last stage of a multistage turbine or

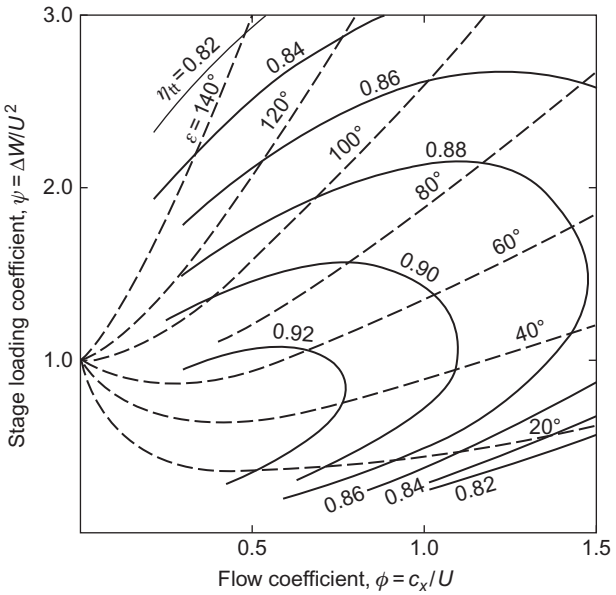

FIGURE 4.14

Design point total-to-total efficiency and deflection angle contours for a turbine stage of 50% reaction.

a single-stage turbine, the kinetic energy in the exit flow would be recovered in a diffuser or used for another purpose (e.g., as a contribution to the propulsive thrust).

From Eq. (4.18c), where it has already been assumed that $c_1 = c_3$ and $T_3 = T_2$, we have

$$\frac{1}{\eta_u} = 1 + \frac{\left(\zeta_R w_3^2 + \zeta_N c_2^2\right)}{2\Delta W}$$

where $\Delta W = \psi U^2$ and, for a 50% reaction, $w_3 = c_2$ and $\zeta_R = \zeta_N = \zeta$:

$$w_3^2 = c_x^2 \sec^2 \beta_3 = c_x^2(1 + \tan^2 \beta_3)$$

Therefore,

$$\frac{1}{\eta_u} = 1 + \frac{\zeta\phi^2}{\psi}(1 + \tan^2 \beta_3) = 1 + \frac{\zeta\phi^2}{\psi}\left[1 + \left(\frac{1+\psi}{2\phi}\right)^2\right]$$

as $\tan \beta_3 = (\psi + 1)/2\phi$ and $\tan \beta_2 = (\psi - 1)/2\phi$.

From these expressions combined with Soderberg's correlation given in Eq. (3.46), the performance chart, shown in Figure 4.14, was derived for specified values of ψ and ϕ. From this chart it can be seen that the peak total-to-total efficiency, η_{tt}, is obtained at very low values of ϕ and ψ. As indicated in a survey by Kacker and Okapuu (1982), most aircraft gas turbine designs operate with flow coefficients in the range, $0.5 \leq \phi \leq 1.5$, and values of stage loading coefficient in the range, $0.8 \leq \psi \leq 2.8$.

Total-to-total efficiency of a zero reaction stage

The degree of reaction will normally vary along the length of the blade depending upon the type of design specified. The performance for $R = 0$ represents a limit, lower values of reaction are possible but undesirable as they would give rise to large losses in efficiency. For $R < 0$, $w_3 < w_2$, which means the relative flow decelerates across the rotor.

Referring to Figure 4.6, for zero reaction $\beta_2 = \beta_3$, and from Eq. (4.15)

$$\tan \alpha_2 = 1/\phi + \tan \beta_2 \quad \text{and} \quad \tan \alpha_3 = \tan \beta_3 - 1/\phi$$

Also, $\psi = \Delta W/U^2 = \phi(\tan \alpha_2 + \tan \alpha_3) = \phi(\tan \beta_2 + \tan \beta_3) = 2\phi \tan \beta_2$; therefore,

$$\tan \beta_2 = \frac{\psi}{2\phi}$$

Thus, using the preceding expressions,

$$\tan \alpha_2 = \frac{(\psi/2) + 1}{\phi} \quad \text{and} \quad \tan \alpha_3 = \frac{(\psi/2) - 1}{\phi}$$

From these expressions, the flow angles can be calculated if values for ψ and ϕ are specified. From an inspection of the velocity diagram,

$$\begin{aligned} c_2 &= c_x \sec \alpha_2, \quad \text{hence, } c_2^2 = c_x^2(1 + \tan^2 \alpha_2) = c_x^2[1 + (\psi/2+1)^2/\phi^2] \\ w_3 &= c_x \sec \beta_3, \quad \text{hence, } w_3^2 = c_x^2(1 + \tan^2 \beta_3) = c_x^2[1 + (\psi/2\phi)^2] \end{aligned}$$

Substituting these expressions into Eq. (4.20),

$$\frac{1}{\eta_{tt}} = 1 + \frac{\zeta_R w_3^2 + \zeta_N c_2^2}{2\psi U^2}$$

$$\frac{1}{\eta_u} = 1 + \frac{1}{2\psi}\left\{\zeta_R\left[\phi^2 + \left(\frac{\psi}{2}\right)^2\right] + \zeta_N\left[\phi^2 + \left(1 + \frac{\psi}{2}\right)^2\right]\right\}$$

The performance chart shown in Figure 4.15 was derived using these expressions. This is similar in its general form to Figure 4.14 for a 50% reaction, with the highest efficiencies being obtained at the lowest values of ϕ and ψ, except that higher efficiencies are obtained at higher values of the stage loading but at reduced values of the flow coefficient.

Total-to-static efficiency of stage with axial velocity at exit

A single-stage axial turbine will have axial flow at exit and the most appropriate efficiency is usually total to static. To calculate the performance, Eq. (4.21) is used:

$$\frac{1}{\eta_{ts}} = 1 + \frac{\zeta_R w_3^2 + \zeta_N c_2^2 + c_1^2}{2\Delta W} = 1 + \frac{\phi^2}{2\psi}\left(\zeta_R \sec^2 \beta_3 + \zeta_N \sec^2 \alpha_2 + 1\right)$$

With axial flow at exit, $c_1 = c_3 = c_x$, and from the velocity diagram, Figure 4.16,

$$\tan \beta_3 = U/c_x, \tan \beta_2 = \tan \alpha_2 - \tan \beta_3$$

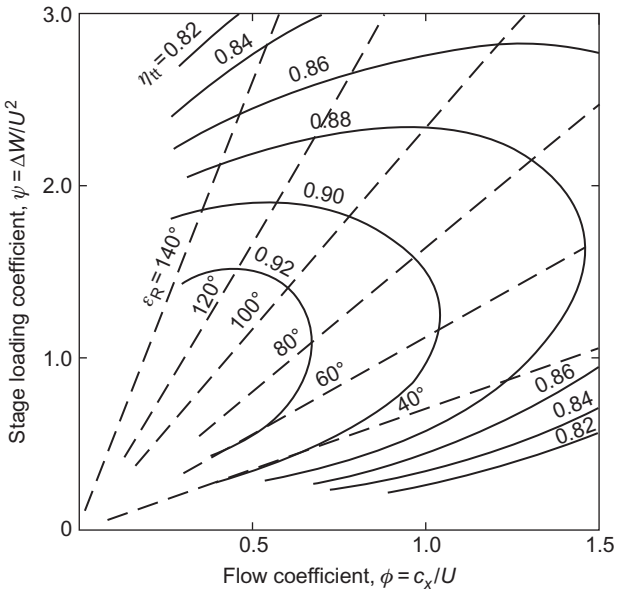

FIGURE 4.15

Design point total-to-total efficiency and rotor flow deflection angle for a zero reaction turbine stage.

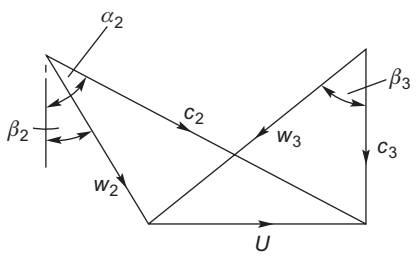

FIGURE 4.16

Velocity diagram for a turbine stage with axial exit flow.

$$\sec^2 \beta_3 = 1 + \tan^2 \beta_3 = 1 + 1/\phi^2$$

$$\sec^2 \alpha_2 = 1 + \tan^2 \alpha_2 = 1 + (\psi/\phi)^2$$

Therefore,

$$\frac{1}{\eta_{ts}} = 1 + \frac{1}{2\phi}\left[\zeta_R(1+\phi^2) + \zeta_N(\psi^2+\phi^2) + \phi^2\right]$$

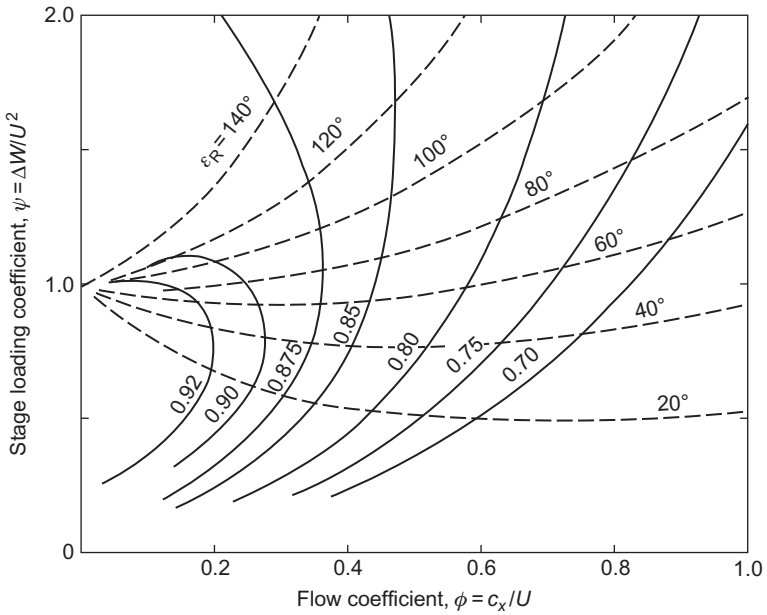

FIGURE 4.17

Total-to-static efficiency contours for a stage with axial flow at exit.

Specifying ϕ and ψ, the unknown values of the loss coefficients, ζ_R and ζ_N, can be derived using Soderberg's correlation, Eq. (3.50), in which

$$\varepsilon_N = \alpha_2 = \tan^{-1}(\psi/\phi) \quad \text{and} \quad \varepsilon_R = \beta_2 + \beta_3 = \tan^{-1}(1+\phi) + \tan^{-1}[(\psi - 1)/\phi]$$

From these expressions the performance chart, Figure 4.17, was derived.

An additional limitation is imposed on the performance chart because of the reaction, which must remain greater than or, in the limit, equal to zero. From Eq. (4.14) for zero interstage swirl,

$$\psi = 2(1 - R)$$

Thus, at the limit, $R = 0$, and the stage loading coefficient, $\psi = 2$.

4.13 Stresses in turbine rotor blades

Although this chapter is primarily concerned with the fluid mechanics and thermodynamics of turbines, some consideration of stresses in rotor blades is needed as these can place restrictions on the allowable blade height and annulus flow area, particularly in high temperature, high stress situations. Only a very brief outline is attempted here of a very large subject, which is treated at much greater length by Horlock (1966), in texts dealing with the mechanics of solids, e.g., Den Hartog (1952) and Timoshenko (1956), and in specialized discourses, e.g., Japiske (1986) and Smith (1986). The stresses in turbine

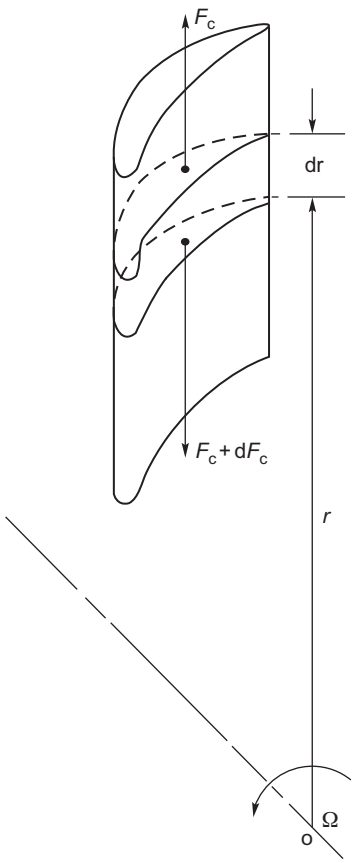

FIGURE 4.18

Centrifugal forces acting on rotor blade element.

blades arise from centrifugal loads, from gas bending loads, and from vibrational effects caused by non-constant gas loads. Although the centrifugal stress produces the biggest contribution to the total stress, the vibrational stress is very significant and thought to be responsible for fairly common vibratory fatigue failures (Smith, 1986). The direct and simple approach to blade vibration is to "tune" the blades so that resonance does not occur in the operating range of the turbine. This means obtaining a blade design in which none of its natural frequencies coincides with any excitation frequency. The subject is complex and interesting, but outside of the scope of the present text.

Centrifugal stresses

Consider a blade rotating about an axis O as shown in Figure 4.18. For an element of the blade of length dr at radius r, at a rotational speed Ω, the elementary centrifugal load dF_c is given by

$$dF_c = -\Omega^2 r dm$$

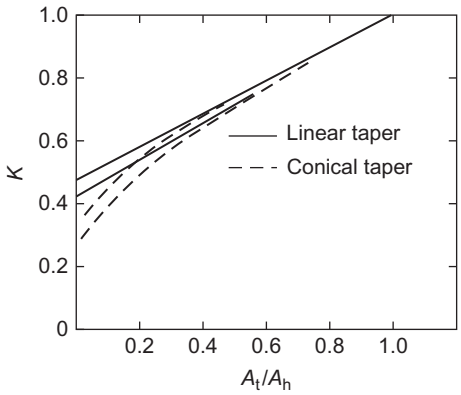

FIGURE 4.19

Effect of tapering on centrifugal stress at blade root.

(Adapted from Emmert, 1950)

where $dm = \rho_m A dr$ and the negative sign accounts for the direction of the stress gradient (i.e., zero stress at the blade tip to a maximum at the blade root),

$$\frac{d\sigma_c}{\rho_m} = \frac{dF_c}{\rho_m A} = -\Omega^2 r dr$$

For blades with a constant cross-sectional area, we get

$$\frac{\sigma_c}{\rho_m} = \Omega^2 \int_{r_h}^{r_t} r dr = \frac{U_t^2}{2}\left[1 - \left(\frac{r_h}{r_t}\right)^2\right] \tag{4.34a}$$

A rotor blade is usually tapered both in chord and in thickness from root to tip, such that the area ratio A_t/A_h is between 1/3 and 1/4. For such a blade taper, it is often assumed that the blade stress is reduced to two-thirds of the value obtained for an untapered blade. A blade stress taper factor can be defined as

$$K = \frac{\text{stress at root of tapered blade}}{\text{stress at root of untapered blade}}$$

Thus, for tapered blades

$$\frac{\sigma_c}{\rho_m} = \frac{KU_t^2}{2}\left[1 - \left(\frac{r_h}{r_t}\right)^2\right] \tag{4.34b}$$

Values of the taper factor K quoted by Emmert (1950) are shown in Figure 4.19 for various taper geometries.

Typical data for the allowable stresses of commonly used alloys are shown in Figure 4.20 for the "1000-h rupture life" limit with maximum stress allowed plotted as a function of blade temperature. It can be seen that, in the temperature range 900−1100 K, nickel or cobalt alloys are likely to be suitable and for temperatures up to about 1300 K molybdenum alloys would be needed.

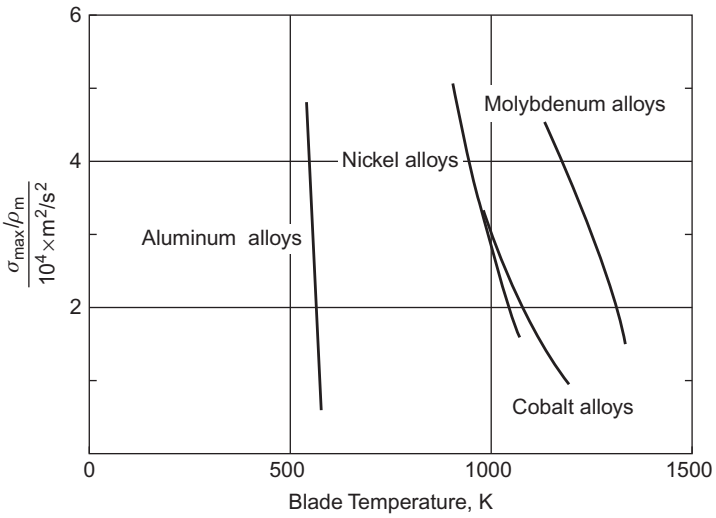

FIGURE 4.20

Maximum allowable stress for various alloys (1000-h rupture life).

(Adapted from Freeman, 1955).

Further detailed information on one of the many alloys used for gas turbines blades is shown in Figure 4.21. This material is Inconel, a nickel-based alloy containing 13% chromium, 6% iron, with a little manganese, silicon, and copper. Figure 4.21 shows the influence of the "rupture life" and also the "percentage creep," which is the elongation strain at the allowable stress and temperature of the blade. To enable operation at high temperatures and for long life of the blades, the creep strength criterion is the one usually applied by designers.

An estimate of the average rotor blade temperature T_b can be made using the approximation

$$T_b = T_2 + 0.85 w_2^2/(2C_p) \tag{4.35}$$

that is, 85% temperature recovery of the inlet *relative kinetic energy*.

EXAMPLE 4.5

Combustion products enter the first stage of a gas turbine at a stagnation temperature and pressure of 1200 K and 4.0 bar. The rotor blade tip diameter is 0.75 m, the blade height is 0.12 m, and the shaft speed is 10,500 rev/min. At the mean radius the stage operates with a reaction of 50%, a flow coefficient of 0.7, and a stage loading coefficient of 2.5.

Assuming the combustion products are a perfect gas with $\gamma = 1.33$ and $R = 287.8$ kJ/kg K, determine:

1. the relative and absolute flow angles for the stage;
2. the velocity at nozzle exit;
3. the static temperature and pressure at nozzle exit assuming a nozzle efficiency of 0.96 and the mass flow;

4. the rotor blade root stress assuming the blade is tapered with a stress taper factor K of 2/3 and the blade material density is 8000 kg/m^2;
5. the approximate mean blade temperature;
6. taking only the centrifugal stress into account suggest a suitable alloy from the information provided that could be used to withstand 1000 h of operation.

Solution

1. The stage loading is

$$\psi = \Delta h_0/U^2 = (w_{\theta 3} + w_{\theta 2})/U = \phi(\tan\beta_3 + \tan\beta_2)$$

From Eq. (4.13b), the reaction is

$$R = \phi(\tan\beta_3 - \tan\beta_2)/2$$

Adding and subtracting these two expressions, we get

$$\tan\beta_3 = (\psi/2 + R)/\phi \quad \text{and} \quad \tan\beta_2 = (\psi/2 - R)/\phi$$

Substituting values of ψ, ϕ, and R into the preceding equations, we obtain

$$\beta_3 = 68.2^\circ, \quad \beta_2 = 46.98^\circ$$

and for similar triangles (i.e., 50% reaction),

$$\alpha_2 = \beta_3 \quad \text{and} \quad \alpha_3 = \beta_2$$

2. At the mean radius, $r_m = (0.75-0.12)/2 = 0.315$ m, the blade speed is $U_m = \Omega r_m = (10{,}500/30) \times \pi \times 0.315 = 1099.6 \times 0.315 = 346.36$ m/s. The axial velocity $c_x = \phi U_m = 0.5 \times 346.36 = 242.45$ m/s and the velocity of the gas at nozzle exit is $c_2 = c_x/\cos\alpha_2 = 242.45/\cos 68.2 = 652.86$ m/s.
3. To determine the conditions at nozzle exit, we have

$$T_2 = T_{02} = \frac{1}{2}c_2^2/C_p = 1200 - 652.86^2/(2 \times 1160) = 1016.3 \text{ K}$$

The nozzle efficiency is

$$\eta_N = \frac{h_{01} - h_2}{h_{01} - h_{2s}} = \frac{1 - (T_2/T_{01})}{1 - (p_2/p_{01})^{(\gamma-1)/\gamma}}$$

Therefore,

$$\left(\frac{p_2}{p_{01}}\right)^{(\gamma-1)/\gamma} = 1 - \frac{1 - (T_2/T_{01})}{\eta_N} = 1 - \frac{1 - (1016.3/1200)}{0.96} = 0.84052$$

and

$$p_2 = 4 \times 0.840052^{4.0303} = 1.986 \text{ bar}$$

The mass flow is found from the continuity equation:

$$\dot{m} = \rho_2 A_2 c_{x2} = \left(\frac{p_2}{RT_2}\right) A_2 c_{x2}$$

therefore,

$$\dot{m} = \left(\frac{1.986 \times 10^5}{287.8 \times 1016.3}\right) \times 0.2375 \times 242.45 = 39.1 \text{ kg/s}$$

4. For a tapered blade, Eq. (4.34b) gives

$$\frac{\sigma_c}{\rho_m} = \frac{2}{3} \times \frac{412.3^2}{2}\left[1 - \left(\frac{0.51}{0.75}\right)^2\right] = 30,463.5 \text{ m}^2/\text{s}^2$$

where $U_t = 1099.6 \times 0.375 = 412.3$ m/s.

The density of the blade material is taken to be 8000 kg/m^3 and so the root stress is

$$\sigma_c = 8000 \times 30,463.5 = 2.437 \times 10^8 \text{ N/m}^2 = 243.7 \text{ MPa}$$

5. The approximate average mean blade temperature is

$$T_b = 1016.3 + 0.85 \times (242.45/\cos 46.975)^2/(2 \times 1160) = 1016.3 + 46.26 = 1062.6 \text{ K}$$

6. The data in Figure 4.20 suggest that, for this moderate root stress, cobalt or nickel alloys would not withstand a lifespan of 1000 h to rupture and the use of molybdenum would be necessary. However, it would be necessary to take account of bending and vibratory stresses and the decision about the choice of a suitable blade material would be decided on the outcome of these calculations.

   Inspection of the data for Inconel 713 cast alloy, Figure 4.21, suggests that it might be a better choice of blade material as the temperature–stress point of the preceding calculation is to the left of the line marked creep strain of 0.2% in 1000 h. Again, account must be taken of the additional stresses due to bending and vibration.

   Design is a process of trial and error; changes in the values of some of the parameters can lead to a more viable solution. In this case (with bending and vibrational stresses included), it might be necessary to reduce one or more of the values chosen, e.g., the rotational speed, the inlet stagnation temperature, and the flow area.

   Note: The combination of values for ψ and ϕ at $R = 0.5$ used in this example was selected from data given by Wilson (1987) and corresponds to an optimum total-to-total efficiency of 91.9%.

4.14 Turbine blade cooling

In the gas turbine industry, there has been a continuing trend towards higher turbine inlet temperatures to give increased specific thrust (thrust per unit air mass flow) and to allow the specific fuel consumption to be reduced. The highest allowable gas temperature at entry to a turbine with uncooled blades is 1000°C while, with a sophisticated blade cooling system, gas temperatures up to

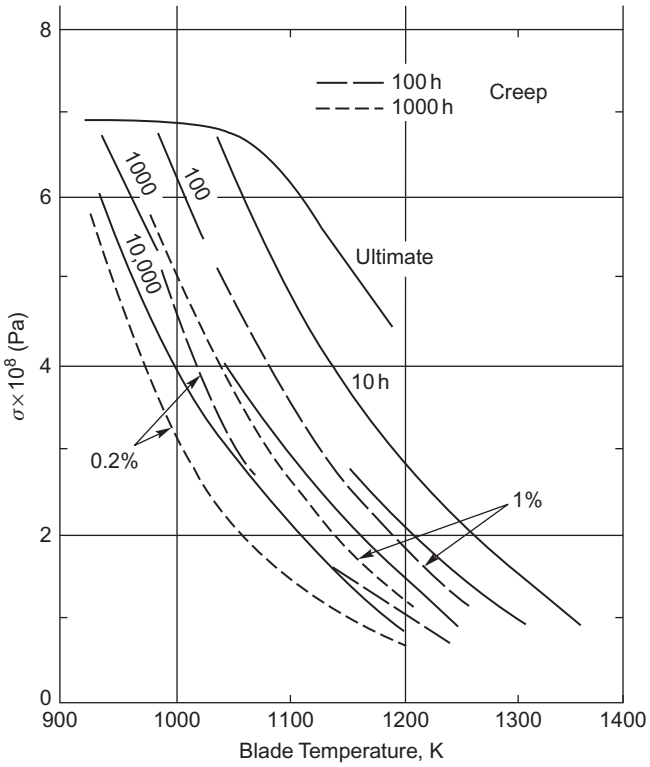

FIGURE 4.21

Properties of Inconel 713 Cast Alloy.

(Adapted from Balje, 1981)

about 1800°C are possible, depending on the nature of the cooling system. Such high temperatures are well in excess of the melting point of the leading nickel-based alloys from which the blades are cast.

Various types of cooling system for gas turbines have been considered in the past and a number of these are now in use. In the Rolls-Royce Trent engines (Rolls-Royce, 2005), the HP turbine blades, nozzle guide vanes, and seal segments are cooled internally and externally using cooling air from the final stage of the HP compressor. This cooling air is itself at a temperature of over 700°C and at a pressure of 3.8 MPa. The hot gas stream at the turbine inlet is at a pressure of over 3.6 MPa so the pressure margin is quite small and maintaining that margin is critical to the lifespan of the engine. Figure 4.22 illustrates a high-pressure turbine rotor blade, sectioned to show the intricate labyrinth of passages through which the cooling air passes before part of it is vented to the blade surface via the rows of tiny holes along and around the hottest areas of the blade. Ideally, the air emerges with little velocity and forms a film of cool air around the blade surface (hence, the term *film cooling*), insulating it from the hot gases. This type of cooling system enables turbine

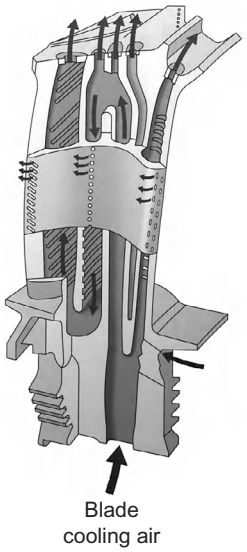

FIGURE 4.22

Cooled HP turbine rotor blade showing the cooling passages.

(Courtesy of Rolls-Royce plc)

entry temperatures up to 1800 K to be used. Figure 4.23 shows the way the cooling air is used to cool HP nozzle guide vanes in a modern jet engine.

The cooling system performance can be quantified using the *cooling effectiveness* defined as

$$\varepsilon = \frac{T_{0g} - T_b}{T_{0g} - T_{0c}} \tag{4.36}$$

where T_{0g} is the stagnation temperature of the hot gas stream, T_b is the blade metal temperature, and T_{0c} is the coolant stagnation temperature. A typical value for ε is around 0.6. Equation (4.36) can be used to look at the effect of changes in the cooling system on the blade metal temperature. As shown by Figure 4.21, relatively small changes in the blade metal temperature will lead to large changes in the creep life of the component.

A rising thermodynamic penalty is incurred with blade cooling systems as the turbine entry temperature rises due to the energy required to pressurize the air bled off from the compressor and the viscous and mixing losses incurred. Figure 4.24 is taken from Wilde (1977) showing how the net turbine efficiency decreases with increasing turbine entry temperature. Several in-service gas turbine engines for that era are included in the graph. Wilde did question whether turbine entry temperatures >1600 K could really be justified in turbofan engines because of the effect on the internal aerodynamic efficiency and specific fuel consumption. However, turbine entry temperatures continue to rise and experience continues to show the important operational advantage of using complex blade cooling systems.

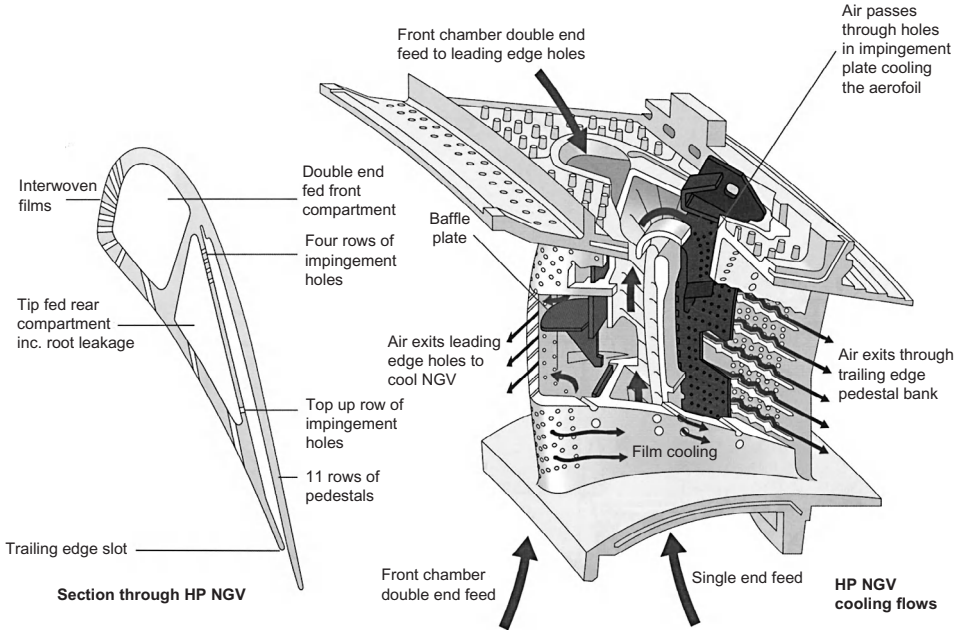

FIGURE 4.23

Cooling arrangement for a nozzle guide vane in a HP turbine of a modern turbofan.

(Courtesy of Rolls-Royce plc)

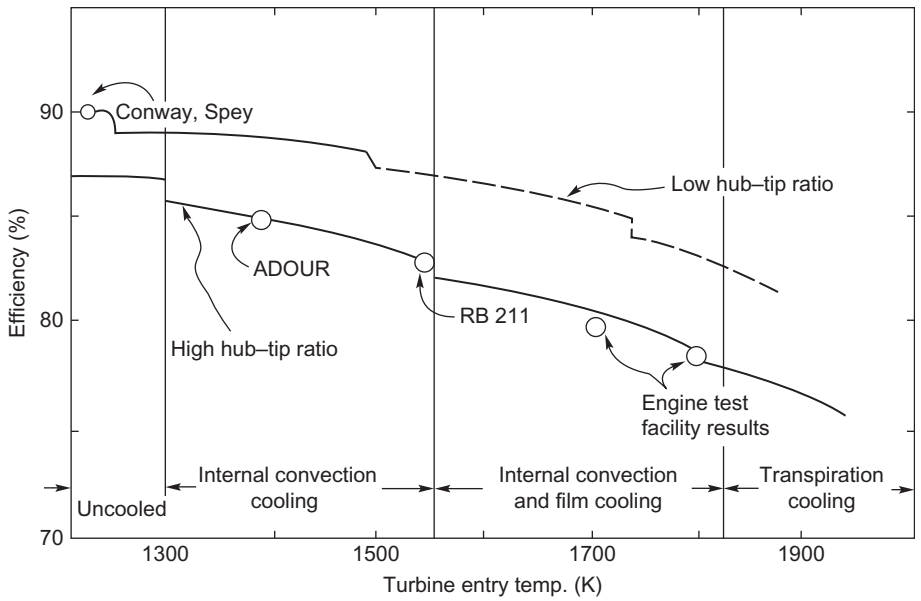

FIGURE 4.24

Turbine thermal efficiency versus inlet gas temperature.

(Wilde, 1977)

4.15 Turbine flow characteristics

An accurate knowledge of the flow characteristics of a turbine is of considerable practical importance as, for instance, in the matching of flows between a compressor and turbine of a jet engine. Figure 4.25, after Mallinson and Lewis (1948), shows a comparison of typical characteristics for one, two, and three stages plotted as turbine overall pressure ratio p_{01}/p_{0e} against a mass flow coefficient $\dot{m}(\sqrt{T_{01}})/p_{01}$. There is a noticeable tendency for the characteristic to become more ellipsoidal as the number of stages is increased. At a given pressure ratio the mass flow coefficient, or "swallowing capacity," tends to decrease with the addition of further stages to the turbine. One of the earliest attempts to assess the flow variation of a multistage turbine is credited to Stodola (1945), who formulated the much used "ellipse law." The curve labeled *multistage* in Figure 4.25 is in agreement with the "ellipse law" expression

$$\dot{m}(\sqrt{T_{01}})/p_{01} = k[1-(p_{0e}/p_{01})^2]^{1/2} \tag{4.37}$$

where k is a constant.

This expression has been used for many years in steam turbine practice, but an accurate estimate of the variation in swallowing capacity with pressure ratio is of even greater importance in gas turbine technology. Whereas, the average condensing steam turbine, even at part-load, operates at very high-pressure ratios, some gas turbines may work at rather low-pressure ratios, making flow matching with a compressor a more difficult problem.

Note that, when the pressure ratio across a single-stage turbine exceeds about 2, the turbine stator blades choke and the flow capacity becomes constant. Beyond this point the turbine behaves

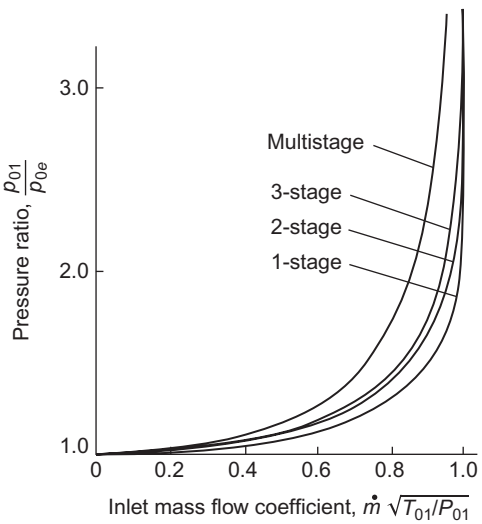

FIGURE 4.25

Turbine flow characteristics

(After Mallinson and Lewis, 1948)

much the same as a choked nozzle and the performance is fairly independent of the turbine rotational speed. For multistage turbines, the choking pressure ratio increases as more stages are added.

Flow characteristics of a multistage turbine

Several derivations of the ellipse law are available in the literature. The derivation given here is a slightly amplified version of the proof given by Horlock (1958). A more general method has been given by Egli (1936), which takes into consideration the effects when operating outside the normal low loss region of the blade rows.

Consider a turbine comprising a large number of normal stages, each of 50% reaction; then, referring to the velocity diagram of Figure 4.26(a), $c_1 = c_3 = w_2$ and $c_2 = w_3$. If the blade speed is maintained constant and the mass flow is reduced, the fluid angles at exit from the rotor (β_3) and nozzles (α_2) will remain constant and the velocity diagram then assumes the form shown in Figure 4.26(b). The turbine, if operated in this manner, will be of low efficiency, as the fluid direction at inlet to each blade row is likely to produce a negative incidence stall. To maintain high efficiency, the fluid inlet angles must remain fairly close to the design values. It is therefore assumed that the turbine operates at its highest efficiency at *all off-design conditions* and, by implication, the blade speed is changed in direct proportion to the axial velocity. The velocity triangles are similar at off-design flows but of different scale.

Now the work done by unit mass of fluid through one stage is $U(c_{\theta 2} + c_{\theta 3})$ so that, assuming a perfect gas,

$$C_p \Delta T_0 = C_p \Delta T = U c_x (\tan \alpha_2 + \tan \alpha_3)$$

and, therefore,

$$\Delta T \propto c_x^2$$

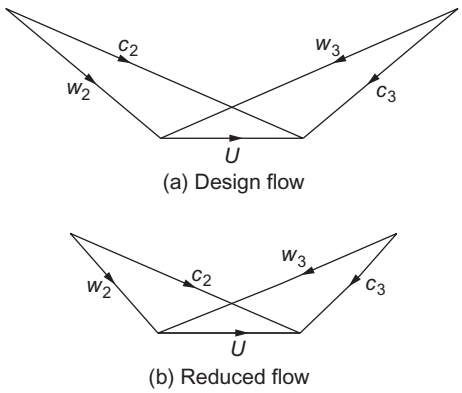

FIGURE 4.26

Change in turbine stage velocity diagram with mass flow at constant blade speed.

Denoting design conditions by subscript d, then

$$\frac{\Delta T}{\Delta T_d} = \left(\frac{c_x}{c_{xd}}\right)^2 \tag{4.38}$$

for equal values of c_x/U.

From the continuity equation, at off-design, $\dot{m} = \rho A_x c_x = \rho_1 A_{x1} c_{x1}$, and at design, $\dot{m}_d = \rho_d A_x c_{xd} = \rho_1 A_{x1} c_{x1}$, hence,

$$\frac{c_x}{c_{xd}} = \frac{\rho_d}{\rho}\frac{c_{x1}}{c_{x1d}} = \frac{\rho_d}{\rho}\frac{\dot{m}}{\dot{m}_d} \tag{4.39}$$

Consistent with the assumed mode of turbine operation, the polytropic efficiency is taken to be constant at off-design conditions and, from Eq. (1.50), the relationship between temperature and pressure is, therefore,

$$T/p^{\eta_p(\gamma-1)/\gamma} = \text{constant}$$

Combined with $p/\rho = RT$, the above expression gives, on eliminating p, $\rho/T^n = \text{constant}$, hence,

$$\frac{\rho}{\rho_d} = \left(\frac{T}{T_d}\right)^{\mathrm{n}} \tag{4.40}$$

where $n = \gamma/[\eta_p(\gamma-1)] - 1$.

For an infinitesimal temperature drop, Eq. (4.38) combined with Eqs. (4.39) and (4.40) gives, with little error,

$$\frac{\mathrm{d}T}{\mathrm{d}T_d} = \left(\frac{c_x}{c_{xd}}\right)^2 = \left(\frac{T_d}{T}\right)^{2n}\left(\frac{\dot{m}}{\dot{m}_d}\right) \tag{4.41}$$

Integrating Eq. (4.41),

$$T^{2n+1} = \left(\frac{\dot{m}}{\dot{m}_d}\right)T_d^{2n+1} + K$$

where K is an arbitrary constant.

To establish a value for K, it is noted that if the turbine entry temperature is constant $T_d = T_1$ and $T = T_1$ also. Thus, $K = \left[1 + (\dot{m}+\dot{m}_d)^2\right]T_1^{2n+1}$ and

$$\left(\frac{T}{T_1}\right)^{2n+1} - 1 = \left(\frac{\dot{m}}{\dot{m}_d}\right)^2\left[\left(\frac{T_d}{T_1}\right)^{2n+1} - 1\right] \tag{4.42}$$

Equation (4.42) can be rewritten in terms of pressure ratio since $T/T_1 = (p/p_l)^{\eta_p(\gamma-1)/\gamma}$. As $2n+1 = 2\gamma/[\eta_p(\gamma-1)] - 1$, then

$$\frac{\dot{m}}{\dot{m}_d} = \left\{\frac{1-(p/p_1)^{2-\eta_p(\gamma-1)/\gamma}}{1-(p_d/p_1)^{2-\eta_p(\gamma-1)/\gamma}}\right\}^{1/2} \tag{4.43a}$$

With $\eta_p = 0.9$ and $\gamma = 1.3$, the pressure ratio index is about 1.8; thus, the approximation is often used:

$$\frac{\dot{m}}{\dot{m}_d} = \left\{ \frac{1-(p/p_1)^2}{1-(p_d/p_1)^2} \right\}^{1/2} \tag{4.43b}$$

which is the ellipse law of a multistage turbine.

PROBLEMS

1. Show, for an axial-flow turbine stage, that the *relative* stagnation enthalpy across the rotor row does not change. Draw an enthalpy−entropy diagram for the stage labeling all salient points. Stage reaction for a turbine is defined as the ratio of the static enthalpy drop in the rotor to that in the stage. Derive expressions for the reaction in terms of the flow angles and draw velocity triangles for reactions of 0.0, 0.5, and 1.0.

2. **a.** An axial-flow turbine operating with an overall stagnation pressure of 8−1 has a polytropic efficiency of 0.85. Determine the total-to-total efficiency of the turbine.
b. If the exhaust Mach number of the turbine is 0.3, determine the total-to-static efficiency.
c. If, in addition, the exhaust velocity of the turbine is 160 m/s, determine the inlet total temperature.
Assume for the gas that $C_p = 1.175$ kJ/(kg K) and $R = 0.287$ kJ/(kg K).

3. The mean blade radii of the rotor of a mixed flow turbine are 0.3 m at inlet and 0.1 m at outlet. The rotor rotates at 20,000 rev/min and the turbine is required to produce 430 kW. The flow velocity at nozzle exit is 700 m/s and the flow direction is at 70° to the meridional plane. Determine the absolute and relative flow angles and the absolute exit velocity if the gas flow is 1 kg/s and the velocity of the through-flow is constant through the rotor.

4. In a Parson's reaction turbine, the rotor blades are similar to the stator blades but with the angles measured in the opposite direction. The efflux angle relative to each row of blades is 70° from the axial direction, the exit velocity of steam from the stator blades is 160 m/s, the blade speed is 152.5 m/s, and the axial velocity is constant. Determine the specific work done by the steam per stage. A turbine of 80% internal efficiency consists of 10 such stages as just described and receives steam from the stop valve at 1.5 MPa and 300°C. Determine, with the aid of a Mollier chart, the condition of the steam at outlet from the last stage.

5. Values of pressure (kPa) measured at various stations of a zero reaction gas turbine stage, all at the mean blade height, are shown in the following table:

Stagnation Pressure	Static Pressure
Nozzle entry 414	Nozzle exit 207
Nozzle exit 400	Rotor exit 200

The mean blade speed is 291 m/s, inlet stagnation temperature 1100 K, and the flow angle at nozzle exit is 70° measured from the axial direction. Assuming the magnitude and direction

of the velocities at entry and exit of the stage are the same, determine the total-to-total efficiency of the stage. Assume a perfect gas with $C_p = 1.148$ kJ/(kg °C) and $\gamma = 1.333$.

6. In a certain axial-flow turbine stage, the axial velocity c_x is constant. The absolute velocities entering and leaving the stage are in the axial direction. If the flow coefficient c_x/U is 0.6 and the gas leaves the stator blades at 68.2° from the axial direction, calculate

a. the stage loading factor, $\Delta W/U^2$;
b. the flow angles relative to the rotor blades;
c. the degree of reaction;
d. the total-to-total and total-to-static efficiencies.
The Soderberg loss correlation, Eq. (3.46), should be used.

7. **a.** Sketch the velocity triangles for a repeating stage turbine with 50% reaction. Show that the ratio of the exit velocity from the stator c_2 to the rotor blade speed U is given by

$$\frac{c_2}{U} = \sqrt{\varphi^2 + \left(\frac{\psi+1}{2}\right)^2}$$

where ϕ is the flow coefficient and ψ is the stage loading.

b. The total-to-total efficiency for an axial turbine stage is given by the following relationship:

$$\eta_{tt} = 1 - \frac{0.04}{\psi}\left[\left(\frac{c_2}{U}\right)^2 + \left(\frac{w_3}{U}\right)^2\right]$$

where w_3 is the relative velocity at exit from the rotor. Using the result from part (a) shows that a repeating stage turbine with 50% reaction and a flow coefficient of 0.5 have maximum efficiency when the stage loading is equal to $\sqrt{2}$. For this design, determine the total-to-total efficiency and the total-to-static efficiency of the stage. Also calculate the flow angles at inlet and exit from the turbine stator.

c. The repeating stage design parameters in part (b) are used in a four-stage air turbine. The turbine is to have a mass flow rate of 25 kg/s and a power output of 3.5 MW. The rotational speed is 3000 rpm and the density of the air at the inlet is 1.65 kg/m^3. Determine the mean radius of the turbine, the flow velocity at inlet and the height of the stator blades in the first stage.

8. A steam turbine stage of high hub–tip ratio is to receive steam at a stagnation pressure and temperature of 1.5 MPa and 325°C, respectively. It is designed for a blade speed of 200 m/s and the following *blade* geometry was selected:

	Nozzles	Rotor
Inlet angle (°)	0	48
Outlet angle (°)	70.0	56.25
Space–chord ratio (s/l)	0.42	–
Blade length–axial chord ratio (H/b)	2.0	2.1
Maximum thickness–axial chord	0.2	0.2

The deviation angle of the flow from the rotor row is known to be 3° on the evidence of cascade tests at the design condition. In the absence of cascade data for the nozzle row, the designer estimated the deviation angle from the approximation $0.19\theta s/l$, where θ is the blade camber in degrees. Assuming the incidence onto the nozzles is 0, the incidence onto the rotor is 1.04°, and the axial velocity across the stage is constant, determine

a. the axial velocity;
b. the stage reaction and loading factor;
c. the approximate total-to-total stage efficiency on the basis of Soderberg's loss correlation, assuming Reynolds number effects can be ignored;
d. by means of a steam chart the stagnation temperature and pressure at stage exit.

9. **a.** A single-stage axial-flow turbine is to be designed for zero reaction without any absolute swirl at rotor exit. At the nozzle inlet, the stagnation pressure and temperature of the gas are 424 kPa and 1100 K, respectively. The static pressure at the mean radius between the nozzle row and rotor entry is 217 kPa and the nozzle exit flow angle is 70°. Sketch an appropriate Mollier diagram (or a $T-s$ diagram) for *this* stage allowing for the effects of losses and sketch the corresponding velocity diagram. Hence, using Soderberg's correlation to calculate blade row losses, determine for the mean radius

i. the nozzle exit velocity;
ii. the blade speed;
iii. the total-to-static efficiency.

b. Verify for this turbine stage that the total-to-total efficiency is given by

$$\frac{1}{\eta_{\mathrm{tt}}} = \frac{1}{\eta_{\mathrm{ts}}} - \left(\frac{\phi}{2}\right)^2$$

where $\phi = c_x/U$. Hence, determine the value of the total-to-total efficiency. Assume for the gas that $C_p = 1.15$ kJ/(kg K) and $\gamma = 1.333$.

10. **a.** Prove that the centrifugal stress at the root of an untapered blade attached to the drum of an axial-flow turbomachine is given by

$$\sigma_{\mathrm{c}} = \pi \rho_{\mathrm{m}} N^2 A_x / 1800,$$

where ρ_{m} = density of blade material, N = rotational speed of drum, in rpm, and A_x = area of the flow annulus.

b. The preliminary design of an axial-flow gas turbine stage with stagnation conditions at stage entry of $p_{01} = 400$ kPa, $T_{01} = 850$ K, is to be based upon the following data *applicable to the mean radius*:

i. flow angle at nozzle exit, $\alpha_2 = 63.8°$;
ii. reaction, $R = 0.5$;
iii. flow coefficient, $c_x/U_{\mathrm{m}} = 0.6$;
iv. static pressure at stage exit, $p_3 = 200$ kPa;
v. estimated total-to-static efficiency, $\eta_{\mathrm{ts}} = 0.85$.
vi. Assuming that the axial velocity is unchanged across the stage, determine the specific work done by the gas;

the blade speed;
the static temperature at stage exit.

c. The blade material has a density of 7850 kg/m^3 and the maximum allowable stress in the rotor blade is 120 MPa. Taking into account only the centrifugal stress, assuming untapered blades and constant axial velocity at all radii, determine for a mean flow rate of 15 kg/s

i. the rotor speed (rev/min);
ii. the mean diameter;
iii. the hub−tip radius ratio.

For the gas assume that $C_p = 1050$ J/(kg K) and $R = 287$ J/(kg K).

11. The design of a single-stage axial-flow turbine is to be based on constant axial velocity with axial discharge from the rotor blades directly to the atmosphere. The following design values have been specified:

Mass flow rate	16.0 kg/s
Initial stagnation temperature, T_{01}	1100 K
Initial stagnation pressure, p_{01}	230 k N/m^2
Density of blading material, ρ_m	7850 kg/m^3
Maximum allowable centrifugal stress at blade root	1.7×10^8 N/m^2
Nozzle profile loss coefficient, $Y_p = (p_{01} - p_{02})/(p_{02} - p_2)$	0.06
Taper factor for blade stressing, K	0.75

In addition, the following may be assumed:

Atmospheric pressure, p_3	102 kPa
Ratio of specific heats, γ	1.333
Specific heat at constant pressure, C_p	1150 J/(kg K)

In the design calculations, values of the parameters at the mean radius are as follows:

Stage loading coefficient, $\psi = \Delta W/U^2$	1.2
Flow coefficient, $\phi = c_x/U$	0.35
Isentropic velocity ratio, U/c_0	0.61

where $c_0 = \sqrt{2(h_{01} - h_{3ss})}$. Determine

i. the velocity triangles at the mean radius;
ii. the required annulus area (based on the density at the mean radius);
iii. the maximum allowable rotational speed;
iv. the blade tip speed and the hub−tip radius ratio.

12. Draw the velocity triangles for a repeating stage of an axial turbine that has a blade speed of 200 m/s, a constant axial velocity of 100 m/s, a stator exit angle of 65°, and no interstage

swirl. Assuming that the working fluid is air, calculate the stage loading coefficient and the degree of reaction of the machine.

13. Determine the total-to-total efficiency of a low speed axial turbine stage that at the design condition has a stator exit flow angle of 70°, zero swirl at inlet and exit, constant axial velocity, and 50% reaction. Assume that the kinetic energy loss coefficient of both the stator blades and the rotor blades is 0.09.

References

Ainley,D. G., & Mathieson, G. C. R. (1951). A method of performance estimation for axial flow turbines. *ARC Reports and Memoranda*, *2974*.

Balje, O. E. (1981). *Turbomachines: A guide to design, selection and theory* New York: Wiley.

Bindon, J. P. (1989). The measurement and formation of tip clearance loss. *ASME Journal of Turbomachinery*, *111*, 257–263.

Craig, H. R. M., & Cox, H. J. A. (1971). Performance estimation of axial flow turbines. *Proceedings of the Institution of Mechanical Engineers*, *185*, 407–424.

Den Hartog, J. P. (1952). *Advanced strength of materials* New York: McGraw-Hill.

Denton, J. D. (1993). Loss mechanisms in turbomachines. 1993 IGTI scholar lecture. *Journal of Turbomachinery*, *115*, 621–656.

Egli, A. (1936). The flow characteristics of variable-speed reaction steam turbines. *Transactions of the American Society of Mechanical Engineers*, *58*.

Emmert, H. D. (1950). Current design practices for gas turbine power elements. *Transactions of the American Society of Mechanical Engineers*, *72* (Part 2).

Freeman, J. A. W. (1955). High temperature materials. *Gas turbines and free piston engines*, Lecture 5, University of Michigan, Summer Session.

Havakechian, S., & Greim, R. (1999). Aerodynamic design of 50 per cent reaction steam turbines. *Proceedings of the Institution of Mechanical Engineers, Part C*, *213*.

Hesketh, J. A., & Walker, P. J. (2005). Effects of wetness in steam turbines. *Proceedings of the Institution of Mechanical Engineers, Part C*, *219*.

Horlock, J. H. (1958). A rapid method for calculating the "off-design" performance of compressors and turbines. *Aeronautics Quarterly*, *9*.

Horlock, J. H. (1966). *Axial flow turbines* London: Butterworth, (1973 reprint with corrections, Huntington, New York: Krieger).

Japikse, D. (1986). Life evaluation of high temperature turbomachinery. In D. Japikse (Ed.), Advanced topics in turbomachine technology. *Principal Lecture Series, No. 2* (pp. 51–547). White River Junction, VT: Concepts ETI.

Kacker, S. C., & Okapuu, U. (1982). A mean line prediction method for axial flow turbine efficiency. *Journal of Engineering Power. Transactions of the American Society of Mechanical Engineers*, *104*, 111–119.

Lewis, R. I. (1996). *Turbomachinery performance analysis.* London: Arnold.

Mallinson, D. H., & Lewis, W. G. E. (1948). The part-load performance of various gas-turbine engine schemes. *Proceedings of the Institution of Mechanical Engineers*, *159*.

McCloskey, T. H. (2003). Steam turbines. In E. Logan, & R. Roy (Eds.), *Handbook of turbomachinery* (2nd ed.). New York: Marcel Dekker, Inc..

National Advisory Committee for Aeronautics (1953). *Equations, tables and charts for compressible flow*. *NACA Report 1135* CA, USA: Ames Aero Lab.

Rolls-Royce (2005). *The jet engine* (5th ed.). Stamford, UK: Key Publishing.

Shapiro, A. H., Soderberg, C. R., Stenning, A. H., Taylor, E. S., & Horlock, J. H. (1957). *Notes on turbomachinery*. Department of Mechanical Engineering, Massachusetts Institute of Technology (Unpublished).

Smith, G. E. (1986). Vibratory stress problems in turbomachinery. In D. Japikse (Ed.), Advanced topics in turbomachine technology, *Principal Lecture Series No. 2* (pp. 8.1–8.23). White River Junction, VT: Concepts ETI.

Smith, S. F. (1965). A simple correlation of turbine efficiency. *Journal of the Royal Aeronautical Society*, *69*, 467–470.

Soderberg C. R. (1949). Unpublished note. Gas Turbine Laboratory, Massachusetts Institute of Technology.

Stodola, A. (1945). *Steam and gas turbines* (6th ed.). New York: Peter Smith.

Timoshenko, S. (1956). *Strength of materials.* New York: Van Nostrand.

Walker, P. J., & Hesketh, J. A. (1999). Design of low-reaction steam turbine blades. *Proceedings of the Institution of Mechanical Engineers, Part C*, *213*.

Wilde, G. L. (1977). The design and performance of high temperature turbines in turbofan engines. *Tokyo joint gas turbine congress*, co-sponsored by Gas Turbine Society of Japan, the Japan Society of Mechanical Engineers, and the American Society of Mechanical Engineers, pp. 194–205.

Wilson, D. G. (1987). New guidelines for the preliminary design and performance prediction of axial-flow turbines. *Proceedings of the Institution of Mechanical Engineers*, *201*, 279–290.

CHAPTER

Axial-Flow Compressors and Ducted Fans

5

A solemn, strange and mingled air, 't was sad by fits, by starts was wild.
W. Collins, *The Passions*

5.1 Introduction

The idea of using a form of *reversed turbine* as an axial compressor is as old as the reaction turbine itself. It is recorded by Stoney (1937) that Sir Charles Parsons obtained a patent for such an arrangement as early as 1884. However, simply reversing a turbine for use as a compressor gives efficiencies that are, according to Howell (1945), less than 40% for machines of high pressure ratio. Parsons actually built a number of these machines (ca. 1900), with blading based upon improved propeller sections. The machines were used for blast furnace work, operating with delivery pressures between 10 and 100 kPa above atmospheric pressure. The efficiency attained by these early, low-pressure compressors was about 55%; the reason for this low efficiency is now attributed to blade stall. A high pressure ratio compressor (550 kPa delivery pressure) was also built by Parsons but is reported by Stoney to have "run into difficulties." The design, comprising two axial compressors in series, was abandoned after many trials, the flow having proved to be unstable (presumably due to *compressor surge*). As a result of low efficiency, axial compressors were generally abandoned in favor of multistage centrifugal compressors with their higher efficiency of 70−80%.

It was not until 1926 that any further development on axial compressors was undertaken, when Griffith outlined the basic principles of his aerofoil theory of compressor and turbine design. The subsequent history of the axial compressor is closely linked with that of the aircraft gas turbine and has been recorded by Cox (1946) and Constant (1950). The work of the team under Griffith at the Royal Aircraft Establishment, Farnborough, led to the conclusion (confirmed later by rig tests) that efficiencies of at least 90% could be achieved for "small" stages, i.e., low-pressure ratio stages.

The early difficulties associated with the development of axial-flow compressors stemmed mainly from the fundamentally different nature of the flow process compared with that in axial-flow turbines. In the axial turbine, the flow relative to each blade row is *accelerated*, whereas in axial compressors, it is *decelerated*. It is now widely known that although a fluid can be rapidly accelerated through a passage and sustain a small or moderate loss in total pressure the same is not true for a rapid deceleration. In the latter case, large losses would arise as a result of severe stall caused by a large adverse pressure gradient. So as to limit the total pressure losses during flow

Fluid Mechanics and Thermodynamics of Turbomachinery. DOI: http://dx.doi.org/10.1016/B978-0-12-415954-9.00005-X

diffusion it is necessary for the rate of deceleration (and turning) in the blade passages to be severely restricted. (Details of these restrictions are outlined in Chapter 3 in connection with the correlations of Lieblein and Howell.) It is mainly because of these restrictions that axial compressors need to have many stages for a given pressure ratio compared with an axial turbine, which needs only a few. Thus, the reversed turbine experiment tried by Parsons was doomed to a low operating efficiency.

The performance of axial compressors depends on their usage category. Carchedi and Wood (1982) described the design and development of a single-shaft 15-stage axial-flow compressor that provided a 12:1 pressure ratio at a mass flow of 27.3 kg/s for a 6 MW industrial gas turbine. The design was based on subsonic flow and the compressor was fitted with variable stagger stator blades to control the position of the low-speed surge line. In the field of aircraft gas turbines, however, the engine designer is more concerned with *maximizing* the work done per stage while retaining an acceptable level of overall efficiency. Increased stage loading almost inevitably leads to some aerodynamic constraint. This constraint is more severe at increased Mach number, when shock-induced boundary layer separation or increased losses can arise from poor diffusion of the flow. Wennerstrom (1990) outlined the history of highly loaded axial-flow compressors with special emphasis on the importance of reducing the number of stages and the ways that improved performance can be achieved. Since about 1970, a significant and special change occurred with respect to one design feature of the axial compressor and that was the introduction of low aspect ratio blading. It was not at all obvious why blading of large chord would produce any performance advantage, especially as the trend was to try to make engines more compact and lighter by using high aspect ratio blading. Wennerstrom (1989) reviewed the increased usage of low aspect ratio blading in aircraft axial-flow compressors and reported on the high loading capability, high efficiency, and good range obtained with this type of blading. One early application was an axial-flow compressor that achieved a pressure ratio of 12.1 in only five stages, with an isentropic efficiency of 81.9% and an 11% stall margin. The blade tip speed was 457 m/s and the flow rate per unit frontal area was 192.5 kg/s/m^2. It was reported that the mean aspect ratio ranged from a "high" of 1.2 in the first stage to less than 1.0 in the last three stages. A related later development pursued by the US Air Force was an alternative inlet stage with a rotor mean aspect ratio of 1.32 that produced, at design, a pressure ratio of 1.912 with an isentropic efficiency of 85.4% and an 11% stall margin. A maximum efficiency of 90.9% was obtained at a pressure ratio of 1.804 and lower rotational speed.

The flow within an axial-flow compressor is exceedingly complex, which is one reason why research and development on compressors has proliferated over the years. In the following sections, a simplified approach is taken so that students can grasp the essentials.

5.2 Mean-line analysis of the compressor stage

Most of the analysis in this chapter is simplified (as it was for axial turbines) by considering the variation in the flow along a mean radius through the machine. Significant spanwise variations are neglected and the parameters determined using this type of analysis are those representative of average conditions. This approach is appropriate for initial design and performance calculations of a compressor, and it is more accurate if the blade height is small compared with the mean radius.

In addition, as for axial turbines, the flow is assumed to be invariant in the circumferential direction, with negligible spanwise (radial) velocities. The 3D flow effects that occur within axial turbomachines are considered in Chapter 6.

To illustrate the layout of an axial compressor, Figure 5.1 shows a sectional drawing of the core compression system of the Rolls-Royce Trent family of gas turbine engines. This consists of an eight-stage intermediate pressure compressor and a six-stage high-pressure compressor. A *compressor stage* is defined as a rotor blade row followed by a stator blade row. The rotor blades are fixed to the rotor drum and the stator blades are fixed to the outer casing. The blades upstream of the first rotor row are inlet guide vanes. These are not considered to be a part of the first stage and are treated separately. Their function is quite different from the other blade rows since, by directing the flow away from the axial direction, they act to *accelerate* the flow rather than diffuse it. Note that the first three sets of stator vanes in the intermediate pressure compressor have variable settings. This enables the inlet angles to the rotor blades to be modified giving greater operating range at low rotational speeds (see Section 5.9).

5.3 Velocity diagrams of the compressor stage

The velocity diagrams for the stage are given in Figure 5.2, and the convention is adopted throughout this chapter of accepting all angles and swirl velocities in this figure as positive. As for axial turbine stages, a *normal* compressor stage is one where the absolute velocities and flow directions

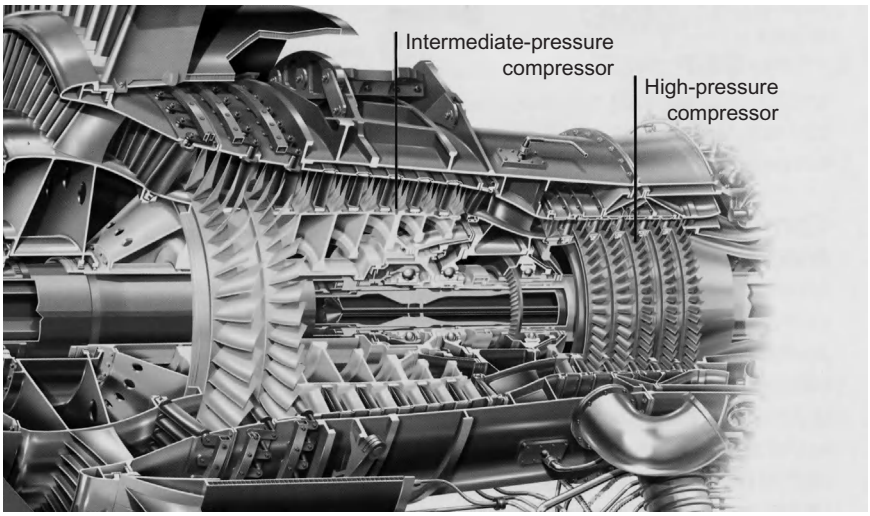

FIGURE 5.1

Section of the compression system of a gas turbine engine.

(*Courtesy of Rolls-Royce plc*)

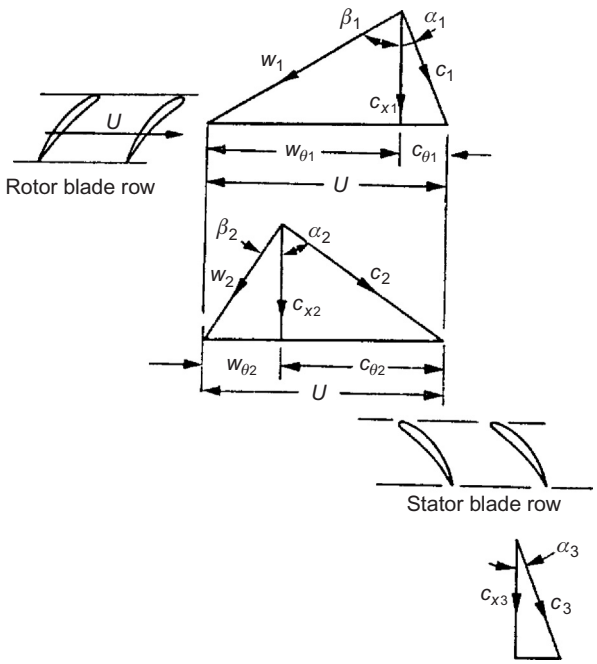

FIGURE 5.2

Velocity diagrams for a compressor stage.

at stage outlet are the same as at stage inlet. The flow from a previous stage (or from the guide vanes) has a velocity c_1 and direction α_1; subtracting vectorially the blades speed U gives the inlet relative velocity w_1 at angle β_1 (the axial direction is the datum for all angles). Relative to the blades of the rotor, the flow is turned to the direction β_2 at outlet with a relative velocity w_2. By vectorially adding the blade speed U onto w_2 gives the absolute velocity from the rotor, c_2 at angle α_2. The stator blades deflect the flow toward the axis, and the exit velocity is c_3 at angle α_3. For the normal repeating stage in a multistage compressor, $c_3 = c_1$ and $\alpha_3 = \alpha_1$. In Figure 5.2, it is noted that both the relative velocity in the rotor and the absolute velocity in the stator decrease. As shown later in this chapter, this diffusion of kinetic energy in the rotor and stator rows significantly influences the stage efficiency.

5.4 Thermodynamics of the compressor stage

The specific work done by the rotor on the fluid, from the steady flow energy equation (assuming adiabatic flow) and momentum equation is

$$\Delta W = \dot{W}_p/\dot{m} = h_{02} - h_{01} = U(c_{\theta 2} - c_{\theta 1}) \tag{5.1}$$

In Chapter 1, it was shown that the Euler work equation can be written as $h_{0,\mathrm{rel}} - U^2 = \text{constant}$. For axial machines where there is no radial shift of the streamlines across the rotor (i.e., $U_1 = U_2$), then $h_{0,\mathrm{rel}} = h + (1/2)w^2$ is constant in the rotor. Thus,

$$h_1 + \frac{1}{2}w_1^2 = h_2 + \frac{1}{2}w_2^2 \tag{5.2}$$

Across the stator, h_0 is constant, and

$$h_2 + \frac{1}{2}c_2^2 = h_3 + \frac{1}{2}c_3^2 \tag{5.3}$$

The compression process for the complete stage is represented on a Mollier diagram in Figure 5.3, which is generalized to include the effects of irreversibility.

5.5 Stage loss relationships and efficiency

From Eqs (5.1) and (5.3) the actual work performed by the rotor on unit mass of fluid is $\Delta W = h_{03} - h_{01}$. Referring to Figure 5.3, the reversible or *minimum* work required to attain the same final stagnation pressure as the real process is

$$\Delta W_{\min} = h_{03\mathrm{ss}} - h_{01} = (h_{03} - h_{01}) - (h_{03} - h_{03\mathrm{ss}})$$

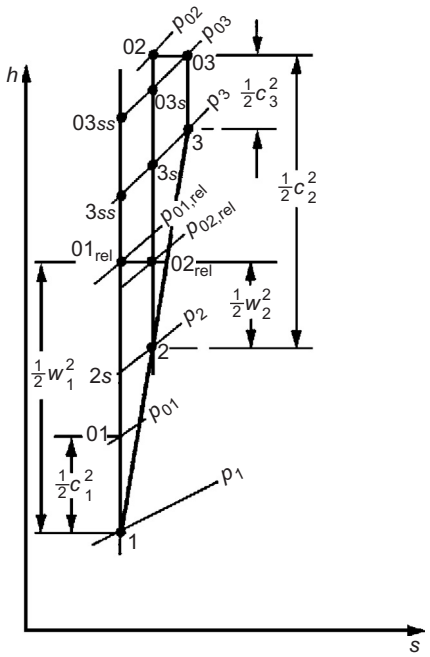

FIGURE 5.3

Mollier diagram for an axial compressor stage.

Applying the equation for the second law of thermodynamics, $T\mathrm{d}s = \mathrm{d}h - \mathrm{d}p/\rho$, along the curve of constant pressure, $p = p_{03}$, the approximation that $\Delta h = T\Delta s$ can be used such that

$$\Delta W_{\min} \cong \Delta W - T_{03}\Delta s_{\text{stage}}$$

where Δs_{stage} is the total entropy change through the stage such that $\Delta s_{\text{stage}} = \Delta s_{\text{rotor}} + \Delta s_{\text{stator}}$. The total-to-total efficiency of the compressor stage can, therefore, be written as

$$\eta_{\text{tt}} = \frac{\Delta W_{\min}}{\Delta W} \cong 1 - \frac{T_{03}\Delta s_{\text{stage}}}{h_{03} - h_{01}} \tag{5.4}$$

Note also that the total-to-static efficiency, as defined in Chapter 1, is given by

$$\eta_{\text{ts}} = \frac{h_{3\text{ss}} - h_{01}}{h_{03} - h_{01}} \cong \frac{h_{03} - h_{01} - (h_{03} - h_{3\text{ss}})}{h_{03} - h_{01}} \cong 1 - \frac{0.5c_3^2 + T_3\Delta s_{\text{stage}}}{h_{03} - h_{01}} \tag{5.5}$$

Therefore, to determine the efficiency of the stage, we need to determine the entropy changes through the rotor and stator. This can be done by using the loss coefficients, $Y_{\text{p,rotor}}$ and $Y_{\text{p,stator}}$, which are defined as

$$Y_{\text{p,rotor}} = \frac{p_{01,\text{rel}} - p_{02,\text{rel}}}{p_{01,\text{rel}} - p_1}$$

and

$$Y_{\text{p,stator}} = \frac{p_{02} - p_{03}}{p_{02} - p_2} \tag{5.6}$$

Consider the process of a perfect gas passing through the rotor at constant relative stagnation enthalpy, $h_{01,\text{rel}}$ (i.e., $U_1 = U_2$). The second law of thermodynamics, $T\,\mathrm{d}s = \mathrm{d}h - \mathrm{d}p/\rho$, can be written for this process as

$$T_{01,\text{rel}}\Delta s_{\text{rotor}} \cong \frac{\Delta p_{0,\text{rotor}}}{\rho_{01,\text{rel}}}$$

where

$$\Delta p_{0,\text{rotor}} = p_{01,\text{rel}} - p_{02,\text{rel}} \tag{5.7}$$

Using the equation of state, $p = \rho RT$, this can be written as

$$\Delta s_{\text{rotor}} \cong \frac{R\Delta p_{0,\text{rotor}}}{p_{01,\text{rel}}} = RY_{\text{p,rotor}}(1 - p_1/p_{01,\text{rel}}) \tag{5.8}$$

Note that the negative sign in the $T\,\mathrm{d}s$ equation disappears since the relative stagnation pressure is decreasing through the rotor, giving an increase in entropy. Also note that a key advantage of using entropy here is that it is independent of the frame of reference in which it is evaluated. The entropy change through the stator is found similarly to that for the rotor, and the total entropy change through the stage is simply the sum of the two. In terms of the loss coefficients,

$$\Delta s_{\text{stage}} = \Delta s_{\text{rotor}} + \Delta s_{\text{stator}} \cong R[Y_{\text{p,rotor}}(1 - p_1/p_{01,\text{rel}}) + Y_{\text{p,stator}}(1 - p_2/p_{02})] \tag{5.9}$$

Hence, the total-to-total efficiency can be written as

$$\eta_{tt} \cong 1 - \frac{(\gamma - 1)}{\gamma} \frac{[Y_{p,rotor}(1 - p_1/p_{01,rel}) + Y_{p,stator}(1 - p_2/p_{02})]}{1 - T_{01}/T_{03}} \tag{5.10}$$

For a low-speed machine, where the flow is incompressible as well as the density being constant, it can be assumed that temperature changes throughout the stage are negligible. Applying the second law equation, $T\,ds = dh - dp/\rho$, for the flow through the rotor and the stator then gives

$$T\Delta s_{rotor} \cong \frac{\Delta p_{0,rotor}}{\rho} = \frac{1}{2} w_1^2 Y_{p,rotor}$$

and

$$T\Delta s_{stator} \cong \frac{\Delta p_{0,stator}}{\rho} = \frac{1}{2} c_2^2 Y_{p,stator} \tag{5.11}$$

Thus, by combining Eqs (5.4) and (5.11), the efficiency can be expressed for a low-speed machine as

$$\eta_{tt} \cong 1 - \frac{T\Delta s_{stage}}{h_{03} - h_{01}} = 1 - \frac{\Delta p_{0,rotor} + \Delta p_{0,stator}}{\rho(h_{03} - h_{01})} \tag{5.12a}$$

or as

$$\eta_{tt} \cong 1 - \frac{0.5(w_1^2 Y_{p,rotor} + c_2^2 Y_{p,stator})}{h_{03} - h_{01}} \tag{5.12b}$$

Compressor loss sources

In a compressor stage, there are numerous loss sources that cause entropy creation. It is the sum of all the entropy creation in a blade row that determines the loss coefficients, $Y_{p,rotor}$ and $Y_{p,stator}$, which are used in mean-line analysis to determine the efficiency in Eqs (5.10) and (5.12b). The discussion of the various loss sources for turbines given in Section 4.6 is, in general, also applicable to compressors. There are, however, some key differences that are covered later.

The loss sources can be categorized as 2D and 3D. The possible 2D loss sources are the same as for turbines: (i) the *blade boundary layers*, (ii) *trailing edge mixing*, (iii) *flow separation*, and (iv) *shock waves*. The total 2D loss for a compressor can be determined through cascade tests or 2D computational methods (see Chapter 3), but there are no general correlations that can be applied to all cases. All compressor blades will suffer from boundary layer and trailing edge mixing loss, and Section 3.5 shows how these losses are strongly dependent on the blade surface pressure distribution. Well-designed compressor blades should not suffer from flow separation losses at their design operating conditions. However, at off-design conditions, when the diffusion levels on the blade surfaces become too high, the flow can separate leading to excessive loss and possible stall or surge (see Section 5.11). Shock wave losses are only present in compressor stages with supersonic inlet flow and these are discussed further in Section 5.10.

The main 3D loss sources in a compressor are (i) *end wall loss,* and (ii) *tip leakage loss*. However, in practice, it is difficult to isolate these loss sources as they interact strongly and the total 3D loss is often simply described as loss due to *secondary flow*.

Annulus boundary layers rapidly build up on the hub and casing of a compressor. As shown later in Section 5.9, these boundary layers are thicker than in a turbine due to the adverse pressure gradients they are exposed to. They are swept across the blade passage by the pressure difference between the pressure and the suction surfaces, leading to a complex and extensive 3D flow field. These end wall flows cause loss through viscous shear and through mixing with the mainstream flow in the blade passages. In addition, they interact with the boundary layers on the blade surfaces, potentially causing further loss. There have been several attempts to model and predict the loss caused by compressor end wall flow, see Koch and Smith (1976) for a more successful example. However, because the end wall boundary layers are large and the flow field is particular to each compressor stage, test results or advanced 3D computational methods are nowadays used to determine end wall loss.

The flow through the clearance gap above the tips of compressor rotor blades interacts with the end wall flow and the flow in the passage creating further loss through mixing and shear. The leakage flow also causes blockage, reducing the overall flow capacity of the compressor stage and, more seriously, reduces the stable operating range, see Freeman (1985). The aim is always to minimize the clearance gap to improve the stability margin and to reduce the losses, but the minimum clearance is usually determined by manufacturing and mechanical considerations.

Leakage flows are not only found in the rotor tip gaps. Stator blades are often cantilevered from the compressor casing to minimize weight. This leads to a clearance gap at the stator hub. The leakage flow that arises can help relieve high diffusion at the stator hub, but it also adds to blockage and loss. In addition, leakage flows arise from any gaps or seals that are present in the real geometry of a compressor.

The 3D flows described earlier will typically contribute 50% or more of the losses within a compressor (the other 50% coming from the 2D loss). They also lead to reduced flow capacity due to the additional blockage, reduced work input, and more limited operating range. They need to be accounted for in the preliminary design by using average loss coefficients for the whole flow field and by factoring the velocity triangle parameters appropriately such that they represent the average flow conditions.

Note that 3D effects and secondary flows are covered in detail in Chapter 6. Further details of compressor loss sources can be found in Koch and Smith (1976) and Denton (1993).

5.6 Mean-line calculation through a compressor rotor

Calculation of the flow through a row of rotor blades is similar to that through a stationary cascade, as described in Chapter 3. The minor complication is the use of relative rather than absolute properties.

Compressible case

Consider the transonic compressor rotor shown in Figure 5.4. The velocity triangle at inlet has been scaled so that it is a Mach number triangle, which is often a useful transformation for high-speed stages.

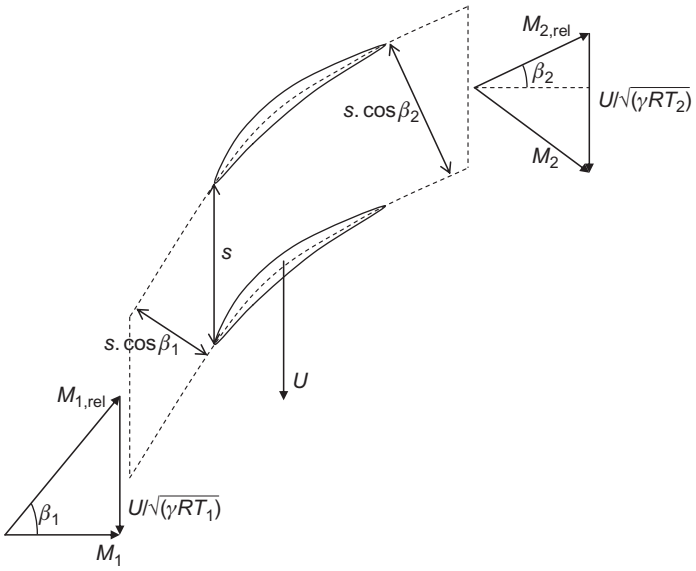

FIGURE 5.4

Mean-line flow through a high-speed compressor rotor.

If the conditions at inlet to the rotor are known, the nondimensional mass flow rate at inlet can be determined from compressible flow tables:

$$\frac{\dot{m}\sqrt{C_\mathrm{p}T_{01,\mathrm{rel}}}}{A_{1n}p_{01,\mathrm{rel}}} = \frac{\dot{m}\sqrt{C_\mathrm{p}T_{01,\mathrm{rel}}}}{Hs\cos\beta_1 p_{01,\mathrm{rel}}} = Q(M_{1,\mathrm{rel}})$$

where A_{1n} is the area normal to the flow at inlet, and the projected frontal area of the rotor (or annulus area) is Hs and taken to be constant through the rotor. To find the conditions at exit, the nondimensional mass flow rate at exit can be written in terms of the preceding, using the fact that through a rotor blade with constant mean radius, $T_{01,\mathrm{rel}} = T_{02,\mathrm{rel}}$:

$$Q(M_{2,\mathrm{rel}}) = \frac{\dot{m}\sqrt{C_\mathrm{p}T_{02,\mathrm{rel}}}}{Hs\cos\beta_2 p_{02,\mathrm{rel}}} = Q(M_{1,\mathrm{rel}}) \times \frac{p_{01,\mathrm{rel}}}{p_{02,\mathrm{rel}}} \times \frac{\cos\beta_1}{\cos\beta_2} \tag{5.13}$$

The ratio of relative total pressures can be determined from the rotor loss coefficient. Using the definition given in Eq. (5.6),

$$\frac{p_{02,\mathrm{rel}}}{p_{01,\mathrm{rel}}} = 1 - Y_{\mathrm{p,rotor}}(1 - p_1/p_{01,\mathrm{rel}}) \tag{5.14}$$

Once the exit relative Mach number and flow angle from the rotor blade are known, the other properties at exit from the rotor can be determined (via compressible flow relations and the velocity triangle) in order to fully specify the conditions at inlet to the stator. This is demonstrated in Example 5.1.

Incompressible case

In the low speed, incompressible case the equivalent calculations are more straightforward. The continuity equation reduces to

$$\rho Hs \cos \beta_1 w_1 = \rho Hs \cos \beta_2 w_2 \Rightarrow \frac{w_2}{w_1} = \frac{\cos \beta_1}{\cos \beta_2} \tag{5.15}$$

The loss in relative total pressure through the rotor can be related to the loss coefficient, since $p_{01,\text{rel}} = p_{02,\text{rel}} + (1/2)\rho w_1^2 Y_{\text{p,rotor}}$. The static pressure at rotor exit can, therefore, be found as follows:

$$p_2 = p_{02,\text{rel}} - \frac{1}{2}\rho w_2^2 = p_{01,\text{rel}} - \frac{1}{2}\rho(w_1^2 Y_{\text{p,rotor}} + w_2^2) \tag{5.16}$$

Once the exit static pressure is known all other quantities at rotor exit can be found since the density is fixed and the velocities are known.

EXAMPLE 5.1

A single-stage transonic compressor operates with axial flow at inlet. The inlet absolute stagnation temperature is 288 K and the inlet absolute stagnation pressure is 101 kPa. The relative flow angle at inlet to the rotor is 45° and the inlet relative Mach number is 0.9.

a. Calculate the rotor blade speed and the inlet relative stagnation pressure.
b. The mean radius and the mass flow rate per unit annulus area are constant through the rotor. If the rotor loss coefficient is 0.068 and the rotor exit relative Mach number is 0.5, find the rotor exit relative flow angle and determine the static pressure ratio across the rotor.
c. Show that the absolute stagnation temperature and pressure at entry to the stator are 322 K and 145 kPa, respectively. Determine the total-to-total isentropic efficiency of the compressor stage if the stagnation pressure loss coefficient for the stator is 0.04.

Solution

a. $T_{01} = 288$ K, $p_{01} = 101$ kPa. Given that the flow is axial at inlet, the absolute inlet Mach number can be calculated (using the Mach number triangles shown in Figure 5.4):

$$M_1 = M_{1,\text{rel}} \cos 45^\circ = 0.9/\sqrt{2} = 0.6364$$

The inlet static temperature can be calculated from the inlet Mach number and inlet stagnation temperature as follows:

$$T_1 = T_{01}(1 + (\gamma - 1)M_1^2/2)^{-1} = 266.4 \text{ K}$$

The blade speed can then be determined from the inlet Mach number triangle and the fact that the relative inflow angle is 45°:

$$U = M_1\sqrt{\gamma R T_1} = 0.634 \times \sqrt{1.4 \times 287.15 \times 266.4} = 208.3 \text{ m/s}$$

The blade relative stagnation pressure can be found from compressible flow tables:

$$p_{01,\text{rel}} = \frac{p_{01} \times p_1/p_{01}}{p_1/p_{01,\text{rel}}} = \frac{101 \times 0.7614}{0.5913} = 130 \text{ kPa}$$

Note that $p_1 = 101 \times 0.7614 = 76.9$ kPa.

b. To relate the conditions across the rotor, first calculate the ratio of relative stagnation pressures:

$$Y_\text{p} = \frac{1 - p_{02,\text{rel}}/p_{01,\text{rel}}}{1 - p_1/p_{01,\text{rel}}}, \text{which implies that } \frac{p_{02,\text{rel}}}{p_{01,\text{rel}}} = 1 - Y_p(1 - p_1/p_{01,\text{rel}})$$

Therefore,

$$\frac{p_{02,\text{rel}}}{p_{01,\text{rel}}} = 1 - 0.068 \times (1 - 0.5913) = 0.9722$$

Applying continuity across the rotor,

$$\frac{\dot{m}\sqrt{C_\text{p}T_{01,\text{rel}}}}{A_x \cos\beta_1 p_{01,\text{rel}}} = Q(M_{1,\text{rel}}) = \frac{\dot{m}\sqrt{C_\text{p}T_{02,\text{rel}}}}{A_x \cos\beta_2 p_{02,\text{rel}}} \times \frac{\cos\beta_2}{\cos\beta_1} \times \frac{p_{02,\text{rel}}}{p_{01,\text{rel}}}$$

Therefore,

$$\cos\beta_2 = \frac{Q(M_{1,\text{rel}})}{Q(M_{2,\text{rel}})} \times \cos\beta_1 \times \frac{p_{01,\text{rel}}}{p_{02,\text{rel}}}$$

This is true since $T_{02,\text{rel}} = T_{01,\text{rel}}$ (constant radius) and $\dot{m}/A_x$ is constant. Putting in the values from the question and using the compressible flow tables:

$$\cos\beta_2 = \frac{Q(0.9)}{Q(0.5)} \times \cos 45^\circ \times \frac{1}{0.9722} = \frac{1.2698}{0.9561} \times \frac{1}{\sqrt{2}} \times \frac{1}{0.9722} = 0.9659$$

which implies that $\beta_2 = 15^\circ$.

The static pressure ratio is then determined from the various ratios just derived:

$$\frac{p_2}{p_1} = \frac{p_2/p_{02,\text{rel}} \times p_{02,\text{rel}}/p_{01,\text{rel}}}{p_1/p_{01,\text{rel}}} = \frac{0.8430 \times 0.9722}{0.5913} = 1.386$$

Note that $p_2 = 0.8430 \times 0.9722 \times 130 = 106.6$ kPa.

c. To calculate the conditions at stator inlet, apply the exit Mach number triangle from the rotor (as shown in Figure 5.4) to convert the properties from the relative to absolute frame of reference. Using the compressible flow tables, the static temperature and relative velocity at rotor exit can be found:

$$T_2 = \frac{T_1 \times T_2/T_{02,\text{rel}}}{T_1/T_{01,\text{rel}}} = \frac{266.4 \times 0.9524}{0.8606} = 294.8 \text{ K (since } T_{02,\text{rel}} = T_{01,\text{rel}})$$

$$W_2 = M_{2,\text{rel}}\sqrt{\gamma R T_2} = 0.5 \times \sqrt{1.4 \times 287.15 \times 294.8} = 172.1 \text{ m/s}$$

The velocity triangle can be used to find the absolute flow Mach number, which is needed to determine the absolute stagnation quantities:

$$M_2 = \frac{c_2}{\sqrt{\gamma R T_2}} = \frac{\sqrt{(W_2 \cos 15^\circ)^2 + (U - W_2 \sin 15^\circ)^2}}{\sqrt{\gamma R T_2}} = 0.6778$$

It then follows that

$$T_{02} = T_2[1 + (\gamma - 1)M_2^2/2] = 321.9 \text{ K}$$

$$p_{02} = p_2(1 + (\gamma - 1)M_2^2/2)^{\gamma/(\gamma-1)} = 145 \text{ kPa}$$

The overall stage efficiency can now be calculated, using Eqs (5.4) and (5.8):

$$\eta_{tt} = \frac{T_{02s} - T_{01}}{T_{02} - T_{01}} = 1 - \frac{T_{02} - T_{02s}}{T_{02} - T_{01}} = 1 - \frac{T_{02}(\Delta s_{rotor} + \Delta s_{stator})/C_p}{T_{02} - T_{01}}$$

which implies that

$$\Delta s_{rotor} = R Y_p \left(1 - \frac{p_1}{p_{01,rel}}\right) = 287.15 \times 0.068 \times (1 - 76.9/130) = 7.98 \, J/\text{kg K}$$

and

$$\Delta s_{stator} = R Y_p \left(1 - \frac{p_2}{p_{02}}\right) = 287.15 \times 0.04 \times (1 - 106.6/145) = 3.04 \, J/\text{kg K}$$

Thus,

$$\eta_{tt} = 1 - \frac{321.9 \times (7.98 + 3.04)/1005}{321.9 - 288} = 0.896$$

This is a realistic efficiency value for a single-stage transonic compressor.

5.7 Preliminary compressor stage design

By fixing the stage loading ψ, the flow coefficient ϕ, and the reaction R, the velocity triangles at the design condition are specified. However, as well as fixing the velocity triangles such that the compressor will achieve the required pressure rise with high efficiency, it is critically important for a compressor that it operates with an adequate stability margin. As will be explained later in this chapter, if too much pressure rise is demanded of a compressor it can become unstable and enter an unacceptable operating regime (stall or surge). The choice of the velocity triangle parameters is therefore a compromise between the best performance at the design condition and the sufficient operating range.

Many axial compressors are multistage devices and, for simplicity, *repeating stages* are initially assumed in which the velocity triangles for all stages are similar, the mean radius is constant, and

the axial velocity through the machine is constant. In such machines, the flow coefficient, stage loading, and reaction are the same in every stage.

Note that this section only briefly covers the main preliminary design considerations and the associated mean-line analysis. If further details are needed, complete descriptions of the compressor design process can be found in Gallimore (1999) and Calvert and Ginder (1999).

Stage loading

The blades of a compressor behave like diffusers, each row of rotors and stators slowing down the local relative velocity (see Chapter 3). The amount of diffusion possible is limited, because if too much diffusion is demanded, the flow will separate from the blades leading to compressor stall or surge. DeHaller (1953) proposed that the relative velocity at exit from a blade row should be at least 72% of the inlet relative velocity for satisfactory performance. This is equivalent to limiting the pressure rise across each blade row and the maximum stage loading possible.

The stage loading ψ for a *normal*, or repeating, stage can be written as

$$\psi = \frac{h_{03} - h_{01}}{U^2} = \frac{\Delta c_\theta}{U} = \frac{c_{\theta 2} - c_{\theta 1}}{U} = \phi(\tan \alpha_2 - \tan \alpha_1) \tag{5.17a}$$

Referring to the velocity triangles in Figure 5.2, it is clear that $c_{\theta 1} = U - w_{y1}$ and $c_{\theta 2} = U - w_{\theta 2}$. Thus, this equation can be rewritten as

$$\psi = \phi(\tan \beta_1 - \tan \beta_2) \tag{5.17b}$$

or,

$$\psi = 1 - \phi(\tan \alpha_1 + \tan \beta_2) \tag{5.17c}$$

where $\phi = c_x/U$ is the flow coefficient.

The choice of stage loading at the compressor design point is critical. A value that is too low will lead to an excessive number of compressor stages to achieve a required pressure ratio. A value that is too high will limit the operating range of the compressor and increase the number of aerofoils needed to remove the risk of flow separation. As shown in Chapter 3, Lieblein's diffusion factor, DF, is a useful parameter for determining the blade pitch−chord ratio needed for acceptable performance. Based on Eq. (3.32), this can be written for a compressor rotor as

$$\mathrm{DF} = \left(1 - \frac{w_2}{w_1}\right) + \frac{\Delta c_\theta}{2w_1}\frac{s}{l} \tag{5.18}$$

A larger stage loading requires more flow turning Δc_θ and, therefore, to maintain an acceptable level of diffusion, the pitch−chord ratio of the blades must be reduced. This leads to a higher number of aerofoils, which tends to increase profile losses due to the higher wetted area and also leads to problems at high Mach numbers since the increased number of aerofoils will increase the likelihood of choking. For these reasons, pitch-to-chord ratios are typically in the range of 0.8−1.2 and the stage loading is limited to values around 0.4. However, more advanced compressor designs for aeroengines, where the need to reduce the number of stages is most pressing, may have higher stage loadings. A recent study by Dickens and Day (2011), looking at highly loaded axial compressors with stage loadings up to 0.75, shows that higher stage loading is possible but it

inevitably leads to greater blade losses and, in particular, significant extra loss is generated by the blade pressure surface boundary layers.

Flow coefficient

From Eq. (5.17b), $\psi = \phi\ (\tan\beta_1 - \tan\beta_2)$, which shows that for a fixed stage loading, as the flow coefficient increases, the flow turning required reduces. Hence, the diffusion through the blades is found to reduce as flow coefficient increases. Equally, for a fixed level of diffusion, the stage loading can increase as the flow coefficient rises. This suggests that a high flow coefficient is beneficial. In addition, higher values of flow coefficient correspond to higher inlet mass flow per unit area, which is a significant advantage as it implies a smaller diameter machine for a given mass flow.

However, in axial compressors, stage performance is often limited by Mach number effects and, for a fixed level of blade speed, high values of flow coefficient will lead to higher relative Mach number and potentially greater losses from choking and shock waves. Another disadvantage of a higher flow coefficient design concerns the tolerance of the compressor to nonuniform inflow. Compressors need to remain stable in the event of a disturbance in the inlet flow, and lower flow coefficient designs are found to absorb fluctuations more readily than high flow coefficient designs. The reasons for this are detailed in Smith (1958).

As a result of these considerations, typical values of ϕ used in designs are between 0.4 and 0.8 and often, for initial designs, 0.5 is chosen.

Reaction

The general definition of R for a compressor is the ratio of the rotor static enthalpy rise to the stage static enthalpy rise:

$$R = (h_2 - h_1)/(h_3 - h_1) \tag{5.19}$$

From Eq. (5.2), $h_2 - h_1 = (1/2)(w_1^2 - w_2^2)$. For normal stages ($c_1 = c_3$), $h_3 - h_1 = h_{03} - h_{01} = U(c_{\theta 2} - c_{\theta 1})$. Substituting into Eq. (5.19),

$$R = \frac{w_1^2 - w_2^2}{2U(c_{\theta 2} - c_{\theta 1})} = \frac{(w_{\theta 1} + w_{\theta 2})(w_{\theta 1} - w_{\theta 2})}{2U(c_{\theta 2} - c_{\theta 1})} \tag{5.20}$$

where it is assumed that c_x is constant across the stage. From Figure 5.2, $c_{\theta 2} = U - w_{\theta 2}$ and $c_{\theta 1} = U - w_{\theta 1}$ so that $c_{\theta 2} - c_{\theta 1} = w_{\theta 1} - w_{\theta 2}$. Thus,

$$R = (w_{\theta 1} + w_{\theta 2})/(2U) = \frac{1}{2}\phi(\tan\beta_1 + \tan\beta_2) \tag{5.21}$$

An alternative useful expression for the reaction can be found in terms of the fluid outlet angles from each blade row in a stage. With $w_{\theta 1} = U - c_{\theta 1}$, Eq. (5.21) gives

$$R = \frac{1}{2} + (\tan\beta_2 - \tan\alpha_1)\phi/2 \tag{5.22}$$

Eliminating β_2 between Eqs (5.22) and (5.17c) gives an equation in ψ, ϕ, and R and the interstage swirl angle, α_1

$$\psi = 2(1 - R - \phi \tan \alpha_1) \tag{5.23}$$

Equation (5.23) is identical to Eq. (4.14) derived for turbines, except for the sign convention. This equation shows that a higher reaction tends to reduce the stage loading, which is good for a compressor. However, stages having 50% reaction are widely used as the adverse (retarding) pressure gradient through the rotor rows and stator rows are equally shared. A 50% reaction also means that the rotor and stator blades will have similar shapes. Parametric design studies, as presented in Cumpsty (1989), suggest that the reaction is not such a critical parameter in determining compressor efficiency. However, Dickens and Day (2011) show that for stages with high stage loading, high reaction is required to achieve optimum efficiency. This appears to be necessary to reduce the pressure rise across the stator row which is more susceptible than the rotor to large separations. In many cases, though, the reaction is not a free design variable since it is determined by other factors. For example, in a design where the stage loading and flow coefficients have already been chosen, if the inlet swirl angle α_1 is fixed, by having either an axial inlet flow or an inlet guide vanes, then the reaction must also be fixed (as indicated by Eq. (5.23)).

If $R = 0.5$, then $\alpha_1 = \beta_2$ from Eq. (5.22), and the velocity diagram is symmetrical. The stage enthalpy rise is equally distributed between the rotor and the stator rows.

If $R > 0.5$, then $\beta_2 > \alpha_1$ and the velocity diagram is skewed to the *right* as shown in Figure 5.5(a). The static enthalpy rise in the rotor exceeds that in the stator (this is also true for the static pressure rise).

If $R < 0.5$, then $\beta_2 < \alpha_1$ and the velocity diagram is skewed to the *left* as shown in Figure 5.5(b). Clearly, the stator enthalpy (and pressure) rise exceeds that in the rotor.

In advanced compressor designs, particularly in jet engine compressors, high reaction is common and values between 0.5 and 0.8 are typical.

Interstage swirl

From Eq. (5.23), it can be seen that introducing positive swirl between the stages helps reduce stage loading. Positive swirl also reduces the relative inlet Mach number at inlet to the rotor. Therefore, advanced multistage compressors, particularly those within gas turbines, will often have an interstage swir1 angle of around 20−30°.

Blade aspect ratio

Once ψ, ϕ, and R are fixed at the design condition, the number of stages for a multistage compressor can be determined (see Example 5.3). Given a mass flow and blade speed, the mean radius of the compressor and the blade heights can also be calculated, using the calculations shown in Chapter 4. The overall compressor length and the number of blades can then be estimated by choosing suitable values of aspect ratio, *H/l*, for each blade row.

The choice of aspect ratio is important as this influences the blade losses and the stage stability margin. Lower aspect ratios will tend to have greater losses due to increased wetted area and the build up of boundary layers. However, as shown in Koch (1997), lower aspect ratios tend to give

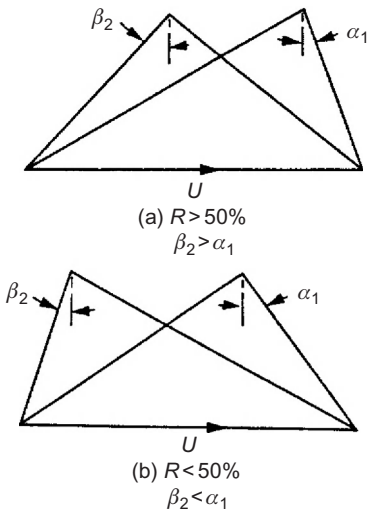

FIGURE 5.5

Asymmetry of velocity diagrams for reactions greater (a) greater than 50%, and (b) less than 50%.

higher surge margin. This is why modern multistage compressors have lower aspect ratio values than might be expected, and 1−2 is typical.

The choice of aspect ratio, combined with the blade height, fixes the blade chord, l. The pitch-to-chord ratio, s/l, is determined by Eq. (5.18) combined with a choice of an acceptable level of diffusion factor, DF. With the blade chord known this then sets the number of blades in each row. Example 5.2 shows how this is done in practice for a low-speed compressor stage.

The overall compressor length depends on the axial gaps between blade rows. These will be set to limit the vibration and noise generated by rotor−stator interaction and spaces between the rows of about half an axial chord are typical.

EXAMPLE 5.2

A low-speed single-stage rig is required to simulate a repeating stage of an air compressor with a flow coefficient of 0.5, a stage loading of 0.45 and 25° of preswirl at stage inlet. The motor that will drive the rig runs at 500 rpm. The aspect ratio of the rotor blade is to be 1.3 and its hub-to-tip radius ratio is 0.8.

a. If the Reynolds number needs to be 3×10^5, determine the mean radius for the rig, the rotor blade height and the motor power required. Use the following definition of Reynolds number based on midspan rotor chord:

$$Re = \frac{\rho c_x l}{\mu}, \text{where } \mu = 1.8 \times 10^{-5} \text{ kg/ms and } \rho = 1.2 \text{ kg/m}^3$$

b. Calculate the stage reaction, the rotor relative flow angles, and the stator inlet flow angle. If the Lieblein diffusion factor for the rotor at the design point cannot exceed 0.55 and for the stator cannot exceed 0.5, determine the number of rotor and stator blades required. Assume that the stator aspect ratio is 1.5.
c. Confirm that the rig is low speed by estimating the rotor tip relative Mach number.

Solution

a. Use the hub-to-tip ratio to relate the mean radius to the blade height:

$$\frac{r_h}{r_t} = \frac{r_m - H/2}{r_m + H/2} = 0.8 \quad \therefore 0.2r_m = 0.9H \quad \Rightarrow r_m = 4.5H$$

Expressing the *Re* in terms of *H*:

$$Re = \frac{\rho c_x l}{\mu} = \frac{\rho \phi r_m \Omega l}{\mu} = \frac{\rho \phi r_m \Omega H}{\mu(H/l)} = \frac{4.5\rho\phi\Omega H^2}{\mu(H/l)}$$

$$\therefore H = \sqrt{\frac{\mu(H/l)Re}{4.5\rho\phi\Omega}} = \sqrt{\frac{1.8\times10^{-5}\times1.3\times3\times10^5}{4.5\times1.2\times0.5\times100\times\pi/6}} = 0.223 \text{ m}$$

$$\Rightarrow r_m = 4.5H = 4.5\times0.223 = 1.003 \text{ m}$$

The motor power can be found from the stage loading and the rig mass flow:

$$\dot{W} = \dot{m}\Delta h_0 = \dot{m}\psi U^2$$

$$\therefore \dot{W} = (2\pi r_m H \rho c_x)\psi(r_m\Omega)^2 = (2\pi\rho r_m H \phi r_m \Omega)\psi(r_m\Omega)^2 = 2\pi\rho\phi\psi H r_m^4\Omega^3$$

$$\dot{W} = 2\pi\times1.2\times0.5\times0.45\times0.223\times1.003^4\times(100\pi/6)^3 = 54.96 \text{ kW}$$

This power requirement is reasonable for a large low-speed rig. The large blade size (0.223 m span) would enable high resolution measurements to be made at the correct *Re* number.

b. From Eq. (5.23):

$$\psi = 2(1 - R - \phi\tan\alpha_1) \Rightarrow R = 1 - \psi/2 - \phi\tan\alpha_1 = 1 - 0.45/2 - 0.5\tan25^\circ = 0.542$$

$$\tan\beta_1 = \frac{1}{\phi} - \tan\alpha_1 = \frac{1}{0.5} - \tan25^\circ \Rightarrow \beta_1 = 56.9^\circ$$

From Eq (5.17b):

$$\tan\beta_2 = \tan\beta_1 - \frac{\psi}{\phi} = 1.5337 - \frac{0.45}{0.5} \Rightarrow \beta_2 = 32.4^\circ$$

$$\tan\alpha_2 = \frac{1}{\phi} - \tan\beta_2 = \frac{1}{0.5} - \tan32.4^\circ \Rightarrow \alpha_2 = 53.8^\circ$$

For the rotor, the pitch-to-chord ratio is found from Eq. (3.36), which is the incompressible version of Eq. (5.18),

$$\mathrm{DF} = \left(1 - \frac{\cos\alpha_1}{\cos\alpha_2}\right) + \frac{s}{l}\frac{\cos\alpha_1}{2}(\tan\alpha_1 - \tan\alpha_2)$$

This must be applied to the relative angles of the rotor:

$$\frac{s}{l} = 2\left(\frac{\cos\beta_1}{\cos\beta_2} - 1 + \mathrm{DF}\right)/\cos\beta_1(\tan\beta_1 - \tan\beta_2)$$

$$\frac{s}{l} \le 2\left(\frac{\cos 56.9}{\cos 32.4} - 1 + 0.55\right)/\cos 56.9(\tan 56.9 - \tan 32.4) = 0.801$$

The inequality is used so that the DF used is a maximum. The number of rotor blades is then,

$$\mathrm{Z_{rotor}} = \frac{2\pi r_\mathrm{m}}{s} = \frac{2\pi(H/l)r_\mathrm{m}/H}{s/l} \Rightarrow \mathrm{Z_{rotor}} \ge \frac{2\pi \times 1.3 \times 4.5}{0.801} = 45.87 \quad \therefore \mathrm{Z_{rotor}} = 46$$

For the stator,

$$\frac{s}{l} = 2\left(\frac{\cos\alpha_2}{\cos\alpha_3} - 1 + \mathrm{DF}\right)/\cos\alpha_2(\tan\alpha_2 - \tan\alpha_3)$$

$$\frac{s}{l} \le 2\left(\frac{\cos 53.8}{\cos 25} - 1 + 0.5\right)/\cos 53.8(\tan 53.8 - \tan 25) = 0.571$$

The number of stator blades is then,

$$\mathrm{Z_{stator}} = \frac{2\pi r_\mathrm{m}}{s} = \frac{2\pi(H/l)r_\mathrm{m}/H}{s/l} \quad \Rightarrow \mathrm{Z_{stator}} \ge \frac{2\pi \times 1.5 \times 4.5}{0.571} = 74.3 \quad \therefore \mathrm{Z_{stator}} = 75$$

c. The rotor relative Mach number is given by

$$M_{1,\mathrm{rel}} = \frac{w_1}{\sqrt{\gamma RT_1}} = \frac{c_x/\cos\beta_1}{\sqrt{\gamma RT_1}} = \frac{\phi r\Omega}{\cos\beta_1\sqrt{\gamma RT_1}}$$

Assuming the flow angles are the same at the tip, this will simply scale with the radius. Hence, the tip relative Mach number is

$$M_{1\mathrm{t,rel}} = \frac{\phi r_\mathrm{m}\Omega}{\cos\beta_1\sqrt{\gamma RT_1}}\frac{r_\mathrm{t}}{r_\mathrm{m}} = \frac{0.5 \times 1.003 \times (100\pi/6)}{\cos 56.9\sqrt{1.4 \times 287 \times 288}}\frac{5}{4.5} = 0.16$$

This will be close to the highest Mach number in the rig, and therefore the flow can be treated as incompressible throughout.

5.8 Off-design performance

As mentioned previously, it is critical for a compressor stage to have adequate stable operating range. A characteristic map for a single-stage high-speed compressor is shown in Figure 2.4. The design operating point will typically be at 100% speed, at the condition where the design pressure ratio is achieved with sufficient margin to the instability (or surge) line. As the compressor moves off-design at fixed rotational speed, the nondimensional mass flow is either increased or decreased from the design value. If the mass flow is reduced, the incidence onto the blades increases and the stage moves toward instability. At increased mass flow the incidence decreases becoming negative, and the blade passages may become choked. The effects of incidence on compressor blade aerodynamics are covered in Section 3.5.

For a low-speed compressor, the operation is independent of rotational speed, and there is no risk of the flow choking. As shown in Chapter 2, the performance characteristic can be presented as a single curve relating stage loading ψ to flow coefficient ϕ. Horlock (1958) considered how the off-design performance of a low-speed repeating compressor stage is influenced by the choice of design parameters. He made a simplification, based on cascade data, that that the fluid outlet angles β_2 for the rotor and $\alpha_1 (= \alpha_3)$ for the stator do not change appreciably over a range of incidence. This assumption is expected to be valid, since the flow should broadly be aligned with the exit metal angles of the blade rows, but it neglects any variations in flow deviation.

The simplification can be written, for a given compressor stage, as

$$\tan \alpha_1 + \tan \beta_2 = t = \text{constant} \tag{5.24}$$

Inserting this expression into Eq. (5.17c) gives

$$\psi = 1 - \phi t \tag{5.25a}$$

An inspection of Eqs (5.24) and (5.25a) suggests that, provided t is positive, the stage stagnation enthalpy rise, ψ, increases as the flow coefficient, ϕ, is reduced, when running at constant rotational speed.

Writing $\psi = \psi_d$ and $\phi = \phi_d$ for conditions at the design point, then

$$\psi_d = 1 - \phi_d t \tag{5.25b}$$

Hence, the values of ψ_d and ϕ_d chosen for a particular stage design determines the value of t. It is instructive to learn how off-design test results obtained from a compressor stage compare with this simplified performance model. Test results for a low-speed compressor stage were obtained by Howell (1945) in the early days of axial-flow compressor design but they are still valid for our purpose. Figure 5.6 shows the variation of the stage loading coefficient ψ plotted against the flow coefficient ϕ. The design point for this stage is actually at about $\phi = 0.80$, which corresponds to the maximum efficiency condition. At this flow coefficient, the relative flow angles are $\beta_1 = 45.8^\circ$ and $\beta_2 = 12.2^\circ$. From these data we can derive a value for $t = \tan \alpha_1 + \tan \beta_2$. Now,

$$\tan \alpha_1 = 1/\phi - \tan \beta_1 = 1/0.8 - \tan 45.8^\circ = 0.2217$$

Hence,

$$t = \tan \alpha_1 + \tan \beta_1 = 0.2217 + 0.2166 = 0.4383$$

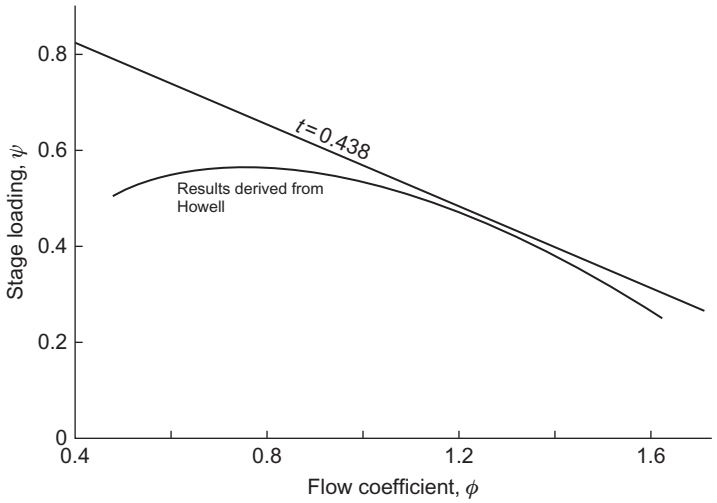

FIGURE 5.6

Compressor stage performance: comparison of simplified analysis with measured performance.

Substituting for t in Eq. (5.25b), the theoretical relationship is found:

$$\psi = 1 - 0.438\phi$$

which is plotted in Figure 5.6. The comparison of the measured results with the theoretical result clearly demonstrates that there is a fault in the assertion that the flow outlet angle from a blade row does not change.

Figure 5.7 shows velocity triangles for a compressor stage operating at the design point and at a reduced, off-design flow coefficient. In this, the effects of deviation have been included, and it can be seen that the rotor deviation *reduces* the tangential flow velocity at rotor exit, $c_{\theta 2}$, and the (upstream) stator deviation *increases* the rotor inlet tangential flow velocity, $c_{\theta 1}$. Hence, the stage loading, from Eq. (5.17a), $\psi = (c_{\theta 2} - c_{\theta 1})/U$, is expected to be significantly reduced by the effects of deviation, as is evident in Figure 5.6. The impact on performance is more pronounced at very low flow coefficients, where the high incidence can also lead to flow separations and increased 3D effects.

5.9 Multistage compressor performance

For preliminary design and analysis purposes, a multistage compressor is thought of as a series of single-stage compressors, each performing as it would in isolation. However, to understand the performance of a real machine, the behavior of the overall system must be considered in more detail. This is particularly important to understand the off-design operation.

Overall pressure ratio and efficiency

It is possible to apply some of the earlier analysis to the determination of the overall pressure ratio of a multistage compressor. A possible procedure requires the calculation of pressure and

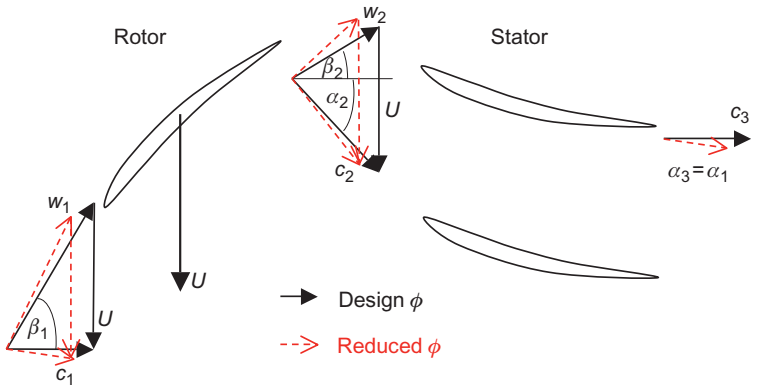

FIGURE 5.7

Velocity triangles showing a compressor stage operating off-design

temperature changes for a single stage, the stage exit conditions enabling the density at entry to the following stage to be found. This calculation can be repeated for each stage in turn until the required final conditions are satisfied. However, for a compressor made up of repeating stages, operating at its design point, it is possible to apply a simple compressible flow analysis for all the stages at once. This is described in Example 5.3.

EXAMPLE 5.3

A multistage axial compressor is required for compressing air at 293 K, through a pressure ratio of 5:1. Each stage is to be a 50% reaction and the mean blade speed of 275 m/s, flow coefficient 0.5, and stage loading factor 0.3 are taken, for simplicity, as constant for all stages. Determine the flow angles and the number of stages required if the polytropic efficiency is 88.8%. Take $C_p = 1.005$ kJ/(kg °C) and $\gamma = 1.4$ for air.

Solution

From Eq. (5.17b), the stage load factor can be written as

$$\psi = \phi(\tan \beta_1 - \tan \beta_2)$$

From Eq. (5.21), the reaction is

$$R = \frac{\phi}{2}(\tan \beta_1 + \tan \beta_2)$$

Solving for $\tan \beta_1$ and $\tan \beta_2$ gives

$$\tan \beta_1 = (R + \psi/2)/\phi$$

and

$$\tan \beta_2 = (R - \psi/2)/\phi$$

Calculating β_1 and β_2 and observing for $R = 0.5$ that the velocity diagram is symmetrical,

$$\beta_1 = \alpha_2 = 52.45^\circ$$

and

$$\beta_2 = \alpha_1 = 35^\circ$$

Writing the stage load factor as $\psi = C_p \Delta T_0 / U^2$, the stage stagnation temperature rise is

$$\Delta T_0 = \psi U^2 / C_p = 0.3 \times 275^2 / 1005 = 22.5^\circ\text{C}$$

It is reasonable here to take the stage efficiency as equal to the polytropic efficiency since the stage temperature rise of an axial compressor is small. Denoting compressor inlet and outlet conditions by subscripts 1 and e, respectively, from Eq. (1.50),

$$\frac{T_{0e}}{T_{01}} = 1 + \frac{n\Delta T_0}{T_{01}} = \left(\frac{p_{0e}}{p_{01}}\right)^{(\gamma-1)/\eta_p \gamma}$$

where n is the required number of stages. Thus,

$$n = \frac{T_{01}}{\Delta T_0}\left[\left(\frac{p_{0e}}{p_{01}}\right)^{(\gamma-1)/\eta_p \gamma} - 1\right] = \frac{293}{22.5}\left[5^{1/3.11} - 1\right] = 8.86$$

A suitable number of stages is therefore 9.

The overall efficiency is found from Eq. (1.53):

$$\eta_{tt} = \left[\left(\frac{p_{0e}}{p_{01}}\right)^{(\gamma-1)/\gamma} - 1\right] \Bigg/ \left[\left(\frac{p_{0e}}{p_{01}}\right)^{(\gamma-1)/\eta_p \gamma} - 1\right] = \left[5^{1/3.5} - 1\right] \Big/ \left[5^{1/3.11} - 1\right] = 86.3\%$$

Note that the total-to-total efficiency is significantly lower than the polytropic (or small stage) efficiency. This difference is to be expected, as shown in Chapter 1. It is more usual in compressor design and analysis to quote polytropic efficiencies, as these are independent of the pressure ratio of the multistage machine and therefore a fairer way to compare the losses.

Off-design operation and stage matching

The *operating line* of a multistage compressor describes the off-design variation of pressure ratio with nondimensional mass flow for a given exit configuration. For example, most compressors when tested will be connected to a downstream throttle, and it is the size of this throttle that determines the test operating line. The operating line that the compressor runs on when in normal use is the *working line* and this should pass through the design operating point on the compressor characteristic. It is possible to determine the working line of a compressor, provided the exit configuration is known.

Consider a multistage compressor connected to a downstream nozzle (or throttle), which is choked. In this case, the nondimensional mass flow through the nozzle will be fixed,

$$\frac{\dot{m}\sqrt{C_p T_{0e}}}{A_N p_{0e}} = Q(1) = \text{Constant}$$

where e denotes conditions at exit from the compressor and A_N is the choked nozzle area. The compressor inlet nondimensional mass flow can be expressed in terms of the exit nondimensional mass flow as follows,

$$\frac{\dot{m}\sqrt{C_p T_{01}}}{D^2 p_{01}} = \frac{\dot{m}\sqrt{C_p T_{0e}}}{A_N p_{0e}} \frac{A_N}{D^2} \frac{p_{0e}}{p_{01}} \sqrt{\frac{T_{01}}{T_{0e}}} \tag{5.26a}$$

Using the definition of polytropic efficiency to relate the stagnation temperature ratio to the stagnation pressure ratio, this can be simplified to

$$\frac{\dot{m}\sqrt{C_p T_{01}}}{D^2 p_{01}} = C\left(\frac{p_{0e}}{p_{01}}\right)^{1-(\gamma-1/2\gamma\eta_p)} \tag{5.26b}$$

which is the equation of the operating line on the compressor characteristic. The constant, C, depends on the exit nozzle area ratio, A_N/D^2, and it can be determined for the working line by the requirement for this to pass through the design point on the compressor characteristic. In Example 5.4, the working line for a 10-stage high-speed compressor is determined using Eq. (5.26b) and the results are plotted on Figure 5.8.

It is essential for multistage compressors to operate satisfactorily at part speed, for example during startup or at low-power settings. This situation is complicated in a multistage machine because different stages in the compressor operate at different conditions simultaneously. The front stages

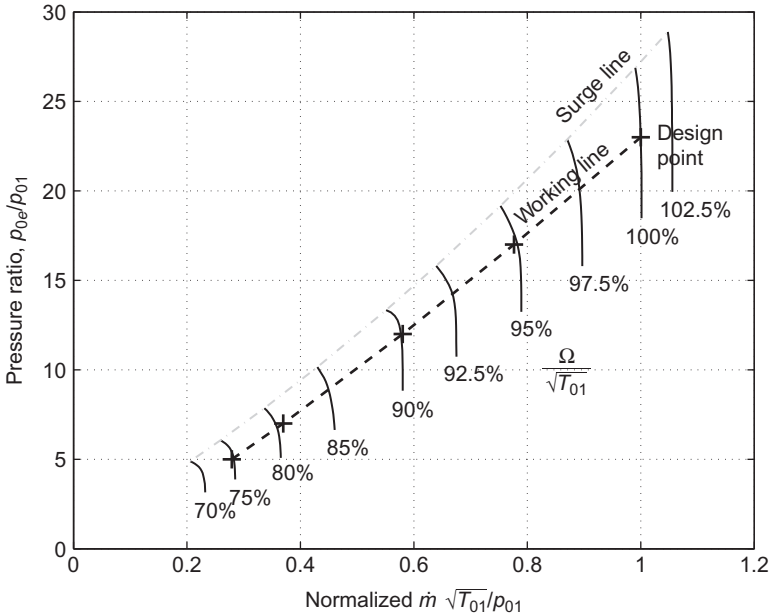

FIGURE 5.8

Characteristic of a high-speed 10-stage compressor showing the working line calculated in Example 5.4.

of the compressor will tend to operate toward stall at part speed because the mass flow rate is reduced and the incidence of the flow onto the rotor blades increased (as demonstrated in Example 5.4). Rear stages, on the other hand, tend to operate toward choke because the annulus area decrease that occurs through the compressor is specified for the design pressure ratio. At part speed, when the pressure ratio is low, the density in the rear stages is also low, leading to high axial velocity relative to the design condition and possible choking. This variation in operating point between the front and the rear stages is described as a stage matching problem. It can be relieved by bleeding off some air from the middle stages and by using variable stator blades to correct the incidence onto the rotor blades in the front stages (see Figure 5.1).

EXAMPLE 5.4

At the design operating point, the 10-stage air compressor represented in Figure 2.5, rotates at 100% speed and has a stagnation pressure ratio of 23. The compressor is operated with a fixed area downstream throttle that is always choked.

a. Using the data on the characteristic, determine the design polytropic efficiency. Assuming that this polytropic efficiency is constant (a fairly accurate simplification in this case), determine the working line of the compressor and plot this on the characteristic.
b. If the flow coefficient of the first compressor stage is 0.6 at the design point, calculate the flow coefficient for the first stage when operating on the working line at 80% speed. What would be the effect of this change in flow coefficient on the incidence onto the rotor blades?

Solution

a. At the design point the compressor isentropic efficiency is 81% (see Figure 2.5)

$$\frac{T_{0e}}{T_{01}} = 1 + \frac{1}{\eta_c}\left[\left(\frac{p_{0e}}{p_{01}}\right)^{(\gamma-1)/\gamma} - 1\right] = 1 + \frac{1}{0.81}\left[23^{0.4/1.4} - 1\right] = 2.789$$

From Eq. (1.50):

$$\eta_p = \frac{\gamma - 1}{\gamma}\frac{\ln(p_{0e}/p_{01})}{\ln(T_{0e}/T_{01})} = \frac{0.4}{1.4}\frac{\ln 23}{\ln 2.789} = 0.873$$

Applying Eq. (5.26b) to the design point (taking the nondimensional mass flow here as 1),

$$\frac{\dot{m}\sqrt{C_p T_{01}}}{D^2 p_{01}} = C\left(\frac{p_{0e}}{p_{01}}\right)^{1-\frac{\gamma-1}{2\gamma\eta_p}} = C \times 23^{1-0.4/2\times 1.4\times 0.873} \Rightarrow C = 1/23^{0.8363} = 0.07263$$

It is now possible to calculate the various operating points on the working line. For example, if we look at the 95%, 90%, 80%, and 70% speed lines, we expect pressure ratios around 17, 12, 7, and 5, respectively. The corresponding normalized nondimensional mass flows are

$$\frac{\dot{m}\sqrt{C_p T_{01}}}{D^2 p_{01}} = C\left(\frac{p_{0e}}{p_{01}}\right)^{1-\frac{\gamma-1}{2\gamma\eta_p}} = 0.07263\left(\frac{p_{0e}}{p_{01}}\right)^{0.8363}$$

$$0.07263 \times 17^{0.8363} = 0.7765, \quad 0.07263 \times 12^{0.8363} = 0.5803$$

$$0.07263 \times 7^{0.8363} = 0.3697, \quad 0.07263 \times 5^{0.8363} = 0.2790$$

The above points are plotted on Figure 5.8. Note that the working line is close to being a straight line. This is because the exponent in Eq. (5.26b), $1 - (\gamma - 1)/2\gamma\eta_p$, is close to unity.

b. At 80% speed on the working line, the normalized nondimensional mass flow rate is 0.36.

As shown in Chapter 2,

$$\phi = \frac{c_x}{U} \propto \frac{\dot{m}\sqrt{T_{01}}}{p_{01}} \Big/ \frac{\Omega}{\sqrt{T_{01}}}$$

$$\therefore \frac{\phi_{80\%}}{\phi_{100\%}} = \left(\frac{\dot{m}\sqrt{T_{01}}}{p_{01}} \Big/ \frac{\Omega}{\sqrt{T_{01}}}\right)_{80\%} \Big/ \left(\frac{\dot{m}\sqrt{T_{01}}}{p_{01}} \Big/ \frac{\Omega}{\sqrt{T_{01}}}\right)_{100\%} = \frac{0.36}{80} \Big/ \frac{1}{100} = 0.45$$

$$\Rightarrow \phi_{80\%} = 0.45\phi_{100\%} = 0.45 \times 0.6 = 0.27$$

Hence, the flow coefficient in the front stage reduces from 0.6 down to 0.27 as the compressor moves down the working line from 100% speed to 80% speed. This reduction in flow coefficient would correspond to a large increase in incidence onto the front rotors leading to possible flow separation and stall. Variable stator vanes would be required for the first few stages to limit this incidence increase at reduced speed and thereby maintain sufficient operating range.

Stage stacking

Suppose that, the performance of a multistage compressor is required, but the compressor has not been tested and therefore the overall performance characteristics are not available. Given the blade speed and inlet flow conditions, the performance of the first stage could be determined using its single-stage performance characteristic. This would enable the inlet conditions to the second stage to be determined, which can be used to determine its operating point and performance. The process can be repeated throughout a multistage compressor to build up the overall performance characteristics. This approach is known as *stage stacking* and various automated methods have been developed for this purpose, e.g., Howell and Calvert (1978). These methods require single-stage characteristics for each of the stages, which can be derived from measured single-stage characteristics or from empirical correlations based on the mean-line analysis of the individual compressor stages, as done by Wright and Miller (1991).

Estimation of the compressor surge margin is critical, but the prediction of when a multistage compressor becomes unstable remains notoriously difficult. In the preliminary design phase, the performance of similar machines can be used for calibration. For example, if a similar design of compressor stage was found to stall when the diffusion factor exceeded 0.6, then this diffusion factor value could be used to estimate where stall occurs in the new design. Within the stage stacking methods, the stall conditions of the individual stages are used to determine the stall margin of the overall machine. However, this approach is problematic since in practice part of a compressor can be stalled when overall the compressor operation is stable.

Annulus wall boundary layers

In multistage axial compressors, the annulus wall boundary layers rapidly thicken through the first few stages and the axial velocity profile becomes increasingly nonuniform. This effect is illustrated in Figure 5.9, from the experimental results of Howell (1945), which shows axial velocity traverses through a four-stage compressor. Over the central region of the blade, the axial velocity is higher than the mean value based on the through-flow. The mean blade section (and most of the span) will, therefore, do less work than is estimated from the velocity triangles based on the mean axial velocity. In theory, it would be expected that the tip and root sections would provide a compensatory effect because of the low axial velocity in these regions. Due to the end wall and tip leakage flows no such work increase actually occurs, and the net result is that the work done by the whole blade is below the design figure. Howell (1945) suggested that the stagnation enthalpy rise across a stage could be expressed as

$$h_{03} - h_{01} = \lambda U(c_{\theta 2} - c_{\theta 1})$$

where λ is a *work done factor*. For multistage compressors, Howell recommended for λ a mean value of 0.86. Other workers have suggested that λ should be high at entry (0.96) where the annulus wall boundary layers are thin, reducing progressively in the later stages of the compressor (0.85).

Smith (1970) commented upon the rather pronounced deterioration of compressor performance implied by the example given in Figure 5.9 and suggested that things are not as bad as suggested. Figure 5.10(a) shows the axial velocity distributions through a 12-stage axial compressor. This does illustrate that rapid changes in velocity distribution still occur in the first few stages, but the profile

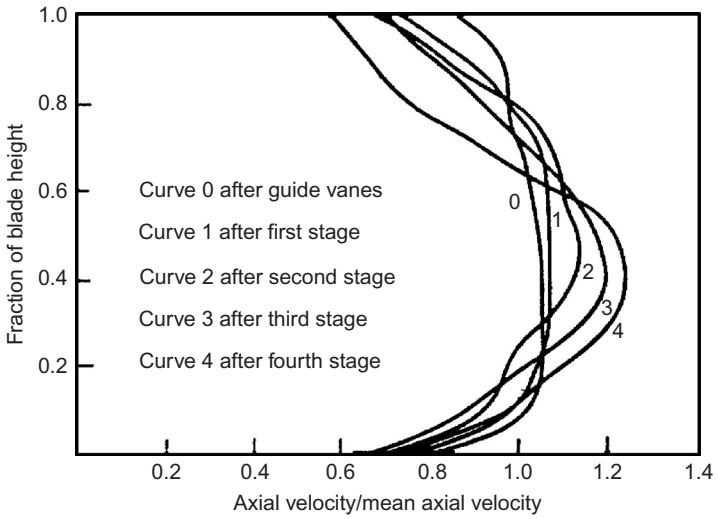

FIGURE 5.9

Axial velocity profiles in a compressor.

(*Howell. 1965, courtesy of the Institution of Mechanical Engineers*)

settles down to a fairly constant shape thereafter. This phenomenon has been referred to as *ultimate steady flow*, which Horlock (2000) described as "a stage deeply embedded in the compressor where an axial equilibrium state is reached."

Smith also provided curves of the spanwise variation in total temperature, Figure 5.10(b), which shows the way losses increase from mid passage toward the annulus walls. An inspection of this figure shows also that the excess total temperature near the end walls increases in magnitude and extent as the flow passes through the compressor. Work on methods of predicting annulus wall boundary layers in turbomachines and their effects on performance have been actively pursued in many countries. Horlock (2000) reviewed several approaches to end wall blockage in axial compressors, i.e., Khalid et al. (1999), Smith (1970), Horlock and Perkins (1974). It is worth noting that although these approaches can give estimates of the increase in blockage and loss across a blade row they have now been superseded by advanced computational methods that can simulate multiple stages of compressor with end wall boundary layers, tip clearance flows, and other leakage paths.

5.10 High Mach number compressor stages

As introduced in Chapter 3, the performance of compressor blades deteriorate once the relative inlet Mach number exceeds about 0.7, because the relative Mach numbers within the blade passages

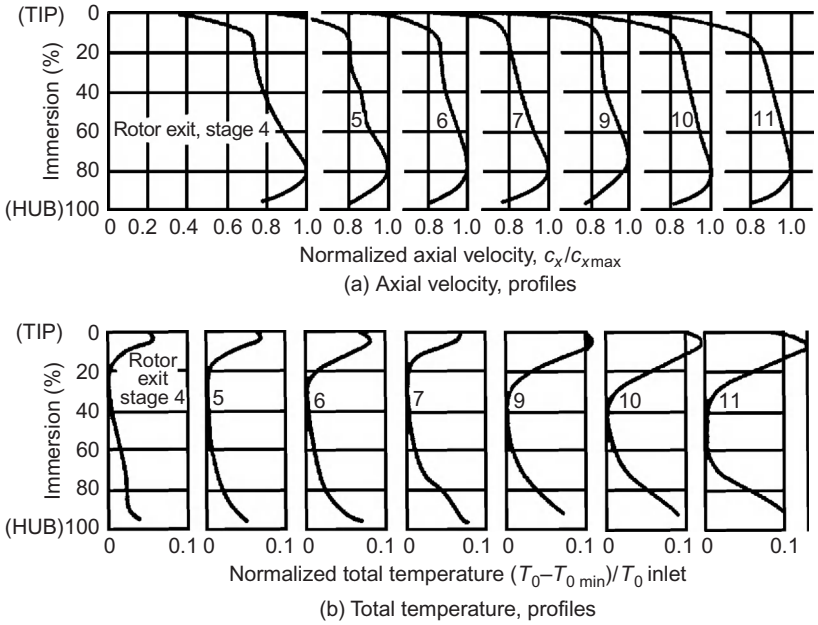

FIGURE 5.10

Traverse measurements obtained from a 12-stage compressor.

(*Smith, 1970, courtesy of the Elsevier Publishing Co.*)

exceeds unity and extra losses are generated by shock waves and thicker boundary layers. Furthermore, high Mach numbers reduce the operating range of a compressor because the flow becomes more sensitive to changes in inlet angle.

However, there are two key advantages of high Mach number compressor stages. Firstly, high relative Mach numbers in a compressor imply a high mass flow per unit area, which leads to a more compact (lower diameter) machine for a given mass flow. Secondly, high Mach numbers are caused by high blade speeds, which enable greater work input to the flow and, hence, higher pressure ratios. Using the definitions of stage loading and polytropic efficiency, the stage pressure ratio for a compressor can be written as

$$\frac{p_{03}}{p_{01}} = \left[\frac{\psi U^2}{C_p T_{01}} + 1\right]^{\gamma \eta_p/(\gamma-1)} \tag{5.27}$$

This shows that high stage pressure ratios can be achieved by high blade speeds combined with high stage loading and efficiency. In modern transonic compressors, rotor inlet relative Mach numbers of up to 1.7 are now used and single-stage pressure ratios greater than 2 are possible.

Calvert and Ginder (1999) detail the design of transonic compressor stages. They also describe the evolution of modern transonic compressors and the major advances that have been made. Transonic compressor stages are currently used within the single-stage fans of high bypass ratio jet engines, in multistage fans within low bypass ratio engines and in the front stages of multistage compressors. The fan of a civil jet engine is a particularly important component as it produces over 80% of the thrust of a modern civil aircraft engine. High mass flow per unit area is needed to minimize the engine size, and inlet relative Mach numbers are around 1.4 at the tip. Polytropic efficiencies above 90% are typical and current design pressure ratios are between 1.6 and 1.8.

To alleviate the effects of high relative Mach numbers in transonic compressors, very thin blades are used to reduce their blockage and typically the thickness-to-chord ratio of the blades is only a few percent. In addition, to reduce the peak Mach number on the blade surface, the blades have very low camber, with only a few degrees of turning. As a result, the blade sections toward the tip of a high-speed compressor resemble sharp, thin, and almost flat plates.

Figure 5.11 shows the flow pattern within a high-speed compressor rotor blade with a supersonic inlet relative Mach number. As the operating point of the compressor changes, the position of the passage shock varies. When the flow is fully choked, the shock moves rearward so that it is fully swallowed within the blade passage. At lower mass flow rates, when the compressor is closer to stall, the shock structure is expelled from the front of the blade passage. The operating point corresponding to peak efficiency usually occurs when the shock wave is close to the blade leading edge.

It is interesting to understand how the shock pattern in Figure 5.11 leads to a very high work input into the flow passing through the compressor. Consider the velocity triangles at inlet and exit from the compressor rotor. Across the passage shock wave, as drawn in Figure 5.11, the flow does not turn significantly, but the density rises sharply. Hence, the relative velocity downstream of the shock will be much lower than upstream. Assuming the blade speed and relative flow angles are the same at rotor inlet and exit, the velocity triangles show that the turning of the flow in the absolute frame is purely a result of the flow slowing down in the relative frame. In contrast, a low-speed compressor rotor achieves a work input to the flow by turning the flow in both the relative and the absolute frames of reference.

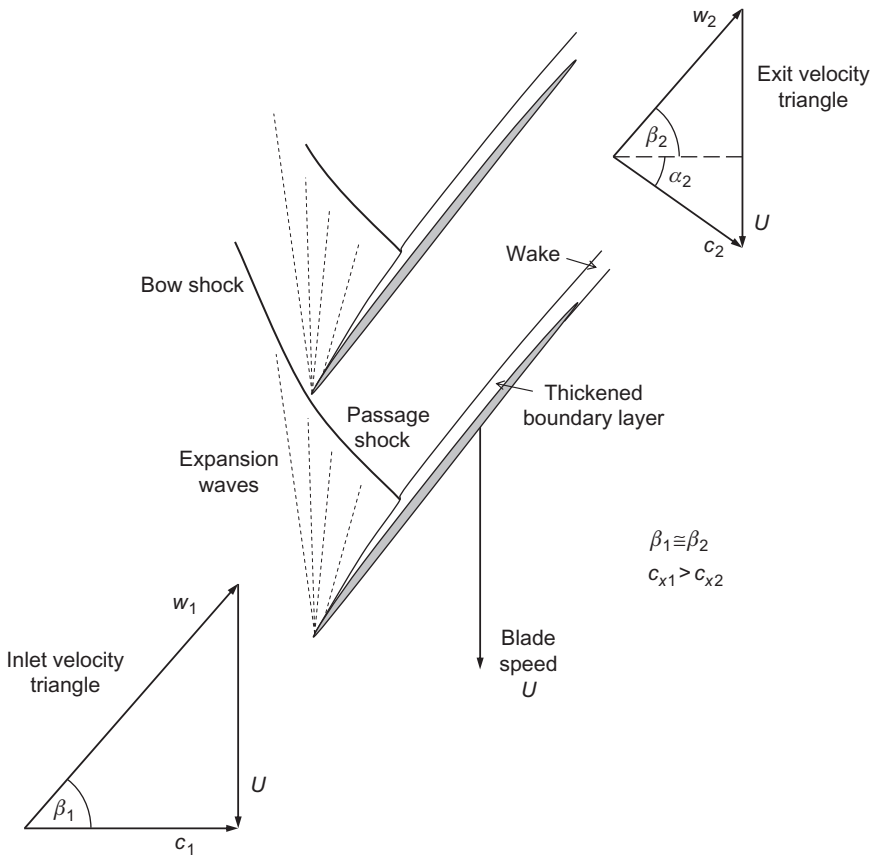

FIGURE 5.11

Flow through a supersonic compressor rotor.

A normal shock wave in a supersonic compressor rotor leads to a rise in entropy in the flow, as given by Eq. (4.21), which can be expressed as a loss coefficient using Eq. (5.8) as

$$Y_{\text{p,shock}} = \frac{1 - \exp(-\Delta s_{\text{shock}}/R)}{(1 - p_1/p_{01,\text{rel}})} \cong \frac{\Delta s_{\text{shock}}}{R(1 - p_1/p_{01,\text{rel}})} \tag{5.28a}$$

which can be expressed as a function of the inlet relative Mach number, $M_{1,\text{rel}}$ and γ. This function is plotted in Figure 5.12 for air as well as the corresponding variation of shock static pressure ratio, given by

$$\frac{p_2}{p_1} = 1 + \frac{2\gamma}{\gamma + 1}(M_{1,\text{rel}}^2 - 1) \tag{5.28b}$$

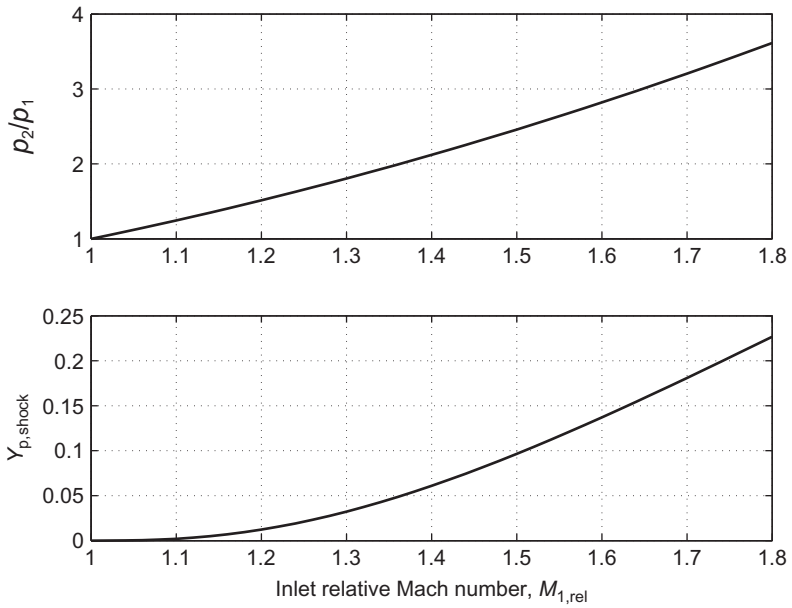

FIGURE 5.12

Variation of static pressure ratio and loss for a normal shock wave.

This shows that the pressure rise delivered by a normal shock wave is high, whereas the shock loss itself is surprisingly low up to inlet relative Mach numbers of 1.5. However, it should be noted that the shock wave also generates loss indirectly through interaction with the blade boundary layers, which are thickened by the shock static pressure rise, and in some cases the flow can separate. Provided this risk of separation is avoided, a shock wave is a highly efficient way to compress flow, as demonstrated by the high efficiencies of modern transonic compressors.

5.11 Stall and surge phenomena in compressors

A noticeable feature of any compressor performance map, such as Figure 5.8, is the *surge line*. This line denotes the limit to stable operation, and it is traditionally referred to as a surge line, even though the instability that occurs may be surge or stall. It can be reached by reducing the mass flow (with a throttle valve), whereas the rotational speed is maintained constant.

When a compressor goes into surge the effects are usually quite dramatic. Generally, an increase in noise level is experienced, indicative of a pulsation of the air flow and of mechanical vibration. Commonly, a small number of predominant frequencies are superimposed on a high background noise. The lowest frequencies are usually associated with what is termed a *Helmholtz-type of resonance* of the flow through the machine, with the inlet and/or outlet volumes. The higher frequencies are known to be due to *rotating stall* and are of the same order as the rotational speed of the impeller.

Rotating stall is a phenomenon of axial compressor flow that has been the subject of many detailed experimental and theoretical investigations. An early detailed survey of the phenomenon was given by Emmons, Kronauer, and Rocket (1959). Briefly, when a blade row (usually the rotor of a compressor) reaches the "stall point," the blades, instead of all stalling together as might be expected, stall in separate patches and these stall patches, moreover, travel around the compressor annulus (i.e., they rotate).

The stall patches *must* propagate from blade to blade has a simple physical explanation. Consider a portion of a blade row, as illustrated in Figure 5.13, to be affected by a stall patch. This patch must cause a partial obstruction to the flow that is deflected on both sides of it. Thus, the incidence of the flow onto the blades on the right of the stall cell is reduced, but the incidence to the left is increased. As these blades are already close to stalling, the net effect is for the stall patch to move to the left; the motion is then self-sustaining.

There is a strong practical reason for the wide interest in rotating stall. Stall patches traveling around blade rows load and unload each blade at some frequency related to the speed and number of the patches. This frequency may be close to a natural frequency of blade vibration and there is clearly a need for accurate prediction of the conditions producing such a vibration. Several cases of blade failure due to resonance induced by rotating stall have been reported, usually with serious consequences to the whole compressor.

It is possible to distinguish between surge and propagating stall by the unsteadiness, or otherwise, of the total mass flow. The characteristic of stall propagation is that the flow passing through the annulus, summed over the whole area, is steady with time; the stall cells merely redistribute the flow over the annulus. Surge, on the other hand, involves an axial oscillation of the total mass flow, a condition highly detrimental to efficient compressor operation.

The point a compressor enters stall or surge still cannot be predicted reliably, even with the most advanced computational methods. However, the understanding of the mechanisms leading to stall and surge have been improved significantly through extensive research.

One early physical explanation of the breakdown of the flow in a compressor is given by Horlock (1958). Figure 5.14 shows a constant rotor speed compressor characteristic (C) of pressure ratio plotted against flow coefficient. A second set of curves (T_1, T_2, etc.) are superimposed on this figure showing the pressure loss characteristics of the throttle for various fixed throttle positions. The intersection of curves T with compressor curve C denotes the various operating points of the combination. A state of *flow stability* exists if the throttle curves at the point of intersection have a greater (positive) slope than

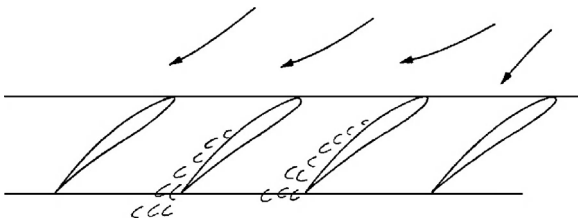

FIGURE 5.13

Model illustrating mechanism of stall cell propagation: partial blockage due to stall patch deflects flow, increasing incidence to the left and decreasing incidence to the right.

the compressor curve. That this is so may be illustrated as follows. Consider the operating point at the intersection of T_2 with C. If a small reduction of flow should momentarily occur, the compressor will produce a greater pressure rise and the throttle resistance will fall. The flow rate must, of necessity, increase so that the original operating point is restored. A similar argument holds if the flow is temporarily augmented, so that the flow is completely stable at this operating condition.

If, now, the operating point is at point U, unstable operation is possible. A small reduction in flow will cause a greater reduction in compressor pressure ratio than the corresponding pressure ratio across the throttle. As a consequence of the increased resistance of the throttle, the flow will decrease even further and the operating point U is clearly unstable. By inference, neutral stability exists when the slopes of the throttle pressure loss curves equal the compressor pressure rise curve.

Tests on low-pressure ratio compressors appear to substantiate this explanation of instability. However, for high rotational speed multistage compressors this argument does not seem sufficient to describe surging. With high speeds no stable operation appears possible on constant speed curves of positive slope and surge appears to occur when this slope is zero or even a little negative. A more complete understanding of surge in multistage compressors is possible only from a detailed study of the individual stages' performance and their interaction with one another.

Casing treatment

It was discovered in the late 1960s that the stall of a compressor could be delayed to a lower mass flow by a suitable treatment of the compressor casing. Given the right conditions this can be of great benefit in extending the range of stall-free operation. Numerous investigations have since been carried out on different types of casing configurations under widely varying flow conditions to demonstrate the range of usefulness of the treatment.

Greitzer, Nikkanen, Haddad, Mazzawy, and Joslyn (1979) observed that two types of stall could be found in a compressor blade row, namely, "blade stall" and "wall stall." Blade stall is, roughly speaking, a 2D type of stall where a significant part of the blade has a large wake leaving the blade suction surface. Wall stall is a stall connected with the boundary layer on the outer casing.

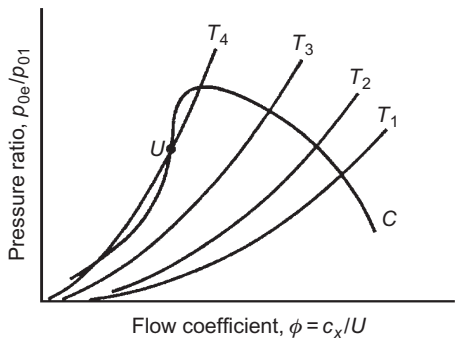

FIGURE 5.14

Stability of operation of a compressor.

(*Adapted from Horlock, 1958*)

Figure 5.15 illustrates the two types of stall. Greitzer et al. found that the response to casing treatment depended conspicuously upon the type of stall encountered.

The influence of a grooved casing treatment on the stall margin of a model axial compressor rotor was investigated experimentally. Two rotor builds of different blade solidities, σ (chord–space ratio), but with all the other parameters identical were tested. Greitzer et al. emphasized that the motive behind the use of different solidities was simply a convenient way to change the type of stall from a blade stall to a wall stall and that the benefit of casing treatment was unrelated to the amount of solidity of the blade row. The position of the casing treatment insert in relation to the rotor blade row is shown in Figure 5.16(a) and the appearance of the grooved surface used is illustrated in Figure 5.16(b). The grooves, described as "axial skewed" and extending over the middle 44% of the blade, have been used in a wide variety of compressors.

As predicted from their design study, the high-solidity blading ($\sigma = 2$) resulted in the production of a wall stall, while the low-solidity ($\sigma = 1$) blading gave a blade stall. Figure 5.17 shows the results obtained for the four conditions tested. The most important difference in performance is the change in the stall point with and without the casing treatment. It can be seen that with the grooved casing a substantial change in the range of ϕ occurred with the high-solidity blading. However, for the low-solidity blading there is only a marginal difference in range. The shape of the performance curve is also significantly affected for the high-solidity rotor blades, with a substantial increase in the peak pressure rise brought about by the grooved casing treatment.

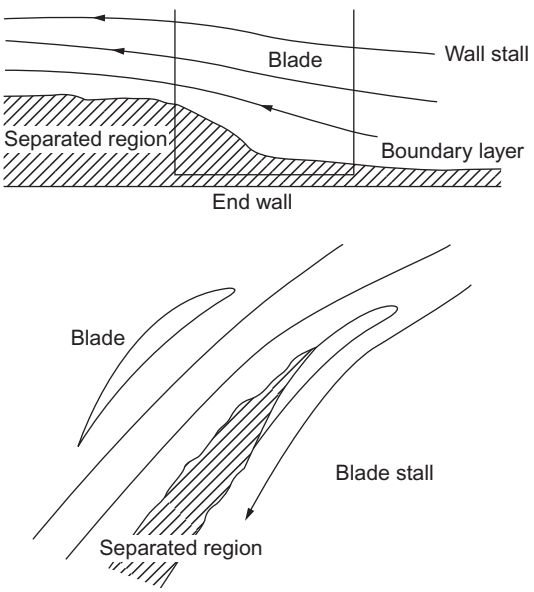

FIGURE 5.15

Compressor stall inception.

(*Adapted from Greitzer et al., 1979*)

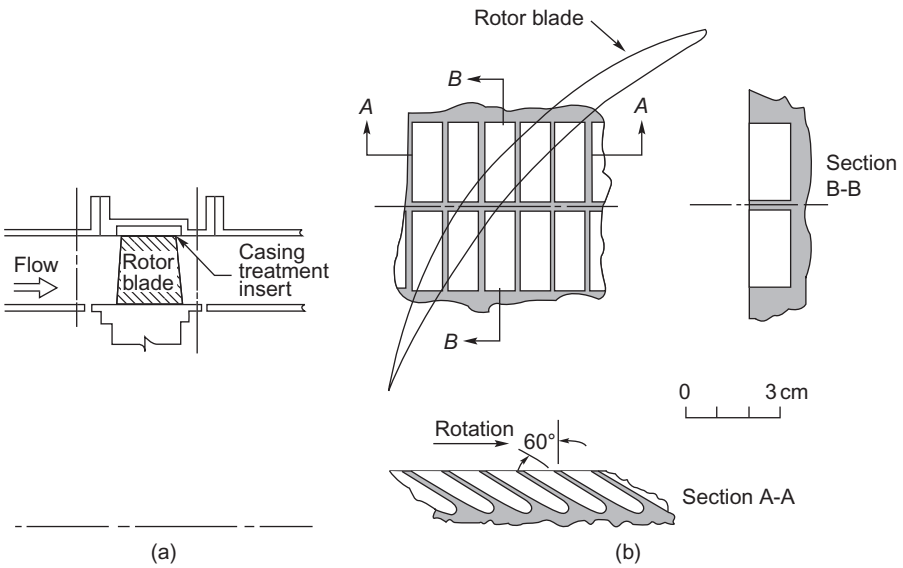

FIGURE 5.16

Position and appearance of casing treatment insert.

(*Adapted from Greitzer et al., 1979*)

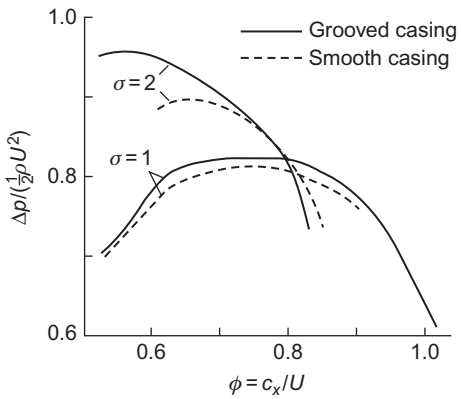

FIGURE 5.17

Effects of casing treatment and solidity on compressor characteristics.

(*Adapted from Greitzer et al., 1979, and data points removed for clarity*)

Casing treatment has not been widely adopted in the aircraft engine industry because of the efficiency penalty that it often causes. Smith and Cumpsty (1984) made an extensive series of experimental investigations to try to discover the cause for this loss in compressor efficiency. At the simplest level, it was realized that the slots provide a route for fluid to pass from the pressure surface to the suction surface allowing a small proportion of the flow to be recirculated. The approaching boundary layer fluid tends to have a high absolute swirl and is, therefore, suitably orientated to enter the slots. Normally, with a smooth wall the high swirl would cause energy to be wasted but, with the casing treatment, the flow entering the slot is turned and reintroduced back into the main flow near the blade's leading edge with its absolute swirl direction reversed. The reentrant flow has, in effect, flowed upstream along the slot to a lower pressure region.

Control of flow instabilities

Important and dramatic advances have been made in recent years in the understanding and controlling of surge and rotating stall. Both phenomena are now regarded as the mature forms of the natural oscillatory modes of the compression system (see Moore and Greitzer, 1986). The flow model they considered predicts that an initial disturbance starts with a very small amplitude but quickly grows into a large amplitude form. Thus, the stability of the compressor is equivalent to the stability of these small amplitude waves that exist just prior to stall or surge (Haynes, Hendricks, & Epstein, 1994). Only a few of the many papers written on the understanding of these unstable flows and the application of control to suppress instability are cited here.

Epstein, Ffowcs Williams, and Greitzer (1989) first suggested that surge and rotating stall could be prevented by using active feedback control to damp the hydrodynamic disturbances while they were still of small amplitude. Active suppression of surge was subsequently demonstrated on a centrifugal compressor by Ffowcs Williams, and Huang (1989), also by Pinsley, Guenette, Epstein, and Greitzer (1991) and on an axial compressor by Day (1993). Shortly after this, Paduano et al. (1993) demonstrated active suppression of rotating stall in a single-stage low-speed axial compressor. By damping the small amplitude waves rotating about the annulus prior to stall, they increased the stable flow range of the compressor by 25%. The control scheme adopted comprised a circumferential array of hot wires just upstream of the compressor and a set of 12 individually actuated vanes upstream of the rotor used to generate the rotating disturbance structure required for control. Haynes et al. (1994), using the same control scheme as Paduano et al., actively stabilized a three-stage, low-speed axial compressor and obtained an 8% increase in the operating flow range. Gysling and Greitzer (1995) employed a different strategy using aeromechanical feedback to suppress the onset of rotating stall in a low-speed axial compressor.

Further methods of active and passive control to prevent stall or surge continue to be extensively researched and new technologies, such as microdevices, are being applied to this purpose. However, there is still very limited adoption of control within commercially available compressors and even casing treatment is used in only a few jet engine compressor designs. Further application of these technologies in the future will be realized only if their robustness and reliability can match that of existing compressor components.

5.12 Low speed ducted fans

In essence, these widely used fans are simply low-speed single-stage compressors with a low pressure (and temperature) rise, so that much of the foregoing theory of this chapter is valid for this class of machine. However, because of the high space−chord ratio used in many of these fans, a simplified theoretical approach based on *isolated aerofoil theory* is often used. This method can be of use in the design of ventilating fans in which aerodynamic interference between adjacent blades can be assumed negligible. Attempts have been made to extend the scope of isolated aerofoil theory to less widely spaced blades by the introduction of an *interference factor*; for instance, the ratio k of the lift force of a single blade in a cascade to the lift force of a single isolated blade. As a guide to the degree of this interference, an exact mathematical solution obtained by Weinig (1935) and used by Wislicenus (1947) for a row of thin flat plates is of value and is shown in Figure 5.18. This illustrates the dependence of k on space−chord ratio for several stagger angles. The rather pronounced effect of stagger for moderate space−chord ratios should be noted as well as the asymptotic convergence of k toward unity for higher space−chord ratios.

Two simple types of axial-flow fan are shown in Figure 5.19 in which the inlet and outlet flows are entirely axial. In the first type (a), a set of guide vanes provides a contra-swirl and the flow is restored to the axial direction by the rotor. In the second type (b), the rotor imparts swirl in the direction of blade motion and the flow is restored to the axial direction by the action of outlet *straighteners* (or outlet guide vanes). The theory and design of both these types of fan have been investigated by Van Niekerk (1958) who was able to formulate expressions for calculating the optimum sizes and fan speeds using blade element theory.

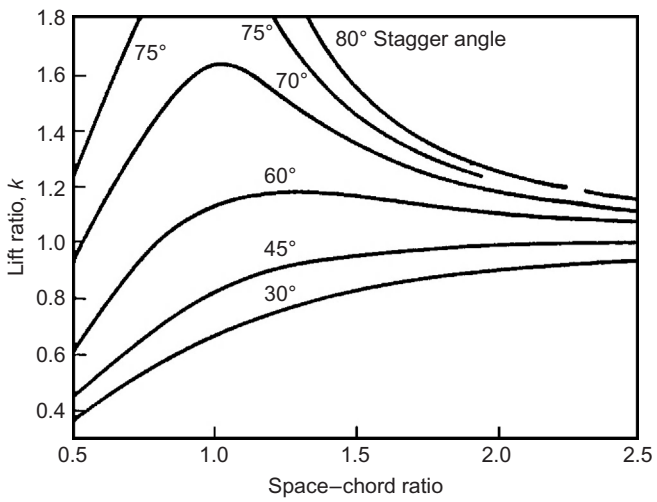

FIGURE 5.18

Weinig's results for lift ratio of a cascade of thin flat plates, showing dependence on stagger angle and space−chord ratio.

(*Adapted from Wislicenus, 1947*)

Note that the analysis in this section uses cartesian (x and y) coordinates in order to be consistent with the low-speed cascade analysis presented in Section 3.4.

Lift and drag coefficients

For a low-speed fan the stage loading factor may be expressed in terms of the lift and drag coefficients for the *rotor*. From Figure 3.12, replacing α_m with β_m, the tangential blade force on the *moving* blades per unit span is

$$Y = L\cos\beta_m + D\sin\beta_m = L\cos\beta_m\left(1 + \frac{C_D}{C_L}\tan\beta_m\right)$$

where $\tan\beta_m = (1/2)(\tan\beta_1 + \tan\beta_2)$.

Now $C_L = L/((1/2)\rho w_m^2 l)$; hence, substituting for L,

$$Y = \frac{1}{2}\rho c_x^2 l C_L \sec\beta_m(1 + \tan\beta_m C_D/C_L) \tag{5.29}$$

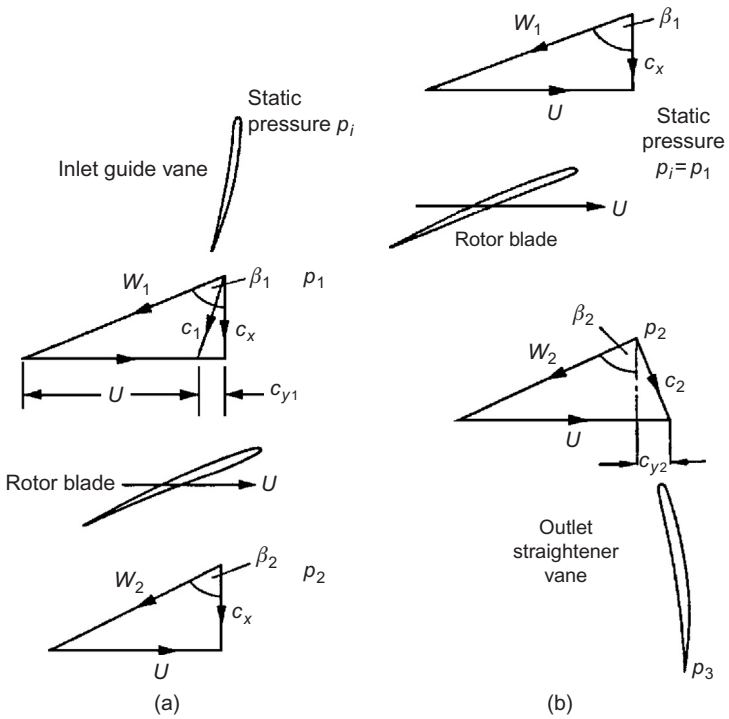

FIGURE 5.19

Two simple types of axial-flow fan and their associated velocity diagrams: (a) fan with inlet guide vanes, and (b) fan with outlet guide vanes.

(*After Van Niekerk, 1958*)

The work done by *each* moving blade per second is YU and is transferred to the fluid through *one* blade passage during that period. Thus, $YU = \rho s c_x (h_{03} - h_{01})$.

Therefore, the stage loading factor may now be written as

$$\psi = \frac{h_{03} - h_{01}}{U^2} = \frac{Y}{\rho s c_x U} \tag{5.30a}$$

Substituting Eq. (5.29) in Eq. (5.30a), the final result is

$$\psi = (\phi/2) \sec \beta_m (l/s)(C_L + C_D \tan \beta_m) \tag{5.30b}$$

In Chapter 3, the approximate analysis indicated that maximum efficiency is obtained when the mean flow angle is 45°. The corresponding optimum stage loading factor at $\beta_m = 45°$ is

$$\psi_{opt} = \left(\phi/\sqrt{2}\right)(l/s)(C_L + C_D) \tag{5.31}$$

Since $C_D \ll C_L$ in the normal low loss operating range, it is permissible to drop C_D from Eq. (5.31).

Blade element theory

A blade element at a given radius can be defined as an aerofoil of vanishingly small span. In fan design theory, it is commonly assumed that each such element operates as a 2D aerofoil, behaving completely independently of conditions at any other radius. Now the forces impressed upon the fluid by unit span of a single stationary blade have been considered in some detail already, in Chapter 3. Considering an *element of a rotor* blade dr, at radius r, the elementary axial and tangential forces, dX and dY, respectively, exerted on the fluid are, referring to Figure 3.12,

$$dX = (L \sin \beta_m - D \cos \beta_m) dr \tag{5.32}$$

$$dY = (L \cos \beta_m + D \sin \beta_m) dr \tag{5.33}$$

where $\tan \beta_m = (1/2)\{\tan \beta_1 + \tan \beta_2\}$ and L, D are the lift and drag on unit span of a blade.

Writing $\tan \gamma = D/L = C_D/C_L$,

$$dX = L(\sin \beta_m - \tan \gamma \cos \beta_m) dr$$

Introducing the lift coefficient $C_L = L/((1/2)\rho w_m^2 l)$ for the rotor blade (cf. Eq. (3.23)) into the preceding expression and rearranging,

$$dX = \frac{\rho c_x^2 l C_L \, dr}{2 \cos^2 \beta_m} \times \frac{\sin(\beta_m - \gamma)}{\cos \gamma} \tag{5.34}$$

where $c_x = w_m \cos \beta_m$.

The torque exerted by *one* blade element at radius r is $r\,\mathrm{d}Y$. If there are Z blades, the elementary torque is

$$\mathrm{d}\tau = rZ\,\mathrm{d}Y = rZL(\cos\beta_\mathrm{m} + \tan\gamma\,\sin\beta_\mathrm{m})\mathrm{d}r$$

after using Eq. (5.33). Substituting for L and rearranging,

$$\mathrm{d}\tau = \frac{\rho c_x^2 l Z C_\mathrm{L} r\,\mathrm{d}r}{2\cos^2\beta_\mathrm{m}} \times \frac{\cos(\beta_\mathrm{m} - \gamma)}{\cos\gamma} \tag{5.35}$$

Now the work done by the rotor in unit time equals the product of the stagnation enthalpy rise and the mass flow rate; for the elementary ring of area $2\pi r\,\mathrm{d}r$,

$$\Omega\mathrm{d}\tau = (C_\mathrm{p}\Delta\mathrm{T}_0)\mathrm{d}\dot{m} \tag{5.36}$$

where Ω is the rotor angular velocity and the element of mass flow, $\mathrm{d}\dot{m} = \rho c_x 2\pi r\,\mathrm{d}r$.

Substituting Eq. (5.35) into Eq. (5.36),

$$C_\mathrm{p}\Delta T_0 = C_\mathrm{p}\Delta T = C_\mathrm{L}\frac{U_{Cx} l\cos(\beta_\mathrm{m} - \gamma)}{2s\cos^2\beta_\mathrm{m}\cos\gamma} \tag{5.37}$$

where $s = 2\pi r/Z$. Now the static temperature rise equals the stagnation temperature rise when the velocity is unchanged across the fan; this, in fact, is the case for both types of fan shown in Figure 5.19.

The increase in static pressure of the *whole* of the fluid crossing the rotor row may be found by equating the total axial force on all the blade elements at radius r with the product of static pressure rise and elementary area $2\pi r\,\mathrm{d}r$, or

$$Z\,\mathrm{d}X = (p_2 - p_1)2\pi r\,\mathrm{d}r$$

Using Eq. (5.34) and rearranging,

$$p_2 - p_1 = C_\mathrm{L}\frac{\rho c_x^2 l\sin(\beta_\mathrm{m} - \gamma)}{2s\cos^2\beta_\mathrm{m}\cos\gamma} \tag{5.38}$$

Note that, so far, all these expressions are applicable to both types of fan shown in Figure 5.19.

Blade element efficiency

Consider the fan type shown in Figure 5.19(a) fitted with guide vanes at inlet. The pressure rise across this fan is equal to the rotor pressure rise, $p_2 - p_1$, minus the drop in pressure across the guide vanes, $p_i - p_1$. The ideal pressure rise across the fan is given by the product of density and $C_\mathrm{p}\Delta T_0$. Fan designers define a blade element efficiency as

$$\eta_\mathrm{b} = \{(p_2 - p_1) - (p_i - p_1)\}/(\rho C_\mathrm{p}\Delta T_0) \tag{5.39}$$

The drop in static pressure across the guide vanes, assuming *frictionless* flow for simplicity, is

$$p_i - p_1 = \frac{1}{2}\rho(c_1^2 - c_x^2) = \frac{1}{2}\rho c_{y1}^2 \tag{5.40}$$

Now, since the change in swirl velocity across the rotor is equal and opposite to the swirl produced by the guide vanes, the work done per unit mass flow, $C_p\Delta T_0$ is equal to Uc_{y1}. Thus, the second term in Eq. (5.39) is

$$(p_i - p_1)/(\rho C_p \Delta T_0) = c_{y1}/(2U) \tag{5.41}$$

Combining Eqs (5.37), (5.38), and (5.41) in Eq. (5.39) then,

$$\eta_b = (c_x/U)\tan(\beta_m - \gamma) - c_{y1}/(2U) \tag{5.42a}$$

The foregoing exercise can be repeated for the second type of fan having outlet straightening vanes, and assuming frictionless flow through the "straighteners," the rotor blade element efficiency becomes

$$\eta_b = (c_x/U)\tan(\beta_m - \gamma) + c_{y2}/(2U) \tag{5.42b}$$

Some justification for ignoring the losses occurring in the guide vanes is found by observing that the ratio of guide vane pressure change to rotor pressure rise is normally small in ventilating fans. For example, in the first type of fan,

$$(p_i - p_1)/(p_2 - p_1) = \left(\frac{1}{2}\rho c_{y1}^2\right)/(\rho U c_{y1}) = c_{y1}/2(U)$$

the tangential velocity c_{y1} being rather small compared with the blade speed U.

Lift coefficient of a fan aerofoil

For a specified blade element geometry, blade speed, and lift−drag ratio, the temperature and pressure rises can be determined if the lift coefficient is known. An estimate of lift coefficient is most easily obtained from 2D aerofoil potential flow theory. Glauert (1959) showed, for isolated aerofoils of small camber and thickness, that

$$C_L = 2\pi \sin\alpha \tag{5.43a}$$

where α is the angle between the flow direction and the *line of zero lift* of the aerofoil. For an isolated, cambered aerofoil Wislicenus (1947) suggested that the zero lift line may be found by joining the trailing edge point with the point of maximum camber, as depicted in Figure 5.20(a). For fan blades experiencing some interference effects from adjacent blades, the modified lift coefficient of a blade may be estimated by assuming that Weinig's results for flat plates (Figure 5.18) are valid for the slightly cambered, finite thickness blades, and

$$C_L = 2\pi k \sin\alpha \tag{5.43b}$$

When the vanes overlap (as they may do at sections close to the hub), Wislicenus suggested that the zero lift line may be obtained by the line connecting the trailing edge point with the maximum camber of that portion of blade that is not overlapped, Figure 5.20(b).

The extension of both blade element theory and cascade data to the design of complete fans was discussed in considerable detail by Wallis (1961).

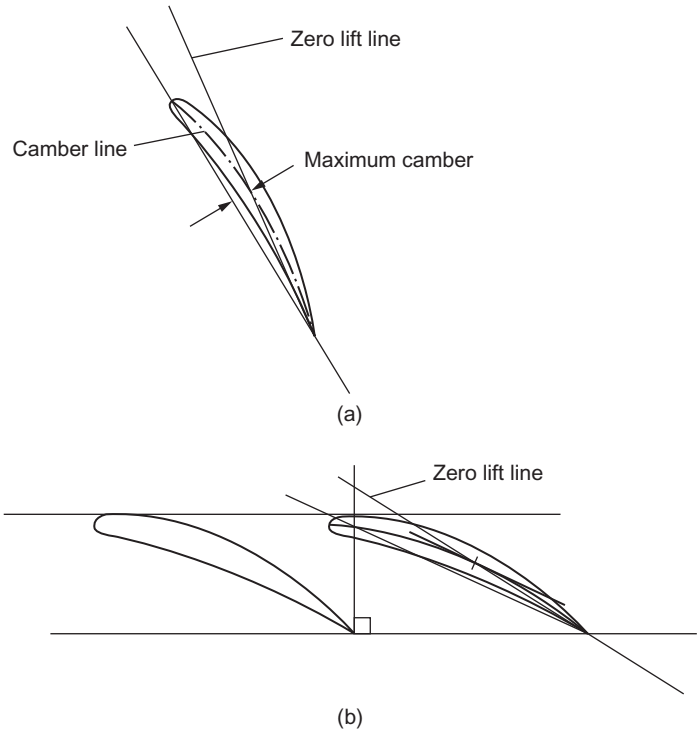

FIGURE 5.20

Method suggested by Wislicenus (1947) for obtaining the zero lift line of cambered aerofoils.

PROBLEMS

(*Note:* In questions 1−4, 6 and 8 take $R = 287$ J/kg °C and $\gamma = 1.4$.)

1. An axial-flow compressor is required to deliver 50 kg/s of air at a stagnation pressure of 500 kPa. At inlet to the first stage, the stagnation pressure is 100 kPa and the stagnation temperature is 23°C. The hub and tip diameters at this location are 0.436 and 0.728 m. At the mean radius, which is constant through all stages of the compressor, the reaction is 0.50 and the absolute air angle at stator exit is 28.8° for all stages. The speed of the rotor is 8000 rev/min. Determine the number of similar stages needed, assuming that the polytropic efficiency is 0.89 and that the axial velocity at the mean radius is constant through the stages and equal to 1.05 times the average axial velocity.

2. Derive an expression for the degree of reaction of an axial compressor stage in terms of the flow angles relative to the rotor and the flow coefficient. Data obtained from early cascade tests suggested that the limit of efficient working of an axial-flow compressor stage occurred when a *relative* Mach number of 0.7 on the rotor is reached;
the flow coefficient is 0.5;

the relative flow angle at rotor outlet is 30° measured from the axial direction; the stage reaction is 50%.

Find the limiting stagnation temperature rise obtained in the first stage of an axial compressor working under these conditions and compressing air at an inlet *stagnation* temperature of 289 K. Assume the axial velocity is constant across the stage.

3. Each stage of an axial-flow compressor is of 0.5 reaction and has the same mean blade speed and the same flow outlet angle of 30° relative to the blades. The mean flow coefficient is constant for all stages at 0.5. At entry to the first stage, the stagnation temperature is 278 K, the stagnation pressure is 101.3 kPa, the static pressure is 87.3 kPa, and the flow area is 0.372 m^2. Using compressible flow analysis determine the axial velocity and the mass flow rate. Determine also the shaft power needed to drive the compressor when there are six stages and the mechanical efficiency is 0.99.

4. A 16-stage axial-flow compressor is to have a pressure ratio of 6.3. Tests have shown that a stage total-to-total efficiency of 0.9 can be obtained for each of the first six stages and 0.89 for each of the remaining 10 stages. Assuming constant work done in each stage and similar stages find the compressor overall total-to-total efficiency. For a mass flow rate of 40 kg/s determine the power required by the compressor. Assume an inlet total temperature of 288 K.

5. At a particular operating condition an axial-flow compressor has a reaction of 0.6, a flow coefficient of 0.5, and a stage loading, defined as $\Delta h_0/U^2$ of 0.35. If the flow exit angles for each blade row may be assumed to remain unchanged when the mass flow is throttled, determine the reaction of the stage and the stage loading when the air flow is reduced by 10% at constant blade speed. Sketch the velocity triangles for the two conditions. Comment upon the likely behavior of the flow when further reductions in air mass flow are made.

6. A high-pressure axial compressor for a jet engine rotates at 15,000 rpm with an overall stagnation pressure ratio of 8.5. The mass flow rate of air through the compressor is 16 kg/s and the stagnation conditions at inlet are 200 kPa and 450 K. The polytropic efficiency is 91%.

a. If the mean radius is 0.24 m and this is constant throughout the compressor, calculate the total-to-total isentropic efficiency of the compressor and show that, for the stage loading to be less than 0.4 in all stages, eight stages are required.

b. The compressor is designed with repeating stages and zero inlet swirl. If the inlet axial Mach number is 0.52, calculate the mean flow coefficient and sketch the velocity triangles for one stage. Show that the blade height at exit from the compressor is about 7.8 mm.

7. At the design operating point, the stage characteristics of a low-speed compressor are as follows:

Reaction	0.5
Flow coefficient	0.4
Stage loading	0.4

Assuming constant axial velocity across the stage and equal absolute velocities at inlet and outlet, determine the exit relative flow angle from the rotor and the exit absolute flow angle from the stator. At an off-design condition, the flow coefficient is reduced to 0.3. Assuming that the deviation from the rotor and stator are unchanged from the design condition, determine the new stage loading. If instead, the deviations from both the rotor and the stator increase by 3°, determine the new stage loading at the off-design condition.

8. Air enters an axial-flow compressor with a stagnation pressure and temperature of 100 kPa and 293 K, leaving at a stagnation pressure of 600 kPa. The hub and tip diameters at entry to the first stage are 0.3 and 0.5 m. The flow Mach number *after* the inlet guide vanes is 0.7 at the mean diameter (0.4 m). At this diameter, which can be assumed constant for all the compressor stages, the reaction is 50%, the axial velocity to mean blade speed ratio is 0.6, and the absolute flow angle is 30° at the exit from all stators. The type of blading used for this compressor is designated "free vortex" and the axial velocity is constant for each stage. Assuming isentropic flow through the inlet guide vanes and a small stage efficiency of 0.88, determine

a. the air velocity at exit from the inlet guide vanes at the mean radius;
b. the air mass flow and rotational speed of the compressor;
c. the specific work done in each stage;
d. the overall efficiency of the compressor;
e. the number of compressor stages required and the power needed to drive the compressor;
f. consider the implications of rounding the number of stages to an integer value if the pressure ratio *must* be maintained at 6 for the same values of blade speed and flow coefficient.

9. The compressor represented in Figure 5.8 has a mean blade speed of 350 m/s when operating at its design point. At the design point, all 10 stages of the compressor can be treated as repeating stages with a flow coefficient of 0.5 and a reaction of 0.6.

Take the inlet stagnation temperature to be 300 K, $\gamma = 1.4$ and $C_p = 1005$ J/kg K.

a. Find the stage loading and the interstage swirl angle that applies to all the stages at the design point.
b. When operating on the working line at 90% speed, estimate the flow coefficients for the first stage and the last stage (for the last stage assume that the nondimensional mass flow is equal to that at compressor exit). Assuming the interstage swirl angles are unchanged from the design point, find the rotor relative inlet angles for the first and last stages at this condition. Hence, determine the change in incidence from the design point, for the last stage rotor and the first stage rotor.
c. The swirl angle at inlet to the first stage can be adjusted by a variable guide vane. Find the inlet swirl angle required at 90% speed to give the same incidence onto the first stage rotor as at the design point.

10. A transonic fan used in a jet engine operates with axial flow at inlet and a flow coefficient of 0.5. The rotor inlet relative Mach number is 1.6 and this is equal to the Mach number just

upstream of the passage normal shock wave. The relative flow angles at inlet and exit from the rotor are equal and there is no change in flow radius.

a. Using Eqs (4.21) and (5.28a), determine the rotor loss coefficient if all of the loss is shock loss. Check this using Figure 5.12.

b. The following equation relates the relative Mach number downstream of the passage shock wave to the upstream relative Mach number:

$$M_{2,\text{rel}} = \left[\frac{1+(\gamma-1/2)M_{1,\text{rel}}^2}{\gamma M_{1,\text{rel}}^2-(\gamma-1/2)}\right]^{1/2}$$

Referring to the velocity triangles in Figure 5.11, use the above equation to determine the stage loading of the fan stage.

c. Show that the stagnation temperature ratio across the fan stage can be written as:

$$\frac{T_{02}}{T_{01}} = \frac{U^2\psi}{C_pT_{01}} + 1 = \frac{2(\gamma-1)M_{1,\text{rel}}^2 \sin^2\beta_1}{2+(\gamma-1)M_{1,\text{rel}}^2}\psi + 1$$

By combining the above result with the rotor loss coefficient, determine the rotor alone total-to-total efficiency and the stagnation pressure ratio across the rotor.

Note: In the following problems on low-speed axial-flow fans the medium is air for which the density is taken to be 1.2 kg/m^3.

11. **a.** The volume flow rate through an axial-flow fan fitted with inlet guide vanes is 2.5 m^3/s and the rotational speed of the rotor is 2604 rev/min. The rotor blade tip radius is 23 cm and the root radius is 10 cm. Given that the stage static pressure increase is 325 Pa and the blade element efficiency is 0.80, determine the angle of the flow leaving the guide vanes at the tip, mean, and root radii.

b. A diffuser is fitted at exit to the fan with an area ratio of 2.5 and an effectiveness of 0.82. Determine the overall increase in static pressure and the air velocity at diffuser exit.

12. The rotational speed of a four-bladed axial-flow fan is 2900 rev/min. At the mean radius of 16.5 cm, the rotor blades operate at $C_L = 0.8$ with $C_D = 0.045$. The inlet guide vanes produce a flow angle of 20° to the axial direction and the axial velocity through the stage is constant at 20 m/s. For the mean radius, determine

a. the rotor relative flow angles;

b. the stage efficiency;

c. the rotor static pressure increase;

d. the size of the blade chord needed for this duty.

13. A diffuser, fitted to the axial fan in the previous problem, has an efficiency of 70% and an area ratio of 2.4. Assuming that the flow at entry to the diffuser is uniform and axial in direction, and the losses in the entry section and the guide vanes are negligible, determine

a. the static pressure rise and the pressure recovery factor of the diffuser;

b. the loss in total pressure in the diffuser;

c. the overall efficiency of the fan and diffuser.

References

Calvert, W. J., & Ginder, R. B. (1999). Transonic fan and compressor design. *Proceedings of the Institution of Mechanical Engineers, Part C: Journal of Mechanical Engineering Science*, *213*(5), 419–436.

Carchedi, F., & Wood, G. R. (1982). Design and development of a 12:1 pressure ratio compressor for the Ruston 6-MW gas turbine. *Journal of Engineering for Power, Transactions of the American Society of Mechanical Engineers*, *104*, 823–831.

Constant, H. (1950). The gas turbine in perspective. *Proc. Inst. Mech. Eng.*, *163*(1), 185–192.

Cox, H. R. (2012). British aircraft gas turbines. *Journal of the Aeronautical Sciences (Institute of the Aeronautical Sciences)*, *13*(2), 53–83.

Cumpsty, N. A. (1989). *Compressor aerodynamics.* New York, NY: Longman.

Day, I. J. (1993). Stall inception in axial flow compressors. *Journal of Turbomachinery, Transactions of the American Society of Mechanical Engineers*, *115*, 1–9.

Denton, J. D. (1993). Loss mechanisms in turbomachines. 1993 IGTI scholar lecture. *Journal of Turbomachinery*, *115*, 621–656.

Dickens, T., & Day, I. J. (2011). The design of highly loaded axial compressors. *Journal of Turbomachinery, Transactions of the American Society of Mechanical Engineers*, *133*, 1–10.

Emmons, H. W., Kronauer, R. E., & Rocket, J. A. (1959). A survey of stall propagation—Experiment and theory. *Transactions of the American Society of Mechanical Engineers, Series D*, *81*, 409–416.

Epstein, A. H., Ffowcs Williams, J. E., & Greitzer, E. M. (1989). Active suppression of aerodynamic instabilities in turbomachines. *Journal of Propulsion and Power*, *5*, 204–211.

Ffowcs Williams, J. E., & Huang, X. Y. (1989). Active stabilization of compressor surge. *Journal of Fluid Mechanics*, *204*, 204–262.

Freeman, C. (1985). Effect of tip clearance flow on compressor stability and engine performance. Von Karman Institute for Fluid Dynamics, Lecture Series 1985-0.

Gallimore, S. J. (1999). Axial flow compressor design. *Proceedings of the Institution of Mechanical Engineers, Part C: Journal of Mechanical Engineering Science*, *213*(5), 437–449.

Glauert, H. (1959). *The elements of aerofoil and airscrew theory.* Cambridge, UK: Cambridge University Press.

Greitzer, E. M., Nikkanen, J. P., Haddad, D. E., Mazzawy, R. S., & Joslyn, H. D. (1979). A fundamental criterion for the application of rotor casing treatment. *Journal of Fluid Engineering, Transactions of the American Society of Mechanical Engineers*, *101*, 237–243.

Gysling, D. L., & Greitzer, E. M. (1995). Dynamic control of rotating stall in axial flow compressors using aeromechanical feedback. *Journal of Turbomachinery, Transactions of the American Society of Mechanical Engineers*, *117*, 307–319.

de Haller, P. (1953). Das verhalten von tragflügelgittern in axialverdichtern und im windkanal. *Brennstoff-Wärme-Kraft*, *Band 5*(*Heft 10*).

Haynes, J. M., Hendricks, G. J., & Epstein, A. H. (1994). Active stabilization of rotating stall in a three-stage axial compressor. *Journal of Turbomachinery, Transactions of the American Society of Mechanical Engineers*, *116*, 226–237.

Horlock, J. H. (1958). *Axial flow compressors.* London: Butterworth-Heinemann, (1973). (Reprint with supplemental material, Huntington, NY: Kreiger.).

Horlock, J. H. (2000). The determination of end-wall blockage in axial compressors: A comparison between various approaches. *Journal of Turbomachinery, Transactions of the American Society of Mechanical Engineers*, *122*, 218–224.

Horlock, J. H., & Perkins, H. J. (1974). Annulus wall boundary layers in turbomachines. *AGARDograph AG-185*.

Howell, A. R. (1945). Fluid dynamics of axial compressors. *Proc. Inst. Mech. Eng.*, *153*(1), 441–452.

Howell, A. R., & Calvert, W. J. (1978). A new stage stacking technique for axial flow compressor performance prediction. Transactions of the American Society of Mechanical Engineers, *Journal of Engineering for Power*, *100*, 698–703.

Khalid, S. A., Khalsa, A. S., Waitz, I. A., Tan, C. S., Greitzer, E. M., Cumpsty, N. A., et al. (1999). Endwall blockage in axial compressors. *Journal of Turbomachinery, Transactions of the American Society of Mechanical Engineers*, *121*, 499–509.

Koch, C. C. (1997). Stalling pressure rise capability of axial flow compressors. *Transactions of the American Society of Mechanical Engineer*, paper 97-GT-535.

Koch, C. C., & Smith, L. H. (1976). Loss sources and magnitudes in axial flow compressors. *Journal of Engineering for Power, Transactions of the American Society of Mechanical Engineers*, *98*, 411–424.

Moore, F. K., & Greitzer, E. M. (1986). A theory of post stall transients in axial compression systems: Parts I and II. *Journal of Engine Gas Turbines Power, Transactions of the American Society of Mechanical Engineers*, *108*, 68–76.

Paduano, J. D., Epstein, A. H., Valavani, L., Longley, J. P., Greitzer, E., & Guenette, G. R. (1993). Active control of rotating stall in a low-speed axial compressor. *Journal of Turbomachinery, Transactions of the American Society of Mechanical Engineers*, *115*(1), 48–56.

Pinsley, J. E., Guenette, G. R., Epstein, A. H., & Greitzer, E. M. (1991). Active stabilization of centrifugal compressor surge. *Journal of Turbomachinery, Transactions of the American Society of Mechanical Engineers*, *113*, 723–732.

Smith, G. D. J., & Cumpsty, N. A. (1984). Flow phenomena in compressor casing treatment. *Journal of* Engineering *Gas Turbines and Power, Transactions of the American Society of Mechanical Engineers*, *106*, 532–541.

Smith, L. H. (1958). Recovery ratio—A measure of the loss recovery potential of compressor stages. *Transactions of the American Society of Mechanical Engineers*, *80*, 3.

Smith, L. H., Jr. (1970). Casing boundary layers in multistage compressors. In L. S. Dzung (Ed.), *Proceedings of symposium on flow research on blading*. Burlington, MA: Elsevier.

Stoney, G. (1937). Scientific activities of the late Hon. Sir Charles Parsons, F.R.S. *Engineering*, *144,* 632–695.

Van Niekerk, C. G. (1958). Ducted fan design theory. *Journal of Applied Mechanics*, *25,* 325.

Wallis, R. A. (1961). *Axial flow fans, design and practice.* London: Newnes.

Weinig, F. (1935). *Die stroemung um die schaufeln von turbomaschinen.* Leipzig, Germany: J. A. Barth.

Wennerstrom, A. J. (1989). Low aspect ratio axial flow compressors: Why and what it means. *Journal of Turbomachinery, Transactions of the American Society of Mechanical Engineers*, *111*, 357–365.

Wennerstrom, A. J. (1990). Highly loaded axial flow compressors: History and current development. *Journal of Turbomachinery, Transactions of the American Society of Mechanical Engineers*, *112*, 567–578.

Wislicenus, G. F. (1947). *Fluid mechanics of turbomachinery.* New York, NY: McGraw-Hill.

Wright, P. I., & Miller, D. C. (1991). An improved compressor performance prediction model. *Institution of Mechanical Engineers Conference Proceedings*, CP1991-3, paper C423/028.

CHAPTER

Three-Dimensional Flows in Axial Turbomachines

6

It cost much labour and many days before all these things were brought to perfection.
Defoe, *Robinson Crusoe*

6.1 Introduction

In Chapters 4 and 5, the fluid motion through the blade rows of axial turbomachines was assumed to be two-dimensional in the sense that radial (i.e., spanwise) velocities did not exist. This assumption is not unreasonable for axial turbomachines of high hub−tip ratio. However, with hub−tip ratios less than about 4/5, radial velocities through a blade row may become appreciable, the consequent redistribution of mass flow (with respect to radius) seriously affecting the outlet velocity profile (and flow angle distribution). The temporary imbalance between the strong centrifugal forces exerted on the fluid and radial pressures restoring equilibrium is responsible for these radial flows. Thus, to an observer traveling with a fluid particle, radial motion will continue until sufficient fluid is transported (radially) to change the pressure distribution to that necessary for equilibrium. The flow in an annular passage in which there is no radial component of velocity, whose streamlines lie in circular, cylindrical surfaces and which is axisymmetric, is commonly known as *radial equilibrium* flow.

An analysis called *the radial equilibrium method*, widely used for design calculations in axial compressors and turbines, is based upon the assumption that any radial flow that may occur is completed *within* a blade row, the flow *outside* the row then being in radial equilibrium (Smith, 1966). Figure 6.1 illustrates the nature of this assumption. The other assumption, that the flow is axisymmetric, implies that the effect of the discrete blades is not transmitted to the flow.

6.2 Theory of radial equilibrium

Consider a small element of fluid of mass dm, shown in Figure 6.2, of unit depth and subtending an angle dθ at the axis, rotating about the axis with tangential velocity, c_θ, at radius r. The element is in radial equilibrium so that the pressure forces balance the centrifugal forces:

Fluid Mechanics and Thermodynamics of Turbomachinery. DOI: http://dx.doi.org/10.1016/B978-0-12-415954-9.00006-1

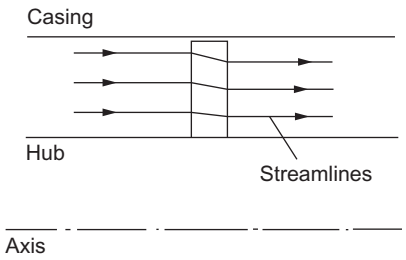

FIGURE 6.1

Radial equilibrium flow through a rotor blade row.

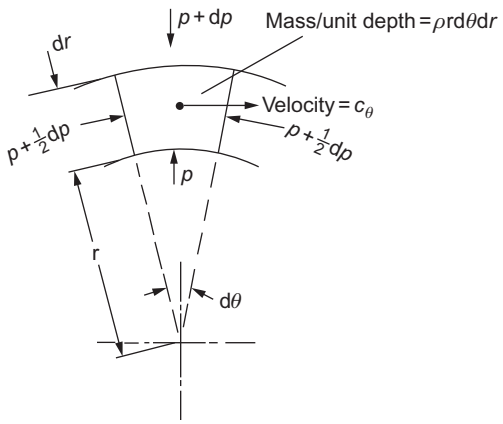

FIGURE 6.2

Fluid element in radial equilibrium ($c_r = 0$).

$$(p + \mathrm{d}p)(r + \mathrm{d}r)\mathrm{d}\theta - pr\mathrm{d}\theta - \left(p + \frac{1}{2}\mathrm{d}p\right)\mathrm{d}r\mathrm{d}\theta = \mathrm{d}mc_\theta^2/r$$

Writing $\mathrm{d}m = \rho r\mathrm{d}\theta\mathrm{d}r$ and ignoring terms of the second order of smallness, this equation reduces to

$$\frac{1}{\rho}\frac{\mathrm{d}p}{\mathrm{d}r} = \frac{c_\theta^2}{r} \tag{6.1}$$

If the swirl velocity c_θ and density are known functions of the radius, the radial pressure variation along the blade length can be determined as

$$p_{\mathrm{tip}} - p_{\mathrm{root}} = \int_{\mathrm{root}}^{\mathrm{tip}} \rho c_\theta^2 \frac{\mathrm{d}r}{r} \tag{6.2a}$$

For an incompressible fluid,

$$p_{\text{tip}} - p_{\text{root}} = \rho \int_{\text{root}}^{\text{tip}} c_\theta^2 \frac{\mathrm{d}r}{r} \tag{6.2b}$$

The stagnation enthalpy is written as (with $c_r = 0$)

$$h_0 = h + \frac{1}{2}\left(c_x^2 + c_\theta^2\right) \tag{6.3}$$

therefore,

$$\frac{\mathrm{d}h_0}{\mathrm{d}r} = \frac{\mathrm{d}h}{\mathrm{d}r} + c_x \frac{\mathrm{d}c_x}{\mathrm{d}r} + c_\theta + \frac{\mathrm{d}c_\theta}{\mathrm{d}r} \tag{6.4}$$

The thermodynamic relation $T\mathrm{d}s = \mathrm{d}h - (1/\rho)\mathrm{d}p$ can be similarly written as

$$T\frac{\mathrm{d}s}{\mathrm{d}r} = \frac{\mathrm{d}h}{\mathrm{d}r} - \frac{1}{\rho}\frac{\mathrm{d}p}{\mathrm{d}r} \tag{6.5}$$

Combining Eqs (6.1), (6.4), and (6.5), eliminating $\mathrm{d}p/\mathrm{d}r$ and $\mathrm{d}h/\mathrm{d}r$, the *radial equilibrium equation* may be obtained as

$$\frac{\mathrm{d}h_0}{\mathrm{d}r} - T\frac{\mathrm{d}s}{\mathrm{d}r} = c_x \frac{\mathrm{d}c_x}{\mathrm{d}r} + \frac{c_\theta}{r}\frac{\mathrm{d}}{\mathrm{d}r}(rc_\theta) \tag{6.6a}$$

If the stagnation enthalpy h_0 and entropy s remain the same at all radii, $\mathrm{d}h_0/\mathrm{d}r = \mathrm{d}s/\mathrm{d}r = 0$, then Eq. (6.6a) becomes

$$c_x \frac{\mathrm{d}c_x}{\mathrm{d}r} + \frac{c_\theta}{r}\frac{\mathrm{d}}{\mathrm{d}r}(rc_\theta) = 0 \tag{6.6b}$$

Equation (6.6b) will hold for the flow between the rows of an adiabatic, reversible (ideal) turbomachine in which rotor rows either deliver or receive equal work at all radii. Now if the flow is incompressible, instead of Eq. (6.3) use $p_0 = p + (1/2)/\rho(c_x^2 + c_\theta^2)$ to obtain

$$\frac{1}{\rho}\frac{\mathrm{d}p_0}{\mathrm{d}r} = \frac{1}{\rho}\frac{\mathrm{d}p}{\mathrm{d}r} + c_x \frac{\mathrm{d}c_x}{\mathrm{d}r} + c_\theta \frac{\mathrm{d}c_\theta}{\mathrm{d}r} \tag{6.7}$$

Combining Eqs (6.1) and (6.7), we obtain

$$\frac{1}{\rho}\frac{\mathrm{d}p_0}{\mathrm{d}r} = c_x \frac{\mathrm{d}c_x}{\mathrm{d}r} + \frac{c_\theta}{r}\frac{\mathrm{d}}{\mathrm{d}r}(rc_\theta) \tag{6.8}$$

Equation (6.8) clearly reduces to Eq. (6.6b) in a turbomachine in which equal work is delivered at all radii and the total pressure losses across a row are uniform with radius.

Equation (6.6b) may be applied to two sorts of problem: the design (or indirect) problem, in which the tangential velocity distribution is specified and the axial velocity variation is found, or the direct problem, in which the swirl angle distribution is specified, the axial and tangential velocities being determined.

6.3 The indirect problem

Free-vortex flow

This is a flow where the product of radius and tangential velocity remains constant (i.e., $rc_\theta = K$, a constant). The term *vortex free* might be more appropriate as the vorticity (to be precise we mean *axial* vorticity component) is then zero.

Consider an element of an ideal inviscid fluid rotating about some fixed axis, as indicated in Figure 6.3. The *circulation* Γ is defined as the line integral of velocity around a curve enclosing an area A, or $\Gamma = \oint c\mathrm{d}s$. The *vorticity* at a point is defined as the limiting value of circulation $\delta\Gamma$ divided by area δA, as δA becomes vanishingly small. Thus, vorticity, $\omega = \mathrm{d}\Gamma/\mathrm{d}A$.

For the element shown in Figure 6.3, $c_r = 0$ and

$$\mathrm{d}\Gamma = (c_\theta + \mathrm{d}c_\theta)(r + \mathrm{d}r)\mathrm{d}\theta - c_\theta r\mathrm{d}\theta = \left(\frac{\mathrm{d}c_\theta}{\mathrm{d}r} + \frac{c_\theta}{r}\right) r\mathrm{d}\theta\,\mathrm{d}r$$

ignoring the product of small terms. Thus, $\omega = \mathrm{d}\Gamma/\mathrm{d}A = (1/r)\mathrm{d}(rc_\theta)/\mathrm{d}r$. If the vorticity is zero, $\mathrm{d}(rc_\theta)/\mathrm{d}r$ is also zero and, therefore, rc_θ is constant with radius.

Putting $rc_\theta =$ constant in Eq. (6.6b), then $\mathrm{d}c_x/\mathrm{d}r = 0$ and so $c_x =$ a constant. This information can be applied to the incompressible flow through a free-vortex compressor or turbine stage, enabling the radial variation in flow angles, reaction, and work to be found.

Compressor stage

Consider the case of a compressor stage in which $rc_{\theta 1} = K_1$ before the rotor and $rc_{\theta 2} = K_2$ after the rotor, where K_1 and K_2 are constants. The work done by the rotor on unit mass of fluid is

$$\Delta W = U(c_{\theta 2} - c_{\theta 1}) = \Omega r(K_2/r - K_1/r) = \text{constant}$$

Thus, the work done is equal at all radii.

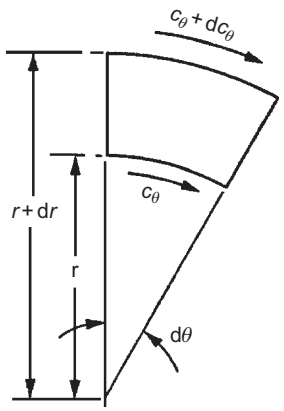

FIGURE 6.3

Circulation about an element of fluid.

The relative flow angles (Figure 5.2) entering and leaving the rotor are

$$\tan \beta_1 = \frac{U}{c_x} - \tan \alpha_1 = \frac{\Omega r - K_1/r}{c_x}$$

$$\tan \beta_2 = \frac{U}{c_x} - \tan \alpha_2 = \frac{\Omega r - K_2/r}{c_x}$$

in which $c_{x1} = c_{x2} = c_x$ for incompressible flow.

In Chapter 5, reaction in an axial compressor is defined by

$$R = \frac{\text{static enthalpy rise in the rotor}}{\text{static enthalpy rise in the stage}}$$

For a normal stage ($\alpha_1 = \alpha_3$) with c_x constant across the stage, the reaction was shown to be, from Eq. (5.21),

$$R = \frac{c_x}{2U}(\tan \beta_1 + \tan \beta_2)$$

Substituting values of $\tan \beta_1$ and $\tan \beta_2$ into Eq. (5.21), the reaction becomes

$$R = 1 - \frac{k}{r^2} \tag{6.9}$$

where

$$k = (K_1 + K_2)/(2\Omega)$$

It will be clear that, as k is positive, the reaction increases from root to tip. Likewise, from Eq. (6.1) we observe that as c_θ^2/r is always positive (excepting $c_\theta = 0$), so static pressure increases from root to tip. For the free-vortex flow $rc_\theta = K$, the static pressure variation can be shown to be $p/\rho = \text{constant} - K^2/(2r^2)$ upon integrating Eq. (6.1).

EXAMPLE 6.1

An axial-flow compressor stage is designed to give free-vortex tangential velocity distributions for all radii before and after the rotor blade row. The tip diameter is constant and 1.0 m; the hub diameter is 0.9 m and constant for the stage. At the rotor tip, the flow angles are as follows:

absolute inlet angle, $\alpha_1 = 30°$;
relative inlet angle, $\beta_1 = 60°$;
absolute outlet angle, $\alpha_2 = 60°$;
relative outlet angle, $\beta_2 = 30°$.

Determine

a. the axial velocity;
b. the mass flow rate;
c. the power absorbed by the stage;

d. the flow angles at the hub;
e. the reaction ratio of the stage at the hub;

given that the rotational speed of the rotor is 6000 rev/min and the gas density is 1.5 kg/m^3, which can be assumed constant for the stage. It can be further assumed that stagnation enthalpy and entropy are constant before and after the rotor row for the purpose of simplifying the calculations.

Solution

a. The rotational speed, $\Omega = 2\pi N/60 = 628.4$ rad/s. Therefore, blade tip speed, $U_t = \Omega r_t = 314.2$ m/s, and blade speed at hub, $U_h = \Omega r_h = 282.5$ m/s. From the velocity diagram for the stage (e.g., Figure 5.2), the blade tip speed is

$$U_t = c_x(\tan 60^\circ + \tan 30^\circ) = 2.309 c_x$$

Therefore, $c_x = 136$ m/s, constant at all radii because the flow is a free vortex.

b. The rate of mass flow, $\dot{m} = \pi(r_t^2 - r_h^2)\rho c_x = \pi(0.5^2 - 0.45^2)1.5 \times 136 = 30.4$ kg/s

c. The power absorbed by the stage,

$$\begin{aligned}\dot{W}e &= \dot{m}U_t(c_{\theta 2t} - c_{\theta 1t}) \\ &= \dot{m}U_t c_x(\tan\alpha_{2t} - \tan\alpha_{1t}) \\ &= 30.4 \times 314.2 \times 136(\sqrt{3} - 1/\sqrt{3}) \\ &= 1.5 \text{ MW}\end{aligned}$$

d. At inlet to the rotor tip,

$$c_{\theta 1t} = c_x \tan\alpha_1 = 136/\sqrt{3} = 78.6\ m/s$$

The absolute flow is a free vortex, $rc_\theta = $ constant. Therefore, $c_{\theta 1h} = c_{\theta 1t}(r_t/r_h) = 78.6 \times 0.5/0.45 = 87.3$ m/s. At outlet to the rotor tip,

$$c_{\theta 2t} = c_x \tan\alpha_2 = 136 \times \sqrt{3} = 235.6\ m/s$$

Therefore, $c_{\theta 2h} = c_{\theta 2t}(r_t/r_h) = 235.6 \times 0.5/0.45 = 262$ m/s. The flow angles at the hub are

$$\begin{aligned}\tan\alpha_1 &= c_{\theta 1h}/c_x = 87.3/136 = 0.642 \\ \tan\beta_1 &= U_h/c_x - \tan\alpha_1 = 1.436 \\ \tan\alpha_2 &= c_{\theta 2h}/c_x = 262/136 = 1.928 \\ \tan\beta_2 &= U_h/c_x - \tan\alpha_2 = 0.152\end{aligned}$$

Thus, $\alpha_1 = 32.75^\circ$, $\beta_1 = 55.15^\circ$, $\alpha_2 = 62.6^\circ$, $\beta_2 = 8.64^\circ$ at the hub.

e. The reaction at the hub can be found by several methods. With Eq. (6.9),

$$R = 1 - k/r^2$$

and noticing that, from symmetry of the velocity triangles,

$$R = 0.5 \text{ at } r = r_t, \text{ then } k = 0.5r_t^2$$

Therefore,

$$R_h = 1 - 0.5(0.5/0.45)^2 = 0.382$$

The velocity triangles will be asymmetric and similar to those in Figure 5.5(b).

The simplicity of the flow under free-vortex conditions is, superficially, very attractive to the designer and many compressors have been designed to conform to this flow. Figure 6.4 illustrates the variation of fluid angles and Mach numbers of a typical compressor stage designed for free-vortex flow. Characteristic of this flow are the large fluid deflections near the inner wall and high Mach numbers near the outer wall, both effects being deleterious to efficient performance. A further serious disadvantage is the large amount of rotor twist from root to tip, which adds to the difficulty of blade manufacture.

Many types of vortex design have been proposed to overcome some of the disadvantages set by free-vortex design and several of these are compared by Horlock (1958). Radial equilibrium solutions for the work and axial velocity distributions of some of these vortex flows in an axial compressor stage follow.

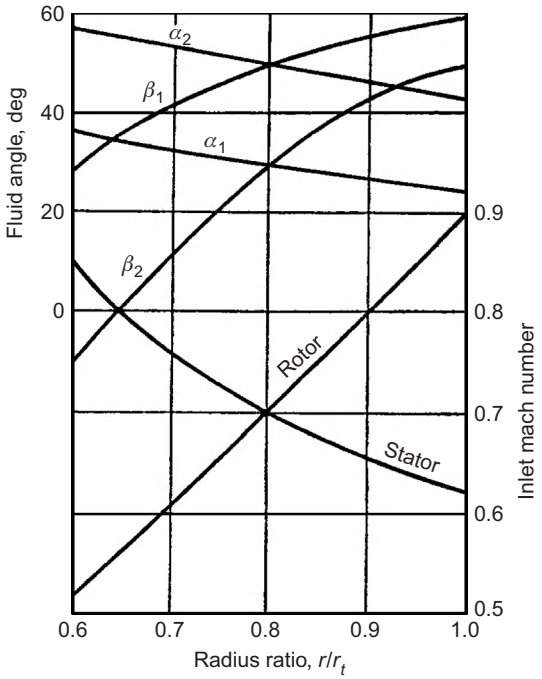

FIGURE 6.4

Variation of fluid angles and Mach numbers of a free-vortex compressor stage with radius.

(*Adapted from Howell, 1945*)

Forced vortex

This is sometimes called *solid-body* rotation because c_θ varies directly with r. At entry to the rotor assume h_{01} is constant and $c_{\theta 1} = K_1 r$.

With Eq. (6.6b),

$$\frac{\mathrm{d}}{\mathrm{d}r}\left(\frac{c_{x1}^2}{2}\right) = -K_1 \frac{\mathrm{d}}{\mathrm{d}r}(K_1 r^2)$$

and, after integrating,

$$c_{x1}^2 = \text{constant} - 2K_1^2 r^2 \tag{6.10}$$

After the rotor $c_{\theta 2} = K_2 r$ and $h_{02} - h_{01} = U(c_{\theta 2} - c_{\theta 1}) = \Omega(K_2 - K_1)r^2$. Thus, as the work distribution is nonuniform, the radial equilibrium equation in the form Eq. (6.6a) is required for the flow after the rotor:

$$\frac{\mathrm{d}h_{02}}{\mathrm{d}r} = 2\Omega(K_2 - K_1)r = \frac{\mathrm{d}}{\mathrm{d}r}\left(\frac{c_{x2}^2}{2}\right) + K_2 \frac{\mathrm{d}}{\mathrm{d}r}(K_2 r^2)$$

After rearranging and integrating,

$$c_{x2}^2 = \text{constant} - 2[K_2^2 - \Omega(K_2 - K_1)]r^2 \tag{6.11}$$

The constants of integration in Eqs (6.10) and (6.11) can be found from the continuity of mass flow, i.e.,

$$\frac{\dot{m}}{2\pi\rho} = \int_{r_\mathrm{h}}^{r_2} c_{x1} r \mathrm{d}r = \int_{r_\mathrm{h}}^{r_2} c_{x2} r \mathrm{d}r \tag{6.12}$$

which applies to the assumed incompressible flow.

Variable vortex design

In this case the tangential velocity distribution is given by

$$c_{\theta 1} = ar^n - b/r \quad \text{(before rotor)} \tag{6.13a}$$

$$c_{\theta 2} = ar^n + b/r \quad \text{(after rotor)} \tag{6.13b}$$

The distribution of work for all values of the index n is constant with radius so that if h_{01} is uniform, h_{02} is also uniform with radius. From Eqs (6.13a) and (6.13b),

$$\Delta W = h_{02} - h_{01} = U(c_{\theta 2} - c_{\theta 1}) = 2b\Omega \tag{6.14}$$

Selecting different values of n gives several of the tangential velocity distributions commonly used in compressor design. With $n = 0$, or zero power blading, it leads to the so-called exponential type of stage design (included as an exercise at the end of this chapter). With $n = 1$, or *first power blading*, the stage design is called (incorrectly, as it transpires later) *constant reaction*.

Mixed vortex design

A problem arises with the use of the free-vortex solution, especially when it is applied to low hub−tip ratio stages, which is the large radial variation in flow angles, reaction, and tangential velocities that results from its use. This leads to highly twisted blades which are difficult and expensive to manufacture and can be the cause of large total pressure losses. Turbomachinery designers have been aware for some time of this difficulty and have attempted various strategies to reduce these flow extremes. One of these attempts is the use of the so-called "mixed vortex," which combines a *free vortex* with a *forced vortex* or solid-body rotation. For the flow after a rotor row, this combined flow produces a tangential velocity distribution given by

$$c_{\theta 2} = \frac{a}{r} + br \tag{6.15}$$

First power stage vortex design

For a given stage temperature rise, the discussion in Chapter 5 would suggest the choice of 50% reaction at all radii for the highest stage efficiency. With swirl velocity distributions,

$$c_{\theta 1} = ar - b/r, \quad c_{\theta 2} = ar + b/r \tag{6.16}$$

before and after the rotor, respectively; and rewriting the expression for reaction, Eq. (5.21), as

$$R = 1 - \frac{c_x}{2U}(\tan \alpha_1 + \tan \alpha_2)$$

then, using Eq. (6.16),

$$R = 1 - a/\Omega = \text{constant} \tag{6.17}$$

Implicit in Eq. (6.17) is the assumption that the axial velocity across the rotor remains constant which, of course, is tantamount to ignoring radial equilibrium. The axial velocity *must* change in crossing the rotor row so that Eq. (6.17) is only a crude approximation at the best.

Assuming constant stagnation enthalpy at entry to the stage, integrating Eq. (6.6b), the axial velocity distributions before and after the rotor are

$$c_{x1}^2 = \text{constant} - 4a\left(\frac{1}{2}ar^2 - b \ln r\right) \tag{6.18a}$$

$$c_{x2}^2 = \text{constant} - 4a\left(\frac{1}{2}ar^2 - b \ln r\right) \tag{6.18b}$$

More conveniently, these expressions can be written nondimensionally as

$$\left(\frac{c_{x1}}{U_t}\right)^2 = A_1 - \left(\frac{2a}{\Omega}\right)^2 \left[\frac{1}{2}\left(\frac{r}{r_t}\right)^2 - \frac{b}{ar_t^2} \ln\left(\frac{r}{r_t}\right)\right] \tag{6.19a}$$

$$\left(\frac{c_{x2}}{U_t}\right)^2 = A_2 - \left(\frac{2a}{\Omega}\right)^2 \left[\frac{1}{2}\left(\frac{r}{r_t}\right)^2 + \frac{b}{ar_t^2}\ln\left(\frac{r}{r_t}\right)\right] \tag{6.19b}$$

in which $U_t = \Omega r_t$ is the tip blade speed. The constants A_1, A_2 are not arbitrary as the continuity equation, Eq. (6.12), must be satisfied.

EXAMPLE 6.2
A DESIGN PROBLEM

By careful selection of the values of the constants a and b in Eq. (6.15), the radial distribution of the blade loading can be optimized for a mixed vortex design. However, it was suggested by Lewis (1996) that a better design strategy would be to consider instead the work coefficient, ψ, and attempt to make this more uniform. Consider a single compressor *rotor* in incompressible flow with purely axial-flow upstream of the rotor, $c_{\theta 1} = 0$. In this case, the variation of work coefficient is given by

$$\psi = \frac{\Delta p_0}{\rho U^2} = \frac{c_{\theta 2}}{U} = \frac{1}{\Omega}\left(\frac{a}{r^2} + b\right)$$

By choosing values of the work coefficient at two radii, the values of a and b can then be found. Let $\psi = \psi_m = 0.3$ at the root mean square radius, $r = r_m = \sqrt{(1/2)(r_h^2 + r_t^2)}$ and $\psi = \psi_h = 0.6$ at $r = r_h$. The values of the hub-to-tip radius ratio are $r_h/r_t = 0.4$, $r_m/r_t = 0.7616$, and $r_t = 0.5$ m. These choices of r_h and r_t and the values of the work coefficients are quite arbitrary and other values could be selected by the designer. Also, for use later, assume the local flow coefficient, $\phi_m = c_{xm}/U_m = 0.5$ and the rotational speed, $\Omega = 500$ rad/s. By substitution into the above equation for work coefficient, it is possible to evaluate a and b as

$$a = 8.286 \text{ and } b = 92.86$$

At this point, it is useful to compare some of the values determined for a free-vortex design and the mixed vortex design, as shown in Table 6.1. Note that from Eq. (5.23), it is apparent that the reaction $R = 1 - \psi/2$ when $c_{\theta 1} = 0$. From Table 6.1, it is seen for the free-vortex design that there is a considerable variation of the work coefficient ψ and the reaction R, whereas for the mixed vortex design only moderate variations are determined.

Solving for the axial velocity

For the mixed vortex, the solution for the axial velocity (for $h_0 =$ constant and $s =$ constant) is found as follows:

$$c_x \frac{dc_x}{dr} + \frac{c_\theta}{r}\frac{d(rc_\theta)}{dr} = 0 \text{ or } \frac{d}{dr}(c_x^2) = -2\frac{c_\theta}{r}\frac{d}{dr}(rc_\theta)$$

With $c_{\theta 2} = (a/r) + br$, we get

$$c_{x2}^2 = -4b\int\left(\frac{a}{r} + br\right)dr = C - 4b\left[a\ln r + \frac{b}{2}r^2\right]$$

Table 6.1 Tangential Velocity Ratio, Work Coefficient, and Reaction Distributions for the Two Designs.

	Free vortex			Mixed vortex		
r/r_t	$c_{\theta 2}/\overline{c}_x$	ψ	R	$c_{\theta 2}/\overline{c}_x$	ψ	R
0.4	1.142	1.088	0.456	0.630	0.600	0.700
0.5	0.913	0.696	0.652	0.592	0.451	0.775
0.6	0.761	0.483	0.758	0.583	0.370	0.815
0.7	0.653	0.355	0.822	0.590	0.321	0.840
0.8	0.571	0.272	0.864	0.608	0.289	0.855
0.9	0.508	0.215	0.893	0.632	0.268	0.866
1.0	0.457	0.174	0.913	0.662	0.252	0.874

Table 6.2 Mixed vortex calculation results

Radius r (m)	0.20	0.25	0.30	0.35	0.40	0.45	0.50
$4b[a \ln r + br^2/2]$	− 4264	− 3190	− 2153	− 1119	− 60.5	1035	2178
$C - 4b[a \ln r + br^2/2]$	12,764	11,690	10,653	9619	8560	7465	6322
$c_{x2}(m/s)$	113.0	108.1	103.2	98.08	92.52	86.4	79.5
c_{x2} at mid-ordinates	110.5	105.6	100.64	95.3	89.46	82.95	
Mid-ordinate radius (m)	0.225	0.275	0.325	0.375	0.425	0.475	

where C is an arbitrary constant, which is found using the continuity equation. The *average* value of the axial velocity is $\overline{c}_x = \phi_m U_m = 95.2$ m/s. The volume flow rate Q for the flow upstream of the rotor is

$$Q/\pi = \overline{c}_x(r_t^2 - r_h^2) = 20.0 \text{ m}^3/\text{s}$$

and the volume flow rate downstream is given by

$$Q/\pi = \int_{r_h}^{r_t} c_{x2} r \mathrm{d}r = \int_{r_h}^{r_t} \sqrt{C - 4b[a \ln r + br^2/2]} \times r \mathrm{d}r$$

To solve for C an iterative method of calculation is required. The preferred method uses the "mid-ordinate rule" and the details of the final iteration (with $C = 8500$) are shown in the Table 6.2. Using the results in the table, $Q/\pi = \sum c_{x2} r_{\text{mid}} \times 0.1 = 19.98 \text{ m}^3/\text{s}$ for the flow downstream of the rotor.

This result is approximately equal to the value of Q/π determined for the flow upstream of the rotor. The details of the absolute and relative flow angles, α_2, β_1, and β_2, and the fluid

deflection angle, ε, are given in Table 6.3. The flow angles follow the generalized notation given in Figure 5.2 with $c_{\theta 1} = 0^\circ$. The various angles are determined using the following formulae:

$$\tan \beta_1 = \frac{U}{c_{x2}}, \tan \beta_2 = \frac{U}{c_{x2}}(1 - \psi), \tan \alpha_2 = \psi \frac{U}{c_{x2}}, \text{and } \varepsilon = \beta_1 - \beta_2$$

The velocity triangles at radii $r/r_t = 0.4, 0.7, \text{and } 1.0$ are shown in Figure 6.5. Note that for simplicity, these are drawn with equal axial velocity at inlet and exit. In reality, the axial velocity upstream of the rotor does not vary with radius because the flow there is not swirling.

Table 6.3 Flow angles for the mixed vortex design

r/r_t	0.40	0.50	0.60	0.70	0.80	0.90	1.00
β_1^0	41.5	49.15	55.47	60.73	65.17	70.0	72.36
β_2^0	19.49	32.4	42.47	50.46	56.95	62.32	66.97
ε^0	22.01	16.75	13.0	10.27	8.22	7.68	5.39
α_2^0	27.97	27.53	28.26	29.8	32.0	34.91	38.4
$\phi = c_{x2}/U_t$	1.13	0.865	0.688	0.561	0.463	0.384	0.318

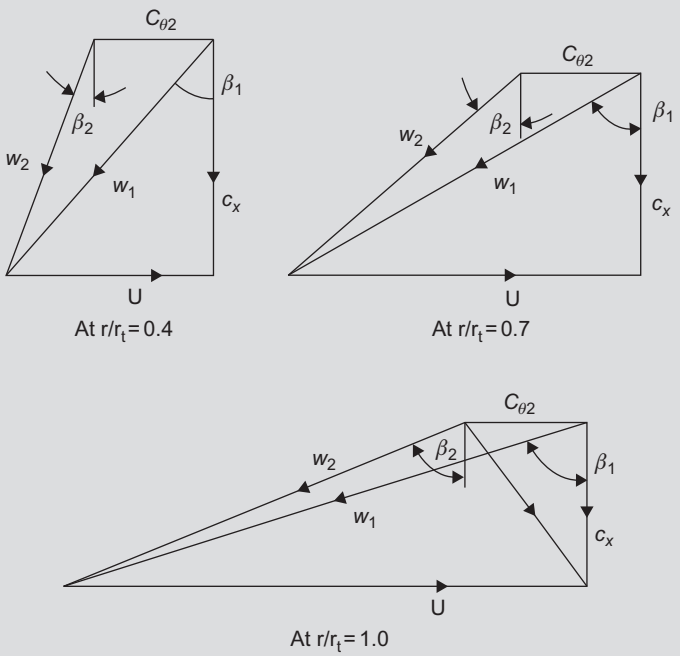

FIGURE 6.5

Velocity triangles for the mixed vortex design.

Meridional flow reversal as a result of excessive swirl

A noticeable feature of the downstream velocity profile is the tendency of the axial velocity to reduce rapidly as $r \to r_t$. Any increase in the swirl velocity will cause the axial velocity to reduce further and this can ultimately lead to flow reversal. This is a real physical limit and mathematically no real solution is possible in the above equations. In the problem solved, a fairly uniform distribution of work transfer was stipulated. Any increase in the exit swirl energy (by increasing the factor b) would reduce the energy contribution to the axial velocity component, which could lead to flow failure. Lewis (1996) suggested that designers have two options available in order to avoid this flow problem:

1. prescribe a less powerful vortex type, or
2. increase the hub/tip ratio.

6.4 The direct problem

The flow angle variation is specified in the direct problem and the radial equilibrium equation enables the solution of c_x and c_θ to be found.

The radial equilibrium equation is

$$c_x \frac{\mathrm{d}c_x}{\mathrm{d}r} + \frac{c_\theta}{r}\frac{\mathrm{d}}{\mathrm{d}r}(rc_\theta) = \frac{\mathrm{d}h_0}{\mathrm{d}r} - T\frac{\mathrm{d}s}{\mathrm{d}r} \tag{6.20a}$$

Substituting $c_\theta = c \sin\alpha$ and $c_x = c\cos\alpha$, we get

$$c_x \frac{\mathrm{d}c_x}{\mathrm{d}r} + \frac{c\sin\alpha}{r}\frac{\mathrm{d}}{\mathrm{d}r}(rc\sin\alpha) = \frac{\mathrm{d}h_0}{\mathrm{d}r} - T\frac{\mathrm{d}s}{\mathrm{d}r}$$

$$\therefore \frac{c\sin\alpha}{r}\frac{\mathrm{d}}{\mathrm{d}r}(rc\sin\alpha) + c\cos\alpha\frac{\mathrm{d}}{\mathrm{d}r}(c\cos\alpha) = \frac{\mathrm{d}h_0}{\mathrm{d}r} - T\frac{\mathrm{d}s}{\mathrm{d}r}$$

$$\therefore \frac{c\sin\alpha}{r}\left[c\sin\alpha + r\sin\alpha\frac{\mathrm{d}c}{\mathrm{d}r} + rc\cos\alpha\frac{\mathrm{d}\alpha}{\mathrm{d}r}\right] + c\cos\alpha\left[\frac{\mathrm{d}c}{\mathrm{d}r}\cos\alpha - c\sin\alpha\frac{\mathrm{d}\alpha}{\mathrm{d}r}\right] = \frac{\mathrm{d}h_0}{\mathrm{d}r} - T\frac{\mathrm{d}s}{\mathrm{d}r}$$

Multiplying out and simplifying we then get

$$c\frac{\mathrm{d}c}{\mathrm{d}r} + \frac{c^2}{r}\sin^2\alpha = \frac{\mathrm{d}h_0}{\mathrm{d}r} - T\frac{\mathrm{d}s}{\mathrm{d}r} \tag{6.20b}$$

Note the similarities between Eqs (6.20a) and (6.20b).

Some special cases

1. If both $\mathrm{d}h_0/dr$ and $\mathrm{d}s/dr$ are zero, Eq. (6.20b) integrated gives

$$\ln c = -\int \sin^2\alpha\frac{\mathrm{d}r}{r} + \text{a constant}$$

If $c = c_\mathrm{m}$ at $r = r_\mathrm{m}$, then

$$\frac{c}{c_\mathrm{m}} = \exp\left(-\int \sin^2\alpha\frac{\mathrm{d}r}{r}\right) \tag{6.21}$$

2. If the flow angle α is made constant, then the above equation simplifies to

$$\frac{c}{c_{\mathrm{m}}} = \frac{c_x}{c_{x\mathrm{m}}} = \frac{c_\theta}{c_{\theta\mathrm{m}}} = \left(\frac{r}{r_{\mathrm{m}}}\right)^{-\sin^2\alpha} \tag{6.22}$$

The vortex distribution represented by Eq. (6.22) is often employed in practice as untwisted blades are much simpler to manufacture.

The general solution of the radial equilibrium equation

A more general case applies when $h_0 = h_0(r)$, $\alpha = \alpha(r)$, and s = a constant. This specification gives the designer a much wider choice. A solution can be contrived as follows. From Eq. (6.20b), i.e.,

$$c\frac{\mathrm{d}c}{\mathrm{d}r} + \frac{c^2}{r}\sin^2\alpha = \frac{\mathrm{d}h_0}{\mathrm{d}r}$$

we can solve this by introducing a suitable *integrating factor*. Multiplying throughout by

$$\exp\left[2\int \sin^2\alpha\frac{\mathrm{d}r}{r}\right]$$

$$\therefore \frac{\mathrm{d}}{\mathrm{d}r}\left\{c^2\exp\left[2\int\sin^2\alpha\frac{\mathrm{d}r}{r}\right]\right\} = 2\left(\frac{\mathrm{d}h_0}{\mathrm{d}r}\right)\exp\left[2\int\sin^2\alpha\mathrm{d}r/r\right]$$

The solution for the velocity is

$$c^2 = \frac{2\int\{\mathrm{e}^D\}(\mathrm{d}h_0/dr)\mathrm{d}r + K}{\{\mathrm{e}^D\}}$$

where $\mathrm{e}^D = \exp(2\int(\sin^2\alpha/r)\mathrm{d}r)$ and K is a constant.

Let $c = c_{\mathrm{m}}$ at $r = r_{\mathrm{m}}$, so that K can be evaluated. The final expression for the velocity is

$$\frac{c^2}{c_{\mathrm{m}}^2} = \frac{2\int_{r_{\mathrm{m}}}^{r}\left[\exp\left(2\int_{r_{\mathrm{m}}}^{r}(\sin^2\alpha/r)\mathrm{d}r\right)\right](\mathrm{d}h_0/dr)\mathrm{d}r}{\exp\left(2\int_{r_{\mathrm{m}}}^{r}(\sin^2\alpha/r)\mathrm{d}r\right)} + \exp\left(-2\int_{r_{\mathrm{m}}}^{r}(\sin^2\alpha/r)\mathrm{d}r\right)$$

or more concisely

$$\frac{c^2}{c_{\mathrm{m}}^2} = \frac{2\int_{r_{\mathrm{m}}}^{r} e^D(\mathrm{d}h_0/dr) + 1}{e^D} \tag{6.23a}$$

A special case

Let $2\mathrm{d}h_0/\mathrm{d}r = kc_{\mathrm{m}}^2/r_{\mathrm{m}}$ and let $a = 2\sin^2\alpha$, then $\exp\left[2\int\sin^2\alpha\mathrm{d}r/r\right] = r^a$ and hence

$$\left(\frac{c}{c_{\mathrm{m}}}\right)^2\left(\frac{r}{r_{\mathrm{m}}}\right)^a = 1 + \frac{k}{1+k}\left[\left(\frac{r}{r_{\mathrm{m}}}\right)^{1+a} - 1\right] \tag{6.23b}$$

If the variation of α is specified by $b(r/r_m) = 2\sin^2\alpha$, where b is a constant, it can be shown that

$$\left(\frac{c}{c_m}\right)^2 = \frac{k}{b} + \left(1 - \frac{k}{b}\right)\exp\left[b\left(1 - \frac{r}{r_m}\right)\right] \tag{6.23c}$$

where k is a constant of integration.

These sort of analyses can be used in the preliminary design of blading and some computational methods use them to prescribe their boundary conditions, see Lakshminarayana (1996).

6.5 Compressible flow through a fixed blade row

In the blade rows of high-performance gas turbines, fluid velocities approaching, or even exceeding, the speed of sound are common and compressibility effects may no longer be ignored. A simple analysis is outlined here for the inviscid flow of a perfect gas through a *fixed* row of blades which, nevertheless, can be extended to the flow through moving blade rows.

The radial equilibrium equation, Eq. (6.6a), applies to *compressible* flow as well as incompressible flow. With constant stagnation enthalpy and constant entropy, a free-vortex flow therefore implies uniform axial velocity downstream of a blade row, regardless of any *density* changes incurred in passing through the blade row. In fact, for high-speed flows there *must* be a density change in the blade row, which implies a streamline shift as shown in Figure 6.1. This may be illustrated by considering the free-vortex flow of a perfect gas as follows. In radial equilibrium,

$$\frac{1}{\rho}\frac{dp}{dr} = \frac{c_\theta^2}{r} = \frac{K^2}{r^3} \quad \text{with} \quad c_\theta = \frac{K}{r}$$

For reversible adiabatic flow of a perfect gas, $\rho = Ep^{1/y}$, see Eq. (1.35), where E is constant. Thus,

$$\int p^{-1/\gamma}dp = EK^2\int r^{-3}dr + \text{constant}$$

therefore,

$$p = \left[\text{constant} - \left(\frac{\gamma-1}{\gamma}\right)\frac{EK^2}{r^2}\right]^{\gamma/(\gamma-1)} \tag{6.24}$$

For this free-vortex flow the pressure, and therefore the density also, must be larger at the casing than at the hub. The density difference from hub to tip may be appreciable in a high velocity, high swirl angle flow. If the fluid is without swirl at entry to the blades, the density will be uniform. Therefore, from continuity of mass flow there must be a redistribution of fluid in its passage across the blade row to compensate for the changes in density. Thus, for this blade row, the continuity equation is

$$\dot{m} = \rho_1 A_1 c_{x1} = 2\pi c_{x2}\int_{r_h}^{r_t}\rho_2 r dr \tag{6.25}$$

where ρ_2 is the density of the swirling flow, obtainable from Eq. (6.24).

6.6 Constant specific mass flow

Although there appears to be no evidence that the redistribution of the flow across blade rows is a source of inefficiency, it has been suggested by Horlock (1966) that the radial distribution of c_θ for each blade row is chosen so that the product of axial velocity and density is constant with radius, i.e.,

$$\mathrm{d}\dot{m}/\mathrm{d}A = \rho c_x = \rho c \cos\alpha = \rho_\mathrm{m} c_\mathrm{m} \cos\alpha_\mathrm{m} = \text{constant} \tag{6.26}$$

where subscript m denotes conditions at $r = r_\mathrm{m}$. This *constant specific mass flow design* is the logical choice when radial equilibrium theory is applied to compressible flows as the assumption that $c_\mathrm{r} = 0$ is then likely to be realized.

Solutions may be determined by means of a simple numerical procedure and, as an illustration of one method, a turbine stage is considered here. It is convenient to assume that the stagnation enthalpy is uniform at nozzle entry, the entropy is constant throughout the stage, and the fluid is a perfect gas. At nozzle exit under these conditions the equation of radial equilibrium, Eq. (6.20), can be written as

$$\mathrm{d}c/c = -\sin^2\alpha \mathrm{d}r/r \tag{6.27}$$

From Eq. (6.1), noting that at constant entropy the acoustic velocity $\alpha = \sqrt{\mathrm{d}p/\mathrm{d}\rho}$,

$$\frac{1}{\rho}\frac{\mathrm{d}p}{\mathrm{d}r} = \frac{1}{\rho}\left(\frac{\mathrm{d}p}{\mathrm{d}\rho}\right)\left(\frac{\mathrm{d}\rho}{\mathrm{d}r}\right) = \frac{a^2}{\rho}\frac{\mathrm{d}\rho}{\mathrm{d}r} = \frac{c^2}{r}\sin^2\alpha$$

therefore,

$$\mathrm{d}\rho/\rho = M^2 \sin^2\alpha \mathrm{d}r/r \tag{6.28a}$$

where the flow Mach number

$$M = c/a = c/\sqrt{\gamma RT} \tag{6.28b}$$

The isentropic relation between temperature and density for a perfect gas is

$$T/T_\mathrm{m} = (\rho/\rho_\mathrm{m})^{\gamma-1}$$

which after logarithmic differentiation gives

$$\mathrm{d}T/T = (\gamma - 1)\mathrm{d}\rho/\rho \tag{6.29}$$

Using this set of equations, the procedure for determining the nozzle exit flow is as follows. Starting at $r = r_\mathrm{m}$, values of c_m, α_m, T_m, and ρ_m are assumed to be known. For a small finite interval Δr, the changes in velocity Δc, density $\Delta\rho$, and temperature ΔT can be computed using Eqs (6.27), (6.28), and (6.29), respectively. Hence, at the new radius $r = r_\mathrm{m} + \Delta r$, the velocity $c = c_\mathrm{m} + \Delta c$, the density $\rho = \rho_\mathrm{m} + \Delta\rho$, and temperature $T = T_\mathrm{m} + \Delta T$ are obtained. The corresponding flow angle α and Mach number M can now be determined from Eqs (6.26) and (6.28b), respectively. Thus, all parameters of the problem are known at radius $r = r_\mathrm{m} + \Delta r$. This procedure is repeated for further increments in radius to the casing and again from the mean radius to the hub.

Figure 6.6 shows the distributions of flow angle and Mach number computed with this procedure for a turbine nozzle blade row of 0.6 hub−tip radius ratio. The input data used was

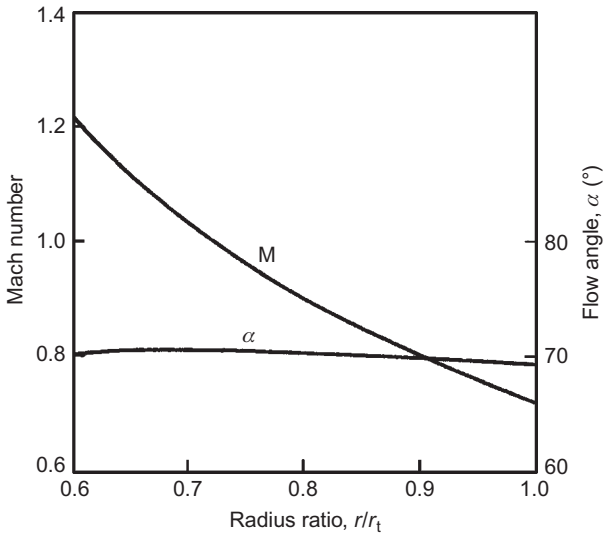

FIGURE 6.6

Flow angle and Mach number distributions with radius of a nozzle blade row designed for constant specific mass flow.

$\alpha_m = 70.4°$ and $M = 0.907$ at the mean radius. Air was assumed at a stagnation pressure of 859 kPa and a stagnation temperature of 465°K. A remarkable feature of these results is the almost uniform swirl angle that is obtained.

With the nozzle exit flow fully determined the flow at rotor outlet can now be computed by a similar procedure. The procedure is a little more complicated than that for the nozzle row because the specific work done by the rotor is not uniform with radius. Across the rotor, using the notation of Chapter 4,

$$h_{03} - h_{03} = U(c_{\theta 2} + c_{\theta 3}) \tag{6.30a}$$

and, hence, the gradient in stagnation enthalpy after the rotor is

$$\mathrm{d}h_{03}/dr = -\,d[U(c_{\theta 2} - c_{\theta 3})]/dr = -\,d(Uc_{\theta 2})/\mathrm{d}r - \,d(Uc_3 \sin \alpha_3)/dr$$

After differentiating the last term,

$$-\mathrm{d}h_0 = d(Uc_{\theta 2}) + U(c \sin \alpha \mathrm{d}r/r + \sin \alpha \mathrm{d}c + c \cos \alpha \mathrm{d}\alpha) \tag{6.30b}$$

the subscript 3 having now been dropped.

From Eq. (6.20b), the radial equilibrium equation applied to the rotor exit flow is

$$\mathrm{d}h_0 = c^2 \sin^2 \alpha \mathrm{d}r/r + c\mathrm{d}c \tag{6.30c}$$

After logarithmic differentiation of $\rho c \cos \alpha = \text{constant}$,

$$\mathrm{d}\rho/\rho + \mathrm{d}c/c = \tan \alpha \mathrm{d}\alpha \tag{6.31}$$

Eliminating successively $\mathrm{d}h_0$ between Eqs (6.30b) and (6.30c), $\mathrm{d}\rho/\rho$ between Eqs (6.28) and (6.31), and finally $\mathrm{d}\alpha$ from the resulting equations gives

$$\frac{\mathrm{d}c}{c}\left(1+\frac{c_\theta}{U}\right) = -\sin^2\alpha\left[\frac{d(rc_\theta)}{rc_\theta}+\left(1+\frac{c_\theta}{U}+M_x^2\right)\frac{\mathrm{d}r}{r}\right] \tag{6.32}$$

where $M_x = M\cos\alpha = c\cos\alpha/\sqrt{\gamma RT}$. and the static temperature

$$T = T_3 = T_{03} - c_3^2/(2C_p) = T_{02} - \left[U(c_{\theta 2}+c_{\theta 3})+(1/2)c_3^2\right]/C_p \tag{6.33}$$

The verification of Eq. (6.32) is left as an exercise for the diligent student.

Provided that the exit flow angle α_3 at $r = r_\mathrm{m}$ and the mean rotor blade speeds are specified, the velocity distribution, etc., at rotor exit can be readily computed from these equations.

6.7 Off-design performance of a stage

A turbine stage is considered here although, with some minor modifications, the analysis can be made applicable to a compressor stage.

Assuming the flow is at constant entropy, apply the radial equilibrium equation, Eq. (6.6a), to the flow on both sides of the rotor:

$$\frac{\mathrm{d}h_{03}}{\mathrm{d}r} = \frac{\mathrm{d}h_{02}}{\mathrm{d}r} - \Omega\frac{\mathrm{d}}{\mathrm{d}r}(rc_{\theta 2}+rc_{\theta 3}) = c_{x3}\frac{\mathrm{d}c_{x3}}{\mathrm{d}r}+\frac{c_{\theta 3}}{r}\frac{\mathrm{d}}{\mathrm{d}r}(rc_{\theta 3})$$

Therefore,

$$c^{x2}\frac{\mathrm{d}c_{x2}}{\mathrm{d}r}+\left(\frac{c_{\theta 2}}{r}-\Omega\right)\frac{\mathrm{d}}{\mathrm{d}r}(rc_{\theta 2}) = c_{x3}\frac{\mathrm{d}c^{x3}}{\mathrm{d}r}+\left(\frac{c^{\theta 3}}{r}+\Omega\right)\frac{\mathrm{d}}{\mathrm{d}r}(rc_{\theta 3})$$

Substituting $c_{\theta 3} = c_{x3}\tan\beta_3 - \Omega r$ into this equation, after some simplification,

$$c_{x2}\frac{\mathrm{d}c_{x2}}{\mathrm{d}r}+\left(\frac{c_{\theta 2}}{r}-\Omega\right)\frac{\mathrm{d}}{\mathrm{d}r}(rc_{\theta 2}) = c_{x3}\frac{\mathrm{d}c_{x3}}{\mathrm{d}r}+\frac{c_{x3}}{r}\tan\beta_3\frac{\mathrm{d}}{\mathrm{d}r}(rc_{x3}\tan\beta_3)-2\Omega c_{x3}\tan\beta_3 \tag{6.34}$$

In a particular problem, the quantities c_{x2}, $c_{\theta 2}$, β_3 are known functions of radius and Ω can be specified. Equation (6.34) is thus a first-order differential equation in which c_{x3} is unknown and may best be solved, in the general case, by numerical iteration. This procedure requires a guessed value of c_{x3} at the hub and, by applying Eq. (6.34) to a small interval of radius Δr, a new value of c_{x3} at radius $r_\mathrm{h}+\Delta r$ is found. By repeating this calculation for successive increments of radius, a complete velocity profile c_{x3} can be determined. Using the continuity relation

$$\int_{r_\mathrm{k}}^{r_\mathrm{t}} c_{x3}r\mathrm{d}r = \int_{r_\mathrm{k}}^{r_\mathrm{t}} c_{x2}r\mathrm{d}r$$

this initial velocity distribution can be integrated and a new, more accurate, estimate of c_{x3} at the hub is then found. Using this value of c_{x3}, the step-by-step procedure is repeated as described and again checked by continuity. This iterative process is normally rapidly convergent and, in most cases, three cycles of the calculation enable a sufficiently accurate exit velocity profile to be found.

The off-design performance may be obtained by making the approximation that the rotor relative exit angle β_3 and the nozzle exit angle α_2 remain constant at a particular radius with a change in mass flow. This approximation is not unrealistic as cascade data (see Chapter 3) suggest that fluid angles at outlet from a blade row alter very little with change in incidence up to the stall point.

Although any type of flow through a stage may be successfully treated using this method, rather more elegant solutions in closed form can be obtained for a few special cases. One such case is outlined next for a free-vortex turbine stage whilst other cases are already covered by Eqs (6.21)–(6.23).

6.8 Free-vortex turbine stage

Suppose, for simplicity, a free-vortex stage is considered where, at the design point, the flow at rotor exit is completely axial (i.e., without swirl). At stage entry, the flow is again supposed completely axial and of constant stagnation enthalpy h_{01}. Free-vortex conditions prevail at entry to the rotor, $rc_{\theta 2} = rc_{x2} \tan \alpha_2 = \text{constant}$. The problem is to find how the axial velocity distribution at rotor exit varies as the mass flow is altered away from the design value.

At off-design conditions, the relative rotor exit angle β_3 is assumed to remain equal to the value β^* at the design mass flow (* denotes design conditions). Thus, referring to the velocity triangles in Figure 6.7, at off-design conditions the swirl velocity $c_{\theta 3}$ is evidently nonzero:

$$c_{\theta 3} = c_{x3} \tan \beta_3 - U = c_{x3} \tan \beta_3^* - \Omega r \tag{6.35}$$

At the design condition, $c_{\theta 3}^* = 0$ and so

$$c_{x3}^* \tan \beta_3^* = \Omega r \tag{6.36}$$

Combining Eqs (6.35) and (6.36),

$$c_{\theta 3} = \Omega r \left(\frac{c^{x3}}{c_{x3}^*} - 1 \right) \tag{6.37}$$

The radial equilibrium equation at rotor outlet gives

$$\frac{\mathrm{d}h_{03}}{\mathrm{d}r} = c_{x3} \frac{\mathrm{d}c_{x3}}{\mathrm{d}r} + \frac{c_{\theta 3}}{r} \frac{\mathrm{d}}{\mathrm{d}r}(rc_{\theta 3}) = -\Omega \frac{\mathrm{d}}{\mathrm{d}r}(rc_{\theta 3}) \tag{6.38}$$

after combining with Eq. (6.33), noting that $\mathrm{d}h_{02}/\mathrm{d}r = 0$ and that $(\mathrm{d}/\mathrm{d}r)(rc_{\theta 2}) = 0$ at all mass flows. From Eq. (6.37),

$$\Omega + \frac{c_{\theta 3}}{r} = \Omega \frac{c_{x3}}{c_{x3}^*}, \quad rc_{\theta 3} = \Omega r^2 \left(\frac{c_{x3}}{c_{x3}^*} - 1 \right)$$

which when substituted into Eq. (6.38) gives

$$\frac{\mathrm{d}c_{x3}}{\mathrm{d}r} = \frac{\Omega^2}{c_{x3}^*} \left[2r \left(\frac{c_{x3}}{c_{x3}^*} - 1 \right) + \frac{r^2}{c_{x3}^*} \frac{\mathrm{d}c_{x3}}{\mathrm{d}r} \right]$$

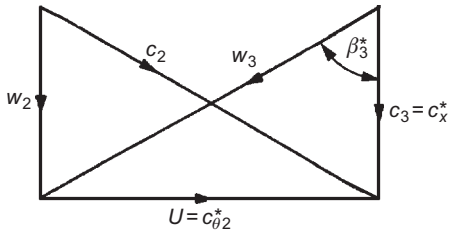

(a) Design

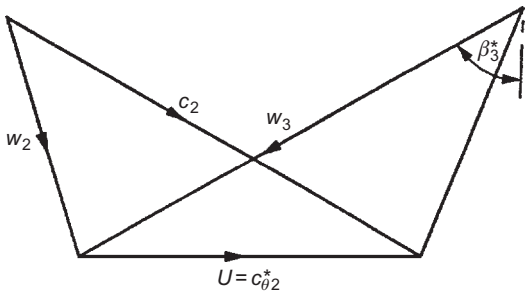

(b) Off-design

FIGURE 6.7

Design (a) and off-design (b) velocity triangles for a free-vortex turbine stage.

After rearranging,

$$\frac{\mathrm{d}c_{x3}}{c_{x3} - c_{x3}^*} = \frac{-\,d(\Omega^2 r^2)}{(c_{x3}^{*2} + \Omega^2 r^2)} \tag{6.39}$$

Equation (6.39) is immediately integrated in the form

$$\frac{c_{x3} - c_{x3}^*}{c_{x3\mathrm{m}} - c_{x3}^*} = \frac{c_{x3}^{*2} + \Omega^2 r_{\mathrm{m}}^2}{c_{x3}^{*2} + \Omega^2 r^2} \tag{6.40a}$$

where $c_{x3} = c_{x3\mathrm{m}}$ at $r = r_{\mathrm{m}}$. Equation (6.40a) is more conveniently expressed in a nondimensional form by introducing flow coefficients $\phi = c_{x3}/U_{\mathrm{m}}$, $\phi^* = c_{x3}^*/U_{\mathrm{m}}$, and $\phi_{\mathrm{m}} = c_{x3\mathrm{m}}/U_{\mathrm{m}}$. Thus,

$$\frac{\phi/\phi^* - 1}{\phi_{\mathrm{m}}/\phi^* - 1} = \frac{\phi^{*2} + 1}{\phi^{*2} + (r/r_{\mathrm{m}})^2} \tag{6.40b}$$

If r_{m} is the mean radius, then $c_{x3\mathrm{m}} \cong c_{x1}$ and, therefore, ϕ_{m} provides an approximate measure of the overall flow coefficient for the machine (*note*: c_{x1} is uniform).

The results of this analysis are shown in Figure 6.8 for a representative design flow coefficient $\phi^* = 0.8$ at several different off-design flow coefficients ϕ_{m}, with $r/r_{\mathrm{m}} = 0.8$ at the hub and $r/r_{\mathrm{m}} = 1.2$ at the tip. It is apparent for values of $\phi_{\mathrm{m}} < \phi^*$ that c_{x3} increases from hub to tip; conversely for $\phi_{\mathrm{m}} > \phi^*$, c_{x3} decreases towards the tip.

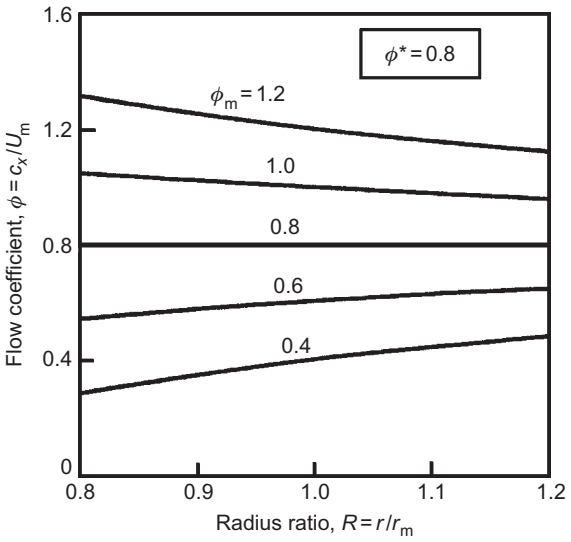

FIGURE 6.8

Off-design rotor exit flow coefficients.

The foregoing analysis is only a special case of the more general analysis of free-vortex turbine and compressor flows (Horlock & Dixon, 1966), in which rotor exit swirl, $rc^*_{\theta 3}$ is constant (at design conditions), is included. However, from Horlock and Dixon, it is quite clear that even for fairly large values of α^*_{3m}, the value of ϕ is little different from the value found when $\alpha^*_3 = 0$, all other factors being equal. In Figure 6.8, values of ϕ are shown when $\alpha^*_{3m} = 31.4^\circ$ at $\phi_m = 0.4$ ($\phi^* = 0.8$) for comparison with the results obtained when $\Delta_0 = (1/2)(c_{x\infty 1} - c_{x\infty 2})$.

It should be noted that the rotor efflux flow at off-design conditions is *not* a free vortex.

6.9 Actuator disc approach

In the radial equilibrium design method it was assumed that all radial motion took place within the blade row. However, in most turbomachines of low hub−tip ratio, appreciable radial velocities can be measured outside of the blade row. Figure 6.9, taken from a review paper by Hawthorne and Horlock (1962), shows the distribution of the axial velocity component at various axial distances upstream and downstream of an isolated row of stationary inlet guide vanes. This figure clearly illustrates the appreciable redistribution of flow in regions outside of the blade row and that radial velocities must exist in these regions. For the flow through a single row of rotor blades, the variation in pressure (near the hub and tip) and variation in axial velocity (near the hub), both as functions of axial position, are shown in Figure 6.10, also taken from Hawthorne and Horlock. Clearly, radial equilibrium is not established entirely within the blade row.

A more accurate form of flow analysis than radial equilibrium theory is obtained with the *actuator disc* concept. The idea of an actuator disc is quite old and appears to have been first used in the

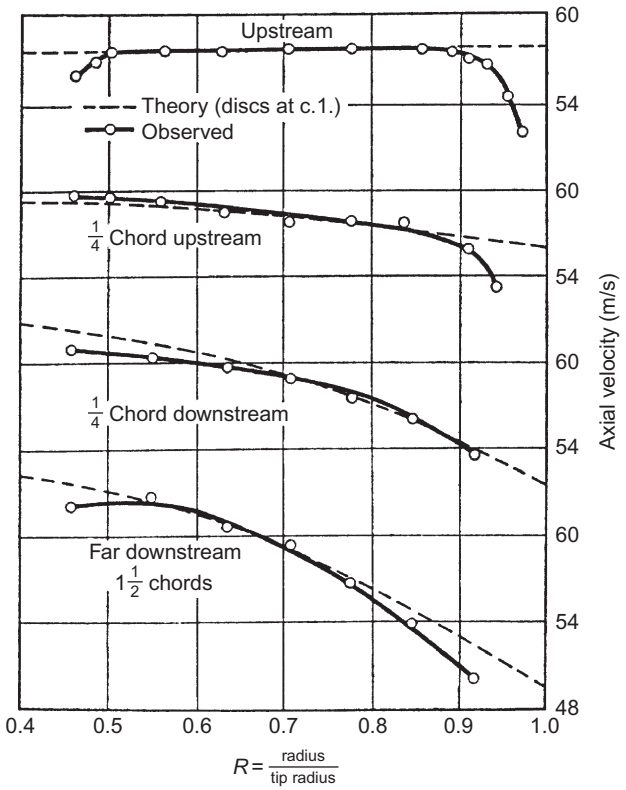

FIGURE 6.9

Variation of the distribution in axial velocity through a row of guide vanes.

(*Adapted from Hawthorne & Horlock, 1962*)

theory of propellers; it has since evolved into a fairly sophisticated method of analyzing flow problems in turbomachinery. To appreciate the idea of an actuator disc, imagine that the axial width of each blade row is shrunk while, at the same time, the space–chord ratio, the blade angles, and overall length of machine are maintained constant. As the deflection through each blade row for a given incidence is, apart from Reynolds number and Mach number effects (cf. Chapter 3 on cascades), fixed by the cascade geometry, a blade row of reduced width may be considered to affect the flow in exactly the same way as the original row. In the limit as the axial width vanishes, the blade row becomes, conceptually, a *plane discontinuity* of tangential velocity—the actuator disc. Note that while the tangential velocity undergoes an abrupt change in direction, the axial and radial velocities are continuous across the disc.

An isolated actuator disc is depicted in Figure 6.11 with radial equilibrium established at fairly large axial distances from the disc. An approximate solution to the velocity fields upstream and downstream of the actuator can be found in terms of the axial velocity distributions *far upstream* and *far downstream* of the disc. The detailed analysis exceeds the scope of this book, involving the solution of the

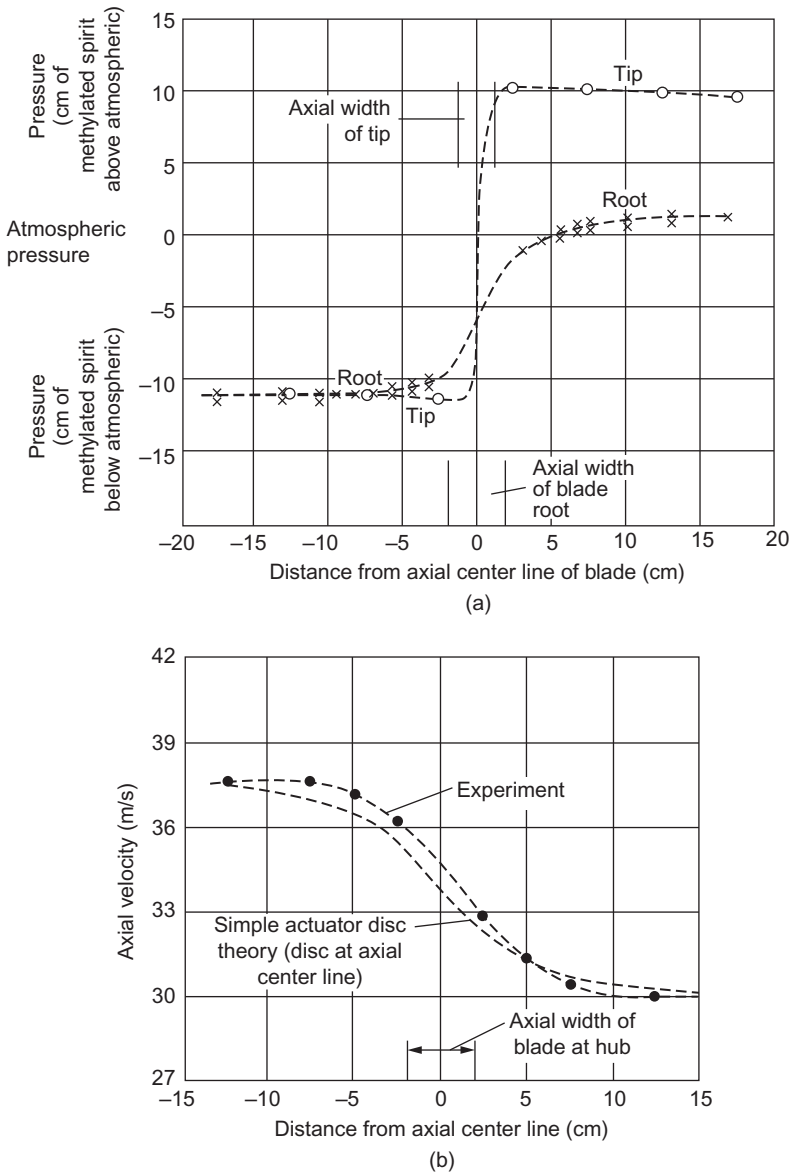

FIGURE 6.10

(a) Pressure variation in the neighborhood of a rotating blade row and (b) axial velocity at the hub in the neighborhood of a rotating blade row.

(*Adapted from Hawthorne & Horlock, 1962*)

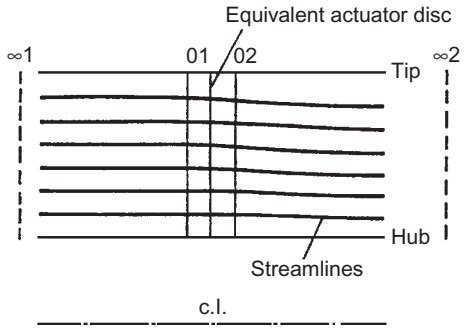

FIGURE 6.11

The actuator disc assumption.

(*After Horlock, 1958*)

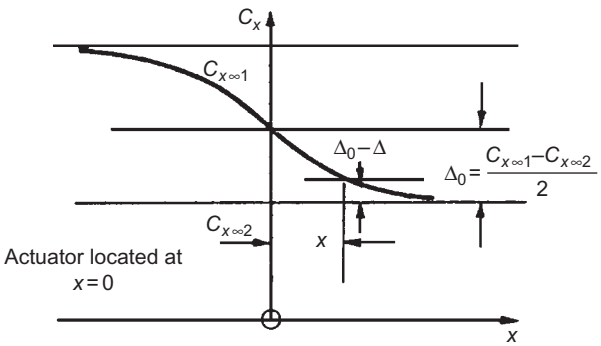

FIGURE 6.12

Variation in axial velocity with axial distance from the actuator disc.

equations of motion, the equation of continuity, and the satisfaction of boundary conditions at the walls and disc. The form of the approximate solution is of considerable interest and is quoted here.

For convenience, conditions far upstream and far downstream of the disc are denoted by subscripts $\infty 1$ and $\infty 2$, respectively (Figure 6.11). Actuator disc theory proves that at the disc ($x = 0$), at any given radius, the axial velocity is equal to the *mean* of the axial velocities at $\infty 1$ and $\infty 2$ at the *same* radius, or

$$c_{x01} = c_{x02} = \frac{1}{2}(c_{x\infty 1} + c_{x\infty 2}) \tag{6.41}$$

Subscripts 01 and 02 denote positions immediately upstream and downstream, respectively, of the actuator disc. Equation (6.41) is known as the *mean-value rule*.

In the downstream flow field ($x \geq 0$), the *difference* in axial velocity at some position (x, r_A) to that at position ($x = \infty$, r_A) is conceived as a velocity perturbation. Referring to Figure 6.12, the axial velocity perturbation at the disc ($x = 0$, r_A) is denoted by Δ_0 and at position (x, r_A) by Δ. The important

result of actuator disc theory is that velocity perturbations *decay exponentially* away from the disc. This is also true for the upstream flow field ($x \leq 0$). The result obtained for the decay rate is

$$\Delta/\Delta_0 = 1 - \exp[\mp \pi x/(r_t - r_h)] \tag{6.42}$$

where the minus and plus signs apply to the flow regions $x \geq 0$ and $x \leq 0$, respectively. Equation (6.42) is often called the *settling-rate rule*. Since $c_{x1} = c_{x01} + \Delta$, $c_{x2} = c_{x02} - \Delta$ and noting that $\Delta_0 = (1/2)(c_{x\infty 1} - c_{x\infty 2})$, Eqs (6.41) and (6.42) combine to give

$$c_{x1} = c_{x\infty 1} - \frac{1}{2}(c_{x\infty 1} - c_{x\infty 2})\exp\left[\pi x/(r_t - r_h)\right] \tag{6.43a}$$

$$c_{x2} = c_{x\infty 2} + \frac{1}{2}(c_{x\infty 1} - c_{x\infty 2})\exp\left[-\pi x/(r_t - r_h)\right] \tag{6.43b}$$

At the disc, $x = 0$, Eqs (6.43a) and (6.43b) reduce to Eq. (6.41). It is of particular interest to note, in Figures 6.9 and 6.10, how closely isolated actuator disc theory compares with experimentally derived results.

Blade row interaction effects

The spacing between consecutive blade rows in axial turbomachines is usually sufficiently small for mutual flow interactions to occur between the rows. This interference may be calculated by an extension of the results obtained from isolated actuator disc theory. As an illustration, the simplest case of two actuator discs situated a distance δ apart from one another is considered. The extension to the case of a large number of discs is given in Hawthorne and Horlock (1962).

Consider each disc in turn as though it was in isolation. Referring to Figure 6.13, disc A, located at $x = 0$, changes the far upstream velocity $c_{x\infty 1}$ to $c_{x\infty 2}$ far downstream. Let us suppose for simplicity that the effect of disc B, located at $x = \delta$, exactly cancels the effect of disc A (i.e., the velocity far upstream of disc B is $c_{x\infty 2}$, which changes to $c_{x\infty 1}$ far downstream). Thus, for disc A in isolation,

$$c_x = c_{x\infty 1} - \frac{1}{2}(c_{x\infty 1} - c_{x\infty 2})\exp\left[\frac{-\pi|x|}{H}\right], \quad x \leq 0 \tag{6.44}$$

$$c_x = c_{x\infty 2} + \frac{1}{2}(c_{x\infty 1} - c_{x\infty 2})\exp\left[\frac{-\pi|x|}{H}\right], \quad x \geq 0 \tag{6.45}$$

where $|x|$ denotes modulus of x and $H = r_t - r_h$.

For disc B in isolation,

$$c_x = c_{x\infty 2} - \frac{1}{2}(c_{x\infty 2} - c_{x\infty 1})\exp\left[\frac{-\pi|x-\delta|}{H}\right], \quad x \leq \delta \tag{6.46}$$

$$c_x = c_{x\infty 1} + \frac{1}{2}(c_{x\infty 2} - c_{x\infty 1})\exp\left[\frac{-\pi|x-\delta|}{H}\right], \quad x \geq \delta \tag{6.47}$$

Now the combined effect of the two discs is most easily obtained by extracting from the preceding four equations the velocity perturbations appropriate to a given region and adding these to the

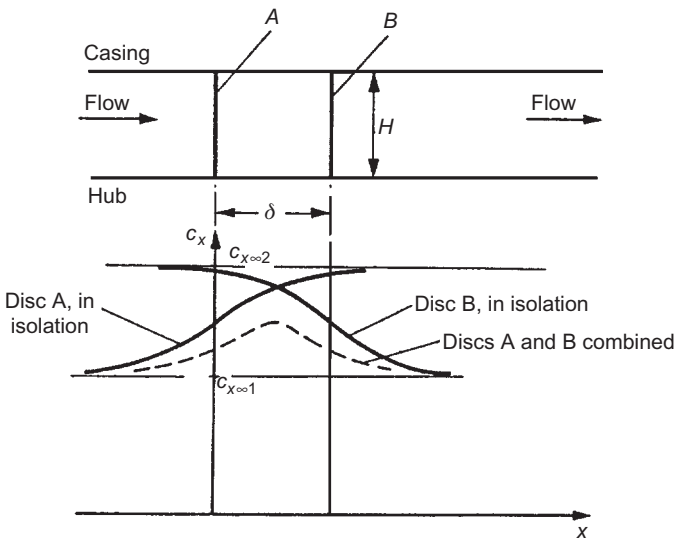

FIGURE 6.13

Interaction between two closely spaced actuator discs.

related radial equilibrium velocity for $x \leq 0$, and to $c_{x\infty 1}$ the perturbation velocities from Eqs (6.44) and (6.46):

$$c_x = c_{x\infty 1} - \frac{1}{2}(c_{x\infty 1} - c_{x\infty 2})\left\{\exp\left[\frac{-\pi|x|}{H}\right] - \exp\left[\frac{-\pi|x-\delta|}{H}\right]\right\} \tag{6.48}$$

For the region $0 \leq x \leq \delta$,

$$c_x = c_{x\infty 2} + \frac{1}{2}(c_{x\infty 1} - c_{x\infty 2})\left\{\exp\left[\frac{-\pi|x|}{H}\right] + \exp\left[\frac{-\pi|x-\delta|}{H}\right]\right\} \tag{6.49}$$

For the region $x \geq \delta$,

$$c_x = c_{x\infty 1} + \frac{1}{2}(c_{x\infty 1} - c_{x\infty 2})\left\{\exp\left[\frac{-\pi|x|}{H}\right] - \exp\left[\frac{-\pi|x-\delta|}{H}\right]\right\} \tag{6.50}$$

Figure 6.13 indicates the variation of axial velocity when the two discs are regarded as *isolated* and when they are *combined*. It can be seen from these equations that as the gap between these two discs is increased, the perturbations tend to vanish. Thus, in turbomachines where δ/r is fairly small (e.g., the front stages of aircraft axial compressors or the rear stages of condensing steam turbines), interference effects are strong and then the simpler radial equilibrium analysis is inadequate.

Application to compressible flow

An elegant analysis to the problem of compressible flow through a multistage turbomachine has been developed by Lewis (1995) using an innovative application of actuator disc theory, which

models the influence of density gradients on the meridional flow through the turbomachine. The analysis takes advantage of previous solutions for the flow induced by source discs and the analogy between compressible flows and incompressible flows with source distributions. The following conclusions were drawn by Lewis:

1. Vortex actuator disc theory can be extended to include compressibility effects, which may be superimposed linearly upon rotational effects. The influence of density gradients upon the meridional flow is considerable for typical free-vortex axial turbine stages.
2. Plane actuator discs can be easily replaced by *smeared actuator discs* distributed uniformly between the leading and trailing edge planes of each blade row.
3. A simple analysis extending cylindrical compressible actuator disc theory to axial turbines with flared annuli has been completed for application to multistage turbines.
4. The method is ideal for rapid computational analysis.

Figure 6.14 illustrates the predicted axial velocity distribution at the hub and tip radii of a model turbine stage (Table 6.4 gives the main details) resulting from axially smeared actuator discs to represent the blade rows. This smearing spreads the density gradient fairly realistically between the blade leading and trailing edges. The rather large change in axial velocity observed is the result of the overall decrease in density—the stage chosen was cylindrical. Usual design practice would be to increase the annular area to maintain a more or less constant value of axial velocity.

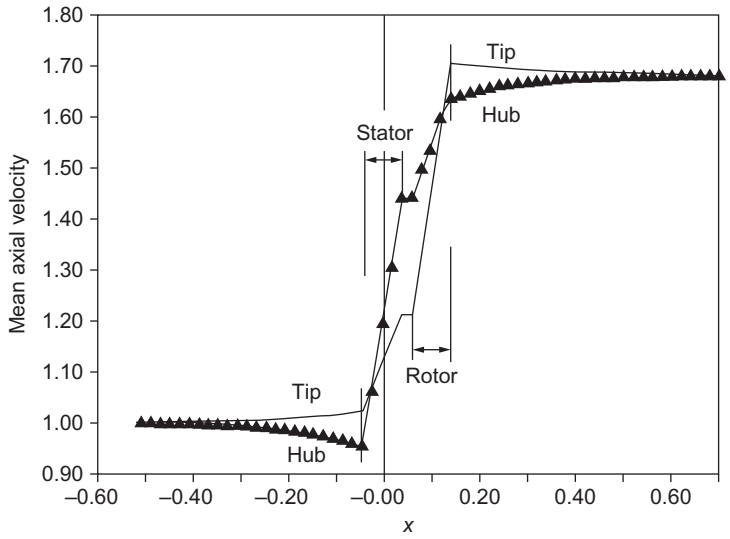

FIGURE 6.14

Flow through turbine stage in cylindrical annulus with smeared actuator disc representation of the blade rows .

(*Adapted from Lewis, 1995 with the permission of Elsevier Science Ltd.*)

Table 6.4 Specification of Model Turbine Stage

Hub/tip ratio, r_h/r_t	0.6
Flow coefficient at r.m.s. radius	0.5
Work coefficient at r.m.s. radius	1.0
Exit mach number M_{2h} at root radius	1.0
Total-to-total efficiency	92%
Zero swirl flow upstream of stator	
Free-vortex flow downstream of stator	
Perfect gas (air) assumed	

6.10 Computational through-flow methods

Actuator disc theory gives some understanding of the meridional through-flow in turbomachines of simple geometry and flow conditions, but its application to design and analysis is now quite limited. Numerous computational methods have evolved for predicting the meridional flow field for single-stage and multistage turbomachines with nonaxial annulus lines, compressible flow, and blade losses. These are known as through-flow methods and are discussed below.

In any through-flow method, the equations of motion to be solved are simplified. First, the flow is taken to be steady in both the absolute and relative frames of reference. Second, the flow is assumed to be axisymmetric. Outside of the blade rows, the effects of wakes from the upstream blade row are "mixed out" so as to give uniform circumferential conditions. Within the blade rows, the effects of the blades themselves are modeled by passage-averaged body forces and loss coefficients. Clearly, with these major assumptions, solutions from through-flow methods are only approximations to the real flow but, if used appropriately, they can accurately reproduce the meridional variations.

Three techniques for solving through-flow problems are

1. *Stream function methods*, in which a *stream function* is employed as the primary variable. This approach has the advantage of simplifying the numerics by satisfying the continuity equation via the boundary conditions of the stream function at the hub and casing. However, it fails when the flow becomes transonic.
2. *Matrix through-flow or finite difference solutions* (Marsh, 1968), in which computations of the radial equilibrium flow field are made at a number of locations *within* each blade row as well as at the leading and trailing edges and outside of the blade row. An illustration of a typical computing mesh for a single blade row taken from Macchi (1985) is shown in Figure 6.15.
3. *Time-marching solutions of the streamline curvature equation* (Denton, 1985), in which the computation starts from some assumed flow field and the governing equations are marched forward with time. The method requires a large number of iterations to converge but with modern computers, a solution can be obtained within a matter of seconds.

As stated in Denton and Dawes (1999), the time-marching streamline curvature method remains the dominant numerical scheme because of its simplicity and ability to cope with mixed subsonic

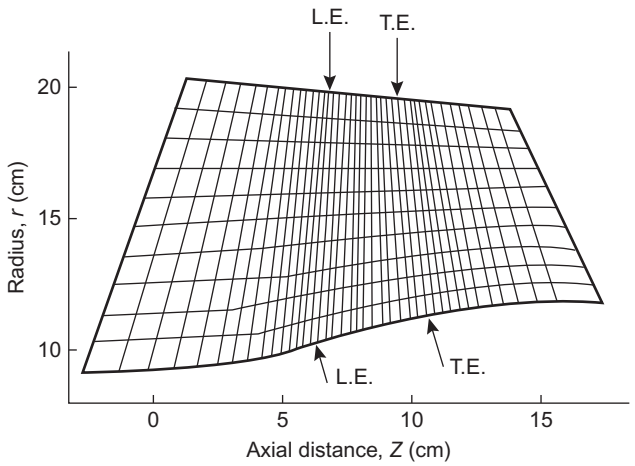

FIGURE 6.15

Typical computational mesh for a single blade row.

(*Adapted from Macchi, 1985*)

and supersonic flows. However, all three approaches essentially solve the same equations of momentum, energy, continuity, and state, for axisymmetric flow through a turbomachine with varying hub and tip radii.

A form of the streamline curvature equation can be derived following the approach presented in Section 6.2. Consider the axisymmetric stream surface and components of acceleration shown in Figure 6.16. In this case, the radial velocity component cannot be neglected and the stagnation enthalpy is written as

$$h_0 = h + \frac{1}{2}(c_{\mathrm{m}}^2 + c_\theta^2), \quad \text{where } c_{\mathrm{m}}^2 = c_x^2 + c_{\mathrm{r}}^2 \tag{6.51a}$$

Note that in this section, c_{m} represents the *meridional velocity*, which is a variable, and not the mean velocity as it was defined earlier in this chapter. Applying the momentum equation in the radial direction (Figure 6.16),

$$-\frac{1}{\rho}\frac{\partial p}{\partial r} = -\frac{c_\theta^2}{r} + \frac{c_{\mathrm{m}}^2}{R_{\mathrm{c}}}\cos\phi + c_{\mathrm{m}}\frac{\partial c_{\mathrm{m}}}{\partial m}\sin\phi \tag{6.51b}$$

Using the second law of thermodynamics,

$$\frac{\partial h}{\partial r} = T\frac{\partial s}{\partial r} + \frac{1}{\rho}\frac{\partial p}{\partial r} \tag{6.51c}$$

Combining Eqs (6.51a), (6.51b), and (6.51c) gives

$$\frac{\partial h_0}{\partial r} - T\frac{\partial s}{\partial r} = \mathrm{c_m}\frac{\partial \mathrm{c_m}}{\partial r} + c_\theta\frac{\partial c_\theta}{\partial \mathrm{r}} + \frac{c_\theta^2}{r} - \frac{c_{\mathrm{m}}^2}{R_{\mathrm{c}}}\cos\phi - \mathrm{c_m}\frac{\partial \mathrm{c_m}}{\partial m}\sin\phi \tag{6.52a}$$

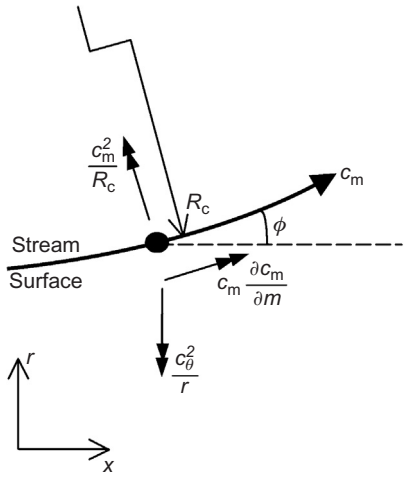

FIGURE 6.16

Acceleration components for a point on an axisymmetric stream surface.

This equation can be rewritten as

$$\frac{\partial h_0}{\partial r} - T\frac{\partial s}{\partial r} = \mathrm{c_m}\frac{\partial \mathrm{c_m}}{\partial r} + \frac{c_\theta}{r}\frac{\partial (rc_\theta)}{\partial r} - \frac{c_m^2}{R_c}\cos\phi - \mathrm{c_m}\frac{\partial \mathrm{c_m}}{\partial m}\sin\phi. \tag{6.52b}$$

The above streamline curvature equation reduces to simple radial equilibrium, Eq. (6.6a), when the radial velocity is zero, since $\phi \to 0$, $R_c \to \infty$, $c_m \to c_x$. The last term on the right-hand side of Eq. (6.52b) represents the radial component of acceleration along the stream surface. The term before this represents the radial component of centripetal acceleration due to meridional curvature. Equation (6.52b) can be solved numerically to find the variations of c_θ and c_m for given stagnation enthalpy and entropy variations. The solution is combined with the continuity equation to give the velocity levels that match the total mass flow using

$$\dot{m} = \int_h^t \rho c_m \mathrm{d}A_n \tag{6.53}$$

Along the streamlines, the tangential velocity, c_θ, is found from specified flow angles within blade rows and conservation of angular momentum outside of blade rows, $rc_\theta = \text{constant}$. The Euler equation can be used to find the variation of stagnation enthalpy within blade rows, $h_0 - r\Omega c_\theta = \text{constant}$. The entropy variation along streamlines is zero outside of blade rows and specified via loss coefficients within the blade rows.

In practice, the solution procedure is further complicated as the directions of the streamlines are not known at the outset and the method must iterate further to find the pitch angle ϕ at each location, such that the streamline curvature equation balances. In general, initial streamline paths are assumed and these are adjusted as the solution progresses. Figure 6.17 shows an example solution for a single-stage fan rig using a code based on the method by Denton (1978).

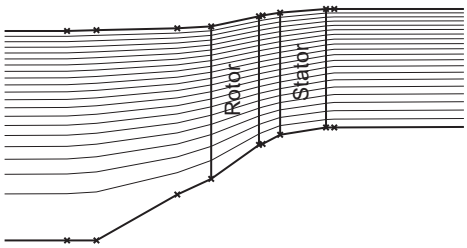

FIGURE 6.17

Solution for a fan test rig from a time-marching through-flow computation.

Through-flow methods can be applied in *design* or *analysis* mode. In analysis mode, the blade row flow angles and loss coefficients are specified and the method determines the velocity field and the spanwise variation of work from the rotor blades. In design mode, the main difference is that the work distribution will be specified and the flow angles and velocity field are determined.

6.11 3D flow features

Radial equilibrium and through-flow methods determine the meridional variations in the velocity field, but they assume that the turbomachinery flow field is axisymmetric. Cascade analysis and blade-to-blade computational methods consider the flow variations across the blade passages, but they neglect spanwise variations and radial flows (see Chapter 3). These two views of a turbomachine are very useful and both are essential in the design process, but in reality the flow field in all axial turbomachinery, to some degree, varies in the axial, radial, and tangential directions. The flow features that lead to fully 3D variations are discussed below.

Secondary flow

When a fluid particle possessing *rotation* is turned (e.g., by a cascade), its axis of rotation is deflected in a direction perpendicular to the direction of turning. The rotation of the fluid particles is known as *vorticity*, which is a vector quantity with a direction along the axis of rotation. The result of deflecting the axis of rotation is a component of vorticity in the direction of the flow streamlines, and whenever this occurs there are *secondary flows*.

Consider the flow at inlet to the guide vanes of a compressor to be completely axial and with a velocity profile as illustrated in Figure 6.18. This velocity profile is nonuniform as a result of friction between the fluid and the wall; the vorticity of this boundary layer is normal to the approach velocity c_1 and of magnitude

$$\omega_1 = \frac{\partial c_1}{\partial z} \tag{6.54}$$

where z is distance from the wall.

The direction of ω_1 follows from the right-hand screw rule and it will be observed that ω_1 is in opposite directions on the two annulus walls. This vector is turned by the cascade, thereby

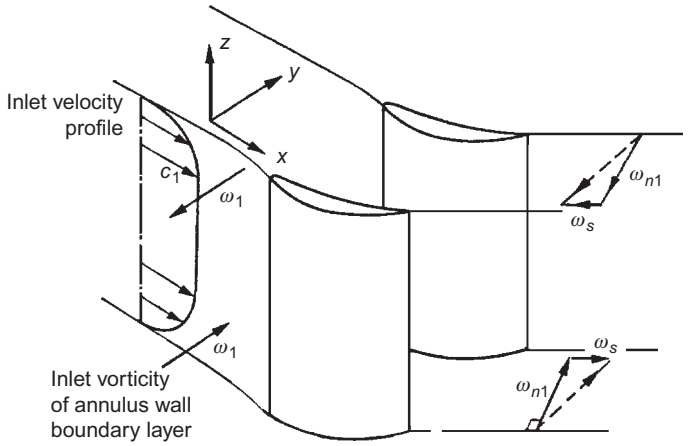

FIGURE 6.18

Secondary vorticity produced by a row of guide vanes.

generating *secondary vorticity* parallel to the outlet stream direction. If the deflection angle ε is not large, the magnitude of the secondary vorticity ω_s is, approximately,

$$\omega_s = -2\varepsilon \frac{\partial c_1}{\partial z} \tag{6.55}$$

A swirling motion of the cascade exit flow is associated with the vorticity ω_s, which is in opposite directions for the two wall boundary layers. This generates simultaneous velocity variations in the spanwise and tangential directions that cannot be captured within two-dimensional models of the flow field (see Dixon, 1974).

The secondary flow structure in a blade passage is further complicated by the flow around the leading edge, as illustrated in Figure 6.19. The vorticity within the annulus wall boundary layer is split into two vortices as the flow stagnates. One vortex enters the blade passage near the pressure surface and the other vortex enters beside the suction surface. The vortex that starts beside the pressure surface is rapidly swept towards the suction surface by the cross-passage pressure gradient and forms what is known as the passage vortex. The other vortex, known as the counter vortex, sticks to the suction surface hub. In addition to these vortices, boundary layer fluid on the endwalls is swept from the pressure surface towards the suction surface. The result is a collection of highly rotational fluid on the suction surface near the hub and casing endwalls. This fluid leads to increased loss through viscous shear and mixing and forms a 3D wake structure downstream of the blades.

As well as increasing the loss, secondary flow affects the variation of exit flow angle from a blade row. The flow is *overturned* close to the endwalls, where the boundary layer fluid has been strongly turned by the cross-passage pressure gradients, and *underturned* some distance away from the endwalls, where the influence of the passage vortex is stronger. Hawthorne (1955) developed some of the first models of secondary flow in turbomachinery and showed how the exit flow angle distribution could be calculated using theoretical analysis. Figure 6.20 shows a comparison by Horlock (1963) between corrected exit flow angles calculated using such an analysis and

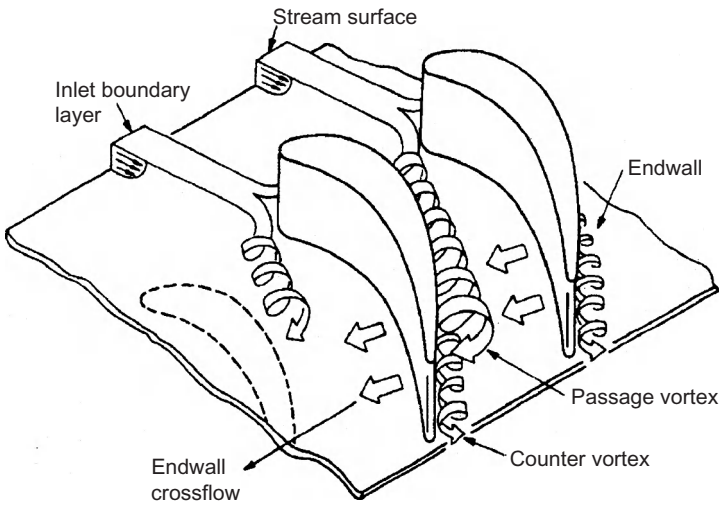

FIGURE 6.19

Secondary flow structure within a blade passage.

(*Adapted from Langston, 1980*)

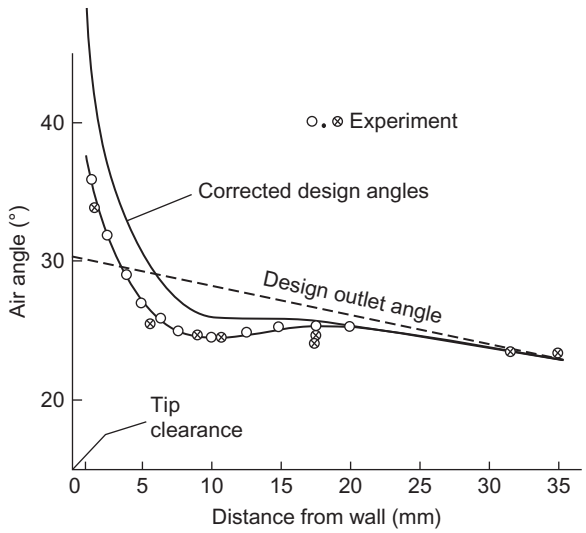

FIGURE 6.20

Exit air angle from inlet guide vanes.

(*Adapted from Horlock, 1963*)

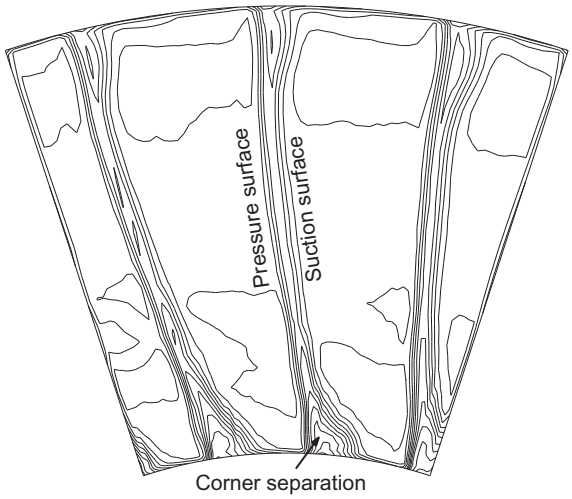

FIGURE 6.21

Stagnation pressure contours measured downstream of a rig compressor stage.

experimental results. The regions of underturning and overturning of the flow are predicted, although the magnitude of the variation is not the same as measured.

Note that secondary flow phenomena occur in all axial turbomachines. In turbines they can be stronger because of the large amount of flow turning and the high cross-passage pressure gradients that exist. However, in compressors, secondary flow effects are often more apparent and can have greater consequences because of the thick boundary layers on the annulus walls and the highly adverse pressure gradients in the streamwise direction.

Figure 6.21 shows stagnation pressure contours measured downstream of a stator row in a compressor test rig. This shows the increased regions of loss near the endwalls beside the suction surfaces of the stator blades. In the case shown the aspect ratio of the blading is high and the majority of the wakes are still quite two-dimensional. In compressors, the low momentum fluid from the endwall boundary layers often separates on the suction surface due to the high level of diffusion there. This is known as a *corner separation*, which is also visible in Figure 6.21.

Figure 6.22 shows measured contours of normalized total pressure loss coefficient downstream of a turbine cascade trailing edge, from Pullan and Harvey (2008). Just downstream of the trailing edge, Figure 6.22(a), the wake is radial with a clear region of high loss around $z/b = 0.2$. This is the passage vortex, which has carried inlet endwall boundary layer fluid from upstream of the leading edge. This vortex overturns the flow below it and underturns the flow above it. Further downstream, Figure 6.22(b), this vortex combined with the other secondary flows present have distorted and twisted the wake.

Leakage flows

Turbomachinery blades require clearance gaps between the rotating and stationary components and these lead to leakage paths. Figure 6.23 illustrates the flow field over the tip of a rotor blade,

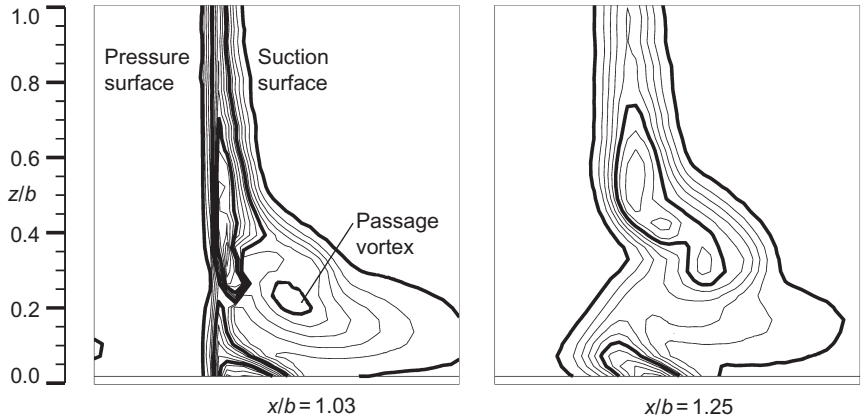

FIGURE 6.22

Stagnation pressure contours measured downstream of a turbine cascade: (a) just downstream of the trailing edge and (b) a quarter-chord downstream of the trailing edge.

(*Adapted from Pullan & Harvey, 2008*)

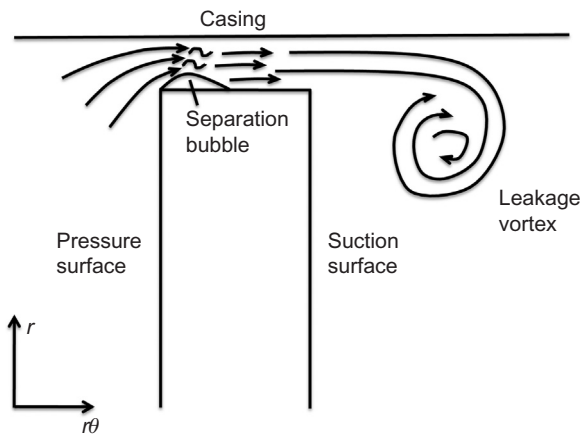

FIGURE 6.23

Schematic of tip leakage flow.

although the flow through a hub clearance gap of a stator blade cantilevered from the casing is similar. The leakage flow is driven by the pressure difference between the pressure surface and suction surface. The flow usually separates from the pressure side corner of the blade tip, which leads to a contraction of the flow area available. If the blade thickness is small compared to the tip gap, the leakage flow may not reattach (as is the case in many compressors). However, in thicker blades a separation bubble forms. The leakage flow then emerges as a high velocity jet at the suction surface tip, almost perpendicular to the free stream flow. The shear between the leakage jet and the free

stream flow generates a tip leakage vortex, with a rotation axis aligned with the streamwise direction. Losses are generated through viscous shear in the clearance gap as well as shear and mixing of the leakage jet with the free stream. Tip leakage losses typically account for around one-third of the total losses in a turbomachine (Denton, 1993). In addition, the leakage flow leads to blockage reducing the total mass flow and work transfer. In compressors, increased leakage significantly reduces the stability margin.

Note that some turbomachinery, particularly axial turbines, use a *shroud*. This is a band that covers and connects the blade tips (an example is shown in Figure 4.22). This prevents the tip leakage flow described above. However, a leakage path still exists above the shroud from the high-pressure end to the low-pressure end (upstream to downstream in a turbine). Shrouded blades are also significantly heavier with greater centrifugal stresses.

6.12 3D design

Until the 1980s, almost all turbomachinery design could be described as two-dimensional. Following the preliminary design using mean-line analysis, through-flow methods were used to set the spanwise variations and suitable blade sections were specified using cascade test results and blade-to-blade methods. Many turbomachines are still designed in this way without significant consideration of 3D effects. However, the development of 3D computational analysis (see following section) and the improved understanding of 3D flow have enabled more widespread application of 3D design effects. In general, these effects are used to control spanwise variations in the flow field and to reduce secondary flow features.

A detailed explanation of 3D design effects is given in Denton and Xu (1999). In this section, a brief outline is given of how different 3D design changes impact on the flow field and how they can be used to improve a design.

Sweep

Sweep is where the leading edge (or trailing edge) of a blade row is not perpendicular to the local meridional velocity, as illustrated in Figure 6.24(a). One effect of sweep is to reduce the effective velocity perpendicular to the blade surfaces and thus reduce the local blade loading and surface Mach numbers. This can be thought of in a similar way to the use of swept wings on aircraft to reduce transonic losses from shock waves. The normal velocity is reduced from c_m to $c_m \cos \lambda$, where λ is the leading edge sweep angle. For transonic compressor rotors, sweep can be applied to control the shock strength and position. However, this is a complex problem since a shock of a particular strength is required to provide the rotor pressure rise (see Chapter 5) and the position of the shock relative to the blade leading edge influences stability. As found by Wadia, Szucs, and Crall (1997), swept back transonic compressor blades have reduced stability margin because the shock is closer to the leading edge, whereas swept forward blades typically have better stability and they can still be designed to be highly efficient. Modern fan blades for large jet engines typically have a combination of both rearward sweep and forward sweep above mid span.

The effects of sweep near to the endwalls can be determined by considering the fact that pressure gradients perpendicular to the hub and casing must be small (Figure 6.24a). This is true

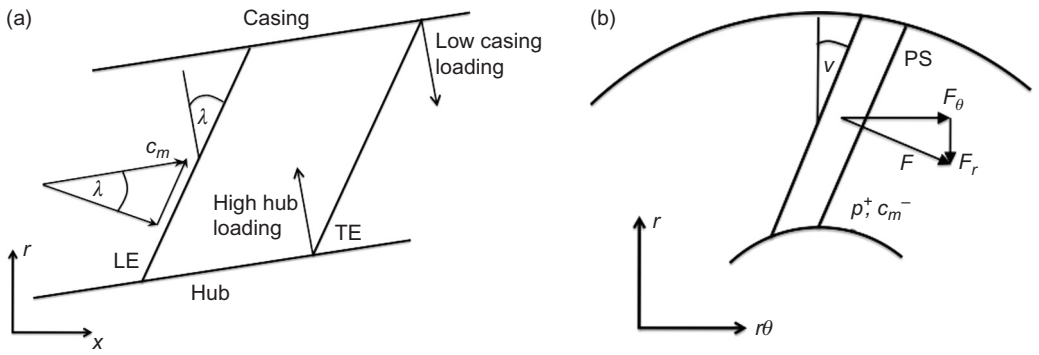

FIGURE 6.24

The application of 3D design: (a) sweep and (b) lean.

because there can be no fluid acceleration perpendicular to the endwalls. Given the normal pressure gradient is small, if the blade sweep is such that moving perpendicularly away from the endwall is moving towards a region with low loading (or where there is no blade) then at the endwall the loading must also be low. Conversely, if moving perpendicularly from the endwall is moving rearward in the blade to higher loading, the endwall loading must be high. Blades that are swept forward towards the hub and casing will, therefore, have reduced loading at the leading edge, which can be beneficial in reducing losses.

Lean

Lean is where a blade row is not stacked in the radial direction, as illustrated in Figure 6.24(b). It is more applicable to stators than rotors, since the centrifugal stresses in a rotor will usually demand radial stacking. The effect of lean is to introduce a radial component of the blade force, which acts in addition to the radial pressure gradient and hence modifies the spanwise velocity field. For example, if a stator blade row is leant with the pressure surface towards the hub, the static pressure at the hub will be increased and the meridional velocity will be decreased. This effect has been applied with great success in high aspect ratio steam turbines (Grant and Borthwick, 1987). In these turbines, the hub reaction is very low and decreasing the hub velocity with lean increases this reaction and can significantly improve efficiency.

Endwall profiling

Shaping the hub and casing annulus lines of a turbomachine can be applied to control blade velocity distributions by changing the local meridional curvature and by varying the annulus area. This is, strictly speaking, a two-dimensional effect as it could be predicted by a through-flow method, and the flow field can still be described with axisymmetric stream surfaces. However, endwall profiling in the meridional plane will also affect 3D flow features and it can be applied to reduce secondary flow effects.

It is also possible to use nonaxisymmetric endwall profiling to reduce secondary flow effects. Varying the endwall shape in the tangential direction modifies the endwall pressure distribution,

and this can be used to reduce secondary flows or to limit leakage flows between stationary and moving endwalls (Rose, 1994).

Leakage paths, seals, and gaps

In recent years, more attention has been paid to the complete real geometry of turbomachinery, which includes steps and bumps, fillets, seals and gaps. These geometrical imperfections can have significant effects on efficiency, particularly where they influence secondary flows, leakage losses, or flow separations. Many modern 3D computational methods can now include these geometrical features and through examining the predicted flow field, fairly modest changes to the location and shape of the detailed geometry have been proposed that are shown to reduce losses. This is an active field of research that is expected to become of increasing importance now that most other sources of loss in turbomachinery designs have been minimized.

6.13 The application of 3D computational fluid dynamics

Three-dimensional computational fluid dynamics (CFD) started to be developed in the 1970s and early 1980s. The first methods were inviscid and ran on very coarse meshes of only a few thousand points per blade passage. These methods were generally based on the Euler blade-to-blade approach, described in Chapter 3, extended to three dimensions. Viscous 3D CFD became possible in the 1980s due to the advances made in computing. Much larger meshes, of the order of 100,000 points, are required to resolve viscous flow features like boundary layers close to the blade surfaces. More powerful computers enabled the full equations of motion, with viscous terms, to be solved for such meshes. 3D CFD is now routinely applied to the analysis and design of turbomachinery, and solutions with mesh sizes of around 1 million points can be computed in less than a few hours on a modern workstation. Figure 6.25 shows an example of a viscous CFD mesh for a low-speed fan with 1 million points in the rotor mesh and 0.64 million in the stator. Note how the mesh points are clustered together close to the blade and endwall surfaces.

Most methods applied to turbomachinery use time-marching algorithms, where the solution iterates towards convergence. These methods require a turbulence model to "close" the equations of motion and this introduces an element of uncertainty into the accuracy of a prediction, even when an extremely fine mesh is used. In general, flow features that are not particularly sensitive to turbulence are still well predicted, whereas some viscous and 3D flow features are difficult to reproduce accurately (Denton and Dawes, 1999). A modern 3D CFD method, if applied carefully, should reliably predict the blade surface pressure distribution, the primary flow field, transonic effects, any effects of lean and sweep, and any leakage flows. However, secondary flows and surface boundary layers, which depend on the parameters of the inlet boundary layers and on the turbulence model, may be inaccurate. For example, 3D CFD has difficulty predicting the extent of corner separations in compressors and often some empirical calibration is required. Figure 6.26 shows the predicted flow downstream of the fan stage illustrated in Figure 6.25. Results are shown for the stator with no hub gap, Figure 6.26(a), and for a small stator hub gap of 0.2% span, Figure 6.26(b). The computed results in Figure 6.26(a) can be compared directly with the measured results given earlier in Figure 6.21. Although the predicted flow field includes comparable features, there are significant

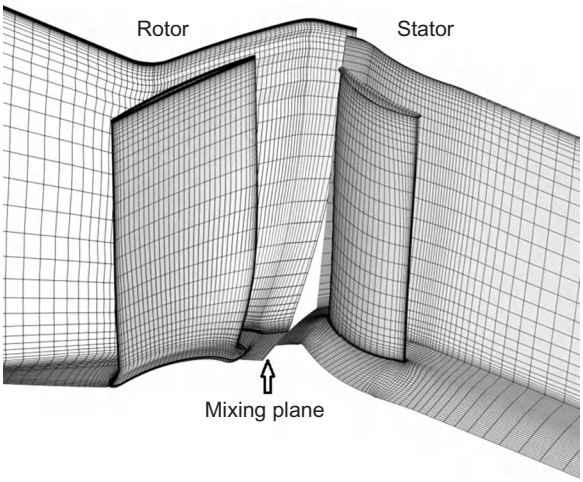

FIGURE 6.25

3D CFD mesh for a test rig fan stage.

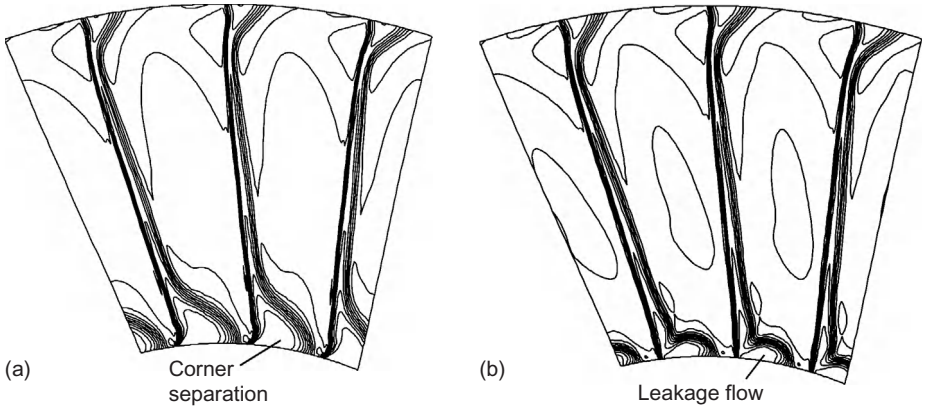

FIGURE 6.26

Computed stagnation pressure contours downstream of the fan stage shown in Figure 6.25: (a) zero stator hub gap and (b) stator hub gap of 0.2% span.

differences: the predicted corner separation is larger, the predicted wake has higher loss, and the flow structure close to the casing is different. Figure 6.26(b) shows that a small amount of leakage flow is potentially beneficial in reducing the size of the corner separation.

A comprehensive presentation of the limitations of CFD is given in Denton (2010) and phenomena that are shown to be particularly difficult to predict include boundary layer transition, viscous shear and mixing, trailing edge flows, and compressor stall. Despite these issues, CFD remains an

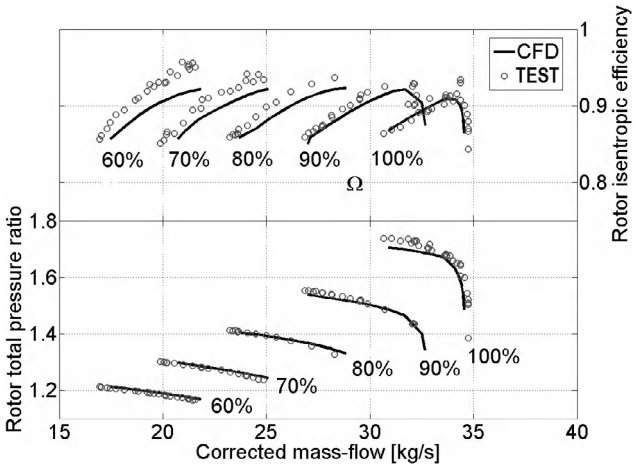

FIGURE 6.27

Rotor alone characteristic map for a transonic fan: single blade row CFD compared with test results.

(*Adapted from Jerez-Fidalgo, et al., 2012*)

invaluable tool for turbomachinery design and analysis, provided it is applied carefully with a full understanding of its capabilities.

Single-passage steady computations

Many single-passage computations are still performed for turbomachinery design and analysis, and before the introduction of multirow computations, CFD could only be applied to single blade rows in isolation. For such computations, it is essential to ensure that the boundary conditions applied are accurate. These can be extracted from a through-flow computation of the whole machine, and this is the normal approach for design work, or alternatively, experimental measurements of the inlet and exit flow field are applied as boundary conditions.

Figure 6.27 shows an example of predicted performance results from single-passage steady CFD of a transonic fan rotor, from Jerez-Fidalgo, Hall, and Colin (2012). The agreement between CFD and experimental data shown here is better than average. There is a close match in the shape of all the characteristic curves and the absolute levels of pressure ratio and choking mass flow are accurately reproduced. However, the stall point is not predicted accurately, and should not be expected to be, since stall is inherently unsteady and involves the full-annulus flow field. Also, at part speeds, the predicted efficiency values are noticeably lower than the measured values.

Multiple blade row steady computations

In general, the flow around a rotor blade is steady in the *relative* frame and the flow around a stator blade is steady in the *stationary* frame. However, wakes and pressure perturbations generated by a rotor will be perceived by an adjacent downstream stator as unsteady fluctuations.

Unsteady interactions between the components are, therefore, always present, but rather than compute the complete time-accurate unsteady flow field, which is computationally very expensive, there are some techniques that enable the time-averaged unsteady flow to be predicted for multistage machines using just steady computations.

The most straightforward and common approach is to simply average the flow field in the circumferential direction at the exit of each blade row. The flow conditions will then be steady in both frames of reference and they can then be exchanged as a boundary condition to the downstream blade row. The averaging process is equivalent to mixing the flow and, therefore, the interfaces between the rotating and stationary blade rows are called *mixing planes* (as shown in Figure 6.25). The problem with mixing planes is that the mixing, or averaging, introduces extra loss at the interfaces and, in general, this will be different from the loss that would have occurred if the circumferentially nonuniform flow had been allowed to interact and mix unsteadily in the downstream blade passage.

Another approach developed by Adamczyk (1985) was to use *deterministic stresses* that describe all the effects of unsteadiness linked to the machine shaft rotation rate. This method allows steady computations to be used, but extra terms are included in the momentum equations that capture the gradual mixing of the flow from upstream blade rows. This has been shown to give improved results relative to mixing planes, but it requires a more complex computational method, and either a model of the deterministic stresses must be provided or larger, overlapping grids are required to calculate how these stresses vary downstream of each blade row.

Unsteady computations

Unsteady 3D computations are currently too expensive and time-consuming to perform routinely for turbomachinery design. However, they are necessary for problems where unsteady phenomena are important and they are widely used in research and development. For example, unsteady CFD can be applied to investigating blade row interactions, compressor stall and surge, noise generation, nonuniform installation effects, and unsteady secondary flow features. These fields are active areas of research and well beyond the scope of this book, but it is worth stating that advanced unsteady CFD methods combined with huge computational resources are enabling continuous improvements in our understanding of complex turbomachinery aerodynamic problems.

Current and future application of CFD to turbomachinery

Over the last 20 years, turbomachinery design has becoming increasingly more dependent on 3D CFD, and this trend is set to continue. Simple methods of determining performance with empirical input, such as described in this book, are still needed for the mean radius design and for through-flow calculations. It is often emphasized by experienced designers that, if the one-dimensional preliminary design is incorrect, e.g., the blade diffusion factors and stage loading, then no amount of CFD will produce a good design! However, CFD does provide the ability to exploit the 3D nature of the flow to suppress deleterious features, such as corner stall in compressors or strong secondary flows in turbines. It is also a quick means to provide better understanding of the flow field for a given design.

As indicated by Horlock and Denton (2003), loss predictions from CFD are still not accurate and interpretation of the computations requires considerable skill and experience. Denton (2010)

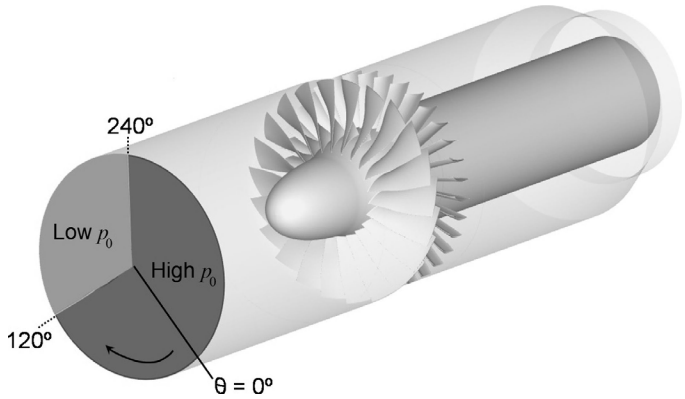

FIGURE 6.28

Computational domain for full annulus, unsteady CFD of a transonic fan operating with nonuniform inlet stagnation pressure.

(*Adapted from Jerez-Fidalgo et al., 2012*)

shows there are still a large number of limitations in CFD that users need to be aware of and these are areas requiring further research and development.

The outlook for CFD is that its capabilities will continue to develop and that it will be used more routinely to tackle more complex turbomachinery design and analysis problems. This trend has been apparent for some time and, at the turn of the century, Adamczyk (2000) outlined the shift towards multistage and unsteady flow computations with more detailed geometrical features and larger computational meshes. The speed and availability of cluster computing has enabled larger computations to be done in shorter and shorter timescales. Figure 6.28 shows the computational domain for the calculation of a high-speed fan stage operating within a test facility with a nonuniform inlet flow field (Jerez-Fidalgo et al., 2012). The mesh contains over 40 million points and the CFD used is fully viscous and unsteady. Computations of this type, in just the last few years, have gone from taking months to run, to just weeks and now, in some cases, days. In the future, computations that were previously barely feasible for research will become routine and possible within design timescales. The growing challenge will be to process the large quantities of data produced by such computations and to interpret the results correctly. Also, with greater computational capabilities, there are inevitably going to be fewer rig tests, which tend to be very expensive, and, therefore, fewer opportunities for experimental validation. The future CFD user should maintain a healthy amount of skepticism in their results!

PROBLEMS

1. Derive the radial equilibrium equation for an incompressible fluid flowing with axisymmetric swirl through an annular duct. Air leaves the inlet guide vanes of an axial-flow compressor in radial equilibrium and with a free-vortex tangenital velocity distribution. The absolute static

pressure and static temperature at the hub, radius 0.3 m, are 94.5 kPa and 293 K, respectively. At the casing, radius 0.4 m, the absolute static pressure is 96.5 kPa. Calculate the flow angles at exit from the vanes at the hub and casing when the inlet absolute stagnation pressure is 101.3 kPa. Assume the fluid to be inviscid and incompressible. Take $R = 0.287$ kJ/(kg °C) for air.

2. A gas turbine stage has an initial absolute pressure of 350 kPa and a temperature of 565°C with negligible initial velocity. At the mean radius, 0.36 m, conditions are as follows:

Nozzle exit flow angle	68°
Nozzle exit absolute pressure	207 kPa
Stage reaction	0.2

Determine the flow coefficient and stage loading factor at the mean radius and the reaction at the hub, radius 0.31 m, at the design speed of 8000 rev/min, given that stage is to have a free-vortex swirl at this speed. You may assume that losses are absent. Comment upon the results you obtain. Take $C_p = 1.148$ kJ/(kg °C) and $\gamma = 1.33$.

3. Gas enters the nozzles of an axial-flow turbine stage with uniform total pressure at a uniform velocity c_1 in the axial direction and leaves the nozzles at a constant flow angle α_2 to the axial direction. The absolute flow leaving the rotor c_3 is completely axial at all radii. Using radial equilibrium theory and assuming no losses in total pressure show that

$$(c_3^2 - c_1^2)/2 = U_{\mathrm{m}} c_{\theta \mathrm{m}2} \left[1 - \left(\frac{r}{r_{\mathrm{m}}} \right)^{\cos^2 \alpha_2} \right]$$

where U_{m} is the mean blade speed and $c_{\theta \mathrm{m}2}$ is the tangential velocity component at nozzle exit at the mean radius $r = r_{\mathrm{m}}$. (*Note*: The approximate $c_3 = c_1$ at $r = r_{\mathrm{m}}$ is used to derive this expression.)

4. Gas leaves an untwisted turbine nozzle at an angle α to the axial direction and in radial equilibrium. Show that the variation in axial velocity from root to tip, assuming total pressure is constant, is given by

$$c_x r^{\sin^2 \alpha} = \text{constant}$$

Determine the axial velocity at a radius of 0.6 m when the axial velocity is 100 m/s at a radius of 0.3 m. The outlet angle α is 45°.

5. The flow at the entrance and exit of an axial-flow compressor rotor is in radial equilibrium. The distributions of the tangential components of absolute velocity with radius are

$$c_{\theta 1} = ar - b/r, \quad \text{before the rotor}$$

$$c_{\theta 2} = ar + b/r, \quad \text{after the rotor}$$

where a and b are constants. What is the variation of work done with radius? Deduce expressions for the axial velocity distributions before and after the rotor, assuming

incompressible flow theory and that the radial gradient of stagnation pressure is zero. At the mean radius, $r = 0.3$ m, the stage loading coefficient, $\psi = \Delta W / U_t^2$, is 0.3, the reaction ratio is 0.5, and the mean axial velocity is 150 m/s. The rotor speed is 7640 rev/min. Determine the rotor flow inlet and outlet angles at a radius of 0.24 m given that the hub−tip ratio is 0.5. Assume that at the mean radius the axial velocity remained unchanged ($c_{x1} = c_{x2}$ at $r = 0.3$ m). (*Note*: ΔW is the specific work and U_t the blade tip speed.)

6. An axial-flow turbine stage is to be designed for free-vortex conditions at exit from the nozzle row and for zero swirl at exit from the rotor. The gas entering the stage has a stagnation temperature of 1000 K, the mass flow rate is 32 kg/s, the root and tip diameters are 0.56 m and 0.76 m, respectively, and the rotor speed is 8000 rev/min. At the rotor tip, the stage reaction is 50% and the axial velocity is constant at 183 m/s. The velocity of the gas entering the stage is equal to that leaving. Determine

a. the maximum velocity leaving the nozzles;
b. the maximum absolute Mach number in the stage;
c. the root section reaction;
d. the power output of the stage;
e. the stagnation and static temperatures at stage exit.

Take $R = 0.287$ kJ/(kg K) and $C_p = 1.147$ kJ/(kg K).

7. The rotor blades of an axial-flow turbine stage are 100 mm long and are designed to receive gas at an incidence of 3° from a nozzle row. A free-vortex whirl distribution is to be maintained between nozzle exit and rotor entry. At rotor exit, the absolute velocity is 150 m/s in the axial direction at all radii. The deviation is 5° for the rotor blades and 0° for the nozzle blades at all radii. At the hub, radius 200 mm, the conditions are as follows:

Nozzle outlet angle	70°
Rotor blade speed	180 m/s
Gas speed at nozzle exit	450 m/s

Assuming that the axial velocity of the gas is constant across the stage, determine

a. the nozzle outlet angle at the tip;
b. the rotor blade inlet angles at hub and tip;
c. the rotor blade outlet angles at hub and tip;
d. the degree of reaction at root and tip.

Why is it essential to have a *positive* reaction in a turbine stage?

8. The rotor and stator of an isolated stage in an axial-flow turbomachine are to be represented by two actuator discs located at axial positions $x = 0$ and $x = \delta$, respectively. The hub and tip diameters are constant and the hub−tip radius ratio r_h/r_t is 0.5. The rotor disc considered on its own has an axial velocity of 100 m/s far upstream and 150 m/s downstream at a constant radius $r = 0.75 r_t$. The stator disc in isolation has an axial velocity of 150 m/s far upstream and 100 m/s far downstream at radius $r = 0.75 r_t$. Calculate and plot the axial velocity variation between $-0.5 \leq x/r_t \leq 0.6$ at the given radius for each actuator disc in isolation and for the combined discs when (a) $\delta = 0.1 r_t$, (b) $\delta = 0.25 r_t$, and (c) $\delta = r_t$.

9. **a.** For the fluid element rotating in radial equilibrium about the axis of a turbomachine (Figure 6.2) prove the generalized radial equilibrium equation:

$$\frac{\mathrm{d}h_0}{\mathrm{d}r} - T\frac{\mathrm{d}s}{\mathrm{d}r} = c_x\frac{\mathrm{d}c_x}{\mathrm{d}r} + \frac{c_\theta}{r}\frac{\mathrm{d}}{\mathrm{d}r}(rc_\theta)$$

b. At entry to an axial-flow hydraulic turbine, the flow passes through a row of inlet guide vanes giving the water a free-vortex swirl prior to it entering the rotor blade row. The rotor has a root radius of 0.5 m and a tip radius of 1.2 m and the volume flow of water is 45 m^3/s. A pressure probe inserted radially into the flow upstream of the rotor to the mean radius indicates a flow angle of 26.1° from the axial direction.

Assuming that the stagnation pressure is constant, determine the static pressure difference between the hub and tip upstream of the rotor as measured on a vertical mercury manometer. Take the density of water as 1000 kg/m^3 and the density of mercury as 13.6×10^3 kg/m^3.

10. A single-stage axial-flow gas turbine stage with a hub/tip ratio of 0.85 is to be designed to give a free-vortex flow after the rotor row and is required to develop 2.6 MW from a gas flow of 30 kg/s. The gas admitted is at a stagnation temperature and pressure of 1100 K and 430 kPa (abs) and the relevant gas properties are $C_p = 1.15$ kJ/kg and $\gamma = 1.333$. At the mean radius the blade speed is to be 250 m/s, the flow coefficient $\phi = 0.5$, the absolute flow angle $\alpha_2 = 67°$, and the reaction is 0.5. The static pressure at exit is 1.02 kPa.

Sketch an appropriate velocity diagram for the stage and determine

a. the blade loading coefficient, $\psi = \Delta W/U^2$

b. the flow area and the hub and tip radii

c. the absolute tangential velocity components, $c_{\theta 2}$ and $c_{\theta 3}$, following the expansion through the nozzle

d. the reaction at the hub and tip.

11. **a.** An axial-flow fan comprising a stator followed by a rotor is to be made with swirl distributions specified by

$$c_{\theta 1} = ar - b/r \text{ downstream of the stator and}$$

$$c_{\theta 2} = ar + b/r \text{ downsream of the rotor.}$$

Show that:

i. the specific work ΔW at any radius is constant and equal to $2b\Omega$, where Ω is the rotational speed, in rad/s;

ii. the work done factor at the mean radius, $\psi_\mathrm{m} = (\Delta h_0/U_\mathrm{m}^2) = (2b/c_x) \times (\psi_\mathrm{m}/\phi_\mathrm{m})$;

iii. the reaction, $R = 1 - (a/\Omega)$ (is this always true?);

iv. at the mean radius, $(a/c_x) = (c_{\theta 1} + c_{\theta 2})/2c_x r_\mathrm{m} = (1 - R_\mathrm{m})/\phi_\mathrm{m} r_\mathrm{m}$.

b. Assuming incompressible flow, with constant enthalpy and entropy, show that the axial velocity distributions upstream and downstream of the rotor are given by the expressions:

$$\left(\frac{c_{x1}}{U_\mathrm{t}}\right)^2 = A_1 - \left(\frac{2a}{\Omega}\right)^2\left(\frac{1}{2}\left(\frac{r}{r_\mathrm{t}}\right)^2 - \frac{b}{ar^2}\ln\left(\frac{r}{r_\mathrm{t}}\right)\right)$$

$$\left(\frac{c_{x2}}{U_t}\right)^2 = A_2 - \left(\frac{2a}{\Omega}\right)^2 \left[\frac{1}{2}\left(\frac{r}{r_t}\right)^2 + \frac{b}{ar_t^2}\ln\left(\frac{r}{r_t}\right)\right]$$

where A_1 and A_2 are constants.

c. For the above fan the hub/tip radius ratio is 0.6, the rotational speed is 4010 rpm, the rotor diameter is 1.0 m, the mean reaction is 0.5, the flow coefficient upstream of the rotor at the mean radius $\phi = c_{x1}/U_t = 0.5$, and the stagnation temperature rise is 10°C. Determine

i. the value of A_1, and values of c_{x1}/U_t in the range, $0.6 \leq 0.05 \leq 1.0$ for r/r_t and hence find the volume flow rate using the mid-ordinate method;

ii. a value of A_2 by repeated iteration of the velocity profile until the correct value of the volume flow is achieved.

Hence, plot the final axial velocity profiles for the upstream and downstream flows.

12. **a.** A solution of the so-called "direct problem" of the flow in an axial-flow turbomachine can be found using the radial equilibrium equation when the absolute flow angle α is constant and a radial gradient in stagnation enthalpy $(dh_0/dr) = (k/2)(c_m^2/r_m)$ is present (where k is a constant).

If the variation of α is specified by $a = 2\sin^2\alpha$, prove that the velocity variation across the duct is given by

$$\left(\frac{c}{c_m}\right)^2 \left(\frac{r}{r_m}\right)^a = 1 + \frac{k}{1+a}\left[\left(\frac{r}{r_m}\right)^{a+1} - 1\right]$$

where c_m is the velocity at radius $r = r_m$.

b. An axial-flow fan with a hub/tip ratio of 0.4, a tip diameter of 1 m is used to compress air at normal temperature and pressure. The rotational speed of the fan is 500 rad/s. The radial gradient of stagnation enthalpy from hub to tip is to be estimated from the following data:

At $r/r_t = 0.4$, the work coefficient $\psi_h = 0.6$. At $r = r_t$, the work coefficient $\psi_t = 0.25$. The entropy is to be assumed constant.

Determine the velocity of the air as a function of radius and plot the results you obtain for

i. $k = 0.6$ at $\alpha = 30$, 45, and 60°.

ii. $k = -1$, 0, 1.0 with $\alpha = 45°$.

Comment on the trends caused by the choice of these variables.

13. **a.** Inlet guide vanes are to be tested to produce a flow with a tangential velocity distribution $c_\theta = k\,r$, where k and K are arbitrary constants. Show that the axial velocity distribution is given by

$$c_x = \sqrt{K - 2k^2r^2}$$

b. Using the continuity equation derive the following solution for the axial velocity:

$$c_x\left(r_t^2 - r_h^2\right) = \frac{1}{3k^2}\left[\left(K - 2k^2 r_h^2\right)^{3/2} - \left(K - 2k^2 r_t^2\right)^{3/2}\right]$$

c. Several arithmetical methods are available for solving this quite complicated equation, one of which is to get an approximate solution for the axial velocity at the root mean square radius: $r_{rms} = ((1/2)(r_h^2 + r_t^2))^{0.5}$. Designating this special axial velocity as X, you should be able to find that

$$K = X^2 + 2(c_{\theta rms})^2 = X^2 + c_{\theta t}^2(1 + \upsilon^2)$$

where $1 + \nu^2 = 2(r_{ms}/r_t)^2$. Finally, after some working you should get

$$\frac{c_x}{X} = \left[1 + \left(1 + \nu^2 - 2\left(\frac{r}{r_t}\right)^2\right)\left(\frac{c_{\theta t}}{X}\right)^2\right]^{0.5}$$

d. For the solid-body inlet guide vane design, the cascade has a hub/tip radius ratio of 0.5, the tip radius is 0.7 m, the value of X is 50 m/s and $k = 25$. Determine the flow angles at the hub and tip and the volume flow rate using the above approximate analysis.

14. An axial-flow compressor has a hub-to-tip radius ratio of 0.5. At the arithmetic mean radius, $r_m = 0.15$ m, the following conditions apply:
the total temperature at stage entry, $T_{01} = 580$ K;
the shaft rotational speed, $N = 20,000$ rpm;
absolute velocity, $c = c_m = 250\ m/s$;
absolute flow angle, $\alpha = \alpha_{2m} = 30^\circ$;
static density, $\rho = \rho_{2m} = 5.0\ \text{kg}/m^3$;
flow incidence angle onto the rotor, $\beta = \beta_m = 0^\circ$.
the tangential velocity swirl distribution is in radial equilibrium after the stator and varies according to $rc_\theta^2 = A$ (a constant). The stagnation enthalpy is constant;
the rotor blade inlet angle, β_1' is 5° at $r = r_h$ and 50° at $r = r_t$;
the average specific heat C_p is 1.157 kJ/(kg K) and $\gamma = 1.33$.
Calculate the following:

a. The rotor blade incidence angles at the hub, mean, and tip radii.

b. The stagnation pressure difference between the hub and tip ($p_{0hub} - p_{0tip}$) at entry to the rotor, assuming (for simplicity) that the static density at the mean radius applies to all radii.

15. **a.** The general solution of the radial equilibrium equation is given as

$$\frac{\mathrm{d}}{\mathrm{d}r}\left\{c^2 \exp\left[2\int \sin^2\alpha \frac{\mathrm{d}r}{r}\right]\right\} - c_m^2 \exp\left[2\int^{r_m} \sin^2\alpha \frac{\mathrm{d}r}{r}\right] = 2\left(\frac{\mathrm{d}h_0}{\mathrm{d}r} - T\frac{\mathrm{d}s}{\mathrm{d}r}\right)\exp\left[2\int \sin^2\alpha \mathrm{d}r/r\right]$$

If the variation of α is specified by the formula $b(r/r_m) = 2\sin^2\alpha$ and the stagnation enthalpy gradient by

$$\frac{\mathrm{d}h_0}{\mathrm{d}r} = \frac{k}{2}\frac{c_m^2}{r_m}$$

show that the velocity varies according to the expression:

$$\left(\frac{c}{c_m}\right)^2 = \frac{k}{b} + \left(1 - \frac{k}{b}\right)\exp\left[b\left(1 - \frac{r}{r_m}\right)\right]$$

where k is a constant of integration.

b. Using the operational data and sizes given in Problem 12, determine the velocity variation c/c_m of an axial fan using the expression given for $\alpha = 30, 45,$ and 60° and $k = 0.6$. Plot your results (c/c_m) versus (r/r_t) and compare these with the results of problem 6.12. Repeat this calculation for $k = 1.2$ and $\alpha = 45^\circ$. What conclusion do you draw about the effect made by the increased stagnation enthalpy gradient on the spanwise velocity distribution?

References

Adamczyk, J. J. (1985). Model equation for simulating flows in multistage turbomachinery. *ASME Paper 85-GT-22*.

Adamczyk, J. J. (2000). Aerodynamic analysis of multistage turbomachinery flows in support of aerodynamic design. *Journal of Turbomachinery*, *122*(2), 189–217.

Denton, J. D. (1978). Through flow calculations for axial flow turbines. *Journal of Engineering for Power, Transactions of ASME*, *100*.

Denton, J. D. (1985). Solution of the Euler equations for turbomachinery flows. Part 2. Three-dimensional flows. In: A. S. Ücer, P. Stow, & C. Hirsch (Eds.), Thermodynamics and fluid mechanics of turbomachinery, *NATO Science Series E.* (Vol. 1, pp. 313–347). Leiden, the Netherlands: Springer.

Denton, J. D. (1993). Loss mechanisms in turbomachines. 1993 IGTI scholar lecture. *Journal of Turbomachinery*, *115*, 621–656.

Denton, J. D. (2010). Some limitations of turbomachinery CFD. *ASME Paper GT2010-22540*.

Denton, J. D., & Dawes, W. N. (1999). Computational fluid dynamics for turbomachinery design. Proceedings of the Institution of Mechanical Engineers, *Part C*, *213*.

Denton, J. D., & Xu, L. (1999). The exploitation of three-dimensional flow in turbomachinery design. Proceedings of the Institution of Mechanical Engineers, *Part C*, *213*.

Dixon, S.L.(1974). Secondary vorticity in axial compressor blade rows. *NASA SP 304*, Vol. 1.

Grant, J. & Borthwick, D. (1987). Fully three dimensional inviscid flow calculations for the final stage of a large low pressure steam turbine. *IMechE Paper C281/87*.

Hawthorne, W. R. (1955). Some formulae for the calculation of secondary flow in cascades. *ARC Report*, *17*, 519.

Hawthorne, W. R., & Horlock, J. H. (1962). Actuator disc theory of the incompressible flow in axial compressors. *Proceedings of the Institution of Mechanical Engineers*, *176*, 789.

Horlock, J. H. (1958). *Axial flow compressors* London: Butterworths.

Horlock, J. H. (1963). Annulus wall boundary layers in axial compressor stages. Transactions of the American Society of Mechanical Engineers, *Series D*, *85*.

Horlock, J. H. (1966). *Axial flow turbines* London: Butterworths.

Horlock, J. H., & Denton, J. D. (2003). A review of some early design practice using CFD and a current perspective. *Proceedings of the American Society of Mechanical Engineers Turbo Expo*, *2003*.

Horlock, J. H., & Dixon, S. L. (1966). The off-design performance of free vortex turbine and compressor stages. *ARC Report*, *27*, 612.

Howell, A. R. (1945). Fluid dynamics of axial compressors. *Proceedings of the Institution of Mechanical Engineers*, *153*.

Jerez-Fidalgo, V., Hall, C. A., & Colin, Y. (2012). A study of fan-distortion interaction within the NASA Rotor 67 transonic stage. *ASME Journal of Turbomachinery*, *134*, *1−12*.

Lakshminarayana, B. (1996). Fluid dynamicsand heat transfer of turbomachines. Hoboken, NJ: Wiley.

Langston, L. S. (1980). Crossflows in a turbine cascade passage. *Journal of Engineering for Power, Transactions of ASME*, *102*, 866−874.

Lewis, R. I. (1996). *Turbomachinery performance analysis.* London: Arnold.

Lewis, R. I. (1995). Developments of actuator disc theory for compressible flow through turbomachines. *International Journal of Mechanical Sciences*, *37*, 1051−1066.

Macchi, E. (1985). The use of radial equilibrium and streamline curvature methods for turbomachinery design and prediction. In: A. S. Ücer, P. Stow, & C. Hirsch (Eds.), Thermodynamics and fluid mechanics of turbomachinery*, NATO Science Series E* (Vol. 1, pp. 133−166). Leiden, the Netherlands: Springer.

Marsh, H. (1968). A digital computer program for the through-flow fluid mechanics on an arbitrary turbomachine using a matrix method. *ARC, R&M 3509*.

Pullan, G., & Harvey, N. W. (2008). The influence of sweep on axial flow turbine aerodynamics in the endwall region. *ASME Journal of Turbomachinery*, *130041011*

Rose, M. G. (1994). Non-axisymmetric endwall profiling in the HP NGV's of an axial flow gas turbine. *ASME Paper 94-GT-249*.

Smith, L. H., Jr. (1966). The radial-equilibrium equation of turbomachinery. Transactions of the American Society of Mechanical Engineers*, Series A*, *88*.

Wadia, A. R., Szucs, P. N. & Crall, W.W. (1997). Inner workings of aerodynamic sweep. *ASME Paper 97-GT-401*.

CHAPTER

Centrifugal Pumps, Fans, and Compressors

7

And to thy speed add wings
Milton, *Paradise Lost*

7.1 Introduction

This chapter is concerned with the elementary flow analysis and preliminary design of work-absorbing turbomachines comprising pumps, low-speed fans, and compressors. The major part of the analysis is centered on the compressor since the basic action of all these machines is, in most respects, similar.

Turbomachines employing centrifugal effects for increasing fluid pressure have been in use for more than a century. The earliest known machines using this method were hydraulic pumps followed later by ventilating fans and blowers. Cheshire (1945) recorded that a centrifugal compressor was incorporated in the build of the Whittle turbojet engine. Figure 7.1 is a version of this compressor illustrating, for that period, a rather complex flow path of the air. By way of contrast, a modern centrifugal compressor is shown as one component of a composite compressor of a jet engine in Figure 7.2.

Development of the centrifugal compressor for aircraft propulsion continued into the mid-1950s but, long before this, it had become clear that axial-flow compressors were better able to meet the needs of larger engines. Not only were the frontal area (and drag) smaller with engines using axial compressors but also the efficiency for the same duty was better by as much as 3 or 4%. However, for very small compressors with low flow rates, the efficiency of axial compressors drops sharply, blading is small and difficult to make accurately, and the centrifugal compressor is again the king. Many applications are found in small gas turbines for road vehicles and commercial helicopters as well as bigger applications, e.g., diesel engine turbochargers, chemical plant processes, factory workshop air supplies, and large-scale air-conditioning plant.

Centrifugal compressors were the choice for refrigerating plants and compression-type heat pumps used in district heating schemes described by Hess (1985). These compressors with capacities ranging from below 1 MW up to nearly 30 MW were preferred because of their good economy, low maintenance, and absolute reliability.

Palmer and Waterman (1995) gave some details of an advanced two-stage centrifugal compressor used in a helicopter engine with a pressure ratio of 14, a mass flow rate of 3.3 kg/s, and an overall total-to-total efficiency of 80%. Both stages employed backswept vanes (approximately 47°) with a

Fluid Mechanics and Thermodynamics of Turbomachinery. DOI: http://dx.doi.org/10.1016/B978-0-12-415954-9.00007-3

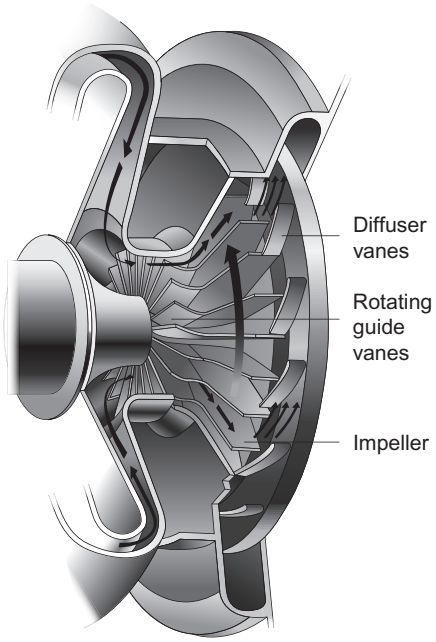

FIGURE 7.1

A version of the centrifugal compressor used by Sir Frank Whittle.

(*With Kind Permission of Rolls-Royce plc*)

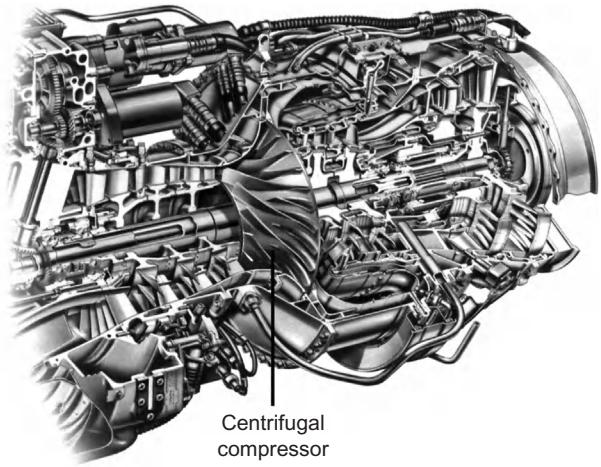

FIGURE 7.2

The turbomeca centrifugal compressor fitted to the RTM322 engine.

(*With kind permission of Rolls-Royce plc*)

low aerodynamic loading achieved by having a relatively large number of vanes (19 full vanes and 19 splitter vanes). Some basic details are given in this chapter for calculating the performance of centrifugal compressors with backward swept impeller vanes. Figure 7.3 is a picture of a compressor that features a high-performance centrifugal compressor impeller with 15 backswept main vanes (and 15 splitter vanes) and its surrounding wedge diffuser is fitted with 24 vanes.

7.2 Some definitions

As well as axial-flow compressors and fans, which we dealt with in Chapter 5, most of the pressure-increasing turbomachines in use are of the radial-flow type and vary from fans that produce pressure rises equivalent to a few millimeters of water to pumps producing pressure heads of many hundreds of meters of water. The term *pump* refers to machines that increase the pressure of a flowing liquid. The term *fan* is used for machines imparting only a small increase in pressure to a flowing gas. In this case, the pressure rise is usually so small that the gas can be considered as being incompressible. A *compressor* gives a substantial rise in pressure to a flowing gas. To make a distinction, a compressor can be defined as a pressure-increasing machine where the *density ratio* across it is 1.05 or greater.

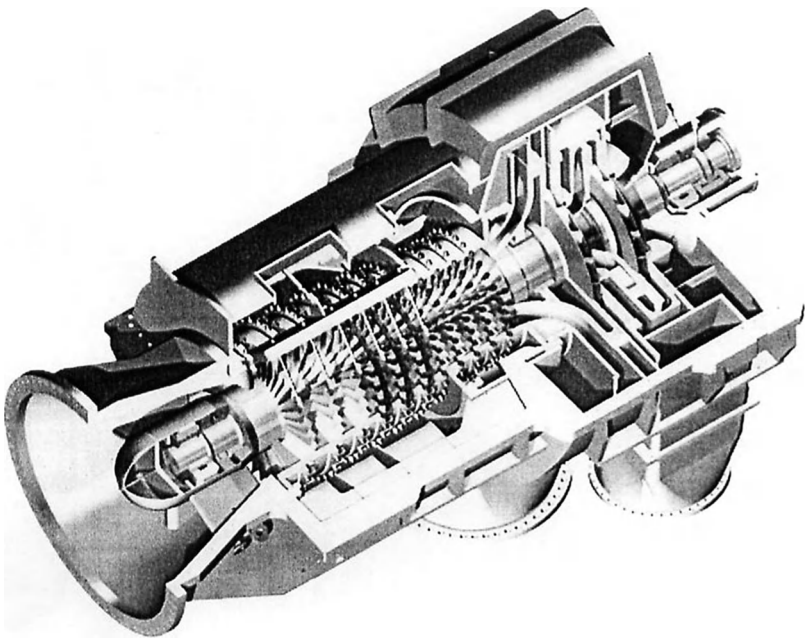

FIGURE 7.3

An axial–radial flow compressor for applications requiring high-pressure ratios and intercooling.

(*With Kind Permission of Siemens AG*)

A centrifugal compressor or pump consists essentially of a rotating *impeller* followed by a *diffuser*. Figure 7.4 shows diagrammatically the various elements of a centrifugal compressor. Fluid is drawn in through the *inlet casing* into the *eye* of the impeller. The function of the impeller is to increase the energy level of the fluid by whirling it outward, thereby increasing the angular momentum of the fluid. Both the static pressure and the velocity are increased within the impeller. The purpose of the diffuser is to convert the kinetic energy of the fluid leaving the impeller into pressure energy. This process can be accomplished by free diffusion in the annular space surrounding the impeller or, as indicated in Figure 7.4, by incorporating a row of fixed diffuser vanes that allows the diffuser to be made very much smaller. Outside the diffuser is a *scroll* or *volute* whose function is to collect the flow from the diffuser and deliver it to the outlet pipe. In low-speed compressors and pump applications where simplicity and low cost count for more than efficiency, the volute follows immediately after the impeller (as shown later in Figures 7.22 and 7.23).

The *hub* is the curved surface of revolution of the impeller $a-b$; the *shroud* is the curved surface $c-d$ forming the outer boundary to the flow of fluid. At entry to the impeller, the relative flow has a velocity w_1 at angle β_1 to the axis of rotation. This relative flow is turned into the axial direction by the *inducer section* or *rotating guide vanes* as they are sometimes called. The inducer starts at the eye and usually finishes in the region where the flow is beginning to turn into the radial direction. Some compressors of advanced design extend the inducer well into the radial flow region, apparently to reduce the amount of relative velocity diffusion.

To simplify manufacture and reduce cost, the impellers of *many fans and pumps* are confined to a 2D radial section as shown in Figure 7.5. With this arrangement some loss in efficiency can be

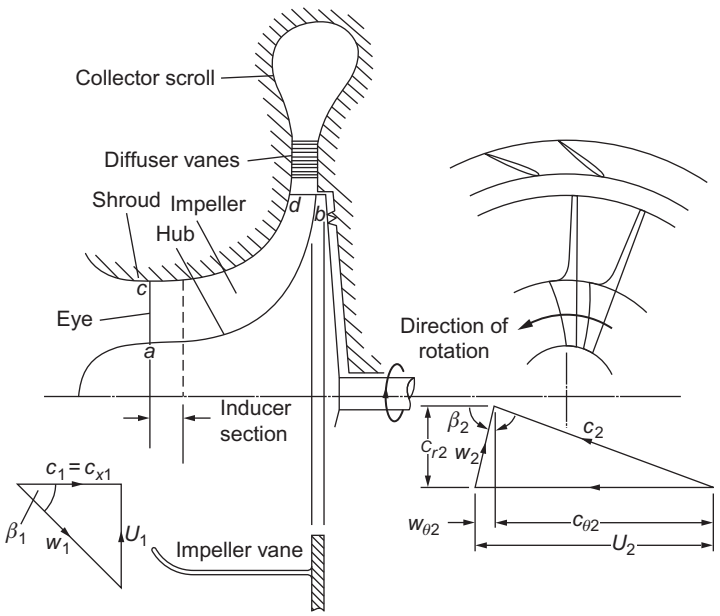

FIGURE 7.4

Centrifugal compressor stage and velocity diagrams at impeller entry and exit.

expected. For the purpose of greatest utility, relations obtained in this chapter are generally in terms of the 3D compressor configuration as shown in Figure 7.4.

7.3 Thermodynamic analysis of a centrifugal compressor

The flow through a centrifugal compressor stage is a highly complicated 3D motion and a full analysis presents many problems. Fortunately, we can obtain approximate solutions by simplifying the flow model, e.g., by adopting the so-called *1D* approach that assumes that the fluid conditions are uniform over certain flow cross sections. These cross sections are conveniently taken immediately before and after the impeller as well as at inlet and exit of the entire machine. Where inlet vanes are used to give prerotation to the fluid entering the impeller, the 1D treatment is no longer valid and an extension of the analysis is then required. (Examples of 3D flows are given in Chapter 6.)

The impeller

The general 3D motion has components of velocity c_r, c_θ, and c_x, respectively, in the radial, tangential, and axial directions and $c^2 = c_r^2 + c_\theta^2 + c_x^2$.

From Eq. (1.20a), rothalpy can be rewritten as

$$I = h + \frac{1}{2}(c_r^2 + c_\theta^2 + c_x^2 - 2Uc_\theta)$$

Adding and subtracting $(1/2)U^2$ this becomes

$$I = h + \frac{1}{2}(U^2 - 2Uc_\theta + c_\theta^2) + \frac{1}{2}(c_r^2 + c_x^2 - U^2) = h + \frac{1}{2}(U - c_\theta)^2 + \frac{1}{2}(c_x^2 + c_r^2 - U^2) \qquad (7.1)$$

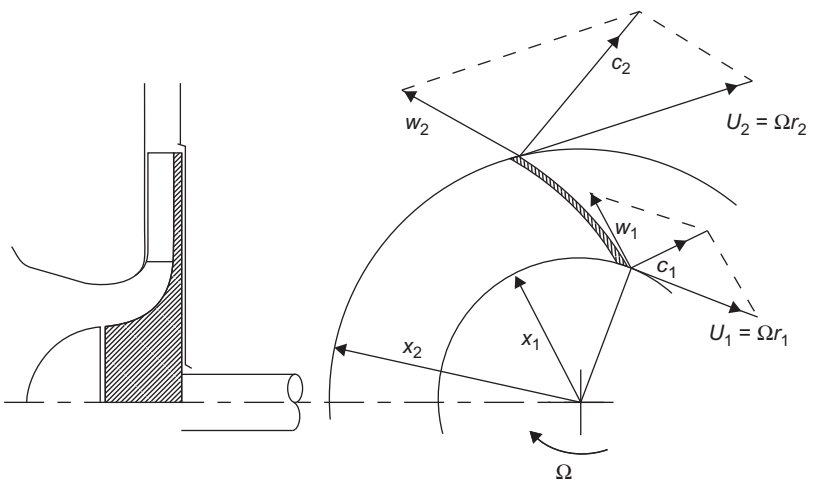

FIGURE 7.5

Centrifugal pump and velocity triangles.

From the velocity triangle, Figure 7.4, $U - c_\theta = w_\theta$, and with $w^2 = c_r^2 + w_\theta^2 + c_x^2$, Eq. (7.1) becomes

$$I = h + \frac{1}{2}(w^2 - U^2)$$

or

$$I = h_{0\text{rel}} - \frac{1}{2}U^2$$

since $h_{0\text{rel}} = h + (1/2)w^2$. Across the impeller, $I_1 = I_2$ so

$$h_2 - h_1 = \frac{1}{2}(U_2^2 - U_1^2) + \frac{1}{2}(w_1^2 - w_2^2) \tag{7.2}$$

This expression provides the reason why the static enthalpy rise in a centrifugal compressor is so large compared with a single-stage axial compressor. On the right-hand side of Eq. (7.2), the second term, $(1/2)(w_1^2 - w_2^2)$, is the contribution from the diffusion of relative velocity, also obtained for axial compressors. The first term, $(1/2)(U_2^2 - U_1^2)$, is the contribution from the centrifugal action caused by the change in radius. The relation between the enthalpies at state points 1 and 2 can be traced in Figure 7.6 with the aid of Eq. (7.2).

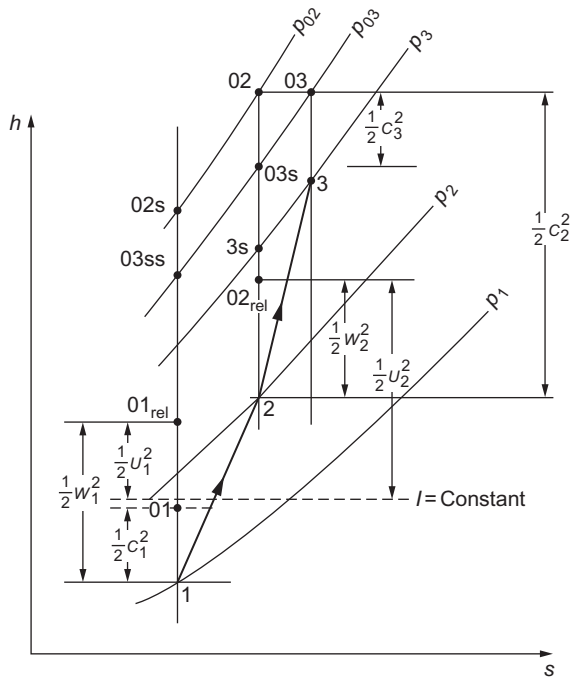

FIGURE 7.6

Mollier diagram for the compressor stage (impeller and diffuser only).

Referring to Figure 7.4, and in particular the inlet velocity diagram, the absolute flow has no whirl component or angular momentum and $c_{\theta 1} = 0$. In centrifugal compressors and pumps, this is the normal situation where the flow is free to enter axially. For such a flow, the specific work done on the fluid, from Eq. (1.18b), is written as

$$\Delta W = U_2 c_{\theta 2} = h_{02} - h_{01} \tag{7.3}$$

in the case of compressors, and

$$\Delta W = U_2 c_{\theta 2} = g H_{\mathrm{i}} \tag{7.4}$$

in the case of pumps, where H_{i} (the "ideal" head) is the total head rise across the pump *excluding all internal losses*. In high-pressure ratio compressors, it may be necessary to impart *prerotation* to the flow entering the impeller as a means of reducing a high relative inlet velocity. The effects of high relative velocity at the impeller inlet are experienced as Mach number effects in compressors and cavitation effects in pumps. The usual method of establishing prerotation requires the installation of a row of inlet guide vanes upstream of the impeller, the location depending upon the type of inlet. Unless contrary statements are made, it will be assumed for the remainder of this chapter that there is no prerotation (i.e., $c_{\theta 1} = 0$).

The diffuser

The diffuser is an important element of a compressor or pump. Its purpose is to reduce the velocity of the flow leaving the impeller resulting in an increase in pressure. The diffuser can be simply depicted as a nonrotating channel whose flow area increases in the direction of flow (Figure 7.7).

Although the basic diffuser *appears* to be a geometrically simple device, it is beset by two serious fluid mechanical problems. The primary problem is the tendency of the boundary layers to

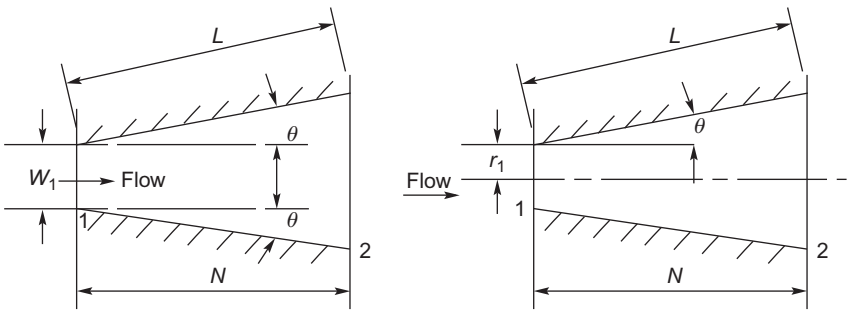

FIGURE 7.7

Some diffuser geometries and their notation: (a) 2D and (b) conical.

separate from the diffuser walls if the local rate of diffusion is too rapid resulting in flow mixing and large losses in stagnation pressure. On the other hand, if the diffusion rate is too low, the fluid is exposed to a long length of wall and fluid friction losses again become excessive. Clearly, there has to be an *optimum rate of diffusion* between these two extremes for which the losses are minimized. Test results indicate that a diffuser with an included angle of about 7° or 8° gives the optimum recovery for both 2D and conical diffusers. Some further details of the performance of rectilinear diffusers taking into account the classical work of Sovran and Klomp (1967) is given later in this chapter.

7.4 Inlet velocity limitations at the compressor eye

The inlet eye is an important and critical region in both centrifugal pumps and compressors and requires careful consideration at the design stage. If the relative velocity of the inlet flow is too large in pumps, cavitation (details in next section) may result with consequent blade erosion or even reduced performance. In compressors, large relative velocities can cause an increase in the impeller total pressure losses. In high-speed centrifugal compressors Mach number effects may become important with high relative velocities in the inlet. By suitable sizing of the eye, the maximum relative velocity, or some related parameter (e.g., maximum relative Mach number), can be minimized to give the optimum inlet flow conditions. As an illustration, the following analysis shows a simple optimization procedure for a low-speed compressor based upon incompressible flow theory.

For the inlet geometry shown in Figure 7.4, the absolute eye velocity is assumed to be uniform and axial. The inlet relative velocity is $w_1 = (c_{x1}^2 + U^2)^{1/2}$, which, of course, is a maximum at the inducer's tip. The volume flow rate is

$$Q = c_{x1}A_1 = \pi(r_{s1}^2 - r_{h1}^2)(w_{s1}^2 - \Omega^2 r_{s1}^2)^{1/2} \tag{7.5}$$

It is worth noticing that with both Q and r_{h1} are fixed:

i. if r_{s1} is made large then, from continuity, the axial velocity is low but the blade speed is high;
ii. if r_{s1} is made small, the blade speed is small but the axial velocity is high.

Both extremes produce large relative velocities and there must exist some optimum radius r_{s1} for which the relative velocity is a minimum.

For maximum volume flow, differentiating Eq. (7.5) with respect to r_{s1} (keeping w_{s1} constant) and equating to zero,

$$\frac{1}{\pi}\frac{\partial Q}{\partial r_{s1}} = 0 = 2r_{s1}(w_{s1}^2 - \Omega^2 r_{s1}^2)^{1/2} - (r_{s1}^2 - r_{h1}^2)\Omega^2 r_{s1}^2/(w_{s1}^2 - \Omega^2 r_{s1}^2)^{1/2}$$

After simplifying,

$$2(w_{s1}^2 - \Omega^2 r_{s1}^2) = (r_{s1}^2 - r_{h1}^2)\Omega^2$$

therefore,

$$2c_{x1}^2 = kU_{s1}^2 \tag{7.6}$$

where $k = 1(r_{h1}/r_{s1})^2$ and $U_{s1} = \Omega r_{s1}$. Hence, the optimum inlet velocity coefficient is

$$\phi = c_{x1}/U_{s1} = \cot \beta_{s1} = (k/2)^{1/2} \tag{7.7}$$

Equation (7.7) specifies the optimum conditions for the inlet velocity triangles in terms of the hub−tip radius ratio. For typical values of this ratio (i.e., $0.3 \leq r_{h1}/r_{s1} \leq 0.6$), the optimum relative flow angle at the inducer tip β_{s1} lies between 56° and 60°.

7.5 Design of a pump inlet

A crucial factor in good pump design is the *avoidance of cavitation* both on account of obtaining good efficiency and the possibility of damage to the impeller blades. In Chapter 2, a brief description of cavitation was given and the *net positive suction head*, NPSH, was defined as

$$H_s = (p_0 - p_v)/\rho$$

where p_0 is the absolute stagnation pressure of the liquid and p_v is its absolute vapor pressure.

The pump considered in the following analysis is assumed to have the flow geometry shown in Figure 7.4. As liquid passes through the impeller, there are changes in the pressure levels. In the vicinity of the impeller blades' leading edges on the suction surfaces there will be a rapid increase in velocity and a corresponding decrease in pressure. If the absolute pressure of the liquid drops below the vapor pressure then cavitation will occur. The fluid then moves into the impeller and the dynamic action of the blades causes the pressure to increase. This pressure rise causes the cavitation bubbles' collapse and the resulting implosion of the bubbles and consequent shock waves can cause pitting of the impeller blades and, eventually, structural failure.

Cavitation can also occur near the impeller exit of radial flow and mixed flow impellers where the velocities are greatest. The blade tip of the axial-flow pump has been found to be the most vulnerable location for cavitation. At inception of cavitation, at some point on the surface of the pump the pressure is equal to the vapor pressure, i.e.,

$$p = p_v = p_1 - \sigma_b \left(\frac{1}{2}\rho w_1^2\right)$$

where σ_b is the *blade cavitation coefficient* corresponding to the cavitation point.

Figure 9.20 is an example of the severe cavitation damage sustained by the runner of a Francis turbine. Similar damage can occur in pump impellers. Pearsall (1972) found that this coefficient lies in the range

$$0.2 \leq \sigma_b \leq 0.4$$

Thus, just upstream of impeller entry at cavitation inception we have

$$p_1 = p_{01} - \sigma_b \left(\frac{1}{2}\rho w_1^2\right)$$

Referring to the velocity triangles (Figure 7.4),

$$gH_s = (p_{01} - p_v)/\rho = \frac{1}{2}c_{x1}^2 + \sigma_b\left(\frac{1}{2}w_1^2\right) = \frac{1}{2}c_{x1}^2(1 + \sigma_b) + \frac{1}{2}\sigma_b U_{s1}^2$$

where H_s is the NPSH measured at the shroud radius, $r = r_{s1}$.

To obtain the optimum inlet design conditions consider the suction specific speed, defined as $\Omega_{ss} = \Omega Q^{1/2}/(gH_s)^{3/4}$, where $\Omega = U_{s1}/r_{s1}$ and $Q = c_{x1}A_1 = \pi k r_{s1}^2 c_{x1}$. Thus,

$$\frac{\Omega_{ss}^2}{\pi k} = \frac{U_{s1}^2 c_{x1}}{\left[(1/2)c_{x1}^2(1+\sigma_b)+(1/2)\sigma_b U_{s1}^2\right]^{3/2}} = \frac{\phi}{\left[(1/2)(1+\sigma_b)\phi^2+(1/2)\sigma_b\right]^{3/2}} \tag{7.8}$$

where $\phi = c_{x1}/U_{s1}$. To obtain the condition of maximum Ω_{ss}, Eq. (7.8) is differentiated with respect to ϕ and the result set equal to zero. From this procedure, the optimum conditions are found:

$$\phi = \left\{\frac{\sigma_b}{2(1+\sigma_b)}\right\}^{1/2} \tag{7.9a}$$

$$gH_s = \frac{3}{2}\sigma_b\left(\frac{1}{2}U_{s1}^2\right) \tag{7.9b}$$

$$\Omega_{ss}^2 = \frac{2\pi k(2/3)^{1.5}}{\sigma_b(1+\sigma_b)^{0.5}} = \frac{3.420k}{\sigma_b(1+\sigma_b)^{0.5}} \tag{7.9c}$$

EXAMPLE 7.1

The inlet of a centrifugal pump of the type shown in Figure 7.4 is to be designed for optimum conditions when the flow rate of water is 25 dm^3/s and the impeller rotational speed is 1450 rev/min. The maximum suction specific speed $\Omega_{ss} = 3.0$ (rad) and the inlet eye radius ratio is to be 0.3. Determine

a. the blade cavitation coefficient;
b. the shroud diameter at the eye;
c. the eye axial velocity;
d. the NPSH.

Solution

a. From Eq. (7.9c), squaring both sides,

$$\sigma_b^2(1+\sigma_b) = (3.42k)^2/\Omega_{ss}^4 = 0.1196$$

with $k = 1-(r_{h1}/r_{s1})^2 = 1-0.3^2 = 0.91$. Solving iteratively (e.g., using the Newton–Raphson approximation), we get $\sigma_b = 0.3030$.

b. As $Q = \pi k r_{s1}^2 c_{x1}$ and $c_{x1} = \phi r_{s1}\Omega$, $r_{s1}^3 = Q/(\pi k\Omega\phi)$ and, hence, $\Omega = 1450\pi/30 = 151.84$ rad/s. From Eq. (7.9a), $\phi = [0.303/(2\times 1.303)]^{0.5} = 0.3410$

$$r_{s1}^3 = 0.025/(\pi \times 0.91 \times 151.84 \times 0.341) = 1.689 \times 10^{-4}$$

$$r_{s1} = 0.05528 \text{ m}$$

The required diameter of the eye is 110.6 mm.

c. $c_{x1} = \phi\phi\Omega r_{s1} = 0.341 \times 151.84 \times 0.05528 = 2.862$ m/s

d. From Eq. (7.9b), the *NPSH* is

$$H_s = \frac{0.75\sigma_b c_{x1}^2}{g\phi^2} = \frac{0.75 \times 0.303 \times 2.862^2}{9.81 \times 0.341^2} = 1.632 \text{ m}$$

7.6 Design of a centrifugal compressor inlet[1]

To obtain high efficiencies from high-pressure ratio compressors, it is necessary to limit the relative Mach number at the eye. In the following paragraphs, two analyses are given, the first for an axial flow at inlet, $\alpha_1 = 0°$, and the second when prewhirl vanes are used and $\alpha_1 > 0°$. The analyses are applied to the shroud radius r_{s1} at the impeller eye.

Case A ($\alpha_1 = 0°$)

The flow area at the eye is

$$A_1 = \pi r_{s1}^2 k$$

where $k = 1 - (r_{h1}/r_{s1})^2$. Hence,

$$A_1 = \pi k U_{s1}^2/\Omega^2 \tag{7.10}$$

with $U_{s1} = \Omega r_{s1}$. Assuming a uniform axial velocity, the continuity equation is, $\dot{m} = \rho_1 A_1 c_{x1}$.

From the inlet velocity diagram (Figure 7.4), $c_{x1} = w_{s1} \cos \beta_{s1}$ and $U_{s1} = w_{s1} \sin \beta_{s1}$. Using (Eq. 7.10),

$$\frac{\dot{m}\Omega^2}{\rho_1 k \pi} = w_{s1}^3 \sin^2 \beta_{s1} \cos \beta_{s1} \tag{7.11}$$

For a perfect gas, the static density ρ is

$$\rho = \rho_0 \left(\frac{p}{p_0}\right)\left(\frac{T_0}{T}\right)$$

With $C_p T_0 = C_p T + (1/2)c^2$ and $C_p = \gamma R/(\gamma - 1)$,

$$\frac{T_0}{T} = 1 + \frac{\gamma - 1}{2} M^2 = \frac{a_0^2}{a^2}$$

where the Mach number, $M = c/(\gamma RT)^{1/2} = c/a$, a_0 and a being the stagnation and local (static) speeds of sound. For isentropic flow,

$$\frac{p}{p_0} = \left(\frac{T}{T_0}\right)^{\gamma/(\gamma-1)}$$

[1]This section is rather more difficult and could be left for a later reading.

Thus,

$$\frac{\rho_1}{\rho_0} = \left(\frac{T_1}{T_0}\right)^{1-\gamma/(\gamma-1)} = \left(1+\frac{\gamma-1}{2}M_1^2\right)^{-1/(\gamma-1)}$$

where $\rho_0 = p_0/(RT_0)$.

The absolute Mach number M_1 and the relative Mach number $M_{1,\text{rel}}$ are defined as

$$M_1 = c_{x1}/a_1 = M_{1,\text{rel}} \cos \beta_{s1} \text{ and } w_{s1} = M_{1,\text{rel}} a_1$$

Using these two relations together with Eq. (7.11), we obtain

$$\frac{\dot{m}\Omega^2 RT_{01}}{k\pi p_{01}} = \frac{M_{1,\text{rel}}^3 a_1^3}{[1+(1/2)(\gamma-1)M_1^2]^{1/(\gamma-1)}} \sin^2 \beta_{s1} \cos \beta_{s1}$$

Since $a_{01}/a_1 = [1+(1/2)(\gamma-1)M_1^2]^{1/2}$ and $a_{01} = (\gamma RT_{01})^{1/2}$ this equation is reworked to give

$$\frac{\dot{m}\Omega^2}{\gamma\pi k p_{01}(\gamma RT_{01})^{1/2}} = \frac{M_{1,\text{rel}}^3 \sin^2 \beta_{s1} \cos \beta_{s1}}{[1+(1/2)(\gamma-1)M_{1,\text{rel}}^2 \cos^2 \beta_{s1}]^{1/(\gamma-1)+3/2}} \tag{7.12a}$$

Although it looks rather cumbersome the preceding equation is really quite useful. For a particular gas, by specifying values of γ, R, p_{01}, and T_{01}, we obtain $\dot{m}\Omega^2/k$ as a function of $M_{1,\text{rel}}$ and β_{s1}. Choosing a particular value of $M_{1,\text{rel}}$ as a limit, an optimum value of β_{s1} *for maximum mass flow* can then be found.

Taking air as an example and assuming $\gamma = 1.4$, Eq. (7.12a) becomes

$$f(M_{1,\text{rel}}, \beta_{s1}) = \dot{m}\Omega^2/(1.4\pi k p_{01} a_{01}) = \frac{M_{1,\text{rel}}^3 \sin^2 \beta_{s1} \cos \beta_{s1}}{(1+(1/5)M_{1,\text{rel}}^2 \cos^2 \beta_{s1})^4} \tag{7.13a}$$

The right-hand side of Eq. (7.13a) is plotted in Figure 7.8 as a function of β_{s1} for $M_{1,\text{rel}} = 0.8$ and 0.9. It has been shown that these curves are a maximum when

$$\cos^2 \beta_{s1} = A - \sqrt{A^2 - 1/M_{1,\text{rel}}^2}$$

where $A = 0.7 + 1.5/M_{1,\text{rel}}^2$.

Case B ($\alpha_1 > 0°$)

The effect of prewhirl on the mass flow function can be determined by a similar analysis. From the velocity triangles in Figure 7.4,

$$c_1 = c_x/\cos \alpha_1 = w_1 \cos \beta_1/\cos \alpha_1$$

$$\dot{m} = \rho A c_r = 2\pi r b \rho c_r$$

Also, $U_1 = w_1 \sin \beta_1 + c_1 \sin \alpha_1 = w_1 \cos \beta_1 (\tan \beta_1 + \tan \alpha_1)$,

$$\dot{m} = \rho_1 A_1 c_{x1}$$

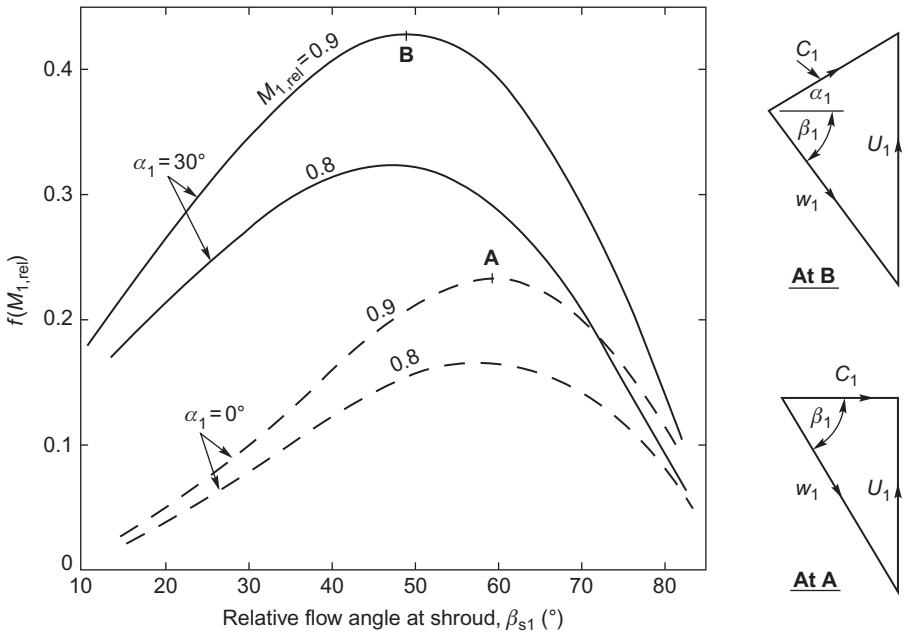

FIGURE 7.8

Variation of mass flow function $f(M_{1,rel})$ as a function of β_{s1} for the inducer of a centrifugal compressor: Case A, no guide vanes, $\alpha_1 = 0$; Case B, with guide vanes, $\alpha_1 > 0$.

It is better to refer to the shroud radius r_{s1} from this point on. Following the previous procedure, we get

$$\dot{m} = \frac{\pi k}{\Omega^2}\rho_1 U_{s1}^2 w_{s1}\cos\beta_{s1} = \left(\frac{\pi k \rho_1}{\Omega^2}\right) w_1^3 \cos^3\beta_{s1}(\tan\beta_{s1}+\tan\alpha_{s1})^2$$

Using the relations developed earlier for T_{01}/T_1, p_{01}/p_1, and ρ_{01}/ρ_1, we obtain

$$f(M_{1,rel},\beta_{s1}) = \frac{\dot{m}\Omega^2}{\pi k \rho_{01} a_{01}^3} = \frac{M_{1,rel}^3\cos^3\beta_{s1}(\tan\beta_{s1}+\tan\alpha_{s1})^2}{(1+(\gamma-1/2)M_{1,rel}^2\cos^2\beta_{s1}/\cos^2\alpha_{s1})^{(1/\gamma-1)+(3/2)}} \tag{7.12b}$$

Substituting $\gamma = 1.4$ for air into Eq. (7.12b), we get

$$f(M_{1,rel}) = \frac{\Omega^2\dot{m}}{\pi k \rho_{01}\alpha_{01}^3} = \frac{M_{1,rel}^3\cos^2\beta_{s1}(\tan\beta_{s1}+\tan\alpha_{s1})^2}{(1+(1/5)M_{1,rel}^2\cos^2\beta_{s1}/\cos^2\alpha_{s1})^4} \tag{7.13b}$$

The right-hand side of Eq. (7.13b) is plotted in Figure 7.8 with $\alpha_1 = 30°$ and $M_{1,rel} = 0.8$ and 0.9, showing that the peak values of $\dot{m}\Omega^2/k$ are significantly increased but arise at much lower values of β_{s1}.

EXAMPLE 7.2

The inlet of a centrifugal compressor is fitted with free-vortex guide vanes to provide a positive prewhirl of 30° at the shroud. The inlet hub−shroud radius ratio is 0.4 and a requirement of the design is that the relative inlet Mach number, $M_{1,\text{rel}}$, does not exceed 0.9. The air mass flow is 1 kg/s, the stagnation pressure and temperature are 101.3 kPa and 288 K. For air, take $R = 287$ J/(kg K) and $\gamma = 1.4$.

Assuming optimum conditions at the shroud, determine

a. the rotational speed of the impeller;
b. the inlet static density downstream of the guide vanes at the shroud and the axial velocity;
c. the inducer tip diameter and velocity.

Solution

a. From Figure 7.9, the peak value of $f(M_{1,\text{rel}}) = 0.4307$ at a relative flow angle $\beta_1 = 49.4°$. The constants needed are $a_{01}\sqrt{\gamma RT_{01}} = 340.2$ m/s, $\rho_{01} = p_{01}/RT_{01} = 1.2255$ kg/m^3, and $k = 1-0.4^2 = 0.84$. From Eq. (7.13b), we find $\Omega^2 = \pi f k \rho_{01} a_{01}^3 = 5.4843 \times 10^7$. Hence,

$$\Omega = 7405.6 \text{ rad/s and } N = 70,718 \text{ rev/min}$$

b.

$$\rho_1 = \frac{\rho_{01}}{[1+(1/5)(M_{1,\text{rel}} \cos \beta_1)^2]^{2.5}} = \frac{1.2255}{1.06973^{2.5}} = 0.98464 \text{ kg/m}^3$$

The axial velocity is found from

$$(w_1 \cos \beta_1)^3 = c_x^3 = \frac{\Omega^2 \dot{m}}{\pi k \rho_1 (\tan \beta_1 + \tan \alpha_1)^2} = \frac{5.4843 \times 10^7}{\pi \times 0.84 \times 0.98464 \times 3.0418} = 6.9388 \times 10^6$$

therefore,

$$c_x = 190.73 \text{ m/s}$$

c.

$$A_1 = \frac{\dot{m}}{\rho_1 c_x} = \pi k r_{s1}^2$$

therefore,

$$r_{s1}^2 = \frac{\dot{m}}{\pi \rho_1 c_x k} = \frac{1}{\pi \times 0.98464 \times 190.73 \times 0.84} = 2.0178 \times 10^{-3}$$

$$r_{s1} = 0.04492 \text{ m and } d_{s1} = 8.984 \text{ cm}$$

$$U = \Omega r_{s1} = 7405.6 \times 0.04492 = 332.7 \text{ m/s}$$

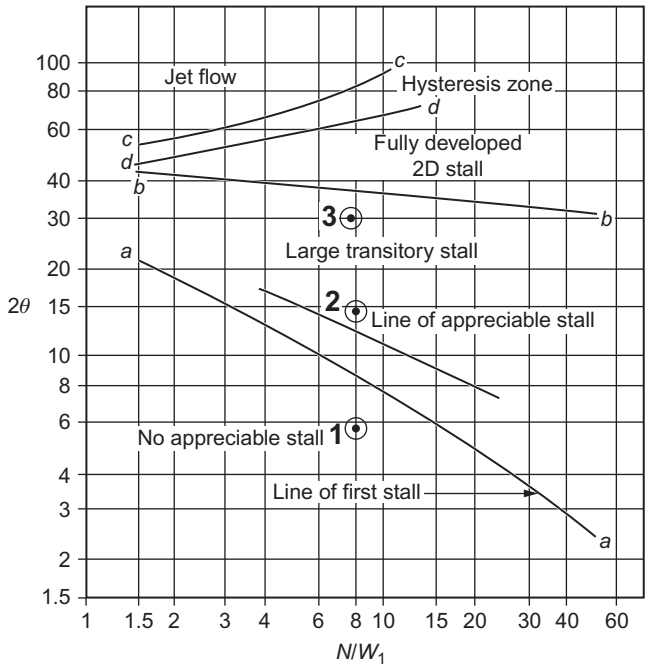

FIGURE 7.9

Chart depicting flow regimes for 2D diffusers.

(*Adapted from Sovran and Klomp, 1967*)

Some remarks on the use of prewhirl vanes at entry to the impeller

Introducing positive prewhirl (i.e., in the direction of impeller rotation) can give a significant reduction of w_1 and the inlet Mach number $M_{1,\text{rel}}$ but, as can be seen from the Euler pump equation, Eq. (1.18b), it reduces the specific work done on the gas. Thus, it is necessary to increase the blade tip speed to maintain the same level of impeller pressure ratio as was obtained without prewhirl.

Prewhirl is obtained by fitting guide vanes upstream of the impeller. One arrangement for doing this is shown in Figure 7.10(a). The velocity triangles, Figure 7.10(b) and (c), suggest how the guide vanes reduce the relative inlet velocity. Guide vanes are designed to produce either a free vortex or some form of forced-vortex velocity distribution. In Chapter 6, it was shown that for a free-vortex flow ($rc_\theta = \text{constant}$) the axial velocity, c_x, is constant (in the ideal flow). It was shown by Wallace, Whitfield, and Atkey (1975) that the use of free-vortex prewhirl vanes leads to a significant increase in incidence angle with low inducer radius ratios. The use of some forced-vortex velocity distribution does alleviate this problem. Whitfield and Baines (1990) have reviewed some of the effects resulting from the adoption of various forms of a *generalized forced-vortex*,

$$c_\theta = A\left(\frac{r}{r_{s1}}\right)^n \tag{7.14}$$

where n is any integer value in the range -1 to 2.

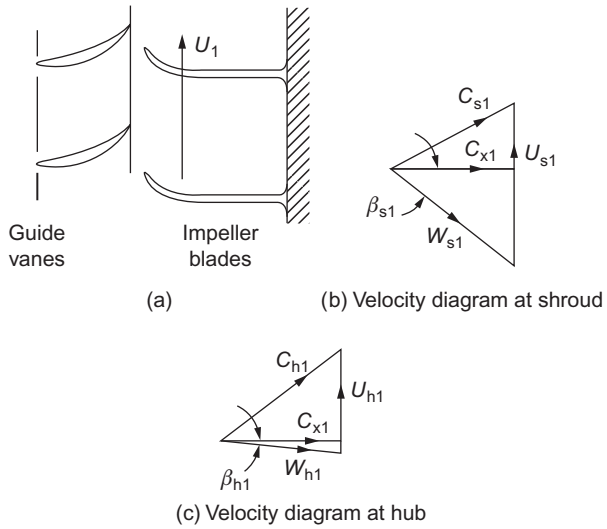

FIGURE 7.10

Effect of free-vortex prewhirl vanes upon the relative velocity at impeller inlet.

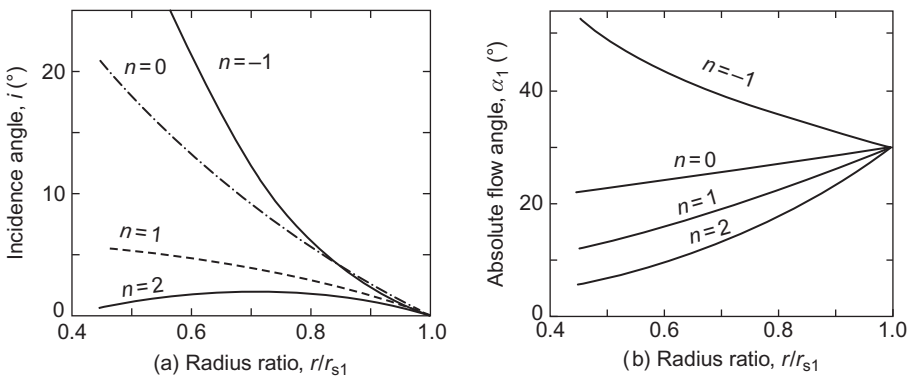

FIGURE 7.11

Effect of prewhirl vanes on (a) incidence angle and (b) absolute flow angle with $\alpha_{s1} = 30°$, $\beta_{s1} = 60°$.

Figure 7.11(a) shows (for a particular case in which $\alpha_{s1} = 30°$, $\beta_{s1} = 60°$) the effect of prewhirl on the variation of the incidence angle, $i = \beta_1 - \beta_2'$, with radius ratio, r/r_{s1}, for several whirl distributions. Figure 7.11(b) shows the corresponding variations of the absolute flow angle, α_1. It is apparent that a high degree of prewhirl vane twist is required for either a free-vortex design or the quadratic ($n = 2$) design. The advantage of the quadratic design is the low variation of incidence with radius, where it is evident that the free-vortex design produces a wide variation of incidence.

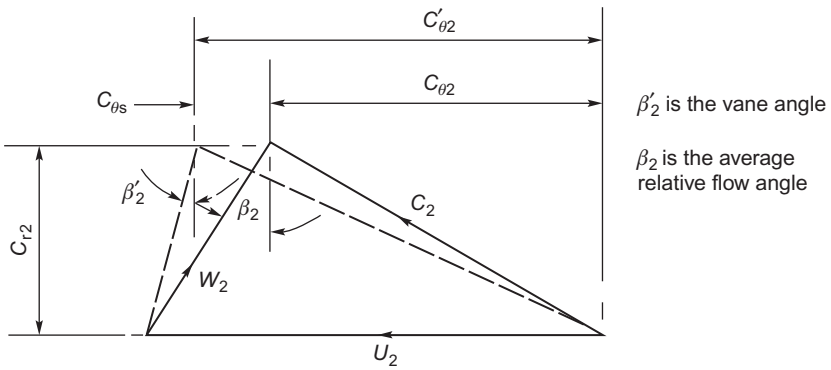

FIGURE 7.12

Effect of slip (in the velocity diagram) on the relative flow angle β_2 at exit from an impeller with backswept vanes at a vane angle of β'_2.

Wallace et al. (1975) adopted the simple untwisted blade shape ($n = 0$), which proved to be a reasonable compromise.

7.7 The slip factor

Introduction

Even under ideal (i.e., frictionless) conditions, the relative flow leaving the impeller of a compressor or pump will receive less than perfect guidance from the vanes and the real flow is said to *slip*. If the impeller could be imagined as being made with an infinite number of infinitesimally thin vanes, then an ideal flow would be perfectly guided by the vanes and would leave the impeller at the vane angle. Figure 7.12 compares the relative flow angle, β_2, obtained with a finite number of vanes, with the vane angle, β'_2.

A *slip factor* may be defined as[2]

$$\sigma = c_{\theta 2}/c_{\theta 2'} \tag{7.15a}$$

where $c_{\theta 2}$ is the tangential component of the absolute velocity and related to the relative flow angle β_2. The *hypothetical tangential velocity* component is related to the vane angle β'_2. The *slip velocity* is given by $c_{\theta s} = c_{\theta 2'} - c_{\theta 2}$ so that the slip factor can be written as

$$\sigma = 1 - c_{\theta s}/c_{\theta 2'} \tag{7.15b}$$

The slip factor is a vital piece of information needed by pump and compressor designers (also by designers of radial turbines as it turns out!) as its accurate estimation allows the pressure rise, the work input, and the velocity triangles at the impeller exit to be determined. There have been many attempts to determine correlations for the slip factor starting, apparently, with that of Busemann (1928) and followed by Stanitz (1952), Wiesner (1967), and many other researchers.

[2]This is now known as the European definition of slip factor. The American definition is $\sigma = 1 - c_{\theta s}/U_2$.

Wiesner (1967) has given an extensive review of the various expressions used for determining slip factors. Most of the expressions derived relate to radially vaned impellers ($\beta'_2 = 0$) or to mixed flow designs, but some are given for *backward swept vane* (bsv) *designs*. Most of the correlations presented work well for one type of impeller at the design point but fail for other designs. A recent paper presented by Qiu et al. (2011) has presented what is now called a *unified slip factor model* that can be applied to axial, mixed flow, and radial flow impellers and capable of being applied at both the design condition and the off-design conditions.

The relative eddy concept

Suppose that an irrotational and frictionless fluid flow is possible that passes through an impeller. If the absolute flow enters the impeller without spin, then at outlet the spin of the absolute flow *must still be zero*. The impeller itself has an angular velocity Ω so that, relative to the impeller, the fluid has an angular velocity of $-\Omega$; this is termed as the *relative eddy* (Figure 7.13(a)). A simple explanation for the slip effect in an impeller is obtained from the idea of a relative eddy.

At outlet from the impeller, the relative flow can be regarded as a through-flow on which is superimposed a relative eddy. The net effect of these two motions is that the average relative flow emerging from the impeller passages is at an angle to the vanes and in a direction opposite to the blade motion, as indicated in Figure 7.13(b). This is the basis of the various early theories of slip.

Slip factor correlations

One of the earliest and simplest expressions for the slip factor was obtained by Stodola (1945). Referring to Figure 7.13(c), the *slip velocity*, $c_{\theta s} = c_{\theta 2} - c_{\theta 2}$, is considered to be the product of the relative eddy and the radius $d/2$ of a circle, which can be inscribed within the channel.

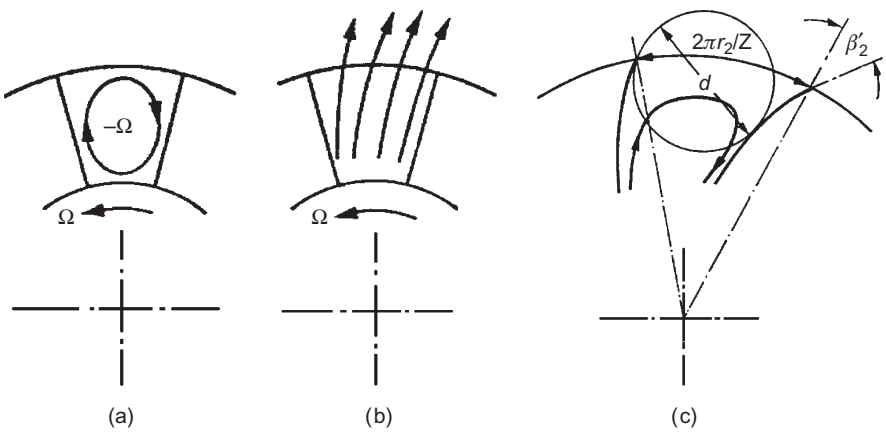

FIGURE 7.13

(a) Relative eddy without any through-flow; (b) relative flow at impeller exit (through-flow added to relative eddy); and (c) Stodola flow model.

Thus, $c_{\theta s} = \Omega d/2$. If the number of vanes is denoted by Z, then an approximate expression, $d \cong (2\pi r_2/Z)\cos \beta'_2$, can be written if Z is not small. Since $\Omega = U_2/r_2$,

$$c_{\theta s} = \frac{\pi U_2 \cos \beta'_2}{Z} \tag{7.15c}$$

Now as $c_{\theta 2'} = U_2 - c_{r2} \tan \beta'_2$then the Stodola slip factor becomes

$$\sigma = \frac{c_{\theta 2}}{c'_{\theta 2}} = 1 - \frac{c_{\theta s}}{U_2 - c_{r2} \tan \beta'_2} \tag{7.16}$$

or

$$\sigma = 1 - \frac{(\pi/Z)\cos \beta'_2}{1 - \phi_2 \tan \beta'_2} \tag{7.17}$$

where $\phi_2 = c_{r2}/U_2$.

A number of "mathematically exact" solutions have been evolved of which the best known is that of Busemann (1928). This theory applies to the special case of 2D vanes curved as logarithmic spirals as shown in Figure 7.14.

Considering the geometry of the vane element shown, it can be proved that

$$\kappa = \tan \beta' \ln(r_2/r_1) \tag{7.18}$$

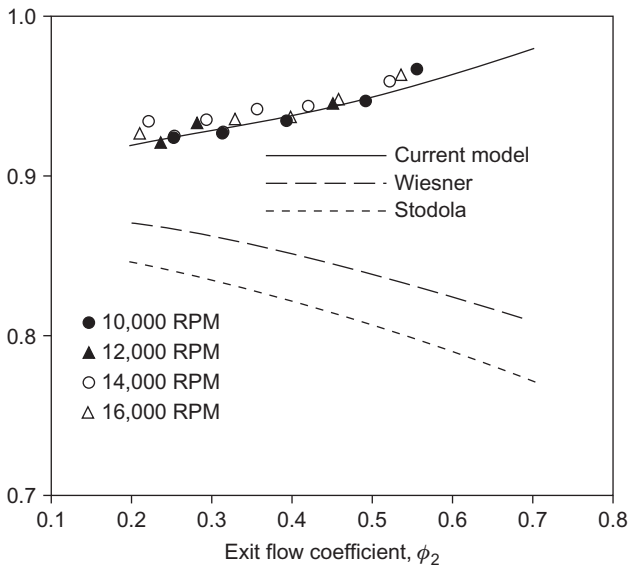

FIGURE 7.14

Calculated experimental results for the Eckardt rotor A slip factor and comparison with results from the Wiesner and Stodola theories.

and that the ratio of vane length to equivalent blade pitch is

$$\frac{l}{s} = \frac{Z}{2\pi \cos \beta'} \ln\left(\frac{r_2}{r_1}\right) \tag{7.19}$$

Hence, the equivalent pitch is

$$s = \frac{2\pi(r_2 - r_1)}{Z \ln(r_2/r_1)} \tag{7.20}$$

The equiangular or logarithmic spiral is the simplest form of radial vane system and has been frequently used for *pump impellers* in the past. The Busemann slip factor can be written as

$$\sigma = (A - B\phi_2 \tan \beta_2')/(1 - \phi_2 \tan \beta_2') \tag{7.21}$$

where both A and B are functions of r_2/r_1, β_2', and Z. For typical pump and compressor impellers, the dependence of A and B on r_2/r_1 is negligible when the equivalent l/s exceeds unity. From Eq. (7.19), the requirement for $l/s \geq 1$ is that the radius ratio must be sufficiently large, i.e.,

$$r_2/r_1 \geq \exp(2\pi \cos \beta'/Z) \tag{7.22}$$

This criterion is often applied to other than logarithmic spiral vanes, then β_2' is used instead of β'. Radius ratios of typical centrifugal pump impeller vanes normally exceed the preceding limit. For instance, blade outlet angles of impellers are usually in the range $50^\circ \leq \beta_2' \leq 70^\circ$ with between 5 and 12 vanes. Taking representative values of $\beta_2' = 60^\circ$ and $Z = 8$ the right-hand side of Eq. (7.22) is equal to 1.48, which is not particularly large for a pump.

So long as these criteria are obeyed, the value of B is constant and practically equal to unity for all conditions. Similarly, the value of A is independent of the radius ratio r_2/r_1 and depends on β_2' and Z only. Values of A given by Csanady (1960) are shown in Figure 7.15 and may also be interpreted as the value of σ_B for zero through-flow ($\phi_2 = 0$).

The *mathematically* exact solution of Busemann makes it possible to check the validity of approximate methods of calculation, such as the Stodola expression. By putting $\phi_2 = 0$ in Eqs (7.17) and (7.21) a comparison of the Stodola and Busemann slip factors at the zero through-flow condition can be made. The Stodola value of slip comes close to the exact correction if the vane angle is within the range $50^\circ \leq \beta_2' \leq 70^\circ$ and the number of vanes exceeds six.

Stanitz (1952) applied the mathematical method called *relaxation* to solve the potential flow field between the blades of eight impellers with blade tip angles β_2' varying between 0° and 45°. The conclusions drawn were that the computed slip velocity, $c_{\theta s}$, was independent of vane angle, β_2', and depended only on blade spacing (number of blades). He also found that compressibility effects did not affect the slip factor. Stanitz's expression for slip velocity is

$$c_{\theta s} = 0.63 U_2 \pi/Z \tag{7.23a}$$

and it is easily shown that the corresponding slip factor using Eq. (7.16) is

$$\sigma = 1 - \frac{0.63\pi/Z}{1 - \phi_2 \tan \beta_2'} \tag{7.23b}$$

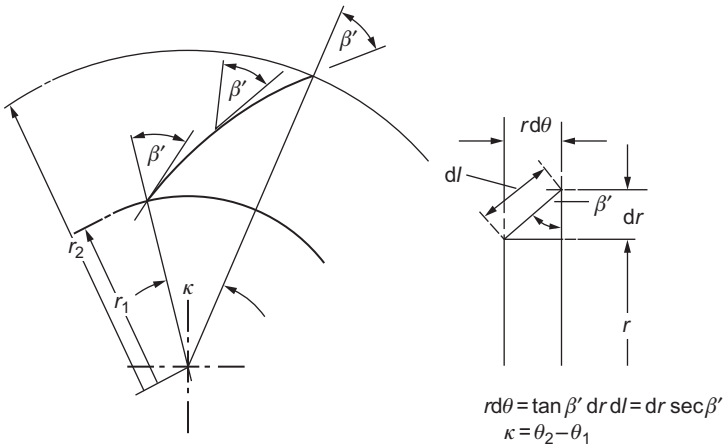

FIGURE 7.15

Logarithmic spiral vane; vane angle β' is constant at all radii.

For radial-vaned impellers this becomes $\sigma = 1-0.63\pi/Z$ but is often written for initial approximate calculations as $\sigma = 1-2/Z$.

Wiesner (1967) reviewed all available methods and concluded that Busemann's procedure was still the most generally applicable predictor for determining the slip factor of centripetal impellers. Wiesner obtained the following simple empirical expression for the slip velocity,

$$c_{\theta s} = \frac{U_2\sqrt{\cos\beta'_2}}{Z^{0.7}} \tag{7.24a}$$

and the corresponding slip factor,

$$\sigma = 1 - \frac{\sqrt{\cos\beta'_2}}{z^{0.7}(1-\phi_2\tan\beta'_2)} \tag{7.24b}$$

which, according to Wiesner, fitted the Busemann results "extremely well over the whole range of practical blade angles and number of blades."

The preceding equation is applicable to a limiting mean radius ratio for the impeller given by the empirical expression

$$\varepsilon = \left(\frac{r_1}{r_2}\right)_{\lim} = \exp\left(\frac{-8.16\cos\beta'_2}{Z}\right) \tag{7.24c}$$

For values of $r_1/r_2 > \varepsilon$, the following empirical expression is useful:

$$\sigma'_w = \sigma_w\left[1-\left(\frac{r_1/r_2-\varepsilon}{1-\varepsilon}\right)^3\right] \tag{7.24d}$$

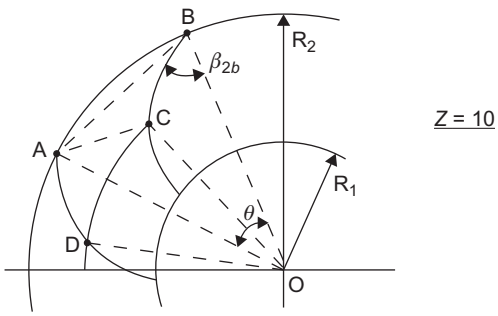

FIGURE 7.16

Flow model used by Qiu.

7.8 A unified correlation for slip factor[3]

It will have been noticed for the preceding correlations of slip factor that once the geometry of an impeller is defined (i.e., the exit blade angle, the number of blades and (possibly) the inlet blade angle), then the slip factor is firmly fixed. However, a new, unified slip factor has been defined by Qiu et al. (2011) which is applicable to axial, radial, and mixed flow impellers and, importantly, takes into account the effect of the flow coefficient. This is a most interesting and significant development of slip factor theory. According to the paper's authors, slip factor is affected by the impeller rotation as well as by the blade turning rate at the point of impeller discharge.

For an axial impeller (i.e., a compressor blade row), there is no radial effect and the resulting slip factor is comparable to the deviation rule of Howell, Carter, and others (see Eqs (3.34) and (3.35)). However, for many radial impellers it turns out that the blade turning term is significant and is actually the key factor that dominates the variation of the slip factor at off-design conditions.

Eck (1973) extended the theory originally advanced by Stodola in which it was asserted that it was the relative eddy which caused the slip in centrifugal impellers. Velocity differences are created in the blade passages so that the velocity on the pressure side of a blade is less than that on the suction side. In Figures 7.13 and 7.16, the pressure side of the passage is, of course, on the right. The relative eddy is imagined to be circular in shape with a diameter d, (shown as AC in Figure 7.16) rotating as a solid body with an angular velocity Ω. The slip velocity is then determined from,

$$c_{\theta s} = \frac{d}{2}\omega = \frac{\omega s_2 \cos \beta_{2b}}{2} \tag{7.25}$$

where the angular velocity in Stodola's flow model is the same as the wheel speed but in the opposite direction.

[3]The word "unified" refers to the intention of the authors to bring into one theory all varieties of compressor. It is not the intention of the present authors to verify the wider aspects of the paper (i.e., application to axial and mixed flow compressors) only to centrifugal compressors.

The pressure inequality includes the effect of blade rotation as well as the effect of blade turning. In his book, Eck stated "the linear velocity gradient is equivalent to a rotation of the total flow across the passage" and from this he recalculated the angular velocity of this rotation as follows:

$$\omega^1 = \frac{w_s - w_p}{2a} \tag{7.26}$$

The slip velocity can now be related to the blade loading, i.e., the velocity difference on the blade suction and pressure surfaces at impeller discharge:

$$c_{\theta s} = \frac{a}{2}\omega^1 = \frac{w_s - w_p}{4} \tag{7.27}$$

Inside the impeller passage, the flow is loaded by the Coriolis force, the centrifugal force, and the blade turning force. According to Qiu, these forces vanish when the flow reaches the line AC with the result that the flow deviates from its expected path. This is the crucial point of Qiu's argument.

The next step is to quantify the blade loading up to AC so that the right-hand side of Eq. (7.27) can be evaluated.

Qiu assumed that the velocity difference between D and A is small so that the blade loading at AC can be determined (approximately) by the loading on the arc DC. Following fairly recent work by Johnson (1986) and Cumpsty (1989), Qiu found that the loading on the arc DC could be expressed by the following equation:

$$\frac{w_s - w_p}{DC} = 2\omega \sin\gamma \cos\beta - w\left(\frac{d\beta}{dm} - \frac{\cos\beta \sin\beta}{\rho b}\left\langle\frac{d(\rho b)}{dm}\right\rangle\right) \tag{7.28}$$

The length of the arc DC is related to the pitch length at the impeller exit s_2 through a shape factor, F, i.e.,

$$DC = F \times s_2 \tag{7.28a}$$

where the F factor can be determined from the following equation:

$$F = 1 - \sin\left(\frac{\pi}{Z}\right)\sin\left(\frac{\pi}{Z} + \beta_{2b}\right)\cos\beta_{2b} \sin\gamma_2 - \frac{t_2}{s_2 \cos\beta_{2b}} \tag{7.29}$$

The detailed derivation of this equation is given later in this section.

Combining Eqs (7.27), (7.28), and (7.28a), we arrive at the final expression for the slip velocity

$$c_{\theta s} = F\left\{\frac{\omega s_2 \cos\beta_{2b} \sin\gamma}{2} + \frac{w_2 s_2}{4}\left(\frac{d\beta}{dm}\right)_2 - \frac{w_2 s_2 \sin 2\beta_{2b}}{8\rho_2\beta_2}\left(\frac{d}{dm}(\rho b)\right)_2\right\} \tag{7.30}$$

The final form of the slip factor is obtained when Eq. (7.30) is divided by the rotational speed, i.e.,

$$\sigma = 1 - \frac{c_{\theta s}}{U_2} = 1 - \frac{F\pi \cos\beta_{2b} \sin\gamma_2}{Z} - \frac{F s_2 \phi_2}{4\cos\beta_{2b}}\left(\frac{d\beta}{dm}\right)_2 + \frac{F\phi_2 s_2 \sin\beta_{2b}}{4\rho_2 b_2}\left(\frac{d\langle\rho b\rangle}{dm}\right)_2 \tag{7.31}$$

Now, in order to better understand the above equation, an inspection of each term is given after labeling them.

Equation (7.31) can be written as

$$\sigma = 1 - \Delta\sigma_{\text{radial}} - \Delta\sigma_{\text{turn}} - \Delta\sigma_{\text{passage}} \tag{7.32}$$

where

$$\Delta\sigma_{\text{radial}} = \frac{F\pi \cos\beta_{2b} \sin\gamma_2}{Z} \tag{7.32a}$$

is the decrement in slip due to the effect of radial rotation,

$$\Delta\sigma_{\text{turn}} = \frac{Fs_2\phi_2}{4\cos\beta_{2b}}\left(\frac{d\beta}{dm}\right)_2 \tag{7.32b}$$

is the decrement due to blade turning, and

$$\Delta\sigma_{\text{passage}} = -\frac{F\phi_2 s_2 \sin\beta_{2b}}{4\rho_2 b_2}\left(\frac{d\langle\rho b\rangle}{dm}\right)_2 \tag{7.32c}$$

is the decrement due to any variations of passage width and density.

Qiu stated that the radical term in Eq. (7.32c) will be very small compared with the other terms and that its contribution to the slip factor would be minimal. Therefore, this last term is disregarded in all the following calculations.

Comparison of the new slip factor theory with experimental results

Method of Calculating the Shape Factor F

Referring to Figure 7.16, the line AC is drawn from point A and is perpendicular to the adjacent blade. The line AC is referred to as the exit throat. The object of the following method is to calculate the length of the arc DC.

The angle between two adjacent blades is $\Delta\theta = 2\pi/Z$, where Z is the number of blades.

The chord AB can now be calculated as

$$\overline{\text{AB}} = 2R_2 \sin\left(\frac{\Delta\theta}{2}\right)$$

Since

$$\angle\text{OBA} = (\pi - \Delta\theta)/2 \text{ then } \angle\text{ABC} = \angle\text{OBA} - \beta_{2b} = \frac{\pi}{2} - \frac{\Delta\theta}{2} - \beta_{2b}$$

We can now calculate the length of the line BC

$$\text{BC} = \text{AB}\cos(\angle\text{ABC}) = \text{AB}\sin\left(\frac{\Delta\theta}{2} + \beta_{2b}\right)$$

The radius reduction from the tip of the impeller (at B) to point C can now be determined approximately as

$$\text{BE} = \text{BC}\cos(\beta_{2b})\sin(\gamma_2) = 2R_2 \sin\left(\frac{\Delta\theta}{2}\right)\sin\left(\frac{\Delta\theta}{2} + \beta_{2b}\right)\cos(\beta_{2b})\sin(\gamma_2)$$

The presence of the angle γ_2 is because the whole calculation is projected onto the radial plane so as to determine the reduction in radius. Therefore, the radius of the arc DC is

$$\mathrm{OC} \approx \mathrm{OB} - \mathrm{BE} = R_2\left[1 - 2\sin\left(\frac{\pi}{Z}\right)\sin\left(\frac{\pi}{Z} + \beta_{2b}\right)\cos(\beta_{2b})\sin(\gamma_2)\right]$$

For a blade of finite thickness, the length of arc DC is then

$$\mathrm{DC} = \mathrm{OC} \times \Delta\theta - \frac{t_2}{\cos\,\beta_{2b}}$$

The F factor is the ratio of the lengths DC to AB, i.e.,

$$F = 1 - 2\sin\left(\frac{\pi}{Z}\right)\sin\left(\frac{\pi}{Z} + \beta_{2b}\right)\cos(\beta_{2b})\sin(\gamma_2) - \frac{t_2}{s_2\cos\,\beta_{2b}}$$

Illustrative exercise (determining a value for *F*)

For the Eckardt (1980) rotor A, the following parameters apply.

$R_2 = 0.2$ m, $\beta_{2b} = 30°$ (backswept), $\gamma_2 = 90°, Z = 20, \mathrm{d}\beta/dm = -9/m$ (and this corresponds to $-0.5°$/mm of radius increment).

Referring to Figure 7.16,

$$\mathrm{AB} = 2\pi R_2/Z = 0.0626 \text{ m}, \angle\mathrm{OBA} = (\pi - \Delta\theta)/2 = 81°$$
$$\angle\mathrm{ABC} = \angle\mathrm{OBA} - \beta_{2b} = 81 - 30 = 51° \quad \therefore \mathrm{BC} = \mathrm{AB}\cos(\angle\mathrm{ABC}) = 0.0626\cos 51°$$

$\mathrm{BC} = 0.0394$ m.

$$\therefore \mathrm{BE} = \mathrm{BC} \times \cos 30° = 0.03412 \text{ and } \mathrm{OE} = \mathrm{OB} - \mathrm{EB} = 0.2 - 0.03412 = 0.1659 \text{ m}$$

Finally, although no information is given about the thickness t_2 at the trailing edge of the blade, we shall assume here a value of 2 mm

$$\therefore t_2/s_2 = \frac{0.002}{2 \times \pi \times 0.2 \times 0.866} = 1.838 \times 10^{-3}$$

$$\therefore F = \frac{0.1659 - .001838}{0.2} = 0.82$$

An approximate confirmation of this result can be made by making a careful scale drawing of the impeller geometry.

Results

Values of the slip factor calculated by Qiu for the Eckardt rotor A are shown in Figure 7.14 as a function of the exit flow coefficient Φ_2. By way of contrast, the results determined using the Stodola and Wiesner formulae are shown. It is clear that the current model matched the experimental values measured for this rotor closely at all speeds whereas the Stodola and Wiesner did not come close. This seems to be a remarkable achievement by the authors and they deserve everyone's congratulations! It should be mentioned that Qiu and his colleagues were supported in their conclusions by a vast number of confirmatory tests on many other types of rotors and pumps.

Qiu expressed the view that the negative blade turning rate was responsible for the upward trend of the slip factor with the exit flow coefficient. Finally, Qiu emphasized how all the data points for all four speeds closely followed a single curve. This observation confirmed that the slip factor correlated with a single parameter—the exit flow coefficient.

It may have been noticed from the references at the end of this chapter that some attempts have been made by various authors to include the variation of the flow rate in their predictions of the slip factor.

7.9 Head increase of a centrifugal pump

The actual delivered head H, measured as the *head difference* between the inlet and the outlet flanges of the pump and sometimes called the *manometric head*, is less than the ideal head H_i defined in Eq. (7.4) by the amount of the internal losses. The hydraulic efficiency of the pump is defined as

$$\eta_h = \frac{H}{H_i} = \frac{gH}{U_2 c_{\theta 2}} \tag{7.33a}$$

From the velocity triangles of Figure 7.5,

$$c_{\theta_2} = U_2 - c_{r2} \tan \beta_2$$

Therefore,

$$H = \eta_h U_2^2 (1 - \phi_2 \tan \beta_2)/g \tag{7.33b}$$

where $\phi_2 = c_{r2}/U_2$ and β_2 is the actual averaged relative flow angle at impeller outlet.

With the definition of slip factor, $\sigma = c_{\theta 2}/c'_{\theta 2}$, H can, more usefully, be directly related to the impeller vane outlet angle as

$$H = \eta_h \sigma U_2^2 (1 - \phi_2 \tan \beta'_2)/g \tag{7.33c}$$

In general, centrifugal pump impellers have between 5 and 12 vanes inclined backward to the direction of rotation, as suggested in Figure 7.5, with a vane tip angle β'_2 of between 50° and 70°. A knowledge of blade number, β'_2 and ϕ_2 (usually small and on the order of 0.1), generally enables σ to be found using the Busemann formula. The effect of slip, it should be noted, causes the relative flow angle β_2 to become larger than the vane tip angle β'_2.

EXAMPLE 7.3

A centrifugal pump delivers 0.1 m^3/s of water at a rotational speed of 1200 rev/min. The impeller has seven vanes, which lean backward to the direction of rotation such that the vane tip angle β'_2 is 50°. The impeller has an external diameter of 0.4 m, an internal diameter of 0.2 m, and an axial width of 31.7 mm. Assuming that the diffuser efficiency is 51.5%, that the impeller head losses are 10% of the ideal head rise, and that the diffuser exit is 0.15 m in diameter, estimate the slip factor, the manometric head, and the hydraulic efficiency.

Solution

The criterion given as Eq. (7.24c) is employed *prior* to estimating the slip factor. As $\exp(2\pi \cos \beta_2'/Z) = \exp(2\pi \times 0.643/7) = 1.78$ (which is less than $r_2/r_1 = 2$), then $B = 1$ and $A \approx 0.77$. *Note:* This value of A is obtained by replotting values of A given in Figure 7.17 for $\beta_2' = 50^\circ$ and interpolating.

The vane tip speed

$$U_2 = \pi N D_2/60 = \pi \times 1200 \times 0.4/6 = 25.13 \text{ m/s}$$

The radial velocity

$$c_{r2} = Q/(\pi D_2 b_2) = 0.1/(\pi \times 0.4 \times 0.0317) = 2.51 \text{ m/s}$$

Hence, the Busemann slip factor is

$$\sigma = (0.77 - 0.1 \times 1.192)/(1 - 0.1 \times 1.192) = 0.739$$

Hydraulic losses occur in the impeller, in the diffuser, and in the volute. The loss in head in the diffuser is

$$\Delta H_D = (p_{02} - p_{03})/(\rho g) = (p_2 - p_3)/(\rho g) + (c_2^2 - c_3^2)/(2g)$$

and, from Eq. (7.52) for incompressible flow,

$$p_3 - p_2 = \frac{1}{2}\eta_D \rho (c_2^2 - c_3^2)$$

Substituting in the previous equation, we find

$$\Delta H_D = (1 - \eta_D)(c_2^2 - c_3^2)/(2g)$$

The kinetic energy leaving the diffuser is only partly recovered. Watson and Janota (1982) ascribe the total loss in the volute as about *half the dynamic head leaving the diffuser*, and this is also assumed in this calculation. The exit head loss is $0.5 \times c_3^2/(2g)$ and the head loss in the impeller is $0.1 \times U_2 c_{\theta 2}/g$.

Summing all the losses,

$$H_L = 0.485 \times (c_2^2 - c_3^2)/(2g) + 0.1 \times U_2 c_{\theta 2}/g + 0.5 \times c_3^2/(2g)$$

Determining the velocities and heads needed,

$$c_{\theta 2} = \sigma U_2 (1 - \phi_2 \tan \beta_{2'}) = 0.739 \times 25.13 \times 0.881 = 16.35 \text{ m/s}$$

$$H_i = U_2 c_{\theta 2}/g = 25.13 \times 16.35/9.81 = 41.8 \text{ m}$$

$$c_2^2/(2g) = (16.35^2 + 2.51^2)/19.62 = 13.96 \text{ m}$$

$$c_3 = 4Q/(\pi d^2) = 0.4/(\pi \times 0.15^2) = 5.65 \text{ m/s}$$

$$c_3^2/(2g) = 1.63 \text{ m}$$

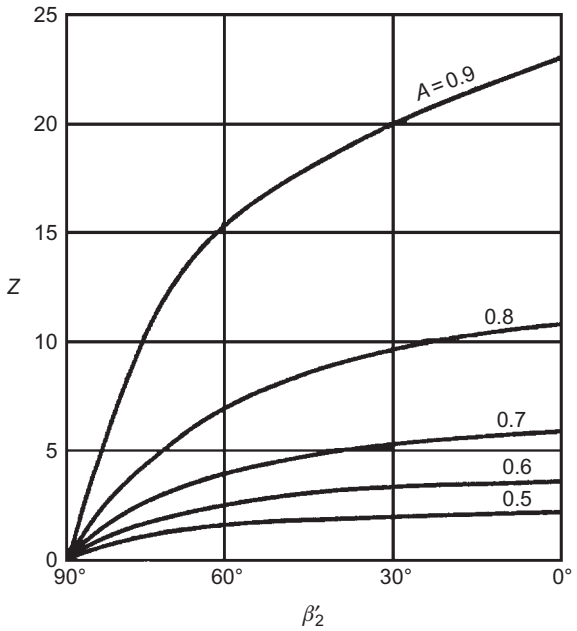

FIGURE 7.17

Head correction factors for centrifugal impellers.

(*Adapted from Csanady, 1960*)

Therefore,

$$H_L = 4.18 + 0.485(13.96 - 1.63) + 1.63/2 = 10.98 \text{ m}$$

The manometric head is

$$H = H_i - H_L = 41.8 - 10.98 = 30.82 \text{ m}$$

and the hydraulic efficiency is

$$\eta_h = H/H_i = 73.7\%$$

7.10 Performance of centrifugal compressors

Determining the pressure ratio

Consider a centrifugal compressor having zero inlet swirl, compressing a perfect gas. With the usual notation, the energy transfer is

$$\Delta W = \dot{W}_c/\dot{m} = h_{02} - h_{01} = U_2 c_{\theta 2}$$

The overall or total-to-total efficiency η_c is

$$\eta_c = \frac{h_{03ss} - h_{01}}{h_{03} - h_{01}} = \frac{C_p T_{01}(T_{03ss}/T_{01} - 1)}{h_{02} - h_{01}} = C_p T_{01}(T_{03ss}/T_{01} - 1)/(U_2 c_{\theta 2}) \tag{7.34}$$

Now the overall pressure ratio is

$$\frac{p_{03}}{p_{01}} = \left(\frac{T_{03ss}}{T_{01}}\right)^{\gamma/(\gamma-1)} \tag{7.35}$$

Substituting Eq. (7.34) into Eq. (7.35) and noting that $C_p T_{01} = \gamma R T_{01}/(\gamma - 1) = a_{01}^2/(\gamma - 1)$, the pressure ratio becomes

$$\frac{p_{03}}{p_{01}} = \left[1 + \frac{(\gamma-1)\eta_c U_2 c_{r2} \tan \alpha_2}{a_{01}^2}\right]^{\gamma/(\gamma-1)} \tag{7.36}$$

From the velocity triangle at impeller outlet (Figure 7.4),

$$\phi_2 = c_{r2}/U_2 = (\tan \alpha_2 + \tan \beta_2)^{-1}$$

and, therefore,

$$\frac{p_{03}}{p_{01}} = \left[1 + \frac{(\gamma-1)\eta_c U_2^2 \tan \alpha_2}{a_{01}^2(\tan \alpha_2 + \tan \beta_2)}\right]^{\gamma/(\gamma-1)} \tag{7.37a}$$

This formulation is useful if the flow angles can be specified. Alternatively, and more usefully, as $c_{\theta 2} = \sigma c_{\theta 2'} = \sigma(U_2 - c_{r2} \tan \beta_2')$, then

$$\frac{p_{03}}{p_{01}} = [1 + (\gamma-1)\eta_c \sigma(1 - \phi_2 \tan \beta_2')M_u^2]^{\gamma/(\gamma-1)} \tag{7.37b}$$

where $M_u = U_2/a_{01}$ is now defined as a blade Mach number.

It is useful and of interest to calculate the variation of the pressure ratio of a radially vaned ($\beta_2' = 0$) centrifugal air compressor to show the influence of blade speed and efficiency on the performance. With $\gamma = 1.4$ and $\sigma = 0.9$ (i.e., using the Stanitz slip factor, $\sigma = 1 - 1.98/Z$) and assuming $Z = 20$, the results evaluated are shown in Figure 7.18 It is clear that both the efficiency and the blade speed have a strong effect on the pressure ratio.

In the 1970s the limit on blade speed due to centrifugal stress was about 500 m/s and compressor efficiency seldom exceeded 80%. With a slip factor of 0.9, a radial-vaned impeller and an inlet temperature of 288 K, the pressure ratio achieved was barely above 5. More recently quite significant improvements in the performance of centrifugal compressors have been obtained, brought about by the development of computer-aided design and analysis techniques. According to Whitfield and Baines (1990), the techniques employed consist of "a judicious mix of empirical correlations and detailed modeling of the flow physics"! However, it is possible to use these computer packages and arrive at a design solution without any real appreciation of the flow phenomena involved. In *all* compressors, the problematic part of the flow process is the *diffusion*; boundary layers are very prone to separate and the flow can become very complicated with separated wakes in the flow and unsteady flow downstream of the impeller. It must be stressed that *a broad*

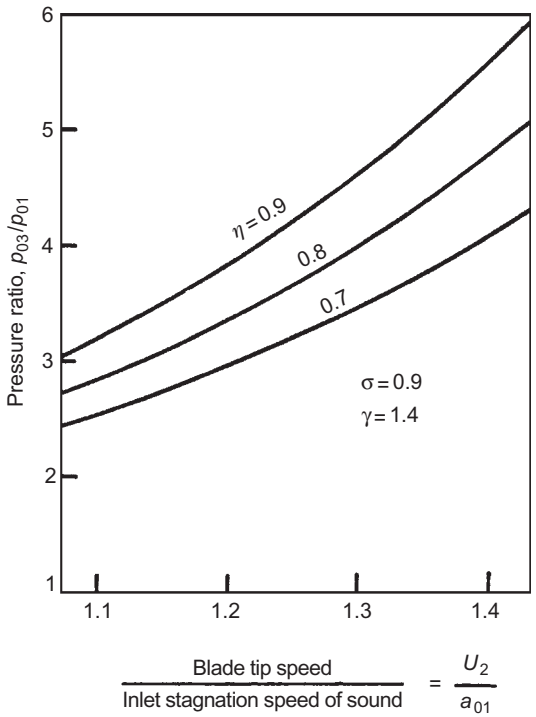

FIGURE 7.18

Variation of pressure ratio with blade speed for a radial-bladed compressor ($\beta_2' = 0$) at various values of efficiency.

understanding of the flow processes within a centrifugal compressor is still a vital requirement for the more advanced student and for the further progress of new design methods.

A characteristic of all high-performance compressors is that as the design pressure ratio has increased, so the range of mass flow between surge and choking has diminished. In the case of the centrifugal compressor, choking can occur when the Mach number entering the diffuser passages is just in excess of unity. This is a severe problem that is aggravated by any shock-induced separation of the boundary layers on the vanes, which will worsen the problem of flow blockage.

Effect of backswept vanes

Came (1978) and Whitfield and Baines (1990) have commented upon the trend of obtaining higher pressure ratios from *single-stage compressors* leading to more highly stressed impellers. The increasing use of backswept vanes and higher blade tip speeds results in higher direct stress in the impeller and bending stress in the nonradial vanes. However, methods of computing the stresses in impellers are available, capable of determining both the direct and the bending stresses caused by the impeller rotation.

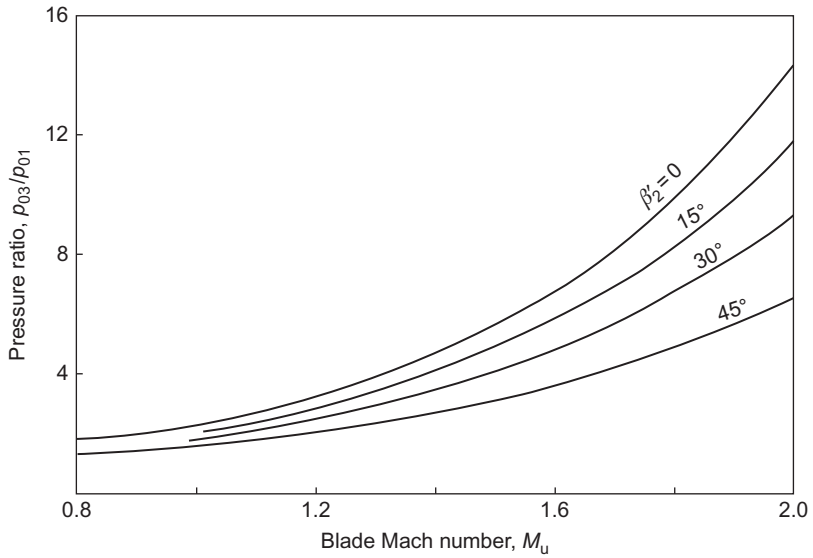

FIGURE 7.19

Variation of pressure ratio versus blade Mach number of a centrifugal compressor for selected backsweep angles ($\gamma = 1.4$, $\sigma = 0.9$, $\phi_2 = 0.375$, $\eta_c = 0.8$).

The effect of using backswept impeller vanes on the pressure ratio is shown in Figure 7.19 for a range of blade Mach numbers. The use of backswept vanes at a given blade speed causes some loss in pressure ratio. In order to maintain a given pressure ratio, it is therefore necessary to increase the design speed, which increases the blade stresses.

With high blade tip speeds the Mach number of the absolute flow leaving the impeller may exceed unity. As this Mach number can be related to the Mach number at entry to the diffuser vanes, it is of some advantage to be able to calculate the former.

Assuming a perfect gas, the Mach number at impeller exit M_2 can be written as

$$M_2^2 = \frac{c_2^2}{a_2^2} = \frac{c_2^2}{T_{01}} \times \frac{T_{01}}{T_2} \times \frac{T_2}{a_2^2} = \frac{c_2^2}{a_{01}^2}\frac{T_{01}}{T_2} \tag{7.38}$$

since $a_{01}^2 = \gamma R T_{01}$ and $a_2^2 = \gamma R T_2$.

Referring to the outlet velocity triangle, Figure 7.12 (for the impeller with backswept vanes),

$$c_2^2 = c_{r2}^2 + c_{\theta 2}^2 = c_{r2}^2 + (\sigma c_{\theta 2'})^2$$

where

$$c_{\theta 2'} = U_2 - c_{r2} \tan \beta_{2'}$$

$$\left(\frac{c_2}{U_2}\right)^2 = \phi_2^2 + \sigma^2(1 - \phi_2 \tan \beta_{2'})^2 \tag{7.39}$$

Assuming that rothalpy remains constant, Eq. (7.2), gives

$$h_2 = \left(h_1 + \frac{1}{2}w_1^2 - \frac{1}{2}U_1^2\right) + \frac{1}{2}(U_2^2 - w_2^2) = h_{01} + \frac{1}{2}(U_2^2 - w_2^2)$$

hence,

$$\frac{T_2}{T_{01}} = 1 + \frac{(U_2^2 - w_2^2)}{a_{01}^2/(\gamma - 1)} = 1 + \frac{1}{2}(\gamma - 1)M_u^2\left(1 - \frac{w_2^2}{U_2^2}\right) \tag{7.40}$$

since $h_{01} = C_p T_{01} = a_{01}^2/(\gamma - 1)$.

From the exit velocity triangle, Figure 7.12,

$$\begin{aligned} w_2^2 &= c_{r2}^2 + (U_2 - c_{\theta 2})^2 = c_{r2}^2 + (U_2 - \sigma c_{\theta 2'})^2 \\ &= c_{r2}^2 + [U_2 - \sigma(U_2 - c_{r2}\tan\beta_2')]^2 \end{aligned} \tag{7.41}$$

$$1 - \left(\frac{w_2}{U_2}\right)^2 = 1 - \phi s_2^2 - [1 - \sigma(1 - \phi_2 \tan\beta_2')]^2 \tag{7.42}$$

Substituting Eqs (7.39), (7.40), and (7.42) into Eq. (7.38), we get

$$M_2^2 = \frac{M_u^2[\sigma^2(1 - \phi_2\tan\beta_{2'})^2 + \phi_2^2]}{1 + (1/2)(\gamma - 1)M_u^2\{1 - \phi_2^2 - [1 - \sigma(1 - \phi_2\tan\beta_{2'})]^2\}} \tag{7.43a}$$

Although Eq. (7.43a) may look rather complicated at first sight, it reduces into an easily managed form when a few constant values are inserted. Assuming the same values, we used previously, i.e., $\gamma = 1.4$, $\sigma = 0.9$, $\phi_2 = 0.375$, and $\beta_2' = 0°, 15°, 30°$, and $45°$, the solution for M_2 simplifies to

$$M_2 = \frac{AM_u}{\sqrt{1 + BM_u^2}} \tag{7.43b}$$

where the values of A and B are given in Table 7.1 and from which the curves of M_2 against M_u in Figure 7.19 have been calculated.

Whitfield and Baines (1990) *assert* that the two most important aerodynamic parameters at impeller exit are the magnitude and direction of the absolute Mach number M_2. If M_2 has too high a value, the process of efficient flow deceleration within the diffuser itself is more difficult leading to high friction losses as well as the increased possibility of shock losses. If the flow angle α_2 is

Table 7.1 Values of Constants Used to Evaluate M_2

	β_2'			
Constant	**0°**	**15°**	**30°**	**45°**
A	0.975	0.8922	0.7986	0.676
B	0.1669	0.1646	0.1545	0.1336

large, then the flow path in the vaneless diffuser will be excessively long resulting in high friction losses and possible stall and flow instability. Several researchers, e.g., Rodgers and Sapiro (1972), have shown that the optimum flow angle is in the range $60^\circ < \alpha_2 < 70^\circ$.

Backswept vanes give a reduction of the impeller discharge Mach number, M_2, at any given tip speed. A designer making the change from radial vanes to backswept vanes will incur a reduction in the design pressure ratio if the vane tip speed remains the same. To recover the original pressure ratio, the designer needs to *increase* the blade tip speed, which, in turn, increases the discharge Mach number. Fortunately, it turns out that this increase in M_2 is rather less than the reduction obtained by the use of backsweep.

Illustrative exercise

Consider a centrifugal compressor design that assumes the previous design data (Figures 7.19 and 7.20) together with $\beta_2' = 0^\circ$ and a blade speed such that $M_u = 1.6$. From Figure 7.19, the pressure ratio at this point is 6.9 and, from Figure 7.20, the value of $M_2 = 1.3$. Choosing another impeller with a backsweep angle, $\beta_{2'} = 30^\circ$, the pressure ratio is 5.0 from Figure 7.19 at the *same value* of M_u. So, to restore the original pressure ratio of 6.9 the blade Mach number must be increased to

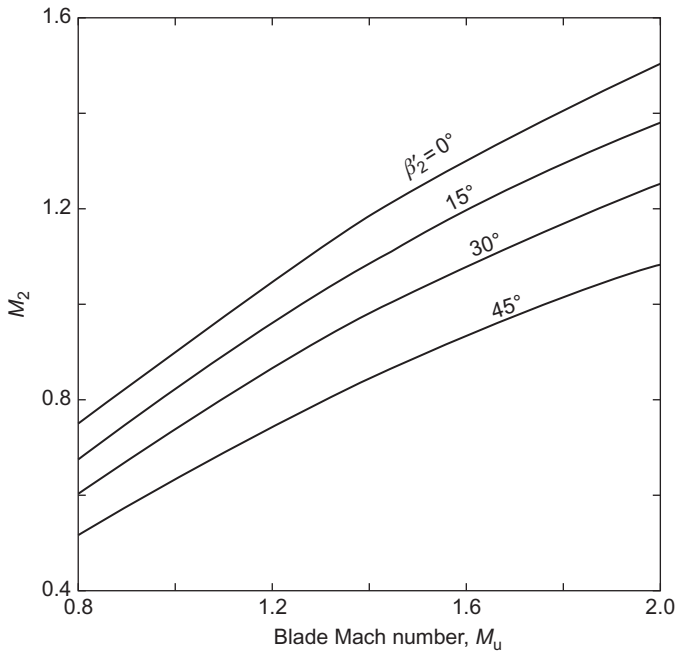

FIGURE 7.20

Variation of impeller exit mach number versus blade Mach number of a centrifugal compresor for selected backsweep angles ($\gamma = 1.4, \sigma = 0.9, \phi_2 = 0.375$).

$M_u = 1.81$. At this new condition a value of $M_2 = 1.178$ is obtained from Figure 7.20, a significant reduction from the original value. Greater values of backsweep may produce even further benefits!

The absolute flow angle can now be found from the exit velocity triangle, Figure 7.12:

$$\tan \alpha_2 = \frac{c_{\theta 2}}{c_{r2}} = \frac{\sigma(U_2 - c_{r2} \tan \beta_{2'})}{c_{r2}} = \sigma\left(\frac{1}{\phi_2} - \tan \beta_{2'}\right)$$

Assuming again the values $\sigma = 0.9$, $\sigma_2 = 0.375$, then with $\beta'_2 = 0°$, the value of $\alpha_2 = 67.38°$. Similarly, with $\beta'_2 = 30°$, the value of $\alpha_2 = 62°$, i.e., both values of α_2 are within the prescribed acceptible range.

Kinetic energy leaving the impeller

According to van den Braembussche (1985), "the kinetic energy available at the diffuser inlet easily amounts to more than 50% of the total energy added by the impeller." Using the foregoing analysis, we can determine whether this statement is true or not. If the magnitude of the kinetic energy is so large, then the importance of efficiently converting this energy into pressure energy can be appreciated. The conversion of the kinetic energy to pressure energy is considered in the following section on diffusers.

We can define the fraction of the kinetic energy at impeller exit to the specific work input as

$$f_{KE} = \frac{1}{2} c_2^2 / \Delta W \tag{7.44}$$

where

$$\begin{aligned} \Delta W = \sigma U_2^2 (1 - \phi_2 \tan \beta'_2) \text{ and } \left(\frac{c_2}{U_2}\right)^2 &= \left(\frac{c_2}{a_2} \times \frac{a_2}{a_{01}} \times \frac{a_{01}}{U_2}\right)^2 \\ &= \left(\frac{M_2}{M_u}\right)^2 \left(\frac{a_2}{a_{01}} \times \frac{a_{02}}{a_{01}}\right)^2 \end{aligned} \tag{7.45}$$

Defining the total-to-total efficiency of the impeller as

$$\eta_1 = \frac{h_{02s} - h_{01}}{h_{02} - h_{01}} = \frac{h_{01}((T_{02s}/T_{01}) - 1)}{h_{02} - h_{01}} = \frac{h_{01}(p_R^{(\gamma-1)/\gamma} - 1)}{\Delta W}$$

where p_R is the total-to-total pressure ratio across the impeller, then

$$\left(\frac{a_{02}}{a_{01}}\right)^2 = \frac{T_{02}}{T_{01}} = 1 + \frac{\Delta T_0}{T_{01}} = 1 + \frac{\Delta W}{C_p T_{01}} = 1 + \frac{1}{\eta_1}(p_R^{(\gamma-1)\gamma} - 1) \tag{7.46}$$

$$\left(\frac{a_{02}}{a_2}\right)^2 = \frac{T_{02}}{T_2} = 1 + \frac{1}{2}(\gamma - 1) M_2^2 \tag{7.47}$$

Substituting Eqs (7.48), (7.49), and (7.50) into Eq. (7.47), we get

$$f_{KE} = \frac{c_2^2/U_2^2}{2\sigma(1 - \phi_2 \tan \beta'_2)} = \frac{(M_2/M_u)^2[1 + (1/\eta_1)(p_R^{(\gamma-1)/\gamma} - 1)]}{2\sigma(1 - \phi_2 \tan \beta'_2)[1 + (1/2)(\gamma - 1)M_2^2]} \tag{7.48}$$

Illustrative exercise

Determine f_{KE} assuming that $\beta_2' = 0,\ \sigma = 0.9,\ \eta_I = 0.8,\ p_r = 4,$ and $\gamma = 1.4$.

Note: It is very convenient to assume that Figures 7.19 and 7.20 can be used to derive the values of the Mach numbers M_u and M_2. From Figure 7.19, we get $M_u = 1.32$ and from Figure 7.20, we get $M_2 = 1.13$. Substituting these results into Eq. (7.48), we obtain the result

$$f_{KE} = \frac{1}{2 \times 0.9}\left(\frac{1.13}{1.32}\right)^2 \frac{[1 + (1/0.8)(4^{1/3.5} - 1)]}{1 + (1/5) \times 1.13^2} = 0.5213$$

This calculation has thus verified the assertion of van den Braembussche (given previously) that the kinetic energy available at diffuser inlet amounts to more than 50% of ΔW. This, clearly, is an extra incentive to seek an efficient diffuser system!

Calculations of f_{KE} at other pressure ratios and sweepback angles show that its value remains about 0.52 provided that σ and η_1 do not change.

EXAMPLE 7.4

Air at a stagnation temperature of 22°C enters the impeller of a centrifugal compressor in the axial direction. The rotor, which has 17 radial vanes, rotates at 15,000 rev/min. The stagnation pressure ratio between diffuser outlet and impeller inlet is 4.2 and the overall efficiency (total-to-total) is 83%. Determine the impeller tip radius and power required to drive the compressor when the mass flow rate is 2 kg/s and the mechanical efficiency is 97%. Given that the air density at impeller outlet is 2 kg/m^3 and the axial width at entrance to the diffuser is 11 mm, determine the absolute Mach number at that point. Assume that the slip factor $\sigma = 1 - 2/Z$, where Z is the number of vanes. (For air, take $\gamma = 1.4$ and $R = 0.287$ kJ/(kg K).)

Solution

From Eq. (7.3), the specific work is

$$\Delta W = h_{02} - h_{01} = U_2 c_{\theta 2}$$

as $c_{\theta 1} = 0$. For a radial impeller, $\beta_2' = 0$, so $c_{\theta 2} = \sigma U_2$. With Eq. (7.28) and some rearranging:

$$U_2^2 = \frac{C_p T_{01}(p_{03}/p_{02}{}^{(\gamma-1)/\gamma} - 1)}{\sigma \eta_c}$$

where $p_{03}/p_{01} = 4.2$; $C_p = \gamma R/(\gamma - 1) = 1.005$ kJ/kg K, $\sigma_s = 1 - 2/17 = 0.8824$. Therefore,

$$U_2^2 = \frac{1005 \times 295(4.2^{0.286} - 1)}{0.8824 \times 0.83} = 20.5 \times 10^4$$

and $U_2 = 452$ m/s.

The rotational speed is $\Omega = 15{,}000 \times 2\pi/60 = 1570$ rad/s and the impeller tip radius is $r_t = U_2/\Omega = 452/1570 = 0.288$ m.

The actual shaft power is obtained from

$$\dot{W}_{act} = \dot{W}_c/\eta_m = \dot{m}\Delta W/\eta_m = 2 \times 0.8824 \times 452^2/0.97 = 373 \text{ kW}$$

Although the absolute Mach number at the impeller tip can be obtained almost directly from Eq. (7.46a), it may be instructive instead to find it from its basic definition:

$$M_2 = \frac{c_2}{a_2} = \frac{c_2}{(\gamma R T_2)^{1/2}}$$

where

$$c_2 = (c_{\theta 2}^2 + c_{r2}^2)^{1/2}$$

$$c_{r2} = \dot{m}/(\rho_2 2\pi r_t b_2) = 2/(2 \times 2\pi \times 0.288 \times 0.011) = 50.3 \text{ m/s}$$

$$c_{\theta 2} = \sigma U_2 = 400 \text{ m/s}$$

Therefore,

$$c_2 = \sqrt{400^2 + 50.3^2} = 402.5 \text{ m/s}$$

Since

$$h_{02} = h_{01} + \Delta W$$

$$h_2 = h_{01} + \Delta W - \frac{1}{2}c_2^2$$

Therefore,

$$T_2 = T_{01} + \left(\Delta W - \frac{1}{2}c_2^2\right)/C_p = 295 + (18.1 - 8.1)10^4/1005 = 394.5 \text{ K}$$

Hence,

$$M_2 = \frac{402.5}{\sqrt{402 \times 394.5}} = 1.01$$

7.11 The diffuser system

Centrifugal compressors and pumps are, in general, fitted with either a vaneless or a vaned diffuser to transform the kinetic energy at the impeller outlet into static pressure. The *volute* or *scroll* is the final component of a centrifugal compressor or pump (Figure 7.21). This is a spiral-shaped channel of increasing cross-sectional area whose purpose is to collect the flow from the diffuser (or impeller) and deliver it to the exit pipe. The volute for compressors is almost always of the overhung type, usually the choice is imposed by constraints of space. Figure 7.22 shows two types of volute cross section.

According to Whitfield and Johnson (2002), it is well known that the volute of a centrifugal compressor can cause a circumferential pressure distortion around the impeller at all flow rates other than at design.

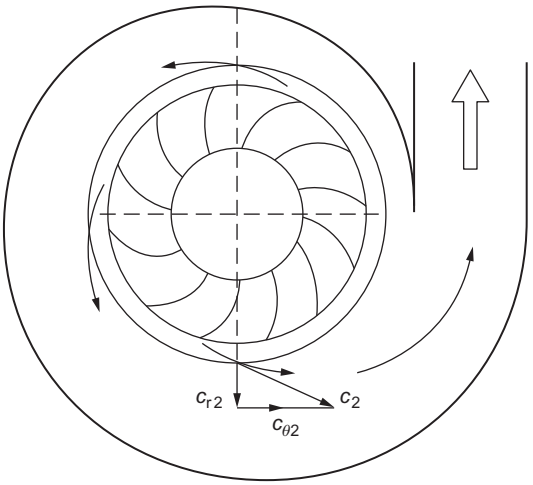

FIGURE 7.21

Volute of a centrifugal compressor or pump.

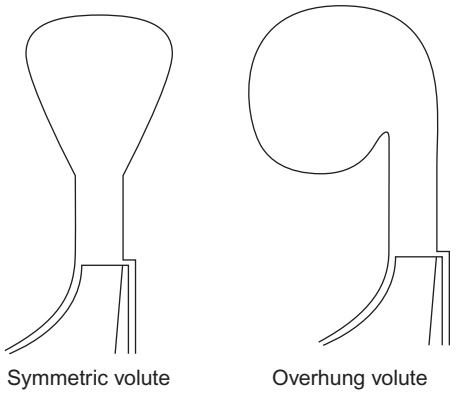

FIGURE 7.22

Two types of volute.

Vaneless diffusers or volutes

The simplest method of diffusion in a radial flow machine is one where the swirl velocity is reduced by an increase in radius (conservation of angular momentum) and the radial component of velocity is controlled by the radial flow area. From continuity, since $\dot{m} = \rho A c_r = 2\pi r b \rho c_r$, where b is the width of passage, then the radial velocity c_r at radius r is

$$c_r = \frac{r_2 b_2 \rho_2 c_{r2}}{r b \rho} \tag{7.49}$$

Assuming the flow is frictionless in the diffuser, the angular momentum is constant and $c_\theta = c_{\theta 2} r_2 / r$. Now the tangential velocity component c_θ is usually very much larger than the radial velocity component c_r; therefore, the ratio of inlet-to-outlet diffuser velocities c_2/c_3 is approximately r_3/r_2. Clearly, to obtain useful reductions in velocity, volutes must be large. This may not be a disadvantage in industrial applications where weight and size may be of secondary importance compared with the cost of a vaned diffuser. A factor in favor of volutes is their wide operating range, vaned diffusers being more sensitive to flow variation because of incidence effects.

For a parallel-walled radial diffuser in incompressible flow, the continuity equation requires that rc_r is constant. Assuming that rc_θ remains constant, then the absolute flow angle $\alpha_2 = \tan^{-1}(c_\theta / c_r)$ is also constant as the fluid is diffused outward. Under these conditions, the flow follows a *logarithmic spiral*. The relationship between the change in the circumferential angle $\Delta\theta$ and the radius ratio of the flow in the diffuser can be found by considering an element of the flow geometry, shown in Figure 7.23. For an increment in radius Dr we have, $r\mathrm{d}\theta = \mathrm{D}r \tan \alpha_2$. Integrating between stations 2 and 3, gives

$$\Delta\theta = \theta_3 - \theta_2 = \tan \alpha_2 \ln\left(\frac{r_3}{r_2}\right) \tag{7.50}$$

Values of $\Delta\theta$ are shown in Figure 7.24 plotted against r_3/r_2 for several values of α_2. It can be readily seen that when $\alpha_2 > 70^\circ$, rather long flow paths are implied, friction losses will be greater and the diffuser efficiency will be lower. Further information about volute design and testing can be found in a paper by Whitfield and Johnson (2002).

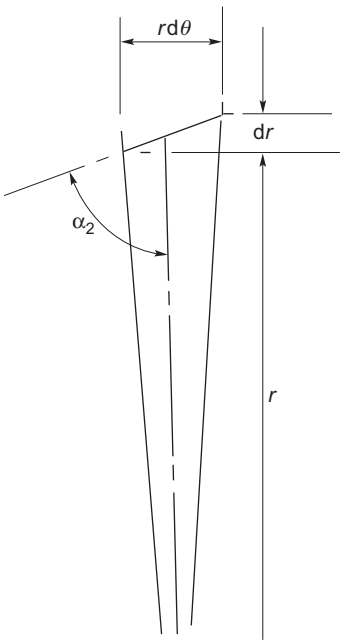

FIGURE 7.23

Element of flow in a radial diffuser.

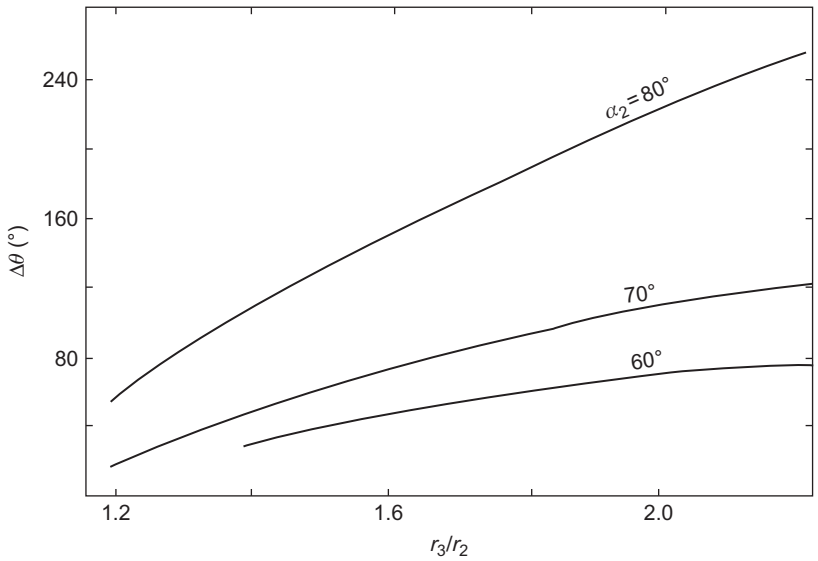

FIGURE 7.24

Variation of flow path parameters for parallel-walled radial diffuser (incompressible flow).

Vaned diffusers

With vaned diffusers, the vanes are used to remove the swirl of the fluid at a higher rate than is possible by a simple increase in radius, thereby reducing the length of flow path and diameter. The vaned diffuser is clearly advantageous where small unit size is important.

There is a clearance between the impeller and the vane leading edges amounting to about $0.04D_2$ for pumps and between $0.1D_2$ and $0.2D_2$ for compressors. This space constitutes a *vaneless diffuser* and its functions are (i) to reduce the circumferential pressure gradient at the impeller tip, (ii) to smooth out velocity variations between the impeller tip and the vanes, and (iii) for compressors, to reduce the Mach number at entry to the vanes. Flow calculations in this space follow the same procedure as for vaneless diffusers.

The flow follows an approximately logarithmic spiral path to the vanes after which it is constrained by the diffuser channels. For rapid diffusion, the axis of the channel is straight and tangential to the spiral as shown. The passages are generally designed on the basis of simple channel theory with an equivalent angle of divergence of between 8° and 10° to control separation.

In many applications of the centrifugal compressor, size is important and the outside diameter must be minimized. With a vaned diffuser, the channel length can be crucial when considering the final size of the compressor. Clements and Artt (1988) considered this and performed a series of experiments aimed at determining the optimum diffuser channel length to width ratio, L/W. They found that, on the compressor they tested, increasing L/W beyond 3.7 did not produce any improvement in the performance, the pressure gradient at that point having reached zero. Another significant result found by them was that the pressure gradient in the diffuser channel when $L/W > 2.13$

was no greater than that which could be obtained in a vaneless diffuser. Hence, removing completely that portion of the diffuser after this point would yield the same pressure recovery as with the full diffuser.

The number of diffuser vanes can also have a direct bearing on the efficiency and surge margin of the compressor. Surge occurs at higher flow rates when vaned diffusers are used than when a simple vaneless diffuser design is adopted. It is better to have fewer diffuser vanes than impeller vanes (about half) in order to achieve a wide range of surge-free flow.

With several adjacent diffuser passages sharing the gas from one impeller passage, the uneven velocity distribution from that passage results in alternate diffuser passages being either starved or choked. This is an unstable situation leading to flow reversal in the passages and to surge of the compressor. When the number of diffuser passages is *less* than the number of impeller passages a more uniform total flow results.

Figure 7.9 shows the occurrence of flow unsteadiness or nonuniform flow at the exit from 2D diffusers. The line marked $a-a$ will be of most interest for turbomachinery diffuser applications. Note that this sharply marked transition line is not necessarily true and exact and a certain amount of arbitrariness and subjectivity attends the occurrence of "first stall."

Figure 7.25 shows typical performance curves for a rectangular diffuser with a fixed sidewall to length ratio, $L/W_1 = 8.0$, given by Kline, Abbott, and Fox (1959). On the line labeled C_p, points numbered 1, 2, and 3 are shown. These numbered points correspond to those shown in Figure 7.9 where they lie in relation to the various flow regimes. Inspection of the location of point 2 shows that optimum recovery at constant length occurs slightly above the line marked ***No appreciable***

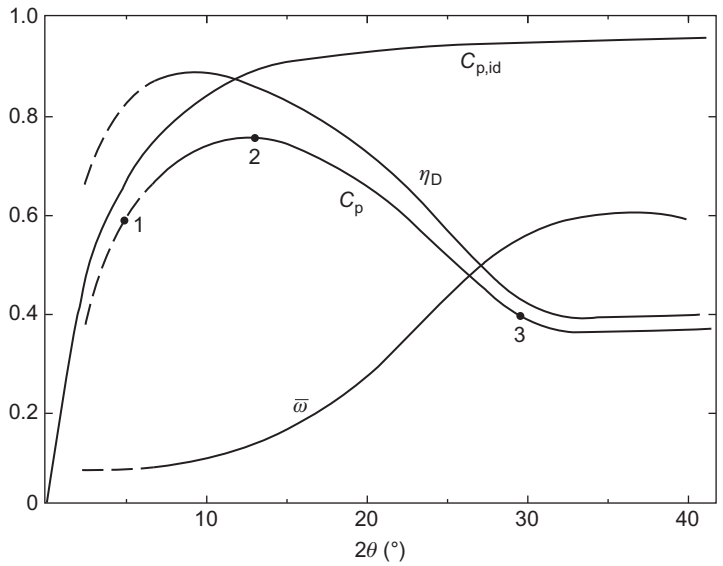

FIGURE 7.25

Typical diffuser performance curves for a 2D diffuser with $L/W_1 = 8{:}0$.

(*Adapted from Kline et al., 1959*)

stall. The performance of the diffuser between points 2 and 3 in Figure 7.9 shows a very significant deterioration and is in the regime of large amplitude, very unsteady flow.

7.12 Diffuser performance parameters

The diffusion process can be represented on a Mollier diagram, Figure 7.26, by a change of state from point 1 to point 2, and the corresponding changes in pressure from p_1 to p_2 and velocity from c_1 to c_2.

Several ways are available for expressing diffuser performance in *compressible flow*:

i. Diffuser efficiency, η_D = ratio of actual change in enthalpy to the isentropic change in enthalpy. For steady and adiabatic flow in stationary passages, $h_{01} = h_{02}$, so that

$$h_2 = h_1 = \frac{1}{2}(c_1^2 - c_2^2) \tag{7.51a}$$

For the equivalent reversible adiabatic process from state point 1 to state point 2s,

$$h_{2s} - h_1 = \frac{1}{2}(c_1^2 - c_{2s}^2) \tag{7.51b}$$

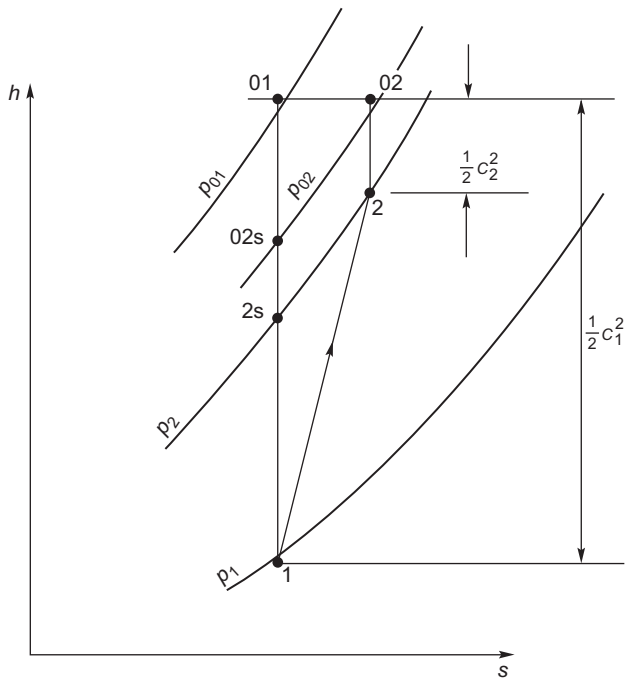

FIGURE 7.26

Mollier diagram for a diffuser flow.

Hence,

$$\eta_D = (h_{2s} - h_1)/(h_2 - h_1) = (c_1^2 - c_{2s}^2)/(c_1^2 - c_2^2) \tag{7.52}$$

ii. A total pressure recovery factor, p_{02}/p_{01}, can be used as a measure of diffuser performance. The diffuser efficiency is

$$\eta_D = (T_{2s}/T_1 - 1)/(T_2/T_1 - 1) \tag{7.53}$$

It may be more convenient to represent this efficiency in terms of pressure ratios as follows: For the isentropic process 1−2s,

$$\frac{T_{2s}}{T_1} = \left(\frac{p_2}{p_1}\right)^{(\gamma-1)/\gamma}$$

For the constant temperature process, 01−02, we obtain $T\,\mathrm{d}s = -\mathrm{d}p/\rho$, which, when combined with the gas law, $p/\rho = RT$, gives $\mathrm{d}s = R\,\mathrm{d}p/p$. Upon integrating for the whole process, we get

$$\Delta s = R \ln\left(\frac{p_{01}}{p_{02}}\right)$$

For the constant pressure process, $2s - 2$, $T\,\mathrm{d}s = \mathrm{d}h = C_p\,\mathrm{d}T$, therefore,

$$\Delta s = C_p \ln\left(\frac{T_2}{T_{2s}}\right)$$

Equating these expressions for the entropy increase and using $R/C_p - (\gamma - 1)/\gamma$, we find

$$\frac{T_2}{T_{2s}} = \left(\frac{p_{01}}{p_{02}}\right)^{(\gamma-1)/\gamma}$$

Therefore,

$$\frac{T_2}{T_1} = \left(\frac{T_2}{T_{2s}}\right)\left(\frac{T_{2s}}{T_1}\right) = \left[\left(\frac{p_{01}}{p_{02}}\right)\left(\frac{p_2}{p_1}\right)\right]^{(\gamma-1)/\gamma}$$

Substituting these expressions into Eq. (7.53), we get

$$\eta_D = \frac{(p_2/p_1)^{(\gamma-1)/\gamma} - 1}{[(p_{01}/p_{02})(p_2/p_1)]^{(\gamma-1)/\gamma} - 1} \tag{7.54}$$

EXAMPLE 7.5

Air enters the diffuser of a compressor with a velocity of 300 m/s at a stagnation pressure of 200 kPa and a stagnation temperature of 200°C and leaves the diffuser with a velocity of 50 m/s. Using compressible flow relations and assuming the diffuser efficiency, $\eta_D = 0.9$, determine

a. the static temperatures at inlet and outlet of the diffuser and the inlet Mach number;

b. the static pressure at diffuser inlet;
c. the increase in entropy caused by the diffusion process.

Take $\gamma = 1.4$ and $C_p = 1005$ J/kg K

Solution

Note: When solving diffuser problems it is advisable and always useful to make a sketch of the Mollier diagram of the diffusion process. In this case, we refer to Figure 7.25.

The expression for the diffuser efficiency, which is most useful for this example, is Eq. (7.53):

$$\eta_D = (T_{2s}/T_1 - 1)/(T_2/T_1 - 1)$$

From the energy equation, $h_{01} - h_1 = (1/2)c_1^2$ we obtain,

$$\frac{T_1}{T_{01}} = 1 - \frac{c_1^2}{2C_pT_{01}} = 1 - \frac{300^2}{2 \times 1050 \times 473} = 0.90533$$

Therefore,

$$T_1 = 428.2 \text{ K as } T = 473 \text{ K}$$

The Mach number at diffuser entry is

$$M_1 = c_1/a_1 \text{ where } a_1 = \sqrt{\gamma RT_1} = \sqrt{1.4 \times 287 \times 428.2} = 414.8 \text{ m/s}$$

Therefore,

$$M_1 = 0.7233.$$

Again, from the energy equation, $h_{02} - h_2 = (1/2)c_2^2$, hence,

$$\frac{T_2}{T_{02}} = 1 - \frac{c_2^2}{2C_pT_{02}} = 1 - \frac{50^2}{2 \times 1050 \times 473} = 0.9974$$

and

$$T_2 = 471.7 \text{ K}$$

From the diffuser efficiency definition above, we get

$$\frac{T_{2s}}{T_1} = \eta_D\left(\frac{T_2}{T_1} - 1\right) + 1 = 1 + 0.9\left(\frac{471.7}{428.2} - 1\right) = 1.0915$$

$$\frac{p_2}{p_1} = \left(\frac{T_{2s}}{T_1}\right)^{\gamma/(\gamma-1)} = 1.0915^{3.5} = 1.3588$$

$$\frac{p_{01}}{p_1} = \left(\frac{T_{02}}{T_1}\right)^{\gamma/(\gamma-1)} = \left(\frac{473}{428.2}\right)^{3.5} = 1.4166$$

Therefore,

$$p_1 = 141.2 \text{ kPa}$$

and

$$p_2 = 1.3588 \times 141.2 = 191.8 \text{ kPa}$$

From the thermodynamic relation, namely $T\,\mathrm{d}s = \mathrm{d}h - (1/\rho)\mathrm{d}p$, we obtain

$$s_2 - s_1 = C_p \ln\frac{T_2}{T_1} - R\ln\frac{p_2}{p_1} = 1005 \ln\frac{471.7}{428.2} - 287 \ln 1.3588 = 97.2 - 88.0 = 9.2 \text{ J/kg K}$$

Diffuser design calculation

The performance of a *conical diffuser* has been chosen as an illustration using data presented by Sovran and Klomp (1967). This is shown in Figure 7.27 as contour plots of C_p in terms of the geometry of the diffuser, N/R_1 and the area ratio A_R ($=A_2/A_1$). Two optimum diffuser lines, useful for design purposes, were added by the authors. The first is the line C_p^*, the locus of points that defines the diffuser area ratio A_R, producing the *maximum pressure recovery* for a prescribed nondimensional length, N/R_1. The second is the line C_p^{**}, the locus of points defining the diffuser

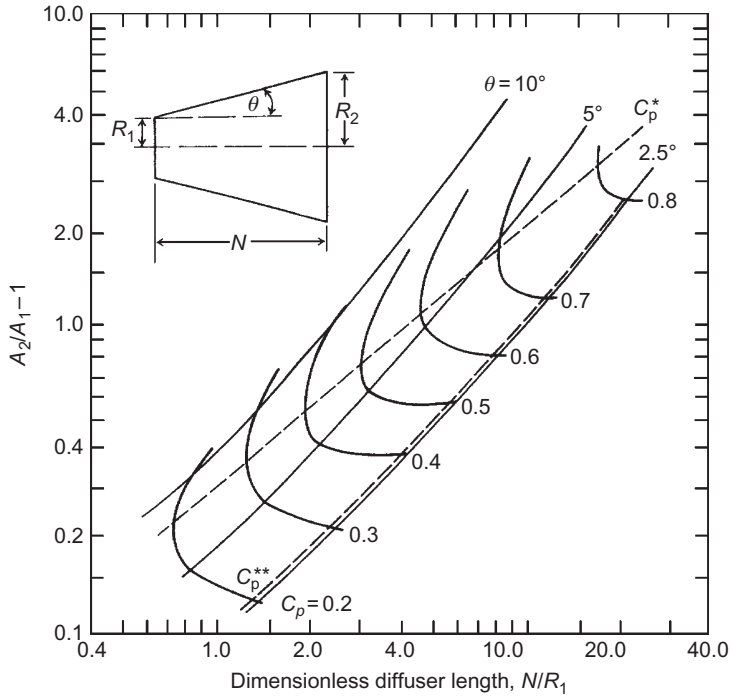

FIGURE 7.27

Performance chart for conical diffusers.

(*Adapted from Sovran and Klomp, 1967*)

nondimensional length, producing the *maximum pressure recovery at a prescribed area ratio*. *Note:* Compressible flow data was not available and incompressible data has been used.

EXAMPLE 7.6

Using the performance chart given by Sovran and Klomp (Figure 7.27) determine the efficiency of a conical low-speed diffuser to give maximum pressure recovery with a prescribed nondimensional length of 8.0 and evaluate the included angle of the cone.

Solution

From Figure 7.26 at $N/R = 8.0$, we find $C_p = 0.7$ and $A_g = 2.8$. The efficiency of the diffuser is

$$\eta_D = C_p / C_{p,id}$$

where

$$C_{p,id} = 1 - [1/A_R^2] = 0.872$$

therefore,

$$\eta_D = 0.802$$

From the geometric expression given for the diffuser shown in Figure 7.7(b), the included angle is

$$2\theta = 2\tan^{-1}\left[\frac{R_1}{N}\left(A_R^{\frac{1}{2}} - 1\right)\right] = 2\tan^{-1}\left[\frac{1}{8}\left(\sqrt{2.8} - 1\right)\right] = 9.6^\circ$$

Note: This angle may be slightly on the high side and a small modification to the area ratio would seem advisable.

7.13 Choking in a compressor stage

When the through-flow velocity in a passage reaches the speed of sound at some cross section, the flow *chokes*. For the stationary inlet passage, this means that no further increase in mass flow is possible, either by decreasing the back pressure or by increasing the rotational speed. Now the choking behavior of rotating passages differs from that of stationary passages, making separate analyses for the inlet, impeller, and diffuser a necessity. For each component, a simple, 1D approach is used assuming that all flow processes are adiabatic and that the fluid is a perfect gas.

Inlet

Choking takes place when $c^2 = a^2 = \gamma RT$. Since $h_0 = h + (1/2)c^2$, $C_pT_0 = C_pT + (1/2)\gamma RT$, and

$$\frac{T_0}{T_0} = \left(1 + \frac{\gamma R}{2C_p}\right)^{-1} = \frac{2}{\gamma + 1} \tag{7.55)}$$

Assuming the flow in the inlet is isentropic,

$$\frac{\rho}{\rho_0} = \frac{p}{p_0}\frac{T_0}{T} = \left[1 + \frac{1}{2}(\gamma - 1)M^2\right]^{-1/(\gamma-1)}$$

and when $c = a$, $M = 1$, so that

$$\frac{\rho}{\rho_0} = \left(\frac{2}{\gamma+1}\right)^{1/(\gamma-1)} \tag{7.56}$$

Substituting Eqs (7.55) and (7.56) into the continuity equation, $\dot{m}/A = \rho c = \rho(\gamma RT)^{1/2}$,

$$\frac{\dot{m}}{A} = \rho_0 a_0 \left(\frac{2}{\gamma+1}\right)^{(\gamma+1)/2(\gamma-1)} \tag{7.57}$$

Thus, $\rho_0 a_0$ refer to inlet stagnation conditions that remain unchanged, the mass flow rate at choking is constant.

Impeller

In the rotating impeller passages, flow conditions are referred to the factor $I = h + (1/2)(w^2 - U^2)$, which is constant according to Eq. (7.2). At the impeller inlet and for the special case $c_{\theta 1} = 0$, note that $I_1 = h_1 + (1/2)c_1^2 = h_{01}$. When choking occurs in the impeller passages, the *relative velocity* w equals the speed of sound at some section. Now $w^2 = a^2 = \gamma RT$ and $T_{01} = T + (\gamma RT/2C_p) - (U^2/2C_p)$, therefore,

$$\frac{T}{T_{01}} = \left(\frac{2}{\gamma + 1}\right)\left(1 + \frac{U^2}{2C_p T_{01}}\right) \tag{7.58}$$

Assuming isentropic flow, $\rho/\rho_{01} = (T/T_{01})^{1/(\gamma-1)}$. Using the continuity equation,

$$\begin{aligned}\frac{\dot{m}}{A} &= \rho_{01} a_{01}\left(\frac{T}{T_{01}}\right)^{(\gamma+1)/2(\gamma-1)} = \rho_{01} a_{01}\left[\frac{2}{\gamma+1}\left(1 + \frac{U^2}{2C_p T_{01}}\right)\right]^{(\gamma+1)/2(\gamma-1)} \\ &= \rho_{01} a_{01}\left[\frac{2 + (\gamma-1)U^2/a_{01}^2}{\gamma+1}\right]^{(\gamma+1)/2(\gamma-1)}\end{aligned} \tag{7.59}$$

If choking occurs in the rotating passages, Eq. (7.59) indicates that the mass flow is dependent on the blade speed. As the speed of rotation is increased, the compressor can accept a *greater* mass flow, unless choking occurs in some other component of the compressor. The fact that the choking flow in an impeller can vary, depending on blade speed, may seem at first rather surprising; this analysis gives the *reason* for the variation of the choking limit of a compressor.

Diffuser

The relation for the choking flow, Eq. (7.57) holds for the diffuser passages, it being noted that stagnation conditions now refer to the diffuser and not the inlet. Thus,

$$\frac{\dot{m}}{A_2} = \rho_{02} a_{02} \left(\frac{2}{\gamma+1}\right)^{(\gamma+1)/2(\gamma-1)} \tag{7.60}$$

Clearly, stagnation conditions at the diffuser inlet are dependent on the impeller process. To find how the choking mass flow limit is affected by blade speed it is necessary to refer back to inlet stagnation conditions.

Assuming a radial blade impeller of efficiency η_i then,

$$T_{02s} - T_{01} = \eta_i (T_{02} - T_{01}) = \eta_i \sigma U_2^2 / C_p$$

Hence,

$$p_{02}/p_{01} = (T_{02s}/T_{01})^{\gamma/(\gamma-1)} = \left[1 + \eta_i \sigma U_2^2 / C_p T_{01}\right]^{\gamma/(\gamma-1)}$$

therefore,

$$\frac{\dot{m}}{A_2} = \rho_{01} a_{01} \frac{[1 + (\gamma-1)\eta_i \sigma U_2^2 / a_{01}^2]^{\gamma/(\gamma-1)}}{[1 + (\gamma-1)\sigma U_2^2 / a_{01}]^{1/2}} \left(\frac{2}{\gamma+1}\right)^{(\gamma+1)/2(\gamma-1)} \tag{7.61}$$

In this analysis, it should be noted that the diffuser process has been assumed to be isentropic but the impeller process has been assumed anisentropic. Equation (7.61) indicates that the choking mass flow can be varied by changing the impeller speed of rotation.

Note: The preliminary design of centrifugal compressor for a turbocharger is given in Appendix B.

PROBLEMS

Note: In problems 1−6 assume γ and R are 1.4 and 287 J/(kg °C), respectively. In problems 2−6 assume the stagnation pressure and stagnation temperature at compressor entry are 101.3 kPa and 288 K, respectively.

1. A cheap radial-vaned centrifugal fan is required to provide a supply of pressurized air to a furnace. The specification requires that the fan produce a total pressure rise equivalent to 7.5 cm of water at a volume flow rate of 0.2 m^3/s. The fan impeller is fabricated from 30 thin sheet metal vanes, the ratio of the passage width to circumferential pitch at the impeller exit being specified as 0.5, and the ratio of the radial velocity to blade tip speed as 0.1. Assuming that the overall isentropic efficiency of the fan is 0.75 and that the slip can be estimated from Stanitz's expression, Eq. (7.34b), determine

a. the vane tip speed;
b. the rotational speed and diameter of the impeller;
c. the power required to drive the fan if the mechanical efficiency is 0.95;
d. the specific speed.

For air assume the pressure is 10^5 Pa and the temperature is 20°C.

2. The air entering the impeller of a centrifugal compressor has an absolute axial velocity of 100 m/s. At rotor exit the relative air angle measured from the radial direction is 26°36′, the radial component of velocity is 120 m/s, and the tip speed of the radial vanes is 500 m/s.

Determine the power required to drive the compressor when the air flow rate is 2.5 kg/s and the mechanical efficiency is 95%. If the radius ratio of the impeller eye is 0.3, calculate a suitable inlet diameter assuming the inlet flow is incompressible. Determine the overall total pressure ratio of the compressor when the total-to-total efficiency is 80%, assuming the velocity at exit from the diffuser is negligible.

3. A centrifugal compressor has an impeller tip speed of 366 m/s. Determine the absolute Mach number of the flow leaving the radial vanes of the impeller when the radial component of velocity at impeller exit is 30.5 m/s and the slip factor is 0.90. Given that the flow area at impeller exit is 0.1 m^2 and the total-to-total efficiency of the impeller is 90%, determine the mass flow rate.

4. The eye of a centrifugal compressor has a hub−tip radius ratio of 0.4, a maximum relative flow Mach number of 0.9, and an absolute flow that is uniform and completely axial. Determine the optimum speed of rotation for the condition of maximum mass flow given that the mass flow rate is 4.536 kg/s. Also, determine the outside diameter of the eye and the ratio of axial velocity−blade speed at the eye tip. Figure 7.12 may be used to assist the calculations.

5. An experimental centrifugal compressor is fitted with free-vortex guide vanes to reduce the relative air speed at inlet to the impeller. At the outer radius of the eye, air leaving the guide vanes has a velocity of 91.5 m/s at 20° to the axial direction. Determine the inlet relative Mach number, assuming frictionless flow through the guide vanes, and the impeller total-to-total efficiency. Other details of the compressor and its operating conditions are:

Radial vanes at impeller exit
Impeller entry tip diameter, 0.457 m;
Impeller exit tip diameter, 0.762 m;
Slip factor, 0.9 radial blades at impeller exit;
Radial component of velocity at impeller exit, 53.4 m/s;
Rotational speed of impeller, 11,000 rev/min;
Static pressure at impeller exit, 223 kPa (abs).

6. A centrifugal compressor has an impeller with 21 vanes, which are radial at exit, a vaneless diffuser, and no inlet guide vanes. At inlet, the stagnation pressure is 100 kPa (abs) and the stagnation temperature is 300 K.

a. Given that the mass flow rate is 2.3 kg/s, the impeller tip speed is 500 m/s and the mechanical efficiency is 96%, determine the driving power on the shaft. Use Eq. (7.34b) for the slip factor.

b. Determine the total and static pressures at diffuser exit when the velocity at that position is 100 m/s. The total-to-total efficiency is 82%.

c. The reaction, which may be defined as for an axial-flow compressor by Eq. (5.19), is 0.5, the absolute flow speed at impeller entry is 150 m/s, and the diffuser efficiency is 84%. Determine the total and static pressures, absolute Mach number, and radial component of velocity at the impeller exit.

d. Determine the total-to-total efficiency for the impeller.

e. Estimate the inlet–outlet radius ratio for the diffuser assuming the conservation of angular momentum.
f. Find a suitable rotational speed for the impeller given an impeller tip width of 6 mm.

7. A centrifugal pump is used to raise water against a static head of 18.0 m. The suction and delivery pipes, both 0.15 m diameter, have, respectively, friction head losses amounting to 2.25 and 7.5 times the dynamic head. The impeller, which rotates at 1450 rev/min, is 0.25 m diameter with eight vanes, radius ratio 0.45, inclined backward at $\beta_2' = 60^\circ$. The axial width of the impeller is designed so as to give constant radial velocity at all radii and is 20 mm at impeller exit. Assuming a hydraulic efficiency of 0.82 and an overall efficiency of 0.72, determine
a. the volume flow rate;
b. the slip factor using Busemann's method;
c. the impeller vane inlet angle required for zero incidence angle;
d. the power required to drive the pump.

8. A centrifugal pump delivers 50 dm^3/s of water at an impeller speed of 1450 rev/min. The impeller has eight vanes inclined backward to the direction of rotation with an angle at the tip of $\beta_2' = 60^\circ$. The diameter of the impeller is twice the diameter of the shroud at inlet and the magnitude of the radial component of velocity at impeller exit is equal to that of the axial component of velocity at the inlet. The impeller entry is designed for the optimum flow condition to resist cavitation (see Eq. (7.20)) has a radius ratio of 0.35 and the blade shape corresponds to a well-tested design giving a cavitation coefficient $\sigma_b = 0.3$. Assuming that the hydraulic efficiency is 70% and the mechanical efficiency is 90%, determine
a. the diameter of the inlet;
b. the NPSH;
c. the impeller slip factor using Wiesner's formula;
d. the head developed by the pump;
e. the power input.
Also calculate values for slip factor using the equations of Stodola and Busemann, comparing the answers obtained with the result found from Wiesner's equation.

9. **a.** Write down the advantages and disadvantages of using free-vortex guide vanes upstream of the impeller of a high-pressure ratio centrifugal compressor. What other sorts of guide vanes can be used and how do they compare with free-vortex vanes?
b. The inlet of a centrifugal air compressor has a shroud diameter of 0.2 m and a hub diameter of 0.105 m. Free-vortex guide vanes are fitted in the duct upstream of the impeller so that the flow on the shroud at the impeller inlet has a relative Mach number, $M_{1,\text{rel}} = 1.0$, an absolute flow angle of $\alpha_1 = 20^\circ$, and a relative flow angle $\beta_1 = 55^\circ$. At inlet the stagnation conditions are 288 K and 10^5 Pa. Assuming frictionless flow into the inlet, determine
i. the rotational speed of the impeller;
ii. the air mass flow.

c. At exit from the radially vaned impeller, the vanes have a radius of 0.16 m and a design point slip factor of 0.9. Assuming an impeller efficiency of 0.9, determine
  i. the shaft power input;
  ii. the impeller pressure ratio.

10. Sketch a Mollier diagram showing all the stagnation and static points needed to represent the complete flow process in a diffuser. Derive the following expression for the diffuser efficiency:

$$\eta_D = \frac{T_{2s}/T_1 - 1}{T_2/T_1 - 1}$$

Air enters a diffuser with an averaged velocity of 360 m/s at a stagnation pressure and temperature of 340 kPa and 420 K and leaves at a stagnation pressure of 300 kPa with an averaged velocity of 120 m/s and a static pressure of 285 kPa. Determine
a. the static pressure and Mach number of the air at inlet;
b. the diffuser efficiency;
c. the Mach number at exit and the overall entropy increase.
Take $\gamma = 1.4$ and $C_p = 287$ J/(kg K).

11. At the inlet to an axial diffuser the velocity of the approaching air is 420 m/s, the stagnation pressure is 300 kPa, and the stagnation temperature is 600 K. At exit the stagnation pressure is 285 kPa and the static pressure is 270 kPa. Using compressible flow analysis, determine
a. the static temperature, static pressure, and Mach number at inlet and the diffuser efficiency;
b. the Mach numbers at exit and entry.
For air take $\gamma = 1.376$ and $R = 287$ J/(kg K).

12. A centrifugal compressor fitted with 21 radial vanes with an outside diameter of 40 cm is designed to operate at a rotational speed of 17,400 rpm. Assuming that the air admitted is at 101.3 kPa and a temperature of 15°C, determine
a. the absolute Mach number of the flow at the impeller tip given that the radial velocity at that location is 30 m/s;
b. the stagnation pressure of the air leaving the impeller if the total-to-total efficiency of the impeller is 92%;
c. the mass flow of air passing through the compressor if the axial width of the passage at impeller exit is 2.0 cm.
Assume the Stanitz expression for the slip factor. Take $C_p = 1005$ J/(kg K) and $\gamma = 1.4$.

13. **a.** A model of low-speed centrifugal compressor (a "blower") runs at 430 rpm and delivers 10 m^3/s of air against a pressure head of 60 mm of water. If the pump efficiency is estimated to be 80%, how much power is required to drive the compressor?
b. A geometrically similar compressor is made with a diameter 1.8 times the size of the model and is required to work against a pressure head of 80 mm of water. Determine the operating speed and the power needed to drive the compressor assuming dynamically similar conditions apply.

14. A centrifugal pump is required to deliver 0.09 m^3/s of water against a back pressure of 100 kPa. The impeller, which rotates at 1250 rpm, is 0.35 m diameter and has nine vanes swept back at 45°. The axial width of the impeller at its tip is 40 mm. Using Wiesner's slip correlation (assuming that $r_1/r_2 = \varepsilon$ in Eq. (7.35d)) determine the specific work done by the impeller. If the efficiency of the pump is 70%, calculate the power needed to drive the pump. Calculate the specific speed and specific diameter of the pump and compare your results with the data given in Chapter 2.

15. Atmospheric air enters the intake diffuser of a jet aircraft flying at a Mach number of 0.9 at a constant altitude where the static pressure and temperature are 25 kPa and 220 K, respectively. The entrance area of the intake is 0.5 m^2 and the area at entry to the compressor is 0.8 m^2. There is a loss of 10% of the stagnation pressure of the air as it flows to the compressor. Using compressible flow theory and assuming adiabatic flow in the intake, determine the Mach number and velocity of the flow entering the compressor.

16. A prototype centrifugal compressor is to be built with an impeller having 19 vanes backswept at $\beta_2' = 30°$, rotating at 12,000 rpm and delivering air at an outlet pressure of 385 kPa. The total-to-total efficiency of the compressor, based upon previous well-established design data, is estimated as 0.82. It can be assumed that the radial component of the air leaving the impeller equals 0.2 times the impeller tip speed. The air enters the inlet axially at a stagnation temperature and pressure of 288 K and 100 kPa. Determine

a. the impeller tip speed and tip diameter using the Wiesner slip factor;

b. the specific speed of the compressor assuming that the axial velocity at entry is equal to the radial component of velocity at impeller outlet. Comment upon whether the chosen value of the efficiency is appropriate.

How well does the specific speed you have found compare with the values shown in Figure 2.7?

17. For the preceding problem determine the size of the compressor eye given that the air flow is 8 kg/s the radius ratio $r_{h1}/r_{s1} = 0.4$. What is the value of the absolute Mach number M_1?

18. A radial-vaned centrifugal compressor is designed for a rotational speed of 2400 rpm and requires 1 MW of power to compress the incoming air at a flow rate of 8 kg/s. The air enters the intake axially and the stagnation conditions are 103 kPa and 288 K. Assuming the slip factor is 0.9 and the specific speed

$$N_S = \phi^{0.5}/\psi^{0.75} = 0.7,$$

where $\phi = c_{x1}/U_2$ and $\psi = \Delta W/U_2^2$, determine

a. the vane tip speed;

b. the axial velocity at inlet, c_{x1};

c. the inlet Mach number, M_1;

d. the inlet area.

19. The final stage of a high-pressure axial compressor is centrifugal of the purely radial type (see Figure 7.5), the flow at all points through the stage having no axial component. At the design point for the stage the following data applies:

Impeller speed, (Ω) = 65,000 rpm
Total pressure at impeller inlet, (p_{01}) = 4.5 bar
Total temperature at impeller inlet, (T_{01}) = 520 K
Total temperature at impeller exit, (T_{02}) = 650 K
Stage isentropic efficiency, (η_c) = 75%
Mach number at impeller exit, (M_2) = 0.85
Impeller blade radius at inlet, (r_1) = 0.08 m
Impeller blade radius at outlet, (r_2) = 0.11 m
Impeller blade axial width at inlet (b_1) = 0.035 m
Impeller blade axial width at outlet (b_2) = 0.018 m
The following assumptions are to be made:
Adiabatic flow throughout the stage
Specific heat at constant pressure, (C_p) = 1.005 kJ/kg K
Specific heat ratio (γ) = 1.4
Determine,

a. the air mass flow, ($\dot{m}$);
b. the extra power needed to drive the stage, (P);
c. the Mach number (M_1) at impeller inlet;
d. the specific speed (compare the value you compute with the data shown in Figure 2.7).

References

Busemann, A. (1928). Lift ratio of radial-flow centrifugal pumps with logarithmic spiral blades. *Zeitschrift für Angewandte Mathematik und Mechanik*, *8*, 372 DSIR translation 621.671.22, Reg.file Ref. DSIR/8082/CT, Feb. 1952

Came, P. (1978). The development, application and experimental evaluation of a design procedure for centrifugal compressors. *Proceedings of the Institution of Mechanical Engineers*, *192*(5), 49–67.

Cheshire, L. J. (1945). The design and development of centrifugal compressors for aircraft gas turbines. *Proceedings of the Institution of Mechanical Engineers, London*, *153*; reprinted by American Society of Mechanical Engineers (1947), *Lectures on the Development of the British Gas Turbine Jet.*

Clements, W. W., & Artt, D. W. (1988). The influence of diffuser channel length to width ratio on the efficiency of a centrifugal compressor. *Proceedings of the Institution of Mechanical Engineers*, *202*(A3), 163–169.

Csanady, G. T. (1960). Head correction factors for radial impellers. *Engineering*, *190*.

Cumpsty, N. A. (1989). *Compressor aerodynamics.* England: Addison-Wesley/Longman.

Eck, B. (1973). *Fans: Design and operation of centrifugal* (First English Edition). *Axial-flow and cross-flow fans* Oxford: Pergamon Press, First English Edition.

Eckardt, D. (1980). Flow field analysis of radial and backswept centrifugal compressor impellers, Part 1: Flow measurement using a laser velocimeter. In *Twenty-fifth ASME Gas turbine conference and twenty-second annual fluids engineering conference*, New Orleans.

Hess, H. (1985). Centrifugal compressors in heat pumps and refrigerating plants. *Sulzer Technical Review*, 27–30.

Johnson, J. P. (1986). *Radial flow turbomachinery. Lecture in series on fluid dynamics of turbomachinery* Ames, IA: ASME Turbomachinery Institute.

Kline, S. J., Abbott, D. E., & Fox, R. W. (1959). Optimum design of straight-walled diffusers. Transactions of the American Society of Mechanical Engineers, *Series D*, *81*, 321–331.

Palmer, D. L., & Waterman, W. F. (1995). Design and development of an advanced two-stage centrifugal compressor. *Journal Turbomachinery, Transactions of the American Society of Mechanical Engineers*, *117*, 205–212.

Pearsall, I. S. (1972). *Cavitation*. M&B Monograph ME/10.

Qiu, X., Japiske, D., Zhao, J., & Anderson, M. R. (2011). Analysis and validation of a unified slip factor model for impellers at design and off-design conditions. *Journal of Turbomachinery, Transactions of the American Society of Mechanical Engineers*, *133* (041018), 1–9.

Rodgers, C., & Sapiro, L. (1972). Design considerations for high pressure ratio centrifugal compressors. *American Society of Mechanical Engineers*, Paper 72-GT-91

Sovran, G., & Klomp, E. (1967). *Experimentally determined optimum geometries for rectilinear diffusers with rectangular, conical and annular cross-sections* (pp. 270–319). *Fluid mechanics of internal flow* Burlingtin, MA: Elsevier Science.

Stanitz, J. D. (1952). Some theoretical aerodynamic investigations of impellers in radial and mixed flow centrifugal compressors. *Transactions of the American Society of Mechanical Engineers*, *74*, 4.

Stodola, A. (1945). *Steam and gas turbines* (Vols. I–II). New York, NY: McGraw-Hill.

Van Den Braembussche, R. (1985). Discussion: "Rotating Stall Induced in Vaneless Diffusers of Very Low Specific Speed Centrifugal Blowers". *Journal of Engineering for Gas Turbines and Power*, *107*(2), 519–520.

Wallace, F. J., Whitfield, A., & Atkey, R. C. (1975). Experimental and theoretical performance of a radial flow turbocharger compressor with inlet prewhirl. *Proceedings of the Institution of Mechanical Engineers*, *189*, 177–186.

Watson, N., & Janota, M. S. (1982). *Turbocharging the internal combustion engine.* London, UK: Macmillan.

Whitfield, A., & Baines, N. C. (1990). *Design of radial turbomachines.* New York, NY: Longman.

Whitfield, A. & Johnson, M. A. (2002). The effect of volute design on the performance of a turbocharger compressor. *International compressor engineering conference*, paper, 1501.

Wiesner, F. J. (1967). A review of slip factors for centrifugal compressors. *Journal of Engineering Power, Transactions of the American Society of Mechanical Engineers*, *89*, 558–572.

CHAPTER

Radial-Flow Gas Turbines

8

I like work; it fascinates me, I can sit and look at it for hours.
Jerome K. Jerome, *Three Men in a Boat*

8.1 Introduction

The radial-flow turbine has had a long history of development being first conceived for the purpose of producing hydraulic power over 180 years ago. A French engineer, Fourneyron, developed the first commercially successful hydraulic turbine (circa 1830) and this was of the *radial-outflow* type. A *radial-inflow* type of hydraulic turbine was built by Francis and Boyden in the United States (circa 1847), which gave excellent results and was highly regarded. This type of machine is now known as the *Francis turbine*, a simplified arrangement of it being shown in Figure 1.1. It will be observed that the flow path followed is from the radial direction to what is substantially an axial direction. A flow path in the reverse direction (radial outflow), for a single-stage turbine anyway, creates several problems, one of which (discussed later) is low specific work. However, as pointed out by Shepherd (1956) radial-outflow steam turbines comprising many stages have received considerable acceptance in Europe. Figure 8.1, from Kearton (1951), shows diagrammatically the *Ljungström steam turbine*, which, because of the tremendous increase in the specific volume of steam, makes the radial-outflow flow path virtually imperative. A unique feature of the Ljungström turbine is that it does not have any stationary blade rows. The two rows of blades constituting each of the stages rotate in opposite directions so that they can both be regarded as rotors.

The inward-flow radial (IFR) turbine covers tremendous ranges of power, rates of mass flow, and rotational speeds, from very large Francis turbines used in hydroelectric power generation and developing hundreds of megawatts (see Figures 9.12 and 9.13) down to tiny closed cycle gas turbines for space power generation of a few kilowatts.

The IFR gas turbine has been, and continues to be, used extensively for powering automotive turbocharges, aircraft auxiliary power units, expansion units in gas liquefaction, and other cryogenic systems and as a component of the small (10 kW) gas turbines used for space power generation (Anon, 1971). It has been considered for primary power use in automobiles and in helicopters. According to Huntsman, Hodson, and Hill (1992), studies at Rolls-Royce have shown that a cooled, high efficiency IFR turbine could offer significant improvement in performance as the gas generator turbine of a high technology turboshaft engine. What is needed to enable this type of application are some small improvements in current technology levels. However, designers of this

Fluid Mechanics and Thermodynamics of Turbomachinery. DOI: http://dx.doi.org/10.1016/B978-0-12-415954-9.00008-5

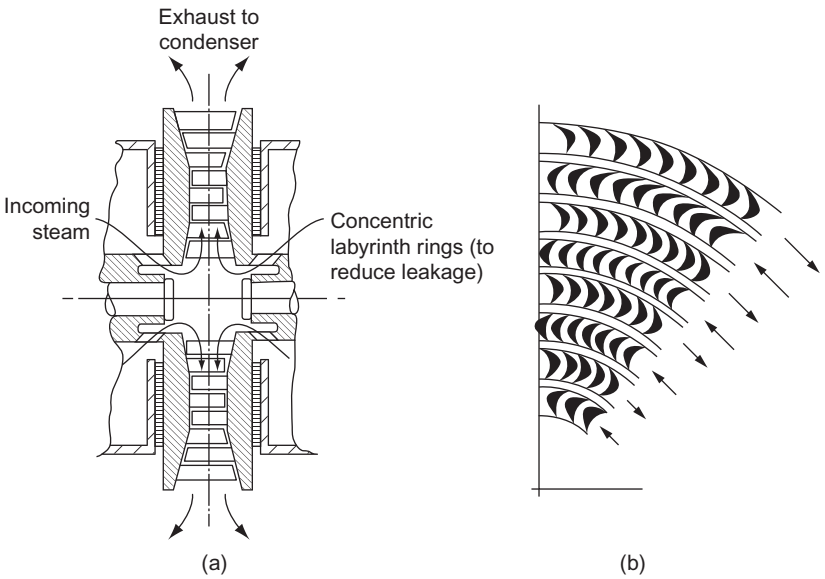

FIGURE 8.1

Ljungström type outward-flow radial turbine: (a) meridional section through turbine and (b) blading arrangement and directions of rotation.

(*Adapted from Kearton, 1951*)

new generation of IFR turbines face considerable problems, particularly in the development of advanced techniques of rotor cooling or of ceramic, shock-resistant rotors.

As indicated later in this chapter, over a limited range of specific speed, IFR turbines provide an efficiency about equal to that of the best axial-flow turbines. The significant advantages offered by the IFR turbine compared with the axial-flow turbine are the greater amount of work that can be obtained per stage, the ease of manufacture, and its superior ruggedness.

8.2 Types of IFR turbine

In the centripetal turbine, energy is transferred from the fluid to the rotor in passing from a large radius to a small radius. For the production of positive work the product of Uc_θ at entry to the rotor must be greater than Uc_θ at rotor exit (Eq. (1.18c)). This is usually arranged by imparting a large component of tangential velocity at rotor entry, using single or multiple nozzles, and allowing little or no swirl in the exit absolute flow.

Cantilever turbine

Figure 8.2(a) shows a *cantilever* IFR turbine where the blades are limited to the region of the rotor tip, extending from the rotor in the *axial* direction. In practice the cantilever blades are usually of

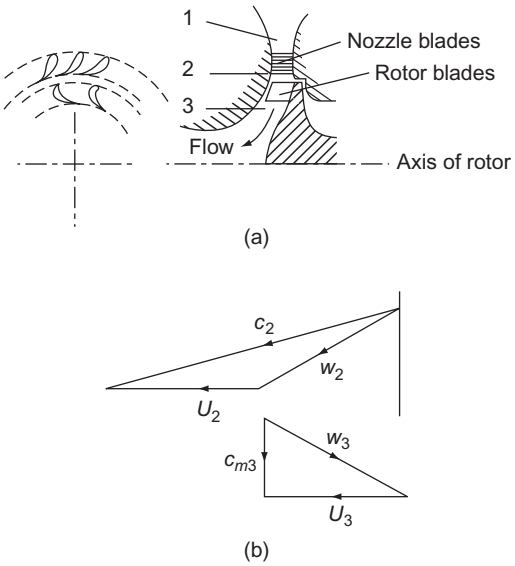

FIGURE 8.2

Arrangement of cantilever turbine and velocity triangles at the design point.

the impulse type (i.e., low reaction), by which it is implied that there is little change in relative velocity at inlet and outlet of the rotor. There is no fundamental reason why the blading should not be of the reaction type. However, the resulting expansion through the rotor would require an increase in flow area. This extra flow area is extremely difficult to accommodate in a small radial distance, especially as the radius decreases through the rotor row.

Aerodynamically, the cantilever turbine is similar to an axial-impulse turbine and can even be designed by similar methods. Figure 8.2(b) shows the velocity triangles at rotor inlet and outlet. The fact that the flow is radially inwards hardly alters the design procedure because the blade radius ratio r_2/r_3 is close to unity anyway.

The 90° IFR turbine

Because of its higher structural strength compared with the cantilever turbine, the 90° IFR turbine is the preferred type. Figure 8.3 shows a typical layout of a 90° IFR turbine; the inlet blade angle is generally made zero, a fact dictated by the material strength and often high gas temperature. The rotor vanes are subject to high stress levels caused by the centrifugal force field, together with a pulsating and often unsteady gas flow at high temperatures. Despite possible performance gains the use of nonradial (or swept) vanes is generally avoided, mainly because of the additional stresses that arise due to bending. Nevertheless, despite this difficulty, Meitner and Glassman (1983) have considered designs using sweptback vanes in assessing ways of increasing the work output of IFR turbines.

From station 2, the rotor vanes extend radially inward and turn the flow into the axial direction. The exit part of the vanes, called the *exducer*, is curved to remove most if not all of the absolute

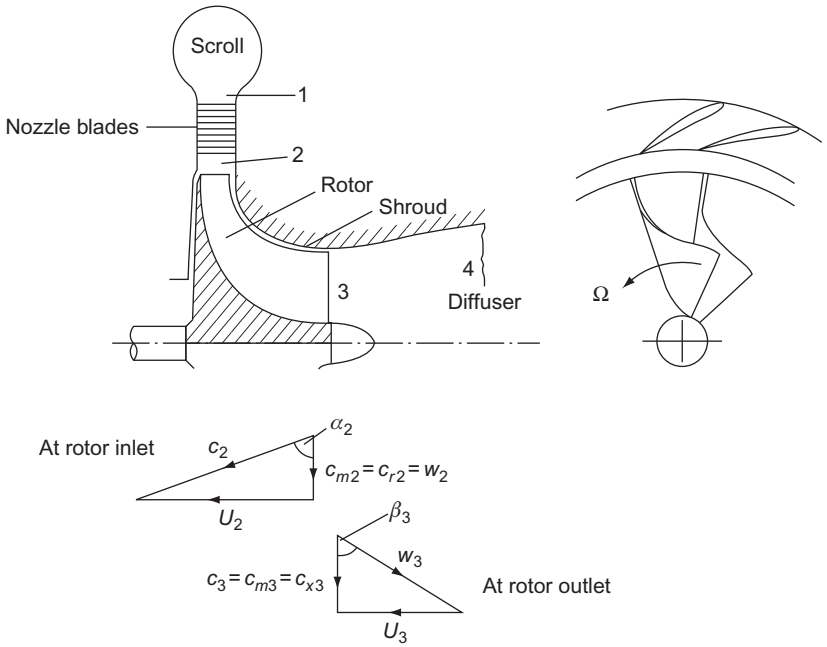

FIGURE 8.3

Layout and velocity diagrams for a 90° IFR turbine at the nominal design point.

tangential component of velocity. The 90° IFR turbine or centripetal turbine is very similar in appearance to the centrifugal compressor of Chapter 7, but with the flow direction and blade motion reversed.

The fluid discharging from the turbine rotor may have a considerable velocity c_3 and an axial diffuser (see Chapter 7) would normally be incorporated to recover most of the kinetic energy, $(1/2)c_3^2$, which would otherwise be wasted. In hydraulic turbines (discussed in Chapter 9), a diffuser is invariably used and is called the *draught tube*.

In Figure 8.3, the velocity triangles are drawn to suggest that the inlet relative velocity, w_2, is *radially* inward, i.e., zero incidence flow, and the absolute flow at rotor exit, c_3, is axial. This configuration of the velocity triangles, popular with designers for many years, is called the *nominal design* condition and will be considered in some detail in the following pages. Following this the so-called optimum efficiency design will be explained.

8.3 Thermodynamics of the 90° IFR turbine

The complete adiabatic expansion process for a turbine comprising (a) the scroll and nozzle blade row, (b) a radial rotor, and (c) a diffuser, corresponding to the layout of Figure 8.3, is represented

by the Mollier diagram shown in Figure 8.4. In the turbine, frictional processes cause the entropy to increase in all components and these irreversibilities are implied in Figure 8.4.

Across the scroll and nozzle blades the stagnation enthalpy is assumed constant, $h_{01} = h_{02}$, and, therefore, the static enthalpy drop is

$$h_1 - h_2 = \frac{1}{2}\left(c_2^2 - c_1^2\right) \tag{8.1}$$

which correspond to the static pressure change from p_1 to the lower pressure p_2. The *ideal* enthalpy change $(h_1 - h_{2s})$ is between these *same* two pressures but is at constant entropy.

In Chapter 7, it was shown that the rothalpy, $I = h_{0,\text{rel}} - (1/2)U^2$, is constant for an adiabatic irreversible flow process, relative to a rotating component. For the rotor of the 90° IFR turbine,

$$h_{02,\text{rel}} - \frac{1}{2}U_2^2 = h_{03,\text{rel}} - \frac{1}{2}U_3^2$$

Thus, as $h = h_{0,\text{rel}} - (1/2)w^2$, then

$$h_2 - h_3 = \frac{1}{2}\left[\left(U_2^2 - U_3^2\right) - \left(w_2^2 - w_3^2\right)\right] \tag{8.2a}$$

In this analysis, the reference point 2 (Figure 8.3) is taken to be at the inlet radius r_2 of the rotor (the blade tip speed $U_2 = \Omega r_2$). This implies that the nozzle irreversibilities are lumped together with any friction losses occurring in the annular space between nozzle exit and rotor entry (usually scroll losses are included as well).

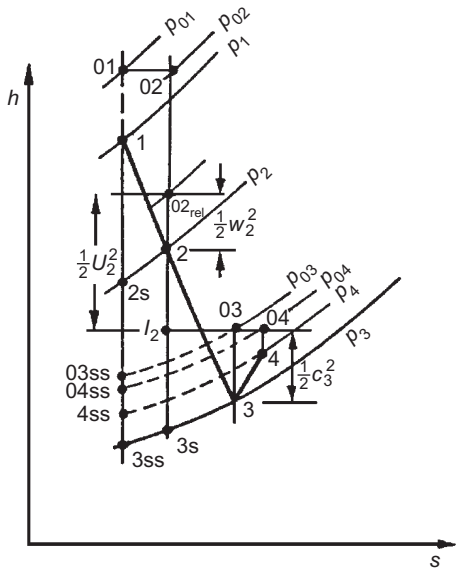

FIGURE 8.4

Mollier diagram for a 90° IFR turbine and diffuser (at the design point).

Across the diffuser the stagnation enthalpy does not change, $h_{03} = h_{04}$, but the static enthalpy *increases* as a result of the velocity diffusion. Hence,

$$h_4 - h_3 = \frac{1}{2}\left(c_3^2 - c_4^2\right) \tag{8.3}$$

The specific work done by the fluid on the rotor is

$$\Delta W = h_{01} - h_{03} = U_2 c_{\theta 2} - U_3 c_{\theta 3} \tag{8.4a}$$

As $h_{01} = h_{02}$,

$$\Delta W = h_{02} - h_{03} = h_2 - h_3 + \frac{1}{2}\left(c_2^2 - c_3^2\right) = \frac{1}{2}\left[\left(U_2^2 - U_3^2\right) - \left(w_2^2 - w_3^2\right) + \left(c_2^2 - c_3^2\right)\right] \tag{8.4b}$$

after substituting Eq. (8.2a).

8.4 Basic design of the rotor

Each term in Eq. (8.4b) makes a contribution to the specific work done on the rotor. A significant contribution comes from the first term, namely, $1/2(U_2^2 - U_1^2)$, and is the main reason why the inward-flow turbine has such an advantage over the outward-flow turbine where the contribution from this term would be negative. For the axial-flow turbine, where $U_2 = U_1$, of course, no contribution to the specific work is obtained from this term. For the second term in Eq. (8.4b), a positive contribution to the specific work is obtained when $w_3 > w_2$. In fact, accelerating the relative velocity through the rotor is a most useful aim of the designer as this is conducive to achieving a low loss flow. The third term in Eq. (8.4b) indicates that the absolute velocity at rotor inlet should be larger than at rotor outlet so as to increase the work input to the rotor. With these considerations in mind the general shape of the velocity diagram shown in Figure 8.3 results.

Nominal design

The *nominal design* is defined by a relative flow of zero incidence at rotor inlet (i.e., $w_2 = c_{r2}$) and an absolute flow at rotor exit, which is axial (i.e., $c_3 = c_{x3}$).[1] Thus, from Eq. (8.4a), with $c_{\theta 3} = 0$ and $c_{\theta 2} = U_2$, the specific work for the nominal design is simply

$$\Delta W = U_2^2 \tag{8.4c}$$

EXAMPLE 8.1

The rotor of an IFR turbine, which is designed to operate at the nominal condition, is 23.76 cm in diameter and rotates at 38,140 rev/min. At the design point, the absolute flow angle at rotor

[1]This arrangement ($c_{\theta 3} = 0$) minimizes the exit kinetic energy loss. However, some designers may opt for some exit swirl in the flow in order to benefit a subsequent diffusion process.

entry is 72°. The rotor mean exit diameter is one-half of the rotor diameter and the relative velocity at rotor exit is twice the relative velocity at rotor inlet.

Determine the relative contributions to the specific work of each of the three terms in Eq. (8.4b).

Solution

The blade tip speed is $U_2 = \pi\Omega D_2/60 = \pi \times 38{,}140 \times 0.2376/60 = 474.5$ m/s.

Referring to Figure 8.3, $w_2 = U_2 \cot \alpha_2 = 154.17$ m/s and $c_2 = U_2/\sin \alpha_2 = 498.9$ m/s

$$c_3^2 = w_3^2 - U_3^2 = (2 \times 154.17)^2 - \left(\frac{1}{2} \times 474.5\right)^2 = 38,786 \text{ m}^2/s^2$$

Hence,

$$U_2^2 - U_2^2 = U_2^2(1 - 1/4) = 168,863 \text{ m}^2/s^2$$
$$w_3^2 - w_2^2 = 3 \times w_2^2 = 71,305 \text{ m}^2/s^2$$

and

$$c_2^2 - c_3^2 = 210,115 \text{ m}^2/s^2$$

Thus, summing the values of the three terms and dividing by 2, we get $\Delta W = 225{,}142$ m^2/s^2.

The fractional inputs from each of the three terms are, for the U^2 terms, 0.375; for the w^2 terms, 0.158; for the c^2 terms, 0.467.

Finally, as a numerical check, the specific work is $\Delta W = U_2^2 = 474.5^2 = 225,150$ m$^2/s^2$, which, apart from some rounding errors, agrees with the preceding computations.

Spouting velocity

The term *spouting velocity* c_0 (originating from hydraulic turbine practice) is defined as that velocity that has an associated kinetic energy equal to the isentropic enthalpy drop from turbine inlet stagnation pressure p_{01} to the final exhaust pressure. The exhaust pressure here can have several interpretations depending upon whether total or static conditions are used in the related efficiency definition and upon whether or not a diffuser is included with the turbine. Thus, when *no* diffuser is used

$$\frac{1}{2}c_0^2 = h_{01} - h_{03ss} \tag{8.5a}$$

or

$$\frac{1}{2}c_0^2 = h_{01} - h_{3ss} \tag{8.5b}$$

for the total and static cases, respectively.

In an *ideal* (frictionless) radial turbine with complete recovery of the exhaust kinetic energy and with $c_{\theta 2} = U_2$,

$$\Delta W = U_2^2 = \frac{1}{2}c_0^2$$

therefore,

$$\frac{U_2}{c_0} = 0.707$$

At the best efficiency point of actual (frictional) 90° IFR turbines, it is found that this velocity ratio is, generally, in the range $0.68 < U_2/c_0 < 0.71$.

8.5 Nominal design point efficiency

Referring to Figure 8.4, the total-to-static efficiency in the absence of a diffuser is defined as

$$\eta_{ts} = \frac{h_{01} - h_{03}}{h_{01} - h_{3ss}} = \frac{\Delta W}{\Delta W + (1/2)c_3^2 + (h_3 - h_{3s}) + (h_{3s} - h_{3ss})} \tag{8.6}$$

The passage enthalpy losses can be expressed as a fraction (ζ) of the exit kinetic energy relative to the nozzle row and the rotor, i.e.,

$$h_3 - h_{3s} = \frac{1}{2} w_3^2 \zeta_R \tag{8.7a}$$

$$h_{3s} - h_{3ss} = \frac{1}{2} c_2^2 \zeta_N (T_3/T_2) \tag{8.7b}$$

for the rotor and nozzles, respectively. It is noted that, for a constant pressure process, $\mathrm{d}s = \mathrm{d}h/T$, hence, the approximation,

$$h_{3s} - h_{3ss} = (h_2 - h_{2s})(T_3/T_2)$$

Substituting for the enthalpy losses in Eq. (8.6),

$$\eta_{ts} = \left[1 + \frac{1}{2}(c_3^2 + w_3^3 \zeta_R + c_2^2 \zeta_N T_3/T_2)/\Delta W\right]^{-1} \tag{8.8}$$

From the design point velocity triangles, Figure 8.3,

$$c_2 = U_2 \operatorname{cosec} a_2, w_3 = U_3 \operatorname{cosec} \beta_3, c_3 = U_3 \cot \beta_3, \Delta W = U_2^2$$

Thus, substituting all these expressions in Eq. (8.8) and noting that $U_3 = U_2 r_3/r_2$,

$$\eta_{ts} = \left\{1 + \frac{1}{2}\left[\zeta_N \frac{T_3}{T_2} \operatorname{cosec}^2 \alpha_2 + \left(\frac{r_3}{r_2}\right)^2 \left(\zeta_R \operatorname{cosec}^2 \beta_3 + \cot^2 \beta_3\right)\right]\right\}^{-1} \tag{8.9a}$$

where r_3 and β_3 are taken to apply at the arithmetic mean radius, i.e., $r_3 = (1/2)(r_{3s} + r_{3h})$. Note that r_{3s} is the shroud radius at rotor exit and r_{3h} is the hub radius at rotor exit. The temperature ratio (T_3/T_2) in Eq. (8.9a) can be obtained as follows.

At the nominal design condition, referring to the velocity triangles of Figure 8.3, $w_3^2 - U_3^2 = c_3^2$, and so Eq. (8.2a) can be rewritten as

$$h_2 - h_3 = \frac{1}{2}(U_2^2 - w_2^2 + c_3^2) \tag{8.2b}$$

This particular relationship, in the form $I = h_{02,\text{rel}} - (1/2)U_2^2 = h_{03}$, can be easily identified in Figure 8.4.

Again, referring to the velocity triangles, $w_2 = U_2 \cot \alpha_2$ and $c_3 = U_3 \cot \beta_3$, a useful alternative form to Eq. (8.2b) is obtained:

$$h_2 - h_3 = \frac{1}{2}U_2^2\left[\left(1 - \cot^2\alpha_2\right) + (r_3/r_2)\cot^2\beta_3\right] \tag{8.2c}$$

where U_3 is written as $U_2 r_3/r_2$. For a perfect gas, the temperature ratio T_3/T_2 can be easily found. Substituting $h = C_p T = \gamma RT/(\gamma - 1)$ in Eq. (8.2c),

$$1 - \frac{T_3}{T_2} = \frac{1}{2}U_2^2\frac{(\gamma - 1)}{\gamma RT_2}\left[1 - \cot^2\alpha_2 + \left(\frac{r_3}{r_2}\right)^2\cot^2\beta_3\right]$$

therefore,

$$\frac{T_3}{T_2} = 1 - \frac{1}{2}(\gamma - 1)\left(\frac{U_2}{a_2}\right)^2\left[1 - \cot^2\alpha_2 + \left(\frac{r_3}{r_2}\right)^2\cot^2\beta_3\right] \tag{8.2d}$$

where $a_2 = (\gamma RT_2)^{1/2}$ is the sonic velocity at temperature T_2.

Generally this temperature ratio will have only a very minor effect upon the numerical value of η_{ts} and so it is often ignored in calculations. Thus,

$$\eta_{\text{ts}} \simeq \left\{1 + \frac{1}{2}\left[\zeta_{\text{N}}\,\text{cosec}^2\,\alpha_2 + \left(\frac{r_3}{r_2}\right)^2(\zeta_{\text{R}}\,\text{cosec}^2\,\beta_3 + \cos^2\,\beta_3)\right]\right\}^{-1} \tag{8.9b}$$

is the expression normally used to determine the total-to-static efficiency. An alternative form for η_{ts} can be obtained by rewriting Eq. (8.6) as

$$\eta_{\text{ts}} = \frac{h_{01} - h_{03}}{h_{01} - h_{3\text{ss}}} = \frac{(h_{01} - h_{3\text{ss}}) - (h_{03} - h_3) - (h_3 - h_{3\text{s}}) - (h_{3\text{s}} - h_{3\text{ss}})}{(h_{01} - h_{3\text{ss}})} = 1 - \left(c_3^2 + \zeta_{\text{N}}c_2^2 + \zeta_{\text{R}}w_3^2\right)/c_0^2 \tag{8.10}$$

where the spouting velocity c_0 is defined by

$$h_{01} - h_{3\text{ss}} = \frac{1}{2}c_0^2 = C_p T_{01}\left[1 - (p_3/p_{01})^{(\gamma-1)/\gamma}\right] \tag{8.11}$$

A simple connection exists between total-to-total and total-to-static efficiency, which can be obtained as follows. Writing

$$\Delta W = \eta_{\text{ts}}\Delta W_{\text{ts}} - \eta_{\text{ts}}(h_{01} - h_{3\text{ss}})$$

then

$$\eta_{\text{tt}} = \frac{\Delta W}{\Delta W_{\text{ts}} - (1/2)c_3^2} = \frac{1}{(1/\eta_{\text{ts}}) - (c_3^2/2\Delta W)}$$

Therefore,

$$\frac{1}{\eta_{tt}} = \frac{1}{\eta_{ts}} - \frac{c_3^2}{2\Delta W} = \frac{1}{\eta_{ts}} - \frac{1}{2}\left(\frac{r_3}{r_2}\cot\beta_3\right)^2 \tag{8.12}$$

EXAMPLE 8.2

Performance data from the CAV type 01 radial turbine (Benson, Cartwright, & Das 1968) operating at a pressure ratio p_{01}/p_3 of 1.5 with zero incidence relative flow onto the rotor is presented in the following form:

$$\dot{m}\sqrt{T_{01}/p_{01}} = 1.44 \times 10^{-5}\ \text{ms}(K)^{1/2}$$
$$\Omega/\sqrt{T_{01}} = 2410\ \ (\text{rev/min})/K^{1/2}$$
$$\tau/p_{01} = 4.59 \times 10^{-6}\ \text{m}^3$$

where τ is the torque, corrected for bearing friction loss. The principal dimensions and angles, etc. are given as follows:

rotor inlet diameter, 72.5 mm;
rotor inlet width, 7.14 mm;
rotor mean outlet diameter, 34.4 mm;
rotor outlet annulus height, 20.1 mm;
rotor inlet angle, 0°;
rotor outlet angle, 53°;
number of rotor blades, 10;
nozzle outlet diameter, 74.1 mm;
nozzle outlet angle, 80°;
nozzle blade number, 15.

The turbine is "cold tested" with air heated to 400 K (to prevent condensation erosion of the blades). At nozzle outlet an estimate of the flow angle is given as 70° and the corresponding enthalpy loss coefficient is stated to be 0.065. Assuming that the absolute flow at rotor exit is without swirl and uniform and the relative flow leaves the rotor without any deviation, determine the total-to-static and overall efficiencies of the turbine, the rotor enthalpy loss coefficient, and the rotor relative velocity ratio.

Solution

The data given are obtained from an actual turbine test and, even though the bearing friction loss has been corrected, there is an additional reduction in the specific work delivered due to disk friction and tip leakage losses, etc. The rotor speed $\Omega = 2410\sqrt{400} = 48,200$ rev/min, the rotor tip speed $U_2 = \pi\Omega D_2/60 = 183$ m/s and, hence, the specific work done by the rotor $\Delta W = U_2^2 = 33.48$ kJ/kg. The corresponding isentropic total-to-static enthalpy drop is

$$h_{01} - h_{3ss} = C_p T_{01}\left[1 - (p_3/p_{01})^{(\gamma-1)/\gamma}\right] = 1.005 \times 400[1 - (1/1.5)^{1/3.5}] = 43.97\ \text{kJ/kg}$$

Thus, the total-to-static efficiency is

$$\eta_{ts} = \Delta W/(h_{01} - h_{3ss}) = 76.14\%$$

The actual specific work output to the shaft, after allowing for the bearing friction loss, is

$$\begin{aligned}\Delta W_{act} = \tau\Omega/\dot{m} &= \left(\frac{\tau}{p_{01}}\right)\frac{\Omega}{\sqrt{T_{01}}}\left(\frac{p_{01}}{\dot{m}\sqrt{T_{01}}}\right)\frac{\pi}{30}T_{01} \\ &= 4.59 \times 10^{-6} \times 2410 \times \pi \times 400/(30 \times 1.44 \times 10^{-5}) \\ &= 32.18 \text{ kJ/kg}\end{aligned}$$

Thus, the turbine overall total-to-static efficiency is

$$\eta_0 = \Delta W_{act}/(h_{01} - h_{3ss}) = 73.18\%$$

By rearranging Eq. (8.9b), the rotor enthalpy loss coefficient can be obtained as

$$\begin{aligned}\zeta_R &= [2(1/\eta_{ts} - 1) - \zeta_N \operatorname{cosec}^2 \alpha_2](r_2/r_3)^2 \sin^2 \beta_3 - \cos^2 \beta_3 \\ &= [2(1/0.7613 - 1) - 0.065 \times 1.1186] \times 4.442 \times 0.6378 - 0.3622 \\ &= 1.208\end{aligned}$$

At rotor exit, the absolute velocity is uniform and axial. From the velocity triangles, Figure 8.3,

$$w_3^2(r) = U_3^2 + c_3^2 = U_3^2\left[\left(\frac{r}{r_3}\right)^2 + \cot^2\beta_3\right]$$

$$w_2 = U_2 \cot \alpha_2$$

ignoring blade-to-blade velocity variations. Hence,

$$\frac{w_3(r)}{w_2} = \frac{r_3}{r_2}\tan\alpha_2\left[\left(\frac{r}{r_3}\right)^2 + \cot^2\beta_3\right]^{1/2} \tag{8.13}$$

The lowest value of this relative velocity ratio occurs when, $r = r_{3h} = (34.4 - 20.1)/2 = 7.15$ mm, so that

$$\frac{w_{3h}}{w_2} = 0.475 \times 2.904[0.415^2 + 0.7536^2]^{1/2} = 1.19$$

The relative velocity ratio corresponding to the mean exit radius is

$$\frac{w_3}{w_2} = 0.475 \times 2.904[1 + 0.7536^2]^{1/2} = 1.73$$

It is worth commenting that higher total-to-static efficiencies have been obtained in other small radial turbines operating at higher pressure ratios. Rodgers (1969) has suggested that

total-to-static efficiencies in excess of 90% for pressure ratios up to 5−1 can be attained. Nusbaum and Kofskey (1969) reported an experimental value of 88.8% for a small radial turbine (fitted with an outlet diffuser, admittedly!) at a pressure ratio p_{01}/p_4 of 1.763. In the design point exercise just given the high rotor enthalpy loss coefficient and the corresponding relatively low total-to-static efficiency may well be related to the low relative velocity ratio determined on the hub. Matters are probably worse than this as the calculation is based only on a simple one-dimensional treatment. In determining velocity ratios across the rotor, account should also be taken of the effect of blade-to-blade velocity variation (outlined in this chapter) as well as viscous effects. The number of vanes in the rotor (10) may be insufficient on the basis of Jamieson's theory (1955), included later in this chapter, which suggests 18 vanes (i.e., $Z_{\min} = 2\pi \tan \alpha_2$). For this turbine, at lower nozzle exit angles, Eq. (8.13) suggests that the relative velocity ratio becomes even less favorable despite the fact that the Jamieson blade spacing criterion is being approached. (For $Z = 10$, the optimum value of α_2 is about 58°.)

8.6 Some Mach number relations

Assuming the fluid is a perfect gas, expressions can be deduced for the important Mach numbers in the turbine. At nozzle outlet, the absolute Mach number at the nominal design point is

$$M_2 = \frac{c_2}{a_2} = \frac{U_2}{a_2}\operatorname{cosec} \alpha_2$$

Now,

$$T_2 = T_{01} - c_2^2/(2C_p) - T_{01} - \frac{1}{2}U_2^2 \operatorname{cosec}^2 \alpha_2/C_p$$

Therefore,

$$\frac{T_2}{T_{01}} = 1 - \frac{1}{2}(\gamma - 1)(U_2/a_{01})^2 \operatorname{cosec}^2 \alpha_2$$

where $a_2 = a_{01}(T_2/T_{01})^{1/2}$. Hence,

$$M_2 = \frac{U_2/a_{01}}{\sin \alpha_2 \left[1-(1/2)(\gamma-1)(U_2/a_{01})^2 \operatorname{cosec}^2 \alpha_2\right]^{1/2}} \tag{8.14}$$

At rotor outlet, the relative Mach number at the design point is defined by

$$M_{3,\text{rel}} = \frac{w_3}{a_3} = \frac{r_3 U_2}{r_2 a_3} \operatorname{cosec} \beta_3$$

Now,

$$h_3 = h_{01} - \left(U_2^2 + \frac{1}{2}c_3^2\right) = h_{01} - \left(U_2^2 + \frac{1}{2}U_3^2 \cot^2\beta_3\right) = h_{01} - U_2^2\left[1 + \frac{1}{2}\left(\frac{r_3}{r_2}\cot\beta_3\right)^2\right]$$

$$a_3^2 = a_{01}^2 - (\gamma - 1)U_2^2\left[1 + \frac{1}{2}\left(\frac{r_3}{r_2}\cot\beta_3\right)^2\right]$$

therefore,

$$M_{3,\text{rel}} = \frac{(U_2/a_{01})(r_3/r_2)}{\sin\beta_3\{1-(\gamma-1)(U_2/a_{01})^2[1+(1/2)((r_3/r_2)\cot\beta_3)^2]\}^{1/2}} \tag{8.15}$$

8.7 The scroll and stator blades

It was pointed out by Artt and Spence (1998) that the division of losses in a radial-inflow turbine is an essential step in attaining a simple performance prediction procedure, one likely to yield useful results. A common procedure is to simply measure the static pressure at the rotor inlet tip diameter. However, without knowledge of the magnitude of the loss occurring in the stator passages the mean velocities cannot be determined.

Many different loss models for one-dimensional performance prediction methods have been published, e.g., Rohlik (1968), Benson (1970), Benson et al. (1968), Spence and Artt (1997), Whitfield (1990), etc. These range from simple loss factors determined from experimental data to more credible attempts at estimating the friction losses in a blade passage. A common fault in most of these loss models was the lack of verification from reliable experimental data. This unsatisfactory state of affairs still holds true. Spence and Artt (1997) published performance data of tests done on a 99 mm turbine rotor tested with seven different sized stator diameters embracing a wide range of rotor speeds and pressure ratios. Despite the ensuing comprehensive test program, these tests were not successful in providing the answers required.

It is worth trying to understand the procedure followed in these tests. The static pressure p_2 was measured just outside the rotor inlet diameter. An isentropic analysis was carried out to determine the stator loss from p_2. The flow was assumed to accelerate isentropically through the nozzle throat, the law of continuity enabling the velocity and ideal static pressure and static temperature to be determined. Conservation of angular momentum was then assumed to apply from the nozzle throat to the rotor inlet. The radial component of velocity at rotor inlet was found from the continuity equation applied to the cylindrical potion of the rotor inlet. Solving for these measurements by iteration enabled the *ideal* velocity, static temperature and pressure at the rotor inlet to be found. The measured static pressure was lower than the ideal calculated value and this difference was equated to the loss through the stator. All of this seemed straightforward enough. However, the resulting pressure loss turned out to be a strong function of the assumed angle of flow through the throat. Assuming a flow angle perpendicular to the geometric nozzle throat predicted a loss in excess of the total loss measured for the turbine stage. Using a flow angle determined from the $\cos^{-1}(o/s)$ proposed by Hiett

and Johnston (1964), resulted in a loss of a more believable magnitude. For the 5.5-mm-diameter nozzle, the angle measured perpendicular to the throat was 62.7° from the radial direction, compared with 75.2° calculated from the cosine rule. The author decided to abandon this method of analysis since it is difficult to justify any angle other than one that is perpendicular to the throat.

Stator loss models

Clearly some theoretical method would be needed to estimate the stator loss. With this the rotor inlet velocity triangles and the rotor losses should then be determinable. Many loss models have been proposed for correlating the scroll and nozzle losses from performance data, but surprisingly few have been successful at predicting the losses based on the geometry alone. One of the main drawbacks with any of the simple loss models is the heavy reliance on existing test data in order to determine a loss coefficient. Also, no account is taken of the geometrical details of the blades. Rohlik (1968) used a more complex stator loss model requiring little empirical data when he presented a design procedure for radial-inflow turbines. This related boundary layer momentum thickness, blade geometry, energy level, and friction loss in the blade passages of axial-flow machines. A single equation (which originated from Stewart, Witney, and Wong, 1960) was given for the overall loss in a blade row:

$$H_f = E\left[\frac{(\theta/l)(l_c/l)(l/s)}{\cos\alpha_1 - t/s - \delta/s}\right]\left(1 + \frac{A_{endwall}}{A_{vane}}\right) \tag{8.16}$$

where

H_f = fraction of the ideal kinetic energy that is lost in the scroll and nozzle passages;
A_{vane} = area of one of the vane walls of the nozzle passage;
$A_{endwall}$ = area of one of the end walls of the nozzle passage;
l = chord length of the nozzle vane;
l_c = mean camber length of the nozzle vane;
s = vane pitch;
σ = vane solidity = l/s;
α_1 = mean angle at nozzle exit, measured from the radial direction;
E = energy factor; from experimental results, $E = 1.8$;
t = trailing edge thickness;
θ/l = momentum thickness ratio, determined from axial cascade data as 0.03;
δ/θ = form factor, determined from correlations of experimental data.

Stewart et al. claimed that the momentum thickness loss parameter varied inversely as the 1/5th power of the Reynolds number. The value of momentum thickness at any Reynolds number could be determined from a reference value of momentum thickness at a known Reynolds number, i.e.,

$$\frac{(\theta/l_c)}{(\theta/l_c)_{ref}} = \left(\frac{Re}{Re_{ref}}\right)^{-0.2} \tag{8.17}$$

This analysis has the advantage of requiring little empirical input data, none of which has to be derived from measured performance data of the turbine being examined. Although there were other analytical

models that were examined only the model presented by Rohlik has the firmest foundation. It was the only model of many that correctly predicted the loss changes that occur for different sized nozzles.

Effects of varying the vaneless space and the vane solidity

An extensive experimental program of tests have been reported by Simpson, Spence, and Watterson (2013) carried out on a 135-mm-tip diameter radial turbine with a variety of stator vane designs. The purpose of these tests was to determine the effects that the parameter R_{te}/R_{le}[2] and the vane solidity had on the stage efficiency. The authors used computational fluid dynamics and reported that it was a reliable tool in predicting trends of both stage efficiency and mass flow. Performance tests were carried out on two series of vaned stator designs in order to measure the efficiency variations with varying values of the parameters R_{te}/R_{le} and solidity c/s. It was found that the aerodynamic optimum values for these two parameters were 1.175 and 1.25, respectively. Increasing the values of both of these parameters led to a reduction of both the measured and predicted static pressure variations at the rotor inlet.

An interesting finding for designers was that increasing the size of the vaneless space was a more aerodynamically efficient method of obtaining a more circumferentially uniform flow around the rotor periphery.

Loss coefficients used in 90° IFR turbines

There are a number of ways of representing the losses in the passages of 90° IFR turbines and these have been listed and interrelated by Benson (1970). As well as the nozzle and rotor passage losses, there is a loss at rotor entry at off-design conditions. This occurs when the relative flow entering the rotor is at some angle of incidence to the radial vanes so that it can be called an *incidence loss*. It is sometimes referred to as *shock loss*. This is a rather misleading term because, normally, there is no shock wave.

Nozzle (or stator) loss coefficients

The enthalpy loss coefficient, which normally includes the inlet scroll and nozzle blade losses, has already been defined and is

$$\zeta_N = \frac{h_2 - h_{2s}}{(1/2)c_2^2} \tag{8.18}$$

the stagnation pressure loss coefficient,

$$Y_N = (p_{01} - p_{02})/(p_{02} - p_2) \tag{8.18a}$$

which can be related, approximately, to ζ_N by

$$Y_N \simeq \zeta_N \left(1 + \frac{1}{2}\gamma M_2^2\right) \tag{8.18b}$$

[2] R_{le} is rotor leading edge radius and R_{te} is stator vane trailing edge radius.

Since

$$h_{01} = h_2 + \frac{1}{2}c_2^2 + h_{2s} + \frac{1}{2}c_{2s}^2,\ h_2 - h_{2s} = \frac{1}{2}\left(c_{2s}^2 - c_2^2\right)$$

and

$$\zeta_N = \frac{1}{\phi_N^2} - 1 \tag{8.19}$$

Practical values of the flow coefficient ϕ_N for well-designed nozzle rows in normal operation are usually in the range $0.90 < \phi_N < 0.97$, therefore, $0.23 < \zeta_N < 0.063$.

Artt and Spence (1998) gave a very detailed review of the many tests made by researchers since the early 1960s on the losses occurring in the nozzles of radial-inflow turbines. They also made many of their own experimental tests on a 99-mm-diameter radial-inflow turbine with seven different nozzle throat areas at two rotor speeds. Plots were presented showing the division of the losses in the several parts of the turbine for the two rotor speeds and for each of the seven stator throat areas.

In a previous report, Spence and Artt (1997) commented that a good efficiency was obtained with a stator–rotor throat area ratio of 0.5. This area ratio seemed to the above authors to be inextricably linked to the optimum blade angles and the more even distribution of the expansion of the flow between the stator and the rotor.

Rotor loss coefficients

At either the design condition (Figure 8.4), or at the off-design condition dealt with later (Figure 8.5), the rotor passage friction losses can be expressed in terms of the following coefficients.

The enthalpy loss coefficient is

$$\zeta_R = \frac{h_3 - h_{3s}}{(1/2)w_3^2} \tag{8.20}$$

The velocity coefficient is

$$\phi_R = w_3/w_{3s} \tag{8.21}$$

which is related to ζ_R by

$$\zeta_R = \frac{1}{\phi_R^2} - 1 \tag{8.22}$$

The normal range of ϕ for well-designed rotors is approximately, $0.70 < \phi_R < 0.85$ and $1.04 < \zeta_R < 0.38$.

8.8 Optimum efficiency considerations

According to Abidat, Chen, Baines, and Firth (1992), the understanding of incidence effects on the rotors of radial- and mixed-flow turbines is very limited. Normally, IFR turbines are made with

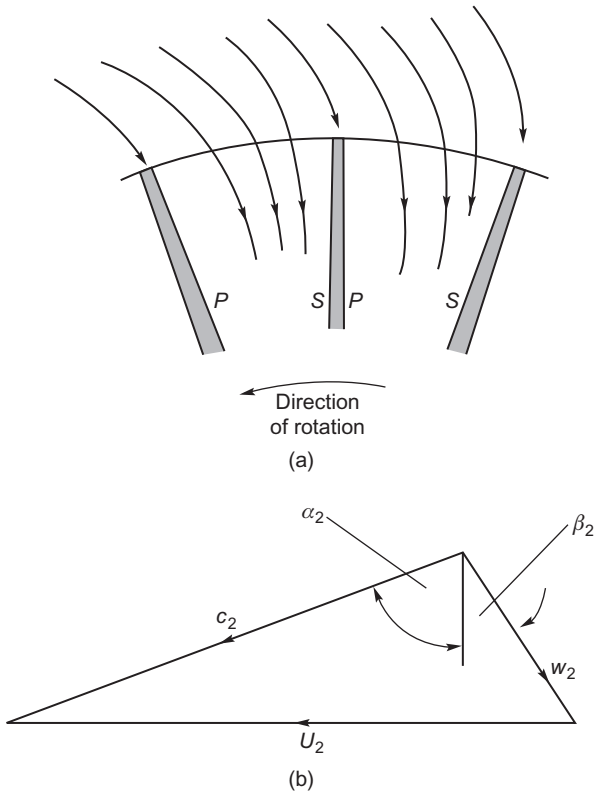

FIGURE 8.5

Optimum flow condition at inlet to the rotor: (a) streamline flow at rotor inlet—P is for pressure surface, S is for suction surface, and (b) velocity diagram for the pitchwise averaged flow.

radial vanes to reduce bending stresses. In most flow analyses that have been published of the IFR turbine, including all earlier editions of this text, it was assumed that the *average* relative flow at entry to the rotor was radial, that is, the incidence of the relative flow approaching the radial vanes was zero. The following discussion of the flow model will show that this is an oversimplification and the flow angle for optimum efficiency is significantly different from zero incidence. Rohlik (1975) had asserted that "there is some incidence angle that provides *optimum flow conditions* at the rotor-blade leading edge. This angle has a value sometimes as high as 40° with a radial blade."

The flow approaching the rotor is assumed to be in the radial plane with a velocity c_2 and flow angle α_2 determined by the geometry of the nozzles or volute. Once the fluid enters the rotor, the process of work extraction proceeds rapidly with reductions in the magnitude of the tangential velocity component and blade speed as the flow radius decreases. Corresponding to these velocity changes is a high blade loading and an accompanying large pressure gradient across the passage from the pressure side to the suction side (Figure 8.5a).

With the rotor rotating at angular velocity Ω and the entering flow assumed to be irrotational, a counter-rotating vortex (or relative eddy) is created in the relative flow, whose magnitude is $-\Omega$, which conserves the irrotational state. The effect is virtually the same as that described earlier for the flow leaving the impeller of a centrifugal compressor but in reverse (see Section 7.8 entitled "Slip Factor"). As a result of combining the incoming irrotational flow with the relative eddy, the relative velocity on the pressure (or trailing) surface of the vane is reduced. Similarly, on the suction (or leading) surface of the vane it is seen that the relative velocity is increased. Thus, a static pressure gradient exists *across* the vane passage in agreement with the reasoning of the preceding paragraph.

Figure 8.5(b) indicates the *average* relative velocity, w_2, entering the rotor at angle β_2 and giving optimum flow conditions at the vane leading edge. As the rotor vanes in IFR turbines are assumed to be radial, the angle β_2 is an angle of incidence, and as drawn it is numerically positive. Depending upon the number of rotor vanes, this angle may be between 20° and 40°. The static pressure gradient across the passage causes a streamline shift of the flow towards the suction surface. Stream function analyses of this flow condition show that the streamline pattern properly locates the inlet stagnation point on the vane leading edge so that this streamline is approximately radial (Figure 8.5a). It is reasoned that only at this flow condition will the fluid move smoothly into the rotor passage. Thus, it is the *averaged* relative flow that is at an angle of incidence β_2 to the vane. Whitfield and Baines (1990, chap. 8) have comprehensively reviewed the computational methods used in determining turbomachinery flows, including stream function methods.

Wilson and Jansen (1965) appear to have been the first to note that the optimum angle of incidence was virtually identical to the angle of "slip" of the flow leaving the impeller of a radially bladed centrifugal compressor with the same number of vanes as the turbine rotor. Following Whitfield and Baines (1990, chap. 8), an *incidence factor*, λ, is defined, analogous to the slip factor used in centrifugal compressors:

$$\lambda = c_{\theta 2}/U_2$$

The slip factor most often used in determining the flow angle at rotor inlet is that devised by Stanitz (1952)[3] for radial-vaned impellers, so for the incidence factor

$$\lambda = 1 - 0.63\pi/Z \approx 1 - 2/Z$$

Thus, from the geometry of Figure 8.5(b), we obtain

$$\tan \beta_2 = (2/Z)U_2/c_{m2} \tag{8.23}$$

To determine the relative flow angle, β_2, we need to know, at least, the values of the flow coefficient, $\phi_2 = c_{m2}/U_2$, and the vane number, Z. A simple method of determining the minimum number of vanes needed in the rotor, due to Jamieson (1955, chap. 9), is given later in this chapter. However, in the next section an optimum efficiency design method devised by Whitfield (1990) provides an alternative way for deriving β_2.

[3]In Chapter 7, a recently modified and improved slip factor for centrifugal compressors has been presented which may have application to the analysis of radial-inflow turbines.

Design for optimum efficiency

Whitfield (1990) presented a general one-dimensional design procedure for the IFR turbine in which, initially, only the required power output is specified. The specific power output is given as

$$\Delta W = \dot{W}\dot{m} = h_{01} - h_{03} = \frac{\gamma R}{\gamma - 1}(T_{01} - T_{03}) \tag{8.24}$$

and, from this a nondimensional *power ratio*, S, is defined as

$$S = \Delta W / h_{01} = 1 - T_{03}/T_{01} \tag{8.25}$$

The power ratio is related to the overall pressure ratio through the total-to-static efficiency:

$$\eta_{\text{ts}} = \frac{S}{\left[1 - (p_3/p_{01})^{(\gamma-1)/\gamma}\right]} \tag{8.26}$$

If the power output, mass flow rate, and inlet stagnation temperature are specified, then S can be directly calculated but, if only the output power is known, then an iterative procedure must be followed.

Whitfield (1990) chose to develop his procedure in terms of the power ratio S and evolved a new nondimensional design method. At a later stage of the design when the rate of mass flow and inlet stagnation temperature can be quantified, the actual gas velocities and turbine size can be determined. Only the first part of Whitfield's method dealing with the rotor design is considered in this chapter.

Solution of Whitfield's design problem

At the design point, it is usually assumed that the fluid discharges from the rotor in the axial direction so that with $c_{\theta 3} = 0$, the specific work is

$$\Delta W = U_2 c_{\theta 2}$$

and, combining this with Eqs (8.24) and (8.25), we obtain

$$U_2 c_{\theta 2}/a_{01}^2 = S/(\gamma - 1) \tag{8.27}$$

where $a_{01} = (\gamma R T_{01})^{1/2}$ is the speed of sound corresponding to the temperature T_{01}.

Now, from the velocity triangle at rotor inlet, Figure 8.5(b),

$$U_2 - c_{\theta 2} = c_{\text{m}2} \tan \beta_2 = c_{\theta 2} \tan \beta_2 / \tan \alpha_2 \tag{8.28}$$

Multiplying both sides of Eq. (8.28) by $c_{\theta 2}/c_{\text{m}2}^2$, we get

$$U_2 c_{\theta 2}/c_{\text{m}2}^2 - c_{\theta 2}^2/c_{\text{m}2}^2 - \tan \alpha_2 \tan \beta_2 = 0$$

But,

$$U_2 c_{\theta 2}/c_{\text{m}2}^2 = (U_2 c_{\theta 2}/c_2^2) \sec^2 \alpha_2 = c(1 + \tan^2 \alpha_2)$$

which can be written as a quadratic equation for tan α_2:

$$(c-1)\tan^2\alpha_2 - b\tan\alpha_2 + c = 0$$

where, for economy of writing, $c = U_2 c_{\theta 2}/c_2^2$ and $b = \tan\beta_2$. Solving for tan α_2,

$$\tan\alpha_2 = \frac{b \pm \sqrt{b^2 + 4c(1-c)}}{2(c-1)} \tag{8.29}$$

For a real solution to exist the radical must be greater than, or equal to, zero, i.e., $b^2 + 4c(1-c) \geq 0$. Taking the zero case and rearranging the terms, another quadratic equation is found, namely,

$$c^2 - c - b^2/4 = 0$$

Hence, solving for c,

$$c = \left(1 \pm \sqrt{1+b^2}\right)/2 = \frac{1}{2}(1 \pm \sec\beta_2) = U_2 c_{\theta 2}/c_2^2 \tag{8.30}$$

From Eq. (8.29) and then Eq. (8.30), the corresponding solution for tan α_2 is

$$\tan\alpha_2 = b/[2(c-1)] = \tan\beta_2/(-1 \pm \sec\beta_2)$$

The correct choice between these two solutions will give a value for $\alpha_2 > 0$; thus

$$\tan\alpha_2 = \frac{\sin\beta_2}{1-\cos\beta_2} \tag{8.31a}$$

It is easy to see from Table 8.1 that a simple numerical relation exists between these two parameters, namely,

$$\alpha_2 = 90 - \beta_2/2 \tag{8.31b}$$

From Eqs (8.27) and (8.30), after some rearranging, a minimum stagnation Mach number at rotor inlet can be found:

$$M_{02}^2 = c_2^2/a_{01}^2 = \left(\frac{S}{\gamma - 1}\right)\frac{2\cos\beta_2}{1+\cos\beta_2} \tag{8.32}$$

and the inlet Mach number can be determined using the equation

$$M_2^2 = \left(\frac{c_2}{a_2}\right)^2 \frac{M_{02}^2}{1-(1/2)(\gamma-1)M_{02}^2} \tag{8.33}$$

assuming that $T_{02} = T_{01}$, as the flow through the stator is adiabatic.

Table 8.1 Variation of α_2 for Several Values of β_2

	Degrees			
β_2	10	20	30	40
α_2	85	80	75	70

Now, from Eq. (8.28)

$$\frac{c_{\theta 2}}{U_2} = \frac{1}{1 + \tan \beta_2 / \tan \alpha_2}$$

After rearranging Eq. (8.31a) to give

$$\tan \beta_2 / \tan \alpha_2 = \sec \beta_2 - 1 \tag{8.34}$$

and, combining these equations with Eq. (8.23),

$$c_{\theta 2}/U_2 = \cos \beta_2 = 1 - 2/Z \tag{8.35}$$

Equation (8.35) is a direct relationship between the number of rotor blades and the relative flow angle at inlet to the rotor. Also, from Eq. (8.31b),

$$\cos 2\alpha_2 = \cos(180 - \beta_2) = -\cos \beta_2$$

so that, from the identity $\cos 2\alpha_2 = 2\cos^2 \alpha_2 - 1$, we get the result

$$\cos^2 \alpha_2 = (1 - \cos \beta_2)/2 = 1/Z \tag{8.31c}$$

using also Eq. (8.35).

EXAMPLE 8.3

An IFR turbine with 12 vanes is required to develop 230 kW from a supply of dry air available at a stagnation temperature of 1050 K and a flow rate of 1 kg/s. Using the optimum efficiency design method and assuming a total-to-static efficiency of 0.81, determine

a. the absolute and relative flow angles at rotor inlet;
b. the overall pressure ratio, p_{01}/p_3;
c. the rotor tip speed and the inlet absolute Mach number.

Solution

a. From the gas tables, e.g., Rogers and Mayhew (1995) or NIST Properties of Fluids Tables, at $T_{01} = 1050$ K, we can find values for $C_p = 1.1502$ kJ/kgK and $\gamma = 1.333$. Using Eq. (8.25),

$$S = \Delta W/(C_p T_{01}) = 230/(1.15 \times 1050) = 0.2$$

From Whitfield's equation (8.31c),

$$\cos^2 \alpha_2 = 1/Z = 0.083333$$

therefore, $\alpha_2 = 73.22^\circ$ and, from Eq. (8.31b), $\beta_2 = 2(90 - \alpha_2) = 33.56^\circ$

b. Rewriting Eq. (8.26),

$$\frac{p_3}{p_{01}} = \left(1 - \frac{s}{\eta_{ts}}\right)^{\gamma/(\gamma-1)} = \left(1 - \frac{0.2}{0.81}\right)^4 = 0.32165$$

therefore, $p_{01}/p_{003} = 3.109$

c. Using Eq. (8.32),

$$M_{02}^2 = \left(\frac{\mathrm{S}}{\gamma - 1}\right)\frac{2\cos\beta_2}{1+\cos\beta_2} = \frac{0.2}{0.333} \times \frac{2 \times 0.8333}{1 + 0.8333} = 0.5460$$

therefore, $M = 0.7389$. Using Eq. (8.33),

$$M_2^2 = \frac{M_{02}^2}{1 - (1/2)(\gamma - 1)M_{02}^2} = \frac{0.546}{1 - (0.333/2) \times 0.546} = 0.6006$$

and $M_2 = 0.775$. To find the rotor tip speed, substitute Eq. (8.35) into Eq. (8.27) to obtain

$$\left(\frac{U_2^2}{a_{01}^2}\right)\cos\beta_2 = \frac{S}{\gamma - 1}$$

therefore,

$$U_2 = a_{01}\sqrt{\frac{S}{(\gamma - 1)\cos\beta_2}} = 633.8\sqrt{\frac{0.2}{0.333 \times 0.8333}} = 538.1 \text{ m/s}$$

where

$$a_{01} = \sqrt{\gamma R T_{01}} = \sqrt{1.333 \times 287 \times 1050} = 633.8 \text{ m/s}$$

and $T_{02} = T_{01}$ is assumed.

8.9 Criterion for minimum number of blades

The following simple analysis of the relative flow in a radially bladed rotor is of considerable interest as it illustrates an important fundamental point concerning blade spacing. From elementary mechanics, the radial and transverse components of acceleration, f_r and f_t, respectively, of a particle moving in a radial plane (Figure 8.6a) are

$$f_\mathrm{r} = \dot{w} - \Omega^2 r \tag{8.36a}$$

$$f_\mathrm{t} = r\dot{\Omega} + 2\Omega w \tag{8.36b}$$

where w is the radial velocity, $\dot{w} = \mathrm{d}w/dt = w\partial w/\partial r$ (for steady flow), Ω is the angular velocity, and $\dot{\Omega} = \mathrm{d}\Omega/dt$ is set equal to zero.

Applying *Newton's second law of motion* to a fluid element (as shown in Figure 6.2) of unit depth, ignoring viscous forces, but putting $c_\mathrm{r} = w$, the radial equation of motion is

$$(p + \mathrm{d}p)(r + \mathrm{d}r)\mathrm{d}\theta - pr\mathrm{d}\theta - p\mathrm{d}r\mathrm{d}\theta = -f_\mathrm{r}\mathrm{d}m$$

where the elementary mass $\mathrm{d}m = \rho r\mathrm{d}\theta\mathrm{d}r$. After simplifying and substituting for f_r from Eq. (8.36a), the following result is obtained,

$$\frac{1}{\rho}\frac{\partial p}{\partial r} + w\frac{\partial w}{\partial r} = \Omega^2 r \tag{8.37}$$

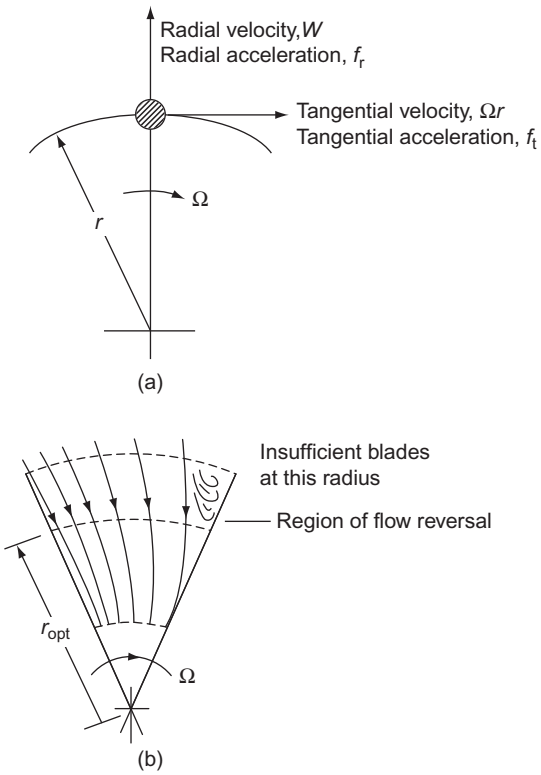

FIGURE 8.6

Flow models used in analysis of minimum number of blades: (a) motion of particle in a radial plane and (b) optimum radius to avoid flow reversal, r_{opt}.

Integrating Eq. (8.37) with respect to r obtains

$$p/\rho + \frac{1}{2}w^2 - \frac{1}{2}U^2 = \text{constant} \tag{8.38}$$

which is merely the *inviscid form* of Eq. (8.2a).

The torque transmitted to the rotor by the fluid manifests itself as a pressure difference across each radial vane. Consequently, there must be a pressure gradient in the *tangential direction* in the space between the vanes. Again, consider the element of fluid and apply Newton's second law of motion in the tangential direction:

$$\mathrm{d}p \times \mathrm{d}r = f_t \mathrm{d}m = 2\Omega w(\rho r \mathrm{d}\theta \mathrm{d}r)$$

Hence,

$$\frac{1}{\rho}\frac{\partial p}{\partial \theta} = 2\Omega r w \tag{8.39}$$

which establishes the magnitude of the tangential pressure gradient. Differentiating Eq. (8.38) with respect to θ,

$$\frac{1}{\rho}\frac{\partial p}{\partial \theta} = -w\frac{\partial w}{\partial \theta} \tag{8.40}$$

Thus, combining Eqs (8.39) and (8.40) gives

$$\frac{\partial w}{\partial \theta} = -2\Omega r \tag{8.41}$$

This result establishes the important fact that *the radial velocity is not uniform across the passage* as is frequently assumed. As a consequence the radial velocity on one side of a passage is lower than on the other side. Jamieson (1955, chap. 9), who originated this method, conceived the idea of determining the *minimum* number of blades based upon these velocity considerations.

Let the mean radial velocity be $\overline{w}$ and the angular space between two adjacent blades be $\Delta\theta = 2\pi/Z$, where Z is the number of blades. The maximum and minimum radial velocities are, therefore,

$$w_{\max} = \overline{w} + \frac{1}{2}\Delta w = \overline{w} + \Omega r\Delta\theta \tag{8.42a}$$

$$w_{\min} = \overline{w} - \frac{1}{2}\Delta w = \overline{w} - \Omega r\Delta\theta \tag{8.42b}$$

using Eq. (8.41).

Making the reasonable assumption that the radial velocity should not drop below zero (Figure 8.6b), the limiting case occurs at the rotor tip, $r = r_2$ with $w_{\min} = 0$. From Eq. (8.42b) with $U_2 = \Omega r_2$, the minimum number of rotor blades is

$$Z_{\min} = 2\pi U_2/\overline{w}_2 \tag{8.43a}$$

At the design condition, $U_2 = \overline{w}_2 \tan \alpha_2$, hence,

$$Z_{\min} = 2\pi \tan \alpha_2 \tag{8.43b}$$

Jamieson's result, Eq. (8.43b), is plotted in Figure 8.7 and shows that a large number of rotor vanes are required, especially for high absolute flow angles at rotor inlet. In practice, a large number of vanes are not used for several reasons, e.g., excessive flow blockage at rotor exit, a disproportionally large "wetted" surface area causing high friction losses, and the weight and inertia of the rotor become relatively high.

Some experimental tests reported by Hiett and Johnston (1964) are of interest in connection with the analysis just presented. With a nozzle outlet angle $\alpha_2 = 77^\circ$ and a 12 vane rotor, a total-to-static efficiency $\eta_{ts} = 0.84$ was measured at the optimum velocity ratio U_2/c_0. For that magnitude of flow angle, Eq. (8.43b) suggests 27 vanes would be required to avoid reverse flow at the rotor tip. However, a second test with the number of vanes increased to 24 produced a gain in efficiency of only 1%. Hiett and Johnston suggested that the criterion for the optimum number of vanes might not simply be the avoidance of local flow reversal but require a compromise between total pressure losses from this cause and friction losses based upon rotor and blade surface areas.

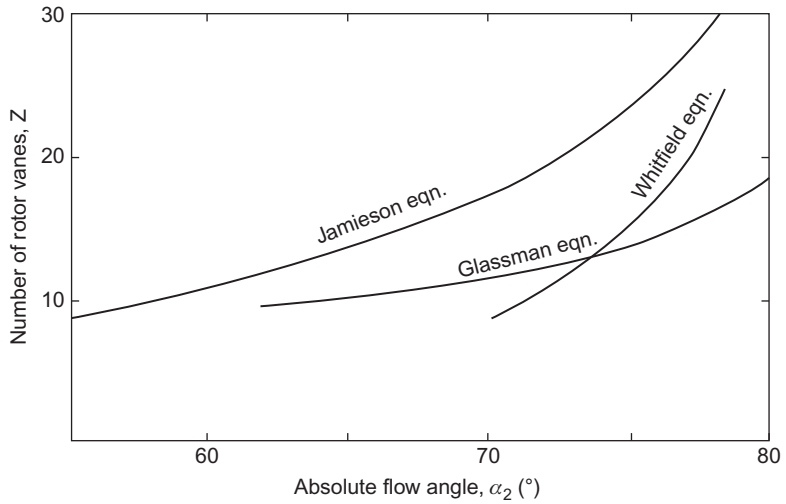

FIGURE 8.7

Flow angle at rotor inlet as a function of the number of rotor vanes.

Glassman (1976) preferred to use an empirical relationship between Z and α_2, namely,

$$Z = \frac{\pi}{30}(110 - \alpha_2)\tan\alpha_2 \tag{8.44}$$

as he also considered Jamieson's result, Eq. (8.43b), gave too many vanes in the rotor. Glassman's result, which gives far fewer vanes than Jamieson's is plotted in Figure 8.7. Whitfield's result, given in Eq. (8.31c), is not too dissimilar from the result given by Glassman's equation, at least for low vane numbers.

8.10 Design considerations for rotor exit

Several decisions need to be made regarding the design of the rotor exit. The flow angle β_3, the meridional velocity to blade tip speed ratio c_{m3}/U_2, the shroud tip to rotor tip radius ratio r_{3s}/r_2, and the exit hub-to-shroud radius ratio $\nu = r_{3h}/r_{3s}$, all have to be considered. It is assumed that the absolute flow at rotor exit is entirely axial so that the relative velocity can be written as

$$w_3^2 = c_{m3}^2 + U_3^2$$

If values of c_{m3}/U_2 and r_3/r_2 can be chosen, then the exit flow angle variation can be found for all radii. From the rotor exit velocity diagram in Figure 8.3,

$$\cot\beta_3(r) = \frac{c_{m3}r_2}{U_2 r} \tag{8.45}$$

The meridional velocity c_{m3} should be kept small in order to minimize the exhaust energy loss, unless an exhaust diffuser is fitted to the turbine.

Rodgers and Geiser (1987) correlated attainable efficiency levels of IFR turbines against the blade tip speed−spouting velocity ratio, U_2/c_0, and the axial exit flow coefficient, c_{m3}/U_2, and their result is shown in Figure 8.8. From this figure, it can be seen that peak efficiency values are obtained with velocity ratios close to 0.7 and with values of exit flow coefficient between 0.2 and 0.3.

Rohlik (1968) suggested that the ratio of mean rotor exit radius to rotor inlet radius, r_3/r_2, should not exceed 0.7 to avoid excessive curvature of the shroud. Also, the exit hub-to-shroud radius ratio, r_{3h}/r_{3s}, should not be <0.4 because of the likelihood of flow blockage caused by closely spaced vanes. Based upon the metal thickness alone, it is easily shown that

$$(2\pi r_3 h/Z)\cos\beta_{3h} > t_{3h}$$

where t_{3h} is the vane thickness at the hub. It is also necessary to allow more than this thickness because of the boundary layers on each vane. Some of the rather limited test data available on the design of the rotor exit comes from Rodgers and Geiser (1987) and concerns the effect of rotor radius ratio and blade solidity on turbine efficiency (Figure 8.9). It is the relative efficiency variation, η/η_{opt}, that is depicted as a function of the rotor inlet radius−exit *root mean square* radius ratio, r_2/r_{3rms}, for various values of a blade solidity parameter, ZL/D_2 (where L is the length of the blade along the mean meridian). This radius ratio is related to the rotor exit hub-to-shroud ratio, ν, by

$$\frac{r_{3rms}}{r_2} = \frac{r_{3s}}{r_2}\left(\frac{1+\nu^2}{2}\right)^{1/2}$$

From Figure 8.9, for r_2/r_{3rms}, a value between 1.6 and 1.8 appears to be the optimum.

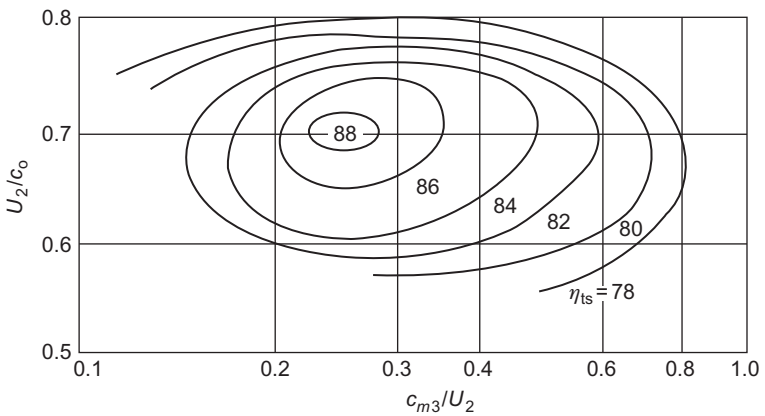

FIGURE 8.8

Correlation of attainable efficiency levels of IFR turbines against velocity ratios.

(*Adapted from Rodgers & Geiser, 1987*)

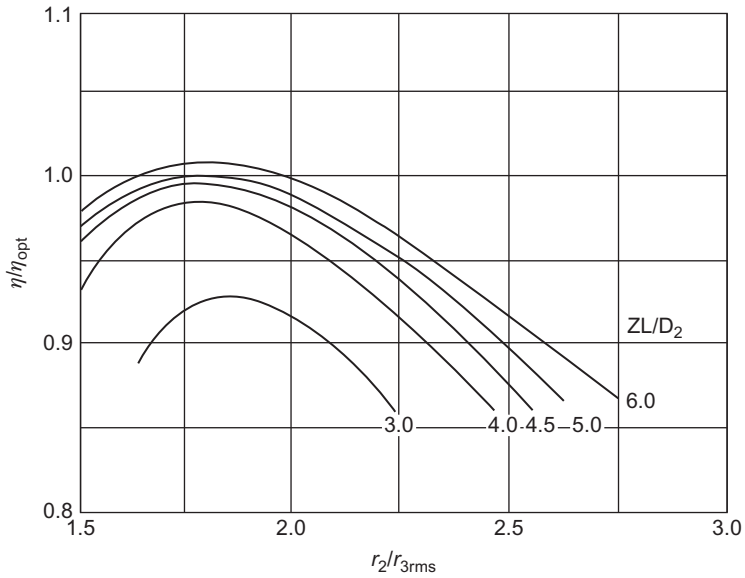

FIGURE 8.9

Effects of vane solidity and rotor radius ratio on the efficiency ratio of the IFR turbine.

(*Adapted from Rodgers & Geiser, 1987*)

Rohlik (1968) suggested that the ratio of the relative velocity at the mean exit radius to the inlet relative velocity, w_3/w_2, should be sufficiently high to assure a low total pressure loss. He gave w_3/w_2 a value of 2.0. The relative velocity at the shroud tip will be greater than that at the mean radius depending upon the radius ratio at rotor exit.

EXAMPLE 8.4

Given the following data for an IFR turbine,

$$c_{m3}/U_2 = 0.25, \quad v = 0.4, r_{3s}/r_2 = 0.7, \text{and} \quad w_3/w_2 = 2.0$$

determine the ratio of the relative velocity ratio, w_{3s}/w_2 at the shroud.

Solution

As $w_{3s}/c_{m3} = \sec\beta_{3s}$ and $w_3/c_{m3} = \sec\beta_3$,

$$\frac{w_{3s}}{w_3} = \frac{\sec\beta_{3s}}{\sec\beta_{3s}}$$

$$\frac{r_3}{r_{3s}} = \frac{1}{2}(1+v) = 0.7 \quad \text{and} \quad \frac{r_3}{r_2} = \frac{r_3}{r_{3s}}\frac{r_{3s}}{r_2} = 0.7 \times 0.7 = 0.49$$

From Eq. (8.45), the angle at mean radius is given by

$$\cot \beta_3 = \frac{c_{m3}}{U_2}\frac{r_2}{r_3} = \frac{0.25}{0.49} = 0.5102$$

hence, $\beta_3 = 62.97°$,

$$\cot \beta_{3s} = \frac{c_{m3}}{U_2}\frac{r_2}{r_{3s}}\frac{0.25}{0.7} = 0.3571$$

hence, $\beta_{3s} = 70.35°$, and, therefore,

$$\frac{w_{3s}}{w_2} = \frac{w_{3s}}{w_3}\frac{w_3}{w_2} = \frac{\sec \beta_{3s}}{\sec \beta_3} \times 2 = \frac{0.4544}{0.3363} \times 2 = 2.702$$

The relative velocity ratio will increase progressively from the hub to the shroud.

EXAMPLE 8.5

Using the data and results given in Examples 8.3 and 8.4 together with the additional information that the static pressure at rotor exit is 100 kPa and the nozzle enthalpy loss coefficient, $\zeta_N = 0.06$, determine

a. the diameter of the rotor and its speed of rotation; and
b. the vane width to diameter ratio, b_2/D_2 at rotor inlet.

Solution

a. The rate of mass flow is given by

$$\dot{m} = \rho_3 c_{m3} A_3 = \left(\frac{p_3}{RT_3}\right)\left(\frac{c_{m3}}{U_2}\right)U_2 \pi \left(\frac{r_{3s}}{r_2}\right)^2 (1 - v^2) r_2^2.$$

From Eq. (8.25), $T_{03} = T_{01}(1 - S) = 1050 \times 0.8 = 840$ K,

$$T_3 = T_{03} - c_{m3}^2/(2C_p) = T_{03} - \left(\frac{c_{m3}}{U_2}\right)^2 \frac{U_2^2}{2C_p} = 840 - 0.25^2 \times 5.38.1^2/(2 \times 1150.2)$$

Hence, $T_3 = 832.1$ K.
Substituting values into this mass flow equation,

$$1 = [10^5/(287 \times 832.1)] \times 0.25 \times 538.1 \times 0.7^2 \times \pi \times (1 - 0.4^2) r_2^2$$

therefore,

$$r_2^2 = 0.01373 \text{ and } r_2 = 0.1172\ m,$$
$$D_2 = 0.2343 \text{ m}$$
$$\Omega = U_2/r_2 = 4591.3 \text{ rad}/s \ \ (43,843 \text{ rev/min}).$$

b. The rate of mass flow equation is now written as

$$\dot{m} = \rho_2 c_{m2} A_2, \quad \text{where } A_2 = 2\pi r_2 b_2 = 4\pi r_2^2 (b_2/D_2)$$

Solving for the absolute velocity at rotor inlet and its components,

$$c_{\theta 2} = SC_p T_{01}/U_2 = 0.2 \times 1150.2 \times 1050/538.1 = 448.9 \text{ m/s}$$

$$c_{m2} = c_{\theta 2}/\tan \alpha_2 = 448.9/3.3163 = 135.4 \text{ m/s}$$

$$c_2 = c_{\theta 2}/\sin \alpha_2 = 448.9/0.9574 = 468.8 \text{ m/s}$$

To obtain a value for the static density, ρ_2, we need to determine T_2 and p_2:

$$T_2 = T_{02} - c_2^2/(2C_p) = 1050 - 468.8^2/(2 \times 1150.2) = 954.5 \, K$$

$$h_{02} - h_2 = \frac{1}{2} c_2^2 \text{ and as } \zeta_N = \frac{h_2 - h_{2s}}{(1/2)c_2^2}, h_{01} - h_{2s} = \frac{1}{2} c_2^2 (1 + \zeta_N)$$

so

$$\frac{T_{02} - T_{2s}}{T_{02}} = \frac{c_2^2 (1 + \zeta_N)}{2C_p T_{02}} = \frac{468.8^2 \times 1.06}{2 \times 1150.2 \times 1050} = 0.096447$$

$$\frac{T_{2s}}{T_{01}} = \left(\frac{p_2}{T_{01}}\right)^{(\gamma-1)/\gamma} = 1 - 0.09645 = 0.90355$$

Therefore,

$$\frac{p_2}{p_{01}} = \left(\frac{T_{2s}}{T_{01}}\right)^{\gamma/(\gamma-1)} = 0.90355^4 = 0.66652$$

$$p_2 = 3.109 \times 10^5 \times 0.66652 = 2.0722 \times 10^5 \text{ Pa}$$

$$\frac{b_2}{D_2} = \frac{1}{4\pi}\left(\frac{RT_2}{p_2}\right)\left(\frac{\dot{m}}{c_{m2} r_2^2}\right) = \frac{1}{4 \times \pi}\left(\frac{287 \times 954.5}{2.0722 \times 10^5}\right)\frac{1}{135.4 \times 0.01373} = 0.0566$$

EXAMPLE 8.6

For the IFR turbine described in Example 8.3 and using the data and results in Examples 8.4 and 8.5, deduce a value for the rotor enthalpy loss coefficient, ζ_R, at the optimum efficiency flow condition.

Solution

From Eq. (8.10), solving for ζ_R,

$$\zeta_R = \left[(1-\eta_{ts})c_0^2 - c_3^2 - \zeta N c_2^2\right]/w_3^2$$

We need to find values for c_0, c_3, w_3, and c_2.
From the data,

$$c_3 = c_{m3} = 0.25 \times 538.1 = 134.5 \text{ m/s}$$
$$w_3 = 2w_2 = 2c_{m2}/\cos\beta_2 = 2 \times 135.4/\cos 33.560 = 324.97 \text{ m/s}$$
$$\frac{1}{2}c_0^2 = \Delta W/\eta_{ts} = 230 \times 10^3/0.81 = 283.95 \times 10^3$$
$$c_2 = 468.8 \text{ m/s}$$

Therefore,

$$\zeta_R = (2 \times 283.95 \times 10^3 \times 0.19 - 134.5^2 - 0.06 \times 468.8^2)/324.97^2$$
$$= 76,624/105,605 = 0.7256$$

8.11 Significance and application of specific speed

The concept of specific speed, Ω_s, has already been discussed in Chapter 2 and some applications of it have been made already. Specific speed is extensively used to describe turbomachinery operating requirements in terms of shaft speed, volume flow rate, and ideal specific work (alternatively, power developed is used instead of specific work). Originally, specific speed was applied almost exclusively to *incompressible* flow machines as a tool in the selection of the optimum type and size of unit. Its application to units handling *compressible* fluids was somewhat inhibited, due, it would appear, to the fact that volume flow rate changes through the machine, which raised the awkward question of which flow rate should be used in the specific speed definition. According to Balje (1981), the significant volume flow rate that should be used for turbines is that in the rotor exit, Q_3. This has now been widely adopted by many authorities.

Wood (1963) found it useful to factorize the basic definition of the specific speed equation, Eq. (2.14a), in terms of the geometry and flow conditions within the radial-inflow turbine. Adopting the nondimensional form of specific speed, to avoid ambiguities,

$$\Omega_s = \frac{\Omega Q_3^{1/2}}{\Delta h_{0s}^{3/4}} \tag{8.46}$$

where Ω is in rad/s, Q_3 is in m^3/s, and the isentropic total-to-total enthalpy drop Δh_{0s} (from turbine inlet to exhaust) is in joules per kilogram (i.e., square meters per second squared).

For the 90° IFR turbine, writing $U_2 = 0.5\Omega D_2$ and $\Delta h_{0s} = (1/2)c_0^2$, Eq. (8.46) can be factorized as follows:

$$\Omega_s = \frac{Q_3^{1/2}}{((1/2)c_0^2)^{3/4}}\left(\frac{2U_2}{D_2}\right)\left(\frac{2U_2}{\Omega D_2}\right)^{1/2} = \left(2\sqrt{2}\right)^{3/2}\left(\frac{U_2}{c_0}\right)^{3/2}\left(\frac{Q_3}{\Omega D_2^3}\right)^{1/2} \tag{8.47a}$$

For the *ideal* 90° IFR turbine and with $c_{\theta 2} = U_2$, it was shown earlier that the blade speed to spouting velocity ratio, $U_2/c_0 = \sqrt{2} = 0.707$. Substituting this value into Eq. (8.47a),

$$\Omega_s = 8\left(\frac{Q_3}{\Omega D_2^3}\right)^{1/2} \tag{8.47b}$$

that is, specific speed is directly proportional to the square root of the volumetric flow coefficient.

To obtain some physical significance from Eqs (8.46) and (8.47b), define a *rotor disc area* $A_d = \pi D_2^2/4$ and assume a uniform axial rotor exit velocity c_3 so that $Q_3 = A_3 c_3$, as

$$\Omega = 2U_2/D_2 = \frac{2c_0\sqrt{2}}{D_2}$$

$$\frac{Q_3}{\Omega D_2^3} = \frac{A_3 c_3 D_2}{2\sqrt{2}c_0 D_2^3} = \frac{A_3}{A_d}\frac{c_3}{c_0}\frac{\pi}{8\sqrt{2}}$$

Hence,

$$\Omega_s = 2.11\left(\frac{c_3}{c_0}\right)^{1/2}\left(\frac{A_3}{A_d}\right)^{1/2} \text{(rad)} \tag{8.47c}$$

In an early study of IFR turbine design for maximum efficiency, Rohlik (1968) specified that the ratio of the rotor shroud diameter to rotor inlet diameter should be limited to a maximum value of 0.7 to avoid excessive shroud curvature and that the exit hub−shroud tip ratio was limited to a minimum of 0.4 to avoid excess hub blade blockage and loss. Using this as data, an upper limit for A_3/A_d can be found,

$$\frac{A_3}{A_d} = \left(\frac{D_{3s}}{D_2}\right)^2\left[1 - \left(\frac{D_{3h}}{D_{3s}}\right)^2\right] = 0.7^2 \times (1 - 0.16) = 0.41$$

Figure 8.10 shows the relationship between Ω_s, the exhaust energy factor $(c_3/c_0)^2$, and the area ratio A_3/A_d based upon Eq. (8.47c). According to Wood (1963), the limits for the exhaust energy factor in gas turbine practice are $0.04 < (c_3/c_0)^2 < 0.30$, the lower value being apparently a flow stability limit.

The numerical value of specific speed provides a general index of flow capacity relative to work output. Low values of Ω_s are associated with relatively small flow passage areas and high values with relatively large flow passage areas. Specific speed has also been widely used as a general indication of achievable efficiency. Figure 8.11 presents a broad correlation of maximum efficiencies for hydraulic and compressible fluid turbines as functions of specific speed. These efficiencies apply to favorable design conditions with high values of flow Reynolds number, efficient diffusers, and low leakage losses at the blade tips. It is seen that over a limited range of specific speed the best radial-flow turbines match the best axial-flow turbine efficiency, but from $\Omega_s = 0.03-10$ no other form of turbine handling compressible fluids can exceed the peak performance capability of the axial turbine.

Over the fairly limited range of specific speed $(0.3 < \Omega_s < 1.0)$ that the IFR turbine can produce a high efficiency, it is difficult to find a decisive performance advantage in favor of either the

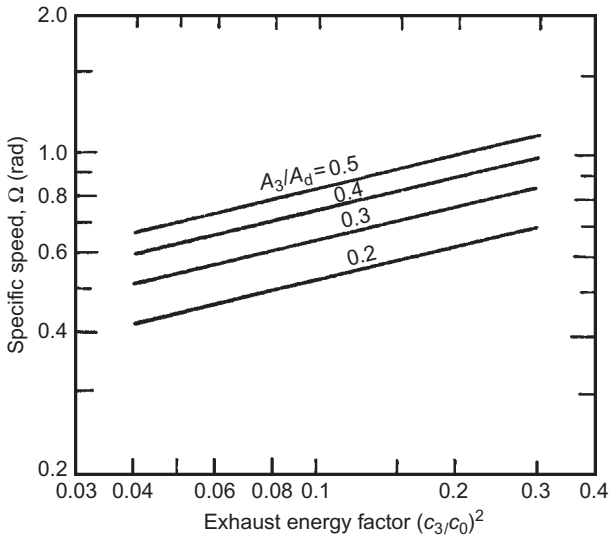

FIGURE 8.10

Specific speed function for a 90° IFR turbine.

(*Adapted from Wood, 1963*)

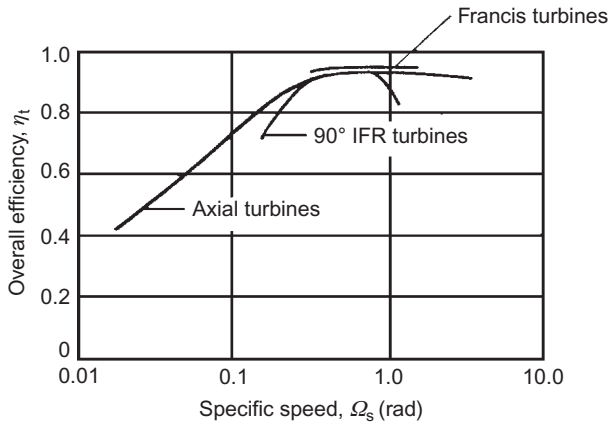

FIGURE 8.11

Specific speed–efficiency characteristics for various turbines.

(*Adapted from Wood, 1963*)

axial-flow turbine or the radial-flow turbine. New methods of fabrication enable the blades of small axial-flow turbines to be cast integrally with the rotor so that both types of turbine can operate at about the same blade tip speed. Wood (1963) compared the relative merits of axial and radial gas

turbines at some length. In general, although weight, bulk, and diameter are greater for radial than axial turbines, the differences are not so large and mechanical design compatibility can reverse the difference in a complete gas turbine power plant. The NASA nuclear Brayton cycle space power studies were all made with 90° IFR turbines rather than with axial-flow turbines.

The design problems of a small axial-flow turbine were discussed by Dunham and Panton (1973), who studied the cold performance measurements made on a single-shaft turbine of 13 cm diameter, about the same size as the IFR turbines tested by NASA. Tests had been performed with four rotors to try to determine the effects of aspect ratio, trailing edge thickness, Reynolds number, and tip clearance. One turbine build achieved a total-to-total efficiency of 90%, about equal to that of the best IFR turbine. However, because of the much higher outlet velocity, the total-to-static efficiency of the axial turbine gave a less satisfactory value (84%) than the IFR type which could be decisive in some applications. They also confirmed that the axial turbine tip clearance was comparatively large, losing 2% efficiency for every 1% increase in clearance. The tests illustrated one major design problem of a small axial turbine that was the extreme thinness of the blade trailing edges needed to achieve the efficiencies stated.

8.12 Optimum design selection of 90° IFR turbines

Rohlik (1968) has examined analytically the performance of 90° IFR turbines to determine *optimum* design geometry for various applications as characterized by specific speed. His procedure, which extends an earlier treatment of Wood (1963), was used to determine the design point losses and corresponding efficiencies for various combinations of nozzle exit flow angle, α_2, rotor diameter ratio, D_2/D_3, and rotor-blade entry height to exit diameter ratio, b_2/D_3. The losses taken into account in the calculations are those associated with

1. nozzle blade row boundary layers;
2. rotor passage boundary layers;
3. rotor-blade tip clearance;
4. disc windage (on the back surface of the rotor);
5. kinetic energy loss at exit.

A mean flow path analysis was used and the passage losses were based upon the data of Stewart et al. (1960). The main constraints in the analysis were

1. $w_3/w_2 = 2.0$;
2. $c_{\theta 3} = 0$;
3. $\beta_2 = \beta_{2,\text{opt}}$, i.e., zero incidence;
4. $r_{3s}/r_2 = 0.7$;
5. $r_{3h}/r_{3s} = 0.4$.

Figure 8.12 shows the variation in total-to-static efficiency with specific speed (Ω_s) for a selection of nozzle exit flow angles, α_2. For each value of α_2 a hatched area is drawn, inside of which the various diameter ratios are varied. The envelope of maximum η_{ts} is bounded by the constraints $D_{3h}/D_{3s} = 0.4$ in all cases and $D_{3s}/D_2 = 0.7$ for $\Omega_s \geq 0.58$ in these hatched regions. This envelope is the *optimum*

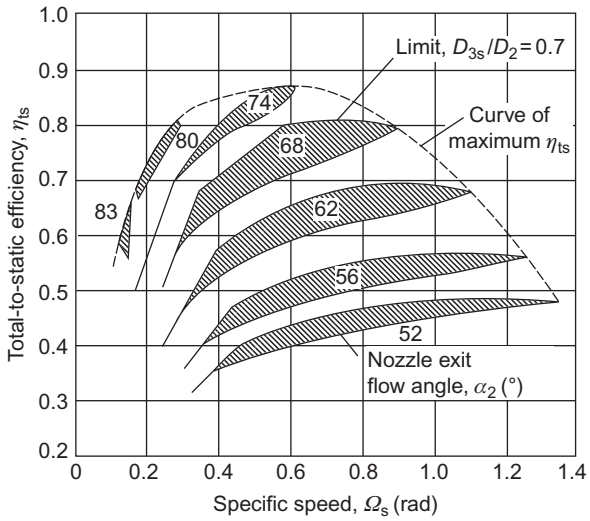

FIGURE 8.12

Calculated performance of 90° IFR turbine.

(*Adapted from Rohlik, 1968*)

geometry curve and has a peak η_{ts} of 0.87 at $\Omega_s = 0.58$ rad. An interesting comparison is made by Rohlik with the experimental results obtained by Kofskey and Wasserbauer (1966) on a single 90° IFR turbine rotor operated with several nozzle blade row configurations. The peak value of η_{ts} from this experimental investigation also turned out to be 0.87 at a slightly higher specific speed, $\Omega_s = 0.64$ rad.

The distribution of losses for optimum geometry over the specific speed range is shown in Figure 8.13. The way the loss distributions change is a result of the changing ratio of flow to specific work. At low Ω_s all friction losses are relatively large because of the high ratios of surface area to flow area. At high Ω_s the high velocities at turbine exit cause the kinetic energy leaving loss to predominate.

Figure 8.14 shows several meridional plane sections at three values of specific speed corresponding to the curve of maximum total-to-static efficiency. The ratio of nozzle exit height−rotor diameter, b_2/D_2, is shown in Figure 8.15, the general rise of this ratio with increasing Ω_s reflecting the increase in nozzle flow area[4] accompanying the larger flow rates of higher specific speed. Figure 8.15 also shows the variation of U_2/c_0 with Ω_s along the curve of maximum total-to-static efficiency.

8.13 Clearance and windage losses

A clearance gap must exist between the rotor vanes and the shroud. Because of the pressure difference between the pressure and suction surfaces of a vane, a leakage flow occurs through the gap

[4]The ratio b_2/D_2 is also affected by the pressure ratio but this has not been shown.

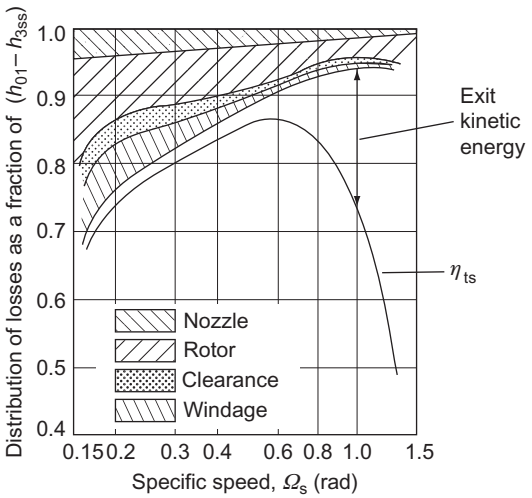

FIGURE 8.13

Distribution of losses along envelope of maximum total-to-static efficiency.

(*Adapted from Rohlik, 1968*)

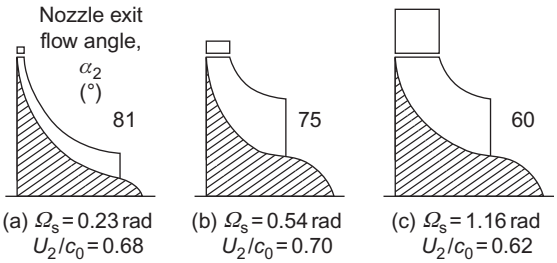

FIGURE 8.14

Sections of radial turbines of maximum static efficiency.

(*Adapted from Rohlik, 1968*)

introducing a loss in efficiency of the turbine. The minimum clearance is usually a compromise between manufacturing difficulty and aerodynamic requirements. Often, the minimum clearance is determined by the differential expansion and cooling of components under *transient* operating conditions that can compromise the steady state operating condition. According to Rohlik (1968), the loss in specific work as a result of gap leakage can be determined with the simple proportionality

$$\Delta h_c = \Delta h_0 (c/b_m) \tag{8.48}$$

where Δh_0 is the turbine specific work uncorrected for clearance or windage losses and c/b_m is the ratio of the gap to average vane height [i.e., $b_m = (1/2)(b_2 + b_3)$]. A constant axial and radial gap,

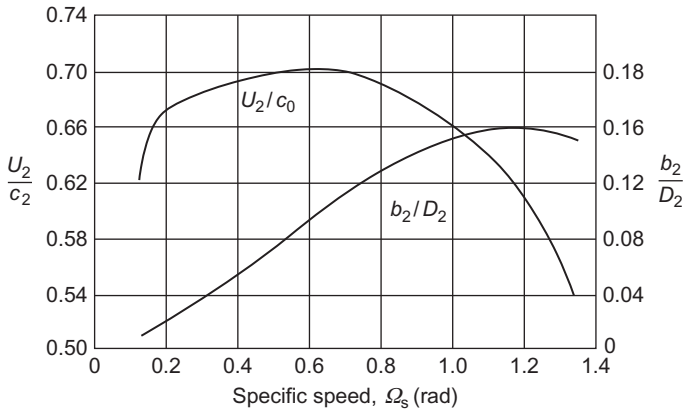

FIGURE 8.15

Variation in blade speed–spouting velocity ratio (U_2/c_0) and nozzle blade height–rotor inlet diameter (b_2/D_2) corresponding to maximum total-to-static efficiency with specific speed.

(*Adapted from Rohlik, 1968*)

$c = 0.25$ mm, was used in the analytical study of Rohlik quoted earlier. According to Rodgers (1969), extensive development on small gas turbines has shown that it is difficult to maintain clearances less than about 0.4 mm. One consequence of this is that as small gas turbines are made progressively smaller the *relative* magnitude of the clearance loss must increase.

The nondimensional power loss due to windage on the back of the rotor has been given by Shepherd (1956) in the form

$$\Delta Pw/(\rho_2 \Omega^3 D_2^2) = \text{constant} \times Re^{-1/5}$$

where Ω is the rotational speed of the rotor and Re is a Reynolds number. Rohlik (1968) used this expression to calculate the loss in specific work due to windage,

$$\Delta h_w = 0.56\ \rho_2 D_2^2 (U_2/100)^3/(\dot{m}\, Re) \tag{8.49}$$

where $\dot{m}$ is the total rate of mass flow entering the turbine and the Reynolds number is defined by $Re = U_2 D_2/\nu_2$, ν_2 being the kinematic viscosity of the gas corresponding to the static temperature T_2 at nozzle exit.

8.14 Cooled 90° IFR turbines

The incentive to use higher temperatures in the basic Brayton gas turbine cycle is well known and arises from a desire to increase cycle efficiency and specific work output. In all gas turbines designed for high efficiency, a compromise is necessary between the turbine inlet temperature desired and the temperature that can be tolerated by the turbine materials used. This problem can be minimized by using an auxiliary supply of cooling air to lower the temperature of the highly

stressed parts of the turbine exposed to the high temperature gas. Following the successful application of blade cooling techniques to axial-flow turbines, methods of cooling small radial gas turbines have been developed.

According to Rodgers (1969), the most practical method of cooling small radial turbines is by film (or veil) cooling (Figure 8.16) where cooling air is impinged on the rotor and vane tips. The main problem with this method of cooling being its relatively low *cooling effectiveness*, defined by

$$\varepsilon = \frac{T_{01} - (T_m + \Delta T_0)}{T_{01} - (T_{0c} + \Delta T_0)} \tag{8.50}$$

where T_m is the rotor metal temperature,

$$\Delta T_0 = \frac{1}{2} U_2^2 / C_p$$

Rodgers refers to tests that indicate the possibility of obtaining $\varepsilon = 0.30$ at the rotor tip section with a cooling flow of approximately 10% of the main gas flow. Since the cool and hot streams rapidly mix, effectiveness decreases with distance from the point of impingement. A model study of the heat transfer aspects of film-cooled radial-flow gas turbines is given by Metzger and Mitchell (1966).

PROBLEMS

1. A small inward radial-flow gas turbine, comprising a ring of nozzle blades, a radial-vaned rotor and an axial diffuser, operates at the nominal design point with a total-to-total efficiency of 0.90. At turbine entry, the stagnation pressure and temperature of the gas are 400 kPa and 1140 K. The flow leaving the turbine is diffused to a pressure of 100 kPa and has negligible final velocity. Given that the flow is just choked at nozzle exit, determine the impeller peripheral speed and the flow outlet angle from the nozzles. For the gas assume $\gamma = 1.333$ and $R = 287$ J/(kg °C).

2. The mass flow rate of gas through the turbine given in Problem 1 is 3.1 kg/s, the ratio of the rotor axial width−rotor tip radius (b_2/r_2) is 0.1, and the nozzle isentropic velocity ratio (ϕ_2) is 0.96. Assuming that the space between nozzle exit and rotor entry is negligible and ignoring the effects of blade blockage, determine

a. the static pressure and static temperature at nozzle exit;

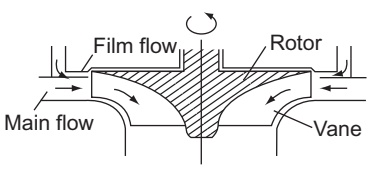

FIGURE 8.16

Cross section of film-cooled radial turbine.

b. the rotor tip diameter and rotational speed;
c. the power transmitted assuming a mechanical efficiency of 93.5%.

3. A radial turbine is proposed as the gas expansion element of a nuclear powered Brayton cycle space power system. The pressure and temperature conditions through the stage at the design point are to be as follows:
upstream of nozzles, $p_{01} = 699$ kPa, $T_{01} = 1145$ K;
nozzle exit, $p_2 = 527.2$ kPa, $T_2 = 1029$ K;
rotor exit, $p_3 = 384.7$ kPa, $T_3 = 914.5$ K; $T_{03} = 924.7$ K.

The ratio of rotor exit mean diameter to rotor inlet tip diameter is chosen as 0.49 and the required rotational speed as 24,000 rev/min. Assuming the relative flow at rotor inlet is radial and the absolute flow at rotor exit is axial, determine
a. the total-to-static efficiency of the turbine;
b. the rotor diameter;
c. the implied enthalpy loss coefficients for the nozzles and rotor row.

The gas employed in this cycle is a mixture of helium and xenon with a molecular weight of 39.94 and a ratio of specific heats of 5/3. The universal gas constant is $R_0 = 8.314$ kJ/(kg-mol K).

4. A film-cooled radial-inflow turbine is to be used in a high-performance open Brayton cycle gas turbine. The rotor is made of a material able to withstand a temperature of 1145 K at a tip speed of 600 m/s for short periods of operation. Cooling air is supplied by the compressor that operates at a stagnation pressure ratio of 4−1, with an isentropic efficiency of 80%, when air is admitted to the compressor at a stagnation temperature of 288 K. Assuming that the effectiveness of the film cooling is 0.30 and the cooling air temperature at turbine entry is the same as that at compressor exit, determine the maximum permissible gas temperature at entry to the turbine. Take $\gamma = 1.4$ for the air. Take $\gamma = 1.333$ for the gas entering the turbine. Assume $R = 287$ J/(kg K) in both cases.

5. The radial-inflow turbine in Problem 3 is designed for a specific speed Ω_s of 0.55 rad. Determine
a. the volume flow rate and the turbine power output;
b. the rotor exit hub and tip diameters;
c. the nozzle exit flow angle and the rotor inlet passage width−diameter ratio, b_2/D_2.

6. An IFR gas turbine with a rotor diameter of 23.76 cm is designed to operate with a gas mass flow of 1.0 kg/s at a rotational speed of 38,140 rev/min. At the design condition, the inlet stagnation pressure and temperature are to be 300 kPa and 727°C. The turbine is to be "cold" tested in a laboratory where an air supply is available only at the stagnation conditions of 200 kPa and 102°C.
a. Assuming dynamically similar conditions between those of the laboratory and the projected design determine, for the "cold" test, the equivalent mass flow rate and the speed of rotation. Assume the gas properties are the same as for air.
b. Using property tables for air, determine the Reynolds numbers for both the hot and cold running conditions. The Reynolds number is defined in this context as

$$Re = \rho_{01}\Omega D^2/\mu_1$$

where ρ_{01} and μ_1 are the stagnation density and viscosity of the air, Ω is the rotational speed (rev/s), and D is the rotor diameter.

7. For the radial-flow turbine described in the previous problem and operating at the prescribed "hot" design point condition, the gas leaves the exducer directly to the atmosphere at a pressure of 100 kPa and without swirl. The absolute flow angle at rotor inlet is 72° to the radial direction. The relative velocity w_3 at the mean radius of the exducer (which is one-half of the rotor inlet radius r_2) is twice the rotor inlet relative velocity w_2. The nozzle enthalpy loss coefficient, $\zeta_N = 0.06$. Assuming the gas has the properties of air with an average value of $\gamma = 1.34$ (this temperature range) and $R = 287$ J/kg K, determine

a. the total-to-static efficiency of the turbine;
b. the static temperature and pressure at the rotor inlet;
c. the axial width of the passage at inlet to the rotor;
d. the absolute velocity of the flow at exit from the exducer;
e. the rotor enthalpy loss coefficient;
f. the radii of the exducer exit given that the radius ratio at that location is 0.4.

8. One of the early space power systems built and tested for NASA was based on the Brayton cycle and incorporated an IFR turbine as the gas expander. Some of the data available concerning the turbine are as follows:
total-to-total pressure ratio (turbine inlet to turbine exit), $p_{01}/p_{03} = 1.560$;
total-to-static pressure ratio, $p_{01}/p_3 = 1.613$;
total temperature at turbine entry, $T_{01} = 1083$ K;
total pressure at inlet to turbine, $T_{01} = 91$ kPa;
shaft power output (measured on a dynamometer), $P_{net} = 22.03$ kW;
bearing and seal friction torque (a separate test), $\tau_f = 0.0794$ Nm;
rotor diameter, $D_2 = 15.29$ cm;
absolute flow angle at rotor inlet, $\alpha_2 = 72°$;
absolute flow angle at rotor exit, $\alpha_3 = 0°$;
the hub-to-shroud radius ratio at rotor exit, $r_{3h/r3s} = 0.35$;
ratio of blade speed to jet speed, $\nu = U_2/c_0 = 0.6958$, c_0 based on total-to-static pressure ratio.

For reasons of crew safety, an inert gas argon ($R = 208.2$ J/(kg K), ratio of specific heats, $\gamma = 1.667$) was used in the cycle. The turbine design scheme was based on the concept of optimum efficiency. Determine, for the design point

a. the rotor vane tip speed;
b. the static pressure and temperature at rotor exit;
c. the gas exit velocity and mass flow rate;
d. the shroud radius at rotor exit;
e. the relative flow angle at rotor inlet;
f. the specific speed.

Note: The volume flow rate to be used in the definition of the specific speed is based on the rotor exit conditions.

9. What is meant by the term *nominal design* in connection with a radial-flow gas turbine rotor? Sketch the velocity diagrams for a 90° IFR turbine operating at the nominal design point. At entry to a 90° IFR turbine, the gas leaves the nozzle vanes at an absolute flow angle, α_2, of 73°. The rotor-blade tip speed is 460 m/s and the relative velocity of the gas at rotor exit is twice the relative velocity at rotor inlet. The rotor mean exit diameter is 45% of the rotor inlet diameter. Determine

a. the exit velocity from the rotor;

b. the static temperature difference, $T_2 - T_3$, of the flow between nozzle exit and rotor exit. Assume the turbine operates at the nominal design condition and that $C_p = 1.33$ kJ/kg K.

10. The initial design of an IFR turbine is to be based upon Whitfield's procedure for optimum efficiency. The turbine is to be supplied with 2.2 kg/s of air, a stagnation pressure of 250 kPa, a stagnation temperature of 800°C, and have an output power of 450 kW. At turbine exit the static pressure is 105 kPA. Assuming for air that $\gamma = 1.33$ and $R = 287$ J/kg K, determine the value of Whitfield's power ratio, S, and the total-to-static efficiency of the turbine.

11. By considering the theoretical details of Whitfield's design problem for obtaining the optimum efficiency of an IFR turbine show that the correct choice for the relationship of the rotor inlet flow angles is obtained from the following equation:

$$\tan \alpha_2 = \frac{\sin \beta_2}{1 - \cos \beta_2}$$

and that a minimum stagnation Mach number at rotor inlet is obtained from

$$M_{02}^2 = \left(\frac{S}{\gamma - 1}\right) \frac{2 \cos \beta_2}{1 + \cos \beta_2}$$

12. An IFR turbine rotor is designed with 13 vanes and is expected to produce 400 kW from a supply of gas heated to a stagnation temperature of 1100 K at a flow rate of 1.2 kg/s. Using Whitfield's optimum efficiency design method and assuming $\eta_{ts} = 0.85$, determine

a. the overall stagnation pressure to static pressure ratio and

b. the rotor tip speed and inlet Mach number, M_2, of the flow.

Assume $C_p = 1.187$ kJ/kg K and $\gamma = 1.33$.

13. Another IFR turbine is to be built to develop 250 kW of shaft power from a gas flow of 1.1 kg/s. The inlet stagnation temperature, T_{01}, is 1050 K, the number of rotor blades is 13, and the outlet static pressure, p_3, is 102 kPa. At rotor exit the area ratio, $\nu = r_{3h}/r_{3s} = 0.4$, and the velocity ratio, $c_{m3}/U_2 = 0.25$. The shroud-to-rotor inlet radius, r_{3s}/r_2, is 0.4. Using the optimum efficiency design method, determine

a. the power ratio, S, and the relative and absolute flow angles at rotor inlet;

b. the rotor-blade tip speed;

c. the static temperature at rotor exit;

d. the rotor speed of rotation and rotor diameter.

Evaluate the specific speed, Ω_s. How does this value compare with the optimum value of specific speed determined in Figure 8.15?

14. Using the same input design data for the IFR turbine given in Problem 5 and given that the total-to-static efficiency is 0.8, determine
- **a.** the stagnation pressure of the gas at inlet and
- **b.** the total-to-total efficiency of the turbine.

15. An IFR turbine is required with a power output of 300 kW driven by a supply of gas at a stagnation pressure of 222 kPa, at a stagnation temperature of 1100 K, and at a flow rate of 1.5 kg/s. The turbine selected by the engineer has 13 vanes and preliminary tests indicate it should have a total-to-static efficiency of 0.86. Based upon the optimum efficiency design method, sketch the appropriate velocity diagrams for the turbine and determine
- **a.** the absolute and relative flow angles at rotor inlet;
- **b.** the overall pressure ratio;
- **c.** the rotor tip speed.

16. For the IFR turbine of the previous problem, the following additional information is made available:

$$c_{m3}/U_2\ 0.25, w_3/w_2 = 2.0, r_{3s}/r_2 = 0.7 \text{ and } v = 0.4.$$

Again, based upon the optimum efficiency design criterion, determine
- **a.** the rotor diameter and speed of rotation;
- **b.** the enthalpy loss coefficients of the rotor and the nozzles given that the nozzle loss coefficient is (estimated) to be one quarter of the rotor loss coefficient.

References

Abidat, M., Chen, H., Baines, N. C., & Firth, M. R. (1992). Design of a highly loaded mixed flow turbine. *Journal of Power and Energy, Proceedings of the Institution Mechanical Engineers*, *206*, 95−107.

Artt, D. W., & Spence, S. W. T. (1998). A loss analysis based on experimental data for a 99 mm radial inflow nozzled turbine with different stator throat areas. Proceedings of the Institution of Mechanical Engineers, London, *Part A*, *212*, 27−42.

Anon. (1971). Conceptual design study of a nuclear Brayton turboalternator compressor. Contractor Report, General Electric Company. *NASA CR-113925*.

Balje, O. E. (1981). *Turbomachines—A guide to design, selection and theory* New York: Wiley.

Benson, R. S. (1970). A review of methods for assessing loss coefficients in radial gas turbines. *International Journal of Mechanical Science*, *12*.

Benson, R. S., Cartwright, W. G., & Das, S. K. (1968). An investigation of the losses in the rotor of a radial flow gas turbine at zero incidence under conditions of steady flow. Proceedings of the Institution Mechanical Engineers London, *Part 3H*, *182*.

Dunham, J., & Panton, J. (1973). Experiments on the design of a small axial turbine. *Conference Publication 3, Institution of Mechanical Engineers*.

Glassman, A. J. (1976). Computer program for design and analysis of radial inflow turbines. *NASA TN 8164*.

Hiett, G. F., & Johnston, I. H. (1964). Experiments concerning the aerodynamic performance of inward radial flow turbines. Proceedings of the Institution Mechanical Engineers, *Part 3I*, *178*.

Huntsman, I., Hodson, H. P., & Hill, S. H. (1992). The design and testing of a radial flow turbine for aerodynamic research. *Journal of Turbomachinery, Transactions of the American Society of Mechanical Engineers*, *114*, 4.

Jamieson, A. W. H. (1955). The radial turbine. In: H. Roxbee-Cox (Ed.), *Gas turbine principles and practice*. London: Newnes.

Kearton, W. J. (1951). *Steam turbine theory and practice* (6th ed.). New York: Pitman.

Kofskey, M. G., & Wasserbauer, C. A. (1966). Experimental performance evaluation of a radial inflow turbine over a range of specific speeds. *NASA TN D-3742*.

Meitner, P. L., & Glassman, J. W. (1983). Computer code for off-design performance analysis of radial-inflow turbines with rotor blade sweep. *NASA TP 2199*, AVRADCOM Technical Report 83-C-4.

Metzger, D. E., & Mitchell, J. W. (1966). Heat transfer from a shrouded rotating disc with film cooling. *Journal of Heat Transfer, Transactions of the American Society of Mechanical Engineers*, *88*.

Nusbaum, W. J., & Kofskey, M. G. (1969). Cold performance evaluation of 4.97 inch radial-inflow turbine designed for single-shaft Brayton cycle space-power system. *NASA TN D-5090*.

Rodgers, C. (1969). A cycle analysis technique for small gas turbines.Technical advances in gas turbine design. *Proceedings of the Institution Mechanical Engineers London, Part 3N*, *183*.

Rodgers, C., & Geiser, R. (1987). Performance of a high-efficiency radial/axial turbine. *Journal of Turbomachinery, Transactions of the American Society of Mechanical Engineers*, *109*.

Rogers, G. F. C., & Mayhew, Y. R. (1995). *Thermodynamic and transport properties of fluids* (5th ed.Malden, MA: Blackwell.

Rohlik, H. E. (1968). Analytical determination of radial-inflow turbine design geometry for maximum efficiency. *NASA TN D-4384*.

Rohlik, H. E. (1975). Radial-inflow turbines. In: A. J. Glassman (Ed.), *Turbine design and applications*. *NASA SP 290*, Vol. 3.

Shepherd, D. G. (1956). *Principles of turbomachinery* New York: Macmillan.

Simpson, A. T., Spence, S. W. T., & Watterson, J. K. (2013). Numerical and experimental study of the performance effects of varying vaneless space and vane solidity in radial turbine stators. *Journal of Turbomachinery, Transactions of the American Society of Mechanical Engineers*, *135*.

Spence, S. W. T., & Artt, D. W. (1997). Experimental performance evaluation of a 99 mm radial inflow inflow-turbine nozzled turbine with different stator throat areas. *Proceedings of the Institution of Mechanical Engineers, Part A, Journal of Power and Energy*, *211*(A6), 477−488.

Stanitz, J. D. (1952). Some theoretical aerodynamic investigations of impellers in radial and mixed flow centrifugal compressors. *Transactions of the American Society of Mechanical Engineers*, *74*, 4.

Stewart, W. L., Witney, W. J., & Wong, R. Y. (1960). A study of boundary layer characteristics of turbomachine blade rows and their relation to overall blade loss. *Journal of Basic Engineering, Transactions of the American Society of Mechanical Engineers*, *82*.

Whitfield, A. (1990). The preliminary design of radial inflow turbines. *Journal of Turbomachinery, Transactions of the American Society of Mechanical Engineers*, *112*, 50−57.

Whitfield, A., & Baines, N. C. (1990). Computation of internal flows. In: A. Whitfield, & N. C. Baines (Eds.), *Design of radial turbomachines*. New York: Longman.

Wilson, D. G., & Jansen, W. (1965). The aerodynamic and thermodynamic design of cryogenic radial-inflow expanders. *ASME Paper 65-WA/PID-6*, pp. 1−13.

Wood, H. J. (1963). Current technology of radial-inflow turbines for compressible fluids. *Journal of Engineering and Power, Transactions of the American Society of Mechanical Engineers*, *85*.

CHAPTER

Hydraulic Turbines

9

Hear ye not the hum of mighty workings?
John Keats, *Sonnet No. 14*

The power of water has changed more in this world than emperors or kings.
Leonardo da Vinci

9.1 Introduction

To put this chapter into perspective, some idea of the scale of hydropower development in the world might be useful before delving into the intricacies of hydraulic turbines. A very detailed and authoritative account of virtually every aspect of hydropower is given by Raabe (1985), and this brief introduction serves merely to illustrate a few aspects of a very extensive subject.

Hydropower is the longest established source for the generation of electric power, which, starting in 1880 as a small DC generating plant in Wisconsin, United States, developed into an industrial size plant following the demonstration of the economic transmission of high-voltage AC at the Frankfurt Exhibition in 1891. Hydropower was expected to have a worldwide yearly growth rate of about 5% (i.e., doubling in size every 15 years), but this rate has now proved to be too optimistic. In 1980, the worldwide installed generating capacity was 460 GW according to the United Nations, but in 2007 the figure was just exceeding 700 GW. This works out at roughly 1.6% annual yearly growth. The smaller growth rate must, primarily, be due to the high costs involved in the civil engineering work, the cost of the power and related electrical plant, and to some extent the human cost due to massive population displacements with necessary new building.

According to the Environmental Resources Group Ltd., in 2007 hydropower constituted about 21% of the world's electrical generating capacity. The theoretical potential of hydropower is believed to be 2800 GW. The main areas with potential for growth are China, Latin America, and Africa.

Table 9.1 is an extract of data quoted by Raabe (1985) of the distribution of harnessed and harnessable potential of some of the countries with the biggest usable potential of hydropower. From this list, it is seen that the People's Republic of China (PRC), the country with the largest harnessable potential in the world had, in 1974, harnessed only 4.22% of this. However, the Three Gorges Dam project on the Yangtze River is now the biggest hydropower plant in the world. It contains 32 Francis turbines, each capable of generating 700 MW, the total generating capacity being 22,500 MW.

Fluid Mechanics and Thermodynamics of Turbomachinery. DOI: http://dx.doi.org/10.1016/B978-0-12-415954-9.00009-7

Table 9.1 Distribution of Harnessed and Harnessable Potential of Hydroelectric Power

Country	Usable Potential (TWh)	Amount of Potential Used (TWh)	Percentage of Usable Potential
1 China (PRC)	1320	55.6	4.22
2 Former USSR	1095	180	16.45
3 USA	701.5	277.7	39.6
4 Zaire	660	4.3	0.65
5 Canada	535.2	251	46.9
6 Brazil	519.3	126.9	24.45
7 Malaysia	320	1.25	0.39
8 Columbia	300	13.8	4.6
9 India	280	46.87	16.7
Sum 1–9	5731	907.4	15.83
Other countries	4071	843	20.7
Total	9802.4	1750.5	17.8

(*From Raabe, 1985*)

Tidal power

This relatively new and very promising technology, in which tidal stream generators are used to generate power, is still under active development. Very large amounts of energy can be obtained by this means and, unlike wind power and solar power, it is available at known times each day. The most efficient type of generator is still to be determined. The world's first commercial tidal stream generator, *SeaGen*, was installed in 2008 at Strangford Lough, Northern Ireland. The prototype version comprises two 600 kW axial-flow turbines, 16 m in diameter. Further details on this tidal turbine are given toward the end of this chapter.

Wave power

Several energy conversion systems have now been developed for obtaining electrical power from sea waves. One notable example is the *Wells turbine*, which uses an oscillating water column generated by the waves to drive this special type of axial-flow turbine. Several of these turbines have been installed (in Scotland and India) and details of their rather special fluid mechanical design are given in this chapter.

Features of hydropower plants

The initial cost of hydropower plants may be much higher than those of thermal power plants. However, the present value of total costs (which includes those of fuel) is, in general, lower in hydropower plants. Raabe (1985) listed the various advantages and disadvantages of hydropower plants and a brief summary of these is given in Table 9.2.

Table 9.2 Features of Hydroelectric Power Plants

Advantages	Disadvantages
Technology is relatively simple and proven. High efficiency. Long useful life. No thermal phenomena apart from those in bearings and generator.	Number of favorable sites limited and available only in some countries. Problems with cavitation and water hammer.
Small operating, maintenance, and replacement costs.	High initial cost especially for low head plants compared with thermal power plants.
No air pollution. No thermal pollution of water.	Inundation of the reservoirs and displacement of the population. Loss of arable land. Facilitates sedimentation upstream and erosion downstream of a barrage.

(*From Raabe, 1985*)

9.2 Hydraulic turbines

Early history of hydraulic turbines

The hydraulic turbine has a long period of development, its oldest and simplest form being the waterwheel, first used in ancient Greece and subsequently adopted throughout medieval Europe for the grinding of grain, etc. A French engineer, Benoit Fourneyron, developed the first commercially successful hydraulic turbine (circa 1830). Later Fourneyron built turbines for industrial purposes that achieved a speed of 2300 rpm, developing about 50 kW at an efficiency of over 80%.

The American engineer James B. Francis designed the first *radial-inflow* hydraulic turbine that became widely used, gave excellent results, and was highly regarded. In its original form, it was used for heads of between 10 and 100 m. A simplified form of this turbine is shown in Figure 1.1(d). It will be observed that the flow path followed is essentially from a radial direction to an axial direction.

The Pelton wheel turbine, named after its American inventor, Lester A. Pelton, was brought into use in the second half of the nineteenth century. This is an impulse turbine in which water is piped at high pressure to a nozzle where it expands completely to atmospheric pressure. The emerging jet impacts onto the blades (or buckets) of the turbine, which produce the required torque and power output. A simplified diagram of a Pelton wheel turbine is shown in Figure 1.1(f). The head of water used originally was between about 90 and 900 m (modern versions operate up to heads of nearly 2000 m).

The increasing need for more power during the early years of the twentieth century also led to the invention of a turbine suitable for small heads of water, i.e., 3−9 m, in river locations where a dam could be built. In 1913, Viktor Kaplan revealed his idea of the propeller (or Kaplan) turbine, see Figure 1.1(e), which acts like a ship's propeller but in reverse. At a later date, Kaplan improved his turbine by means of swiveling blades, which improved the efficiency of the turbine appropriate to the available flow rate and head.

Flow regimes for maximum efficiency

The efficiency of a hydraulic turbine can be defined as the work developed by the rotor in unit time divided by the difference in hydraulic energy between inlet and outlet of the turbine in unit

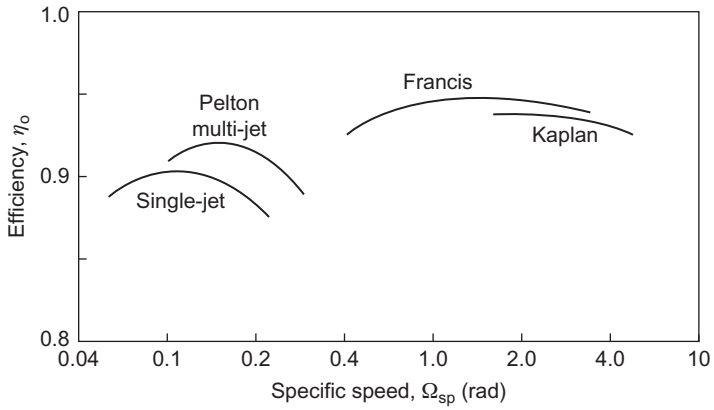

FIGURE 9.1

Typical design point efficiencies of Pelton, Francis, and Kaplan turbines.

Table 9.3 Operating Ranges of Hydraulic Turbines

	Pelton Turbine	Francis Turbine	Kaplan Turbine
Specific speed (rad)	0.05–0.4	0.4–2.2	1.8–5.0
Head (m)	100–1770	20–900	6–70
Maximum power (MW)	500	800	300
Optimum efficiency (%)	90	95	94
Regulation method	Needle valve and deflector plate	Stagger angle of guide vanes	Stagger angle of rotor blades

Note: *Values shown in the table are only a rough guide and are subject to change.*

time. The efficiencies of the three principal types of hydraulic turbine just mentioned are shown in Figure 9.1 as functions of the power specific speed, Ω_{sp}. From Eq. (2.15b), this is

$$\Omega_{sp} = \frac{\Omega\sqrt{P/\rho}}{(gH_E)^{5/4}} \tag{9.1}$$

where P is the power delivered by the shaft, ρ is the density of water, H_E is the effective head at turbine entry, and Ω is the rotational speed in radians per second. It is remarkable that the efficiency of the multistage Pelton turbine has now reached 92.5% at $\Omega_{sp} \cong 0.2$ and that the Francis turbine can achieve an efficiency of 95–96% at an $\Omega_{sp} \cong 1.0–2.0$.

The Ω_{sp} regimes of these turbine types are of considerable importance to the designer as they indicate the most suitable choice of machine for an application. In general, low specific speed machines correspond to low-volume flow rates and high heads, whereas high specific speed machines correspond to high volume flow rates and low heads. Table 9.3 summarizes the normal

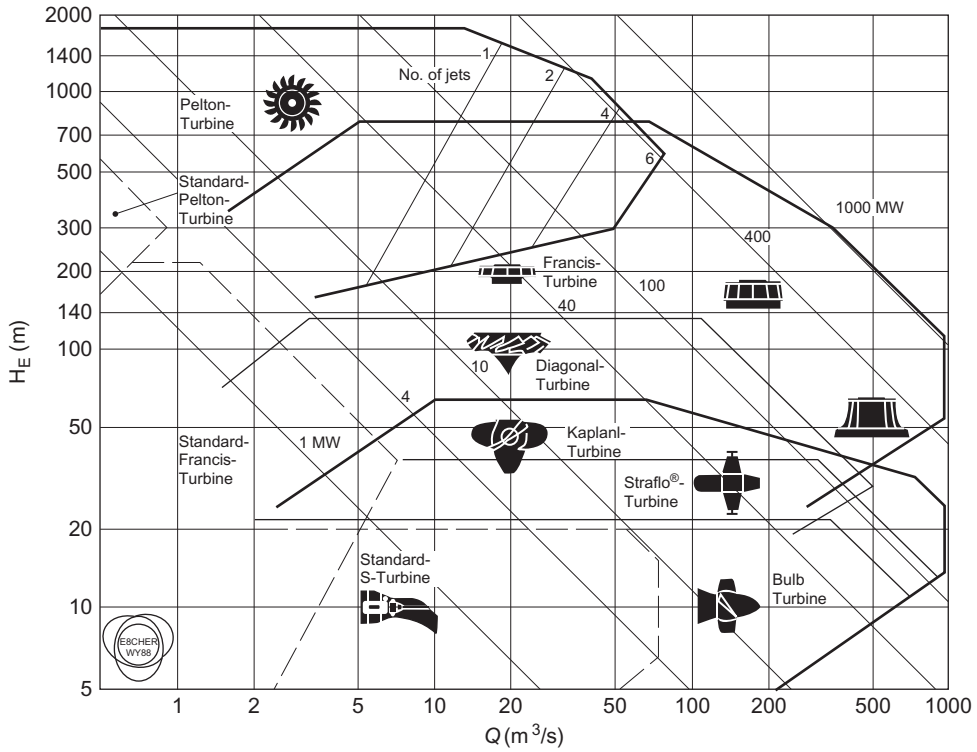

FIGURE 9.2

Application ranges for various types of hydraulic turbomachines, as a plot of Q versus H with lines of constant power determined assuming $\eta_0 = 0.8$.

(*Courtesy Sulzer Hydro Ltd., Zurich*)

operating ranges for the specific speed, the effective head, the maximum power, and best efficiency for each type of turbine.

According to the experience of Sulzer Hydro Ltd., of Zurich, the application ranges of the various types of turbines and turbine pumps (including some not mentioned here) are plotted in Figure 9.2 on a $\ln Q$ versus $\ln H_E$ diagram and reflect the present state of the art of hydraulic turbomachinery design. Also in Figure 9.2, lines of constant power output are conveniently shown and have been calculated as the product $\eta\rho g Q H_E$, where the efficiency η is given the value of 0.8 throughout the chart.

Capacity of large Francis turbines

The size and capacity of some of the recently built Francis turbines is a source of wonder, and they seem so enormous! The size and weight of the runners cause special problems getting them to the site, especially when rivers have to be crossed and the bridges are inadequate.

The largest installation in North America (circa 1998) is at La Grande on James Bay in eastern Canada where 22 units each rated at 333 MW have a total capacity of 7326 MW. A close competitor with the Three Gorges project is the Itaipu hydroelectric plant on the Paraná river (between Brazil and Paraguay), which has a capacity of 12,600 MW in full operation using 18 Francis turbines each sized at 700 MW.

The efficiency of large Francis turbines has gradually risen over the years and now is about 95%. There seems to be little prospect of much further improvement in efficiency as computable values of losses due to skin friction, tip leakage, and exit kinetic energy from the diffuser are reckoned to account for the remaining 5%. Raabe (1985) has given much attention to the statistics of the world's biggest turbines. It would appear at the present time that the largest hydroturbines in the world are the three vertical-shaft Francis turbines installed at Grand Coulee III on the Columbia River, Washington, United States. Each of these leviathans has been uprated to 800 MW, with the delivery (or effective) head, $H_E = 87$ m, $\Omega = 85.7$ rpm, the runner having a diameter of $D = 9.26$ m and weighing 450 ton. Using this data in Eq. (9.1), it is easy to calculate that the power specific speed $\Omega_{sp} = 1.74$ rad.

9.3 The Pelton turbine

This is the only hydraulic turbine of the impulse type now in common use. It is an efficient machine and it is particularly suited to high head applications. The rotor consists of a circular disk with a number of blades (usually called *buckets*) spaced around the periphery. One or more nozzles are mounted in such a way that each nozzle directs its jet along a tangent to the circle through the centers of the buckets. A "splitter" or ridge splits the oncoming jet into two equal streams so that, after flowing round the inner surface of the bucket, the two streams depart from the bucket in a direction nearly opposite to that of the incoming jet.

Figure 9.3 shows the runner of a Pelton turbine and Figure 9.4 shows a six-jet vertical axis Pelton turbine. Considering one jet impinging on a bucket, the appropriate velocity diagram is shown in Figure 9.5. The jet velocity at entry is c_1 and the blade speed is U so that the relative velocity at entry is $w_1 = c_1 - U$. At exit from the bucket, one half of the jet stream flows as shown in the velocity diagram, leaving with a relative velocity w_2 and at an angle β_2 to the original direction of flow. From the velocity diagram, the much smaller absolute exit velocity c_2 can be determined.[1]

From Euler's turbine equation, Eq. (1.18c), the specific work done by the water is

$$\Delta W = U_1 c_{\theta 1} - U_2 c_{\theta 2}$$

For the Pelton turbine, $U_1 = U_2 = U$, $c_{\theta 1} = c_1$, so we get

$$\Delta W = U[U + w_1 - (U + w_2 \cos \beta_2)] = U(w_1 - w_2 \cos \beta_2)$$

in which the value of $c_{\theta 2} < 0$, as defined in Figure 9.5, i.e., $c_{\theta 2} = U + w_2 \cos \beta_2$.

[1]Design practicalities of Pelton turbines suggested by Franzini and Finnemore (1997). For good efficiency, the bucket width should be three to four times the size of the jet diameter. The wheel diameter, also referred to as the pitch diameter, is usually 15−20 times the size of the jet diameter. It is the pitch circle to which the centerline of the jet is tangent. The maximum efficiency of the turbine would be obtained if each bucket completely reversed the relative velocity of the impinging jet. However, this is not possible because the water must be deflected to either side to avoid interfering with the following bucket. As a result, the bucket angle β_2 is usually about 165°.

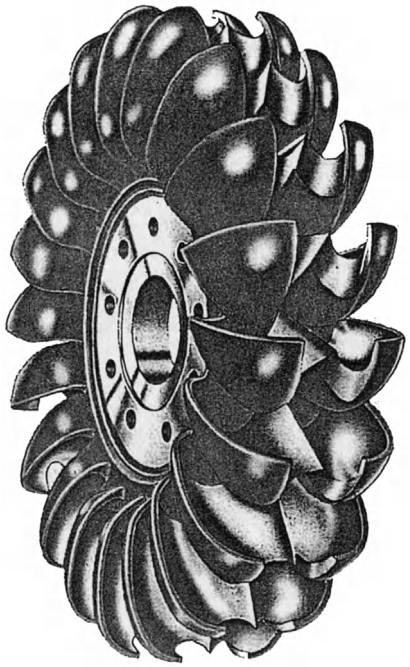

FIGURE 9.3

Pelton turbine runner.

(*Courtesy Sulzer Hydro Ltd., Zurich*)

The effect of friction on the fluid flowing inside the bucket will cause the relative velocity at outlet to be less than the value at inlet. Writing $w_2 = kw_1$, where $0.8 \leq k \leq 0.9$.

$$\Delta W = Uw_1(1 - k\cos\beta_2) = U(c_1 - U)(1 - k\cos\beta_2) \tag{9.2}$$

An efficiency η_R for the runner can be defined as the specific work done ΔW divided by the incoming kinetic energy, i.e.,

$$\eta_R = \Delta W / \left(\frac{1}{2}c_1^2\right) = 2U(c_1 - U)(1 - k\cos\beta_2)/c_1^2 \tag{9.3}$$

Therefore,

$$\eta_R = 2v(1 - v)(1 - k\cos\beta_2) \tag{9.4}$$

where the blade speed to jet speed ratio, $v = U/c_1$.

To find the optimum efficiency, differentiate Eq. (9.4) with respect to the blade speed ratio, i.e.,

$$\frac{d\eta_R}{dv} = 2\frac{d}{dv}(v - v^2)(1 - k\cos\beta_2) = 2(1 - 2v)(1 - k\cos\beta_2) = 0$$

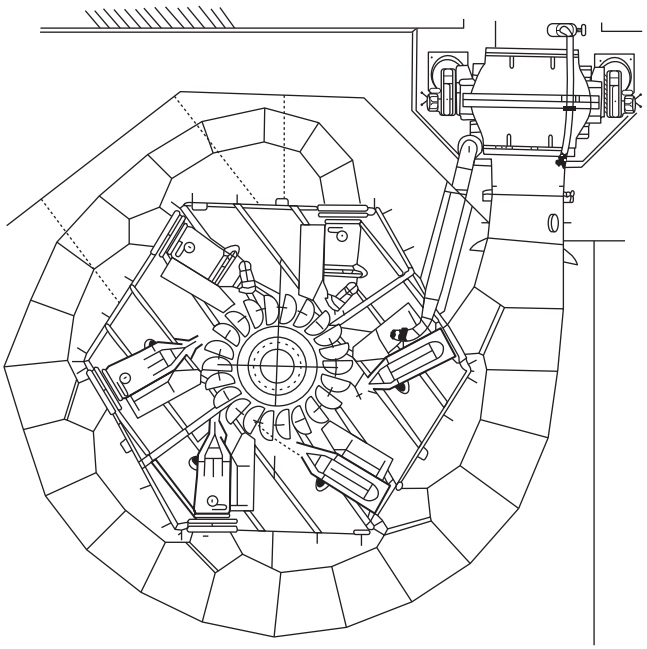

FIGURE 9.4

Six-jet vertical-shaft Pelton turbine, horizontal section; power rating 174.4 MW, runner diameter 4.1 m, speed 300 rpm, head 587 m.

(*Courtesy Sulzer Hydro Ltd., Zurich)*

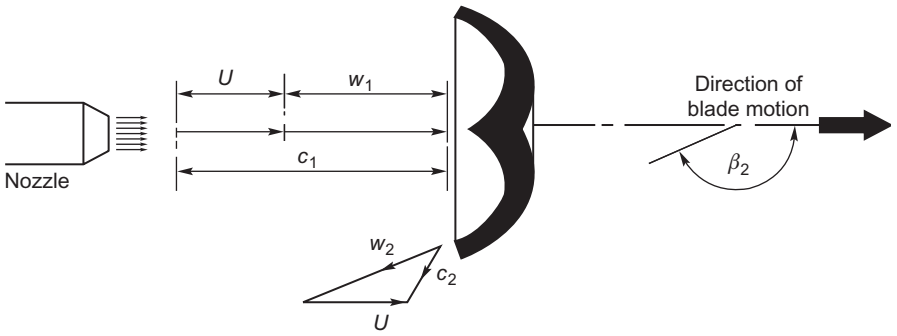

FIGURE 9.5

The Pelton wheel showing the jet impinging onto a bucket and the relative and absolute velocities of the flow (only one half of the emergent velocity diagram is shown).

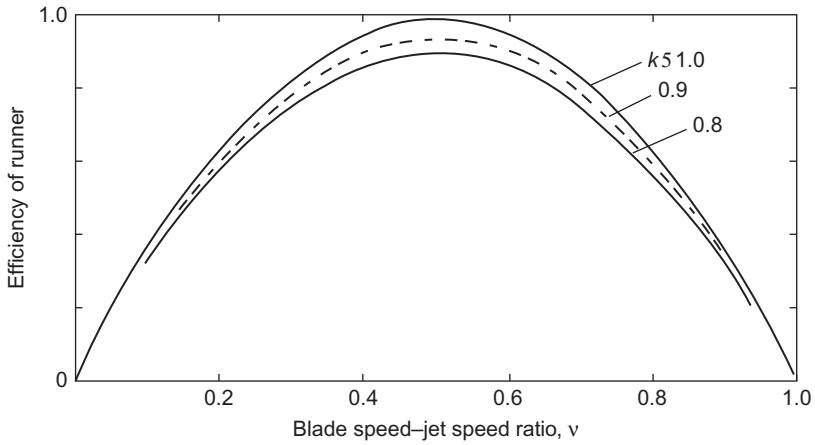

FIGURE 9.6

Theoretical variation of runner efficiency for a Pelton wheel with a blade speed–jet speed ratio for several values of friction factor k.

Therefore, the maximum efficiency of the runner occurs when $\nu = 0.5$, i.e., $U = c_1/2$. Hence,

$$\eta_{\text{R max}} = (1 - k\cos\beta_2) \tag{9.5}$$

Figure 9.6 shows the theoretical variation of the runner efficiency with blade speed ratio for assumed values of $k = 0.8$, 0.9, and 1.0 with $\beta_2 = 165°$. In practice, the value of k is usually found to be between 0.8 and 0.9.

A simple hydroelectric scheme

The layout of a Pelton turbine hydroelectric scheme is shown in Figure 9.7. The water is delivered from a constant level reservoir at an elevation z_R (above sea level) and flows via a pressure tunnel to the penstock head, down the penstock to the turbine nozzles emerging onto the buckets as a high-speed jet. To reduce the deleterious effects of large pressure surges, a *surge tank* is connected to the flow close to the penstock head, which acts so as to damp out transients. The elevation of the nozzles is z_N and the gross head, $H_G = z_R - z_N$.

Controlling the speed of the Pelton turbine

The Pelton turbine is usually directly coupled to an electrical generator that must run at synchronous speed. With large size hydroelectric schemes supplying electricity to a national grid, it is essential for both the voltage and the frequency to closely match the grid values. To ensure that the turbine runs at constant speed despite any load changes that may occur, the rate of flow Q is changed. A spear (or needle) valve, Figure 9.8(a), whose position is controlled by means of a servomechanism, is moved axially within the nozzle to alter the diameter of the jet. This works well for

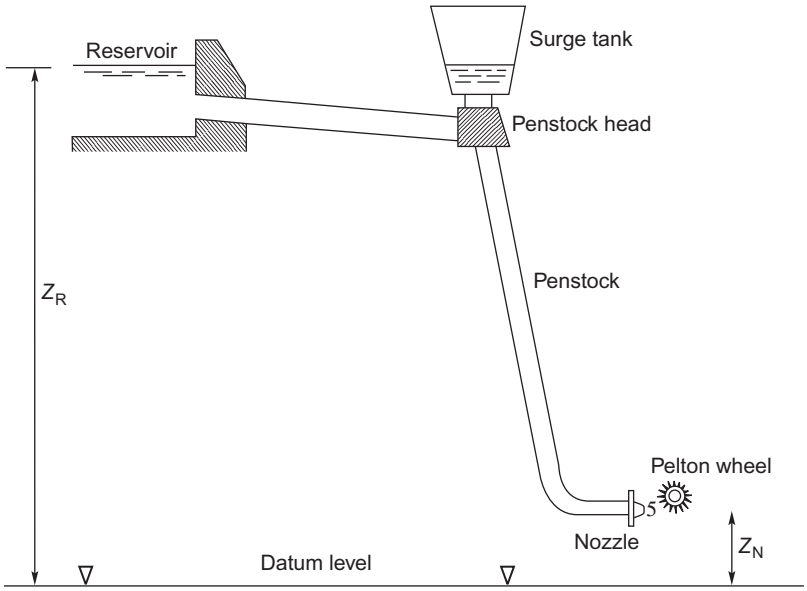

FIGURE 9.7

Pelton turbine hydroelectric scheme.

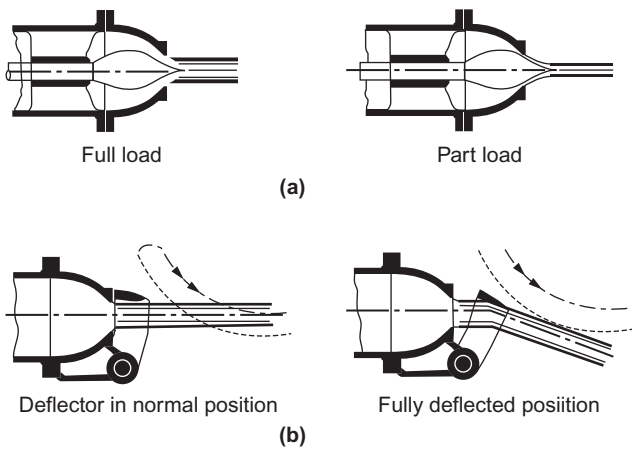

FIGURE 9.8

Methods of regulating the speed of a Pelton turbine: (a) with a spear (or needle) valve, and (b) with a deflector plate.

very gradual changes in load. However, when a sudden loss in load occurs, a more rapid response is needed. This is accomplished by temporarily deflecting the jet with a deflector plate so that some of the water does not reach the buckets, Figure 9.8(b). This acts to prevent over-speeding and allows time for the slower acting spear valve to move to a new position.

It is vital to ensure that the spear valve *does move slowly* as a sudden reduction in the rate of flow could result in serious damage to the system from pressure surges (called *water hammer*). If the spear valve did close quickly, all the kinetic energy of the water in the penstock would be absorbed by the elasticity of the supply pipeline (penstock) and the water, creating very large stresses, which would reach their greatest intensity at the turbine inlet where the pipeline is already heavily stressed. The surge tank, shown in Figure 9.7, has the function of absorbing and dissipating some of the pressure and energy fluctuations created by too rapid a closure of the needle valve.

Sizing the penstock diameter

It is shown in elementary textbooks on fluid mechanics (e.g., Franzini & Finnemore, 1997; White, 2011) that the loss in head with incompressible, steady, turbulent flow in pipes of circular cross-section is given by the Darcy–Weisbach equation (often referred to simply as Darcy's equation):

$$H_{\mathrm{f}} = \frac{flV^2}{2g\mathrm{d}} \tag{9.6}$$

where f is the friction factor, l is the length of the pipe, d is the pipe diameter, and V is the mass average velocity of the flow in the pipe. It is assumed, of course, that the pipe is running full. The value of the friction factor has been determined for various conditions of flow and pipe surface roughness, e, and the results are usually presented in what is called a *Moody diagram*. The penstock (the pipeline bringing the water to the turbine) is long and of large diameter and this can add significantly to the total cost of a hydroelectric power scheme. Using Darcy's equation, Eq. (9.6), it is easy to calculate a suitable pipe diameter for such a scheme if the friction factor is known and an estimate can be made of the allowable head loss. Logically, this head loss would be determined economically on the cost of materials, etc., needed for a large diameter pipe and compared with the value of the useful energy lost from having too small a pipe. A commonly used compromise for the loss in head in the supply pipes is to allow $H_{\mathrm{f}} \leq 0.1H_{\mathrm{G}}$.

A summary of various other factors on which the "economic diameter" of a pipe can be determined is given by Raabe (1985).

From Eq. (9.6), substituting for the velocity, $V = 4Q/(\pi d^2)$, we get

$$H_{\mathrm{f}} = \left(\frac{8fl}{\pi^2 g}\right)\frac{Q^2}{d^5} \tag{9.7}$$

Energy losses in the Pelton turbine

Having accounted for the energy loss due to friction in the penstock, the energy losses in the rest of the hydroelectric scheme must now be considered. The effective head, H_{E} (or delivered head), at entry to the turbine is the gross head minus the friction head loss, H_{f}, i.e.,

$$H_{\mathrm{E}} = H_{\mathrm{G}} - H_{\mathrm{f}} = z_{\mathrm{R}} - z_{\mathrm{N}} - H_{\mathrm{f}}$$

and the spouting (or ideal) velocity, c_o, is

$$c_o = \sqrt{2gH_E}$$

The pipeline friction loss H_f is regarded as an external loss and is not usually included in the losses attributed to the turbine itself. The performance and efficiency of the turbine are, in effect, measured against the total head, H_E, as shown in the following.

The main energy losses of the turbine occur in

i. the nozzles due to fluid friction;
ii. converting the kinetic energy of the jet into mechanical energy of the runner;
iii. external effects (bearing friction and windage).

Each of these energy losses are now considered in turn.

For *item* (i), let the loss in head in the nozzles be ΔH_N. Thus, the available head is

$$H_E = \Delta H_N = c_1^2/(2g) \tag{9.8}$$

where c_1 is the actual velocity of the jet at nozzle exit. The nozzle efficiency is defined by

$$\eta_N = \frac{\text{energy at nozzle exit}}{\text{energy at nozzle inlet}} = \frac{c_1^2}{2gH_E} \tag{9.9a}$$

An often-used alternative to η_N is the nozzle velocity coefficient K_N defined by

$$K_N = \frac{\text{actual velocity at nozzle exit}}{\text{spouting velocity}} = \frac{c_1}{c_0}$$

i.e.,

$$\eta_N = K_N^2 = \frac{c_1^2}{c_0^2} \tag{9.9b}$$

Optimum jet diameter

For any given penstock, there will be a unique jet diameter that will provide a maximum power to the jet. The power available in the jet is given by

$$P = \dot{m}c_1^2/(2g) = \rho Q c_1^2/(2g)$$

where c_1 is the velocity of the jet.

To give further weight to the above statement, consider allowing the flow rate Q to slowly increase, initially allowing the power to increase. As a result of this, the frictional losses must increase and the jet velocity will be reduced. It will be apparent from the above equation that there will be some flow rate at which the power must be at a maximum. This is illustrated in Example 9.1.

EXAMPLE 9.1

Water is supplied to the nozzle of a Pelton turbine through a single penstock 0.3 m internal diameter and 300 m long from a reservoir whose surface level is 180 m above the centerline of the nozzle. The friction factor for the penstock is $f = 0.04$. The head loss of the flow in the nozzle is $0.04c_1^2/(2g)$. Determine the jet diameter that will give the maximum power in the jet.

The energy equation for the pipe flow can be written as

$$H_E - \frac{flc_p^2}{2gd} - \frac{0.04c_1^2}{2g} = \frac{c_1^2}{2g}$$

where H_E is the effective head and c_p is the flow velocity in the pipeline.

Substituting values, we get

$$180 - \frac{0.04 \times 300 \times c_p^2}{2 \times 9.81 \times 0.3} = \frac{1.04 \times c_1^2}{2 \times 9.81} \quad \therefore 180 - 2.039 \times c_p^2 = 0.053 \times c_1^2 \tag{i}$$

From the continuity equation,

$$\therefore d^2 c_1 = d_p^2 c_p \text{ so that } c_p = c_1 \left(\frac{d}{d_p}\right)^2 \tag{ii}$$

Substituting Eq. (ii) into Eq. (i) and simplifying, we get

$$180 = c_1^2(0.053 + 251.7d^4) \tag{iii}$$

Choose a range of values of d, calculate c_1 using Eq. (iii), then Q and P as shown in the table below:

d (m)	$0.053 + 251.7d^4$	c_1 (m/s)	Q (m^3/s)	P (kW)
0.06	0.06015	54.7	0.1547	23.59
0.08	0.06331	53.41	0.2685	39.04
0.10	0.07817	47.99	0.3769	44.24
0.12	0.1052	41.36	0.4677	40.78
0.14	0.1497	34.68	0.5339	32.73
0.16	0.2180	28.73	0.5777	24.30

The maximum power for the jet is 44.24 kW at $d = 0.10$ m.

Of course it is possible to obtain a solution for the jet diameter and maximum power by setting up an expression for the power and differentiating with respect to the diameter. The advantage of the tabular method used here is that of being able to observe the variations of the various factors with the change in diameter of the jet.

As an exercise, it would be useful to determine the nozzle efficiency, η_N, as given in Eq. (9.9a). We must first calculate $H_E = H_g - H_f$, where

$$H_f = \left(\frac{8fl}{\pi^2 g}\right)\frac{Q^2}{d^5} = 57.94 \text{ m}$$

$$\therefore H_E = 180 - 57.94 = 122.06 \text{ m}$$

$$\therefore \eta_N = \frac{c_1^2}{2gH_E} = \frac{47.99^2}{2 \times 9.81 \times 122.06} = 0.9617$$

For *item* (ii), the loss in energy is already described in Eq. (9.2) and the runner efficiency, η_R, by Eqs (9.3) and (9.4). The turbine hydraulic efficiency, η_h, is defined as the specific work done by the rotor, ΔW, divided by the specific energy available at entry to the nozzle, gH_E, i.e.,

$$\eta_h = \frac{\Delta W}{gH_E} = \left(\frac{\Delta W}{(1/2)c_1^2}\right)\left(\frac{(1/2)c_1^2}{gH_E}\right) = \eta_R \eta_N \tag{9.10}$$

after using Eq. (9.9a).

For *item* (iii), the external losses are responsible for the energy deficit between the runner and the shaft. A good estimate of these losses can be made using the following simple flow model where the specific energy loss is assumed to be proportional to the square of the blade speed, i.e.,

$$\text{external loss/unit mass flow} = KU^2$$

where K is a dimensionless constant of proportionality. Thus, the *shaft* work done/unit mass flow is

$$\Delta W - KU^2$$

Therefore, the overall efficiency of the turbine, η_o, including these external losses is

$$\eta_o = (\Delta W - KU^2)/(gH_e)$$

i.e., the shaft work delivered by the turbine/specific energy available at nozzle entry, which

$$= \eta_R \eta_N - 2K\left(\frac{U}{c_1}\right)^2\left(\frac{c_1^2}{2gH_E}\right)$$

Using the definitions of the blade speed–jet speed ratio, $\nu = U/c_1$, and the nozzle efficiency, $\eta_N = c_1^2/c_2^2$,

$$\eta_0 = \eta_N(\eta_R - 2K\nu^2) = \eta_m \eta_R \eta_N \tag{9.11}$$

where the mechanical efficiency, $\eta_m = 1 -$ external losses$/gH_E$, i.e.,

$$\eta_m = 1 - 2K\nu^2/\eta_R \tag{9.12}$$

The variation of the overall efficiency as given by Eq. (9.11) is shown in Figure 9.9 as a function of ν for several values of the windage coefficient K. It will be noted that peak efficiency reduces as the value of K is increased and that it occurs at lower values of ν than the optimum for the runner. This evaluation of the theoretical performance of a Pelton turbine gives a possible

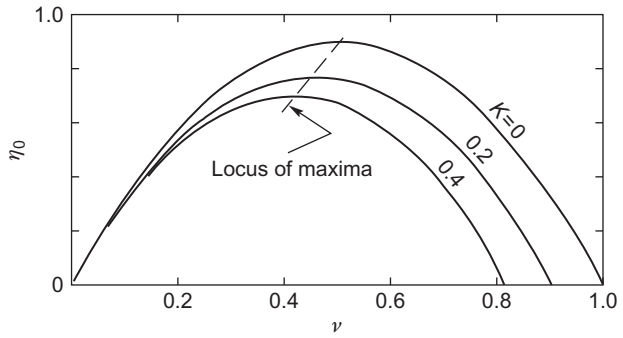

FIGURE 9.9

Variation of overall efficiency of a Pelton turbine with speed ratio for several values of windage coefficient, *K*.

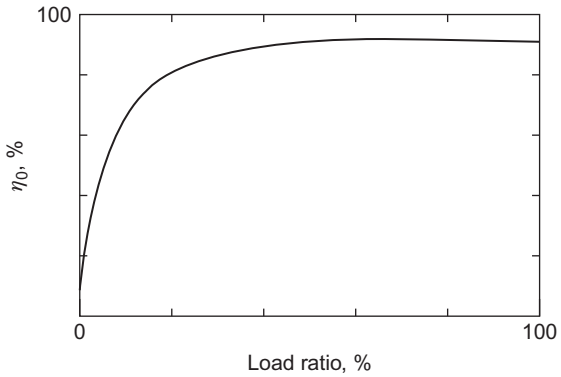

FIGURE 9.10

Pelton turbine overall efficiency variation with load under constant head and constant speed conditions.

reason for the often puzzling result found when experiments are evaluated and that always yield a peak efficiency for values of $\nu < 0.5$.

By differentiating Eq. (9.11), it can be shown that the optimum value of ν occurs when

$$\nu_{\text{opt}} = \frac{A}{2(A + K)}$$

where $A = 1 - k \cos \beta_2$.

Exercise

Let $k = 0.9$, $\beta_2 = 165°$, and $K = 0.1$. Hence, $A = 1.869$ and $\nu = 0.475$.

Typical performance of a Pelton turbine *under conditions of constant head and speed* is shown in Figure 9.10 in the form of the variation of overall efficiency against load ratio. As a result of a

change in the load, the output of the turbine must then be regulated by a change in the setting of the needle valve to keep the turbine speed constant. The observed almost constant value of the efficiency over most of the load range is the result of the *hydraulic losses* reducing in proportion to the power output. However, as the load ratio is reduced to even lower values, the windage and bearing friction losses, which have not diminished, assume a relatively greater importance and the overall efficiency rapidly diminishes toward zero.

EXAMPLE 9.2

A Pelton turbine is driven by two jets, generating 1.4 MW at 375 rpm. The effective head at the nozzles is 200 m of water and the nozzle velocity coefficient, $K_N = 0.98$. The axes of the jets are tangent to a circle 1.5 m in diameter. The relative velocity of the flow across the buckets is decreased by 15% and the water is deflected through an angle of 165°.

Neglecting bearing and windage losses, determine

a. the runner efficiency;
b. the diameter of each jet;
c. the power specific speed.

Solution

a. The blade speed is

$$U = \Omega r = (375 \times \pi/30) \times 1.5/2 = 39.27 \times 1.5/2 = 29.45\ m/s$$

The jet speed is

$$c_1 = K_N\sqrt{2gH_E} = 0.98 \times \sqrt{2 \times 9.81 \times 200} = 61.39\ m/s$$

Therefore, $v = U/c_1 = 0.4798$.
The efficiency of the runner is obtained from Eq. (9.4):

$$\eta_R = 2 \times 0.4798 \times (1 - 0.4798)(1 - 0.85 \times \cos 165^\circ) = 0.9090$$

b. The "theoretical" power is $P_{th} = P/\eta_R = 1.4/0.909 = 1.54$ MW, where $P_{th} = \rho g Q H_E$. Therefore,

$$Q = P_{th}/(\rho g H_E) = 1.54 \times 10^6/(9810 \times 200) = 0.785\ \text{m}^3/\text{s}$$

Each jet must have a flow area of

$$A_j = \frac{Q}{2c_1} = 0.785/(2 \times 61.39) = 0.00639\ \text{m}^2$$

Therefore, $d_j = 0.0902$ m.

Note: The wheel diameter is 16.63 times the jet diameter which is in the acceptable range given earlier, i.e., 15−20 times.

c. Substituting into Eq. (9.1), the power specific speed is

$$\Omega_{sp} = 39.27 \times (1.4 \times 10^3)^{1/2}/(9.81 \times 200)^{5/4} = 0.1125$$

Note: In Figure 9.1, the efficiency for a single-jet Pelton turbine would be about 89% when $\Omega_{sp} = 0.1125$. For a multi-jet turbine at the same specific speed, an efficiency of 92% could be attained.

9.4 Reaction turbines

The primary features of the reaction turbine are:

- **i.** only part of the overall pressure drop has occurred up to turbine entry, the remaining pressure drop takes place in the turbine itself;
- **ii.** the flow completely fills all of the passages in the runner, unlike the Pelton turbine where, for each jet, only one or two of the buckets at a time are in contact with the water;
- **iii.** pivotable guide vanes are used to control and direct the flow;
- **iv.** a draft tube is normally added on to the turbine exit; this is considered as an integral part of the turbine.

The pressure of the water gradually decreases as it flows through the runner and the reaction from this pressure change earns this type of turbine its appellation.

9.5 The Francis turbine

The majority of Francis turbines are arranged so that the axis is vertical (some smaller machines can have horizontal axes). Figure 9.11 illustrates a section through a vertical-shaft Francis turbine with a runner diameter of 5 m, a head of 110 m, and a power rating of nearly 200 MW. Water enters via a spiral casing called a *volute* or *scroll* that surrounds the runner. The area of cross-section of the volute decreases along the flow path in such a way that the flow velocity remains constant. From the volute, the flow enters a ring of stationary guide vanes, which direct it onto the runner at the most appropriate angle.

In flowing through the runner, the angular momentum of the water is reduced and work is supplied to the turbine shaft. At the design condition, the absolute flow leaves the runner axially (although a small amount of swirl may be countenanced) into the *draft tube* and, finally, the flow enters the *tailrace*. It is essential that the exit of the draft tube is submerged below the level of the water in the tailrace in order that the turbine remains full of water. The draft tube also acts as a diffuser; by careful design, it can ensure maximum recovery of energy through the turbine by significantly reducing the exit kinetic energy.

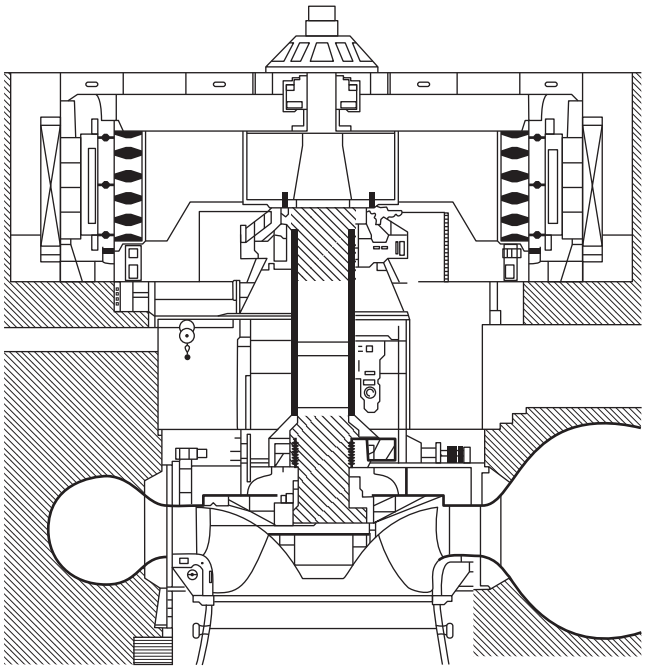

FIGURE 9.11

Vertical-shaft Francis turbine: runner diameter 5 m, head 110 m, power 200 MW.

(*Courtesy Sulzer Hydro Ltd., Zurich*)

Figure 9.12 shows the runner of a small Francis turbine and Figure 9.13 is a sectional view of the turbine together with the velocity triangles at inlet to and exit from the runner at mid-blade height. At inlet to the guide vanes, the flow is in the radial/tangential plane, the absolute velocity is c_1, and the absolute flow angle is α_1. Thus,

$$\alpha_1 = \tan^{-1}(c_{\theta 1}/c_{r1}) \tag{9.13}$$

The flow is turned to angle α_2 and velocity c_2, the absolute condition of the flow at entry to the runner. By vector subtraction, the relative velocity at entry to the runner is found, i.e., $\boldsymbol{w}_2 = \boldsymbol{c}_2 - \boldsymbol{U}_2$. The relative flow angle β_2 at inlet to the runner is defined as

$$\beta_2 = \tan^{-1}[(c_{\theta 2} - U_2)/c_{r2}] \tag{9.14}$$

Further inspection of the velocity diagrams in Figure 9.13 reveals that the direction of the velocity vectors approaching both guide vanes and runner blades are tangential to the camber lines at the leading edge of each row. This is the ideal flow condition for "shockless" low loss entry, although an incidence of a few degrees may be beneficial to output without a significant extra loss penalty. At vane outlet some deviation from the blade outlet angle is to be expected (see Chapter 3). For

FIGURE 9.12

Runner of a small Francis turbine.

(*Permission Granted to Copy Under the Terms of the GNU Free Documentation License*)

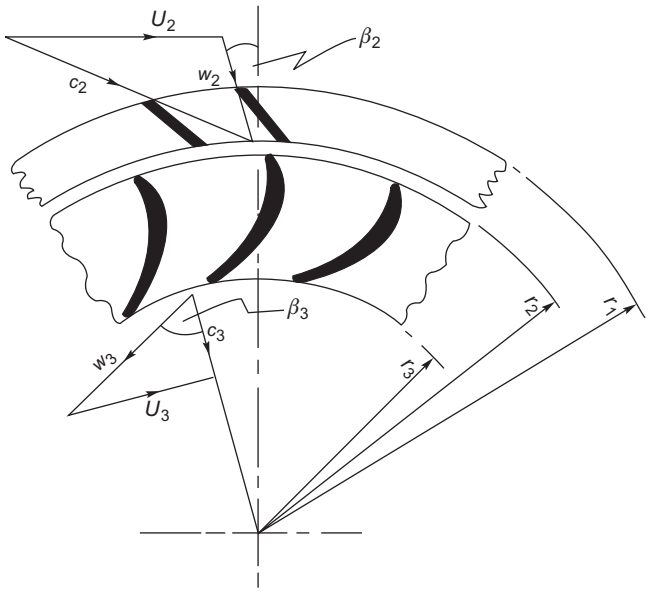

FIGURE 9.13

Sectional sketch of blading for a Francis turbine showing velocity diagrams at runner inlet and exit.

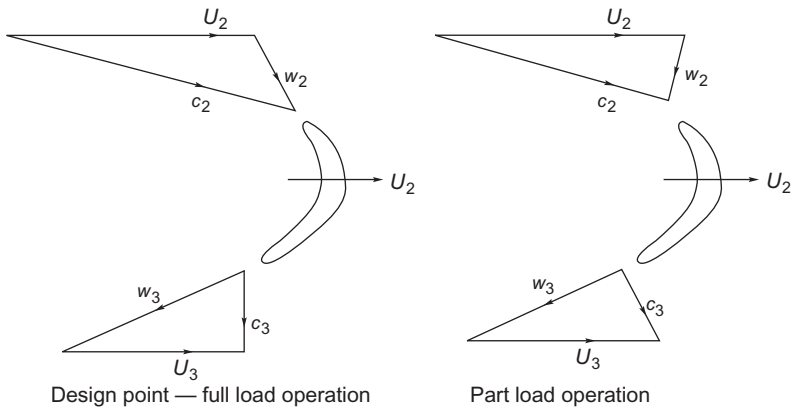

FIGURE 9.14

Comparison of velocity triangles for a Francis turbine at full load and at part load operation.

these reasons, in all problems concerning the direction of flow, it is clear that the angle of the fluid flow is important and not the vane angle as is often quoted in other texts.

At outlet from the runner, the flow plane is simplified as though it were actually in the radial/tangential plane. This simplification will not affect the subsequent analysis of the flow, but it must be conceded that some component of velocity in the axial direction does exist at runner outlet.

The water leaves the runner with a relative flow angle β_3 and a relative flow velocity w_3. The absolute velocity at runner exit is found by vector addition, i.e., $\boldsymbol{c}_3 = \boldsymbol{w}_3 + \boldsymbol{U}_3$. The relative flow angle, β_3, at runner exit is given by

$$\beta_3 = \tan^{-1}[(c_{\theta 3} + U_3)/c_{r3}] \tag{9.15}$$

In this equation it is assumed that some residual swirl velocity $c_{\theta 3}$ is present (c_{r3} is the radial velocity at exit from the runner). In most simple analyses of the Francis turbine, it is assumed that there is no exit swirl. Detailed investigations have shown that some extra *counter-swirl* (i.e., acting so as to increase Δc_θ) at the runner exit does increase the amount of work done by the fluid without a significant reduction in turbine efficiency.

When a Francis turbine is required to operate at part load, the power output is reduced by swiveling the guide vanes to restrict the flow, i.e., Q is reduced, while the blade speed is maintained constant. Figure 9.14 compares the velocity triangles at full load and at part load from which it will be seen that the relative flow at runner entry is at a high incidence and at runner exit the absolute flow has a large component of swirl. Both of these flow conditions give rise to high head losses. Figure 9.15 shows the variation of hydraulic efficiency for several types of turbine, including the Francis turbine, over the full load range at constant speed and constant head.

It is of interest to note the effect that swirling flow has on the performance of the following diffuser. The results of an extensive experimental investigation made by McDonald, Fox, and van Dewoestine (1971) showed that swirling inlet flow *does not* affect the performance of conical diffusers, which are well designed and give unseparated or only slightly separated flow when the flow through them is entirely axial. Accordingly, part load operation of the turbine is unlikely to give adverse diffuser performance.

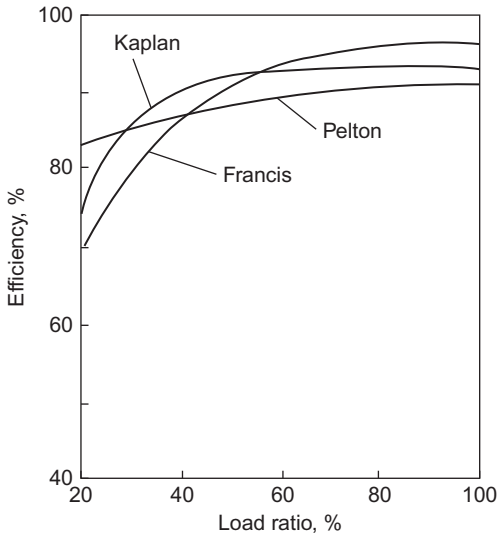

FIGURE 9.15

Variation of hydraulic efficiency for various types of turbine over a range of loading, at constant speed and constant head.

Basic equations

Euler's turbine equation, Eq. (1.18c), in the present notation, is written as

$$\Delta W = U_2 c_{\theta 2} - U_3 c_{\theta 3} \tag{9.16a}$$

If the flow at runner exit is without swirl, then the equation reduces to

$$\Delta W = U_2 c_{\theta 2} \tag{9.16b}$$

The effective head for all reaction turbines, H_E, is the total head available at the turbine inlet *relative to the surface of the tailrace*. At entry to the runner, the energy available is equal to the sum of the kinetic, potential, and pressure energies:

$$g(H_E - \Delta H_N) = \frac{p_2 - p_a}{\rho} + \frac{1}{2}c_2^2 + g z_2 \tag{9.17}$$

where ΔH_N is the loss of head due to friction in the volute and guide vanes and p_2 is the *absolute* static pressure at inlet to the runner.

At runner outlet, the energy in the water is further reduced by the amount of specific work ΔW and by friction work in the runner, $g\Delta H_R$ and this remaining energy equals the sum of the pressure potential and kinetic energies:

$$g(H_E - \Delta H_N - \Delta H_R) - \Delta W = \frac{1}{2}c_3^2 + p_3/\rho - p_a/\rho + g z_3 \tag{9.18}$$

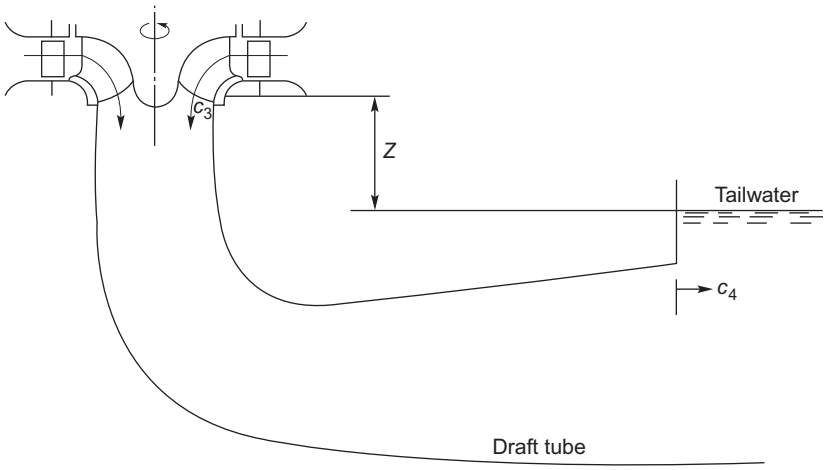

FIGURE 9.16

Location of draft tube in relation to vertical-shaft Francis turbine.

where p_3 is the *absolute* static pressure at runner exit.

By differencing Eqs (9.17) and (9.18), the specific work is obtained:

$$\Delta W = (p_{02} - p_{03})/p - g\Delta H_R + g(z_2 - z_3) \tag{9.19}$$

where p_{02} and p_{03} are the absolute total pressures at runner inlet and exit.

Figure 9.16 shows the draft tube in relation to a vertical-shaft Francis turbine. The most important dimension in this diagram is the vertical distance ($z = z_3$) between the exit plane of the runner and the free surface of the tailrace. The energy equation between the exit of the runner and the tailrace can now be written as

$$p_3/\rho + \frac{1}{2}c_3^2 + gz_3 - g\Delta H_{DT} = \frac{1}{2}c_4^2 + p_a/\rho \tag{9.20}$$

where ΔH_{DT} is the loss in head in the draft tube and c_4 is the flow exit velocity.

The hydraulic efficiency is defined by

$$\eta_h = \frac{\Delta W}{gH_E} = \frac{U_2c_{\theta 2} - U_3c_{\theta 3}}{gH_E} \tag{9.21a}$$

and, whenever $c_{\theta 3} = 0$,

$$\eta_H = \frac{U_2c_{\theta 2}}{gH_E} \tag{9.21b}$$

The overall efficiency is given by $\eta_o = \eta_m\eta_H$. For very large turbines (e.g., 500−1000 MW), the mechanical losses are then relatively small, $\eta \to 100\%$ and effectively $\eta_o \approx \eta_H$.

For the Francis turbine, the ratio of the runner tip speed to the jet velocity, $\nu = U_2/c_1$, is not as critical for high-efficiency operation as it is for the Pelton turbine and can lie in a fairly wide range,

e.g., $0.6 \leq \nu \leq 0.95$. In most applications, the Francis turbine is used to drive a synchronous generator and the rotational speeds chosen are those appropriate to either 50 or 60 cycles per second. The speed must then be maintained constant.

It is possible to obtain part load operation of the turbine by varying the angle of the guide vanes. The guide vanes are pivoted and set to an optimum angle via a gearing mechanism. However, part load operation normally causes a whirl velocity to be set up in the flow downstream of the runner causing a reduction in efficiency. The strength of the vortex may be enough to cause a cavitation bubble to form along the axis of the draft tube (see Section 9.8).

EXAMPLE 9.3

In a vertical-shaft Francis turbine, the available head at the inlet flange is 150 m of water and the vertical distance between the runner and the tailrace is 2.0 m. The runner tip speed is 35 m/s, the meridional velocity of the water through the runner is constant at 10.5 m/s, the flow leaves the runner without whirl and the velocity at exit from the draft tube is 3.5 m/s.

The hydraulic losses for the turbine are as follows:

$$\Delta H_{\mathrm{N}} = 6.0 \text{ m}, \quad \Delta H_{\mathrm{R}} = 10 \text{ m}, \quad \Delta H_{\mathrm{DT}} = 1.0 \text{ m}$$

Determine

a. the specific work, ΔW, and the hydraulic efficiency, η_{h}, of the turbine;
b. the absolute velocity, c_2, at runner entry;
c. the pressure head (relative to the tailrace) at inlet to and exit from the runner;
d. the absolute and relative flow angles at runner inlet; the flow discharged by the turbine is 20 m^3/s and the power specific speed is 0.8 (rad), the speed of rotation and diameter of the runner.

Solution

a. From Eqs (9.18) and (9.20), we can find the specific work:

$$\Delta W = g(H_{\mathrm{E}} - \Delta H_{\mathrm{N}} - \Delta H_{\mathrm{R}} - \Delta H_{\mathrm{DT}}) - \frac{1}{2}c_4^2$$

$$= 9.81 \times (150 - 6 - 10 - 1) - 3.5^2/2 = 1298.6 \text{ m}^2/s^2$$

The hydraulic efficiency, $\eta_{\mathrm{h}} = \Delta W/(gH_{\mathrm{E}}) = 0.8825$.

b. As $c_{\theta 3} = 0$, then $\Delta W = U_2 c_{\theta 2}$ and $c_{\theta 2} = \Delta W/U_2 = 1298.6/35 = 37.1$ m/s, thus,

$$c_2 = \sqrt{c_{\theta 2}^2 + c_{\mathrm{m}}^2} = \sqrt{37.1^2 + 10.5^2} = 38.56 \text{ m/s}$$

c. From Eq. (9.17), the pressure head at inlet to the runner is

$$H_2 = H_{\mathrm{E}} - \Delta H_{\mathrm{N}} - c_2^2/(2g) = 150 - 6 - 38.56^2/(2 \times 9.81) = 68.22 \text{ m}$$

Again, using Eq. (9.20), the pressure head (relative to the tailrace) at runner exit is

$$H_3 = (p_3 - p_a)/(\rho g) = (c_4^2 - c_3^2)/(2g) + \Delta H_{DT} - z_3 = (3.5^2 - 10.5^2)/(2 \times 9.81) + 1 - 2 = -6.0 \text{ m}$$

Note: The minus sign for H_3 indicates that the pressure is below the atmospheric level. This is a matter of considerable importance in the design and operation of hydraulic turbomachinery and is considered in further detail under Section 9.8 later in this chapter.

d. The flow angles at runner inlet are now obtained as follows:

$$\alpha_2 = \tan^{-1}(c_{\theta 2}/c_{r2}) = \tan^{-1}(37.1/10.5) = 74.2^\circ$$

$$\beta_2 = \tan^{-1}[(c_{\theta 2} - U_2)/c_{r2}] = \tan^{-1}[(37.1 - 35)/10.5] = 11.31^\circ$$

From the definition of power specific speed, Eq. (9.1), and using $P/\rho = Q\Delta W$,

$$\Omega = \frac{\Omega_{SP}(gH_E)^{5/4}}{\sqrt{Q\Delta W}} = \frac{0.8 \times 9114}{\sqrt{20 \times 1298.7}} = 45.24 \text{ rad/s}$$

Thus, the rotational speed $\Omega = 432$ rpm and the runner diameter is

$$D_2 = 2U_2/\Omega = 70/45.24 = 1.547 \text{ m}$$

The pump turbine

The pump turbine is an example of a system capable of providing large reserves of power with a very short *start-up time* and its design is generally based on the Francis turbine. It is, essentially, a reversible turbomachine employing two large reservoirs, one at high level able to generate power from the turbines in the daytime when the demand for electricity is high and the other at low level used to store the water which is pumped back at night when the demand for electricity is low. The plant is usually referred to as a *pumped storage scheme*. (For further technical details, consult Stelzer and Walters (1977) or go to URL www.usbr.gov/pmts/hydraulics_lab/pubs/EM/EM39.pdf).

EXAMPLE 9.4

A modern pumped storage scheme, the Gwynedd plant at Llanberis, North Wales, consists of six Francis turbines with a total power output $P = 1728$ MW, a volume flow rate $Q = 60$ m^3/s for each turbine, a head $H = 600$ m at full capacity, operating at a rotational speed of $\Omega = 500$ rpm. When pumping the water back to the upper reservoir, the demand on the electricity supply is 33% greater than it was in the turbine mode.

Determine

a. the efficiency of the turbines and their specific speed, comparing the value you obtain with the range of values shown in Figure 2.8; comment on the suitability of these turbines for the task;

b. the diameter of the turbines assuming a peripheral velocity factor (PVF) for the turbines of 0.75;
c. the efficiency of the system in the pumping mode.

Solution

a. The efficiency of each turbine is

$$\eta = \frac{P}{\rho g H Q} = \frac{(1728/6) \times 10^6}{9810 \times 600 \times 60} = 0.8155$$

with $\Omega = N\pi/30 = 52.36$ rad, the specific speed is

$$\Omega_s = \frac{\Omega Q^{1/2}}{(gH)^{3/4}} = \frac{52.36 \times 60^{1/2}}{(9.81 \times 600)^{3/4}} = 0.604$$

Examining Figure 2.8, this value of specific speed is in the middle of the range shown for Francis turbines confirming that the working values are well chosen.

b.

$$D = \frac{2}{\Omega}\phi\sqrt{2gH} = \frac{2}{52.36} \times 0.75 \times \sqrt{2 \times 9.81 \times 600} = 3.11 \text{ m}$$

c. The efficiency of the system in the pumping mode is

$$\eta_p = \frac{\text{power to pump water}}{\text{input power}} = \frac{\rho g Q H}{1.33 \times 288} = \frac{9810 \times 600 \times 60}{1.33 \times 288 \times 10^6} = 92.2\%$$

9.6 The Kaplan turbine

This type of turbine evolved from the need to generate power from much lower pressure heads than are normally employed with the Francis turbine. To satisfy large power demands, very large volume flow rates need to be accommodated in the Kaplan turbine, i.e., the product QH_E is large. The overall flow configuration is from radial to axial. Figure 9.17(a) is a part sectional view of a Kaplan turbine in which the flow enters from a volute into the inlet guide vanes, which impart a degree of swirl to the flow determined by the needs of the runner. The flow leaving the guide vanes is forced by the shape of the passage into an axial direction and the swirl becomes essentially a free vortex, i.e.,

$$rc_\theta = \text{a constant}$$

The vanes of the runner are similar to those of an axial-flow turbine rotor but designed with a twist suitable for the free-vortex flow at entry and an axial flow at outlet. A picture of a Kaplan (or propeller) turbine runner is shown in Figure 9.17(b). Because of the very high torque that must be transmitted and the large length of the blades, strength considerations impose the need for large

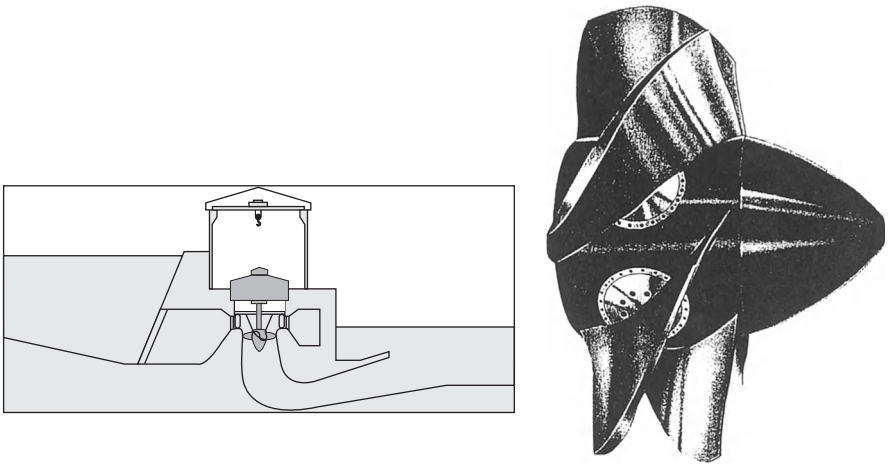

FIGURE 9.17

(a) Part section of a Kaplan turbine *in situ*. (b) Kaplan turbine runner.

(*Courtesy Sulzer Hydro Ltd., Zurich*)

blade chords. As a result, pitch−chord ratios of 1.0−1.5 are commonly used by manufacturers and, consequently, the number of blades is small, usually four, five, or six. The Kaplan turbine incorporates one essential feature not found in other turbine rotors and that is the setting of the stagger angle can be controlled. At part load operation, the setting angle of the runner vanes is adjusted automatically by a servomechanism to maintain optimum efficiency conditions. This adjustment requires a complementary adjustment of the inlet guide vane stagger angle to maintain an absolute axial flow at exit from the runner.

Basic equations

Most of the equations presented for the Francis turbine also apply to the Kaplan (or propeller) turbine, apart from the treatment of the runner. Figure 9.18 shows the velocity triangles and part section of a Kaplan turbine drawn for the mid-blade height. At exit from the runner, the flow is shown leaving the runner without a whirl velocity, i.e., $c_{\theta 3} = 0$ and constant axial velocity. The theory of free-vortex flows was expounded in Chapter 6 and the main results as they apply to an incompressible fluid are given here. The runner blades will have a fairly high degree of twist, the amount depending upon the strength of the circulation function K, and the magnitude of the axial velocity. Just upstream of the runner, the flow is assumed to be a free-vortex and the velocity components are accordingly

$$c_{\theta 2} = K/r, \quad c_x = \text{a constant}$$

The relations for the flow angles are

$$\tan \beta_2 = U/c_x - \tan \alpha_2 = \Omega r/c_x - K/(rc_x) \tag{9.22a}$$

$$\tan \beta_3 = U/c_x = \Omega r/c_x \tag{9.22b}$$

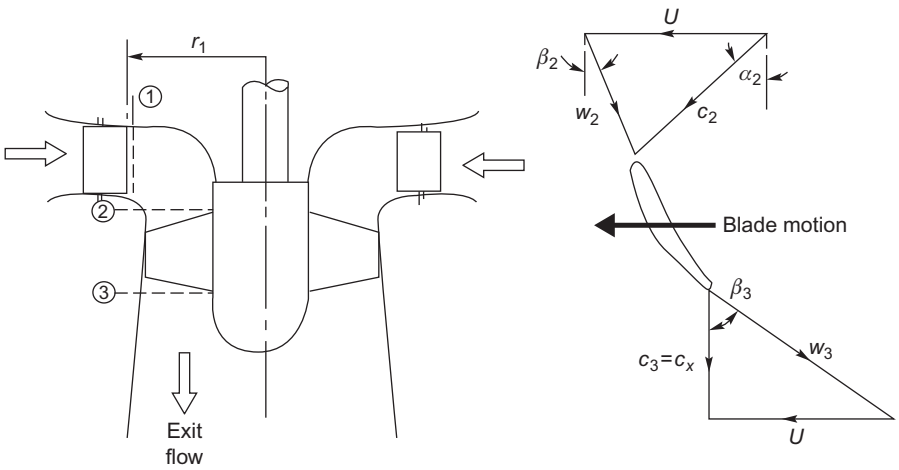

FIGURE 9.18

Section of a Kaplan turbine and velocity diagrams at inlet to and exit from the runner.

EXAMPLE 9.5

A small-scale Kaplan turbine has a power output of 8 MW, an available head at turbine entry of 13.4 m, and a rotational speed of 200 rpm. The inlet guide vanes have a length of 1.6 m and the diameter at the trailing edge surface is 3.1 m. The runner diameter is 2.9 m and the hub−tip ratio is 0.4.

Assuming the hydraulic efficiency is 92% and the runner design is "free-vortex," determine

a. the radial and tangential components of velocity at exit from the guide vanes;
b. the component of axial velocity at the runner;
c. the absolute and relative flow angles upstream and downstream of the runner at the hub, mid-radius, and tip.

Solution

a. As $P = \eta_H \rho g Q H_E$, then the volume flow rate is

$$Q = P/(\eta_H \rho g H_E) = 8 \times 10^6/(0.92 \times 9810 \times 13.4) = 66.15 \text{ m/s}^2$$

Therefore,

$$c_{r1} = Q/(2\pi r_1 L) = 66.15/(2\pi \times 1.55 \times 1.6) = 4.245 \text{ m/s}$$

$$c_{x2} = \frac{4Q}{\pi D_{2t}^2 (1 - \nu^2)} = 4 \times 66.15/(\pi \times 2.9^2 \times 0.84) = 11.922 \text{ m/s}$$

Table 9.4 Calculated Values of Flow Angles for Example 9.5

	Ratio r/r_t		
Parameter	**0.4**	**0.7**	**1.0**
$c_{\theta 2}$ (m/s)	9.955	5.687	3.982
tan α_2	0.835	0.4772	0.334
α_2 (deg)	39.86	25.51	18.47
U/c_{x2}	1.019	1.7832	2.547
β_2 (deg)	10.43	52.56	65.69
β_3 (deg)	45.54	60.72	68.57

b. As the specific work done is $\Delta W = U_2 c_{\theta 2}$ and $\eta_H = \Delta W/(gH_E)$, then at the tip

$$c_{\theta 2} = \frac{\eta_H g H_E}{U_2} = \frac{0.92 \times 9.81 \times 13.4}{30.37} = 3.892 \text{ m/s}$$

where the blade tip speed is $U_2 = \Omega D_2/2 = (200 \times \pi/30) \times 2.9/2 = 30.37$ m/s,

$$c_{\theta 1} = c_{\theta 2} r_2/r_1 = 3.892 \times 1.45/1.55 = 3.725 \text{ m/s}^2$$

$$\alpha_1 = \tan^{-1}\left(\frac{c_{\theta 1}}{c_{r1}}\right) = \tan^{-1}\left(\frac{3.725}{4.245}\right) = 41.26^\circ$$

c. Values α_2, β_2, and β_3 given in Table 9.4 have been derived from the following relations:

$$\alpha_2 = \tan^{-1}\left(\frac{c_{\theta 2}}{c_{x2}}\right) = \tan^{-1}\left(\frac{c_{\theta 2t}}{c_{x2}}\frac{r_t}{r}\right)$$

$$\beta_2 = \tan^{-1}\left(\frac{\Omega r}{c_{x2}} - \tan\alpha_2\right) = \tan^{-1}\left(\frac{U_{2t}}{c_{x2}}\frac{r}{r_t} - \tan\alpha_2\right)$$

$$\beta_3 = \tan^{-1}\left(\frac{U}{c_{x2}}\right) = \tan^{-1}\left(\frac{U_{2t}}{c_{x2}}\frac{r}{r_t}\right)$$

Finally, Figure 9.19 illustrates the variation of the flow angles, from which the large amount of blade twist mentioned earlier can be inferred.

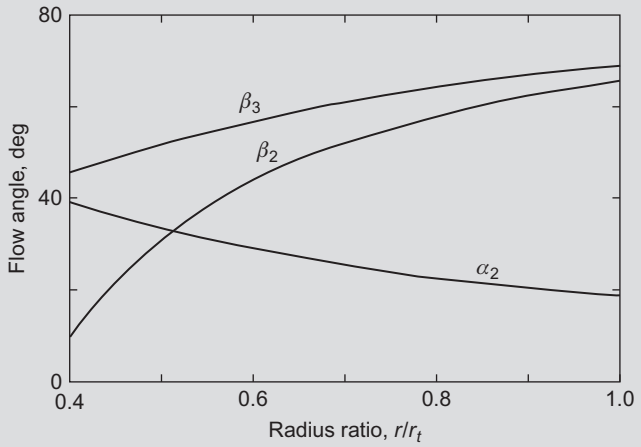

FIGURE 9.19

Calculated variation of flow angles for Kaplan turbine of Example 9.5.

9.7 Effect of size on turbomachine efficiency

Despite careful attention to detail at the design stage and during manufacture, it is a fact that small turbomachines always have lower efficiencies than larger geometrically similar machines. The primary reason for this is that it is not possible to establish perfect dynamical similarity between turbomachines of different size. To obtain this condition, each of the dimensionless terms in Eq. (2.2) would need to be the same for all sizes of a machine.

To illustrate this, consider a family of turbomachines where the loading term, $\psi = gH/\Omega^2 D^2$, is the same and the Reynolds number, $Re = \Omega D^2/\nu$, is the same for every size of machine, then

$$\psi\, Re^2 = \frac{gH}{\Omega^2 D^2} \times \frac{\Omega^2 D^4}{\nu^2} = \frac{gHD^2}{\nu^2}$$

must be the same for the whole family. Thus, for a given fluid (ν is a constant), a reduction in size D must be followed by an increase in the head H. A turbine model of one-eighth the size of a prototype would need to be tested with a head 64 times that required by the prototype! Fortunately, the effect on the model efficiency caused by changing the Reynolds number is not large. In

practice, models are normally tested at conveniently low heads and an empirical correction is applied to the efficiency.

With model testing, other factors affect the results. Exact geometric similarity cannot be achieved for the following reasons:

a. The blades in the model will probably be thicker than in the prototype.
b. The relative surface roughness for the model blades will be greater.
c. Leakage losses around the blade tips of the model will be relatively greater as a result of increased relative tip clearances.

Various simple corrections have been devised (see Addison, 1964) to allow for the effects of size (or scale) on the efficiency. One of the simplest and best known is that due to Moody and Zowski (1969), also reported by Addison (1964) and Massey (1979), which as applied to the efficiency of reaction turbines is

$$\frac{1-\eta_p}{1-\eta_m}=\left(\frac{D_m}{D_p}\right)^n \tag{9.23}$$

where the subscripts p and m refer to prototype and model, respectively, and the index n is in the range 0.2−0.25. From comparison of field tests of large units with model tests, Moody and Zowski concluded that the best value for n was approximately 0.2 rather than 0.25 and for general application this is the value used. However, Addison (1964) reported tests done on a full-scale Francis turbine and a model made to a scale of 1−4.54 that gave measured values of the maximum efficiencies of 0.85 and 0.90 for the model and full-scale turbines, respectively, which agreed very well with the ratio computed with $n = 0.25$ in the Moody formula!

EXAMPLE 9.6

A model of a Francis turbine is built to a scale of one-fifth of full size and when tested it developed a power output of 3 kW under a head of 1.8 m of water, at a rotational speed of 360 rpm and a flow rate of 0.215 m^3/s. Estimate the speed, flow rate, and power of the full-scale turbine when working under dynamically similar conditions with a head of 60 m of water.

By making a suitable correction for scale effects, determine the efficiency and the power of the full-size turbine. Use Moody's formula and assume $n = 0.25$.

Solution

From the group $\psi = gH/(ND)^2$, we get

$$N_p = N_m(D_m/D_p)(H_p/H_m)^{0.5} = (360/5)(60/1.8)^{0.5} = 415.7 \text{ rev/min}$$

From the group $\phi = Q/(ND^3)$, we get

$$Q_p = Q_m(N_p/N_m)(D_p/D_m)^3 = 0.215 \times (415.7/360) \times 5^3 = 31.03 \text{ m}^3/s$$

Lastly, from the group $\hat{P} = P/(\rho N^3 D^3)$, we get

$$P_p = P_m(N_p/N_m)^3(D_p/D_m)^5 = 3 \times (415.7)^3 \times 5^5 = 14,430 \text{ kW} = 14.43 \text{ MW}$$

This result has still to be corrected to allow for scale effects. First we must calculate the efficiency of the model turbine. The efficiency is found from

$$\eta_m = P/(\rho QgH) = 3 \times 10^3/(10^3 \times 0.215 \times 9.81 \times 1.8) = 0.79$$

Using Moody's formula, the efficiency of the prototype is determined:

$$(1 - \eta_p) = (1 - \eta_m) \times 0.2^{0.25} = 0.21 \times 0.6687$$

hence,

$$\eta_p = 0.8596$$

The corresponding power is found by an adjustment of the original power obtained under dynamically similar conditions, i.e.,

$$\text{corrected } P_p = 14.43 \times 0.8596/0.79 = 15.7 \text{ MW}$$

9.8 Cavitation in hydraulic turbines

A description of the phenomenon of cavitation with regard to pumps was given in Chapter 7. In hydraulic turbines, where reliability, long life, and efficiency are all very important, the effects of cavitation must be considered. Two types of cavitation may be in evidence:

a. on the suction surfaces of the runner blades at outlet that can cause severe blade erosion;
b. a twisting "rope type" cavity that appears in the draft tube at off-design operating conditions.

Cavitation in hydraulic turbines can occur on the suction surfaces of the runner blades where the dynamic action of the blades acting on the fluid creates low-pressure zones in a region where the static pressure is already low. Hydraulic turbines are designed to run for many years with very little maintenance. However, if cavitation does occur, then pitting of the surfaces, fatigue cracking, and partial collapse of the blades will reduce performance. Figure 9.20 shows extensive damage due to cavitation of a Francis runner.

Cavitation will commence when the local static pressure is less than the vapor pressure of the water, i.e., where the head is low, the velocity is high and the elevation, z, of the turbine is set too high above the tailrace. For a turbine with a horizontal shaft, the lowest pressure will be located in the upper part of the runner, which could be of major significance in large machines. Fortunately, the runners of large machines are, in general, made so that their shafts are orientated vertically, lessening the problem of cavitation occurrence.

The cavitation performance of hydraulic turbines can be correlated with the Thoma coefficient, σ, defined as

$$\sigma = \frac{H_S}{H_E} = \frac{(p_a - p_0)/(\rho g) - z}{H_E} \tag{9.24}$$

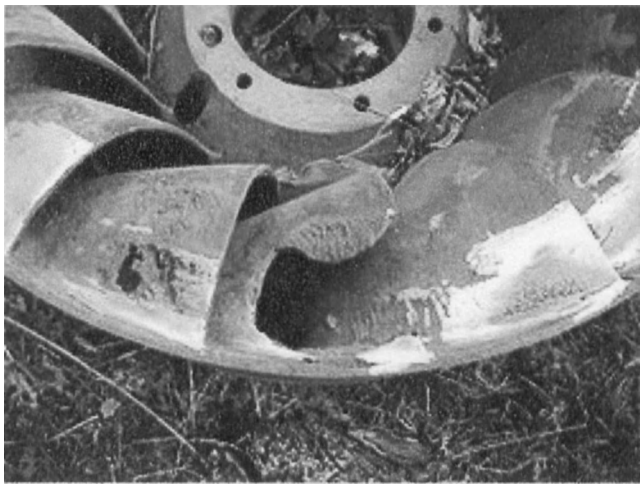

FIGURE 9.20

Cavitation damage to the blades of a Francis turbine.

where H_S is the net positive suction head (NPSH), the amount of head needed to avoid cavitation, the difference in elevation, z, is defined in Figure 9.16 and p_v is the vapor pressure of the water. The Thoma coefficient was, strictly, originally defined in connection with cavitation in turbines and its use in pumps is not appropriate (see Yedidiah, 1981). It is to be shown that σ represents the fraction of the available head H_E, which is unavailable for the production of work. A large value of σ means that a smaller part of the available head can be utilized. In a pump, incidentally, there is no direct connection between the developed head and its suction capabilities, provided that cavitation does not occur, which is why the use of the Thoma coefficient is not appropriate for pumps.

From the energy equation, Eq. (9.20), this can be rewritten as

$$\frac{p_a - p_3}{\rho g} - z = \frac{1}{2g}(c_3^2 - c_4^2) - \Delta H_{DT} \tag{9.25}$$

so that when $p_3 = p_v$, then H_S is equal to the right-hand side of Eq. (9.24).

Figure 9.21 shows a widely used correlation of the Thoma coefficient plotted against specific speed for Francis and Kaplan turbines, approximately defining the boundary between no cavitation and severe cavitation. In fact, there exists a wide range of critical values of σ for each value of specific speed and type of turbine due to the individual cavitation characteristics of the various runner designs. The curves drawn are meant to assist preliminary selection procedures. An alternative method for avoiding cavitation is to perform tests on a model of a particular turbine in which the value of p_3 is reduced until cavitation occurs or a marked decrease in efficiency becomes apparent. This performance reduction would correspond to the production of large-scale cavitation bubbles. The pressure at which cavitation erosion occurs will actually be at some higher value than that at which the performance reduction starts.

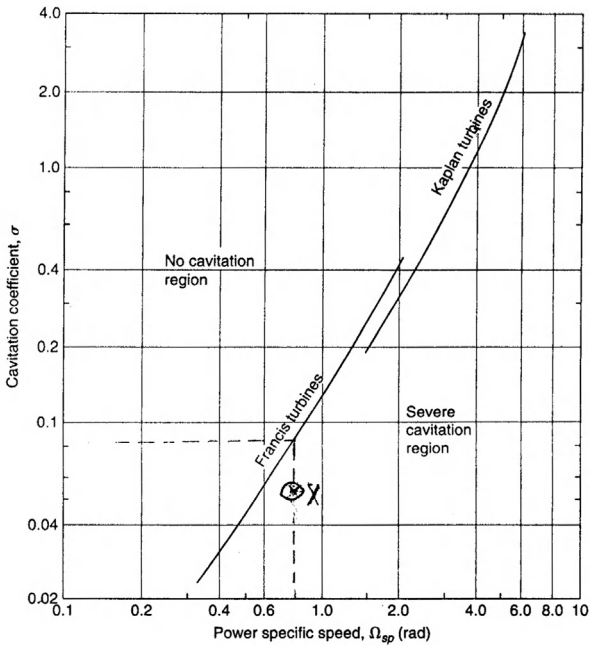

FIGURE 9.21

Variation of critical cavitation coefficient with nondimensional specific speed for Francis and Kaplan turbines.

(*Adapted from Moody and Zowski, 1969*)

For the centerline cavitation that appears downstream of the runner at off-design operating conditions, oscillations of the cavity can cause severe vibration of the draft tube. Young (1989) reported some results of a "corkscrew" cavity rotating at 4 Hz. Air injected into the flow both stabilizes the flow and cushions the vibration.

EXAMPLE 9.7

Using the data for the Francis turbine given in Example 9.3 and the atmospheric pressure is 1.013 bar, and the water is at 25°C, determine the NPSH for the turbine. Hence, using Thoma's coefficient and the data shown in Figure 9.21, determine whether cavitation is likely to occur. Verify the result using Wislicenus's criterion, the result given in Eq. (2.23b).

Solution

From tables of fluid properties, e.g., Rogers and Mayhew (1995), or using the data of Figure 9.22, the vapor pressure for water corresponding to a temperature of 25°C is 0.03166 bar. From the definition of NPSH, Eq. (9.24), we obtain

$$H_S = \frac{p_a - p_v}{\rho g} - z = (1.013 - 0.03166) \times 10^5/(9810) - 2 = 8.003 \text{ m}$$

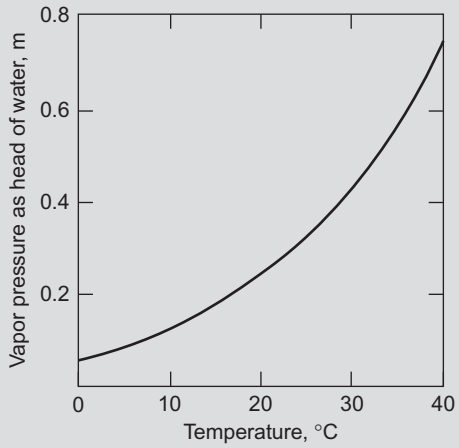

FIGURE 9.22

Vapor pressure of water as head (m) versus temperature.

Thus, from Eq. (9.24) with $H_E = 150$ m, then Thoma's coefficient is, $\sigma = H_S/H_E = 8.003/150 = 0.05336$.

At the value of $\Omega_{sp} = 0.8$ given as data, the value of the critical Thoma coefficient σ_c corresponding to this is 0.083 from Figure 9.21. From the fact that $\sigma < \sigma_c$, then the turbine *will* cavitate**.** The point X in Figure 9.21 is the intercept of σ_c and Ω_{sp} in the severe cavitation zone.

From the definition of the suction specific speed,

$$\Omega_{SS} = \frac{\Omega Q^{1/2}}{(gH_S)^{3/4}} = \frac{44.9 \times 20^{1/2}}{(9.81 \times 8.003)^{3/4}} = 200.8/26.375 = 7.613$$

According to Eq. (2.23b), when Ω_{SS} exceeds 4.0 (rad) cavitation can occur, giving further confirmation of the above conclusion.

Connection between Thoma's coefficient, suction specific speed, and specific speed

The definitions of suction specific speed Ω_{SS} and specific speed Ω_s are

$$\Omega_{SS} = \frac{\Omega Q^{1/2}}{(gH_S)^{3/4}} \text{ and } \Omega_S = \frac{\Omega Q^{1/2}}{(gH_E)^{3/4}}$$

Combining these expressions and using Eq. (9.24), we get

$$\frac{\Omega_S}{\Omega_{SS}} = \left(\frac{gH_S}{gH_E}\right)^{3/4} = \sigma^{3/4}$$

therefore, the cavitation coefficient is,

$$\sigma = \left(\frac{\Omega_S}{\Omega_{SS}}\right)^{4/3} \tag{9.26}$$

Exercise

Verify the value of Thoma's coefficient in Example 9.5 using the values of power specific speed, efficiency, and suction specific speed given or derived.

We use as data $\Omega_{SS} = 7.613$, $\Omega_{SP} = 0.8$, and $\eta_H = 0.896$ so that, from Eq. (2.16),

$$\Omega_S = \Omega_{sp}/\sqrt{\eta_H} = 0.8/\sqrt{0.896} = 0.8452$$

therefore, from Eq. (9.26)

$$\sigma = (0.8452/7.613)^{4/3} = 0.05336$$

This value corresponds to point X shown in Figure 9.21 and corroborates the previous conclusion that cavitation will occur.

Avoiding Cavitation

By rearranging Eq. (9.24) and putting $\sigma = \sigma_c$, a critical value of z can be derived on the boundary curve between cavitation and no cavitation. Thus,

$$z = z_c = \frac{p_a - p_v}{\rho g} - \sigma_c H_E = (101.3 - 3.17)/9.81 - 0.09 \times 150 = -3.5 \text{ m}$$

This means that the turbine would need to be submerged to a depth of 3.5 m or more below the surface of the tailwater and, for a Francis turbine, would lead to problems with regard to construction and maintenance. Equation (9.24) shows that the greater the available head H_E at which a turbine operates, the lower it must be located relative to the surface of the tailrace.

Controversially, some manufacturers might allow for some cavitation damage to occur in large turbines, balancing this against the extra cost. A difficult choice!

Peripheral velocity factor

This is a most useful concept which is often used to verify (and calculate) the size of pumps and turbines. For a pump impeller or for a turbine runner, the PVF is defined as

$$\phi = U_2/\sqrt{2gH}$$

where U_2 is the peripheral velocity or blade tip speed ($\Omega D_2/2$) and H is the net head delivered by the pump or the effective head supplied to a turbine. Thus, from these expressions, we get

$$D_2 = 2U_2/\Omega = 2\phi\sqrt{2gH}/\Omega \tag{9.27}$$

assuming all the parameters are at the respective maximum efficiency condition (BEP).

For the various main types of hydraulic turbine, the approximate values of PVF are as follows:

Pelton Wheel	0.43–0.48
Francis turbine	0.7–0.8
Kaplan turbine	1.4–2.0

Selecting the right turbine

The power specific speed, Eq. (2.15), is often understood to be the best guide in choosing the most appropriate type of turbine for a given duty. From Figure 9.1, it would seem that for high heads and a low Ω_{sp} the most likely choice would be a Pelton wheel, providing the designer with a high efficiency. However, the situation is rather more complicated than at first sight because it is possible for the designer to end up with a very large and costly turbine.

At a give site, options to be considered must include not only the type of turbine but also the number of units to be installed. It is regarded as good practice to have at least two turbines in place so that in the event of essential maintenance of a turbine the plant can continue to operate. Another factor to be considered is the freedom from cavitation. Example 9.8 illustrates the choices to be made.

EXAMPLE 9.8

Two (or more) identical turbines are to be installed where the net available head is 108 m and the total flow rate is 18 m^3/s. You are required to choose appropriate turbines for the site assuming that all the turbines have an efficiency of 90%.

The total power available is

$$P = \eta\rho gQH = 0.9 \times 9810 \times 18 \times 108 = 17.16 \text{ MW}$$

a. Assuming there are actually two turbines operating at $\Omega = 75$ rpm, i.e., $\Omega = 75 \times \pi/30 = 7.854$ rad$/s$, then the power specific speed is

$$\Omega_{sp} = \frac{\Omega\sqrt{P/\rho}}{(gH)^{5/4}} = 7.854 \times \frac{\sqrt{(17.16 \times 10^6/2 \times 10^3)}}{(9.81 \times 108)^{5/4}} = 0.1204$$

From Figure 9.1, it can be seen that the type of turbine best suited to this power specific speed is either a single-jet Pelton wheel or a multi-jet Pelton wheel.

From the definition of the PVF, ϕ, Eq. (9.27), the diameter is

$$D = \frac{2}{\Omega}\phi\sqrt{2gH}$$

where, for a Pelton wheel, $\phi \approx 0.47$

$$\therefore D = \frac{2}{7.854} \times 0.47 \times \sqrt{2 \times 9.81 \times 108} = 5.55 \text{ m}$$

This diameter seems rather large for Pelton wheel turbines and it would be worth looking around to see if suitable alternatives are available.

b. Another solution is to use four Pelton turbines operating at 180 rpm (this would require a generator with 20 pole pairs for a supply at 60 Hz) Thus, $\Omega = (180/30) \times \pi = 18.85$ rad/s.

$$\Omega_{sp} = \frac{18.85 \times \sqrt{17.16 \times 10^3/4}}{(9.81 \times 108)^{5/4}} = 0.204$$

and

$$D_2 = \frac{2\phi\sqrt{2gH}}{\Omega} = \frac{2 \times 0.45\sqrt{2 \times 9.81 \times 108}}{18.85} = 2.198 \text{ m}$$

Thus, the specific speed appears to be satisfactory with a multi-jet Pelton wheel (see Figure 9.1).

The diameter of the impeller wheels is more acceptable with the higher rotational speed and lower flow rate for each turbine.

c. An additional alternative, of many other possible choices, is to use one Francis turbine which operates at some speed still to be selected.

For the generator operating at 60 Hz and having z pole pairs, the operating speed is

$$\Omega = 2\pi \times 60/z$$

The peripheral velocity ratio for a Francis turbine can be assumed to be the accepted average of

$$\phi = 0.75 \quad \therefore D_2 = 2\phi\sqrt{2gH}/\Omega$$

Values for various pole pairs are shown in the table below of rotational speed diameter and power specific speed.

z	8	10	15
Ω (rpm)	450	360	240
Ω (rad/s)	47.12	37.7	25.13
D_2	1.46	1.83	2.75
Ω_{sp}	1.02	0.818	0.545

It would seem that a good choice of Francis turbine would be the one with eight pole pairs operating at 450 rpm and having an impeller diameter of 1.02 m. The power specific speed suggests that the efficiency would be about 95%.

9.9 Application of CFD to the design of hydraulic turbines

With such a long history, the design of hydraulic turbines still depends very much on the experience gained from earlier designs. According to Drtina and Sallaberger (1999), the use of computational fluid dynamics (CFDs) for predicting the flow in these machines has brought further substantial improvements in their hydraulic design and resulted in a more complete understanding of the flow processes and their influence on turbine performance. Details of flow separation, loss sources, and loss distributions in components both at design and off-design as well as detecting low-pressure levels associated with the risk of cavitation are now amenable to analysis with the aid of CFD.

Drtina and Sallaberger presented two examples where the application of CFD resulted in a better understanding of complex flow phenomena. Generally, this better knowledge of the flow has resulted either in design improvements to existing components or to the replacement of components by a completely new design.

9.10 The Wells turbine

Introduction

Numerous methods for extracting energy from the motion of sea waves have been proposed and investigated since the late 1970s. The problem is in finding an efficient and economical means of converting an oscillating flow of energy into a unidirectional rotary motion for driving electrical generators. A novel solution of this problem is the Wells turbine (Wells, 1976), a version of the axial-flow turbine. For countries surrounded by the sea, such as the British Isles and Japan to mention just two, or with extensive shorelines like the United States, wave energy conversion is an attractive proposition. Energy conversion systems based on the *oscillating water column* and the Wells turbine have been installed at several locations (Islay in Scotland and Trivandrum in India). Figure 9.23 shows the arrangement of a turbine and generator together with the oscillating column of seawater. The cross-sectional area of the plenum chamber is made very large compared to the flow area of the turbine so that a substantial air velocity through the turbine is attained.

One version of the Wells turbine consists of a rotor with eight *uncambered* aerofoil section blades set at a stagger angle of 90° (i.e., with their chord lines lying in the plane of rotation). A schematic diagram of such a Wells turbine is shown in Figure 9.24. At first sight, the arrangement might seem to be a highly improbable means of energy conversion. However, once the blades have attained design speed, the turbine is capable of producing a time-averaged positive power output from the *cyclically reversing airflow* with a fairly high efficiency. According to Raghunathan, Curran, and Whittaker (1995), *peak* efficiencies of 65% have been measured at the experimental wave power station on Islay. The results obtained from a theoretical analysis by Gato and de O Falcào (1984) showed that fairly high values of the mean efficiency, on the order of 70−80%, may be attained in an oscillating flow "with properly designed Wells turbines."

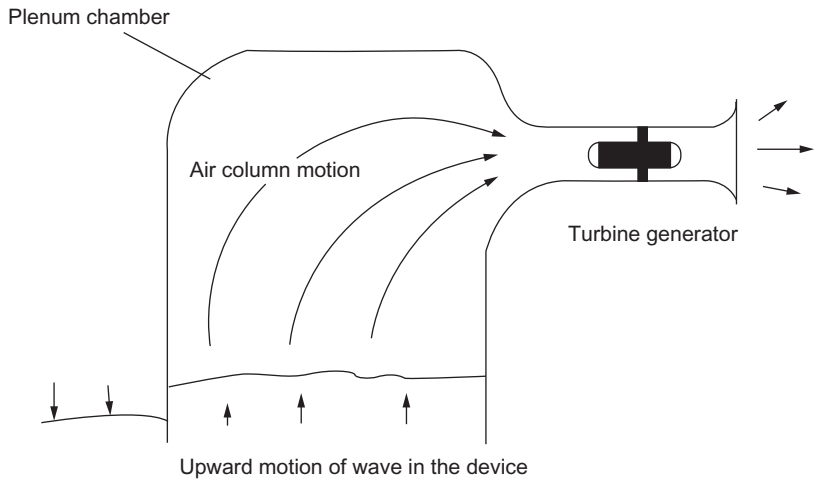

FIGURE 9.23

Arrangement of Wells turbine and oscillating water column.

(*Adapted from Raghunathan et al., 1995*)

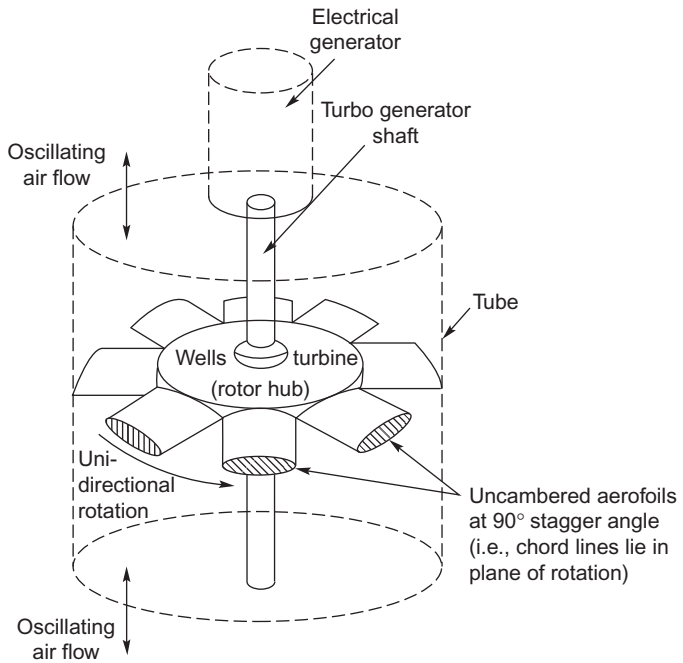

FIGURE 9.24

Schematic of a Wells turbine.

(*Adapted from Raghunathan et al., 1995*)

Operating principles

Figure 9.25(a) shows a blade in motion at the design speed U in a flow with an upward, absolute axial velocity c_1. It can be seen that the *relative velocity* w_1 is inclined to the chord line of the blade at an angle α. According to classical aerofoil theory, an *isolated* aerofoil at an angle of incidence α to a free stream will generate a lift force L normal to the direction of the free stream. In a viscous fluid, the aerofoil will also experience a drag force D in the direction of the free stream. These lift and drag forces can be resolved into the components of force X and Y as indicated in Figure 9.25(a), i.e.,

$$X = L\cos\alpha + D\sin\alpha \tag{9.28a}$$

$$Y = L\sin\alpha - D\cos\alpha \tag{9.28b}$$

The student should note, in particular, that the force Y *acts in the direction of blade motion*, giving positive work production.

For a symmetrical aerofoil, the direction of the tangential force Y is the same for both positive and negative values of α, as indicated in Figure 9.25b. If the aerofoils are secured to a rotor drum to form a turbine row, as in Figure 9.24, they will *always* rotate in the direction of the positive tangential force regardless of whether the air is approaching from above or below. With a time-varying, bidirectional airflow, the torque produced will fluctuate cyclically but can be smoothed to a large extent by means of a high inertia rotor−generator.

It will be observed from the velocity diagrams that a residual swirl velocity is present for both directions of flow. It was suggested by Raghunathan et al. (1995) that the swirl losses at turbine exit can be reduced by the use of guide vanes.

Two-dimensional flow analysis

The performance of the Wells turbine can be predicted by means of blade element theory. In this analysis, the turbine annulus is considered to be made up of a series of concentric elementary rings, each ring being treated separately as a two-dimensional cascade.

The power output from an elementary ring of area $2\pi r\,\mathrm{d}r$ is given by

$$\mathrm{d}W = ZU\,\mathrm{d}y$$

where Z is the number of blades and the tangential force on each blade element is

$$\mathrm{d}Y = C_y\left(\frac{1}{2}\rho\omega_1^2 l\right)\mathrm{d}r$$

The axial force acting on the blade elements at radius r is $Z\,\mathrm{d}X$, where

$$\mathrm{d}X = C_X\left(\frac{1}{2}\rho w_1^2 l\right)\mathrm{d}r$$

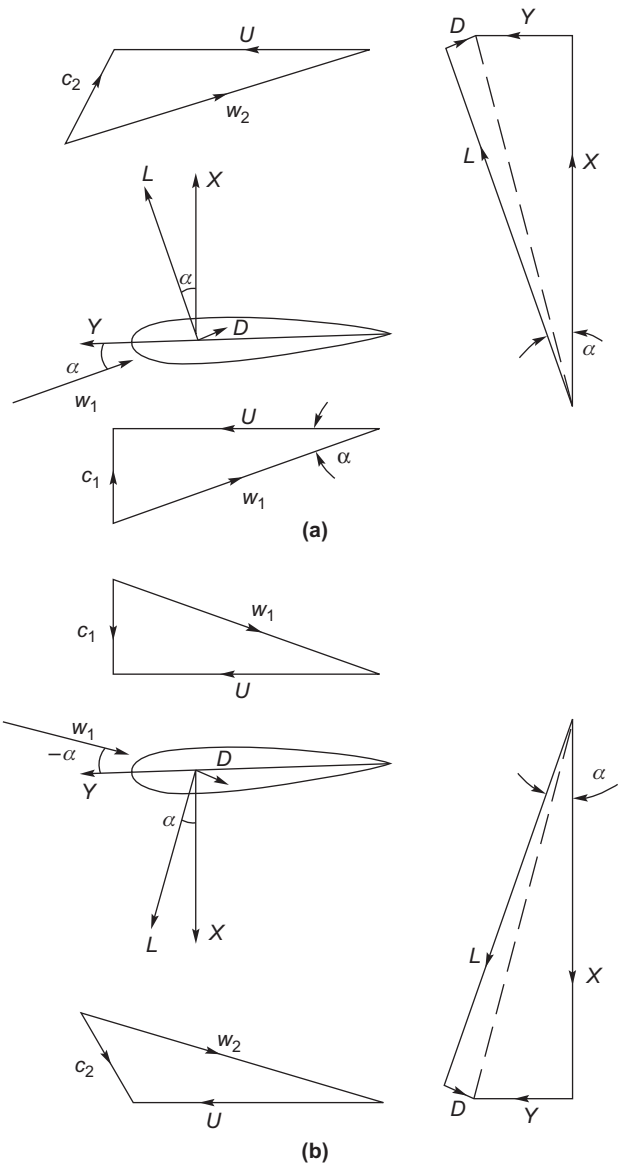

FIGURE 9.25

Velocity and force vectors acting on a blade of a Wells turbine in motion: (a) upward absolute flow onto blade moving at speed U, and (b) downward absolute flow onto blade moving at speed U.

and where C_x, C_y are the axial and tangential force coefficients, respectively. Now the axial force on all the blade elements at radius r can be equated to the pressure force acting on the elementary ring:

$$2\pi r(p_1 - p_2)\mathrm{d}r = ZC_x\left(\frac{1}{2}\rho w_1^2 l\right)\mathrm{d}r$$

so

$$\frac{(p_1 - p_2)}{(1/2)\rho c_x^2} = \frac{ZC_x l}{2\pi r \sin^2 \alpha_1}$$

where $w_1 = cx/\sin \alpha_1$.

An expression for the efficiency can now be derived from a consideration of all the power losses and the power output. The power lost due to the drag forces is $\mathrm{d}W_f = w_1\,\mathrm{d}D$, where

$$\mathrm{d}D = ZC_\mathrm{D}\left(\frac{1}{2}\rho w_1^2 l\right)\mathrm{d}r$$

and the power lost due to exit kinetic energy is given by

$$\mathrm{d}W_\mathrm{k} = \left(\frac{1}{2}c_2^2\right)\mathrm{d}\dot{m}$$

where $\mathrm{d}\dot{m} = 2\pi r\rho c_x \mathrm{d}r$ and c_2 is the absolute velocity at exit. Thus, the aerodynamic efficiency, defined as power output/power input, can now be written as

$$\eta = \frac{\int_\mathrm{h}^\mathrm{t} \mathrm{d}W}{\int_\mathrm{h}^\mathrm{t}(\mathrm{d}W + \mathrm{d}W_\mathrm{f} + \mathrm{d}W_\mathrm{k})} \tag{9.29}$$

The predictions for nondimensional pressure drop p^* and aerodynamic efficiency η determined by Raghunathan et al. (1995) are shown in Figure 9.26(a) and (b), respectively, together with experimental results for comparison.

Design and performance variables

The primary input for the design of a Wells turbine is the air power based upon the pressure amplitude ($p_1 - p_2$) and the volume flow rate Q at turbine inlet. The performance indicators are the pressure drop, power, and efficiency, and their variation with the flow rate. The aerodynamic design and consequent performance is a function of several variables that have been listed by Raghunathan. In nondimensional form, these are

$$\text{flow coefficient } \phi = c_x/U$$

$$\text{solid dity at mean radius } \sigma = \frac{2lZ}{\pi D_\mathrm{t}(1 + v)}$$

$$\text{hub/tip ratio } v = D_\mathrm{h}/D_\mathrm{t}$$

$$\text{blade aspect ratio AR} = \text{blade length chord}$$

$$\text{blade tip clearance ratio} = t_\mathrm{c}/D_\mathrm{t}$$

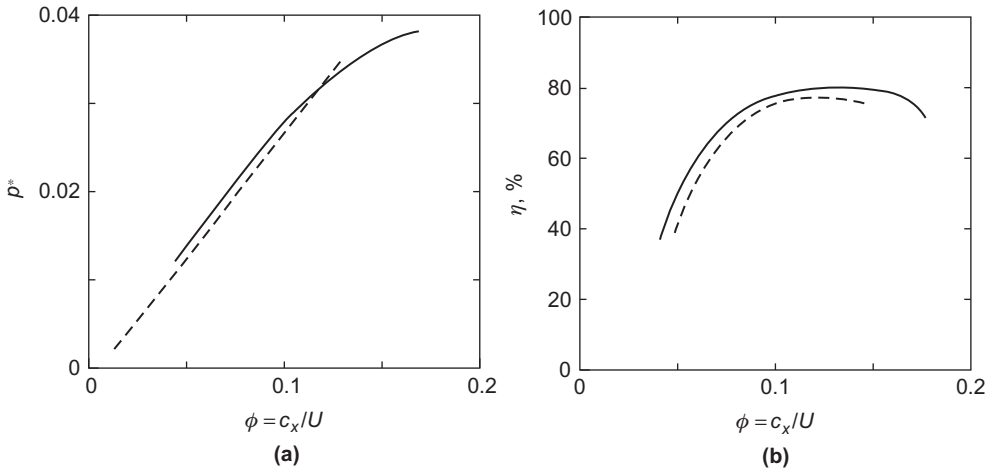

FIGURE 9.26

Comparison of theory with experiment for the Wells turbine: —— Theory – – – Experiment (Adapted from Raghunathan, 1995): (a) Nondimensional pressure drop versus flow coefficient and (b) efficiency versus flow coefficient.

and also blade thickness ratio, turbulence level at inlet to turbine, frequency of waves, and the relative Mach number. It was observed by Raghunathan, Setoguchi, and Kaneko (1987) that the Wells turbine has a characteristic feature that makes it significantly different from most turbomachines: the absolute velocity of the flow is only a (small) fraction of the relative velocity. It is theoretically possible for transonic flow conditions to occur in the relative flow resulting in additional losses due to shock waves and an interaction with the boundary layers leading to flow separation. The effects of these variables on the performance of the Wells turbine have been considered by Raghunathan (1995) and a summary of some of the main findings follow.

Effect of flow coefficient

The flow coefficient ϕ is a measure of the angle of incidence of the flow and the aerodynamic forces developed are critically dependent upon this parameter. Typical results based on predictions and experiments of the nondimensional pressure drop $p^* = \Omega p/(\rho\omega^2 D_t^2)$ and efficiency are shown in Figure 9.26. For a Wells turbine, a linear relationship exists between pressure drop and the flow rate (Figure 9.26(a)), and this fact can be employed when making a match between a turbine and an oscillating water column that also has a similar characteristic.

The aerodynamic efficiency η (Figure 9.26(b)) is shown to increase up to a certain value, after which it decreases, because of boundary layer separation.

Effect of blade solidity

The solidity is a measure of the blockage offered by the blades to the flow of air and is an important design variable. The pressure drop across the turbine is, clearly, proportional to the axial force acting on the blades. An increase of solidity increases the axial force and likewise the pressure

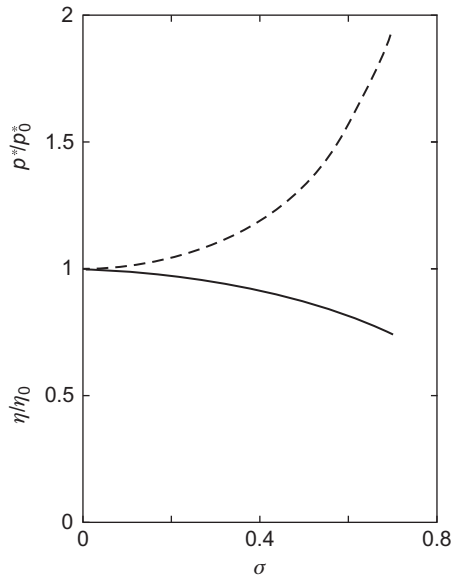

FIGURE 9.27

Variation of peak efficiency and nondimensional pressure drop (in comparison to the values for an isolated aerofoil) versus solidity: ——— Pressure – – – Efficiency.

(*Adapted from Raghunathan et al., 1995*)

drop. Figure 9.27 shows how the variations of peak efficiency and pressure drop are related to the amount of the solidity.

Raghunathan gives correlations between pressure drop and efficiency with solidity:

$$p^*/p_0^* = 1 - \sigma^2 \quad \text{and} \quad \eta/\eta_0 = \frac{1}{2}(1 - \sigma^2)$$

where the subscript 0 refers to values for a two-dimensional isolated aerofoil ($\sigma = 0$). A correlation between pressure drop and solidity (for $\sigma > 0$) was also expressed as

$$p^* = A\sigma^{1.6}$$

where A is a constant.

Effect of hub–tip ratio

The hub–tip ratio ν is an important parameter as it controls the volume flow rate through the turbine but also influences the stall conditions, the tip leakage, and, most importantly, the ability of the turbine to run up to operating speed. Values of $\nu < 0.6$ are recommended for design.

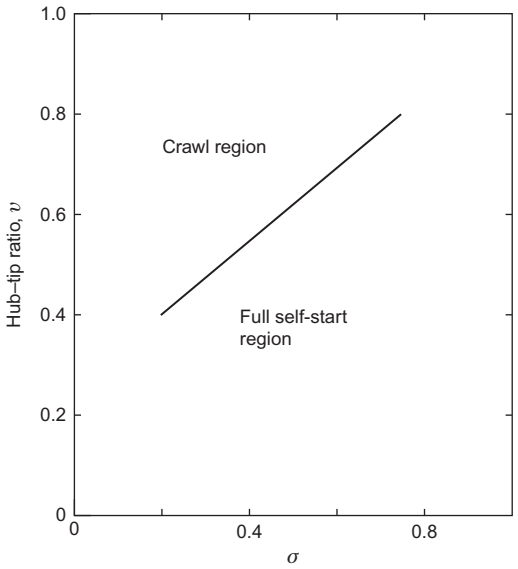

FIGURE 9.28

Self-starting capability of the Wells turbine.

(*Adapted from Raghunathan et al., 1995*)

The starting behavior of the Wells turbine

When a Wells turbine is started from rest, the incoming relative flow will be at 90° to the rotor blades. According to the choice of the design parameters, the blades could be severely stalled and, consequentially, the tangential force Y will be small and the acceleration negligible. In fact, if and when this situation occurs, the turbine may accelerate only up to a speed much lower than the design operational speed, a phenomenon called *crawling*. The problem can be avoided either by choosing a suitable combination of hub−tip ratio and solidity values at the design stage or by some other means, such as incorporating a starter drive. Values of hub−tip ratio and solidity that have been found to allow self-starting of the Wells turbine are indicated in Figure 9.28.

Pitch-controlled blades

Some appreciable improvements have been made in the performance of the Wells turbine as a result of incorporating pitch-controlled blades into the design. The efficiency of the original Wells turbine had a peak of about 80%, but the power output was rather low and the starting performance was poor. One reason for the low-power output was the low tangential force Y and low flow coefficient ϕ as a consequence of the fixed-blade geometry.

A turbine with self-pitch-controlled blades

Performance enhancement of the Wells turbine reported by Kim et al. (2002) was achieved by incorporating *swivelable vanes* instead of fixed vanes in an experimental test rig. The method they

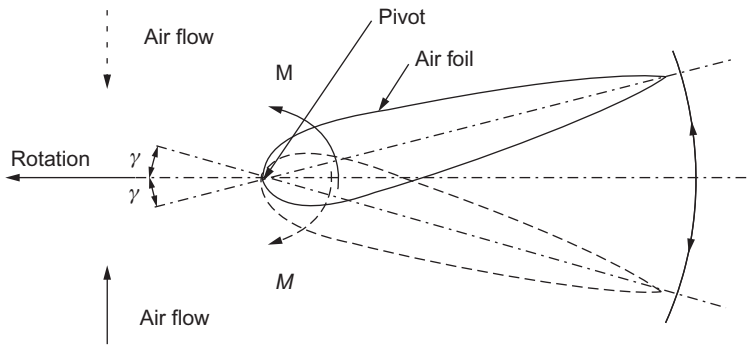

FIGURE 9.29

Air turbine using self-pitch-controlled blades for wave energy conversion.

(*From Kim et al., 2002, with Permission of Elsevier Science*)

Table 9.5 Details of the Turbine Rotor

Blade profile	NACA 0021	Hub–tip ratio	0.7
Blade chord, *l*	75 mm	Tip diameter	298 mm
Number of blades, *Z*	8	Hub diameter	208 mm
Solidity	0.75	Blade length, *H*	45 mm

devised used symmetrical blades that pivot about the nose, whose pitch angle changes by a small amount as a result of the varying aerodynamic forces developed by the oscillating flow. This change to the turbine configuration enables a higher torque and efficiency to be obtained from the reciprocating airflow. According to the authors, the turbine is geometrically simpler and would be less expensive to manufacture than some earlier methods using "active" pitch-controlled blades, e.g., Sarmento, Gato, and de O Falcào (1987) and Salter (1993).

The working principle with self-pitch-controlled blades is illustrated in Figure 9.29. This shows one of the turbine blades fixed to the hub by a pivot located near the leading edge, allowing the blade to move between two prescribed limits, $\pm\gamma$. An aerofoil set at a certain angle of incidence experiences a pitching moment about the pivot, which causes the blade to flip. In this new position, the blade develops a higher tangential force and torque at a lower rotational speed than was obtained with the original fixed-blade design of the Wells turbine.

Kim et al., using a piston-driven wind tunnel, measured the performance characteristics of the turbine under steady flow conditions. To determine its running and starting characteristics, a quasi-steady computer simulation of the oscillating through-flow was used together with the steady state characteristics. Details of the turbine rotor are given in Table 9.5.

The turbine characteristics under steady flow conditions were determined in the form of the output torque coefficient, C_τ, and the input power coefficient, C_P, against the flow coefficient, $\phi = c_x/U_{\text{av}}$, defined as

$$C_\tau = \tau_0/[\rho(c_x^2 + U_{\text{av}}^2)ZlHr_{\text{av}}/2] \tag{9.30}$$

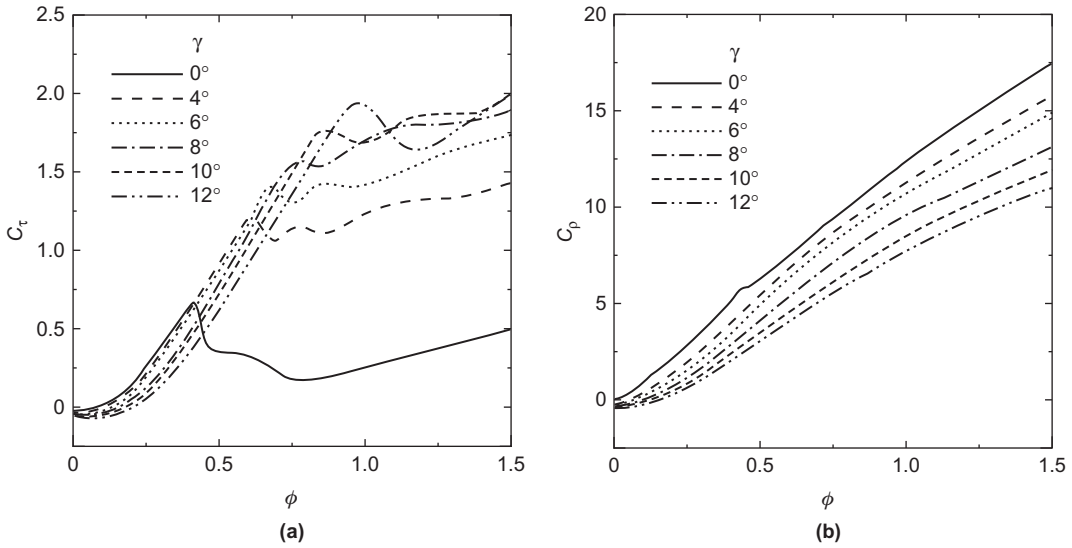

FIGURE 9.30

Turbine characteristics under steady flow conditions: (a) torque coefficient; (b) input power coefficient.

(*From Kim et al., 2002, with Permission of Elsevier Science*)

$$C_p = \Delta p_0/[\rho(c_x^2 + U_{\text{av}}^2)ZlHr_x/2] \tag{9.31}$$

where τ_0 is the output torque and Δp_0 is the total pressure difference across the turbine.

Figure 9.30(a) shows the C_τ versus ϕ characteristics for the turbine for various blade-setting angles. The solid line ($\gamma = 0°$) represents the result obtained for the original, fixed-blade Wells turbine. For values of $\gamma > 0°$, C_τ decreases with increasing γ in the stall-free zone but, beyond the original stall point for $\gamma = 0$, much higher values of C_τ were obtained.

Figure 9.30(b) shows the C_p versus ϕ characteristics for the turbine for various blade-setting angles. This figure indicates that for $\gamma > 0°$, the input power coefficient, C_p, is lower than the case where $\gamma = 0°$ for all values of ϕ. Clearly, this is due to the variation in the rotor blade-setting angle.

The instantaneous efficiency of the turbine is given by

$$\eta = \frac{\Omega\tau_0}{Q\Delta p_0} = \frac{C_\tau}{\phi C_p} \tag{9.32a}$$

and the mean efficiency over the period of the wave, $T = 1/f$, is

$$\eta_{\text{av}} = \left[\frac{1}{T}\int_0^T C_\tau\right] \Big/ \left[\frac{1}{T}\int_0^T \phi C_p \mathrm{d}t\right] \tag{9.32b}$$

Using the measured characteristics for C_τ and C_p and assuming a sinusoidal variation of the axial velocity with a different maximum amplitude[2] for each half cycle, as shown in Figure 9.31,

[2]Kim et al. reported a lower maximum axial velocity c_{xi} during inhalation than exhalation c_{xo}.

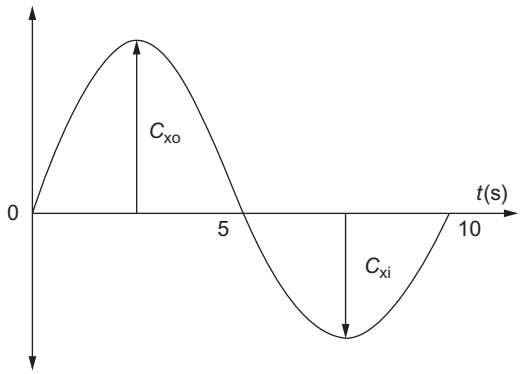

FIGURE 9.31

Assumed axial velocity variation.

(*From Kim et al., 2002, with Permission of Elsevier Science*)

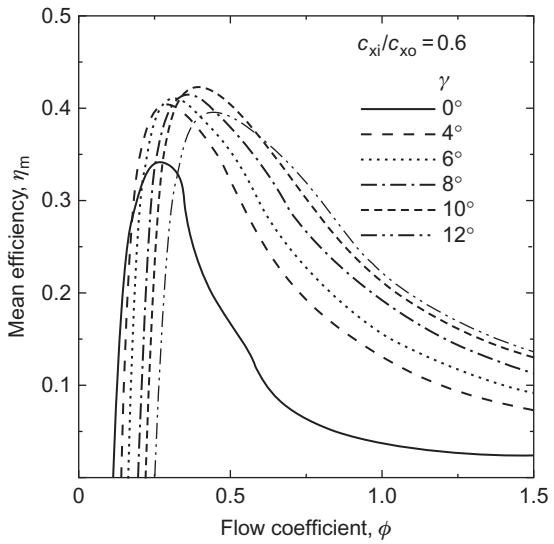

FIGURE 9.32

Mean efficiency under sinusoidally oscillating flow conditions.

(*From Kim et al., 2002, with Permission of Elsevier Science*)

the mean efficiency of the cycle can be computed. Figure 9.32 shows the mean efficiency as a function of the flow coefficient ϕ for a range of γ values with $c_{xi} = 0.6c_{xo}$.

Compared to the basic Wells turbine (with $\gamma = 0°$), the optimum result for $\gamma = 10°$ shows an improved mean efficiency and an optimum flow coefficient of about 0.4. It is apparent that further field testing would be needed to prove the concept.

Further work

Energetech in Sydney, Australia, began (circa 2003) the design of a half-scale test turbine, which will be used for more detailed flow studies and to test new blade–hub arrangements. Also, a full-scale 1.6 m diameter variable-pitch turbine has been constructed for use at the prototype wave energy plant at Port Kembla, New South Wales, Australia. Studies of derivatives of the Wells turbine are also being undertaken at research centers in the United Kingdom, Ireland, Japan, India, and other countries. It is still not clear which type of blading or which pitch-control system will prevail. Kim et al. (2001) attempted a comparison of five derivatives of the Wells turbine using steady flow data and numerical simulation of an irregular wave motion. However, at present a "best" type has still not emerged from a welter of data. A final conclusion must await the outcome of further development and the testing of prototypes subjected to real sea wave conditions.

9.11 Tidal power

Tidal energy is generated by the relative motion of the Earth, Sun, and Moon system whose gravitational forces cause periodic changes to the water levels on the Earth's surface. The magnitude of the tide at any given location is the result of the varying positions of the Moon and Sun relative to that of the Earth, the rotation of the Earth, the shape of the seabed, and the magnifying effects of the coast. The Moon is the main cause of these tides and the Sun to a much lesser extent. When the Sun and Moon are in-line with the Earth (Figure 9.33), the gravitational force is greatest causing bigger tides (so-called spring tides).

With the Sun and Moon disposed at 90° to the Earth, the gravitational pull on the Earth is weakest (the so-called neap tide). It is worth noting that tidal power is inexhaustible for all practical purposes (it is a *renewable energy resource*).[3] At any one moment in time, there are two high tides and two low tides around the Earth. One high tide occurs on the longitude closest to the Moon and the other on the longitude furthest from it. Of course, at the same time, the low tides are occurring at longitudes that are at 90° to those at which the high tides are occurring. The interval between high tide is about 12 h 25 min. The *tidal range* is the difference in height between high and low tides. In mid-ocean, the tidal range is between 0.5 and 1.0 m, but in the coastal regions the range can be significantly enhanced. In the Severn estuary (United Kingdom), the tidal range can be as much as 14 m and other shallow areas, e.g., the Bay of Fundy (Nova Scotia), the tidal range can exceed 13 m. Other coastal regions have enhanced tidal ranges and many are under consideration for the installation of tidal energy generators.

Several of these tidal generators have been installed for long-term evaluations and testing and recent commercial enterprises have produced successful results. Compared to wind and solar energy, tidal power has the great advantage of being entirely predictable.

[3] Williams (2000) records that tidal activity has caused a loss of mechanical energy in the Earth–Moon system due to pumping of water through natural restrictions around coastlines, to viscous dissipation at the seabed and in turbulence. Over the last 620 million years, this loss of energy is estimated to have caused the Earth's speed of rotation to slow down, the period of rotation is estimated to have increased from 21.9 h to the present 24 h. Energy taken from the tides by humankind would be insignificant on a world-scale and would have a negligible effect on the Earth's rotation.

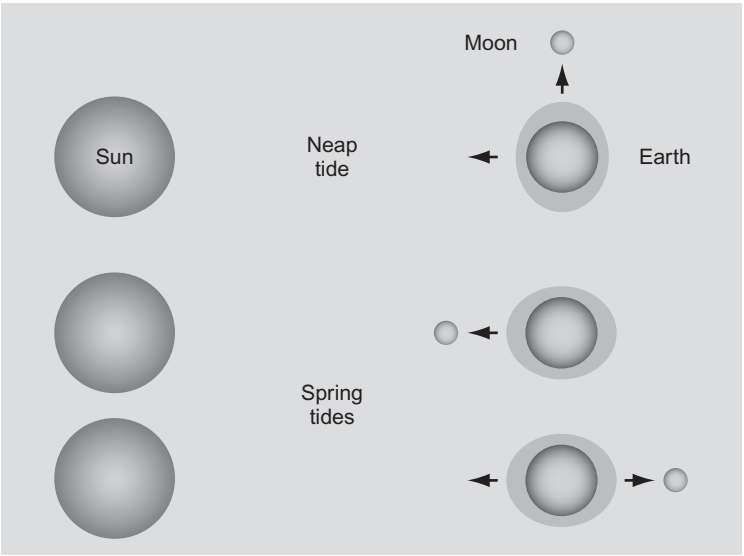

FIGURE 9.33

Sun, Moon, and Earth orientations causing spring and neap tides.

Categories of tidal power

There are two main types of tidal power generator:

a. tidal stream systems that use the kinetic energy of the water to power turbines;
b. barrages that make use of the potential energy of the water trapped between high and low tides.

Barrages are essentially dams stretching across the full width of a tidal estuary. Because of their very high civil engineering construction costs, the environmental problems they can cause, and also a worldwide lack of suitable sites (they require a minimum tidal range of at least 7 m for economic reasons), very few are likely to be made. The *La Rance scheme* in France, however, has been in operation since 1966. It was the first tidal barrage in the world, took 6 years to build, and provides an output of 240 MW. This type of tidal power generator is not considered any further.

Tidal stream generators

This is a relatively new technology and is still under development. It appears that the most successful approach is based on axial turbine practice. Since April 2007, Verdant Power has been running a demonstration project in the East River between Queens and Roosevelt Island in New York City. It is noted that the strength of the currents at that location has posed serious engineering

FIGURE 9.34

Strangford Lough, near Belfast, is about 25 km long. Roughly 1.8×10^6 m^3 of water flow in and out of the lough (loch) each day.

challenges: the blades of the 2006 and 2007 prototypes broke off. Because of the robust underwater environment they encounter, new stronger blades were installed in September 2008. Several other installations based on the axial turbine design have been tried out at Kvalsund in Norway (300 kW) in 2003, and the SeaGen project at Strangford Lough in Northern Ireland has proved successful and has been providing 1.2 MW to the grid.

The SeaGen tidal turbine

Strangford Lough, shown in Figure 9.34, is a large (150 km^2) shallow lagoon situated on the east coast of Northern Ireland, open to the sea. The entrance to the lough is a deep channel (the Narrows) about 8 km long and about 0.5 km wide. The currents through the Narrows are extremely strong and fast, reaching up to about 4 m/s at full flow. At the time this book was being prepared, little technical information had been released by the manufacturers about the SeaGen project, but using the data given and with the aid of actuator disk theory as applied to wind turbines (Chapter 10), some of the leading values of the operating parameters can be estimated. The background to the design philosophy, development, and testing of the pioneering "Seaflow Project,"

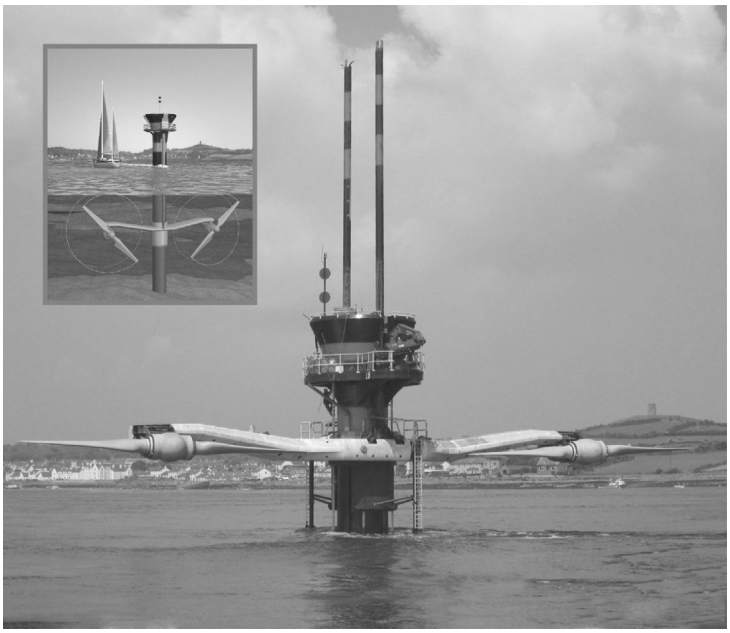

FIGURE 9.35

SeaGen tidal power generator.

(*With permission of Marine Current Turbines, Ltd.*)

which preceded SeaGen, and the preparation for the installation of SeaGen itself is described by Fraenkel (2007). A slightly later technical article by Douglas et al. (2008) gives a detailed assessment of the Seagen including the important information that the energy payback period is approximately 14 months and the CO_2 payback time is around 8 months.

Figure 9.35 shows the structural arrangement of SeaGen comprising two unshrouded axial-flow turbines, 16 m tip diameter, supported on a single beam. At the design speed, given as 14 rpm, each turbine provides 600 kW. The configuration of the turbines appears to be the same as that of horizontal axis wind turbines (HAWTs) studied in Chapter 10. The rotor blades can be pitched through 180″ to allow operation of the turbine on both the ebb and flood tides.

From the actuator disk theory used in Chapter 10, Eq. (10.15b), the turbine *hydrodynamic power output* is

$$P = \frac{1}{2}\rho A C_p c_{x1}^3$$

where A is the blade disk area, C_p is the power coefficient, ρ is the density of seawater, and c_{x1} is the velocity of the water approaching the turbine.

EXAMPLE 9.9

Determine the minimum flow speed of the water approaching the SeaGen tidal turbine in order for the full design power of 600 kW (for each turbine) to be achieved and also the blade tip−speed ratio. Assume the power coefficient $C_p = 0.3$,[4] the blade diameter is 16 m, and the density of seawater is 1025 kg/m^3.

Solution

From the preceding equation,

$$c_{x1}^3 = P/\left(\frac{1}{2}\rho A C_p\right) = P/\left(\frac{\pi}{8}\rho D^2 C_p\right) = \frac{600 \times 10^3}{\pi/8 \times 1025 \times 16^2 \times 0.3} = 19.41$$

Therefore,

$$c_{x1} = 2.69 \text{ m/s}$$

The blade tip speed is

$$U_t = \Omega r_t = \left(\frac{14}{30}\pi\right) \times 8 = 11.73 \text{ m/s}$$

Hence, the blade tip−speed ratio (when full power is reached) is

$$J = \frac{U_t}{c_{x1}} = \frac{11.73}{2.69} = 4.36$$

This value of blade tip−speed ratio conforms with the values found for HAWTs.

PROBLEMS

1. A generator is driven by a small, single-jet Pelton turbine designed to have a power specific speed $\Omega_{sp} = 0.20$. The effective head at nozzle inlet is 120 m and the nozzle velocity coefficient is 0.985. The runner rotates at 880 rpm, the turbine overall efficiency is 88%, and the mechanical efficiency is 96%. If the blade speed−jet speed ratio, $v = 0.47$, determine

- **a.** the shaft power output of the turbine;
- **b.** the volume flow rate;
- **c.** the ratio of the wheel diameter to jet diameter.

2. **a.** Water is to be supplied to the Pelton wheel of a hydroelectric power plant by a pipe of uniform diameter, 400 m long, from a reservoir whose surface is 200 m vertically above the nozzles. The required volume flow of water to the Pelton wheel is 30 m^3/s. If the pipe skin friction loss is not to exceed 10% of the available head and $f = 0.03$, determine the minimum pipe diameter.

[4]Values of C_p for horizontal axis wind turbines are normally found in the range 0.3−0.35. The Betz limit for C_p is 0.593.

b. You are required to select a suitable pipe diameter from the available range of stock sizes to satisfy the criteria given. The ranges of diameters (m) available are 1.6, 1.8, 2.0, 2.2, 2.4, 2.6, and 2.8. For the diameter you have selected, determine
   a. the friction head loss in the pipe;
   b. the nozzle exit velocity assuming no friction losses occur in the nozzle and the water leaves the nozzle at atmospheric pressure;
   c. the total power developed by the turbine assuming that its efficiency is 75% based upon the energy available at turbine inlet.

3. A multi-jet Pelton turbine with a wheel 1.47 m diameter operates under an effective head of 200 m at nozzle inlet and uses 4 m^3/s of water. Tests have proved that the wheel efficiency is 88% and the velocity coefficient of each nozzle is 0.99. Assuming that the turbine operates at a blade speed to jet speed ratio of 0.47, determine
   a. the wheel rotational speed;
   b. the power output and the power specific speed;
   c. the bucket friction coefficient given that the relative flow is deflected 165°;
   d. the required number of nozzles if the ratio of the jet diameter−mean diameter of the wheel is limited to a maximum value of 0.113.

4. A four-jet Pelton turbine is supplied by a reservoir whose surface is at an elevation of 500 m above the nozzles of the turbine. The water flows through a single pipe 600 m long, 0.75 m diameter, with a friction coefficient $f = 0.0075$. Each nozzle provides a jet 75 mm diameter and the nozzle velocity coefficient $K_N = 0.98$. The jets impinge on the buckets of the wheel at a radius of 0.65 m and are deflected (relative to the wheel) through an angle of 160°. Fluid friction within the buckets reduces the relative velocity by 15%. The blade speed−jet speed ratio $\nu = 0.48$ and the mechanical efficiency of the turbine is 98%. Calculate, using an iterative process, the loss of head in the pipeline and, hence, determine for the turbine
   a. the speed of rotation;
   b. the overall efficiency (based on the effective head);
   c. the power output;
   d. the percentage of the energy available at turbine inlet that is lost as kinetic energy at turbine exit.

5. A Francis turbine operates at its maximum efficiency point at $\eta_0 = 0.94$, corresponding to a power specific speed of 0.9 rad. The effective head across the turbine is 160 m and the speed required for electrical generation is 750 rpm. The runner tip speed is 0.7 times the spouting velocity, the absolute flow angle at runner entry is 72° from the radial direction, and the absolute flow at runner exit is without swirl. Assuming there are no losses in the guide vanes and the mechanical efficiency is 100%, determine
   a. the turbine power and the volume flow rate;
   b. the runner diameter;
   c. the magnitude of the tangential component of the absolute velocity at runner inlet;
   d. the axial length of the runner vanes at inlet.

6. The power specific speed of a 4 MW Francis turbine is 0.8, and the hydraulic efficiency can be assumed to be 90%. The head of water supplied to the turbine is 100 m. The runner vanes are radial at inlet and their internal diameter is three-quarters of the external diameter. The

meridional velocities at runner inlet and outlet are equal to 25% and 30%, respectively, of the spouting velocity. Determine

a. the rotational speed and diameter of the runner;
b. the flow angles at outlet from the guide vanes and at runner exit;
c. the widths of the runner at inlet and at exit.
Blade thickness effects can be neglected.

7. **a.** Review, briefly, the phenomenon of cavitation in hydraulic turbines and indicate the places where it is likely to occur. Describe the possible effects it can have upon turbine operation and the turbine's structural integrity. What strategies can be adopted to alleviate the onset of cavitation?

b. A Francis turbine is to be designed to produce 27 MW at a shaft speed of 94 rpm under an effective head of 27.8 m. Assuming that the optimum hydraulic efficiency is 92% and the runner tip speed−jet speed ratio is 0.69, determine

a. the power specific speed;
b. the volume flow rate;
c. the impeller diameter and blade tip speed.

c. A 1/10 scale model is to be constructed to verify the performance targets of the prototype turbine and to determine its cavitation limits. The head of water available for the model tests is 5.0 m. When tested under dynamically similar conditions as the prototype, the NPSH H_S of the model is 1.35 m. Determine for the model

a. the speed and the volume flow rate;
b. the power output, corrected using Moody's equation to allow for scale effects (assume a value for $n = 0.2$);
c. the suction specific speed Ω_{SS}.

d. The prototype turbine operates in water at 30°C when the barometric pressure is 95 kPa. Determine the necessary depth of submergence of that part of the turbine most likely to be prone to cavitation.

8. The preliminary design of a turbine for a new hydroelectric power scheme has under consideration a vertical-shaft Francis turbine with a hydraulic power output of 200 MW under an effective head of 110 m. For this particular design, a specific speed, $\Omega_s = 0.9$ (rad), is selected for optimum efficiency. At runner inlet the ratio of the absolute velocity to the spouting velocity is 0.77, the absolute flow angle is 68°, and the ratio of the blade speed to the spouting velocity is 0.6583. At runner outlet, the absolute flow is to be without swirl. Determine

a. the hydraulic efficiency of the rotor;
b. the rotational speed and diameter of the rotor;
c. the volume flow rate of water;
d. the axial length of the vanes at inlet.

9. A Kaplan turbine designed with a *shape factor* (power specific speed) of 3.0 (rad), a runner tip diameter of 4.4 m, and a hub diameter of 2.0 m operates with a net head of 20 m and a shaft speed of 150 rpm. The absolute flow at runner exit is axial. Assuming that the hydraulic efficiency is 90% and the mechanical efficiency is 99%, determine

a. the volume flow rate and shaft power output;
b. the relative flow angles at the runner inlet and outlet at the hub, at the mean radius and at the tip.

10. A hydroelectric power station is required to generate a total of 4.2 MW from a number of single-jet Pelton wheel turbines each operating at the same rotational speed of 650 rpm, at the same power output and at a power specific speed of 1.0 rev. The nozzle efficiency η_N of each turbine can be assumed to be 0.98, the overall efficiency η_o is assumed to be 0.88, and the blades speed to jet speed ratio v is to be 0.47. If the effective head H_E at the entry to the nozzles is 250 m, determine

a. the number of turbines required (round up the value obtained);
b. the wheel diameter;
c. the total flow rate.

11. **a.** In the previous problem, the reservoir surface is 300 m above the turbine nozzles and the water is supplied to the turbines by three pipelines, each 2 km long and of constant diameter. Using Darcy's formula, determine a suitable diameter for the pipes assuming the friction factor $f = 0.006$.

b. The chief designer of the scheme decides that a *single pipeline* would be more economical and that its cross-sectional area would need to be equal to the total cross-sectional area of the pipelines in the previous scheme. Determine the resulting friction head loss assuming that the friction factor remains the same and that the total flow rate is unchanged.

12. Sulzer Hydro Ltd. of Zurich at one time manufactured a six-jet vertical-shaft Pelton wheel turbine with a power rating of 174.4 MW, with a runner diameter of 4.1 m, and an operating speed of 300 rpm with an effective head of 587 m. Assuming the overall efficiency is 0.90 and the nozzle efficiency is 0.99, determine

a. the power specific speed;
b. the blade speed−jet speed ratio;
c. the volume flow rate.

Considering the values shown in Figure 9.2, comment on your result.

13. A vertical axis Francis turbine has a runner diameter of 0.825 m, operates with an effective head, $H_E = 6.0$ m, and produces 200 kW at the shaft. The rotational speed of the runner is 250 rpm, the overall efficiency is 0.90, and the hydraulic efficiency is 0.96. If the meridional (i.e., flow) velocity of the water through the runner is constant and equal to $0.4\sqrt{2gH_E}$ and the exit absolute flow is without swirl, determine the vane exit angle, the inlet angle of the runner vanes, and the runner height at inlet. Evaluate the power specific speed of the turbine and decide if the data given is consistent with the stated overall efficiency.

14. **a.** A prototype Francis turbine is to be designed to operate at 375 rpm at a power specific speed of 0.8 (rad), with an effective head of 25 m. Assuming the overall efficiency is 92%, the mechanical efficiency is 99%, the runner tip speed to jet speed ratio is 0.68, and the flow at runner exit has zero swirl, determine

i. the shaft power developed;
ii. the volume flow rate;
iii. the impeller diameter and blade tip speed;
iv. the absolute and relative flow angles at runner inlet if the meridional velocity is constant and equal to 7.0 m/s.

b. Using Thoma's coefficient and the data in Figure 9.21, investigate whether the turbine is likely to experience cavitation. The vertical distance between the runner and

the tailrace is 2.5 m, the atmospheric pressure is 1.0 bar, and the water temperature is 20°C.

15. For the previous problem, a 1/5 scale model turbine of the prototype is to be made and tested to check that the performance targets are valid. The test facility has an available head of 3 m. For the model, determine
a. the rotational speed and volume flow rate;
b. the power developed (uncorrected for scale).

16. A radial flow hydraulic turbine whose design is based on a power specific speed, $\Omega_{sp} = 1.707$ is to produce 25 MW from a total head, $H_E = 25$ m. The overall turbine efficiency $\eta_o = 0.92$, the mechanical efficiency is 0.985, and the loss in head in the nozzles is 0.5 m. The ratio of the blade tip speed to jet speed is 0.90. Assuming the meridional velocity is constant and equal to 10 m/s and there is no swirl in the runner exit flow, determine
a. the volume flow rate through the turbine;
b. the rotational speed and diameter of the runner;
c. the absolute and relative flow angles at entry to the runner.

17. An axial-flow hydraulic turbine operates with a head of 20 m at turbine entry and develops 10 MW when running at 250 rpm. The blade tip diameter is 3 m, the hub diameter is 1.25 m, and the runner design is based upon a "free vortex." Assuming the hydraulic efficiency is 94%, the overall efficiency is 92%, and the flow at exit is entirely axial, determine the absolute and relative flow angles upstream of the runner at the hub, mean, and tip radii.

18. **a.** A model of a Kaplan turbine, built to a scale of 1/6 of the full-scale prototype, develops an output of 5 kW from a net head of 1.2 m of water at a rotational speed of 300 rpm and a flow rate of 0.5 m^3/s. Determine the efficiency of the model.
b. By using the scaling laws, estimate the rotational speed, flow rate, and power of the prototype turbine when running with a net head of 30 m.
c. Determine the power specific speed for both the model and the prototype, corrected with Moody's equation. To take account of the effects of size (scale), use the Moody formula

$$(1 - \eta_p) = (1 - \eta_m)(D_m/D_p)^{0.25}$$

to estimate the full-scale efficiency, η_p, and the corresponding power.

19. A Pelton wheel turbine rotates at 240 rpm, has a pitch diameter of 3.0 m, a bucket angle of 165°, and a jet diameter of 5.0 cm. If the jet velocity at nozzle exit is 60 m/s and the relative velocity leaving the buckets is 0.9 times that at entry to the buckets, determine
a. the force acting on the buckets;
b. the power developed by the turbine.

References

Addison, H. (1964). *A treatise on applied hydraulics* (5th ed.London: Chapman and Hall.

Douglas, C. A., Harrison, G. P., & Chick, J. P. (2008). Life Cycle Assessment of the Seagen marine current turbine. *Proceedings of the Institution of Mechanical Engineers for the Maritime Environment*, *222*(*1*)(An online version of the article can be found at: http://pim.sagepub.com/content/222/1/1).

Drtina, P., & Sallaberger, M. (1999). Hydraulic turbines—basic principles and state-of-the-art computational fluid dynamics applications. Proceedingsof the Institution of Mechanical Engineers, *Part C*, *213*, 85−102.

Fraenkel, P. L. (2007). Marine current turbines: Pioneering the development of marine kinetic energy converters, *Proceedings of the Institution of Mechanical Engineers, 221*, Part A: *Journal of Power and Energy* Special Issue Paper.

Franzini, J. B., & Finnemore, E. J. (1997). *Fluid mechanics with engineering applications.* New York, NY: McGraw-Hill.

Gato, L. M. C., & de O Falcao, A. F. (1984). On the theory of the Wells turbine. *Journal of engineering for gas turbines and power*, *106*(3), 628−633.

Kim, T. H., Takao, M., Setoguchi, T., Kaneko, K., & Inoue, M. (2001). Performance comparison of turbines for wave power conversion. *International Journal of Thermal Science*, *40*, 681−689.

Kim, T. H., et al. (2002). Study of turbine with self-pitch-controlled blades for wave energy conversion. *International Journal of Thermal Science*, *41*, 101−107.

Massey, B. S. (1979). *Mechanics of fluids* (4th ed.New York, NY: Van Nostrand.

McDonald, A. T., Fox, R. W., & van Dewoestine, R. V. (1971). Effects of swirling inlet flow on pressure recovery in conical diffusers. *AIAA Journal*, *9*(10), 2014−2018.

Moody, L. F., & Zowski, T. (1969). Hydraulic machinery. In C. V. Davis, & K. E. Sorensen (Eds.), *Handbook of applied hydraulics* (3rd ed.). New York, NY: McGraw-HillSection 26.

Raabe, J. (1985). *Hydro power. The design, use, and function of hydromechanical, hydraulic, and electrical equipment* Germany: VDI Verlag, Düsseldorf.

Raghunathan, S. (1995). A methodology for Wells turbine design for wave energy conversion. *Proceedings of the Institution of Mechanical Engineers*, *209*, 221−232.

Raghunathan, S., Curran, R., & Whittaker, T. J. T. (1995). Performance of the Islay wells air turbine. *Proceedings of the Institution of Mechanical Engineers*, *209*, 55−62.

Raghunathan, S., Setoguchi, T., & Kaneko, K. (1987). The well turbine subjected to inlet flow distortion and high levels of turbulence. *Heat and Fluid Flow*, *8*(2).

Rogers, G. F. C., & Mayhew, Y. R. (1995). *Thermodynamic and transport properties of fluids* (5th ed., (*SI Units*)). Malden, MA: Blackwell, (*SI Units*).

Salter, S. H. (1993). Variable pitch air turbines. *Proceedings of the European wave energy symposium*. Edinburgh, pp. 435−442.

Sarmento, A. J. N. A., Gato, L. M., & de O Falcào, A. F. (1987). Wave-energy absorption by an OWC device with blade-pitch controlled air turbine. *Proceedings of the Sixth International Offshore Mechanics and Arctic Engineering Symposium, American Society of Mechanical Engineers*, *2*, 465−473.

Stelzer, R. S. & Walters, R. N. (1977), *Estimating reversible pump-turbine characteristics*. Engineering Monograph No. 39 A Water Resources Technical Publication, U.S. Department of the Interior.

Wells, A. A. (1976). Fluid driven rotary transducer. British Patent 1595700.

White, F. M. (2011). *Fluid mechanics.* New York, NY: McGraw-Hill.

Williams, G. E. (2000). Geological constraints on the Precambrian history of the earth's rotation and the moon's orbit. *Reviews of geophysics*, *38*, 37−60.

Yedidiah, S. (1981). The meaning and application-limits of Thoma's cavitation number. In J. W. Hoyt (Ed.), Cavitation and polyphase flow forum—198 (*1*, pp. 45−46). New York, NY: American Society of Mechanical Engineers.

Young, F. R. (1989). *Cavitation* New York, NY: McGraw-Hill.

CHAPTER

Wind Turbines

10

Take care your worship, those things over there are not giants but windmills.
M. Cervantes, *Don Quixote*, Part 1, Chapter 8

Like a circle in a spiral
Like a wheel within a wheel
Never ending or beginning
On an ever spinning reel
As the images unwind
Like the circles
That you find
In the windmills of your mind!
Lyric: The Windmills of your Mind (Legrande/Bergman/Bergman)

10.1 Introduction

A modern wind turbine is a machine which converts the power available in the wind into electricity. On the other hand, a windmill is a machine which was used to convert wind power to mechanical power. As generators of electricity, wind turbines are usually connected into some form of electrical network and the larger turbines can form a part of the electrical grid. The largest size single turbines used for this purpose can have an output of around 5−6 MW.

Over the past four decades, there has been a remarkable growth in global installed generating capacity. The data given in Figure 10.1 obtained from statistics published by the *Global Wind Energy Council* (GWEC), the *European Wind Energy Association* (EWEA), the *American Wind Energy Association* (AWEA), and others shows the regional and worldwide growth of installed wind power capacity up to the end of 2011. It is interesting to note that the global wind power capacity is now still doubling every 3 years. The biggest regional contributors to this installed growth in wind power are the Peoples Republic of China. According to the GWEC, the development of wind energy in China in terms of scale is absolutely unparalleled in the world. By the end of 2010, the installed wind power capacity had reached 41.8 GW. Up to May 2009, 80 countries around the world contributed to the generation of wind power on a commercial scale. Predicting the growth of wind power generation is far from reliable. At the end of 2011, the total worldwide wind power capacity had reached 237 GW.

Fluid Mechanics and Thermodynamics of Turbomachinery. DOI: http://dx.doi.org/10.1016/B978-0-12-415954-9.00010-3

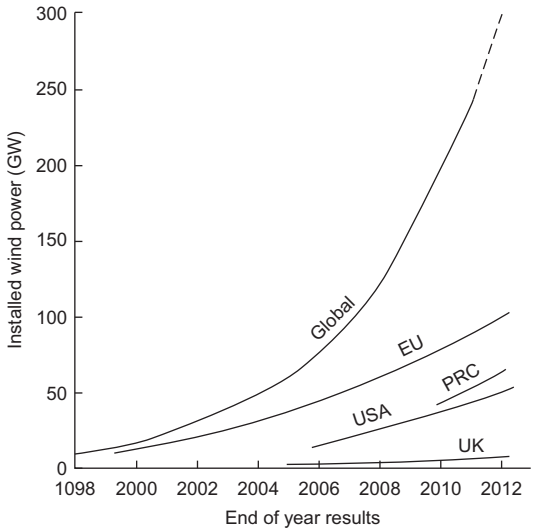

FIGURE 10.1

Installed wind power capacity (global and of some selected countries).

An interesting paper which considers the potential of wind power as a global source of electricity has been presented by Xi, McElroy, and Kiviluoma (2009). The analysis indicates that a network of land based 2.5 MW wind turbines restricted to land based, nonforested, ice free, nonurban areas and operating as little as 20% of their rated capacity could supply more than 40 times the current world capacity of electricity.

Wind characteristics and resource estimation

The Earth receives more energy from the Sun at the equator than at the poles. Dry land heats up (and cools down) more quickly than the oceans. This differential heating and cooling, which is greatest near the equator, drives an atmospheric convection system extending from sea level to the upper atmosphere. The warm air rises, circulates in the atmosphere, and gradually sinks back to the surface in the cooler regions. At the upper levels of the atmosphere, continuous wind speeds are known to exceed 150 km/h. The large-scale motion of the air at altitude causes a circulation pattern with well-known features at sea level such as the trade winds.

The most striking characteristic of wind energy is its variability both spatially and temporally. The variability depends on many factors: climatic region, topography, season of the year, altitude, type of local vegetation, etc. Topography and altitude have a major influence on wind strength. The strength of wind on the high ground and mountain tops is greater than in the sheltered valleys. Coastal regions are often windier than further inland because of the difference in heating between land and sea. The use of available wind resource data is clearly of some importance. Studies have been made in the United States, Europe, and many parts of the world that give an indication of the wind resource (in W/m^2) for many locations. In is not feasible (in this book) to give a sensible

coverage of these extensive results, but an indication is given for some of the chief organizations which give detailed resource references. These are:

1. For world summaries:
   Singh, S., Bhatti, T.S., & Kothari, D.P. (2006). A review of wind-resource-assessment technology. *Journal of Energy Engineering*, *132*(1), 8−14.
   Elliot, D.L. (2002). Assessing the world wind resource. *Power Engineering Review*, *IEEE*, *22*(9).
2. For the United States:
   Elliot, D.L., & Schwartz, M. (2004). *Validation of Updated State Wind Resource Maps for the United States*, NREL/CP−500−36200.
3. For Europe:
   Troen, I., & Petersen, E.L. (1989). *European Wind Atlas*, Risø National Laboratory, Denmark.

A significant change has now taken place with the location and rapid building of many wind turbines in coastal waters. Despite the difficult installation environment and increased cost, the main advantages arise from the significantly higher wind speeds and lower wind turbulence. Often centers of population and industry are situated close to coasts so that the cost of electrical transmission is reduced by the more likely shorter distances required by their supply lines.

At any given location temporal variability can mean that the magnitude and amount of the wind strength can change from 1 year to the next. The cause of these changes are still not well understood but may be generated by large-scale variations in weather systems and ocean currents.

The proper design and size of a wind turbine will depend crucially upon the site under consideration having a favorable wind. Briefly, to be *favorable*, the wind would need to be of sufficient strength and duration at an acceptable height. For the locations being considered as possible sites, extended anemometric surveys (lasting over at least a year) are needed to determine the nature of the wind speed distribution with respect to time and height above the ground. These surveys are generally carried out at a fairly standard height of 30 m above the ground and, when required, some sort of extrapolation is made for estimating wind speeds at other heights.[1] To assess the frequency of the occurrence of wind speeds at a site, a probability distribution function is often employed to fit the observed data. Several types of these distribution functions are commonly used:

i. the simple single-parameter *Rayleigh distribution*;
ii. the complicated but slightly more accurate, two-parameter *Weibull distribution*.

From these data, estimates of power output for a range of turbine designs and sizes can be made. Wind turbine rotors have been known to suffer damage or even destruction from excessive wind speeds and obviously this aspect requires very careful consideration of the worst-case wind conditions so the problem may be avoided.

[1]The NREL has developed an automated method for wind resource mapping in order to quickly generate wind data. Their mapping technique is based on known empirical relationships between the "free-air" wind speed, 100−200 m above the surface, and the actual surface. A so-called "top-down" method is then used to determine the free-air velocity profiles down to the surface (Schwartz, 1999).

An important issue concerning the installation of wind power plants involves their environmental impact. Walker and Jenkins (1997) have outlined the most significant benefits for installing wind turbines as well as the reasons put forward to counter their installation. It is clear that the benefits include the reduction in the use of fossil fuels, leading to a reduction in the emission of pollutants (the most important of these being the oxides of carbon, sulfur, and nitrogen). Any emissions caused by the manufacture of the wind turbine plant itself are offset after a few months of emission-free operation. Similarly, and importantly, the energy expended in the manufacture of a wind turbine, according to the World Energy Council (1994), is paid back after about a year's normal productive operation.

Historical viewpoint

It may be of interest to mention a little about how the modern wind turbine evolved. Of course, the extraction of mechanical power from the wind is an ancient practice dating back at least 3000 years. Beginning with sailing ships, the technical insight gained from them was somehow extended to the early windmills for the grinding of corn, etc. Windmills are believed to have originated in Persia in the seventh century and, by the twelfth century, their use had spread across Europe. The design was gradually improved, especially in England during the eighteenth century where millwrights developed remarkably effective self-acting control mechanisms. A carefully preserved brick built tower windmill, shown in Figure 10.2, a classic version of this type, still exists on Bidston Hill near Liverpool, United Kingdom, and was used to grind corn into flour for 75 years up until 1875. It has now become a popular historical attraction.

The wind pump was first developed in Holland for drainage purposes, while in the United States, the deep-well pump was evolved for raising water for stock watering. Most windmills employ a rotor with a near horizontal axis, the sails were originally of canvas, a type still in use today in Crete. The English windmill employed wooden sails with pivoted slats for control. The US wind pump made use of a large number of sheet-metal sails (Lynette and Gipe, 1998). The remarkable revival of interest in modern wind-powered machines appears to have started in the 1970s because of the so-called fuel crisis. A most interesting brief history of wind turbine design is given by Eggleston and Stoddard (1987). Their focus of attention was the use of wind power for generating electrical energy rather than mechanical energy. A rather more detailed history of the engineering development of windmills from the earliest times leading to the introduction of the first wind turbines is given by Manwell et al. (2009).

10.2 Types of wind turbine

Wind turbines fall into two main categories: those that depend upon aerodynamic drag to drive them (i.e., the old style windmills) and those that depend upon aerodynamic lift. Drag machines such as those developed in ancient times by the Persians were of very low efficiency compared with modern turbines (employing lift forces) and so are not considered any further in this chapter.

The design of the modern wind turbine is based upon aerodynamic principles, which are elaborated later in this chapter. The rotor blades are designed to interact with the oncoming airflow so that an aerodynamic lift force is developed. A drag force is also developed but, in the normal range

FIGURE 10.2

Tower Windmill, Bidston, Wirral, UK (ca. 1875).

of prestall operation, this will amount to only about 1% or 2% of the lift force. The lift force, and the consequent positive torque produced, drives the turbine thereby developing output power.

In this chapter, the focus of attention is necessarily restricted to the aerodynamic analysis of the *horizontal axis wind turbine* (HAWT) although some mention is given of the *vertical axis wind turbine* (VAWT). The VAWT, also referred to as the *Darrieus turbine* after its French inventor in the 1920s, uses vertical and often slightly curved symmetrical aerofoils. Figure 10.3(a) shows a general view of the very large 4.2 MW vertical axis Darrieus wind turbine called the *Eole*́ VAWT installed at Cap-Chat, Quebec, Canada, having an effective diameter of 64 m and a blade height of 96 m.

Figure 10.3(b), from Richards (1987), is a sketch of the major components of this aptly named *eggbeater* wind turbine. Guy cables (not shown) are required to maintain the turbine erect. This

type of machine has one distinct advantage: it can operate consistently without regard to wind direction. However, it does have a number of major disadvantages:

- **i.** wind speeds are low close to the ground so that the lower part of the rotor is rather less productive than the upper part;
- **ii.** high fluctuations in torque occur with every revolution;
- **iii.** negligible self-start capability;
- **iv.** limited capacity for speed regulation in winds of high speed.

Darrieus turbines usually require mechanical power input to start them but have been known to self-start. (Several VAWTs have been destroyed by such self-starts.) For assisted starting, the method used is to run the generator as a motor up to a speed when aerodynamic wind forces can take over. Stopping a VAWT in high winds is difficult as aerodynamic braking has not been successful and friction braking is needed.

According to Ackermann and Söder (2002), VAWTs were developed and produced commercially in the 1970s until the 1980s. Since the end of the 1980s, research and development on VAWTs has virtually ceased in most countries, apart from Canada (see Gasch, 2002; Walker & Jenkins, 1997; Divone, 1998).

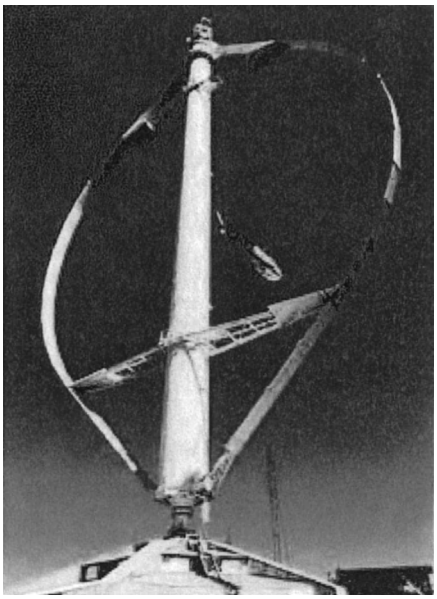

(a)

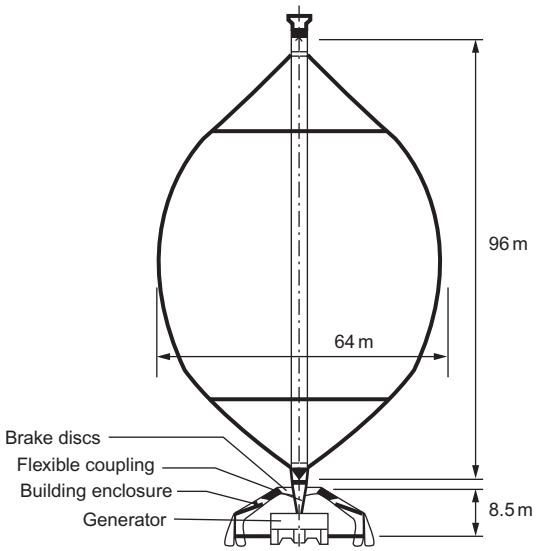

(b)

FIGURE 10.3

(a) The 4 MW Eolé VAWT installed at Cap-Chat, Quebec; (b) sketch of VAWT Eolé showing the major components, including the direct-drive generator.

(*Courtesy AWEA*)

Large HAWTs

The HAWT type is currently dominant in all large-scale applications for extracting power from the wind and seems likely to remain so. The large HAWT, Figure 10.4(a), operating at Barrax, Spain, is 104 m in diameter and can generate 3.6 MW. (This size of wind turbine has become fairly commonplace, especially in the coastal waters around Great Britain.) Basically, a HAWT comprises a nacelle mounted on top of a high tower, containing a generator and, usually, a gearbox to which the rotor is attached. Increasing numbers of wind turbines do not have gearboxes but use a direct drive. A powered *yaw system* is used to turn the turbine so that it faces into the wind. Sensors monitor the wind direction and the nacelle is turned according to some integrated average wind direction. The number of rotor blades employed depends on the purpose of the wind turbine. As a rule, three-bladed rotors are used for the generation of electricity. Wind turbines with only two or three blades have a high ratio of blade tip speed to axial flow velocity (the tip−speed ratio), but only a

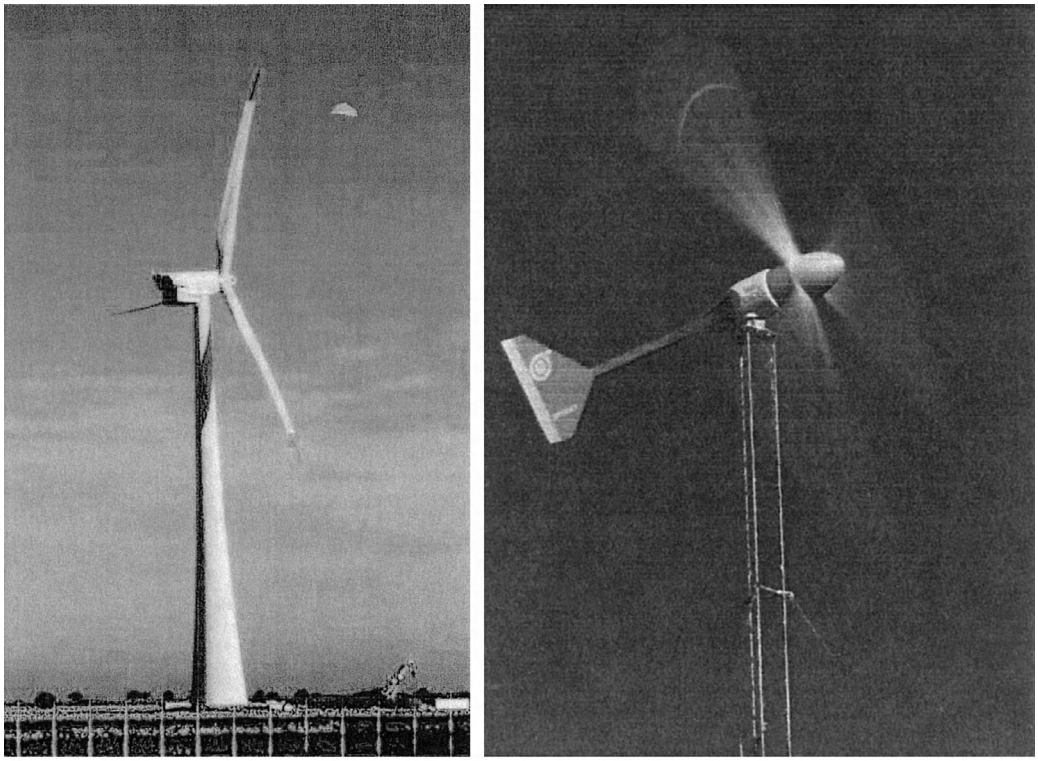

(a) (b)

FIGURE 10.4

(a) First general electric baseline HAWT, 3.6 MW, 104 m diameter, operating at Barrax, Spain, since 2002.
(b) The Bergey Excel-S, three-bladed, 7 m diameter wind turbine, rated at 10 kW at wind speed of 13 m/s.
(*(a) Courtesy US DOE; (b) with permission of Bergey Windpower Company*)

low starting torque and may even require assistance at startup to bring it into the useful power producing range of operation. Commercial turbines range in capacity from a few hundred kilowatts to more than 3 MW. The crucial parameter is the diameter of the rotor blades, the longer the blades, the greater is the "swept" area and the greater the possible power output. Rotor diameters now range to over 100 m. The trend has been toward larger machines as they can produce electricity at a lower price. Most wind turbines of European origin are made to operate upwind of the tower, i.e., they face into the wind with the nacelle and tower downstream. However, there are also wind turbines of downwind design, where the wind passes the tower before reaching the rotor blades. Advantages of the upwind design are that there is little or no tower "shadow" effect and lower noise level than the downwind design.

Small HAWTs

Small wind turbines with a horizontal axis were developed in the nineteenth century for mechanical pumping of water, e.g., the American farm pump. The rotors had 20 or more blades, a low tip−speed ratio but a high starting torque. With increasing wind speed pumping would then start automatically. According to Baker (1985), the outgrowth of the utility grid caused the decline of the wind-driven pump in the 1930s. However, there has been a worldwide revival of interest in small HAWTs of modern design for providing electricity in remote homes and isolated communities that are "off grid." The power output of such a wind-powered unit would range from about 1 to 50 kW. Figure 10.4(b) shows the Bergey Excel-S, which is a three-blade upwind turbine rated at 10 kW at a wind speed of 13 m/s. This is currently America's most popular residential and small business wind turbine.

Effect of tower height

An important factor in the design of HAWTs is the tower height. The wind speed is higher the greater the height above the ground. This is the meteorological phenomenon known as *wind shear*. This common characteristic of wind can be used to advantage by employing wind towers with increased hub heights to capture more wind energy. A study by Livingston and Anderson (2004) investigated the wind velocities at heights up to 125 m on the Great Plains (United States) and provide a compelling case for operating wind turbines with hub heights of at least 80 m. Typically, for daytime temperatures, the variation follows the wind profile one-seventh power law (i.e., wind speed increases proportionally to the one-seventh root of height above the surface):

$$c_x/c_{x,\text{ref}} = (h/h_{\text{ref}})^n$$

where c_x is the wind speed at height h, $c_{x,\text{ref}}$ is the known wind speed at a reference height h_{ref}. The exponent n is an empirically derived coefficient. In a neutrally stable atmosphere and over open ground (the normal condition), $n \approx 1/7$ or 0.143. Over open water, a more appropriate coefficient is $n \approx 0.11$. As an example, it is required to estimate the wind speed at a height of 80 m above the ground using a reference velocity of 15 m/s measured at a hub height of 50 m:

$$c_x = 15(80/50)^{0.143} = 16.04 \text{ m/s}$$

Even a small increase in wind speed can be important. It is shown later that the possible power extracted from the wind varies as the cube of the wind speed. Using this example, the increase in the power extracted would be over 22% as a result of increasing the hub height from 50 to 80 m. Of course, there is a penalty as costs will be greater for the stronger tower structure required.

10.3 Performance measurement of wind turbines

Wind turbine performance relates to the energy availability in the wind at the turbines site. The wind can be described by a probability density distribution of turbulence of various frequencies superimposed on a momentarily steady component. The turbulent wind will have longitudinal, lateral, and vertical components of velocity. In this basic description of the wind, we will be concerned only with its longitudinal component c which will normally be parallel to the axis of rotation of the turbine. In the short term, the speed of the wind is to be considered as a steady component $\overline{c}$ and a fluctuating component c', i.e., $c = \overline{c} + c'$.

Wind speed probability density function

From measurements of wind speeds at any one location and over a long enough period of time, it becomes apparent that the wind speed is more likely to be closer to a mean value than far from it. Also, the measured values will, in all probability, be as much above the mean as below it. The probability density function (p.d.f.) that best fits in with this type of erratic behavior of turbulence is called the *Gaussian probability density distribution* (or normal distribution).

The normal p.d.f. for continuously collected data is given by:

$$p(c) = \frac{1}{\sigma_c\sqrt{2\pi}}\exp\left[-\frac{(c-\overline{c})^2}{2\sigma_c^2}\right]$$

where $\sigma_c^2 = (1/N_s - 1)\sum_{i=1}^{N_s}(c_i - \overline{c})^2$, σ_c is the standard deviation and N_s is the number of readings taken over a time interval of (say) 10 s to determine the short-term wind speed, $c = (1/N_s)\sum_{i=1}^{N_s} c_i$.

Figure 10.5 shows a sample histogram of the wind speeds varying about a mean wind speed. The Gaussian p.d.f. that represents this data is shown drawn onto this histogram.

Prediction of power output. The power output of a wind turbine is obviously a function of the wind speed. We will find that every wind turbine has its own characteristic power curve. From this curve, it is possible to predict the energy output without having to refer to more detailed information about the individual components of the turbine. Figure 10.6 shows the power output curve of a hypothetical wind turbine as a function of the wind speed at hub height.

There are three important key factors included in this diagram and which are applicable to all wind turbines. These are:

1. *Cut-in wind speed*: This is the minimum wind speed that the turbine can deliver useful power. It is usually between 3 and 4 m/s.
2. *Cut-out wind speed*: This is the maximum wind speed that the turbine can safely deliver power. This is a positive limit set by the stresses in the turbine components. If this limit is reached, the control system activates the braking system which brings the rotor to rest.

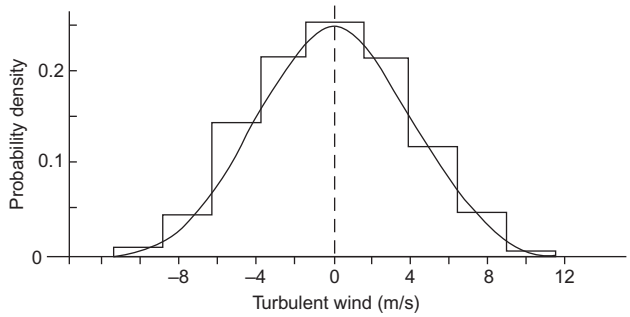

FIGURE 10.5

Gaussian p.d.f. fitted to a sample of wind speed data.

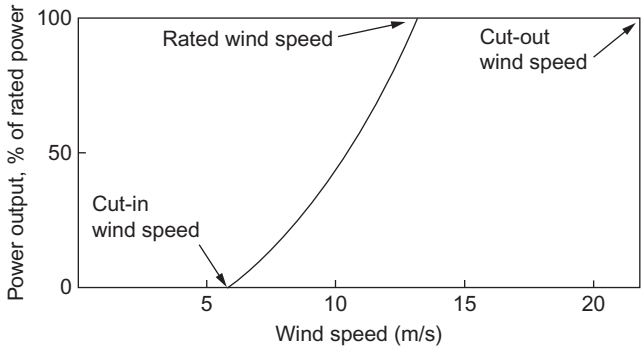

FIGURE 10.6

Idealized power output curve for a wind turbine.

3. *Rated output power and rated output wind speed*: The electrical power output increases rapidly with wind speed. However, usually between 14 and 17 m/s, the maximum permitted power limit of the generator is reached. The rated output power and the corresponding wind speed is called the rated output wind speed. At higher wind speeds, the power output is kept constant by the control system making adjustment of the blade angles.

The kinetic power available in the wind is

$$P_0 = \frac{1}{2}\rho A_2 c_{x1}^3$$

where A_2 is the disc area and c_{x1} is the velocity upstream of the disc. The ideal power generated by the turbine can therefore be expected to vary as the cube of the wind speed. Figure 10.6 shows the idealized power curve for a wind turbine, where the preceding cubic "law" applies between the *cut-in* wind speed and the *rated wind speed* at which the maximum power is first reached. The rated wind speed often corresponds to the point at which the efficiency of energy conversion is close to its maximum.

Storing energy

Because of the intermittency of wind and the unavailability at times of the required energy, it is often claimed by opponents of wind turbines that it is better to rely on other sources of power. Clearly, some form of energy storage can be devised. For instance, in Spain more than 13.8 GW of wind power capacity has been installed, providing about 10% of that country's electricity needs, according to *Renewable Energy World* (September–October, 2009). At *Iberdrola*, *Spain*, a pumped storage scheme (852 MW) is now being used to store the excess wind turbine energy and three further pumped storage plants are likely to be built with a total capacity of 1.64 GW.

In the following sections, the aerodynamic theory of the HAWT is gradually developed, starting with the simple 1D momentum analysis of the actuator disc and followed by the more detailed analysis of the blade element theory. The flow state just upstream of the rotor plane forms the so-called inflow condition for the rotor blades and from which the aerodynamic forces acting on the blades can be determined. The highly regarded blade element momentum (BEM) method[2] is outlined and used extensively. A number of worked examples are included at each stage of development to illustrate the application of the theory. Detailed calculations using the BEM method were made to show the influence of various factors, such as the tip–speed ratio and blade number on performance. Further development of the theory includes the application of Prandtl's tip loss correction factor, which corrects for a finite number of blades. Glauert's optimization analysis is developed and used to determine the ideal blade shape for a given lift coefficient and to show how the optimum rotor power coefficient is influenced by the choice of tip–speed ratio.

Calculating the maximum possible power production of a wind turbine

This method of calculation, devised by Carlin (1997), is based on the Rayleigh probability energy distribution for a HAWT of a given size and determines the maximum possible average power for a given average wind speed $\overline{c}$.

The average wind power produced by the turbine is given by:

$$\overline{P}_{\mathrm{W}} = \frac{1}{2}\rho\frac{\pi}{4}D^2\eta\int_0^{\infty} C_{\mathrm{p}}(\lambda)c^3 p(c)\mathrm{d}c$$

where $\lambda =$ (blade tip speed/wind speed) $= (\Omega R/c)$ and η is the mechanical efficiency of the turbine.

The average machine wind power assuming the Rayleigh distribution applies is

$$\overline{P}_{\mathrm{W}} = \frac{\pi}{8}\rho D^2\eta\int_0^{\infty} C_{\mathrm{p}}(\lambda)c^3\left\{\frac{2c}{c_{\mathrm{c}}^2}\exp\left[-\left(\frac{c}{c_{\mathrm{c}}}\right)^2\right]\right\}\mathrm{d}c$$

where $c_{\mathrm{c}} = 2\overline{c}/\sqrt{\pi}$ is a characteristic wind velocity obtained from the average wind speed, $\overline{c}$.

[2]Details are given in Section 10.8.

Some simplifications can now be made by assuming that the efficiency, $\eta = 1$ and the power coefficient is replaced by the maximum value of the Betz coefficient, $C_{\mathrm{p,Betz}} = 16/27$. This form of the turbine power is the average *idealized* wind turbine power, $P_{W,\mathrm{id}}$

$$\therefore P_{W,\mathrm{id}} = \frac{\pi}{8}\rho D^2 c_{\mathrm{c}}^3 C_{\mathrm{p,Betz}} \int_0^{\infty} \left(\frac{c}{c_{\mathrm{c}}}\right)^3 \left\{\frac{2c}{c_{\mathrm{c}}} \exp\left[-\left(\frac{c}{c_{\mathrm{c}}}\right)^2\right]\right\} \frac{\mathrm{d}c}{c_{\mathrm{c}}}$$

It is usual to further simplify the above equation by the use of a dimensionless wind speed $x = c/c_{\mathrm{c}}$. Hence, we get:

$$\overline{P}_{W,\mathrm{id}} = \frac{\pi}{8}\rho D^2 c_{\mathrm{c}}^3 C_{\mathrm{p,Betz}} \int_0^{\infty} x^3 \left\{2x \exp\left[-(x^2)\right]\right\} \mathrm{d}x$$

The above integral can be easily evaluated and is $(3/4)\sqrt{\pi}$ and so the equation for the averaged *maximum* possible power becomes

$$\overline{P}_{W,\mathrm{id}} = \rho\left(\frac{2}{3}D\right)^2 \overline{c}^3$$

which may be worth remembering. You are reminded that this result is for an idealized wind turbine without losses, the value of C_{p} is assumed to be at the Betz limit and the wind speed probability is given by the Rayleigh distribution.

EXAMPLE 10.1

Determine the annual average energy production (AEP) of a 30 m diameter HAWT for a location at sea level with an annual average wind speed of (a) 6 m/s, (b) 8 m/s, (c) 10 m/s.

Assume that the air density is 1.25 kg/m^3. Assume also that the efficiency is 100% and that $C_{\mathrm{p}} = 0.5926$ (the Betz maximum).

Solution

$$\overline{P}_{\mathrm{W}} = 1.25 \times ((2/3) \times 30)^2 \times c^3 = 500 \times c^3, \text{ hence}$$

a.

$$\overline{P}_{\mathrm{W}} = 108 \text{ kW} \quad \therefore \mathrm{AEP} = 8760 \times 108 = 946 \text{ MWh}$$

b.

$$\overline{P}_{\mathrm{W}} = 256 \text{ kW} \quad \therefore \mathrm{AEP} = 2243 \text{ MWh}$$

c.

$$\overline{P}_{\mathrm{W}} = 500 \text{ kW} \quad \therefore \mathrm{AEP} = 4380 \text{ MWh}$$

Some considerable loss of power can be expected because we have taken $\eta = 1$ and $C_{\mathrm{p}} = 16/27$ as the maximum value given by Betz's theory.

10.4 Annual energy output

The cost effectiveness of a wind turbine is determined by its *average* production of energy over a year. (Of course, some allowance must be made for installation and running costs.) Determining the annual energy output requires detailed information about the *wind speed frequency distribution*, derived from detailed measurements of the wind speed variation at the actual site of the wind turbine. For a HAWT, it is necessary to measure the varying wind speed at the elevation of the turbine's hub over a long period of time, usually over at least a year. The usual procedure adopted is to make these varying wind speed measurements over relatively short time intervals, say 5 min and the averaged values are stored in what are called "wind speed bins." This "*method of bins*" is widely adopted as a reliable way of summarizing wind data.[3]

10.5 Statistical analysis of wind data

Basic equations

The frequency of the occurrence of wind speeds can be described by a *p.d.f.* $p(c)$, of the wind speed c. The probability of a particular value of a wind speed occurring between c_a and c_b may be expressed as

$$p_{a\to b} = \int_{c_a}^{c_b} p(c)\mathrm{d}c$$

and the mean wind speed, $\overline{c} = \int_0^\infty cp(c)\mathrm{d}c$.

The total area under the p.d.f. is

$$\int_0^\infty p(c)\mathrm{d}c = 1$$

and the mean wind speed, $\overline{c} = \int_0^\infty cp(c)\mathrm{d}c$.

The mass flow of air of density ρ passing through a rotor disc of area A with a velocity c (assumed constant) is given by:

$$\frac{\mathrm{d}m}{\mathrm{d}t} = \rho A c$$

[3]Empirical relationships have been found by NREL (see Schwartz, 1999) for well-exposed locations with low surface roughness in diverse parts of the world. Accordingly, the wind resource values presented on NREL maps are for nonsheltered locations with low surface roughness (e.g., short grasslands). NREL uses a so called "top-down" method in the adjustment of much of the available wind resource data. In other words, The NREL approach uses the *free-air wind profile* in the lowest few hundred meters above the surface and adjusts it down to the surface. The NREL took this "top-down" approach because of the many data reliability problems regarding data from many parts of the world. For example, a few of the problems indicated apparently relate to a lack of information about observation procedures, anemometer hardware calibration, height, exposure, and maintenance history.

The kinetic energy per unit time, or wind power of the flow, is

$$P = \frac{1}{2}\frac{\mathrm{d}m}{\mathrm{d}t}U^2 = \frac{1}{2}\rho A c^3 \tag{10.1a}$$

Hence, the mean available wind power is

$$\overline{P} = \frac{\rho A}{2}\int_0^\infty c^3 p(c)\mathrm{d}c = \frac{\rho A}{2}\overline{c^3} \tag{10.1b}$$

Wind speed probability distributions

For the statistical analysis of wind speed distributions, two types of flow model are in use. These are

1. the Rayleigh Distribution;
2. the Weibull Distribution.

The simplest velocity probability distribution for the wind resource is the so-called *Rayleigh distribution* as it only requires knowledge of one parameter namely the mean wind speed $\overline{c}$.

The Rayleigh probability distribution is written as

$$p(c) = \frac{\pi}{2}\left(\frac{c}{\overline{c}^2}\right)\exp\left[-\frac{\pi}{4}\left(\frac{c}{\overline{c}}\right)^2\right]$$

and the cumulative distribution factor is

$$F(c) = 1 - \exp\left[-\frac{\pi}{4}\left(\frac{c}{\overline{c}}\right)^2\right]$$

Figure 10.7 illustrates Rayleigh probability density distributions for a range of different mean wind speeds. It is implied that a bigger value of the mean wind speed gives a higher probability of higher wind speeds. The cumulative distribution function $F(c)$ represents the time fraction that the wind speed is smaller than or equal to a given wind speed, c. This means that $F(c) =$ the probability that $c' \leq c$ where c' is a dummy variable.

It can be shown that

$$F(c) = \int_0^\infty p(c')\mathrm{d}c' = 1$$

and the derivative of the cumulative distribution function equals the p.d.f., i.e.,

$$p(c) = \frac{\mathrm{d}F(c)}{\mathrm{d}c}$$

Note: The mathematics of the Weibull probability distribution are rather more complicated than those of the Rayleigh distribution as it is based upon two parameters and also requires some knowledge of Gamma functions. All we need to know about the wind speed characteristics, for the purposes of this book, can be obtained using the Rayleigh probability distribution function.

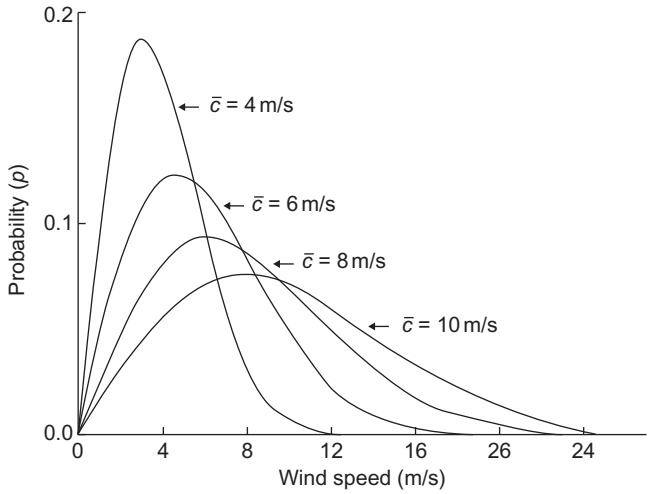

FIGURE 10.7

Rayleigh p.d.f.

Readers wishing to advance their knowledge of the Weibull probability function and its application to wind characteristics can consult Manwell et al. (2009).

Comment: It should be carefully noted that the mean power output of a wind turbine (which includes the effect of the probability function), Eq. (10.1b), is very much less than the rated power of the turbine. This has been a source of some confusion in discussions. The ratio of the mean power produced at a given mean wind speed to the so-called rated power output is called the *capacity factor*. The capacity factor is usually about 0.5 at maximum power output of a turbine.

10.6 Actuator disc approach

Introduction

In the following sections, the aerodynamic theory of the HAWT is gradually developed, starting with the simple 1D momentum analysis of the actuator disc and followed by the more detailed analysis of the blade element theory. The flow state just upstream of the rotor plane forms the so-called inflow condition for the rotor blades and from which the aerodynamic forces acting on the blades can be determined. The highly regarded BEM method is outlined and used extensively. A number of worked examples are included at each stage of development to illustrate the application of the theory. Detailed calculations using the BEM method were made to show the influence of various factors, such as the tip−speed ratio and blade number on performance. Further development of the theory includes the application of Prandtl's tip loss correction factor, which corrects for a finite number of blades. Glauert's optimization analysis is developed and used to determine the ideal blade shape for a given lift coefficient and to show how the optimum rotor power coefficient is influenced by the choice of tip−speed ratio.

The concept of the actuator disc was used in Chapter 6 as a method of determining the 3D flows in compressor and turbine blade rows. Betz (1926) in his seminal work on the flow through windmill blades used a much simpler version of the actuator disc. As a start to understanding the power production process of the turbine consider the flow model shown in Figure 10.8 where the rotor of the HAWT is replaced by an actuator disc. It is necessary to make a number of simplifying assumptions concerning the flow but, fortunately, the analysis yields useful approximate results.

Theory of the actuator disc

The following assumptions are made:

- **i.** steady uniform flow upstream of the disc;
- **ii.** uniform and steady velocity at the disc;
- **iii.** no flow rotation produced by the disc;
- **iv.** the flow passing through the disc is contained both upstream and downstream by the boundary stream tube;
- **v.** the flow is incompressible.

Because the actuator disc offers a resistance to the flow, the velocity of the air is reduced as it approaches the disc and there will be a corresponding increase in pressure. The flow crossing through the disc experiences a sudden drop in pressure below the ambient pressure. This discontinuity in pressure at the disc characterizes the actuator. Downstream of the disc there is a gradual recovery of the pressure to the ambient value.

We define the axial velocities of the flow far upstream ($x \to -\infty$), at the disc ($x = 0$) and far downstream ($x \to \infty$) as c_{x1}, c_{x2} and c_{x3}, respectively. From the continuity equation, the mass flow is

$$\dot{m} = \rho c_{x2} A_2$$

where ρ = air density and A_2 = area of disc.

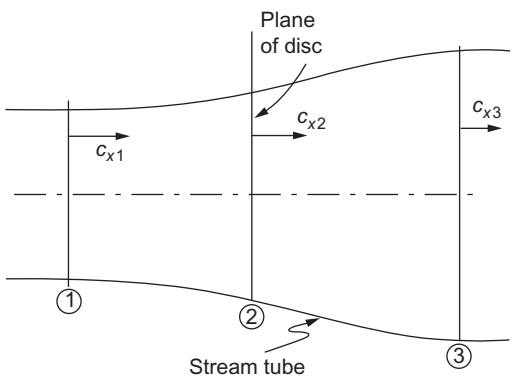

FIGURE 10.8

Actuator disc and boundary stream tube model.

The axial force acting on the disc is

$$X = \dot{m}(c_{x1} - c_{x3}) \tag{10.2}$$

and the corresponding power extracted by the turbine or actuator disc is

$$P = Xc_{x2} = \dot{m}(c_{x1} - c_{x3})c_{x2} \tag{10.3}$$

The rate of energy loss by the wind must then be

$$P_W = \dot{m}(c_{x1}^2 - c_{x3}^2)/2 \tag{10.4}$$

Assuming no other energy losses, we can equate the power lost by the wind to the power gained by the turbine rotor or actuator:

$$P_W = P$$

$$\dot{m}(c_{x1}^2 - c_{x3}^2)/2 = \dot{m}(c_{x1} - c_{x3})c_{x2}$$

therefore,

$$c_{x2} = \frac{1}{2}(c_{x1} + c_{x3}) \tag{10.5}$$

This is the proof developed by Betz (1926) to show that the velocity of the flow in the plane of the actuator disc is the mean of the velocities far upstream and far downstream of the disc. We should emphasize again that wake mixing, which must physically occur far downstream of the disc, has so far been ignored.

An alternative proof of Betz's result

The air passing across the disc undergoes an overall change in velocity $(c_{x1} - c_{x3})$ and a corresponding rate of change of momentum equal to the mass flow rate multiplied by this velocity change. The force causing this momentum change is equal to the difference in pressure across the disc times the area of the disc. Thus,

$$\begin{aligned}(p_{2+} - p_{2-})A_2 = \dot{m}(c_{x1} - c_{x3}) = \rho A_2 c_{x2}(c_{x1} - c_{x3})\\ \Delta p = (p_{2+} - p_{2-}) = \rho c_{x2}(c_{x1} - c_{x3})\end{aligned} \tag{10.6}$$

The pressure difference Δp is obtained by separate applications of Bernoulli's equation to the two flow regimes of the stream tube.

Referring to regions 1−2 in Figure 10.8,

$$p_1 + \frac{1}{2}\rho c_{x1}^2 = p_{2+} + \frac{1}{2}\rho c_{x2}^2$$

and for regions 2−3,

$$p_3 + \frac{1}{2}\rho c_{x3}^2 = p_{2-} + \frac{1}{2}\rho c_{x2}^2$$

By taking the difference of the two equations, we obtain

$$\frac{1}{2}\rho(c_{x1}^2 - c_{x3}^2) = p_{2+} - p_{2-} \tag{10.7}$$

Equating Eqs (10.6) and (10.7), we arrive at the result previously found,

$$c_{x2} = \frac{1}{2}(c_{x1} + c_{x3}) \tag{10.5}$$

By combining continuity with Eq. (10.3),

$$P = \rho A_2 c_{x2}^2 (c_{x1} - c_{x3})$$

and from Eq. (10.5), we can obtain

$$c_{x3} = 2c_{x2} - c_{x1}$$

hence,

$$c_{x1} - c_{x3} = c_{x1} - 2c_{x2} + c_{x1} = 2(c_{x1} + c_{x2})$$

and so

$$P = 2\rho A_2 c_{x2}^2 (c_{x1} - c_{x2}) \tag{10.8}$$

It is convenient to define an *axial flow induction factor*, $\overline{a}$ (assumed to be invariant with radius)[4], for the actuator disc:

$$\overline{a} = (c_{x1} - c_{x2})/c_{x1} \tag{10.9}$$

Hence,

$$\begin{aligned} c_{x2} &= c_{x1}(1 - \overline{a}), \\ P &= 2\overline{a}\rho A_2 c_{x1}^3 (1 - \overline{a})^2 \end{aligned} \tag{10.10a}$$

The power coefficient

For the unperturbed wind (i.e., velocity is c_{x1}) with the *same* flow area as the disc ($A_2 = \pi R^2$), the kinetic power available in the wind is

$$P_0 = \frac{1}{2}c_{x1}^2(\rho A_2 c_{x1}) = \frac{1}{2}\rho A_2 c_{x1}^3$$

A power coefficient C_p is defined as

$$C_p = P/P_0 = 4\overline{a}(1 - \overline{a})^2 \tag{10.11}$$

The maximum value of C_p is found by differentiating C_p with respect to $\overline{a}$, i.e., finally

$$dC_p/d\overline{a} = 4(1 - \overline{a})(1 - 3\overline{a}) = 0$$

[4]Later on this restriction is removed.

which gives two roots, $\overline{a} = 1/3$ and 1.0. Using the first root, the maximum value of the power coefficient is

$$C_{\text{p max}} = 16/27 = 0.593 \tag{10.12}$$

This value of C_p is often referred to as *the Betz limit*, referring to the maximum possible power coefficient of the turbine (with the prescribed flow conditions).

The axial force coefficient

The axial force coefficient is defined as

$$\begin{aligned} C_x &= X \Big/ \left(\frac{1}{2}\rho c_{x1}^2 A_2\right) \\ &= 2\dot{m}(c_{x1} - c_{x2}) \Big/ \left(\frac{1}{2}\rho c_{x1}^2 A_2\right) \\ &= 4c_{x2}(c_{x1} - c_{x2})/c_{x1}^2 \\ &= 4\overline{a}(1 - \overline{a}) \end{aligned} \tag{10.13}$$

By differentiating this expression with respect to $\overline{a}$, we can show that C_x has a maximum value of unity at $\overline{a} = 0.5$. Figure 10.9(a) shows the variation of both C_p and C_x as functions of the axial induction factor, $\overline{a}$.

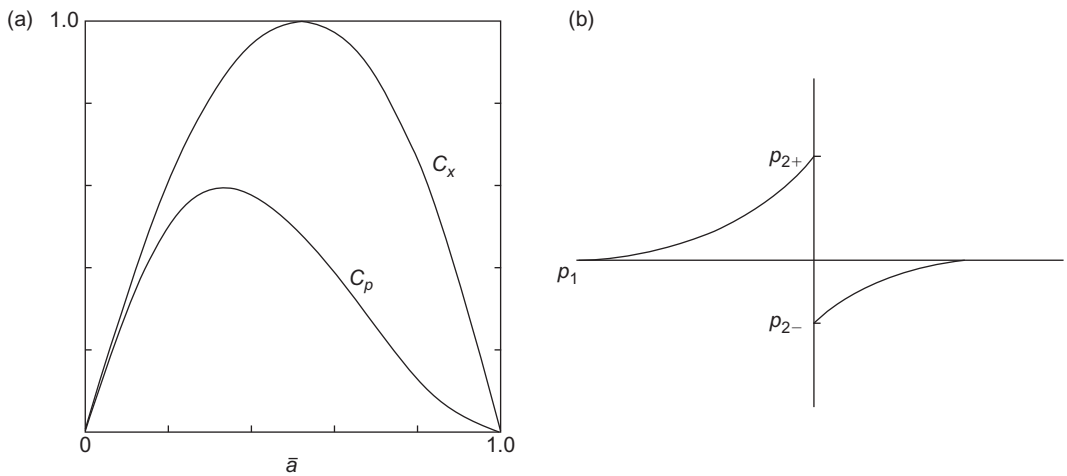

FIGURE 10.9

(a) Variation of C_p and C_x as functions of ā. (b) Schematic of the pressure variation before and after the plane of the actuator disc.

EXAMPLE 10.2

Using the theoretical flow model of a wind turbine proposed by Betz obtain expressions for the static pressure changes:

a. across the actuator disc;
b. up to the disc from far upstream;
c. from the disc to far downstream.

The pressure immediately before the disc is p_{2+}. The pressure immediately after the disc is p_{2-}.

Solution

a. The force acting on the disc is $X = A_2(p_{2+} - p_{2-}) = A_2\Delta p$. The power developed by the disc is

$$P = Xc_{x2} = A_2\Delta p c_{x2}$$

Also, we have

$$P = \frac{1}{2}\dot{m}(c_{x1}^2 - c_{x3}^2)$$

Equating for power and simplifying, we get

$$\Delta p \Big/ \left(\frac{1}{2}\rho c_{x1}^2\right) = \left[1 - (c_{x3}/c_{x1})^2\right] = 1 - (1-2\overline{a})^2 = 4\overline{a}(1-\overline{a})$$

This is the pressure change across the disc divided by the upstream dynamic pressure.

b. For the flow field from far upstream of the disc,

$$p_{01} = p_1 + \frac{1}{2}\rho c_{x1}^2 = p_{2+} + \frac{1}{2}\rho c_{x2}^2$$

$$(p_{2+} - p_1) = \frac{1}{2}\rho(c_{x1}^2 - c_{x2}^2)$$

$$(p_{2+} - p_1) \Big/ \left(\frac{1}{2}\rho c_{x1}^2\right) = 1 - (c_{x2}/c_{x1})^2 = 1 - (1-\overline{a})^2 = \overline{a}(2-\overline{a})$$

c. For the flow field from the disc to far downstream,

$$p_{03} = p_3 + \frac{1}{2}\rho c_{x3}^2 = p_{2-} + \frac{1}{2}\rho c_{x2}^2$$

$$(p_{2-} - p_3) \Big/ \left(\frac{1}{2}\rho c_{x1}^2\right) = (c_{x3}^2 - c_{x2}^2)/c_{x1}^2$$

and, noting that $p_3 = p_1$, we finally obtain

$$(p_{2-} - p_1) \Big/ \left(\frac{1}{2}\rho c_{x1}^2\right) = (1-2\overline{a})^2 - (1-\overline{a})^2 = -\overline{a}(2-3\overline{a})$$

Figure 10.9 (b) indicates, approximately, the way the pressure varies before and after the actuator disc.

EXAMPLE 10.3

Determine the radii of the unmixed slipstream at the disc (R_2) and far downstream of the disc (R_3) compared with the radius far upstream (R_1).

Solution

Continuity requires that

$$\pi R_1^2 c_{x1} = \pi R_2^2 c_{x2} = \pi R_3^2 c_{x3}$$
$$(R_2/R_1)^2 = c_{x1}/c_{x2} = 1/(1-\overline{a}),\ R_2/R_1 = 1/(1-\overline{a})^{0.5}$$
$$(R_3/R_1)^2 = c_{x1}/c_{x3} = 1/(1-2\overline{a}),\ R_3/R_1 = 1/(1-2\overline{a})^{0.5}$$
$$(R_3/R_2) = \left[(1-\overline{a})/(1-2\overline{a})\right]^{0.5}$$

Choosing a value of $\overline{a} = 1/3$, corresponding to the maximum power condition, the radius ratios are $R_2/R_1 = 1.225$, $R_3/R_1 = 1.732$ and $R_3/R_2 = 1.414$.

EXAMPLE 10.4

Using the preceding expressions for an actuator disc, determine the power output of a HAWT of 30 m tip diameter in a steady wind blowing at

a. 7.5 m/s;
b. 10 m/s.

Assume that the air density is 1.2 kg/m^3 and that $\overline{a} = 1/3$.

Solution

Using Eq. (10.10a) and substituting $\overline{a} = 1/3$, $\rho = 1.2$ kg/m^2 and $A_2 = \pi 15^2$,

$$P = 2\overline{a}\rho A_2 c_{x1}^3 (1-\overline{a})^2 \frac{2}{3} \times 1.2 \times \pi 15^2 \times \left(1-\frac{1}{3}\right)^2 c_{x1}^3 = 251.3 c_{x1}^3$$

a. With $c_{x1} = 7.5$ m/s, $P = 106$ kW
b. With $c_{x1} = 10$ m/s, $P = 251.3$ kW

These two results give some indication of the power available in the wind.

Correcting for high values of $\bar{a}$

It is of some interest to examine the theoretical implications of what happens at high values of $\bar{a}$ and compare this with what is found experimentally. From the actuator disc analysis, we found that the velocity in the wake far downstream was determined by $c_{x3} = c_{x1}(1 - 2\bar{a})$, and this becomes zero when $\bar{a} = 0.5$. In other words, the actuator disc model has already failed as there can be no flow when $\bar{a} = 0.5$. It is as if a large flat plate had been put into the flow, completely replacing the rotor. Some opinion has it that the theoretical model does not hold true for values of a even as low as 0.4. So, it becomes necessary to resort to empirical methods to include physical reality.

Figure 10.10 shows experimental values of C_X for heavily loaded turbines plotted against $\bar{a}$, taken from various sources, together with the theoretical curve of C_X versus $\bar{a}$ given by Eq. (10.13). The part of this curve in the range $0.5 < \bar{a} < 1.0$, shown by a broken line, is invalid as already explained. The experiments revealed that the vortex structure of the flow downstream disintegrates and that wake mixing with the surrounding air takes place. Various authors including Glauert (1935), Wilson (1976), and Anderson (1980), have presented curves to fit the data points in the regime $\bar{a} > 0.5$. Anderson obtained a simple "best fit" of the data with a straight line drawn from a point denoted by C_{XA} located at $\bar{a} = 1$ to a tangent point T, the transition point, on the theoretical curve located at $\bar{a} = \bar{a}_T$. It is easy to show, by differentiation of the curve $C_X = 4\bar{a}(1 - \bar{a})$ then fitting a straight line, with the equation,

$$C_X = C_{XA} - 4(C_{XA}^{0.5} - 1)(1 - \bar{a}) \tag{10.14}$$

where

$$\bar{a}_T = 1 - \frac{1}{2}C_{XA}^{0.5}$$

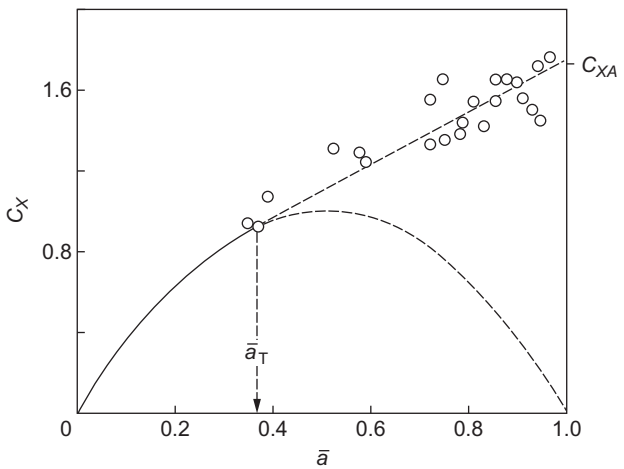

FIGURE 10.10

Comparison of theoretical and measured values of C_x versus $\bar{a}$.

Anderson recommended a value of 1.816 for C_{XA}. Using this value, Eq. (10.14) reduces to

$$C_X = 0.4256 + 1.3904\overline{a} \tag{10.15a}$$

where $\overline{a}_T = 0.3262$.

Sharpe (1990) noted that, for most practical, existent HAWTs, the value of $\overline{a}$ rarely exceeds 0.6.

Estimating the power output

Preliminary estimates of rotor diameter can easily be made using simple actuator disc theory. A number of factors need to be taken into account, i.e., the wind regime in which the turbine is to operate and the tip−speed ratio. Various losses must be allowed for the main ones being the mechanical transmission including gearbox losses and the electrical generation losses. From the actuator disc theory, the turbine aerodynamic power output is

$$P = \frac{1}{2}\rho A_2 C_p c_{x1}^3 \tag{10.15b}$$

Under theoretical ideal conditions, the maximum value of $C_p = 0.593$. According to Eggleston and Stoddard (1987), rotor C_p values as high as 0.45 have been reported. Such high, real values of C_p relate to very precise, smooth aerofoil blades and tip−speed ratios above 10. For most machines of good design a value of C_p from 0.3 to 0.35 would be possible. With a drive train efficiency, η_d, and an electrical generation efficiency, η_g, the output electrical power would be

$$P_{el} = \frac{1}{2}\rho A_2 C_p \eta_g \eta_d c_{x1}^3$$

EXAMPLE 10.5

Determine the size of rotor required to generate 20 kW of electrical power in a steady wind of 7.5 m/s. It can be assumed that the air density, $\rho = 1.2$ kg/m^3, $C_p = 0.35$, $\eta_g = 0.75$, and $\eta_d = 0.85$.

Solution

From this expression, the disc area is

$$A_2 = 2P_{el}/(\rho C_p \eta_g \eta_d c_{x1}^3) = 2 \times 20 \times 10^3/(1.2 \times 0.35 \times 0.75 \times 0.85 \times 7.5^3) = 354.1 \text{ m}^2$$

Hence, the diameter is 21.2 m.

10.7 Blade element theory

Introduction

It has long been recognized that the work of Glauert (1935) in developing the fundamental theory of aerofoils and airscrews is among the great classics of aerodynamic theory. Glauert also

generalized the theory to make it applicable to wind turbines and, with various modifications, it is still used in turbine design. It is often referred to as the *momentum vortex blade element theory* or more simply as the *blade element method*. However, the original work neglected an important aspect: the flow periodicity resulting from the turbine having a finite number of blades. Glauert assumed that elementary radial blade sections could be analyzed independently, which is valid only for a rotor with an infinite number of blades. However, several approximate solutions are available (those of Prandtl and Tietjens (1957) and Goldstein (1929)), which enable compensating corrections to be made for a finite number of blades. The simplest and most often used of these, called the *Prandtl correction factor*, will be considered later in this chapter. Another correction that is considered is empirical and applies only to heavily loaded turbines when the magnitude of the axial flow induction factor a exceeds the acceptable limit of the momentum theory. According to Sharpe (1990), the flow field of heavily loaded turbines is not well understood, and the results of the empirical analysis mentioned are only approximate but better than those predicted by the momentum theory.

The vortex system of an aerofoil

To derive a better understanding of the aerodynamics of the HAWT than was obtained earlier from simple actuator disc theory, it is now necessary to consider the forces acting on the blades. We may regard each radial element of a blade as an aerofoil. The turbine is assumed to have a constant angular speed Ω and is situated in a uniform wind of velocity c_{x1} parallel to the axis of rotation. The lift force acting on each element must have an associated *circulation* (see Section 3.4) around the blade. In effect there is a line vortex (or a set of line vortices) along the aerofoil span. The line vortices that move with the aerofoil are called *bound vortices* of the aerofoil. As the circulation along the blade length can vary, *trailing vortices* will spring from the blade and will be convected downstream with the flow in approximately helical paths, as indicated for a two-bladed wind turbine in Figure 10.11. It will be observed that the helices, as drawn, gradually expand in radius as they move downstream (at the wake velocity) and the pitch between each sheet becomes smaller because of the deceleration of the flow.

Wake rotation

In the previous analysis of the actuator disc, it was assumed that no rotation was imparted to the flow. It is evident that the torque exerted on the rotor disc by the air passing through it requires an equal and opposite torque to be exerted on the air. As a consequence, this reaction torque causes the air leaving the rotor to rotate incrementally in the *opposite direction* to that of the rotor. Thus, the wakes leaving the rotor blades will have a velocity component in the direction tangential to the blade rotation as well as an axial velocity component.

The flow entering the rotor has no rotational motion at all. The flow exiting the rotor has rotation and this remains constant as the flow travels downstream. We can define the change in the tangential velocity in terms of a *tangential flow induction factor*, a'. Downstream of the disc in the induced tangential velocity $c_{\theta 2}$ defined as $2\Omega r a'$ is as shown in Figure 10.12(a). The complete transfer of rotational energy is assumed to take place across the rotor disc. This is actually impossible as the disc is defined as having no thickness. The rotational velocity component $c_{\theta 2}$ develops physically as the actual flow progresses toward the trailing edge plane.

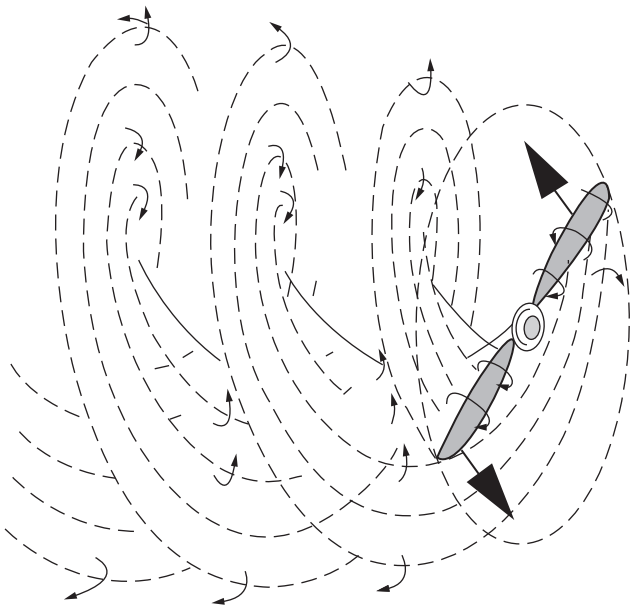

FIGURE 10.11

Schematic drawing of the vortex system being carried downstream from a two-bladed wind turbine rotor.

Glauert regarded the exact evaluation of the interference flow to be of great complexity because of the periodicity of the flow caused by the blades. He asserted that for most purposes it is sufficiently accurate to use circumferentially averaged values, equivalent to assuming that the thrust and the torque carried by the finite number of blades are replaced by uniform distributions of thrust and torque *spread over the whole circumference* at the same radius.

Consider such an elementary annulus of a HAWT of radius r from the axis of rotation and of radial thickness $\mathrm{d}r$. Let $\mathrm{d}\tau$ be the element of torque equal to the rate of decrease in angular momentum of the wind passing through the annulus. Thus,

$$\mathrm{d}\tau = (\mathrm{d}\dot{m}) \times 2a'\Omega r^2 = (2\pi r\, \mathrm{d}r \rho c_{x2}) \times 2a'\Omega r^2 \tag{10.16a}$$

or

$$\mathrm{d}\tau = 4\pi\rho\Omega c_{x1}(1-a)a' r^3\, \mathrm{d}r \tag{10.16b}$$

In the actuator disc analysis, the value of a (denoted by $\overline{a}$) is a constant over the whole of the disc. With blade element theory, the value of a is a function of the radius. This is a fact that must not be overlooked. A constant value of a *could* be obtained for a wind turbine design with blade element theory, but only by varying the chord and the pitch in some special way along the radius. This is not a useful design requirement.

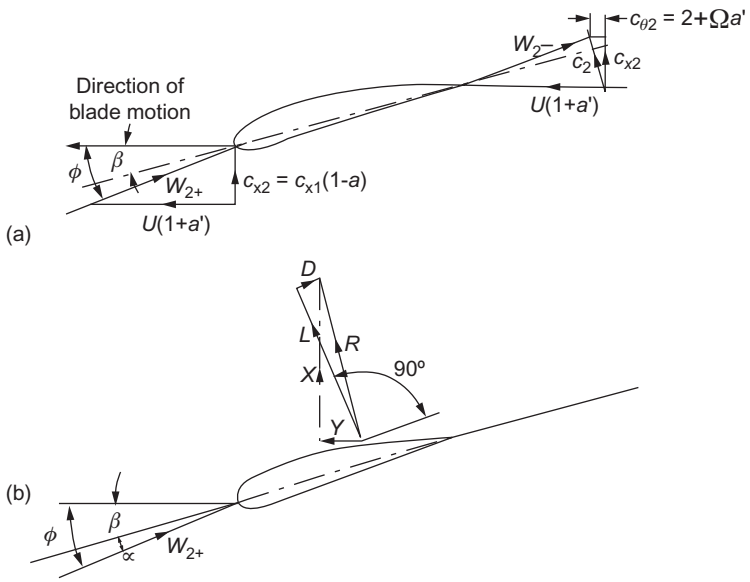

FIGURE 10.12

(a) Blade element at radius r showing the various velocity components. (b) The various components of force acting on the blade.

Assuming the axial and tangential induction factors a and a' are functions of r, we obtain an expression for the power developed by the blades by multiplying the above expression by Ω and integrating from the hub r_h to the tip radius R:

$$P = 4\pi\rho\Omega^2 c_{x1} \int_{r_h}^{R} (1-a)a' r^3 \, dr \tag{10.17}$$

Forces acting on a blade element

Consider now a turbine with Z blades of tip radius R each of chord l at radius r and rotating at angular speed Ω. The pitch angle of the blade at radius r is β measured from the zero lift line to the plane of rotation. The axial velocity of the wind at the blades is the same as the value determined from actuator disc theory, i.e., $c_{x2} = c_{x1}(1-a)$, and is perpendicular to the plane of rotation.

Figure 10.12(a) shows the blade element moving from right to left together with the velocity vectors relative to the blade chord line at radius r. The resultant of the relative velocity immediately upstream of the blades is

$$w_{2+} = [c_{x1}^2(1-a)^2 + (\Omega r)^2(1+a')^2]^{0.5} \tag{10.18}$$

and this is shown as impinging onto the blade element at angle ϕ to the plane of rotation. It will be noticed that the relative velocity at blade exit is reduced to w_{2-} as a result of the wake mentioned earlier. The following relations will be found useful in later algebraic manipulations:

$$\sin\phi = c_{x2}/w_{2+} = c_{x1}(1-a)/w_{2+} \tag{10.19}$$

$$\cos\phi = \Omega r(1+a')/w_{2'} \tag{10.20}$$

$$\tan\phi = \frac{c_{x1}}{\Omega r}\left(\frac{1-a}{1+a'}\right) \tag{10.21}$$

Figure 10.12(b) shows the lift force L and the drag force D drawn (by convention) perpendicular and parallel to the relative velocity at entry, respectively. In the normal range of operation, D although rather small (1−2%) compared with L, is not to be entirely ignored. The resultant force, R, is seen as having a component in the direction of blade motion. This is the force contributing to the positive power output of the turbine.

From Figure 10.12 (b), the force per unit blade length in the direction of motion is

$$Y = L\sin\phi - D\cos\phi \tag{10.22}$$

and the force per unit blade length in the direction perpendicular to the direction of motion is

$$X = L\cos\phi + D\sin\phi \tag{10.23}$$

Lift and drag coefficients

We can define the lift and drag coefficients as

$$C_{\mathrm{L}}(\alpha) = L/\left(\frac{1}{2}\rho w^2 l\right) \tag{10.24}$$

$$C_{\mathrm{D}}(\alpha) = D/\left(\frac{1}{2}\rho w^2 l\right) \tag{10.25}$$

where, by the convention employed for an isolated aerofoil, w is the incoming relative velocity and l is the blade chord. The coefficients C_{L} and C_{D} are functions of the angle of incidence, $\alpha = \phi - \beta$, as defined in Figure 10.12 as well as the blade profile and blade Reynolds number. In this chapter, the angle of incidence is understood to be measured from the *zero lift line* (see Section 5.15) for which the C_{L} versus α curve goes through zero. It is important to note that Glauert (1935), when considering aerofoils of small camber and thickness, obtained a theoretical expression for the lift coefficient,

$$C_{\mathrm{L}} = 2\pi\sin\alpha \tag{10.26}$$

The theoretical slope of the curve of lift coefficient against incidence is 2π per radian (for small values of α) or 0.11 per degree but, from experimental results, a good average generally accepted is 0.1 per degree *within the prestall regime*. This very useful result will be used extensively in calculating results later. However, measured values of the lift-curve slope reported by Abbott and von Doenhoff (1959) for a number of NACA four- and five-digit series and NACA 6-series wing

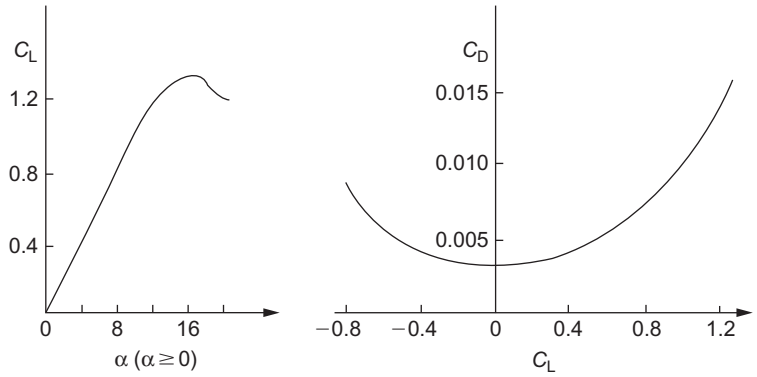

FIGURE 10.13

Typical performance characteristics for a wind turbine blade, C_L versus α and C_D versus C_L.

sections, measured at a Reynolds number of 6×10^6, gave 0.11 per degree. But these blade profiles were intended for aircraft wings, so some departure from the rule might be expected when the application is the wind turbine.

Again, within the prestall regime, values of C_D are small and the ratio of C_D/C_L is usually about 0.01. Figure 10.13 shows typical variations of lift coefficient C_L plotted against incidence α and drag coefficient C_D plotted against C_L for a wind turbine blade tested beyond the stall state. The blades of a wind turbine may occasionally have to operate in *poststall conditions* when C_D becomes large; then the drag term needs to be included in performance calculations. Details of *stall modeling* and formulae for C_D and C_L under poststall conditions are given by Eggleston and Stoddard (1987).

The correct choice of aerofoil sections is very important for achieving good performance. The design details and the resulting performance are clearly competitive and not much information is actually available in the public domain. The US Department of Energy (DOE) developed a series of aerofoils specifically for wind turbine blades. These aerofoils were designed to provide the necessarily different performance characteristics from the blade root to the tip while accommodating the structural requirements. Substantially increased energy output (from 10% to 35%) from wind turbines with these new blades have been reported. The data are cataloged and is available to the US wind industry.[5] Many other countries have national associations, research organizations, and conferences relating to wind energy and contact details are listed by Ackermann and Söder (2002).

Connecting actuator disc theory and blade element theory

The elementary axial force and elementary force exerted on *one* blade of length dr at radius r are

$$\begin{aligned} \mathrm{d}X &= (L\cos\phi + D\sin\phi)\mathrm{d}r \\ \mathrm{d}\tau &= r(L\sin\phi - D\cos\phi)\mathrm{d}r \end{aligned}$$

[5]See Section 10.11, HAWT Blade Section Criteria, for more details.

For a turbine having Z blades and using the definitions for C_L and C_D given by Eqs (10.24) and (10.25), we can write expressions for the elementary torque, power, and thrust as

$$d\tau = \frac{1}{2}\rho w^2 r(C_L \sin\phi - C_D \cos\phi)Zl\, dr \tag{10.27}$$

$$dP = \Omega\, d\tau = \frac{1}{2}\rho w^2 \Omega r(C_L \sin\phi - C_D \cos\phi)Zl\, dr \tag{10.28}$$

$$dX = \frac{1}{2}\rho w^2 (C_L \cos\phi + C_D \sin\phi)Zl\, dr \tag{10.29}$$

It is now possible to make a connection between actuator disc theory and blade element theory. (Values of a and a' are allowed to vary with radius in this analysis.) From Eq. (10.2), for an element of the flow, we obtain

$$dX = d\dot{m}(c_{x1} - c_{x3}) = d\dot{m}c_{x2}2a/(1-a) \tag{10.30}$$

Equating Eqs (10.29) and (10.30) and with some rearranging, we get

$$a/(1-a) = Zl(C_L \cos\phi + C_D \sin\phi)/(8\pi r \sin^2\phi) \tag{10.31}$$

Again, considering the tangential momentum, from Eq. (10.16a) the elementary torque is

$$d\tau = (2\pi r\, dr)\rho c_{x2}(rc_\theta)$$

Equating this with Eq. (10.27) and simplifying, we get

$$c_{x2}c_\theta/w^2 = Zl(C_L \sin\phi - C_D \cos\phi)/(4\pi r) \tag{10.32}$$

Using Eq. (10.20), we find

$$c_\theta/w = Ua' \cos\phi/[U(1+a')] = 2a' \cos\phi/(1+a')$$

and, with Eq. (10.19), Eq. (10.32) becomes

$$a'/(1+a') = Zl(C_L \sin\phi - C_D \cos\phi)/(8\pi r \sin\phi \cos\phi) \tag{10.33}$$

Introducing a useful new dimensionless parameter, the *blade loading coefficient*,

$$\lambda = ZlC_L/(8\pi r) \tag{10.34}$$

into Eqs (10.31) and (10.33), we get

$$a/(1-a) = \lambda(\cos\phi + \varepsilon\sin\phi)/\sin^2\phi \tag{10.35a}$$

$$a'/(1+a') = \lambda(\sin\phi - \varepsilon\cos\phi)/(\sin\phi\cos\phi) \tag{10.36a}$$

$$\varepsilon = \frac{C_D}{C_L} \tag{10.37}$$

Tip–speed ratio

A most important nondimensional parameter for the rotors of HAWTs is the tip–speed ratio, defined as

$$J = \frac{\Omega R}{c_{x1}} \tag{10.38}$$

This parameter controls the operating conditions of a turbine and strongly influences the values of the flow induction factors, a and a'.

Using Eq. (10.38) in Eq. (10.21), we write the tangent of the relative flow angle ϕ as

$$\tan\phi = \frac{R}{rJ}\left(\frac{1-a}{1+a'}\right) \tag{10.39}$$

Turbine solidity

A primary nondimensional parameter that characterizes the geometry of a wind turbine is the blade solidity, σ. The solidity is defined as the ratio of the blade area to the disc area:

$$\sigma = ZA_B/(\pi R^2)$$

where

$$A_B = \int l(r)\mathrm{d}r = \frac{1}{2}Rl_{av}$$

This is usually written as

$$\sigma = Zl_{av}/(2\pi R) \tag{10.40}$$

where l_{av} is the mean blade chord.

Solving the equations

The foregoing analysis provides a set of relations which can be solved by a process of iteration, enabling a and a' to be determined for any specified pitch angle β, provided that convergence is possible. To obtain faster solutions, we will use the approximation that $\varepsilon \cong 0$ in the normal efficient range of operation (i.e., the prestall range). Equations (10.35a) and (10.36a) can now be written as

$$a/(1-a) = \lambda \cot\phi/\sin\phi \tag{10.35b}$$

$$a'/(1+a') = \lambda/\cos\phi \tag{10.36b}$$

These equations are about as simple as it is possible to make them and they will be used to model some numerical solutions.

Table 10.1 BEM Method for Evaluating a and a'

Step	Action Required
1	Initialize a and a' with zero values
2	Evaluate the flow angle using Eq. (10.39)
3	Evaluate the local angle of incidence, $\alpha = \phi - \beta$
4	Determine C_L and C_D from tables (if available) or from formula
5	Calculate a and a'
6	Check on convergence of a and a', if not sufficient go to step 2, else go to step 7
7	Calculate local forces on the element

10.8 The BEM method

All the theory and important definitions to determine the force components on a blade element have been introduced and a first trial approach has been given to finding a solution in Example 10.5. The various steps of the classical BEM model from Glauert are formalized in Table 10.1 as an algorithm for evaluating a and a' for each elementary control volume.

Spanwise variation of parameters

Along the blade span there is a significant variation in the blade-pitch angle β, which is strongly linked to the value of J and to a lesser extent to the values of the lift coefficient C_L and the blade chord l. The ways both C_L and l vary with radius are at the discretion of the turbine designer. In the previous example, the value of the pitch angle was specified and the lift coefficient was derived (together with other factors) from it. We can likewise specify the lift coefficient, keeping the incidence below the angle of stall and from it determine the angle of pitch. This procedure will be used in the next example to obtain the spanwise variation of β for the turbine blade. It is certainly true that for optimum performance the blade *must* be twisted along its length with the result that, near the root, there is a large pitch angle. The blade-pitch angle will decrease with increasing radius so that, near the tip, it is close to zero and may even become slightly negative. The blade chord in the following examples has been kept constant to limit the number of choices. Of course, most turbines in operation have tapered blades whose design features depend upon blade strength as well as economic and aesthetic considerations.

EXAMPLE 10.6

A three-bladed HAWT with a 30 m tip diameter is to be designed to operate with a constant lift coefficient $C_L = 0.8$ along the span, with a tip−speed ratio $J = 5.0$. Assuming a constant chord of 1.0 m, determine, using an iterative method of calculation, the variation along the span ($0.2 \leq r/R \leq 1.0$) of the flow induction factors a and a' and the pitch angle β.

Table 10.2 Summary of Results Following Iterations

r/R	0.2	0.3	0.4	0.6	0.8	0.9	0.95	1.0
ϕ	42.29	31.35	24.36	16.29	11.97	10.32	9.59	8.973
β	34.29	23.35	16.36	8.29	3.97	2.32	1.59	0.97
a	0.0494	0.06295	0.07853	0.1138	0.1532	0.1742	0.1915	0.2054
a'	0.04497	0.0255	0.01778	0.01118	0.00820	0.00724	0.00684	0.00649

Note: $C_L = 0.8$ along the span.

Solution

We begin the calculation at the tip, $r = 15$ m and, as before, take initial values for a and a' of zero. Now,

$$\lambda = (ZlC_L)/(8\pi r) = (3 \times 0.8)/(8 \times \pi \times 15) = 0.116366, \text{ and } 1/\lambda = 157.1$$
$$\tan\phi = (R/rJ)(1-a)/(1+a') = 0.2, \phi = 1131^\circ$$
$$1/a = 1 + 157.1 \times \sin 11.31 \times \tan 11.31 = 7.162, a = 0.1396$$
$$1/a' = 157.1 \times \cos 11.31 - 1 = 153.05, \; a' = 0.00653$$

After a further five iterations (to obtain sufficient convergence), the result is

$$a = 0.2054, \; a' = 0.00649, \text{ and } \beta = 0.97^\circ$$

The results of the computations along the complete span ($0.2 \le r/R \le 1.0$) for a and a' are shown in Table 10.2. It is very evident that the parameter a varies markedly with radius, unlike the actuator disc application where $\overline{a}$ was constant. The spanwise variation of the pitch angle β for $C_L = 0.8$ (as well as for $C_L = 1.0$ and 1.2 for comparison) is shown in Figure 10.14. The large variation of β along the span is not surprising and is linked to the choice of the value of J, the tip−speed ratio. The choice of inner radius ratio $r/R = 0.2$ was arbitrary. However, the contribution to the power developed from choosing an even smaller radius would have been negligible.

Evaluating the torque and axial force

The incremental axial force can be derived from Eqs (10.29) and (10.19) in the form

$$\Delta X = \frac{1}{2}\rho ZlRc_{x1}^2[(1-a)/\sin\phi]^2 C_L \cos\phi \Delta(r/R) \tag{10.41}$$

and the incremental torque can be derived from Eqs (10.27) and (10.20) as

$$\Delta\tau = \frac{1}{2}\rho Zl\Omega^2 R^4[(1+a')/\cos\phi]^2 (r/R)^3 C_L \sin\phi \Delta(r/R) \tag{10.42}$$

In determining numerical solutions, these two equations have proved to be more reliable in use than some alternative forms that have been published. The two preceding equations will now be integrated numerically.

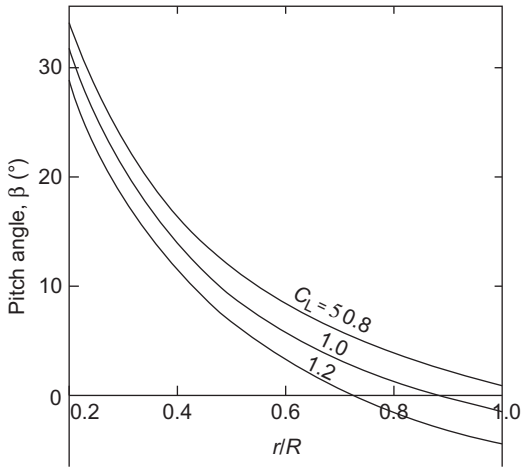

FIGURE 10.14

Variation of blade-pitch angle β with radius ratio *r/R* for $C_L = 0.8$, 1.0, and 1.2.

EXAMPLE 10.7

Determine the total axial force, the torque, the power, and the power coefficient of the wind turbine described in Example 10.5. Assume that $c_{x1} = 7.5$ m/s and that the air density $\rho = 1.2$ kg/m^3.

Solution

Evaluating the elements of axial force ΔX having previously determined the mid-ordinate values of a, a', and ϕ to gain greater accuracy (the relevant data is shown in Table 10.3):

Table 10.3 Data Used for Summing Axial Force

Mid r/R	0.250	0.350	0.450	0.550	0.650	0.750	0.850	0.95
$\Delta r/R$	0.100	0.100	0.100	0.100	0.100	0.100	0.100	0.100
a	0.05565	0.0704	0.0871	0.1053	0.1248	0.1456	0.1682	0.1925
ϕ (deg)	36.193	27.488	21.778	17.818	14.93	12.736	10.992	9.5826
Var.1	0.1648	0.2880	0.4490	0.6511	0.8920	1.172	1.4645	1.8561

$$\Delta X = \frac{1}{2}\rho ZlRc_{x1}^2[(1-a)/\sin\phi]^2 C_{\mathrm{L}} \cos\phi \Delta(r/R)$$

where, in Table 10.3, Var.1 $= [(1 - a)/\sin\phi]^2 C_{\mathrm{L}} \cos\phi\Delta(r/R)$:

$$\sum \text{Var.1} = 6.9682$$

Then with $(1/2)\rho Z l R c_{x1}^2 = (1/2) \times 1.2 \times 3 \times 15 \times 7.5^2 = 1518.8$, we obtain

$$X = 1518.8 \sum \text{Var.1} = 10,583 \text{ N}$$

In Table 10.4, $\text{Var.2} = [(1 + a')/\cos\phi]^2 (r/R)^3 C_L \sin\phi \Delta(r/R)$,

$$\sum \text{Var.2} = 47.509 \times 10^{-3}$$

Table 10.4 Data Used for Summing Torque

Mid r/R	0.250	0.350	0.450	0.550	0.650	0.750	0.850	0.950
a'	0.0325	0.02093	0.0155	0.0123	0.0102	0.0088	0.0077	0.00684
ϕ	36.19	27.488	21.778	17.818	14.93	12.736	10.992	9.5826
$(r/R)^3$	0.0156	0.0429	0.0911	0.1664	0.2746	0.4219	0.6141	0.8574
Var.2 ($\times 10^{-3}$)	1.206	2.098	3.733	4.550	6.187	7.959	9.871	11.905

and with $(1/2)\rho Z l \Omega^2 R^4 = 0.5695 \times 10^6$

$$\tau = 27.058 \times 10^3 \text{ Nm}$$

Hence, the power developed is $P = \tau\Omega = 67.644$ kW. The power coefficient is, see Eq. (10.11), is

$$C_p = \frac{P}{P_0} = \frac{P}{0.5\rho A_2 c_{x1}^3} = \frac{P}{1.789 \times 10^5} = 0.378$$

and the relative power coefficient is, see Eq. (10.12b),

$$\zeta = \frac{27}{16} C_p = 0.638$$

EXAMPLE 10.8

The relationship between actuator disc theory and blade element theory can be more firmly established by evaluating the power again, this time using the actuator disc equations.

Solution

To do this we need to determine the equivalent constant value for $\overline{a}$. From Eq. (10.13),

$$C_x = 4\overline{a}(1 - \overline{a}) = X \Big/ \left(\frac{1}{2}\rho c_{x1}^2 A_2\right)$$

with $X = 10{,}583$ N and $(1/2)\rho c_{x1}^2 A_2 = (1/2) \times 1.2 \times 7.5^2 \times \pi \times 15^2 \times 23,856$, we obtain

$$C_x = 10,583/23,856 = 0.4436$$

$$\overline{a}(1-\overline{a}) = 0.4436/4 = 0.1109$$

Solving the quadratic equation, we get $\overline{a} = 0.12704$.

From Eq. (10.10a), $P = 2\rho A_2 c_{x1}^3 \overline{a}(1-a)^2$, and substituting values,

$$P = 69.286 \text{ kW}$$

and this agrees fairly well with the value obtained in Example 10.8.

Note: The lift coefficient used in this example, admittedly modest, was selected purely to illustrate the method of calculation. For an initial design, the equations just developed would suffice but some further refinements can be added. An important refinement concerns the Prandtl correction for the number of blades.

Correcting for a finite number of blades

So far, the analysis has ignored the effect of having a finite number of blades. The fact is that at a fixed point the flow fluctuates as a blade passes by. The induced velocities at the point are not constant with time. The overall effect is to reduce the net momentum exchange and the net power of the turbine. Some modification of the analysis is needed and this is done by applying a blade tip correction factor. Several solutions are available: (i) an exact one due to Goldstein (1929), represented by an infinite series of modified Bessel functions, and (ii) a closed form approximation due to Prandtl and Tietjens (1957). Both methods give similar results and Prandtl's method is the one usually preferred.

Prandtl's correction factor

The mathematical details of some parts of Prandtl's analysis are beyond the scope of this book, but the result for F is usually expressed as

$$F = (2/\pi)\cos^{-1}[\exp(-\pi d/s)] \tag{10.43}$$

where, as shown in Figure 10.15, s is the pitchwise distance between the successive helical vortex sheets and $d = R - r$. From the geometry of the helices,

$$s = (2\pi R/Z)\sin\phi$$

where $\sin\phi = c_{x2}/w$. Thus,

$$\begin{aligned} s &= 2\pi(1-a)Rc_{x1}/(wZ) \\ \pi d/s &= \frac{1}{2}Z(1-r/R)w/c_{x2} = \frac{1}{2}Z(1-r/R)/\sin\phi \end{aligned} \tag{10.44a}$$

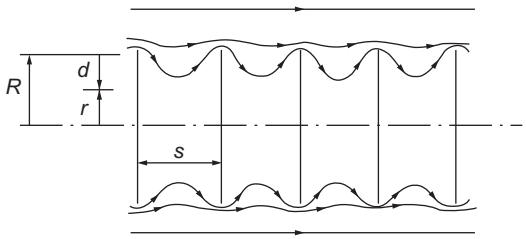

FIGURE 10.15

Prandtl tip loss model showing the distances used in the analysis.

This can be evaluated with sufficient accuracy and perhaps more conveniently with the approximation,

$$\pi d/s = \frac{1}{2} Z(1 - r/R)(1 + J^2)^{0.5} \tag{10.44b}$$

The circulation at the blade tips reduces to zero because of the vorticity shed from it, in the same way as at the tip of an aircraft wing. These expressions ensure that F becomes zero when $r = R$ but rapidly increases toward unity with decreasing radius.

The variation of $F = F(r/R)$ is shown in Figure 10.16 for $J = 5$ and $Z = 2$, 3, 4, and 6. It will be clear from the graph and the preceding equations that the greater the pitch s and the smaller the number of blades Z, the bigger will be the variation of F (from unity) at any radius ratio. In other words, the amplitude of the velocity fluctuations will be increased.

Prandtl's tip correction factor is applied directly to each blade element, modifying the elementary axial force, obtained from Eq. (10.13),

$$\mathrm{d}X = 4\pi\rho a(1 - a) r c_{x1}^2 \, \mathrm{d}r$$

to become

$$\mathrm{d}X = 4\pi\rho a(1 - a) r c_{x1}^2 F \, \mathrm{d}r \tag{10.45}$$

and the elementary torque, Eq. (10.16b),

$$\mathrm{d}\tau = 4\pi\rho\Omega c_{x1}(1 - a) a' r^3 \, \mathrm{d}r$$

is modified to become

$$\mathrm{d}\tau = 4\pi\rho\Omega c_{x1}(1 - a) a' F r^3 \, \mathrm{d}r \tag{10.46}$$

Following the reduction processes that led to Eqs (10.35a) and (10.36a), the last two numbered equations give the following results:

$$a/(1 - a) = \lambda(\cos\phi + \varepsilon \sin\phi)/(F \sin^2\phi) \tag{10.47a}$$

$$a'/(1 + a') = \lambda(s \sin\phi - \varepsilon \cos\phi)/(F \sin\phi \cos\phi) \tag{10.48a}$$

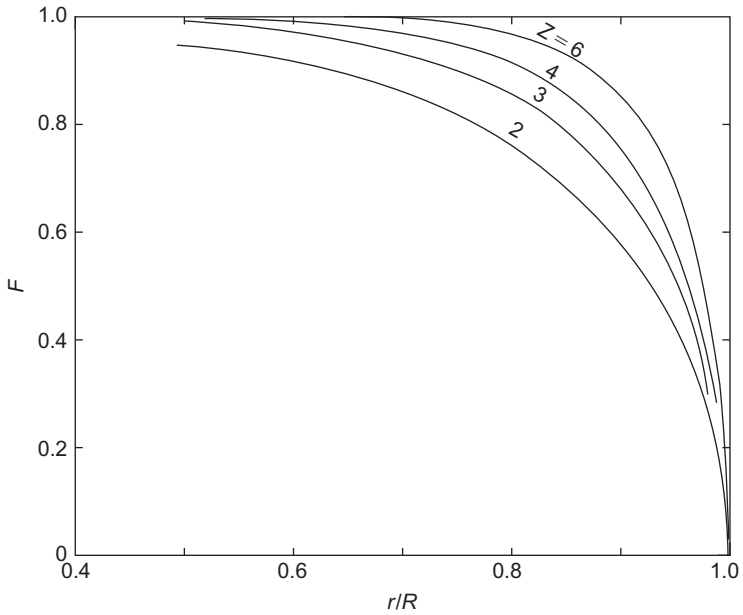

FIGURE 10.16

Variation of Prandtl correction factor F with radius ratio for blade number $Z = 2$, 3, 4, and 6.

The application of the Prandtl tip correction factor to the elementary axial force and elementary torque equations has some important implications concerning the overall flow and the interference factors. The basic meaning of Eq. (10.45) is

$$dX = d\dot{m}(2aFc_{x1})$$

i.e., the average axial induction factor in the far wake is $2aF$ when the correction factor is applied as opposed to $2a$ when it is not. Note also that, in the plane of the disc (or the blades), the average induction factor is aF, and that the axial velocity becomes

$$c_{x2} = c_{x1}(1 - aF)$$

From this, we see that at the tips of the blades $c_{x2} = c_{x1}$, because F is zero at that radius.

Note: It was explained earlier that the limit of application of the theory occurs when $a \rightarrow 0.5$, i.e., $c_{x2} = c_{x1}(1 - 2a)$, and, as the earlier calculations have shown, a is usually greatest toward the blade tip. However, with the application of the tip correction factor F, the limit state becomes $aF = 0.5$. As F progressively reduces to zero as the blade tip is approached, the operational result gives, in effect, some additional leeway in the convergence of the iterative procedure discussed earlier.

Performance calculations with tip correction included

In accordance with the previous approximation (to reduce the amount of work needed), ε is ascribed the value zero, simplifying the preceding equations for determining a and a' to

$$a/(1-a) = \lambda \cos\phi/(F \sin^2\phi) \tag{10.47b}$$

$$a'/(1+a') = \lambda/(F \cos\phi) \tag{10.48b}$$

When using the BEM method, an extra step is required in Table 10.1, between steps 1 and 2, to calculate F, and it is necessary to calculate a new value of C_L for each iteration that, consequently, changes the value of the blade loading coefficient λ as the calculation progresses.

EXAMPLE 10.9

This example repeats the calculations of Example 10.8 using the same blade specification (i.e., the pitch angle $\beta = \beta(r)$) but now it includes the Prandtl correction factor. The results of the iterations to determine a, a', ϕ, and C_L and used as data for the summations are shown in Table 10.5. The details of the calculation for one mid-ordinate radius ($r/R = 0.95$) are shown first to clarify the process.

Solution

At $r/R = 0.95$, $F = 0.522$, using Eqs (10.44b) and (10.43). Thus, with $Z = 3$, $l = 1.0$,

$$F/\lambda = 62.32/C_L$$

In the BEM method, we start with $a = a' = 0$ so, initially, $\tan\phi = (R/r)/J = (1/0.95)/5 = 0.2105$. Thus, $\phi = 11.89°$ and $C_L = (\phi - \beta)/10 = (11.89 - 1.59)/10 = 1.03$. Hence, $F/\lambda = 60.5$. With Eqs (10.47a) and (10.48a), we compute $a = 0.2759$ and $a' = 0.0172$.

The next cycle of iteration gives $\phi = 8.522$, $C_L = 0.693$, $F/\lambda = 89.9$, $a = 0.3338$, and $a' = 0.0114$. Continuing the series of iterations we finally obtain

Table 10.5 Summary of Results for All Mid-ordinates

Mid r/R	0.250	0.350	0.450	0.550	0.650	0.750	0.850	0.950
F	1.0	1.0	0.9905	0.9796	0.9562	0.9056	0.7943	0.522
C_L	0.8	0.8	0.796	0.790	0.784	0.7667	0.7468	0.6115
A	0.055	0.0704	0.0876	0.1063	0.1228	0.1563	0.2078	0.3510
a'	0.0322	0.0209	0.0155	0.01216	0.0105	0.0093	0.00903	0.010
ϕ (deg)	36.4	27.49	21.76	17.80	14.857	12.567	10.468	7.705
Var.1	0.1643	0.2878	0.4457	0.6483	0.8800	1.1715	1.395	0.5803

Table 10.6 Data Used for Summing Torque

Midr/R	0.250	0.350	0.450	0.550	0.650	0.750	0.850	0.950
$(r/R)^3$	0.01563	0.04288	0.09113	0.1664	0.2746	0.4219	0.6141	0.7915
Var.2 $\times 10^{-3}$	1.2203	2.097	3.215	4.541	6.033	7.526	8.773	7.302

Table 10.7 Summary of Results

	Axial Force (kN)	Power (kW)	C_P	ζ
Without tip correction	10.583	67.64	0.378	0.638
With tip correction	9.848	57.96	0.324	0.547

$$a = 0.351,\ a' = 0.010,\ \phi = 7.705,\ \text{and}\ C_L = 0.6115$$

For the elements of force,

$$\Delta X = \frac{1}{2}\rho ZlRc_{x1}^2[(1-a)/\sin\phi]^2\cos\phi C_L\Delta(r/R)$$

where, in Table 10.5, Var.1 $= [(1-a)/\sin\phi]^2\cos\phi C_L\Delta(r/R)$,

$$\sum \text{Var.1} = 6.3416$$

As in Example 10.6, $(1/2)ZlRc_{x1}^2 = 1518.8$, then

$$X = 1518.8 \times 6.3416 = 9631\ N$$

Evaluating the elements of the torque using Eq. (10.42), where, in Table 10.6, Var.2 $= [(1+a')/\cos\phi]^2(r/R)^3C_L\sin\phi\Delta(r/R)$,

$$\sum \text{Var.2} = 40.707 \times 10^{-3} \text{ and } \frac{1}{2}\rho Zl\Omega^2R^4 = 05695 \times 10^6$$

then

$$\tau = 23.183 \times 10^3 \text{ Nm}$$

Hence, $P = \tau\Omega = 57.960$ kW, $C_P = 0.324$, and $\zeta = 0.547$.

These calculations, summarized in Table 10.7, demonstrate that quite substantial reductions occur in both the axial force and the power output as a result of including the Prandtl tip loss correction factor.

10.9 Rotor configurations

Clearly, with so many geometric design and operational variables to consider, it is not easy to give general rules about the way the performance of a wind turbine will be affected by the values of parameters other than (perhaps) running large numbers of computer calculations. The variables for the turbine include the number of blades, blade solidity, blade taper and twist, as well as tip−speed ratio.

Blade planform

In all the preceding worked examples, a constant value of chord size was used, mainly to simplify proceedings. The actual planform used for the blades of most HAWTs is tapered, the degree of taper is chosen for structural, economic, and, to some degree, aesthetic reasons. If the planform is known or one can be specified, the calculation procedure developed previously, i.e., the BEM method, can be easily modified to include the variation of blade chord as a function of radius.

In the following section, Glauert's analysis is extended to determine the variation of the rotor blade planform under *optimum conditions*.

Effect of varying the number of blades

A first estimate of overall performance (power output and axial force) based on actuator disc theory was given earlier. The choice of the number of blades needed is one of the first items to be considered. Wind turbines have been built with anything from 1 to 40 blades. The vast majority of HAWTs, with high tip−speed ratios, have either two or three blades. For purposes such as water pumping, rotors with low tip−speed ratios (giving high starting torques) employ a large number of blades. The chief considerations to be made in deciding on the blade number, Z, are the design tip−speed ratio, J, the effect on the power coefficient, C_P, as well as other factors such as weight, cost, structural dynamics, and fatigue life, which we cannot consider in this short chapter.

Tangler (2000) has reviewed the evolution of the rotor and the design of blades for HAWTs, commenting that, for large commercial machines, the upwind, three-bladed rotor is the industry accepted standard. Most large machines built since the mid-1990s are of this configuration. The blade number choice appears to be guided mainly by inviscid calculations presented by Rohrback and Worobel (1977) and Miller, Dugundji et al. (1978). Figure 10.17 shows the effect on the power coefficient C_P of blade, number for a range of tip−speed ratio, J. It is clear, on the basis of these results, that there is a significant increase in C_P in going from one blade to two blades, rather less gain in going from two to three blades, and so on for higher numbers of blades. In reality, the apparent gains in C_P would be quickly canceled when blade frictional losses are included with more than two or three blades.

Tangler (2000) indicated that considerations of rotor noise and aesthetics strongly support the choice of three blades rather than two or even one. Also, for a given rotor diameter and solidity, a three-bladed rotor will have two-thirds the blade loading of a two-bladed rotor resulting in lower impulsive noise generation.

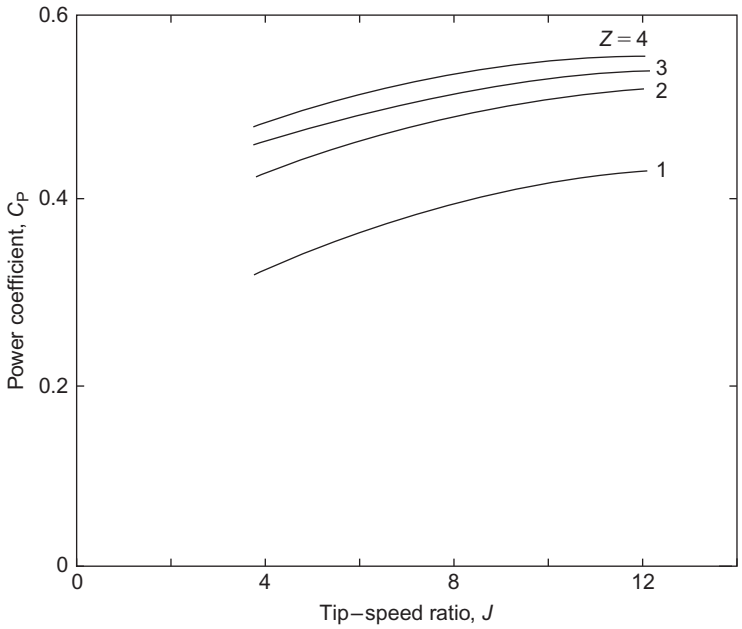

FIGURE 10.17

Theoretical effect of tip−speed ratio and number of blades on power coefficient assuming zero drag.

Effect of varying tip−speed ratio

The tip−speed ratio J is generally regarded as a parameter of some importance in the design performance of a wind turbine. So far, all the examples have been determined with one value of J and it is worth finding out how performance changes with other values of the tip−speed ratio. Using the procedure outlined in Example 10.6, assuming zero drag ($\varepsilon = 0$) and ignoring the correction for a finite number of blades, the overall performance (axial force and power) has been calculated for $C_L = 0.6$, 0.8, and 1.0 (with $l = 1.0$) for a range of J values. Figure 10.18 shows the variation of the axial force coefficient C_X plotted against J for the three values of C_L and Figure 10.19(a) the corresponding values of the power coefficient C_P plotted against J. A point of particular interest is that when C_X is replotted as $C_X/(JC_L)$ all three sets of results collapse onto one straight line, as shown in Figure 10.19(b). The main interest in the axial force would be its effect on the bearings and on the supporting structure of the turbine rotor. A detailed discussion of the effects of both steady and unsteady loads acting on the rotor blades and supporting structure of HAWTs is given by Garrad (1990).

Note: The range of these calculated results is effectively limited by the nonconvergence of the value of the axial flow induction factor a at, or near, the blade tip at high values of J. The largeness of the blade loading coefficient, $\lambda = ZlC_L/(8\pi r)$, is wholly responsible for this nonconvergence of a. In practical terms, λ can be reduced by decreasing C_L or by reducing l (or by a combination of these). Also, use of the tip correction factor in calculations will extend the range of J for which

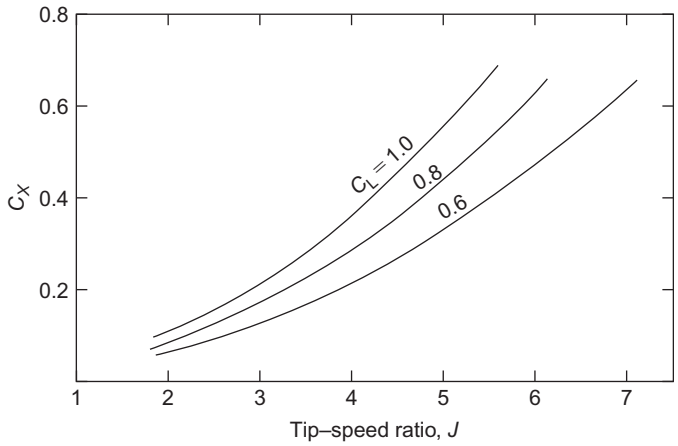

FIGURE 10.18

Variation of the axial force coefficient C_X versus tip–speed ratio J for three values of the lift coefficient $C_L = 0.6$, 0.8, and 1.0.

convergence of a can be obtained. The effect of any of these measures will be to reduce the amount of power developed. However, in the examples throughout this chapter, to make valid comparisons of performance the values of lift coefficients and chord are fixed. It is of interest to note that the curves of the power coefficient C_P all rise to about the same value, approximately 0.48, where the cut-off due to nonconvergence occurs.

Rotor optimum design criteria

Glauert's momentum analysis provides a relatively simple yet accurate framework for the preliminary design of wind turbine rotors. An important aspect of the analysis not yet covered was his development of the concept of the "ideal windmill" that provides equations for the optimal rotor. In a nutshell, the analysis gives a preferred value of the product $C_L l$ for each rotor blade segment as a function of the local speed ratio j defined by

$$j = \frac{\Omega r}{c_{x1}} = \left(\frac{r}{R}\right) J \tag{10.49}$$

By choosing a value for either C_L or l enables a value for the other variable to be determined from the known optimum product $C_L l$ at every radius.

The analysis proceeds as follows. Assuming $C_D = 0$, we divide Eq. (10.36b) by Eq. (10.35b) to obtain

$$\frac{a'(1-a)}{a(1+a')} = \tan^2 \phi \tag{10.50}$$

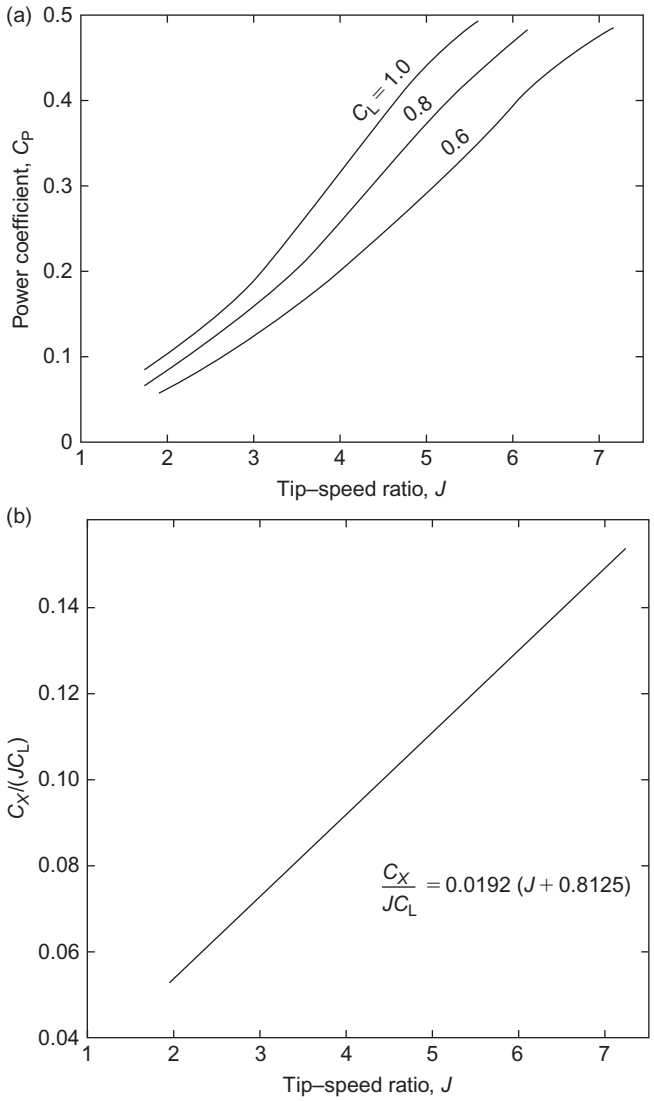

FIGURE 10.19

(a) Variation of the power coefficient C_P versus J for three values of the lift coefficient $C_L = 0.6$, 0.8, and 1.0. (b) Axial force coefficient divided by JC_L and plotted versus J (this collapses all results shown in Figure 10.17 onto a straight line).

Also, from Eqs (10.39) and (10.49), we have

$$\tan\phi = \frac{(1-a)}{j(1+a')} \tag{10.51}$$

We now substitute for tan ϕ in Eq. (10.50) to obtain

$$\frac{1}{j^2} = \frac{a'(1+a')}{a(1-a)} \tag{10.52}$$

Thus, at any radius r, the value of j is constant for a fixed tip−speed ratio J, and the right-hand side is likewise constant. Looking again at Eq. (10.17), for specific values of c_{x1} and Ω, the power output is a maximum when the product $(1-a)a'$ is a maximum. Differentiating this product and setting the result to zero, we obtain

$$a' = \frac{\mathrm{d}a'}{\mathrm{d}a}(1-a) \tag{10.53}$$

From Eq. (10.52), after differentiating and some simplification, we find

$$j^2(1+2a')\frac{\mathrm{d}a'}{\mathrm{d}a} = 1-2a \tag{10.54}$$

Substituting Eq. (10.53) into Eq. (10.54), we get

$$j^2(1+2a')a' = (1-2a)(1-a)$$

Combining this equation with Eq. (10.52), we obtain

$$\frac{1+2a'}{1+a'} = \frac{1-2a}{a}$$

Solving this equation for a',

$$a' = \frac{1-3a}{4a-1} \tag{10.55}$$

Substitute Eq. (10.55) back into Eq. (10.52) and using $1+a' = a/(4a-1)$, we get

$$a'j^2 = (1-a)(4a-1) \tag{10.56}$$

Equations (10.53) and (10.55) can be used to determine the variation of the interference factors a and a' with respect to the coordinate j along the turbine blade length. After combining Eq. (10.55) with Eq. (10.56), we obtain

$$j = (4a-1)\sqrt{\frac{1-a}{1-3a}} \tag{10.57}$$

Equation (10.57), derived for these ideal conditions, is valid only over a very narrow range of a, i.e., $(1/4) < a < (1/3)$. It is important to keep in mind that optimum conditions are much more restrictive than general conditions. Table 10.8 gives the values of a' and j for increments of a in this range (as well as ϕ and λ). It will be seen that for large values of j the interference factor a is

Table 10.8 Relationship Between a', a, ϕ, j, and λ at Optimum Conditions

a	a'	j	ϕ (°)	λ
0.260	5.500	0.0734	57.2	0.4583
0.270	2.375	0.157	54.06	0.4131
0.280	1.333	0.255	50.48	0.3637
0.290	0.812	0.374	46.33	0.3095
0.300	0.500	0.529	41.41	0.2500
0.310	0.292	0.753	35.33	0.1842
0.320	0.143	1.150	27.27	0.1111
0.330	0.031	2.63	13.93	0.0294
0.333	0.003	8.574	4.44	0.0030

only slightly less than $(1/3)$ and a' is very small. Conversely, for small values of j the interference factor a approaches the value $(1/4)$ and a' increases rapidly.

The flow angle ϕ at optimum power conditions is found from Eqs (10.50) and (10.55),

$$\tan^2 \phi = \frac{a'(1-a)}{a(1+a')} = \frac{(1-3a)(1-a)}{a^2}$$

therefore,

$$\tan \phi = \frac{1}{a}\sqrt{(1-3a)(1-a)} \tag{10.58}$$

Again, at optimum conditions, we can determine the blade loading coefficient λ in terms of the flow angle ϕ. Starting with Eq. (10.55), we substitute for a' and a using Eqs (10.36b) and (10.35b). After some simplification, we obtain

$$\lambda^2 = \sin^2 \phi - 2\lambda \cos \phi$$

Solving this quadratic equation, we obtain a relation for the optimum blade loading coefficient as a function of the flow angle ϕ,

$$\lambda = 1 - \cos \phi \equiv \frac{ZlC_L}{8\pi r} \tag{10.59}$$

Returning to the general conditions, from Eq. (10.51) together with Eqs (10.35b) and (10.36b), we obtain

$$\tan \phi = \frac{1(1-a)}{j(1+a')} = \frac{1}{j}\left(\frac{a}{a'}\right)\tan^2 \phi$$

therefore,

$$j = \left(\frac{a}{a'}\right)\tan \phi \tag{10.60}$$

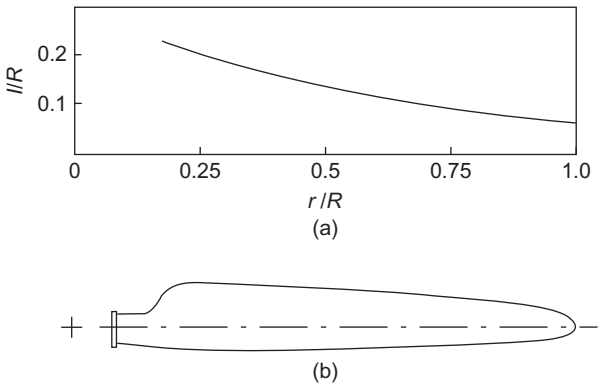

FIGURE 10.20

Examples of variation of chord length with radius: (a) optimal variation of chord length with radius, according to Glauert theory, for $C_L = 1.0$ and (b) a typical blade planform (used for the Micon 65/13 HAWT).

Rewriting Eqs (10.35b) and (10.36b) in the form

$$\frac{1}{a} = 1 + \frac{1}{\lambda}\sin\phi\tan\phi \text{ and } \frac{1}{a'} = \frac{1}{\lambda}\cos\phi - 1$$

and substituting into Eq. (10.60), we get

$$j = \sin\phi\left(\frac{\cos\phi - \lambda}{\lambda\cos\phi + \sin^2\phi}\right) \tag{10.61}$$

Reintroducing optimum conditions with Eq. (10.59),

$$j = \frac{\sin\phi(2\cos\phi - 1)}{(1 - \cos\phi)\cos\phi + \sin 2\phi}$$

therefore,

$$j = \frac{\sin\phi(2\cos\phi - 1)}{(1 + 2\cos\phi)(1 - \cos\phi)} \tag{10.62}$$

$$j\lambda = \frac{\sin\phi(2\cos\phi - 1)}{1 + 2\cos\phi} \tag{10.63}$$

Some values of λ are shown in Table 10.8. Equation (10.62) enables j to be calculated directly from ϕ. These equations also allow the optimum blade layout in terms of the product of the chord l and the lift coefficient C_L (for $C_D = 0$) to be determined. By ascribing a value of C_L at a given radius, the corresponding value of l can be determined.

Figure 10.20 shows the calculated variation of blade chord with radius. The fact that the chord increases rapidly as the radius is reduced would suggest that the blade designer would ignore optimum conditions at some point and accept a slightly reduced performance. A typical blade planform (for the Micon 65/13 HAWT; Tangler et al., 1990) is also included in Figure 10.20 for comparison.

EXAMPLE 10.10

A three-bladed HAWT, with a 30 m tip diameter, is to be designed for optimum conditions with a constant lift coefficient C_L of unity along the span and with a tip−speed ratio $J = 5.0$. Determine a suitable chord distribution along the blade, from a radius of 3 m to the blade tip, satisfying these conditions.

Solution

It is obviously easier to input values of ϕ in order to determine the values of the other parameters than attempting the reverse process. To illustrate the procedure, choose $\phi = 10°$, and so we determine $j\lambda = 0.0567$, using Eq. (10.63). From Eq. (10.59), we determine $\lambda = 0.0152$ and then find $j = 3.733$. Now

$$j = \frac{\Omega r}{c_{x1}} = J\left(\frac{r}{R}\right) = \frac{5}{15}r$$

$$r = 3j = 11.19 \text{ m}$$

As

$$j\lambda = J\left(\frac{r}{R}\right) = \frac{ZlC_L}{8\pi r} = \frac{J}{R}\frac{ZlC_L}{8\pi} = \frac{l}{8\pi}$$

after substituting $J = 5$, $R = 15$ m, $Z = 3$, $C_L = 1.0$. Thus,

$$l = 8\pi \times 0.0567 = 1425 \text{ m}$$

and Table 10.9 shows the optimum blade chord and radius values.

Table 10.9 Values of Blade Chord and Radius (Optimum Conditions)

ϕ (°)	j	$4j\lambda$	r (m)	l (m)
30	1.00	0.536	3.0	3.368
20	1.73	0.418	5.19	2.626
15	2.42	0.329	7.26	2.067
10	3.733	0.2268	11.2	1.433
7.556	5	0.1733	15	1.089

10.10 The power output at optimum conditions

Equation (10.17) expresses the power output under general conditions, i.e., when the rotational interference factor a' is retained in the analysis. From this equation, the power coefficient can be written as

$$C_P = P/\left(\frac{1}{2}\pi\rho R^2 c_{x1}^3\right) = \frac{8}{J^2}\int_{j_k}^{J}(1-a)a'j^3 \, dj$$

Table 10.10 Power Coefficients at Optimum Conditions

J	ζ	C_P	J	ζ	C_P
0.5	0.486	0.288	2.5	0.899	0.532
1.0	0.703	0.416	5.0	0.963	0.570
1.5	0.811	0.480	7.5	0.983	0.582
2.0	0.865	0.512	10.0	0.987	0.584

This equation converts to optimum conditions by substituting Eq. (10.56) into it, i.e.,

$$C_P = \frac{8}{J^2}\int_{j_k}^{J} (1-a)^2(4a-1)j \, dj \tag{10.64}$$

where the limits of the integral are changed to j_h and $J = \Omega R/c_{x1}$. Glauert (1935) derived values for C_P for the limit range $j = 0$ to J (from 0.5 to 10) by numerical integration and the relative maximum power coefficient ζ. These values are shown in Table 10.10. So, to obtain a large fraction of the possible power, it is apparent that the tip−speed ratio J should not be too low.

10.11 HAWT blade section criteria

The essential requirements of turbine blades clearly relate to aerodynamic performance, structural strength and stiffness, ease of manufacture, and ease of maintenance in that order. It was assumed, in the early days of turbine development, that blades with high lift and low drag were the ideal choice with the result that *standard* aerofoils, e.g., NACA 44XX, NACA 230XX, (where the XX denotes thickness to chord ratio, as a percentage), suitable for aircraft were selected for wind turbines. The aerodynamic characteristics and shapes of these aerofoils are summarized by Abbott and von Doenhoff (1959).

The primary factor influencing the lift−drag ratio of a given aerofoil section is the Reynolds number. The analysis developed earlier showed that optimal performance of a turbine blade depends on the product of blade chord and lift coefficient, lC_L. When other turbine parameters such as the tip−speed ratio J and radius R are kept constant, the operation of the turbine at a high value of C_L thus allows the use of narrower blades. Using narrower blades does not necessarily result in lower viscous losses, instead the lower Reynolds number often produces higher values of C_D. Another important factor to consider is the effect on the blade structural stiffness, which decreases sharply as thickness decreases. The standard aerofoils just mentioned also suffered from a serious fault; namely, a gradual performance degradation from roughness effects consequent on leading-edge contamination. Tangler commented that "the annual energy losses due to leading-edge roughness are greatest for *stall-regulated*[6] rotors." Figure 10.21 illustrates the surprising loss in power output of a stall-regulated, three-bladed rotor on a medium scale (65 kW) turbine. The loss

[6]Refer to Section 10.13, Control Methods.

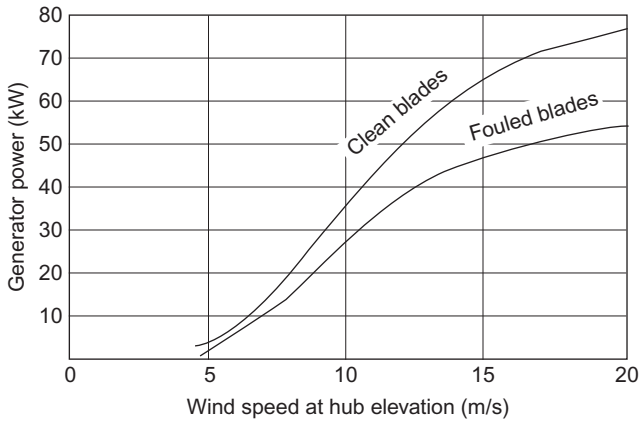

FIGURE 10.21

Power curves from field tests for NACA 4415-4424 blades.

(*Adapted from Tangler, 1990, courtesy of NREL*)

in performance is proportional to the reduction in maximum lift coefficient along the blade. The roughness also degrades the aerofoil's lift-curve slope and increases profile drag, further contributing to losses. Small-scale wind turbines are even more severely affected because their lower elevation allows the accretion of more insects and dust particles and the debris thickness is actually a larger fraction of the leading-edge radius. Some details of the effect of blade fouling on a small-scale (10 m diameter) rotor are given by Lissaman (1998). Estimates of the typical annual energy loss (in the United States) caused by this increased roughness are 20−30%. The newer NREL turbine blades described in the next section are much less susceptible to the effects of fouling.

10.12 Developments in blade manufacture

Snel (1998) remarked, "in general, since blade design details are of a competitive nature, not much information is present in the open literature with regard to these items." Fortunately, for progress, efficiency, and the future expansion of wind energy power plants, the progressive and enlightened policies of the US DOE, NASA, and the National Renewable Energy Laboratory allowed the release of much valuable knowledge to the world concerning wind turbines. Some important aspects gleaned from this absorbing literature follows.

Tangler and Somers (1995) outlined the development of special-purpose aerofoils for HAWTs, which began as a collaborative venture between the National Renewable Energy Laboratory (NREL) and the Airfoils Incorporated. Seven families of blades comprising 23 aerofoils were planned for rotors of various sizes. These aerofoils were designed to have a maximum C_L that was largely insensitive to roughness effects. This was achieved by ensuring that the boundary layer transition from laminar to turbulent flow on the suction surface of the aerofoil occurred very close to the leading edge, just before reaching the maximum value of C_L. These new aerofoils also have

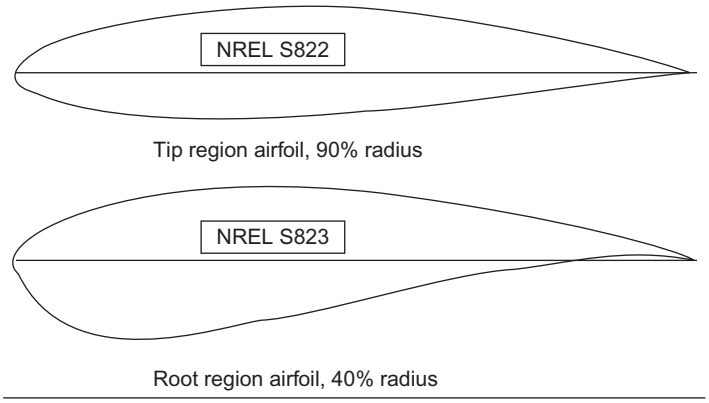

Design specifications

Airfoil	r/R	Re ($\times 10^6$)	t_{max}/l	$C_{L\,max}$	$C_{D\,min}$
S822	0.9	0.6	0.16	1.0	0.010
S823	0.4	0.4	0.21	1.2	0.018

FIGURE 10.22

Thick aerofoil family for HAWTs of diameter 2–11 m ($P = 2$–20 kW).

(*Courtesy of NREL*)

low values of C_D in the clean condition because of the extensive laminar flow over them. The tip–region aerofoils typically have close to 50% laminar flow on the suction surface and over 60% laminar flow on the pressure surface.

The preferred choice of blade from the NREL collection of results rather depends on whether the turbine is to be regulated by stall, by variable blade pitch, or by variable rotor speed. The different demands made of the aerofoil from the hub to the tip preclude the use of a single design type. The changing aerodynamic requirements along the span are answered by specifying different values of lift and drag coefficients (and, as a consequence, different aerofoil sections along the length). For stall-regulated turbines, a limited maximum value of C_L in the blade tip region is of benefit to passively control peak rotor power. Figures 10.22–10.25 show families of aerofoils for rotors originally designated as "small-, medium-, large-, and very large-sized" HAWTs,[7] designed specifically for turbines having low values of maximum blade tip C_L. A noticeable feature of these aerofoils is the substantial thickness–chord ratio of the blades, especially at the root section, needed to address the structural requirements of "flap stiffness" and the high root bending stresses.

According to Tangler (2000), the evolutionary process of HAWTs is not likely to deviate much from the now firmly established three-bladed, upwind rotors, which are rapidly maturing in design. Further refinements, however, can be expected of the various configurations and the convergence

[7]With the top end size of HAWTs growing ever larger with time, the size categories of "large" or "very large" used in the 1990s are rather misleading and, perhaps, better described by stating either the relevant diameter or the power range.

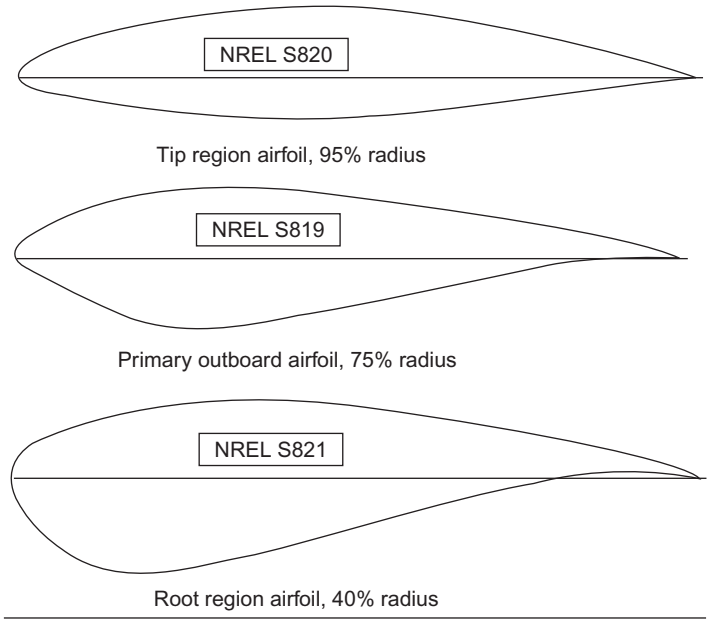

Design specifications

Airfoil	r/R	Re ($\times 10^6$)	t_{max}/l	$C_{L\,max}$	$C_{D\,min}$
S820	0.95	1.3	0.16	1.1	0.007
S819	0.75	1.0	0.21	1.2	0.008
S821	0.40	0.8	0.24	1.4	0.014

FIGURE 10.23

Thick aerofoil family for HAWTs of diameter 11–21 m ($P = 20$–100 kW).

(*Courtesy of NREL*)

toward the best of the three options of stall regulated, variable pitch, and variable speed blades. Blades on large, stall-regulated wind turbines with movable speed control tips may be replaced by variable-pitch blades for more refined peak power control and reliability.

With the very large HAWTs (i.e., 104 m diameter, refer to Figure 10.4(a)) being brought into use, new blade section designs and materials will be needed. Mason (2004) has described "lightweight" blades being made from a carbon/glass fiber composite for the 125 m diameter, 5 MW HAWT to be deployed in the North Sea as part of Germany's first deepwater offshore project.

10.13 Control methods (starting, modulating, and stopping)

Referring to Figure 10.9, the operation of a wind turbine involves starting the turbine from rest, regulating the power while the system is running, and stopping the turbine if and when the wind

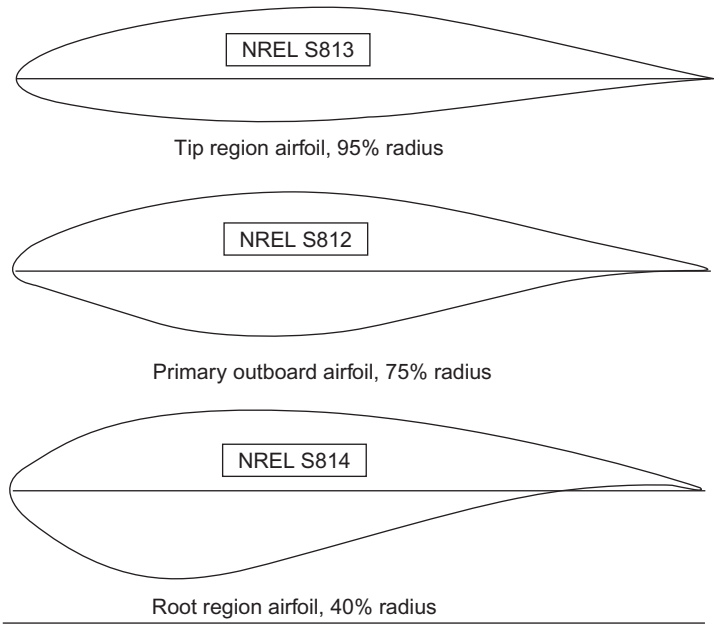

Design Specifications

Airfoil	r/R	Re ($\times 10^6$)	t_{max}/l	$C_{L\,max}$	$C_{D\,min}$
S813	0.95	2.0	0.16	1.1	0.007
S812	0.75	2.0	0.21	1.2	0.008
S814	0.40	1.5	0.24	1.3	0.012
S815	0.30	1.2	0.26	1.1	0.014

FIGURE 10.24

Thick aerofoil family for HAWTs of diameter 21–35 m ($P = 100–400$ kW) (Note: blade profile for S815 was not available).

(*Courtesy of NREL*)

speed becomes excessive. Startup of most wind turbines usually means operating the generator as a motor to overcome initial resistive torque until sufficient power is generated at "cut-in" speed assuming, of course, that a source of power is available.

Blade-pitch control

The angle of the rotor blades is actively adjusted by the machine control system. This, known as *blade-pitch control*, has the advantage that the blades have built-in braking, which brings the blades to rest. Pitching the whole blade requires large actuators and bearings, increasing the weight, and expense of the system. One solution to this problem is to use *partial span blade-pitch control* where only the outer one-third of the blade span is pitched.

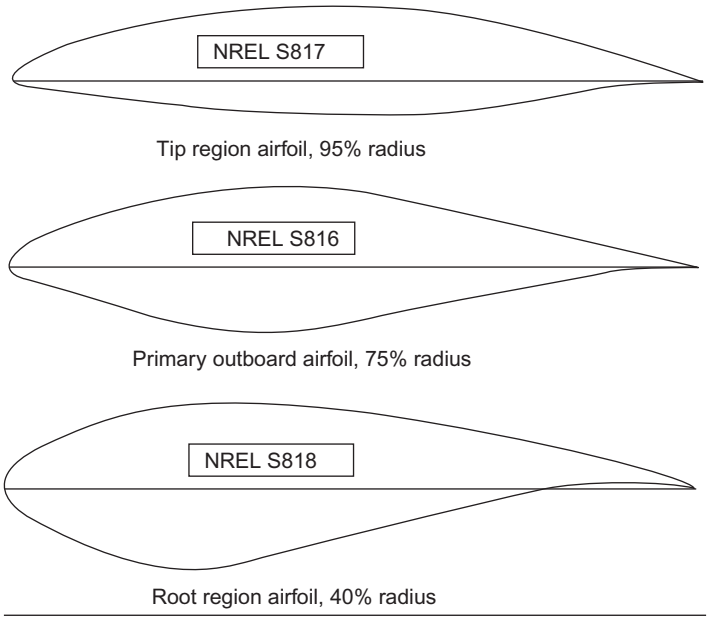

Design specifications

Airfoil	r/R	Re ($\times 10^6$)	t_{max}/l	$C_{L\,max}$	$C_{D\,min}$
S817	0.95	3.0	0.16	1.1	0.007
S816	0.75	4.0	0.21	1.2	0.008
S818	0.40	2.5	0.24	1.3	0.012

FIGURE 10.25

Thick aerofoil family for HAWTs with $D >$ 36 m (blade length = 15–25 m, P = 400–1000 kW).

(*Courtesy of NREL*)

Passive or stall control

The aerodynamic design of the blades (i.e., the distribution of the twist and thickness along the blade length) varies in such a way that blade stall occurs whenever the wind speed becomes too high. The turbulence generated under stall conditions causes less energy to be transferred to the blades minimizing the output of power at high wind speeds.

According to Armstrong and Brown (1990), there is some competition between the advocates of the various systems used in commercial wind farms. The classical European machines are usually stall regulated, while most American designs are now either pitch regulated or, for large turbines, use some form of aileron control.

Aileron control

Aerodynamic control surfaces have been investigated by the US DOE and NASA as an alternative to full blade-pitch control. The aileron control system has the potential to reduce cost and weight

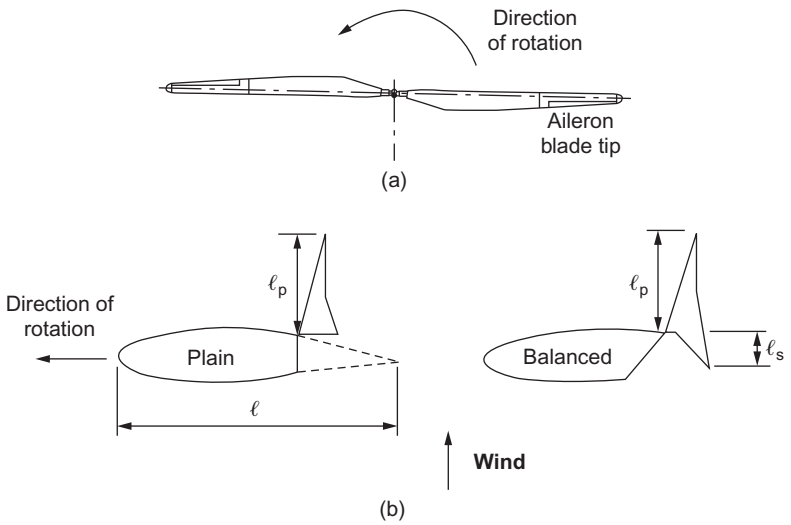

FIGURE 10.26

Aileron control surfaces: (a) showing position of ailerons on two-bladed rotor and (b) two types of aileron in fully deflected position.

(*Adapted from Miller and Sirocky, 1985*)

of the rotors of large HAWTs. The control surfaces consist of a movable flap built into the outer part of the trailing edge of the blade, as shown in Figure 10.26(a). Although they appear similar to the flaps and ailerons used on aircraft wings, *they operate differently*. Control surfaces on an aircraft wing deflect downward toward the high-pressure surface in order to increase lift during takeoff and landing, whereas on a wind turbine blade the flaps deflect toward the low-pressure surface (i.e., downwind side) *to reduce lift and cause a braking effect*. Figure 10.26(b) shows sketches of two typical control surface arrangements in the fully deflected position, included in a paper by Miller and Sirocky (1985). The configuration marked *plain* was found to have the best braking performance. The configuration marked *balanced* has both a low-pressure and a high-pressure control surface, which helps to reduce the control torque.

Ailerons change the lift and drag characteristics of the basic blade aerofoil as a function of the deflection angle. Full-scale field tests were conducted on the Mod-O wind turbine[8] with ailerons of 20% chord and 38% chord. Results from loss of load to shutdown showed that the 38% chord ailerons were the better aerodynamic braking device than the 20% chord ailerons. Also, the 38% chord ailerons effectively regulated the power output over the entire operating range of the Mod-O turbine. Figure 10.27 shows the variation of the lift and drag coefficients for the 38% chord ailerons set at 0°, -60°, and -90°.

[8]Details of the Mod-O wind turbine are given in Divone (1998).

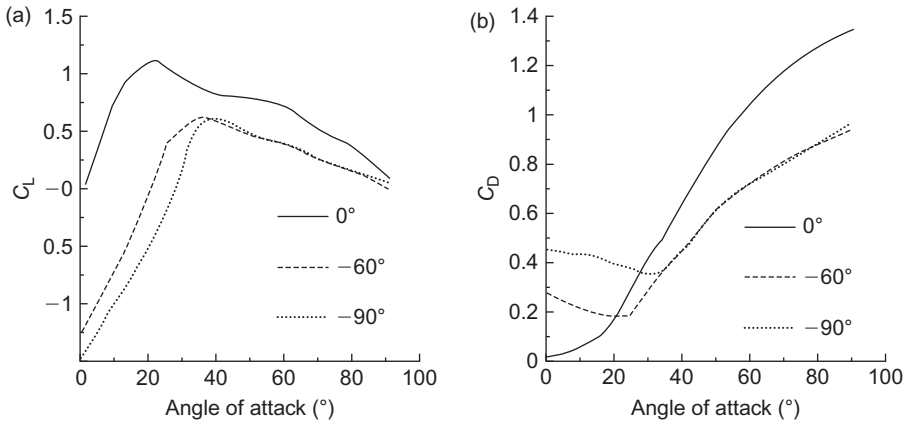

FIGURE 10.27

Variation of (a) lift and (b) drag coefficients for the 38% chord ailerons when set at 0°, −60°, and at −90°.

(*Adapted from Savino, Nyland, and Birchenough, 1985; courtesy of NASA*)

Although wind tunnel tests normally present results in terms of lift and drag coefficients, Miller and Sirocky (1985) wisely chose to represent their aileron-controlled wind turbine results in terms of a *chordwise force coefficient,* C_C (also called a *suction coefficient*). C_C is a combination of both the lift and the drag coefficients, as described next:

$$C_C = C_L \sin \alpha - C_D \cos \alpha \tag{10.65}$$

where α = angle of attack.

The reason for using C_C to describe aileron-control braking effectiveness is that only the chordwise force produces torque (assuming a wind turbine blade with no pitch or twist). Because of this direct relationship between chordwise force and rotor torque, C_C serves as a convenient parameter for evaluating an aileron's braking effectiveness. Thus, if C_C is negative it corresponds to a negative torque producing a rotor deceleration. Clearly, it is desirable to have a negative value of C_C available for all angles of attack. Figure 10.28 shows some experimental results, Snyder, Wentz, and Ahmed (1984) illustrate the variation of the chordwise force coefficient with the angle of attack, *a*, for aileron percent chord of 20% and 30% for several aileron deflection angles. The general conclusions to be drawn from these results are that increasing the aileron chord length and the aileron deflection angle contribute to better aerodynamic braking performance.

10.14 Blade tip shapes

The blade geometry determined with various aerodynamic models gives no guidance of an efficient aerodynamic tip shape. From a basic view of fluid mechanics, a strong shed vortex occurs at the blade tip as a result of the termination of lift and this together with the highly 3D nature of the

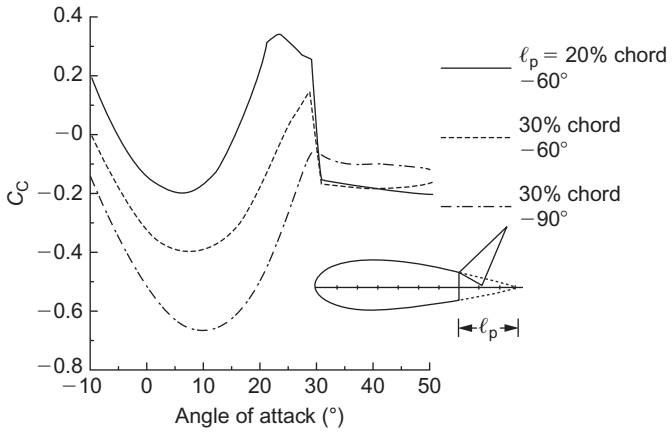

FIGURE 10.28

Effect of chord length on chordwise force coefficient, C_C, for a range of angles of attack.

(*Adapted from Snyder et al., 1984, unpublished*)

flow at the blade tip causes a loss of lift. The effect is exacerbated with a blunt blade end as this increases the intensity of the vortex.

Many attempts have been made to improve the aerodynamic efficiency by the addition of various shapes of "winglet" at the blade ends. Details of field tests on a number of tip shapes intended to improve performance by controlling the shedding of the tip vortex are given by Gyatt and Lissaman (1985). According to Tangler (2000), test experience has shown that rounding the leading-edge corner, Figure 10.29, with a contoured, streamwise edge (a swept tip) yields good performance. Tip shapes of other geometries are widely used. The sword tip also shown is often chosen because of its low noise generation, *but this is at the expense of a reduction in performance*.

10.15 Performance testing

Comparison and improvement of aerodynamic predictive methods for wind turbine performance and field measurements have many inherent limitations. The natural wind is capricious; it is unsteady, nonuniform, and variable in direction, making the task of interpreting performance measurements of questionable value. As well as the nonsteadiness of the wind, nonuniformity is present at all elevations as a result of wind shear, the vertical velocity profile caused by ground friction. The problem of obtaining accurate, measured, steady-state flow conditions for correlating with predictive methods was solved by testing a full-size HAWT in the world's largest wind tunnel, the NASA Ames low speed wind tunnel[9] with a test section of 24.4 m × 36.6 m (80 ft × 120 ft).

[9]Further details of this facility can be found at windtunnels.arc.nasa.gov/80ft1.html.

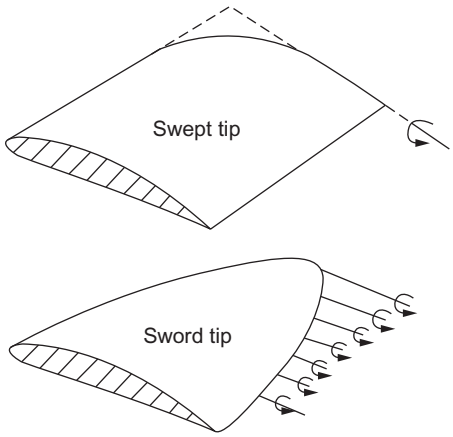

FIGURE 10.29

Blade tip geometries.

(*Tangler, 2000*; *courtesy of NREL*)

Table 10.11 Performance prediction codes

Code Name	Reference
PROP	Wilson and Walker (1976)
PROP93	McCarty (1993)
PROPID	Selig and Tangler (1995)
WTPERF	Buhl (2000)

10.16 Performance prediction codes

BEM theory

The BEM theory presented, because of its relative simplicity, has been the mainstay of the wind turbine industry for predicting wind turbine performance. Tangler (2002) has listed some of the many versions of performance prediction codes based upon the BEM theory and reference to these is shown in Table 10.11.

According to Tangler (2002), some limitations are apparent in the BEM theory that affect its accuracy and are related to simplifications that are not easily corrected. Basically, these errors begin with the assumption of uniform inflow over each annulus of the rotor disc and no interaction between annuli. Also, the tip loss model accounts for blade number effects but not effects due to differences in blade planform.

Lifting surface, prescribed wake theory

Modeling the rotor blades with a lifting surface and its resulting vortex wake is claimed to eliminate the errors resulting from the simplifications mentioned for the BEM theory. The lifting surface, prescribed wake theory (LSWT) is an advanced code capable of modeling complex blade geometries and, according to Kocurek (1987), allows for wind shear velocity profiles, tower shadow, and off-axis operation. Performance predictions are calculated by combining the lifting surface method with blade element analysis that incorporates 2D aerofoil lift and drag coefficients as functions of the angle of attack and the Reynolds number.

It is not possible to pursue the ramifications of this developing theory any further in this introductory text. Gerber et al. (2004) give a useful, detailed description of LSWT methodology and suggestions for its likely future development. Other leading references that give details of LSWT theory are Kocurek (1987) and Fisichella (2001).

Comparison with experimental data

A HAWT with a 10 m diameter rotor was comprehensively tested by NREL in the NASA Ames wind tunnel. Some of these test results are reported by Tangler (2002) and only a brief extract comparing the predicted and measured power is given here. The test configuration comprised a constant speed (72 rpm), two-bladed rotor, which was upwind and stall regulated. Rotor blades (see Giguere and Selig, 1998) for this test had a linear chord taper with a nonlinear twist distribution, as shown in Figure 10.30. It operated with -3° tip pitch relative to the aerofoil chord line. The S809 aerofoil

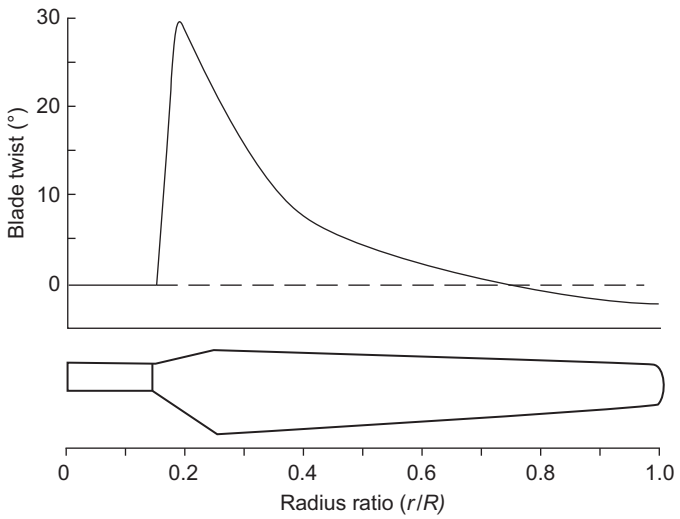

FIGURE 10.30

Rotor blade tested in the NASA Ames wind tunnel showing the chord and twist distributions.

(*Tangler, 2002; courtesy of NREL*)

was used from blade root to tip for simplicity and because of the availability of 2D wind tunnel data for the blade section.

Comparison of the measured power output with the BEM (WTPERF and PROP93) and the LSWT predictions are shown in Figure 10.31, plotted against wind speed. At low wind speeds, up to about 8 m/s, both the BEM and the LSWT predictions are in very good agreement with the measured results. At higher wind speeds both theoretical methods slightly underpredict the power actually measured, the LSWT method rather more than the BEM method. It may be a matter of interpretation but it appears to this writer that only after blade stall (when the measured power sharply decreases) does the LSWT method approach closer to the measured power than the BEM method. Thus, the overall result obtained from wind tunnel measurements appears, in general, to strongly confirm the validity of the BEM theory prior to the onset of stall.

Peak and postpeak power predictions

The comprehensive testing of a highly instrumented 10 m rotor in the NASA Ames 24.4 m × 36.6 m wind tunnel has provided steady-state data that gives better understanding of the complex phenomena of blade stall. Until recently, according to Gerber et al. (2004), peak and

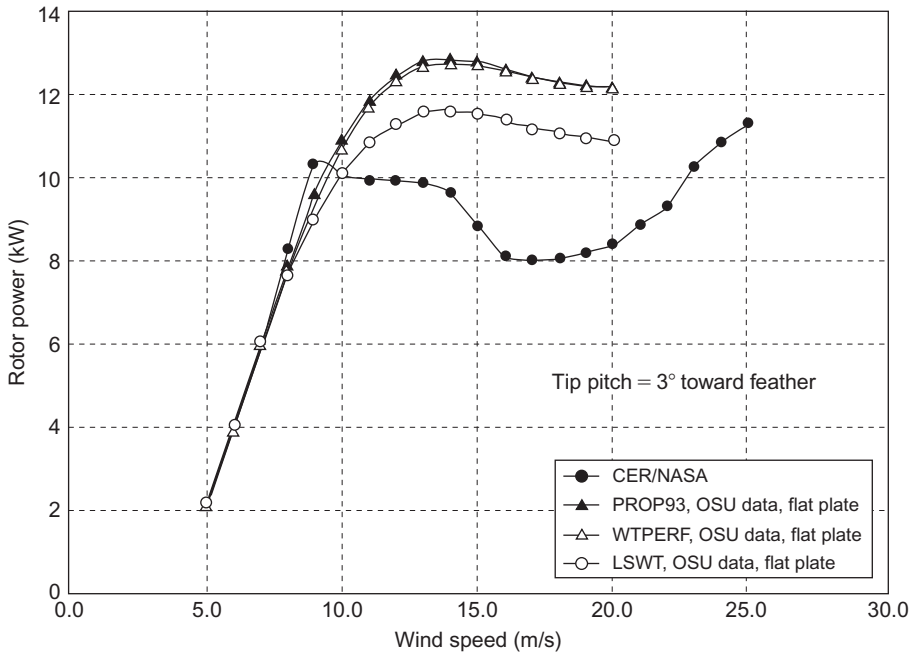

FIGURE 10.31

Measured power output (kW) (CER/NASA) for the 10 m diameter wind turbine versus wind speed (m/s) compared with theoretical predictions.

(*Tangler, 2000; courtesy of NREL*)

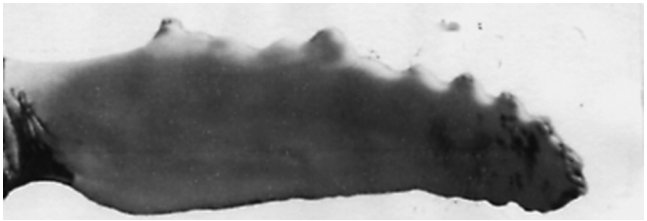

FIGURE 10.32

Large rounded tubercles along the leading edge of the flippers of the baleen whale.

postpeak power were mistakenly thought to coincide with blade stall that originated in the root region and propagated toward the tip with increased wind speed. This rather simplistic scenario does not occur due to 3D *delayed stall* effects. Analysis of some of the more recent data, Tangler (2003), showed leading edge separation to occur in the mid-span region, which spread radially inward and outward with increased wind speed. The BEM approach lacks the ability to model the 3D stall process. Further efforts are being made to take these real effects into account.

Enhanced performance of turbine blades (bioinspired technology)

It has been known for more than a decade that the fins of the baleen whale as shaped by nature, give exceptional swimming performance and maneuverability enabling them to capture prey. Large rounded tubercles along the leading edge of the flippers are morphological structures that are unique in nature (Figure 10.32; Fish et al., 2011). Laboratory experiments on models of these structures have shown that there is a delay in the angle of attack of a blade until the stall point is reached thereby increasing the maximum lift as well as reducing the drag. Figure 10.33 shows some comparative results of the output power of a standard blade and that of a so-called WhalePower blade (of the same shape) plotted against wind speed, obtained by Howle (2009). The tubercles constructed on the leading edges of blades can be applied as a feature to the design of watercraft, aircraft, ventilation fans as well as wind turbines.

10.17 Environmental matters

On what may be classed as aesthetic considerations and environmental objections are the following topics, arguably in decreasing order of importance: (i) visual intrusion, (ii) acoustic emissions, (iii) impact on local ecology, (iv) land usage, and (v) effects on radio, radar, and television reception. Much has been written about all these topics, also numerous websites cover each of them so, for brevity, only a brief recapitulation of some of the main issues regarding the first two are afforded any space in this chapter.

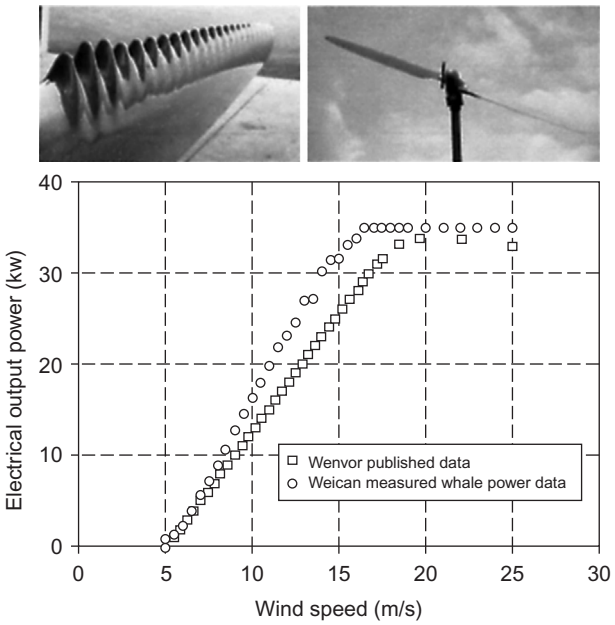

FIGURE 10.33

Wind turbine blade with tubercles (top left) and wind turbine (top right). Graph shows comparison of the output power of a standard blade versus a WhalePower turbine blade.

(*Tests made by the Wind Institute of Canada, Courtesy of WhalePower Corporation*)

Visual intrusion

The matter of public acceptance (in the United Kingdom especially and several other countries) is important and clearly depends upon where the turbines are located and their size. The early investigations of acceptability indicated that the sight of just a few turbines, perhaps a mile or so distant, produced only a few isolated complaints and even appeared to generate some favorable interest from the public. However, any suggestion of locating wind turbines on some nearby *scenic* hillside produced some very strong opposition, comments in the press, and the formation of groups to oppose the proposals. The opposition set up by a few vociferous landowners and members of the public in the 1990s retarded the installation of wind farms for several years in many parts of the United Kingdom. However, wind turbines in larger numbers located in relatively remote upland areas and not occupying particularly scenic ground have been installed. Nowadays, medium- and large-size wind turbines in small numbers (i.e., 20−30) are regarded as beneficial to the community, providing they are not too close. The move to locate wind turbines offshore may have started as a result of this opposition but, as it turned out, there were some hidden benefits. Perhaps they may eventually become tourist attractions in the area. The graceful, almost hypnotic turning of the slender blades of the larger turbines, seemingly in slow motion, has generally led to a more positive aesthetic reaction, in most surveys. Other factors can importantly sway public acceptance of wind turbines. The first factor is the perceived benefit to the community with part or total ownership,

giving lower power costs and possibly even preferential availability of power. The second factor comes from the amount of careful planning and cooperation between the installers and the leaders of the community long before any work on installation commences. It is a strange fact that the old-fashioned, disused windmills, now local landmarks, that abound in many parts of Europe (e.g., see Figure 10.2), are now widely accepted.

Acoustic emissions

Wind turbines undoubtedly generate some noise but, with the improvements in design in recent years, the level of noise emitted by them has dropped remarkably.

Aerodynamic broadband noise is typically the largest contributor to wind turbine noise. The main efforts to reduce this noise have included the use of lower blade tip speeds, lower blade angles of attack, upwind turbine configuration, variable speed operation, and specially modified blade trailing edges and tip shapes. For the new, very large (i.e., 1−5 MW size) wind turbines, the rotor tip speed on land is limited (in the United States the limit is 70 m/s). However, large variable speed wind turbines often rotate at lower tip speeds in low speed winds. As wind speed increases, the rotor speed is allowed to increase until the limit is reached. This mode of operation results in much quieter working at low wind speeds than a comparable constant speed wind turbine.

The study of noise emitted by wind turbines is a large and complex subject. No coverage of the basic theory is given in this chapter. Numerous publications on acoustics are available and one particularly recommended as it covers the study of fundamentals to some extent is the white paper by Rogers and Manwell (2004), prepared by NREL. A wide ranging, deeper approach to turbine noise is given in the NASA/DOE publication "Wind Turbine Acoustics," by Hubbard and Shepherd (1990).

A particular problem occurs in connection with small wind turbines. These turbines are sold in large numbers in areas remote from electric utilities and are often installed close to people's homes, often too close. There is an urgent need for reliable data on the levels of noise generated so that homeowners and communities can then reliably anticipate the noise levels from wind turbines prior to installation. The NREL have performed acoustic tests (Migliore, van Dam, & Huskey, 2004) on eight small wind turbines with power ratings from 400 W to 100 kW to develop a database of acoustic power output of new and existing turbines and to set targets for low noise rotors. Test results will be documented as NREL reports, technical papers, seminars, colloquia, and on the Internet. In comparing the results, Migliore et al. reported that, following improvements to the blading, the noise from the Bergey Excel (see Figure 10.4(b)) was reduced to the point that the turbine noise could not be separated from the background noise. As a result, any further testing will need to be done in a much quieter location.

10.18 The largest wind turbines

Claims are sometimes made that a new wind turbine is the biggest yet and produces more power than any other. Such claims need to be carefully considered and compared with verified performance data. The latest claimant (in 2011) for the title of "largest wind turbine" appears to be the Enercon E-126, a 3-bladed rotor of 127 m diameter and rated at 7.58 MW. The hub height was stated to be 135 m.

The previous record holder was the 5 MW REpower Systems wind turbine installed at Brunsbüttel in Schleswig-Holstein, Germany (October 1, 2004), according to a report in *Renewable Energy World* (November–December 2004). The three-bladed rotor again has a tip diameter of 126.3 m (blade length 61.5 m, maximum chord 4.6 m) and a hub height of 120 m.

The various speeds and rotor speed range quoted (data that may be useful in problem solving) are

Rotor speed	6.9–12.1 rev/min
Rated wind speed	13 m/s
Cut-in wind speed	3.5 m/s
Cut-out wind speed	25 m/s (onshore); 30 m/s (offshore)

The chief factors that influence the higher output of the Enercon E-126 turbine seems to be the increased hub height and possibly the windier location of the site.

A factor of some importance in getting higher performance from HAWT's is the enormous length of the individual blades and transporting them to the site of use often along roads with unhelpful bends. Until recently, the world's longest blades were around 80–100 m. Now blades are being made of carbon fiber (instead of fiberglass) in shorter pieces which are joined up together. This advance makes possible individual offshore wind turbines with an output capacity of 8–10 MW.

What are the limits on the size of wind turbine

A recent investigation by Ceyhan (2012) has been made in a project called UPWIND in which several aspects of the design have been investigated. Due to the increased blade size, 252 m diameter, the local Reynolds number values along the blade were found to be as high as 25×10^6 while the local wind speeds remain constant. Further progress on this advanced project is hampered by the lack of performance data for aerofoils operating at such high Reynolds numbers. The author of this seminal work concludes that high quality measurements will be the key to obtaining cost effective and reliable designs for very large offshore wind turbines.

10.19 Final remarks

This chapter has given an introduction to the aerodynamics of HAWTs. In order to model the performance of a HAWT, it was necessary to give a brief introduction to the mathematics of wind speed probability. By combining the statistical method of probability theory with the important but relatively simple BEM method, the performance of a HAWT over a wide range of wind speeds can be determined.

PROBLEMS

1. Determine the diameter of a HAWT rotor required to generate 0.42 MW of power in a steady wind of 10 m/s at hub height. Assume that the power coefficient $C_P = 0.35$, the air density is 1.2 kg/m^3 and the mechanical efficiency, $\eta = 0.88$.

2. The original 5 MW, three-bladed HAWT, made by RE Systems has a tip diameter of 126.3 m and a rated wind speed of 13 m/s. Determine the rated value of the power coefficient C_P and compare this with the value at the Betz limit. Assume the air density $\rho = 1.2$ kg/m^3.

3. For the preceding problem, using actuator disc theory, determine the *axial flow induction factor,* $\overline{a}$, and the static pressure difference across the disc at the rated wind speed.

4. A HAWT with a hub height of 80 m and blades of 80 m diameter develops 1.824 MW in a wind of 12 m/s with a blade tip−speed ratio of 4.5. Determine

a. the power coefficient, the relative maximum power coefficient, and the rotational speed;

b. for the same wind speed at 80 m height the wind speed that could be expected at a height of 150 m and, if the hub height was raised to that level, the likely power output if the power coefficient remains the same.

Assume the density is constant at 1.2 kg/m^3 and that the one-seventh power law applies.

5. A three-bladed HAWT of 50 m diameter, has a constant blade chord of 2 m. and operates with a tip−speed ratio, $J = 4.5$. Using an iterative method of calculation determine the values of the axial and tangential induction factors (a and a') at a radius ratio of 0.95 and the value of the lift coefficient. Assume the drag coefficient is negligible (and can be ignored) compared with the lift coefficient and that the pitch angle of the blades $\beta = 3°$.

Note: This problem requires the application of the BEM iterative method. Students are recommended to write computer programs for solving problems of this type.

(Stop the calculation after three iterations if solving manually.)

6. Using the methods of probability theory for a Rayleigh distribution of the wind speed, show that

$$\int_0^\infty p(c)\mathrm{d}c = 1 \text{ where } p(c) = \frac{\pi}{2}\left(\frac{c}{\overline{c}}\right)\exp\left[-\frac{\pi}{4}\left(\frac{c}{\overline{c}}\right)^2\right] \text{ and}$$

where c is the fluctuating wind speed and $\overline{c}$ is the mean wind speed.

7. **a.** In calculating the maximum possible power production of a wind turbine (Carlin's method) show that the integral

$$\int_0^\infty c^3\left\{\frac{2c}{c_c^2}\exp\left[-\left(\frac{c}{c_c}\right)^2\right]\right\}\mathrm{d}c \text{ reduces to } \left(\frac{3}{4}\right)\sqrt{\pi}$$

where the characteristic wind velocity $c_c = 2c/\sqrt{\pi}$.

b. Determine the maximum idealized power output using Carlin's formula for a turbine of 28 m diameter in a wind regime with an average wind speed of 10 m/s and an air density of 1.22 kg/m^3.

8. A turbine has a cut-in speed of 4.5 m/s and a cut-out speed of 26 m/s. Assuming that the turbine is located at a favorable site where the mean annual wind speed is 10 m/s and a Rayleigh wind speed distribution may be applied, calculate:

a. the annual number of hours below the cut-in speed when the turbine does not produce any power;

b. the annual number of hours when the turbine is within the usable range of wind speed.

9. A three-bladed rotor of a HAWT with blades of 20 m tip radius is to be designed to work with a constant lift coefficient $C_L = 1.1$ along the length of the span at a tip−speed ratio, $J = 5.5$. Using Glauert's momentum analysis of the "ideal wind turbine," determine the variation of the chord size along the length of the span for the radius range of 2.8 m to a radius of 19.5 m.

Note: It is expected that students attempting this classical problem will need to become familiar with the theory of Glauert outlined in section "rotor optimum design criteria." Also, this problem requires the application of the BEM iterative method of solution. Students are recommended to write a computer program for solving this type of problem, probably saving much time.

References

Abbott, I. H., von Doenhoff, A. E. (1959). *Theory of wing sections* New York, NY: Dover.

Ackermann, T., & Söder, L. (2002). An overview of wind energy—Status 2002. *Renewable and Sustainable Energy Reviews*, *6*(1−2), 67−127.

Anderson, M. B. (1980). A vortex-wake analysis of a horizontal axis wind turbine and a comparison with modified blade element theory. *Proceedings of the third international symposium on wind energy systems*, Copenhagen, BHRA Fluid Engineering, paper no. H1 357−374.

Armstrong, J., Brown, A. (1990). Horizontal axis WECS design. In: L. L. Freris (Ed.), *Wind energy conversion systems*. Englewood Cliffs, NJ: Prentice-Hall.

Baker, T. L. (1985). *A field guide to American windmills* Norman, OK: University of Oklahoma Press.

Betz, A. (1926). Windenergie und ihreAusnutzungdurchWindmühlen, *Vandenhoek und Ruprecht*, Gottingen. Reprint 1982, by öko−Verlag Kassel, Germany.

Buhl, M. L. (2000). *WT_PERF user's guide*, NREL Golden, CO.

Carlin, P. W. (1997) Analytic expressions for maximum wind turbine average power in a Rayleigh wind regime. *Proceedings of the 1997 ASME/AIAA wind symposium* (pp. 255−263).

Ceyhan, O. (2012). Towards 20 MW Wind turbines: high reynolds number effects on rotor design. ECN−M−12−02. *50th AiAA aerospace sciences meeting*, January 2012, Nashville, TN.

Divone, L. V. (1998). Evolution of modern wind turbines. In: D. A. Spera (Ed.), *Wind turbine technology*. New York, NY: ASME Press.

Eggleston, D. M., Stoddard, F. S. (1987). *Wind turbine engineering design,* New York, NY: Van Nostrand Reinhold Co..

Fish, E. F., Weber, P. W., Murray, M. M., Howle, L. E. (2011). The tubercles on humpback whales flippers: Application of bio-inspired technology. *Integrative and Comparitive Biology*, *51*(1), 203−213.

Fisichella, C. J. (2001). *An improved prescribed wake analysis for wind turbine rotors* (Ph.D. thesis). Mechanical Engineering Department, University of Illinois.

Garrad, A. D. (1990). Forces and dynamics of horizontal axis wind turbines. In: L. L. Freris (Ed.), *Wind energy conversion systems*. Englewood Cliffs, NJ: Prentice-Hall.

Gasch, R. (2002). *Wind power plants—fundamentals, design, construction and operation* Solarpraxis, Berlin: German Wind Energy Association, distributed by.

Gerber, B. S., Tangler, J. L., Duque, E. P. N., & Kocurek, D. (2004). *Peak and post-peak power predictions for constant speed rotor operation* U.S. Department of Energy, (off the Internet).

Giguere, P., Selig, M. S. (1998). *Design of a tapered and twisted blade for the NREL combined experiment rotor*, Subcontract No. XAF-4-14076-03.

Glauert, H. (1935). Airplane propellers. In: W. F. Durand, & L. Division (Eds.), *Aerodynamic theory*. Berlin: Springer(Reprinted 1976, Glouster, MA: Peter Smith).

Goldstein, S. (1929). On the vortex theory of screw propellers. *Proceedings of the royal society*, *A123*, 440–465.

Gyatt, G. W., & Lissaman, P. B. S. (1985). *Development of tip devices for HAWTs* Cleveland, OH: NASA Lewis Research Center, NASA CR 174991.

Howle, L. E. (2009). WhalePower Wenvor blade. A report on the efficiency of a Whalepower Corp. 5 m prototype wind turbine blade. BeleQuant Engineering, PLLC.

Hubbard, H. H., Shepherd, K. P. (1990). *Wind turbine acoustics*, NASA Technical paper 3057 DOE/NASA/20320-77.

Kocurek, D. (1987). *Lifting surface performance analysis for HAWTs*, SERI/STR-217-3163.

Lissaman, P. B. S. (1998). Wind turbine airfoils and rotor wakes. In: D. A. Spera (Ed.), *Wind turbine technology*. New York, NY: ASME Press.

Livingston, J. T., Anderson, T. (2004). *Taller turbines, and the effects on wind farm development create a need for greater height wind assessment*, WASWATCH WIND.

Lynette, R., Gipe, P. (1998). Commercial wind turbine systems and applications. In: D. A. Spera (Ed.), *Wind turbine technology*. New York, NY: ASME Press.

Manwell, J. F., McGowan, J. G., Rogers, A. L. (2009). *Wind energy explained (theory, design and application).* New York, NY: John Wiley & Sons, reprinted 2010).

Mason, K. F. (2004). Wind energy: Change in the wind. *Composites Technology*.

McCarty, J. (1993). PROP93 user's guide, *alternative energy institute* Canyon, TX: West Texas State University.

Migliore, P., van Dam, J., Huskey, A. (2004). *Acoustic tests of small wind turbines*, NREL SR-500-34601. AIAA-2004-1185.

Miller, D. R., Sirocky, P. J. (1985). Summary of NASA/DOE aileron-control development program for wind turbines. In *Proceedings Windpower '85 Conference*, Washington, DC: American Wind Energy Association, 537–545 SERI/CP-217-2902.

Miller, R. H., Dugundji, J., Martinez-Sanchez, M., Gohard, J., Chung, S., & Humes, T. (1978). Aerodynamics of horizontal axis wind turbines, *Wind Energy Conversion*, *vol. 2*, MIT Aeroelastic and Structures Research Lab. TR-184-7 through TR-184-16. DOE Contract No. COO-4131-T1. Distribution category UC-60.

Prandtl, L., Tietjens, O. G. (1957). *Applied hydro- and aeromechanics* New York, NY: Dover Publications.

Renewable Energy World (September–October 2009) *12*, 5. Waltham Abbey, UK: PennWell International Ltd.

Richards, B. (1987). Initial operation of project Eolé 4 MW vertical axis wind turbine generator. In *Proceedings Windpower '87 Conference* (pp. 22–27), Washington, DC: American Wind Energy Association.

Rogers, A. L., Manwell, J. F. (2004). *Wind turbine noise issues*. Renewable Energy Research Laboratory 1–19 University of Massachusetts, Amherst.

Rohrback, W. H., Worobel, R. (1977). *Experimental and analytical research on the aerodynamics of wind driven turbines*. Hamilton Standard, COO-2615-T2.

Savino, J. M., Nyland, T. W., Birchenough, A. G. (1985). *Reflection plane tests of a wind turbine blade tip section with ailerons*. NASA TM-87018, DOE/NASA 20320-65.

Schwartz, M. (1999). Wind resource estimation and mapping at the National Renewable Energy Laboratory, Golden, CO (NREL/CP–500–26245).

Selig, M. S., Tangler, J. L. (1995). Development and application of a multipoint inverse design method for HAWTs. *Wind Engineering*, *19*(2), 91–105.

Sharpe, D. J. (1990). Wind turbine aerodynamics. In: L. L. Freris (Ed.), *Wind energy conversion systems*. Englewood Cliffs, NJ: Prentice-Hall.

Snel, H. (1998). Review of the present status of rotor aerodynamics. *Wind Energy*, *1*, 46–49.

Snyder, M. H., Wentz, W. H., Ahmed, A. (1984). *Two-dimensional tests of four airfoils at angles of attack from 0 to 360 deg.* Center for Energy Studies, Wichita State University (unpublished).

Tangler, J. L., Smith, B., Kelley, N. and Jager, D. (1990). *Atmospheric performance of the special purpose SERI thin airfoil family: Final results*. SERI/ TP-257-3939, European Wind Energy Conference, Madrid, Spain.

Tangler, J. L. (2000). *The evolution of rotor and blade design*, NREL/CP—500—28410.

Tangler, J. L. (2002). The nebulous art of using wind-tunnel airfoil data for predicting rotor performance. Presented at the *21st ASME wind energy conference*, Reno, Nevada.

Tangler, J. L. (2003). *Insight into wind turbine stall and post-stall aerodynamics* Austin, TX: AWEA, (off the Internet).

Tangler, J. L., Somers, D. M. (1995). *NREL airfoil families for HAWTs*, NREL/TP-442-7109. UC Category: 1211. DE 95000267.

Walker, J. F., Jenkins, N. (1997). *Wind energy technology* New York, NY: John Wiley & Sons.

Wilson, R. E., (1976). *Performance analysis for propeller type wind turbines*. Ph.D. Thesis. Oregon State University.

World Energy Council (1994). *New renewable energy sources* London: Kogan Pagen.

Xi L., McElroy, M. B. Kiviluoma, J. (2009). *Global potential for wind-generated electricity*. PNAS Early Edition. www.pnas.org/cgi/doi.

Appendix A: Preliminary Design of an Axial-Flow Turbine for a Large Turbocharger

Turbochargers are used to increase the power output of internal combustion engines by compressing the air prior to it being admitted into the engine. This is achieved by employing a centrifugal compressor driven by a turbine that is powered by the engine exhaust gases. Figure A.1 shows the mechanical arrangement with the compressor and turbine on a common shaft. An air or water cooler is often used to reduce the temperature of the air entering the engine, enabling greater power to be achieved by the engine.

There are two basic types of turbocharger:

1. Small units for turbocharging the complete range of automobiles and trucks that incorporate an *inward flow radial turbine*.
2. Large units whose duties include ship propulsion and electrical power generation, typically 1 MW and above, employ an *axial-flow turbine*. The present design study is directed to this larger size of unit. The essential design philosophy of these larger turbochargers is that they have high efficiencies over a limited flow range unlike the automotive turbochargers, which usually have a rather lower efficiency over a wide flow range. All turbochargers need to be compact, durable, and have low unit cost. Typically, for these large units, low unit cost is maintained by using single-stage turbines even for pressure ratios greater than 4.5.

Detailed discussions of the various types and design features of turbochargers are given by Flaxington and Swain (1999) and by Iwaki and Mitsubori (2004).

Design requirements

The total pressure available at turbine inlet	2.1 kPa
The static pressure at turbine exit, p_3	1.05 kPa
Entry temperature of products of combustion to turbine, T_{01}	500°C
Mass flow rate, $\dot{m}$	8 kg/s
Free-vortex design	
Reaction ratio, R	0.4
Flow coefficient, ϕ	0.4
Axial flow at entry and exit of turbine	
Target efficiency, η_{tt}	0.90
Assume a constant value of specific heat at constant pressure, C_p(kJ/kg °C)	1.178
Assume a ratio of specific heats, γ	1.32

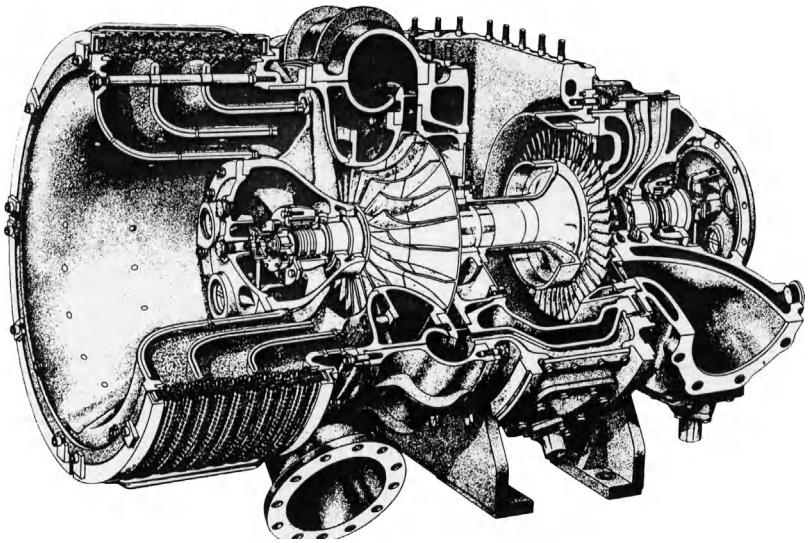

FIGURE A.1

The mechanical arrangement of the centrifugal compressor and axial-flow turbine of a large turbocharger.

(*With permission of ABB Asea Brown Beverl*)

Mean radius design

The steps in a preliminary design of an axial-flow turbine are essentially a process of trial and error and several different approaches are possible depending on the data available, any additional assumptions that may have to be made, and the designer's previous experience. The notation used relates to that of Figure 4.4.

First we need to determine the isentropic enthalpy drop across the stage, $\Delta h_{is} = h_{01} - h_{3ss}$.

The isentropic temperature ratio is

$$\frac{T_{3ss}}{T_{01}} = \left(\frac{p_3}{p_{01}}\right)^{(\gamma-1)/\gamma} = 0.5^{0.2424} = 0.8453$$

Therefore,

$$\Delta h_{is} = C_p T_{01}(1 - T_{3ss}/T_{01}) = 1.178 \times 773 \times (1 - 0.8453) = 140.8 \text{ kJ/kg}$$

and

$$T_{3ss} = 653.4 \text{ K}$$

From Figure 4.4, $\Delta W = h_{01} - h_{03}$ and the total-to-total efficiency can be written as

$$\eta_{tt} = \frac{\Delta W}{h_{01} - h_{03ss}} \approx \frac{\Delta W}{h_{01} - h_{3ss} - (1/2)c_3^2}$$

using the small approximation, $(1/2)c_3^2 \approx (1/2)c_{3ss}^2$. Hence,

$$\Delta h_{is} = \frac{\Delta W}{\eta_{tt}} + \frac{1}{2}c_3^2 = \frac{\Delta W}{\eta_{tt}} + \frac{1}{2}c_x^2$$

From Eq. (4.13a) and with $\alpha_1 = 0$ (axial entry flow),

$$R = 1 - \frac{c_x \tan \alpha_2}{2U} \tag{A.1}$$

therefore,

$$\Delta W = Uc_x \tan \alpha_2 = 2(1-R)U^2 = \eta_{tt}\left(\Delta h_{is} - \frac{1}{2}c_x^2\right) \tag{A.2}$$

after some rearranging.

Using $\phi = c_x/U$ in the preceding and with a little more rearranging we get:

$$U^2 = \frac{\eta_{tt}\Delta h_{is}}{2(1-R) + (1/2)\eta_{tt}\phi^2} \tag{A.3}$$

Using the values of the parameters given in the design requirements, we get

$$U = 315.6 \text{ m/s} \quad \text{and} \quad c_x = 126.3 \text{ m/s}$$

From Eq. (A.2), $\Delta W = 2(1-R)U^2 = 119.6$ kJ/kg,

$$\tan \alpha_2 = \frac{\Delta W}{Uc_x} = \frac{119.55 \times 10^3}{315.6 \times 126.3} = 3.0$$

$$\alpha_2 = 71.56^\circ$$

Determining the mean radius velocity triangles and efficiency

We can easily determine the rest of the data necessary to calculate the total-to-total efficiency. For $\alpha_3 = 0^\circ$,

$$\tan \beta_3 = U/c_x = 1/\phi = 2.5, \text{ so } \beta_3 = 68.2^\circ$$

From Eq. (4.13b) with $\alpha_3 = 0^\circ$,

$$\tan \beta_2 = \tan \beta_3 - 2R/\phi = 0.5, \quad \text{so} \quad \beta_2 = 26.57^\circ$$
$$w_3 = c_x/\cos \beta_3 = 340.1 \text{ m/s}$$
$$c_2 = c_x/\cos \alpha_2 = 399.3 \text{ m/s}$$

From Eq. (4.20b), we use the approximation for the total-to-total efficiency recommended for initial calculations, i.e.,

$$\eta_{tt} = \left[1 + \frac{\zeta_R w_3^2 + \zeta_N c_2^2}{2\Delta W}\right]^{-1}$$

The Soderberg loss coefficients, in their simplest form, are used,

$$\zeta = 0.04[1 + 1.5(\varepsilon/100)^2]$$

For the rotor, $\varepsilon_R = \beta_2 + \beta_3 = 94.77°$, hence, $\zeta = 0.0939$.

For the nozzle row, $\varepsilon_N = \alpha_2 = 71.56°$, hence, $\zeta = 0.0707$.

Evaluating the total-to-total efficiency using these data, $\eta_{tt} = 91.5\%$.

This is fairly close to the value originally used in the calculations and a further iteration at this stage of the design with this new value is not really necessary.

The total-to-static efficiency can be evaluated from Eq. (4.21b), i.e.,

$$\eta_{ts} = \left[1 + \frac{\zeta_R w_3^2 + \zeta_N c_2^2 + c_x^2}{2\Delta W}\right]^{-1}$$

Hence, we get, $\eta_{ts} = 86.26\%$.

It is worth noting that values of total-to-static efficiency are shown in Figure 4.17 for a stage with axial flow at exit with the coordinate axes, stage loading coefficient, $\psi = \Delta W/U^2$, and flow coefficient, $\phi = c_x/U$. In the present design, the value of $\psi = 1.2$ and $R = 0.4$ at the mean radius and, not unexpectedly, we obtain complete accord for the value of η_{ts} from the graph.

The nozzle exit Mach number $M_2 = c_2/\sqrt{\gamma R T_2}$ is now determined:

$$T_2 = T_{01} - c_2^2/(2C_p) = 705.3 \text{ K}$$

$$\gamma R = (\gamma - 1)C_p$$

$$M_2 = 0.774$$

Note: Turbine stages can be designed to operate at much higher loads, i.e., with larger available pressure ratios, resulting in supersonic absolute flow at nozzle exit and possibly supersonic relative flow into the rotor. For such flows, shock wave systems will occur and some loss in efficiency is then inevitable. Supersonic and transonic flows in axial turbine cascades are discussed in Chapter 3.

Determining the root and tip radii

The axial-flow area at nozzle exit is $A_2 = \dot{m}/(\rho_2 c_x)$ where $p_2/(RT_2)$. We need to determine the static pressure p_2 taking into account the nozzle losses. It is easily shown that

$$\frac{p_2}{p_{01}} = \left(\frac{T_{2s}}{T_{01}}\right)^{\gamma/(\gamma-1)}$$

and, for a nozzle,

$$\left(1 - \frac{T_{2s}}{T_{01}}\right) = \left(1 - \frac{T_2}{T_{01}}\right)/\eta_N$$

Table A.1 Results for several values of hub-to-tip radius ratio

r_h/r_t	0.75	0.8	0.85	0.9	Notes
r_t (cm)	25.56	28.17	32.09	38.78	
H (cm)	6.39	5.634	4.814	3.878	Blade height
U_t (m/s)	360.7	350.7	341.2	332.2	Tip speed
$\frac{\sigma_c/\rho_m}{10^4\ m^2/s^2}$	2.846	2.214	1.615	1.048	
σ_c (MPa)	223.4	173.8	126.8	104.8	Centrifugal stress
N (rev/min)	13,476	11,887	10,153	8,180	Rotor speed
R_h	0.18	0.24	0.29	0.33	Reaction at the hub
Z	44	56.5	77.5	119	Number of blades with $H/s = 2$

At this point in the design we have no information on the magnitude of nozzle efficiency. However, in a nozzle the losses will be low and a value $\eta_N = 0.97$ is selected. Using this value and earlier data, determine $T_{2s}/T_{01} = 0.9097$. Hence,

$$p_2 = 0.6768 p_{01} = 1.4213 \times 10^5 \text{ Pa} \quad \text{as} \quad p_{01} = 2.1 \times 10^5 \text{ Pa}$$

Thus, $p_2 = p_2/(RT_2) = 0.7056$ kg/m^3 with $R = 285.6$ kJ/kg °C. Therefore, the flow area

$$A_2 = \frac{\dot{m}}{\rho_2 c_x} = \frac{8}{0.7056 \times 126.3} = 0.08977 \text{ m}^2$$

In Table A.1, several values of hub−tip ratio have been selected to discover the most suitable blade aspect ratio, rotational speed, and blade root stress for the turbine rotor. Equation (4.34a) gives the centrifugal stress developed at the root of the rotor blades. It is assumed that the blades are untapered and made of steel ($\rho_m = 7850$ kg/m^3).

The blade tip radius is determined from Eq. (4.25),

$$r_t = \sqrt{A_2/\pi[1 - (r_h/r_t)^2]}$$

and the average blade temperature $T_b = 721$ K is determined from Eq. (4.35).

Comparing the stress divided by density values with the rather limited data given in Figure 4.20, the stress levels are quite low and there appears to be no limitation in using untapered steel blades.

Variation of reaction at the hub

In Chapter 6, an application of free-vortex flow was made to an axial-flow compressor where it was shown that the reaction increases radially as we go from root to tip, see Eq. (6.9). The same result applies to the axial-flow turbine stage and here our interest must be directed to how small the reaction becomes at the hub. This is important as losses can become large when the reaction is very low or even negative.

Table A.2 Data for the Calculated Velocity Triangles

r/r_t	α_2 (deg)	β_2 (deg)	β_3 (deg)	U (m/s)	R_h
1.0	69.14	−13.0	70.7	360.7	0.54
0.875	71.6	26.6	68.2	315.6	0.4
0.75	74.1	53.7	65.0	270.5	0.183

Note: Axial velocity $c_x = 126.3$ m/s at all radii.

From Eq. (A.1), for all radii,

$$R = 1 - \frac{c_x \tan \alpha_2}{2U} = 1 - \frac{c_{\theta 2}}{2U} = 1 - \frac{K}{2Ur}$$

When referring to particular flow conditions at the mean radius, the subscript m will be added to the variables R and r. Thus,

$$R_m = 1 - \frac{K}{2U_m r_m}$$

Combining these expressions, the radial variation of reaction is

$$R = 1 - (1 - R_m)\left(\frac{r_m}{r}\right)^2$$

Values of R at the hub radius r_h are given in Table A.2 as a function of r_h/r_t. The value of r_h/r_t at which $R = 0$ is 0.632.

Choosing a suitable stage geometry

Deciding on a suitable configuration for the turbine is not so easy as several factors need to be considered in making a decision. The size of the unit can be of importance and usually the turbocharger needs to be made as small as possible. As shown in Table A.1, by making r_t smaller the speed of rotation must increase. As a result both the blade length and the root stress are increased. It is also necessary to check that the blade pitch s is not so small that the blades cannot be safely attached to the rim of the turbine disc. In small turbines such as this design it may be practicable to consider either machining the blades and disc from a single forging or welding the blades onto the disc.

The blade aspect ratio H/s is another factor that can affect the efficient working of the turbine. This ratio needs to be sufficiently large that the end wall losses and secondary flow losses do not become excessive. A just acceptable value of H/s is 2.0 and, in Table A.1, the values of $Z = 2\pi r_m/s$ resulting from this choice are shown.

Although the decision is not absolutely clear cut, on balance the present designer favors the smallest size of the selection, $r_h/r_t = 0.75$ with 44 blades. With the sizing choice having now been made the flow angles at the root and tip radii are determined and the velocity diagrams are added to Figure A.2.

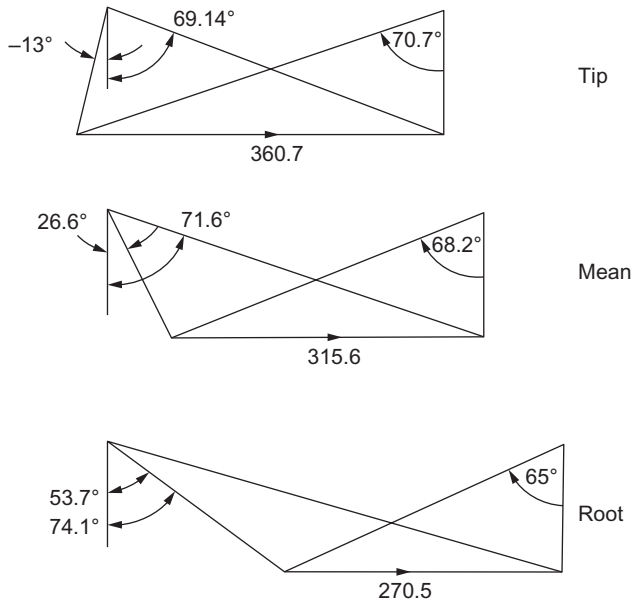

FIGURE A.2

Velocity triangles for root, mean, and tip radii.

As a precaution against the possibility of inducing resonant frequencies between the rotor blades and the nozzle blades, the number of nozzle blades is chosen to be 45, thereby avoiding common multiples.

Estimating the pitch/chord ratio

Referring to the measured profile loss coefficients for turbine nozzle and impulse blades, the data of Figure 3.24, indicate two significant trends:

1. Losses increase generally as the flow deflection increases.
2. The greater the flow deflection required, the lower must be the pitch−chord ratio to minimize the losses.

The simplified form of Zweifel's criterion, Eq. (3.55) can be applied to the mean radius of the rotor:

$$Z = 2(s/b)\cos^2 \beta_3(\tan \beta_3 + \tan \beta_2) = 0.8$$

with $\beta_2 = 26.6^\circ$ and $\beta_3 = 68.2^\circ$, we get

$$s/b = 0.8/0.8275 = 0.967$$

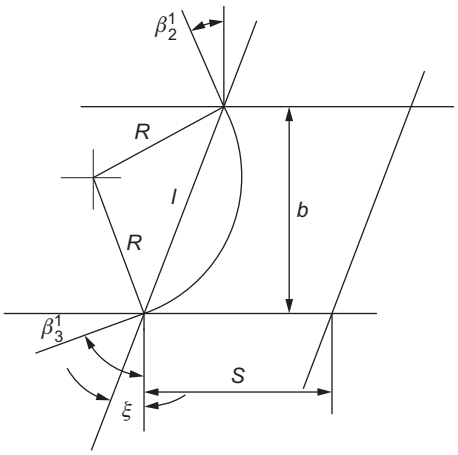

FIGURE A.3

Construction details to determine stagger angle.

The relationship between the axial chord, b, and the true chord, l, of a blade row is not simple or at all obvious. However, a simple, approximate geometric relationship can be found based upon the assumption of a single circular arc to represent the camber line of a turbine blade in a cascade, as shown in Figure A.3. From the construction details shown in this figure, the stagger angle ξ can be obtained from

$$\tan \xi = \frac{\cos \beta_2' - \cos \beta_3'}{\sin \beta_2' + \sin \beta_3'}$$

Making a crude approximation, we can substitute the relative flow angles β_2 and β_3 into this expression and so derive a "stagger" angle,

$$\tan \xi = \frac{\cos 26.6 - \cos 68.2}{\sin 26.6 + \sin 68.2} = \frac{0.5228}{1.376} = 0.3798$$

$$\xi = 20.8^\circ$$

Hence, $s/l = (s/b)(b/l) = 0.967 \times \cos 20.8 = 0.903$.

This space–chord ratio appears to be suitable and is in agreement with the values found by Ainley and Mathieson (1951), Figure 3.24, although the exact value is not crucial.

The velocity triangles for the root, mean, and tip radii are drawn in Figure A.2. Equation (4.15) can be used to obtain the relative flow angles shown in Table A.2 with $\alpha_3 = 0$.

Blade angles and gas flow angles

A point well worth remembering is that the velocity triangles relate to the gas angles and not to the blade angles. Cascade results for impulse and reaction blades, e.g., Figure 3.25, show that the

Table A.3 Results at hub, mid-span and tip.

Radius (cm)	$r_h = 19.17$ cm	$r_m = 22.37$ cm	$r_t = 25.56$ cm
Nozzle exit Mach number	0.906	0.74	0.682
Nozzle exit velocity (m/s)	460	399	355

profile loss coefficients for reaction blades are not very sensitive to the angle of incidence over a wide range (-20° to 15°). This means that in the preliminary design exercise the rotor blades can have less twist along their length, i.e., blade sections may operate at varying amounts of incidence without incurring excessive losses.

Additional information concerning the design

Power output	$\dot{m}\Delta W = 956.4$ kW
Rotational speed	$N = 13{,}476$ rev/min
Rotor tip radius	$r_t = 25.56$ cm
Rotor blade chord	$l = 4.56$ cm
Rotor blade temperature	$T_b = 772$ K

See also Table A.3.

Postscript

The initial design described is one of many possible methods that could be employed and was governed by the initial assumptions (free-vortex design, choices of degree of reaction, and flow coefficient) as well as decisions made about the radius ratio and blading. Students could further investigate the effect of increasing the value of the flow coefficient (so reducing the turbine diameter), increasing the reaction ratio or using a nonfree-vortex flow such as the *first power stage design*, Eq. (6.15). In all such design attempts, it would be wise to check the values of reaction and Mach number at the blade root for reasons given earlier.

References

Ainley, D. G., & Mathieson, G. C. R. (1951). A method of performance estimation for axial flow turbines. *ARC. R. and M.*, 2974.

Flaxington, D., & Swain, E. (1999). Turbocharger aerodynamic design. Proceedings of the Institution of Mechanical Engineers, *Part C: Journal of Mechanical Engineering Science*, *213*(1), 43–57.

Iwaki, F., & Mitsubori, K. (2004). Development of TPL and TPS series marine turbocharger. *IHI Engineering Review*, *37*(1), 35–39.

Appendix B: Preliminary Design of a Centrifugal Compressor for a Turbocharge

This design is a follow-up to the preliminary turbine design given in Appendix A to which it is linked. The power delivered to the compressor will be rather less than that produced by the turbine to allow for bearing frictional losses. The air mass flow entering the compressor will be lower than the products of combustion entering the turbine because of the fuel used by the engine. The rotational speed of the compressor is the same as that of the turbine as they are on the same shaft.

For the turbine, a premium was placed on small size, so that for the compressor a vaned diffuser will be needed to restrict the size of the turbocompressor. Prewhirl of the inlet flow will not be required both to simplify the design and because of the expected fairly low Mach numbers. As this compressor is not a heavily loaded, high-performance design, the use of backward swept impeller vanes is unlikely to confer much advantage in comparison with a design having radial vanes. In fact, certain attributes associated with backward swept vanes suggest that a higher overall efficiency can be achieved although this design study has not been extended to include such vanes.

Design requirements and assumptions

Power supplied by the turbine (allowing for bearing friction), P	947 kW
Rotational speed, N	13,476 rev/min
Air mass flow, $\dot{m}$	7.5 kg/s
Inlet stagnation temperature, T_{01}	293 K
Inlet stagnation pressure, p_{01}	105 kPa
Assume a constant value of specific heat, C_p	1.005 kJ/kg °C
Assume a constant value of ratio of specific heats, γ	1.4
The number of rotor blades, Z	21

Determining the blade speed and impeller radius

The specific work is $\Delta W = P/\dot{m} = 947 \times 10^3/7.5 = \mathbf{126.3 \times 10^3}\ \mathrm{m^2/s^2}$.[1]

The impeller radius is easily found since $\Delta W = U_2 c_{\theta 2}$ and, using the Stanitz expression for the slip factor, $\sigma = 0.63\pi/Z = c_{\theta 2}/U_2 = \mathbf{0.9057}$:

$$U_2 = \sqrt{\Delta W/\sigma} = \mathbf{373.4}\ \mathrm{m/s}$$

[1]Results shown in **bold** will be referred to later.

$$r_2 = U_2/\Omega = \mathbf{0.265}\ \text{m as}\ \Omega = \mathbf{1411}\ \text{rad/s}$$

Design of impeller inlet

Several alternative methods can be used to start the design of the inlet. We can choose a particular ratio of r_{s1}/r_2, usually in the range of 0.35−0.65, and select an axial velocity to blade tip speed ratio at inlet, c_{x1}/U_{s1}, in the range of 0.4−0.5, then proceed from there to calculate the hub−tip radius ratio from the continuity equation. The magnitude of the maximum relative Mach number at the inlet, $M_{1,\text{rel}}$, at the shroud radius r_{s1} can then be checked and further repeated adjustments made as required to the values of r_{h1}/r_2 and c_{x1}/U_{s1}.

A more direct method is available using the theory already developed leading to Eq. (7.13a). The inlet radius ratio can be determined by a suitable choice of the *relative* inlet Mach number $M_{1,\text{rel}}$ at the shroud. Referring to Eq. (7.12a) with $\gamma = 1.4$, this is

$$f(M_{1,\text{rel}}) = \frac{\Omega^2 \dot{m}}{\pi k p_{01} \gamma a_{01}} = \frac{M_{1,\text{rel}}^3 \sin^2 \beta_{s1} \cos \beta_{s1}}{(1+(1/5)M_{1,\text{rel}}^2 \cos^2 \beta_{s1})^4} \tag{7.13a}$$

where $k = 1 - (r_{h1}/r_{s1})^2$. For $\alpha_1 = 0$ and a fixed value of $M_{1,\text{rel}}$, the optimum value of β_{s1}, is at the maximum value of $f(M_{1,\text{rel}})$ (see Figure 7.8). For a fixed value of $M_{1,\text{rel}}$, it can be shown by differentiating the right-hand side of Eq. (7.13a), that this maximum occurs when

$$\cos^2 \beta_{s1} = X - \sqrt{X^2 - 1/M_{1,\text{rel}}^2}$$

where $X = 0.7 + 1.5/M_{1,\text{rel}}^2$.

Using the given or derived data, several optimum values of k and hub−tip ratios have been determined (to illustrate the trend) for a range of values of $M_{1,\text{rel}}$, shown in Table B.1.

The value $r_{h1}/r_{s1} = 0.443$ is in the normal range used in practice and corresponds to $M_{1,\text{rel}} = 0.7$, which seems satisfactory.

The inlet dimensions are now easily found with the equation of continuity, $\dot{m} = \rho_1 A_1 c_{x1}$:

$$r_{x1}^2 = \frac{\dot{m}}{\pi k \rho_1 c_{x1}}$$

where

$$\rho_1 = \rho_{01} \Big/ \left[1 + \frac{1}{5} M_1^2\right]^{2.5}$$

and $c_{x1} = M_1 a_1$,

$$M_1 = M_{1,\text{rel}} \cos \beta_{s1} = 0.7 \times \cos 57.94 = \mathbf{0.3716}$$

Table B.1 Values of k and radius ratio determined for several values of $M_{1,rel}$

$M_{1,\text{rel}}$	0.7	0.75	0.8	0.85
Max of right-hand side of Eq. (7.13a)	0.1173	0.1420	0.1695	0.2000
β_{s1} (deg) at max of $f(M_{1,\text{rel}})$	57.94	58.36	58.78	59.25
k	0.8037	0.6640	0.5560	0.4715
r_{h1}/r_{s1}	0.4430	0.5796	0.666	0.7270

$$a_1 = a_{01}/\left[1+\frac{1}{5}M_1^2\right]^{0.5} = 338.5 \text{ m/s}$$

and

$$c_{x1} = 0.3716 \times 338.5 = 125.8 \text{ m/s}$$

As $\rho_{01} = p_{01}/(RT_{01}) = 1.249 \text{ kg/m}^3$, $\rho_1 = 1.249/1.0704 = 1.1669 \text{ kg/m}^3$. Thus, $r_{s1}^2 = 7.5/(\pi \times 0.8037 \times 1.1669 \times 125.8) = 0.02024$ and

$$r_{s1} = \mathbf{0.1423} \text{ m and } r_{h1} = \mathbf{0.0630} \text{ m.}$$

Efficiency considerations for the impeller

In well-designed radial-vaned impellers, the stagnation pressure losses are not large and isentropic efficiencies up to 92% have been attained at the optimum specific speed, $N_S = 0.6-0.7$.[2] The reason for the high efficiency achieved by centrifugal compressor impellers is because of the major contribution made to the compression process by the *frictionless* centrifugal term $(1/2)(U_2^2 - U_1^2)$, shown in Eq. (7.2). Rodgers (1980) noted that impellers with between 25° and 50° of backsweep were found to give around 2% higher efficiency than those with radial vanes. Notwithstanding the efficiency advantage of backswept vanes we shall persist with radial vanes because of their greater simplicity and obviously lower manufacturing cost. In the present radially bladed impeller, it seems quite reasonable to assume an isentropic efficiency $\eta_i = 92\%$ for the impeller, and this value is used in the following calculations.

Design of impeller exit

Designers often choose a value for the radial component of velocity c_{r2} at impeller exit equal to the axial velocity c_{x1} at impeller entry. Hence, we shall use $c_{r2} = \mathbf{125.8}$ m/s.

As $U_2 = 373.4$ m/s and $\sigma = 0.9057$, then $c_{\theta 2} = \mathbf{338.2}$ m/s

[2] In this design, $N_s = \phi^{0.5}/\psi^{0.75}$, where $\phi = c_{x1}/U_2 = 118.7/373.4 = 0.3179$ and $\psi = \Delta W/U_2^2 = 126.3 \times 10^3/373.4^2 = 0.9058$. Hence, $N_s = 0.607$ (based on inlet axial velocity).

$$c_2 = \sqrt{c_{\theta 2}^2 + c_{\mathrm{r}2}^2} = \mathbf{360.8}\ \mathrm{m/s}$$

and the flow angle $\alpha_2 = \tan^{-1}(c_{\theta 2}/c_{\mathrm{r}2}) = \mathbf{69.60}^\circ$ (measured from the radial direction).

From the continuity equation, Eq. (1.8), $\dot{m} = \rho_2 A_2 c_{\mathrm{r}2} = 7.5$ kg/s and $A_2 = 2\pi r_2 b_2$, so to solve for b_2 we need to determine the density, $\rho_2 = p_2/(RT_2)$.

Now

$$\eta_{\mathrm{i}} = \frac{h_{02\mathrm{s}} - h_{01}}{h_{02} - h_{01}} = \frac{T_{02s}/T_{01} - 1}{T_{02}/T_{01} - 1}$$

and

$$\frac{T_{02}}{T_{01}} = \frac{\Delta W}{C_{\mathrm{p}} T_{01}} + 1 = \mathbf{1.4289}$$

and $T_{02} = \mathbf{418.7}$ K.

Hence, with $\eta_{\mathrm{i}} = 0.92$, we obtain $T_{02s}/T_{01} = \mathbf{1.3946}$ and $p_{02}/p_{01} = \mathbf{3.203}$; therefore,

$$p_{02} = \mathbf{336.3}\ \mathrm{kPa}$$

$$T_2 = T_{02} - \frac{c_2^2}{2C_{\mathrm{p}}} = \mathbf{353.9}\ \mathrm{K}\ \text{ so }\ T_2/T_{01} = \mathbf{1.2080}\ \text{ and }\ T_{02}/T_2 = \mathbf{1.1830}$$

$$p_2 = p_{02} \Big/ \left(\frac{T_{02}}{T_2}\right)^{\gamma(\gamma-1)} = \mathbf{186.7}\ \mathrm{kPa}$$

Hence, $\rho_2 = p_2/RT_2 = 186.7 \times 10^3/(287 \times 353.9) = 1.838\ \mathrm{kg/m^3}$, so

$$b_2 = \dot{m}/(2\pi\rho_2 c_{r2} r_2) = 0.0195\ \mathrm{m} = \mathbf{1.95}\ \mathrm{cm}$$

$$\frac{b_2}{r_2} = \frac{1.95}{26.5} = 0.0736$$

At impeller exit the Mach number, $M_2 = c_2/a_2$, where $a_2 = \sqrt{\gamma RT_2} = 377.1$ m/s,

$$M_2 = 360.8/377.1 = \mathbf{0.957}.$$

Flow in the vaneless space

The region between the impeller exit, radius r_2 and the start of the diffuser vanes at radius $r_{2\mathrm{d}}$ is known as the *vaneless space* and within this space the flow is treated as though it was in a vaneless diffuser (see notes on Vaneless diffusers). The flow leaving the impeller is known to have extensive

regions of separated flow and to be highly nonuniform and may have strong, deleterious effects on the diffuser performance. Having a vaneless space allows some flow diffusion to take place but also allows some reduction of these flow irregularities before entry into the diffuser vanes.

The minimum radius ratio for the vaneless space, r_{2d}/r_2, mentioned by Cumpsty (1989) and others is 1.1, although this ratio could be further increased if necessary to reduce the Mach number of the flow at entry to the vanes. In the case of the present design, the Mach number, M_2, is not excessive so that this measure is not needed. We will assume that the axial width of the vaneless space remains constant at $b_2 = \mathbf{1.95}$ cm.

Despite the known highly irregular flow entering the vaneless space, it is usually assumed for the purposes of a preliminary design that a smoothed out and frictionless flow exists. It is assumed for simplicity that the flow is frictionless, that the tangential momentum is conserved within the vaneless space. In Chapter 7, the flow in a parallel walled diffuser was assumed to be incompressible and this led to the idea of a *logarithmic spiral* flow path as described by Eq. (7.42).

We may determine the tangential velocity at the radius $r_{2d} = 1.1r_2$ from

$$\frac{c_{\theta 2d}}{c_{\theta 2}} = \frac{r_2}{r_{2d}} \quad \text{so} \quad c_{\theta 2d} = 338.2/1.1 = \mathbf{307.5}\ \text{m/s}$$

$$c_{r2d} = \frac{r_2}{r_{2d}} c_{r2} = 114.36\ \text{m/s}, \alpha_{2d} = \cos^{-1}(114.36/307.5) = \mathbf{68.16}^\circ$$

$$c_{2d} = (c_{2d}^2 + c_{r2d}^2)^{0.5} = 328.1\ \text{m/s},\ T_{2d} = T_{02} - c_{2d}^2/(2C_p) = 418.7 - 328.1^2/2010 = 365.2\ \text{K}$$

$$a_{2d} = (\gamma R T_{2d})^{0.5} = 383.0, \quad \text{so} \quad M_{2d} = 328.1/383 = \mathbf{0.856}$$

An iterative procedure

The flow at entry to our vaneless diffuser space is in a high subsonic Mach number range and one might expect a significant change in Mach number to occur across the diffuser. So, in the following analysis, a progressive series of approximations is used to try and discover just how much the density (and Mach number) changes.

In the *first approximation*, the radial velocity at radius r_{2d} is obtained using the incompressible log-spiral approximation:

$$c_{r2d} = c_{r2}(r_2/r_{2d}) = 125.8/1.1 = 114.3$$

Hence,

$$c_{2d} = (c_{\theta 2d}^2 + c_{r2d}^2)^{0.5} = (307.5^2 + 114.3^2)^{0.5} = 328.06\ m/s$$

In the *second approximation*, we can determine T_{2d} and p_{2d} at radius r_{2d}:

$$T_{2d} = T_{02} - c_{2d}^2/2C_p = 418.7 - 328.062/2010 = 365.2\ \text{K}$$

$$p_{2d} = p_{02}/(T_{02}/T_{2d})^{\gamma/(\gamma-1)} = 336.3 \times 10^3/(418.7/365.2)^{3.5} = 208.4\ \text{kPa}$$

$$p_{2d} = \frac{p_{2d}}{RT_{2d}} = \frac{208.4 \times 10^3}{287 \times 365.2} = 1.988\ \text{kg/m}^3$$

$$A_{2d} = 2\pi r_{2d} b_2 = 2\pi \times 0.2915 \times 0.0195 = 0.03572 \text{ m}^2$$

so that

$$c_{r2} = \dot{m}/(\rho_{2d} A_{2d}) = 7.5/(1.988 \times 0.03572) = 105.6 \text{ m/s}$$

$$c_{2d} = (105.6^2 + 307.5^2)^{0.5} = 325.1 \text{ m/s}$$

For the third approximation,

$$T_{2d} = T_{02d} - c_{2d}^2/(2C_p) = 418.7 - 325.1^2/2010 = 366.1 \text{ K}$$

$$p_{2d} = p_{02d}/(T_{02d}/T_2)^{\gamma/(\gamma-1)} = 336.3/(418.7/366.1)^{3.5} = 210.2 \text{ kPa}$$

$$p_{2d} = 210.2/(287 \times 366.1) = 2.000 \text{ kg/m}^3$$

$$c_{r2d} = \dot{m}/(p_{2d} A_{2d}) = 7.5/(2.00 \times 0.03572) = 104.98 \text{ m/s}$$

therefore,

$$c_{2d} = (104.98^2 + 307.5^2)^{0.5} = 324.9 \text{ m/s}$$

This iteration has provided sufficient convergence so that the Mach number M_{2d} and flow angle α_{2d} can be determined:

$$M_{2d} = c_{2d}/\sqrt{\gamma R T_{2d}} = 324.9/\sqrt{1.4 \times 287 \times 366.1} = \mathbf{0.847}$$
$$\alpha_{2d} = \tan^{-1}(c_{\theta 2d}/c_{r2d}) = \tan^{-1}(307.5/104.98) = \mathbf{71.15}^\circ$$

This calculation shows that, for this spiraling flow with a high subsonic Mach number, the change in radius between the impeller exit and the entrance to the vaned diffuser actually causes only a small change in Mach number and flow angle.

A more elegant method of solution for the flow in the vaneless space is to use the compressible flow equation:

$$\frac{\dot{m}}{A_n p_0}\sqrt{C_p T_0} = \frac{\gamma M}{\sqrt{\gamma - 1}}\left(1 + \frac{\gamma - 1}{2} M^2\right)^{(1/2)[(\gamma+1)/(\gamma-1)]} \tag{1.39}$$

In the vaneless space, the values of $\dot{m}$, C_p, T_0, and p_0 are constant by assumption and $\gamma = 1.4$. Thus, the equation reduces to

$$\frac{A_n M}{(1 + (1/5)M^2)^3} = \text{constant}$$

It will be appreciated that A_n is the area $2\pi rb$ and the change in area we are considering is controlled by the radial direction r. It is thus necessary to apply this expression to the change in radius from r_2 to r_{2d} using the radial component of M.

At entry to the vaneless space, $M_2 = 0.957$ and $\alpha_2 = 69.6^\circ$, so that $M_{2r} = 0.957 \cos 69.6^\circ = 0.3336$.

Hence, we need to solve for M_{2r} in the expression

$$\frac{r_2 M_{2r}}{(1+(1/5)M_{2r}^2)^3} = \frac{r_{2d} M_{2dr}}{(1+(1/5)M_{2dr}^2)^3}$$

Substituting $r_{2d}/r_2 = 1.1$ and $M_{2r} = 0.3336$, we can solve iteratively (or using tables) to obtain $M_{2r} = 0.2995$. With $\alpha_2 = 69.6°$, we find $M_{2d} = \mathbf{0.858}$.

Determining the Mach number change across the vaneless space may be regarded (in this instance) as just an exercise in the use of the compressible flow equation. The result obtained varies only slightly from that determined using incompressible flow analysis.

The vaned diffuser

From Figure 7.25 (with $L/W_1 = 8$), a good choice of a plate diffuser would be one with $2\theta = 8°$, corresponding, at this point, to the values $C_p = 0.7$ and $C_{p,id} = 0.8$. This is close to the maximum efficiency condition for this type of diffuser and, according to the data shown in Figure 7.24, is in the flow regime that avoids stall.

From Eq. (7.48), the static pressure at diffuser exit will be

$$p_3 = p_{2d} + C_p q_{2d} = 210.2 + 0.7 \times 105.6 = 284.1 \text{ kPa}$$

and by using Eq. (7.51) the exit velocity will be

$$c_3 = c_{2d}(1 - C_{p,id})^{0.5} = 324.9(1-0.8)^{0.5} = \mathbf{145.3} \text{ m/s}$$

The actual number of diffuser "nozzles" is fairly arbitrary but is usually chosen to be much less than the number of impeller vanes. In this design, the number chosen is $Z = 12$ corresponding with common practice in manufacturing.

The volute

The purpose of the volute (or scroll), shown in Figure 7.4, is simply to collect the compressed air leaving the diffuser and guide it to the engine air intake. The energy losses in the volute are partly the result of the dissipation of the kinetic energy at diffuser exit due to turbulent mixing and partly due to friction on the solid surfaces of the volute. According to Watson and Janota (1982), the total loss in the volute is usually assumed to be (about) half of the dynamic pressure leaving the diffuser. Here, we shall assume this extra loss is exactly half of the available dynamic pressure.

Determining the exit stagnation pressure, p_{03}, and overall compressor efficiency, η_C

We determine the density, $\rho_3 = p_3/RT_3$, where $T_3 = T_{03} - c_3^2/(2C_p) = 411.9$ K and $p_3 = 284.1$ kPa. Hence, $\rho_3 = 2.409$ kg/m^3.

Immediately on leaving the diffuser the total pressure is approximately $p_{03} = p_3 + q_3$ where $q_3 = (1/2)\rho_3 c_3^2$, and $q_3 = 16.4$ kPa, hence, $p_{03} = 300.9$ kPa. Because of the total pressure losses in the volute mentioned previously, the final total pressure at compressor exit is estimated as $p_{03} = p_3 + (1/2)q_3 = \mathbf{293}$ kPa.

The overall compressor efficiency η_C can be found with Eq. (7.10):

$$\eta_C = C_p T_{01}(T_{03ss}/T_{01} - 1)/\Delta W$$

where $T_{03ss}/T_{01} = (p_{03}/p_{01})^{(1/35)} = 1.3407$. Thus,

$$\eta_C = 0.794$$

This value of overall efficiency is rather low and can be attributed to the poor diffuser efficiency ($\eta_D = 0.805$). The performance of the conical diffuser is known to be fairly resistant to stall, particularly with the flow issuing from the impeller, which is turbulent and unsteady. So, another attempt is made to redesign the diffuser with $C_p = C_p^* = 0.8$.

Again, from Figure 7.26 the new values of $A_2/A_1 = 4.42$ and $N/R_1 = 18.8$:

$$C_{p,id}^* = 1 - 1/A_R^2 = 0.9490 \text{ and } \eta_D = C_p^*/C_{p,id}^* = \mathbf{0.843}$$

Following the previous calculations, the results obtained for the new diffuser are

$$p_3 = 295.3 \text{ kPa}$$

$$c_3 = 73.0 \text{ m/s}$$

$$T_3 = 416.0 \text{ K}$$

$$\rho_3 = 2.473 \text{ kg/m}^3$$

and

$$p_{03} = 301.9 \text{ kPa}$$

With the volute loss included, $p_{03'} = 298.6$ kPa.

Thus, $T_{03ss'}/T_{01}(298.6/105)^{(1/35)} - 1.3480$ and the compressor efficiency is

$$\eta_C = 81.1\%$$

This is a substantial improvement on the previous value. The student will have realized that the subject of design provides a seemingly infinite number of choices and the best one can do is to use any well-founded guidance that is available. On this topic, it was remarked by Cumpsty (1989) that the procedures used by most organizations involved in the design of compressors are shrouded in commercial secrecy. New designs are somehow evolved often based upon older successful designs and as long as the new product gives satisfactory test results then some sort progress can be claimed.

References

Cumpsty, N. A. (1989). *Compressor aerodynamics* London: Longman.

Rodgers, C. (1980). Efficiency of centrifugal compressor impellers. Paper 22 of AGARD conference proceedings, No. 282. Centrifugal compressors, flow phenomena and performance conference in Brussells at VKI.

Watson, N., & Janota, M. S. (1982). *Turbocharging the internal combustion engine*.

Appendix C: Tables for the Compressible Flow of a Perfect Gas

The tables in this appendix are required for some of the problems in the book. All results are quoted to four decimal places at equal intervals of Mach number so that linear interpolation can be easily applied where required. In most cases this will give adequate accuracy, but if necessary improved precision can be obtained by direct application of the formulae that follow:

Static and Stagnation Quantities	Flow Relations
$\frac{T}{T_0} = \left(1 + \frac{\gamma-1}{2}M^2\right)^{-1}$	$c = M\sqrt{\gamma \mathrm{RT}}, \frac{c}{\sqrt{C_p T_0}} = M\sqrt{\gamma - 1}\left(1 + \frac{\gamma-1}{2}M^2\right)^{-(1/2)}$
$\frac{p}{p_0} = \left(1 + \frac{\gamma-1}{2}M^2\right)^{-\gamma/(\gamma-1)}$	$\dot{m} = \rho c A_n, \frac{\dot{m}\sqrt{C_p T_0}}{A_n p_0} = \frac{\gamma}{\sqrt{\gamma-1}} M\left(1 + \frac{\gamma-1}{2}M^2\right)^{-(1/2)[(\gamma+1)/(\gamma-1)]}$
$\frac{\rho}{\rho_0} = \left(1 + \frac{\gamma-1}{2}M^2\right)^{-1/(\gamma-1)}$	

Note that in steady, adiabatic flow with no shaft work, T_0 is constant. If the flow is also isentropic, p_0 and ρ_0 are also constant.

Through a steady flow turbomachinery device, the mass flow rate will be conserved such that $\dot{m}$ is constant.

Table C.1 shows results for $\gamma = 1.4$ (applicable to dry air and diatomic gases). Table C.2 shows results for $\gamma = 1.333$ (typical of gas turbine combustion products).

Table C.1 Compressible Flow for a Perfect Gas, $\gamma = 1.4$

M	T/T_0	p/p_0	ρ/ρ_0	$\dot{m}\sqrt{C_pT_0}/A_np_0$	$c/\sqrt{C_pT_0}$
0.00	1.0000	1.0000	1.0000	0.0000	0.0000
0.01	1.0000	0.9999	1.0000	0.0221	0.0063
0.02	0.9999	0.9997	0.9998	0.0443	0.0126
0.03	0.9998	0.9994	0.9996	0.0664	0.0190
0.04	0.9997	0.9989	0.9992	0.0885	0.0253
0.05	0.9995	0.9983	0.9988	0.1105	0.0316
0.06	0.9993	0.9975	0.9982	0.1325	0.0379
0.07	0.9990	0.9966	0.9976	0.1545	0.0443
0.08	0.9987	0.9955	0.9968	0.1764	0.0506
0.09	0.9984	0.9944	0.9960	0.1983	0.0569

(*Continued*)

Table C.1 (Continued)

M	T/T_0	p/p_0	ρ/ρ_0	$\dot{m}\sqrt{C_pT_0}/A_np_0$	$c/\sqrt{C_pT_0}$
0.10	0.9980	0.9930	0.9950	0.2200	0.0632
0.11	0.9976	0.9916	0.9940	0.2417	0.0695
0.12	0.9971	0.9900	0.9928	0.2633	0.0758
0.13	0.9966	0.9883	0.9916	0.2849	0.0821
0.14	0.9961	0.9864	0.9903	0.3063	0.0884
0.15	0.9955	0.9844	0.9888	0.3276	0.0947
0.16	0.9949	0.9823	0.9873	0.3488	0.1009
0.17	0.9943	0.9800	0.9857	0.3699	0.1072
0.18	0.9936	0.9776	0.9840	0.3908	0.1135
0.19	0.9928	0.9751	0.9822	0.4116	0.1197
0.20	0.9921	0.9725	0.9803	0.4323	0.1260
0.21	0.9913	0.9697	0.9783	0.4528	0.1322
0.22	0.9904	0.9668	0.9762	0.4731	0.1385
0.23	0.9895	0.9638	0.9740	0.4933	0.1447
0.24	0.9886	0.9607	0.9718	0.5133	0.1509
0.25	0.9877	0.9575	0.9694	0.5332	0.1571
0.26	0.9867	0.9541	0.9670	0.5528	0.1633
0.27	0.9856	0.9506	0.9645	0.5723	0.1695
0.28	0.9846	0.9470	0.9619	0.5915	0.1757
0.29	0.9835	0.9433	0.9592	0.6106	0.1819
0.30	0.9823	0.9395	0.9564	0.6295	0.1881
0.31	0.9811	0.9355	0.9535	0.6481	0.1942
0.32	0.9799	0.9315	0.9506	0.6666	0.2003
0.33	0.9787	0.9274	0.9476	0.6848	0.2065
0.34	0.9774	0.9231	0.9445	0.7027	0.2126
0.35	0.9761	0.9188	0.9413	0.7205	0.2187
0.36	0.9747	0.9143	0.9380	0.7380	0.2248
0.37	0.9733	0.9098	0.9347	0.7553	0.2309
0.38	0.9719	0.9052	0.9313	0.7723	0.2369
0.39	0.9705	0.9004	0.9278	0.7891	0.2430
0.40	0.9690	0.8956	0.9243	0.8056	0.2490
0.41	0.9675	0.8907	0.9207	0.8219	0.2551
0.42	0.9659	0.8857	0.9170	0.8379	0.2611
0.43	0.9643	0.8807	0.9132	0.8536	0.2671
0.44	0.9627	0.8755	0.9094	0.8691	0.2730
0.45	0.9611	0.8703	0.9055	0.8843	0.2790
0.46	0.9594	0.8650	0.9016	0.8992	0.2850
0.47	0.9577	0.8596	0.8976	0.9138	0.2909
0.48	0.9559	0.8541	0.8935	0.9282	0.2968
0.49	0.9542	0.8486	0.8894	0.9423	0.3027

(*Continued*)

Table C.1 (Continued)

M	T/T_0	p/p_0	ρ/ρ_0	$\dot{m}\sqrt{C_pT_0}/A_np_0$	$c/\sqrt{C_pT_0}$
0.50	0.9524	0.8430	0.8852	0.9561	0.3086
0.51	0.9506	0.8374	0.8809	0.9696	0.3145
0.52	0.9487	0.8317	0.8766	0.9828	0.3203
0.53	0.9468	0.8259	0.8723	0.9958	0.3262
0.54	0.9449	0.8201	0.8679	1.0084	0.3320
0.55	0.9430	0.8142	0.8634	1.0208	0.3378
0.56	0.9410	0.8082	0.8589	1.0328	0.3436
0.57	0.9390	0.8022	0.8544	1.0446	0.3493
0.58	0.9370	0.7962	0.8498	1.0561	0.3551
0.59	0.9349	0.7901	0.8451	1.0672	0.3608
0.60	0.9328	0.7840	0.8405	1.0781	0.3665
0.61	0.9307	0.7778	0.8357	1.0887	0.3722
0.62	0.9286	0.7716	0.8310	1.0990	0.3779
0.63	0.9265	0.7654	0.8262	1.1090	0.3835
0.64	0.9243	0.7591	0.8213	1.1186	0.3891
0.65	0.9221	0.7528	0.8164	1.1280	0.3948
0.66	0.9199	0.7465	0.8115	1.1371	0.4003
0.67	0.9176	0.7401	0.8066	1.1459	0.4059
0.68	0.9153	0.7338	0.8016	1.1544	0.4115
0.69	0.9131	0.7274	0.7966	1.1626	0.4170
0.70	0.9107	0.7209	0.7916	1.1705	0.4225
0.71	0.9084	0.7145	0.7865	1.1782	0.4280
0.72	0.9061	0.7080	0.7814	1.1855	0.4335
0.73	0.9037	0.7016	0.7763	1.1925	0.4389
0.74	0.9013	0.6951	0.7712	1.1993	0.4443
0.75	0.8989	0.6886	0.7660	1.2058	0.4497
0.76	0.8964	0.6821	0.7609	1.2119	0.4551
0.77	0.8940	0.6756	0.7557	1.2178	0.4605
0.78	0.8915	0.6691	0.7505	1.2234	0.4658
0.79	0.8890	0.6625	0.7452	1.2288	0.4711
0.80	0.8865	0.6560	0.7400	1.2338	0.4764
0.81	0.8840	0.6495	0.7347	1.2386	0.4817
0.82	0.8815	0.6430	0.7295	1.2431	0.4869
0.83	0.8789	0.6365	0.7242	1.2474	0.4921
0.84	0.8763	0.6300	0.7189	1.2514	0.4973
0.85	0.8737	0.6235	0.7136	1.2551	0.5025
0.86	0.8711	0.6170	0.7083	1.2585	0.5077
0.87	0.8685	0.6106	0.7030	1.2617	0.5128
0.88	0.8659	0.6041	0.6977	1.2646	0.5179
0.89	0.8632	0.5977	0.6924	1.2673	0.5230

(*Continued*)

Table C.1 (Continued)

M	T/T_0	p/p_0	ρ/ρ_0	$\dot{m}\sqrt{C_pT_0}/A_np_0$	$c/\sqrt{C_pT_0}$
0.90	0.8606	0.5913	0.6870	1.2698	0.5280
0.91	0.8579	0.5849	0.6817	1.2719	0.5331
0.92	0.8552	0.5785	0.6764	1.2739	0.5381
0.93	0.8525	0.5721	0.6711	1.2756	0.5431
0.94	0.8498	0.5658	0.6658	1.2770	0.5481
0.95	0.8471	0.5595	0.6604	1.2783	0.5530
0.96	0.8444	0.5532	0.6551	1.2793	0.5579
0.97	0.8416	0.5469	0.6498	1.2800	0.5628
0.98	0.8389	0.5407	0.6445	1.2806	0.5677
0.99	0.8361	0.5345	0.6392	1.2809	0.5725
1.00	0.8333	0.5283	0.6339	1.2810	0.5774
1.01	0.8306	0.5221	0.6287	1.2809	0.5821
1.02	0.8278	0.5160	0.6234	1.2806	0.5869
1.03	0.8250	0.5099	0.6181	1.2801	0.5917
1.04	0.8222	0.5039	0.6129	1.2793	0.5964
1.05	0.8193	0.4979	0.6077	1.2784	0.6011
1.06	0.8165	0.4919	0.6024	1.2773	0.6058
1.07	0.8137	0.4860	0.5972	1.2760	0.6104
1.08	0.8108	0.4800	0.5920	1.2745	0.6151
1.09	0.8080	0.4742	0.5869	1.2728	0.6197
1.10	0.8052	0.4684	0.5817	1.2709	0.6243
1.11	0.8023	0.4626	0.5766	1.2689	0.6288
1.12	0.7994	0.4568	0.5714	1.2667	0.6333
1.13	0.7966	0.4511	0.5663	1.2643	0.6379
1.14	0.7937	0.4455	0.5612	1.2618	0.6423
1.15	0.7908	0.4398	0.5562	1.2590	0.6468
1.16	0.7879	0.4343	0.5511	1.2562	0.6512
1.17	0.7851	0.4287	0.5461	1.2531	0.6556
1.18	0.7822	0.4232	0.5411	1.2500	0.6600
1.19	0.7793	0.4178	0.5361	1.2466	0.6644
1.20	0.7764	0.4124	0.5311	1.2432	0.6687
1.21	0.7735	0.4070	0.5262	1.2396	0.6730
1.22	0.7706	0.4017	0.5213	1.2358	0.6773
1.23	0.7677	0.3964	0.5164	1.2319	0.6816
1.24	0.7648	0.3912	0.5115	1.2279	0.6858
1.25	0.7619	0.3861	0.5067	1.2238	0.6901
1.26	0.7590	0.3809	0.5019	1.2195	0.6943
1.27	0.7561	0.3759	0.4971	1.2152	0.6984
1.28	0.7532	0.3708	0.4923	1.2107	0.7026
1.29	0.7503	0.3658	0.4876	1.2061	0.7067

(*Continued*)

Table C.1 (Continued)

M	T/T_0	p/p_0	ρ/ρ_0	$\dot{m}\sqrt{C_pT_0}/A_np_0$	$c/\sqrt{C_pT_0}$
1.30	0.7474	0.3609	0.4829	1.2014	0.7108
1.31	0.7445	0.3560	0.4782	1.1965	0.7149
1.32	0.7416	0.3512	0.4736	1.1916	0.7189
1.33	0.7387	0.3464	0.4690	1.1866	0.7229
1.34	0.7358	0.3417	0.4644	1.1815	0.7270
1.35	0.7329	0.3370	0.4598	1.1763	0.7309
1.36	0.7300	0.3323	0.4553	1.1710	0.7349
1.37	0.7271	0.3277	0.4508	1.1656	0.7388
1.38	0.7242	0.3232	0.4463	1.1601	0.7427
1.39	0.7213	0.3187	0.4418	1.1546	0.7466
1.40	0.7184	0.3142	0.4374	1.1490	0.7505
1.41	0.7155	0.3098	0.4330	1.1433	0.7543
1.42	0.7126	0.3055	0.4287	1.1375	0.7581
1.43	0.7097	0.3012	0.4244	1.1317	0.7619
1.44	0.7069	0.2969	0.4201	1.1258	0.7657
1.45	0.7040	0.2927	0.4158	1.1198	0.7694
1.46	0.7011	0.2886	0.4116	1.1138	0.7732
1.47	0.6982	0.2845	0.4074	1.1077	0.7769
1.48	0.6954	0.2804	0.4032	1.1016	0.7805
1.49	0.6925	0.2764	0.3991	1.0954	0.7842
1.50	0.6897	0.2724	0.3950	1.0891	0.7878
1.51	0.6868	0.2685	0.3909	1.0829	0.7914
1.52	0.6840	0.2646	0.3869	1.0765	0.7950
1.53	0.6811	0.2608	0.3829	1.0702	0.7986
1.54	0.6783	0.2570	0.3789	1.0638	0.8021
1.55	0.6754	0.2533	0.3750	1.0573	0.8057
1.56	0.6726	0.2496	0.3710	1.0508	0.8092
1.57	0.6698	0.2459	0.3672	1.0443	0.8126
1.58	0.6670	0.2423	0.3633	1.0378	0.8161
1.59	0.6642	0.2388	0.3595	1.0312	0.8195
1.60	0.6614	0.2353	0.3557	1.0246	0.8230
1.61	0.6586	0.2318	0.3520	1.0180	0.8263
1.62	0.6558	0.2284	0.3483	1.0114	0.8297
1.63	0.6530	0.2250	0.3446	1.0047	0.8331
1.64	0.6502	0.2217	0.3409	0.9980	0.8364
1.65	0.6475	0.2184	0.3373	0.9913	0.8397
1.66	0.6447	0.2151	0.3337	0.9846	0.8430
1.67	0.6419	0.2119	0.3302	0.9779	0.8462
1.68	0.6392	0.2088	0.3266	0.9712	0.8495
1.69	0.6364	0.2057	0.3232	0.9644	0.8527

(*Continued*)

Table C.1 (Continued)

M	T/T_0	p/p_0	ρ/ρ_0	$\dot{m}\sqrt{C_pT_0}/A_np_0$	$c/\sqrt{C_pT_0}$
1.70	0.6337	0.2026	0.3197	0.9577	0.8559
1.71	0.6310	0.1996	0.3163	0.9509	0.8591
1.72	0.6283	0.1966	0.3129	0.9442	0.8622
1.73	0.6256	0.1936	0.3095	0.9374	0.8654
1.74	0.6229	0.1907	0.3062	0.9307	0.8685
1.75	0.6202	0.1878	0.3029	0.9239	0.8716
1.76	0.6175	0.1850	0.2996	0.9172	0.8747
1.77	0.6148	0.1822	0.2964	0.9104	0.8777
1.78	0.6121	0.1794	0.2931	0.9037	0.8808
1.79	0.6095	0.1767	0.2900	0.8970	0.8838
1.80	0.6068	0.1740	0.2868	0.8902	0.8868
1.81	0.6041	0.1714	0.2837	0.8835	0.8898
1.82	0.6015	0.1688	0.2806	0.8768	0.8927
1.83	0.5989	0.1662	0.2776	0.8701	0.8957
1.84	0.5963	0.1637	0.2745	0.8634	0.8986
1.85	0.5936	0.1612	0.2715	0.8568	0.9015
1.86	0.5910	0.1587	0.2686	0.8501	0.9044
1.87	0.5884	0.1563	0.2656	0.8435	0.9072
1.88	0.5859	0.1539	0.2627	0.8368	0.9101
1.89	0.5833	0.1516	0.2598	0.8302	0.9129
1.90	0.5807	0.1492	0.2570	0.8237	0.9157
1.91	0.5782	0.1470	0.2542	0.8171	0.9185
1.92	0.5756	0.1447	0.2514	0.8106	0.9213
1.93	0.5731	0.1425	0.2486	0.8041	0.9240
1.94	0.5705	0.1403	0.2459	0.7976	0.9268
1.95	0.5680	0.1381	0.2432	0.7911	0.9295
1.96	0.5655	0.1360	0.2405	0.7846	0.9322
1.97	0.5630	0.1339	0.2378	0.7782	0.9349
1.98	0.5605	0.1318	0.2352	0.7718	0.9375
1.99	0.5580	0.1298	0.2326	0.7655	0.9402
2.00	0.5556	0.1278	0.2300	0.7591	0.9428

Table C.2 Compressible Flow for a Perfect Gas, $\gamma = 1.333$

M	T/T_0	p/p_0	ρ/ρ_0	$\dot{m}\sqrt{C_pT_0}/A_np_0$	$c/\sqrt{C_pT_0}$
0.00	1.0000	1.0000	1.0000	0.0000	0.0000
0.01	1.0000	0.9999	1.0000	0.0231	0.0058
0.02	0.9999	0.9997	0.9998	0.0462	0.0115
0.03	0.9999	0.9994	0.9996	0.0693	0.0173
0.04	0.9997	0.9989	0.9992	0.0923	0.0231
0.05	0.9996	0.9983	0.9988	0.1153	0.0288
0.06	0.9994	0.9976	0.9982	0.1383	0.0346
0.07	0.9992	0.9967	0.9976	0.1612	0.0404
0.08	0.9989	0.9957	0.9968	0.1841	0.0461
0.09	0.9987	0.9946	0.9960	0.2069	0.0519
0.10	0.9983	0.9934	0.9950	0.2297	0.0577
0.11	0.9980	0.9920	0.9940	0.2523	0.0634
0.12	0.9976	0.9905	0.9928	0.2749	0.0692
0.13	0.9972	0.9888	0.9916	0.2974	0.0749
0.14	0.9967	0.9870	0.9903	0.3197	0.0807
0.15	0.9963	0.9851	0.9888	0.3420	0.0864
0.16	0.9958	0.9831	0.9873	0.3641	0.0921
0.17	0.9952	0.9810	0.9857	0.3861	0.0979
0.18	0.9946	0.9787	0.9840	0.4080	0.1036
0.19	0.99402	0.9763	0.982	0.4298	0.1093
0.20	0.9934	0.9738	0.9803	0.4514	0.1150
0.21	0.9927x	0.9711	0.9783	0.4728	0.4728
0.22	0.9920	0.9684	0.9762	0.4941	0.1264
0.23	0.9913	0.9655	0.9740	0.5152	0.1321
0.24	0.9905	0.9625	0.9717	0.5362	0.1378
0.25	0.9897	0.9594	0.9694	0.5569	0.1435
0.26	0.9889	0.9562	0.9669	0.5775	0.1492
0.27	0.9880	0.9529	0.9644	0.5979	0.1549
0.28	0.9871	0.9494	0.9618	0.6181	0.1605
0.29	0.9862	0.9459	0.9591	0.6380	0.1662
0.30	0.9852	0.9422	0.9563	0.6578	0.1718
0.31	0.9843	0.9384	0.9534	0.6774	0.1775
0.32	0.9832	0.9346	0.9505	0.6967	0.1831
0.33	0.9822	0.9306	0.9475	0.7158	0.1887
0.34	0.9811	0.9265	0.9444	0.7347	0.1943
0.35	0.9800	0.9224	0.9412	0.7533	0.1999
0.36	0.9789	0.9181	0.9379	0.7717	0.2055
0.37	0.9777	0.9137	0.9346	0.7898	0.2111
0.38	0.9765	0.9093	0.9311	0.8077	0.2167
0.39	0.9753	0.9047	0.9276	0.8253	0.2223

(*Continued*)

Table C.2 (Continued)

M	T/T_0	p/p_0	ρ/ρ_0	$\dot{m}\sqrt{C_pT_0}/A_np_0$	$c/\sqrt{C_pT_0}$
0.40	0.9741	0.9001	0.9241	0.8427	0.2278
0.41	0.9728	0.8954	0.9204	0.2334	0.8598
0.42	0.9715	0.8906	0.8906	0.8766	0.2389
0.43	0.9701	0.8857	0.9130	0.8932	0.2444
0.44	0.9688	0.8807	0.9091	0.9095	0.2499
0.45	0.9674	0.8757	0.9052	0.9255	0.2554
0.46	0.9660	0.8706	0.9012	0.9412	0.2609
0.47	0.9645	0.8654	0.8972	0.9567	0.2664
0.48	0.9631	0.8601	0.8931	0.9718	0.2718
0.49	0.9616	0.8548	0.8890	0.9867	0.2773
0.50	0.9600	0.8494	0.8847	1.0012	0.2827
0.51	0.9585	0.8439	0.8805	1.0155	0.2881
0.52	0.9569	0.8384	0.8761	1.0295	0.2935
0.53	0.9553	0.8328	0.8717	1.0431	0.2989
0.54	0.9537	0.8271	0.8673	1.0565	0.3043
0.55	0.9520	0.8214	0.8628	1.0696	0.3097
0.56	0.9504	0.8157	0.8583	1.0823	0.3150
0.57	0.9487	0.8099	0.8537	1.0948	0.3204
0.58	0.9470	0.8040	0.8490	1.1069	0.3257
0.59	0.9452	0.7981	0.8443	1.1188	0.3310
0.60	0.9434	0.7921	0.8396	1.1303	0.3363
0.61	0.9417	0.7861	0.8348	1.1415	0.3416
0.62	0.9398	0.7801	0.8300	1.1524	0.3469
0.63	0.9380	0.7740	0.8252	1.1630	0.3521
0.64	0.9362	0.7679	0.8203	1.1733	0.3573
0.65	0.9343	0.7618	0.8153	1.1833	0.3626
0.66	0.9324	0.7556	0.8104	1.1930	0.3678
0.67	0.9305	0.7494	0.8054	1.2023	0.3729
0.68	0.9285	0.7431	0.8003	1.2114	0.3781
0.69	0.9266	0.7368	0.7953	1.2201	0.3833
0.70	0.9246	0.7306	0.7902	1.2285	0.3884
0.71	0.9226	0.7242	0.7850	1.2367	0.3935
0.72	0.9205	0.7179	0.7799	1.2445	0.3986
0.73	0.9185	0.7116	0.7747	1.2520	0.4037
0.74	0.9164	0.7052	0.7695	1.2592	0.4088
0.75	0.9144	0.6988	0.7643	1.2661	0.4139
0.76	0.9123	0.6924	0.7590	1.2727	0.4189
0.77	0.9102	0.6860	0.7537	1.2790	0.4239
0.78	0.9080	0.6796	0.7484	1.2850	0.4289
0.79	0.9059	0.6732	0.7431	1.2907	0.4339

(*Continued*)

Table C.2 (Continued)

M	T/T_0	p/p_0	ρ/ρ_0	$\dot{m}\sqrt{C_pT_0}/A_np_0$	$c/\sqrt{C_pT_0}$
0.80	0.9037	0.6668	0.7378	1.2961	0.4389
0.81	0.9015	0.6603	0.7325	1.3013	0.4438
0.82	0.8993	0.6539	0.7271	1.3061	0.4487
0.83	0.8971	0.6475	0.7217	1.3107	0.4536
0.84	0.8949	0.6411	0.7164	1.3149	0.4585
0.85	0.8926	0.6346	0.7110	1.3189	0.4634
0.86	0.8904	0.6282	0.7056	1.3226	0.4683
0.87	0.8881	0.6218	0.7002	1.3260	0.4731
0.88	0.8858	0.6154	0.6948	1.3292	0.4779
0.89	0.8835	0.6090	0.6893	1.3321	0.4827
0.90	0.8812	0.6026	0.6839	1.3347	0.4875
0.91	0.8788	0.5963	0.6785	1.3370	0.4923
0.92	0.8765	0.5899	0.6731	1.3391	0.4970
0.93	0.8741	0.5836	0.6676	1.3410	0.5018
0.94	0.8717	0.5773	0.6622	1.3425	0.5065
0.95	0.8694	0.5710	0.6568	1.3439	0.5111
0.96	0.8670	0.5647	0.6514	1.3449	0.5158
0.97	0.8646	0.5585	0.6459	1.3458	0.5205
0.98	0.8621	0.5522	0.6405	1.3464	0.5251
0.99	0.8597	0.5460	0.6351	1.3467	0.5297
1.00	0.8573	0.5398	0.6297	1.3468	0.5343
1.01	0.8548	0.5337	0.6243	1.3467	0.5389
1.02	0.8524	0.5276	1.3464	0.6189	0.5434
1.03	0.8499	0.5215	0.6136	1.3458	0.5479
1.04	0.8474	0.5154	0.6082	1.3450	0.5525
1.05	0.8449	0.5093	0.6028	1.3440	0.5569
1.06	0.8424	0.5033	0.5975	1.3428	0.5614
1.07	0.8399	0.4974	0.5922	1.3414	0.5659
1.08	0.8374	0.4914	0.5869	1.3397	0.5703
1.09	0.8349	0.4855	0.5816	1.3379	0.5747
1.10	0.8323	0.4796	0.5763	1.3359	0.5791
1.11	0.8298	0.4738	0.5710	1.3337	0.5835
1.12	0.8272	0.4680	0.5658	1.3313	0.5878
1.13	0.8247	0.4622	0.5605	1.3287	0.5922
1.14	0.8221	0.4565	0.5553	1.3259	0.5965
1.15	0.8195	0.4508	0.5501	1.3229	0.6008
1.16	0.8170	0.4452	0.5449	1.3198	0.6050
1.17	0.8144	0.4396	0.5398	1.3165	0.6093
1.18	0.8118	0.4340	0.5347	1.3131	0.6135
1.19	0.8092	0.4285	0.5295	1.3094	0.6177

(*Continued*)

Table C.2 (Continued)

M	T/T_0	p/p_0	ρ/ρ_0	$\dot{m}\sqrt{C_pT_0}/A_np_0$	$c/\sqrt{C_pT_0}$
1.20	0.8066	0.4230	0.5245	1.3057	0.6219
1.21	0.8040	0.4176	0.5194	1.3017	0.6261
1.22	0.8014	0.4122	0.5143	1.2976	0.6302
1.23	0.7988	0.4068	0.5093	1.2934	0.6344
1.24	0.7962	0.4015	0.5043	1.2890	0.6385
1.25	0.7936	0.3963	0.4994	1.2845	0.6426
1.26	0.7909	0.3911	0.4944	1.2798	0.6466
1.27	0.7883	0.3859	0.4895	1.2751	0.6507
1.28	0.7857	0.3808	0.4846	1.2701	0.6547
1.29	0.7830	0.3757	0.4798	1.2651	0.6587
1.30	0.7804	0.3706	0.4749	1.2599	0.6627
1.31	0.7778	0.3657	0.4701	1.2547	0.6667
1.32	0.7751	0.3607	0.4654	1.2493	0.6706
1.33	0.7725	0.3558	0.4606	1.2438	0.6746
1.34	0.7698	0.3510	0.4559	1.2382	0.6785
1.35	0.7672	0.3462	0.4512	1.2325	0.6824
1.36	0.7646	0.3414	0.4465	1.2266	0.6862
1.37	0.7619	0.3367	0.4419	1.2207	0.6901
1.38	0.7593	0.3320	0.4373	1.2147	0.6939
1.39	0.7566	0.3274	0.4328	1.2086	0.6977
1.40	0.7540	0.3229	0.4282	1.2025	0.7015
1.41	0.7513	0.3183	0.4237	1.1962	0.7053
1.42	0.7487	0.3139	0.4192	1.1899	0.7090
1.43	0.7460	0.3094	0.4148	1.1835	0.7127
1.44	0.7434	0.3051	0.4104	1.1770	0.7164
1.45	0.7407	0.3007	0.4060	1.1704	0.7201
1.46	0.7381	0.2965	0.4017	1.1638	0.7238
1.47	0.7354	0.2922	0.3974	1.1571	0.7275
1.48	0.7328	0.2880	0.3931	1.1504	0.7311
1.49	0.7301	0.2839	0.3888	1.1367	0.7347
1.50	0.7275	0.2798	0.3846	1.1367	0.7383
1.51	0.7248	0.2758	0.3804	1.1298	0.7419
1.52	0.7222	0.2718	0.3763	1.1228	0.7454
1.53	0.7195	0.2678	0.3722	1.1158	0.7489
1.54	0.7169	0.2639	0.3681	1.1087	0.7524
1.55	0.7143	0.2600	0.3641	1.1016	0.7559
1.56	0.7116	0.2562	0.3600	1.0945	0.7594
1.57	0.7090	0.2524	0.3561	1.0873	0.7629
1.58	0.7064	0.2487	0.3521	1.0801	0.7663
1.59	0.7038	0.2450	0.3482	1.0729	0.7697
1.60	0.7011	0.2414	0.3443	1.0656	0.7731

(*Continued*)

Table C.2 (Continued)

M	T/T_0	p/p_0	ρ/ρ_0	$\dot{m}\sqrt{C_pT_0}/A_np_0$	$c/\sqrt{C_pT_0}$
1.61	0.6985x	0.2378	0.3405	1.0583	1.0583
1.62	0.6959	0.2343	0.3367	1.0510	0.7799
1.63	0.6933	0.2308	0.3329	1.0436	0.7832
1.64	0.6907	0.2273	0.3291	1.0363	0.7865
1.65	0.6881	0.2239	0.3254	1.0289	0.7898
1.66	0.6855	0.2206	0.3217	1.0215	0.7931
1.67	0.6829	0.2172	0.3181	1.0141	0.7964
1.68	0.6803	0.2139	0.3145	1.0066	0.7996
1.69	0.6777	0.2107	0.3109	0.9992	0.8028
1.70	0.6751	0.2075	0.3074	0.9918	0.8061
1.71	0.6726	0.2044	0.3039	0.9843	0.8093
1.72	0.6700	0.2012	0.3004	0.9769	0.8124
1.73	0.6674	0.1982	0.2969	0.9694	0.8156
1.74	0.6649	0.1951	0.2935	0.9620	0.8187
1.75	0.6623	0.1922	0.2901	0.9545	0.8218
1.76	0.6597	0.1892	0.2868	0.9471	0.8249
1.77	0.6572	0.1863	0.2835	0.9396	0.8280
1.78	0.6546	0.1834	0.2802	0.9322	0.8311
1.79	0.6521	0.1806	0.2770	0.9248	0.8341
1.80	0.6496	0.1778	0.2737	0.9173	0.8372
1.81	0.6471	0.1751	0.2706	0.9099	0.8402
1.82	0.6445	0.1723	0.2674	0.9025	0.8432
1.83	0.6420	0.1697	0.2643	0.8951	0.8461
1.84	0.6395	0.1670	0.2612	0.8878	0.8491
1.85	0.6370	0.1644	0.2581	0.8804	0.8521
1.86	0.6345	0.1619	0.2551	0.8731	0.8550
1.87	0.6320	0.1593	0.2521	0.8658	0.8579
1.88	0.6295	0.1568	0.2491	0.8585	0.8608
1.89	0.6271	0.1544	0.2462	0.8512	0.8636
1.90	0.6246	0.1520	0.2433	0.8439	0.8665
1.91	0.6221	0.1496	0.2404	0.8367	0.8693
1.92	0.6197	0.1472	0.2376	0.8295	0.8722
1.93	0.6172	0.1449	0.2348	0.8223	0.8750
1.94	0.6148	0.1426	0.2320	0.8152	0.8778
1.95	0.6123	0.1404	0.2292	0.8081	0.8805
1.96	0.6099	0.1382	0.2265	0.8010	0.8833
1.97	0.6075	0.1360	0.2238	0.7939	0.8860
1.98	0.6051	0.1338	0.2212	0.7869	0.8888
1.99	0.6026	0.1317	0.2185	0.7799	0.8915
2.00	0.6002	0.1296	0.2159	0.7729	0.8942

Appendix D: Conversion of British and American Units to SI Units

Length	***Force***
1 inch = 0.0254 m 1 foot = 0.3048 m	1 lbf = 4.448 N 1 ton f (UK) = 9.964 kN
Area 1 $in^2 = 6.452 \times 10^{-4}$ m^2 1 $ft^2 = 0.09290$ m^2	*Pressure* 1 $lbf/in^2 = 6.895$ kPa 1 ft $H_2O = 2.989$ kPa 1 in Hg = 3.386 kPa 1 bar = 100.0 kPa
Volume 1 $in^3 = 16.39$ cm^3 1 $ft^3 = 28.32$ dm^3 $= 0.02832$ m^3 1 gall (UK) = 4.546 dm^3 1 gall (US) = 3.785 dm^3	*Energy* 1 ft lbf = 1.356 J 1 Btu = 1.055 kJ
Velocity 1 ft/s = 0.3048 m/s 1 mile/h = 0.447 m/s	*Specific energy* 1 ft lbf/lb = 2.989 J/kg 1 Btu/lb = 2.326 kJ/kg
Mass 1 lb = 0.4536 kg 1 ton (UK) = 1016 kg	*Specific heat capacity* 1 ft lbf/(lb °F) = 5.38 J/(kg °C) 1 ft lbf/(slug °F) = 0.167 J/(kg °C) 1 Btu/(lb °F) = 4.188 kJ/(kg °C)
Density 1 $lb/ft^3 = 16.02$ kg/m^3 1 $slug/ft^3 = 515.4$ kg/m^3	*Power* 1 hp = 0.7457 kW

Appendix E: Mollier Chart for Steam

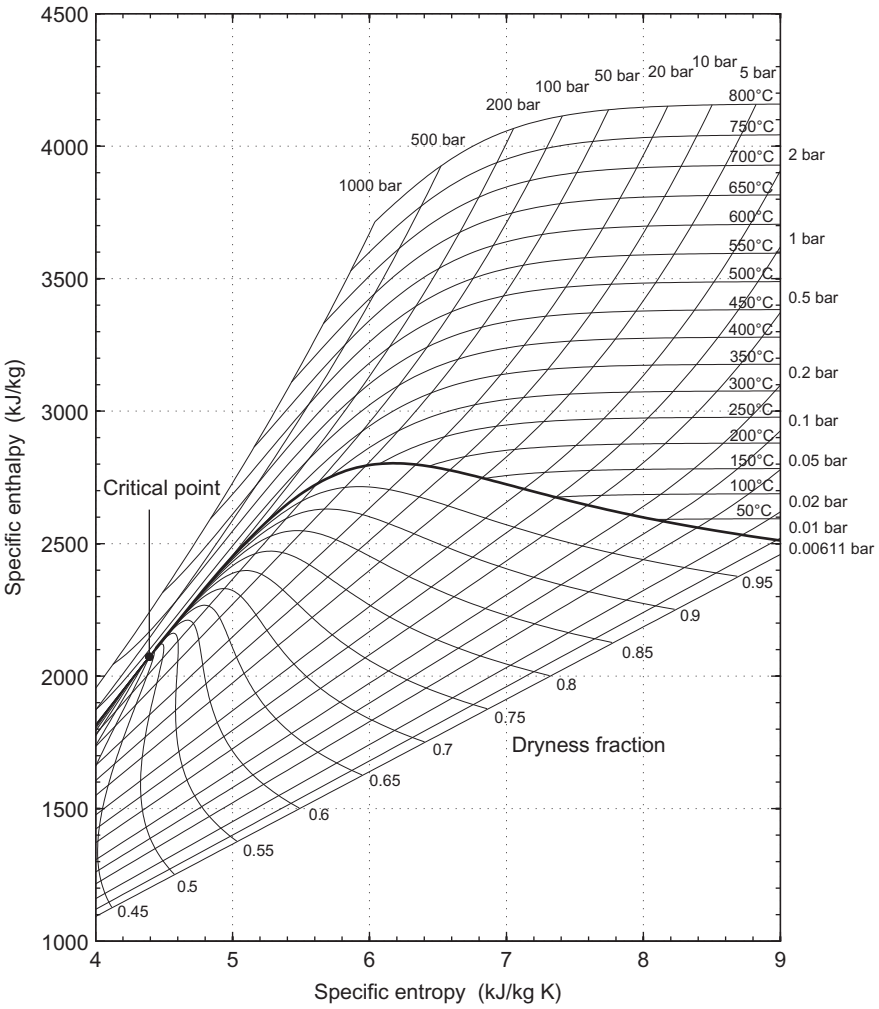

FIGURE E.1

Plotted from the IAPWS equations (http://www.iapws.org) by Peter O'Brien, 2013.

Appendix F: Answers to Problems

Chapter 1

1. (a) 179.9 m/s, 439.1 K; (b) 501.4 kPa, 39.24 J/kg K.
2. (a) 279.9 K, 2.551 bar; (b) 27.16 kg/s.
3. 316.9 m/s, 0.0263 kJ/kg K.
4. 88.1%.
5. (a) 704 K; (b) 750 K; (c) 668 K.
6. 2301.8 kJ/kg, 36.5 kg/s.
7. (a) 500 K, 0.313 m^3/kg; (b) 1.045.
8. 49.1 kg/s; 24 mm.
9. (a) 630 kPa, 275°C; 240 kPa; 201°C; 85 kPa, 126°C; 26 kPa, $x = 0.988$; 7 kPa, $x = 0.95$. (b) 0.638, 0.655, 0.688, 0.726, 0.739. (c) 0.739, 0.724. (d) 1.075.
10. (a) 0.489, (b) 87.4 kPa, (c) 399.6 K, (d) 0.308.
11. 630.6 K, 0.8756.

Chapter 2

1. 6.29 m^3/s.
2. 9.15 m/s, 5.33 atm.
4 551 rev/min, 1:10.8; 0.885 m^3/s; 17.85 MN.
5 4030 rev/min, 31.4 kg/s.
6 (a) 0.501, 4.95, 3.658 kW; (b) 61.19 m, 0.64 m^3/s, 468 kW.
7 (a) 150 rpm, 1500 kW; (b) 0.842 rev or 5.293 rad.
8 (a) 88.9%; (b) 202.4 rpm, 13.9 m^3/s, 4.858 MW.
9 (a) 303 kW, $\Omega_S = 1.632$ (rad), $D_S = 4.09$; (b) 0.0936 m^3/s, 799 rpm, $P = 3.23$ kW.
10 (a) $T_{02} = 305.2$ K; (b) $P_C = 105$ kW.

Chapter 3

1. 49.8°.
2. 0.77; $C_D = 0.048$, $C_L = 2.245$.
3. (b) 57.8°; (c) (a) 357 kPa, (b) 0.0218, 1.075.
4. (a) 1.22, 6°; (b) 19.5°.
5. (a) 41.3°; (b) 0.78; (c) 0.60; (d) −7.95°.
6. (a) 0.178, 0.121; (b) 0.1; (c) 0.342.

7. 141.2 kg/(sm^2), 0.40, 1.30.
8. 0.058.
9. (a) 1.21; (c) 0.19.

Chapter 4

2. (a) 88%; (b) 86.17%; (c) 1170.6 K.
3. $\alpha_2 = 70°$, $\beta_2 = 7.02°$, $\alpha_3 = 18.4°$, $\beta_3 = 50.37°$, 375.3 m/s.
4. 22.7 kJ/kg; 420 kPa, 117°C.
5. 91%.
6. (a) 1.503; (b) 39.9°, 59°; (c) 0.25; (d) 90.5 and 81.6%.
7. (b) 67.5°, 22.5°, 0.90, 0.80; (c) 0.501 m, 85.2 m/s, 61 mm.
8. (a) 215 m/s; (b) 0.098, 2.68; (c) 0.872; (d) 265°C, 0.75 MPa.
9. (a) (a) 601.9 m/s, (b) 282.8 m/s, (c) 79.8%; (b) 89.23%.
10. (b) (a) 130.9 kJ/kg, (b) 301.6 m/s, (c) 707.6 K; (c) (a) 10,200 rev/min, (b) 0.565 m, (c) 0.845.
11. (b) 0.2166; (c) 8740 rev/min; (d) 450.7 m/s, 0.846.
12. 1.07, 0.464.
13. 0.908.

Chapter 5

1. 14 stages.
2. 30.6°C.
3. 132.5 m/s, 56.1 kg/s; 10.1 MW.
4. 86.5%; 9.28 MW.
5. 0.59, 0.415.
6. (a) 0.88; (b) 0.571.
7. 36.9°, 36.9°, 0.55, 0.50.
8. (a) 229.3 m/s; (b) 23.5 kg/s, 15796 rev/min; (c) 33.16 kJ/kg; (d) 84.7%; (e) 5.86 stages, 4.68 MW; (f) with six stages the stage loading will be lower for the same pressure ratio, with five stages the weight and cost would be lower.
9. (a) 0.44, 19.8°; (b) 0.322, 0.556, 70.0°, 55.2°, +11.3°, −3.4°; (c) 55.6°.
10. (a) 0.137; (b) 0.508; (c) 0.872, 2.422.
11. (a) 16.22°, 22.08°, 33.79°; (b) 467.2 Pa, 7.42 m/s.
12. (a) $\beta_1 = 70.79°$, $\beta_2 = 68.24°$; (b) 83.96%; (c) 399.3 Pa; (d) 7.144 cm.
13. (a) 141.1 Pa, 0.588; (b) 60.48 Pa; (c) 70.14%.

Chapter 6

1. 55° and 47°.
2. 0.602, 1.38, −0.08 (i.e., implies large losses near hub).
4. 70.7 m/s.
5. Work done is constant at all radii:

$$c_{x1}^2 = \text{constant} - 2a^2[(r^2 - 1) - 2(b/a)\ln r];$$

$$c_{x2}^2 = \text{constant} - 2a^2[(r^2 - 1) - 2(b/a)\ln r];$$

$$\beta_1 = 47.5^\circ, \beta_2 = 4.6^\circ.$$

6. (a) 469.3 m/s; (b) 0.798; (c) 0.079; (d) 3.244 MW; (e) 911.6 K, 897 K.
7. (a) 62°; (b) 55.3°, 1.54°; (c) 55.19° and 65.95°; (d) −0.175, 0.478.
8. See Figure 6.13. For (a) at $x/r_t = 0.05$, $c_x = 113.2$ m/s.
9. 0.31 m.
10. (a) 1.4; (b) $A_2 = 0.4822$ m^2, $r_t = 0.7737$ m, $r_h = 0.632$ m; (c) $c_{\theta 3h} = 49.49$ m/s, $c_{\theta 3h} = 40.43$ m/s; (d) $R_h = 0.444$, $R_t = 0.546$.
11. Tabulated results. See Solutions Manual.
12. See graphs in Solutions Manual.
13. (d) $\alpha_h = 9.1^\circ$ $\alpha_t = 21.08^\circ$.
14. (a) $i_h = 7.09^\circ$, $i_t = 7.5^\circ$, (b) $p_{0h} - p_{0t} = 0.276$ bar.
15. See Solutions manual.

Chapter 7

1. (a) 27.9 m/s; (b) 880 rev/min, 0.604 m; (c) 182 W; (d) 0.333 (rad).
2. 579 kW; 169 mm; 50.0.
3. 0.875; 5.61 kg/s.
4. 24,430 rev/min; 0.2025 m, 0.5844.
5. 0.735, 90.5%.
6. (a) 542.5 kW; (b) 536 and 519 kPa; (c) 586 and 240.8 kPa, 1.20, 176 m/s; (d) 0.875; (e) 0.22; (f) 28,400 rev/min.
7. (a) 29.4 dm^3/s; (b) 0.781; (c) 77.7°; (d) 7.82 kW.
8. (a) 14.11 m; (b) 2.635 m; (c) 0.7664; (d) 17.73 m; (e) 13.8 kW; $\sigma_S = 0.722$, $\sigma_B = 0.752$.
9. (a) See text; (b) (a) 32,214 rev/min, (b) 5.246 kg/s; (c) (a) 1.254 MW, (b) 6.997.
10. (a) 189.7 kPa, 0.953; (b) 0.751; (c) 0.294, 33.3 J/(kg K)
11. Bookwork: (a) 516 K, 172.8 kPa, 0.890; (b) $M_2 = 0.281$, $M_2 = 0.930$.
12. (a) 0.880; (b) 314.7 kPa; (c) 1.414 kg/s.
13. (a) 7.358 kW; (b) 275.8 rpm, 36.7 kW.
14. (a) $\Delta W = 300$ J/(kg K), power = 38.6 kW; (b) $\Omega_s = 0.545$ (rad), $D_S = 4.85$.
15. $M_2 = 0.4482$, $c_2 = 140.8$ m/s.
16. (a) 465 m/s, 0.740 m; (b) 0.546 (rad).

17. $r_{s1} = 0.164$m, $M_1 = 0.275$.
18. (a) 372.7 m/s; (b) 156 m/s; (c) 0.4685; (d) 0.046 m^2.
19. (a) 11.55 kg/s; (b) 1509 kW; (c) 0.5786; (d) 2.925 rad.

Chapter 8

1. 586 m/s, 73.75°.
2. (a) 205.8 kPa, 977 K; (b) 125.4 mm, 89,200 rev/min; (c) 1 MW.
3. (a) 90.3%; (b) 269 mm; (c) 0.051, 0.223.
4. 1593 K.
5. 2.159 m^3/s, 500 kW.
6. (a) 10.089 kg/s, 23,356 rev/min; (b) 9.063×10^5, 1.879×10^6.
7. (a) 81.82%; (b) 890 K, 184.3 kPa; (c) 1.206 cm; (d) 196.3 m/s; (e) 0.492; (f) $r_{s3} = 6.59$ m, $r_{h3} = 2.636$ cm.
8. (a) 308.24 m/s; (b) 56.42 kPa, 915.4 K; (c) 113.6 m/s, 0.2765 kg/s; (d) 5.452 cm; (e) 28.34°; (f) 0.7385 rad
9. (a) 190.3 m/s; (b) 85.7°C.
10. $S = 0.1648$, $\eta_{ts} = 0.851$.
11. Bookwork.
12. (a) 4.218; (b) 627.6 m/s, $M_3 = 0.896$.
13. (a) $S = 0.1824$, $\beta_2 = 32.2°$, $\alpha_2 = 73.9°$; (b) $U_2 = 518.3$ m/s; (c) $T_3 = 851.4$ K; (d) $N = 38{,}956$ rpm, $D_2 = 0.254$ m, $\Omega_s = 0.5685$, which corresponds (approximately) to the maximum of η_{ts} in Figure 8.15.
14. (a) 361.5 kPa; (b) 0.8205.
15. (a) $\alpha_2 = 73.9°$, $\beta_2 = 32.2°$; (b) 2.205; (c) 486.2 m/s.
16. (a) 0.3194 m, 29.073 rpm; (b) $\zeta_R = 0.330$, $\zeta_N = 0.0826$.

Chapter 9

1. (a) 224 kW; (b) 0.2162 m^3/s; (c) 6.423.
2. (a) 2.138 m. (b) For $d = 2.2$ m, (a) 17.32 m, (b) 59.87 m/s, 40.3 MW.
3. (a) 378.7 rev/min; (b) 6.906 MW, 0.252 (rad); (c) 0.783; (d) 3.
4. Head loss in pipeline is 17.8 m. (a) 672.2 rev/min; (b) 84.5%; (c) 6.735 MW; (d) 2.59%.
5. (a) 12.82 MW, 8.69 m^3/s; (b) 1.0 m; (c) 37.6 m/s; (d) 0.226 m.
6. (a) 663.2 rev/min; (b) 69.55°, 59.2°; (c) 0.152 m and 0.169 m.
7. (b) (a) 1.459 (rad), (b) 107.6 m^3/s, (c) 3.153 m, 15.52 m/s. (c) (a) 398.7 rev/min, 0.456 m^2/s; (b) 20.6 kW (uncorrected), 19.55 kW (corrected); (c) 4.06 (rad). (d) $H_s - H_a = -2.18$ m.
8. (a) 0.94; (b) 115.2 rev/min, 5.068 m; (c) 197.2 m^2/s; (d) 0.924 m.
9. (a) 11.4 m^3/s, 19.47 MW; (b) 72.6°, 75.04° at tip; (c) 25.73°, 59.54° at hub.
10. (a) 6 turbines required; (b) 0.958 m; (c) 1.861 m^3/s.
11. (a) 0.498 m; (b) 28.86 m.

12. (a) 0.262 (rad); (b) 0.603; (c) 33.65 m^3/s.
13. $\alpha_2 = 50.32^\circ$, $\beta_2 = 52.06^\circ$, 0.336 m, $\Omega_{sp} = 2.27$ (rad). Yes, it is consistent with stated efficiency.
14. (a) (a) 390.9 kW, (b) 1.733 m^3/s, (c) 0.767 m and 15.06 m/s, (d) $\alpha_2 = 65.17^\circ$ and $\beta_2 = 0.57^\circ$. (b) $\sigma = 0.298$, at $\Omega_{sp} = 0.8$, $\sigma_c = 0.1$ the turbine is well clear of cavitation (see Figure 9.21).
15. (a) 649.5 rev/min and 0.024 m^3/s; (b) 0.650 kW; (c) 0.579 kW.
16. (a) 110.8 m^3/s; (b) 100 rpm and 3.766 m; (c) $\alpha_2 = 49.26^\circ$ and $\beta_2 = 39.08^\circ$.
17. At hub, $\alpha_2 = 49.92^\circ$, $\beta_2 = 28.22^\circ$; at mean radius, $\alpha_2 = 38.64^\circ$, $\beta_2 = 60.46^\circ$; at tip, $\alpha_2 = 31.07^\circ$,$\beta_2 = 70.34^\circ$.
18. (a) 0.8495; (b) 250 rpm, 90 m^3/s, 22.5 MW; (c) $N_{SP} = 30.77$ rpm for model and 31.73 for prototype.
19. (a) 4910 *N*; (b) 185.1 kW.

Chapter 10

1. $C_p = 0.303$, $\zeta = 0.51$.
2. $\overline{a} = 0.0758$ and $\Delta p = 14.78$ Pa.
3. (a) $C_p = 0.35$, $\zeta = 0.59$, and $N = 12.89$ rpm; (b) 13.13 m/s, 2.388 MW.
4. $a = 0.145$, $a' = 0.0059$, and $C_L = 0.80$.

Index

Note: Page numbers followed by "*f*" and "*t*" refer to figures and tables, respectively.

A

B

C

D

N

O

P

Q

R

S

T

U

V

W

Z